



आंकड़े विवेचन पर प्रतिवेदन / DATA INTERPRETATION REPORT

भारत के स्पष्ट भूवैज्ञानिक संभावित क्षेत्र (ओजीपी) ब्लॉक-6 पर बहु-संवेदी
हवाई भूभौतिकीय सर्वेक्षण
(तेलंगाना, महाराष्ट्र, छत्तीसगढ़ तथा आंध्र प्रदेश के भागों में)
Multi-Sensor Aero-geophysical Surveys over Obvious Geological
Potential (OGP) Areas of India Block-6
(Parts of Telangana, Maharashtra, Chhattisgarh and Andhra Pradesh)



सुदूर संवेदन एवं हवाई सर्वेक्षण / Remote Sensing and Aerial Survey
Geological Survey of India, Bengaluru
बेंगलुरु / Bengaluru

दिसंबर 2024 / DECEMBER 2024





SANDER GEOPHYSICS LIMITED

**260 Hunt Club Road
Ottawa, ON Canada K1V 1C1
Tel: +1 613 521 9626
Fax: +1 613 521 0215
E-mail: info@sgl.com**

Agencies associated with OGP Block-6 Survey

Client	<p>GOVERNMENT OF INDIA Remote Sensing and Aerial Survey Geological Survey of India Vasudha Bhavan, Kumaraswamy Layout Bengaluru - 560111, India Primary contact: Deputy Director General & HOD Tel/Fax: 080 26662574/26662565 Email: rsasddgdp@gmail.com</p>
GSI-TSQC Team	<p>Aerogeophysical Data Processing and Interpretation Centre (APIC) Geophysics Division Remote Sensing and Aerial Survey Geological Survey of India, Bengaluru - 560111</p>
Project Implementing Agency	<p>Sander Geophysics Limited 260 Hunt Club Road Ottawa, ON Canada K1V 1C1 Pan India Consultants Pvt. Ltd. 105, Phase IV, Udyog Vihar, Gurugram- 122015, Haryana, India</p>

**Multi-sensor Aerogeophysical Surveys over
Obvious Geological Potential (OGP) Areas of India
Block-6**

(Parts of Telangana, Maharashtra, Chhattisgarh and Andhra Pradesh)

Submitted to: **Remote Sensing & Aerial Survey**

Geological Survey of India, Bengaluru

AUTHORS

Dr. Martin Bates

Dr. Andrew Palmer

GSi-TSQC TEAM

Ramesh K.

Ashish Kumar Bage

Ramesh Muddammagari

Mallipeddi Nagadivya

Vanga Mounika



Martin Bates, Ph.D., P. Geo
Sander Geophysics Limited, Canada

Table of Contents

1. EXECUTIVE SUMMARY	1
2. INTRODUCTION	2
2.1 Summary	2
2.2 Datum and Units	3
2.3 Survey Parameters	3
3. GEOLOGICAL SETTING	4
3.1 Introduction	4
3.2 Geologic overview of Block-6	6
3.2.1 Archaean Eastern Dharwar Craton	6
3.2.2 Archaean Bastar Craton	7
3.2.3 Eastern Ghats Mobile Belt	8
3.2.4 Pranhita-Godavari Basin Proterozoic Sediments	8
3.2.5 Gondwana Godavari Graben	9
3.2.6 Krishna-Godavari Basin	10
3.2.7 Deccan Traps	10
3.2.8 Geology Map of Block-6	11
3.3 Known Mineral occurrences and deposit types on Block-6	11
3.3.1 Gadchiroli Mining district (Surjagarh Iron Ore Mine)	11
3.3.2 Mailaram Mining District (Copper)	12
3.3.3 Thanewasna, Dubarpeth, and Ghot-Chamorsi Cu-Au Deposits	13
3.3.4 Godavari Valley and Wardha Valley Coal Fields	14
4. MAGNETIC DATA AND DERIVATIVES	16
4.1 Introduction	16
4.2 Anomalous Magnetic Field	16
4.3 Magnetic Anomaly Reduction to the Pole	16
4.4 Vertical Derivatives of Magnetic Anomaly	17
4.5 Total Horizontal Gradient of the Magnetic Anomaly	17
4.6 Amplitude of the Total Gradient of the Magnetic Anomaly (Analytic Signal)	18
4.7 Hanning Convolution Filter	18
4.8 Upward Continuation	19
4.9 Power Spectrum Analysis	19
5. MAGNETIC SOURCE PARAMETER ESTIMATIONS	22
5.1 Introduction	22
5.2 Euler Deconvolution	22
5.3 Trend Analysis	23
5.4 Tilt Derivative	24
5.5 Keating Coefficients	24
6. RADIOMETRIC DATA AND RATIOS	27
6.1 Introduction	27
6.2 Radiometric Data	28
7. REGOLITH MAP	29
8. LEGACY GRAVITY DATA	30
9. SENTINEL-2 SATELLITE DATA	31

10. MINERALIZATION AND GEOPHYSICAL DATA	32
10.1 GAMMA-RAY SIGNATURES OF MINERAL DEPOSITS	32
10.1.1 Uranium Mineralization.....	32
10.1.2 Potassium Alteration and Mineralization.....	32
10.1.3 Thorium Mineralization	33
10.2 Magnetic signatures of Mineral Deposits.....	33
11. LITHO-TECTONIC INTERPRETATION	35
11.1 Introduction	35
11.2 Lithology mapping	35
11.3 Faults, fractures, dykes, and lineaments.....	36
11.4 Areas of Significant Change in the Map.....	36
11.5 Buried Geologic Boundaries.....	37
11.6 Areas of high mineral potential and zones of alteration	37
12. GEOPHYSICAL CHARACTERIZATION OF DOMAINS	38
12.1 Overview of the geophysical signature	38
12.1.1 Magnetic Trends and Graben Related Structures.....	38
12.1.2 Potential Kimberlites from Magnetic Data	40
12.1.3 Baseline Gamma-Ray Statistics.....	41
12.2 Geophysical character and anomalies of the Archaean Eastern Dharwar Craton.....	43
12.3 Geophysical character and anomalies of the Archaean Bastar Craton	48
12.4 Geophysical character and anomalies of the Eastern Ghats Mobile Belt	56
12.5 Geophysical character and anomalies of the Proterozoic Basins	59
12.6 Geophysical character and anomalies of the Phanerozoic Godavari Graben	62
12.7 Geophysical character and anomalies of the Krishna-Godavari Basin	64
12.8 Geophysical character and anomalies of the Deccan Traps	65
12.9 Summary of Anomalies of Potential Economic Interest.....	66
12.9.1 High Priority Target Area A: Northern Bastar Craton Potential Kimberlites	69
12.9.2 High Priority Target Area B: Eastern Ghats Mobile Belt Potential kimberlites	69
12.9.3 High Priority Target Area C: Eastern Ghats Mobile Belt Potential kimberlites	70
12.9.4 High Priority Target Area D: Eastern Dharwar Craton/Godavari Supergroup Unconformity.....	70
12.9.5 High Priority Target Area E: Eastern Ghats Mobile Belt Magmatic Chamber	70
12.9.6 Medium Priority Target Area F: Eastern Dharwar Craton Leucogranite.....	71
12.9.7 Medium Priority Target Area G: Eastern Dharwar Craton Alkaline Potential Intrusive Dykes	71
12.9.8 Medium Priority Target Area H: Eastern Dharwar Craton Potential Alkaline Intrusions.....	71
12.9.9 Medium Priority Target Area I: Eastern Dharwar Craton Potential Alkaline Intrusion	72
12.9.10 Medium Priority Target Area J: Eastern Ghats Mobile Belt Potential Alkaline Intrusion	72
12.9.11 Medium Priority Target Area K: Bastar Craton Potential Magmatic Hosted Alteration	72
12.9.12 Medium Priority Target Area L: Bastar Craton Potential VMS.....	73
12.9.13 Medium Priority Target Area M: Godavari Supergroup Potential Potassium Alteration	73
12.9.14 Medium Priority Target Area N: Bastar Craton Ironstone.....	74
12.9.15 Low Priority Target Area O: Eastern Ghats Mobile Belt Alkaline Granites.....	74
12.9.16 Low Priority Target Area P: Eastern Dharwar Craton Ultramafic outlier	74
12.9.17 Low Priority Target Area Q: Bastar Craton Ironstone	75
12.9.18 Low Priority Target Area R: Bastar Craton supracrustal Rock.....	75
13. FOLLOW UP RECOMMENDATIONS.....	76
14. SUMMARY AND CONCLUSION	79
15. INTERPRETATION PRODUCTS.....	81

15.1 Digital Grids	81
15.2 Euler Solutions	82
15.3 Philips Trend Data	83
15.4 Tilt Depth Estimates	83
15.5 ArcPro Project.....	84
16. REFERENCES	85

Index of Tables

Table 1. Structural indices used in 3D Euler deconvolution	22
Table 2. Coordinates of magnetic anomalies identified as potential kimberlites by the Keating coefficient method.....	26
Table 3. Radio-element statistics of geological domains.....	42
Table 4. Radio-element ratio statistics of geological domains.	42
Table 5. Locations of mineral prospects in Block-6 (Datum WGS-84, UTM coordinates in Zone 44 North). The first column lists the anomaly number plus a letter relating to the target area, which are referenced in the text. Not all numbered anomalies are included in a target area.....	67
Table 6: Coordinates of Target Area A (WGS-84, UTM Zone 44N).	69
Table 7: Coordinates of Target Area B (WGS-84, UTM Zone 44N).	69
Table 8: Coordinates of Target Area C (WGS-84, UTM Zone 44N).	70
Table 9: Coordinates of Target Area D (WGS-84, UTM Zone 44N).	70
Table 10: Coordinates of Target Area E (WGS-84, UTM Zone 44N).	70
Table 11: Coordinates of Target Area F (WGS-84, UTM Zone 44N).	71
Table 12: Coordinates of Target Area G (WGS-84, UTM Zone 44N).	71
Table 13: Coordinates of Target Area H (WGS-84, UTM Zone 44N).	72
Table 14: Coordinates of Target Area I (WGS-84, UTM Zone 44N).	72
Table 15: Coordinates of Target Area J (WGS-84, UTM Zone 44N).	72
Table 16: Coordinates of Target Area K (WGS-84, UTM Zone 44N).	72
Table 17: Coordinates of Target Area L (WGS-84, UTM Zone 44N).	73
Table 18: Coordinates of Target Area M (WGS-84, UTM Zone 44N).	73
Table 19: Coordinates of Target Area N (WGS-84, UTM Zone 44N).	74
Table 20: Coordinates of Target Area O (WGS-84, UTM Zone 44N).	74
Table 21: Coordinates of Target Area P (WGS-84, UTM Zone 44N).	75
Table 22: Coordinates of Target Area Q (WGS-84, UTM Zone 44N).	75
Table 23: Coordinates of Target Area R (WGS-84, UTM Zone 44N).	75
Table 24: Summary of target areas. Target areas A-E are high priority; Target areas F-N are medium priority; Target areas O-R are low priority.	80
Table 25: Digital Grids	81
Table 26: Euler Solution Data Format.....	82
Table 27: Format of Philips trend data.	83
Table 28: Format of tilt depth estimates data.	84

APPENDICES	APPENDIX NAME
APPENDIX I	Additional Litho-Codes
APPENDIX II	Report Figures

1. EXECUTIVE SUMMARY

Geological Survey of India (GSI), Remote Sensing and Aerial Survey (RSAS) is mainly engaged in conducting Aerogeophysical Surveys with magnetic gradiometry and spectrometric sensors with uniform survey parameters to aid in mineral exploration under the National Aerogeophysical Mapping Program (NAGMP) funded by National Mineral Exploration Trust (NMET). The purpose of these surveys is to collect High-Resolution Magnetic and Spectrometric data to cover the entire country. The NAGMP project is carried out by RSAS, GSI in different phases to cover all of India. Phase-I consists of 12 survey Blocks (Blocks 1 to 12) that cover the Obvious Geological Potential (OGP) areas. Phase-II with 10 survey Blocks (Blocks 13 to 22) will cover areas adjoining to the OGP areas.

Under Phase-I of the NAGMP program, OGP Block-6 covering parts of Telangana, Maharashtra, Chhattisgarh and Andhra Pradesh states, with an initially estimated 278,846 line km covering an area of 76,049 km² was awarded to project implementing agency (PIA) M/s. Sander Geophysics Limited, Canada in consortium with M/s. Pan India Consultant Pvt. Ltd., India. The final total flown was 281,963 line km, covering an area of 76,899 km².

The traverse lines of Block-6 are oriented at N45°E and spaced at 300 m, while the control lines are oriented perpendicular to traverse lines and spaced at 3,000 m. A drape surface is created to guide the survey aircraft in the vertical direction, considering the terrain and the performance of the aircraft at the expected altitudes and estimated temperatures. The survey is flown with a target clearance of survey 80 m above ground level. The target average ground speed is 75 m/s.

The primary purpose of this interpretation report is to identify geological structural elements, to map the subsurface geology in areas with sediment cover and to identify areas of high mineral potential. An interpretation of a number of interesting geophysical anomalies has been performed, with eighteen areas of economic potential recommended for suggested follow up work.

2. INTRODUCTION

2.1 Summary

This report describes data interpretation of the airborne survey data of Block-6 of the National Airborne Geophysical Mapping Program (NAGMP) of the Geological Survey of India (GSI) that Sander Geophysics Limited (SGL) flew in 2022 to 2024. Magnetic gradient and gamma-ray were gathered during this survey. The general location of Block-6 in India is shown in Figure 2.1, and the area covered by the survey is shown in Figure 2.2. All figures for this report are provided in Appendix II.

Block-6 is part of the ongoing NAGMP nationwide program of airborne geophysical surveys focusing on “Areas of obvious potential and adjoining areas”. The intent is to compliment other geological methods of hard rock mineral exploration and has been identified by the GSI as the best method to explore for concealed natural mineral resources on a large scale.

Upon completion of data acquisition, the data were processed using SGL's proprietary geophysical software suite. Principal deliverables include magnetic anomaly data sets, radiometric data sets, and final positional and topographic data sets.

Interpretation employed both SGL proprietary geophysical software, and the following commercially or freely available software:

- Geosoft Oasis montaj® suite of modelling and analysis tools
- QGIS geographic information system software
- ArcPro geographic information system software

The interpretation of the radiometric and magnetic data was performed with the following goals:

- Outline the general geological setting of the block
- Identify structural elements such as faults, dykes and lineaments
- Estimate depth to source of magnetic anomalies
- Identify areas of high mineral potential
- Map the subsurface geology in areas with sediment cover

To accomplish this the following were performed:

- Available geoscientific information and data collated and reviewed
- Derivatives and filters of the airborne geophysical data created and analysed
- Anomaly source depths calculated
- Automatic trend analysis carried out
- Automatic detection of cylindrical magnetic anomalies carried out
- A litho-tectonic map incorporating manual fault, fracture, dyke and lineament mapping created
- Description of litho-tectonic domains performed
- Identification of anomalies of interest

This interpretation report is broken down into sixteen sections.

- Section 1 is the executive summary
- Section 2 introduces the project description, units and survey parameters
- Section 3 contains an overview of the geological setting of the survey block
- Section 4 describes the interpretation techniques applied to the magnetic data set
- Section 5 describes magnetic data source detection methods
- Section 6 describes the interpretation techniques applied to the spectrometric data set
- Section 7 describes the generation of a regolith map
- Section 8 describes the legacy gravity data set
- Section 9 describes the Sentinel-2 satellite data set
- Section 10 Gives an overview of the relationship between mineral deposits and the geophysical techniques used on the survey
- Section 11 presents the litho-tectonic interpretation map creation
- Section 12 describes each main geological domain in terms of its geophysical character and anomalies of interest
- Section 13 describes some recommendations for follow up work
- Section 14 summarizes the findings from the previous sections into a concise overall conclusion
- Section 15 describes the products delivered in support of the interpretation
- Section 16 lists the references

2.2 Datum and Units

Within the report the following conventions are employed:

- Maps and coordinates in this report use the Universal Transverse Mercator (UTM) projection in Zone 44 North and/or latitude and longitude, both with respect to the WGS-84 datum in metres.
- Coordinates are stated in meters (m), as X/Y and as Latitude/Longitude in degrees, minutes and seconds.
- Heights and depths are stated in metres (m) on maps and grids with respect to Mean Sea Level (MSL) and stated in metres in the text.
- Magnetic values are stated in nano-Teslas (nT).
- Radiometric values are in counts per second for total count rate (cps), parts per million for equivalent uranium (ppm eU) and thorium (ppm eTh) or in percent concentration for potassium (%K).
- Gravity values are stated in milli-Gals (mGal).

2.3 Survey Parameters

For comprehensive details on the project logistics, data acquisition and data processing for Block-6, please refer to the project Acquisition Report and Data Processing Report. Some salient parameters of the survey design and processing employed are:

- Traverse lines were spaced at 300 m and were oriented at N45°E
- Control lines were spaced at 3000 m and were oriented at N135°E
- Survey target altitude was 80 m above ground level (2D smooth drape)
- Target ground speed was 75 m/s.

3. GEOLOGICAL SETTING

3.1 Introduction

India's geology is complex and varied, shaped by a long and dynamic geological history. The country's geological history spans from the Precambrian to the present and reflects a diverse range of geological processes and events. The structural provinces which are governed by the country's complex tectonic history are described below. The structural provinces include cratons, Proterozoic sedimentary basins, mobile belts, Phanerozoic sedimentary basins, orogenic belts and volcanic provinces (Figure 3.1). A more detailed description of the parts of these provinces that fall within Block-6 follows.

A highly simplified timeline of the major events that impacted the geologic evolution within Block-6 based on the work of Vaidyanadhan and Ramakrishnan (2010) is provided here:

- Archaean: Formation and assembly of cratons, including the Eastern Dharwar and Bastar Cratons.
- Palaeo-Proterozoic: Emplacement of the Dharwar Giant Dyke Swarm at around 2367 Ma (Kumar et al., 2012).
- Palaeo-Proterozoic: Emplacement of late granites, including the Dongargarh Granite at around 2270 Ma to 2465 Ma (Sensarma and Mukhopadhyay, 2014).
- Palaeo-Proterozoic: Formation of the "early" Purana sedimentary basins.
- Meso-Proterozoic: Formation of the Eastern Ghats Mobile Belt during the assembly of the Rodinia Supercontinent at around 1000Ma ("Grenvillian") (Burhanuddin 2017).
- Meso-Proterozoic: Formation of the "late" Purana Sedimentary Basins, including the Pranhita-Godavari Basin and deposition of the Godavari Supergroup sediments in Block-6 spanning from 1330 to 790 Ma (Chaudhuri, 2003).
- Late Meso-Proterozoic: Formation of Gondwana Supercontinent.
- Late Carboniferous/Early Permian to Cretaceous: Development of the Gondwana Basins, including the Godavari Graben and deposition of the Gondwana Supergroup sediments in Block-6 (Sengupta 2003), as well as the Krishna-Godavari Coastal Basin that impinges on the southeast corner of Block-6, in response to the break-up of the Gondwana Supercontinent.
- Upper Cretaceous/Palaeocene: Eruption of the Deccan Traps volcanics in the late Cretaceous.

Cratons are the oldest and most stable parts of the subcontinent of India. They form the basement complexes upon which much of the younger rocks are built on or extruded into. Four tectonically distinct major cratons are described below (Vaidyanadhan and Ramakrishnan, 2010).

The Dharwar Craton, located in southern India is one of the most significant cratons in India. It is divided into the Eastern Dharwar Craton (EDC) and Western Dharwar Craton (WDC) by the north-northwest trending Chitradurga shear zone. It is largely made of Archaean age rocks including granite-greenstone belts and high-grade metamorphic rocks. The two halves of the Dharwar Craton are different in age, lithology and relationships to supra-crustal rocks. The greenbelts of the WDC are rich in gold and base metal deposits and the EDC is dominated by granites and gneisses. A large number of alkali-carbonatite and ultramafic intrusions occur within the Dharwar craton within the Dharmapuri rift in the vicinity of Salem in Tamil Nadu State to the south (Vaidyanadhan and Ramakrishnan 2010). Two minor instances of carbonatite have been identified near but outside the southerly end of Block-6 called Elchuru and Kunavaram (Krishnamurthy 2019), occurring as late-stage veins in peralkaline

syenite complexes, but none have been identified within Block-6 to date.

The Singhbhum Craton, in central west India, is characterized by a complex grouping of Archaean and Proterozoic age granites, greenstones, and iron formations, and is known for uranium and iron deposits.

The Bundelkhand Craton, in central India, consists predominantly of Archaean age granites with smaller occurrences of greenstone belts. The craton is known as a major source of building stones.

The Bastar Craton, located in Central India, is mostly comprised of a range of Archaean to Proterozoic age rocks characterized by granites, gneisses and metasedimentary supracrustal rocks (Mondal et al., 2006). The craton is known for its diamond bearing kimberlite pipes (Mainkar et al., 2008).

Two of these cratons occur within the area of Block-6, the Eastern Dharwar Craton and the Bastar Craton.

Mobile belts are Proterozoic age areas of extensive tectonic activity typically between stable cratons. The Eastern Ghats Mobile Belt of eastern India, Pandyan Mobile Belt of southern India, and the Satpura Mobile Belt (or Central Indian Tectonic Zone) of central India are the most significant occurrences. Of these, the Eastern Ghats Mobile Belt occurs in the southwest part of Block-6.

Palaeo and Mesoproterozoic age sedimentary basins, sometimes referred to as the Purana Basins, are regions where thick sequences of sedimentary rocks have accumulated over geological time, often in response to tectonic subsidence. They are generally unmetamorphosed or deformed and vary between 100 m to 10 km in thickness (Vaidyanadhan and Ramakrishnan, 2010) and occur across India (Figure 3.2).

The Vindhyan Basin, located in northern India, contains one of the largest sedimentary sequences in the world, composed mainly of sandstones, shales, and limestones from the Proterozoic era. This basin is important for understanding the early history of the Indian subcontinent and hosts significant resources, such as limestone and building stone.

The relatively small and less well known Palaeoproterozoic age Abujhmar Basin lies within the Bastar craton just outside Block-6 to the east. It consists of a central area of sediments, mostly sandstone, unconformably overlain by a conglomerate that includes clasts of banded iron formation and overlain by tholeiitic basalts and gabbros (Mishra et al., 1987).

The Pranhita-Godavari basin is located in the middle of Block-6, containing both Mesoproterozoic Godavari Supergroup (Chaudhuri 2003) and later Phanerozoic age Gondwana Supergroup sediments that fill the Godavari valley (Rao et al. 2018). The Pranhita-Godavari basin lies along the boundary of the EDC and the Bastar Craton. The Mesoproterozoic sediments are divided into two sub-parallel basins, separated by the later Gondwana sediments in the Godavari Graben. In some of the literature these basins are referred to as the Pakhal Basin or the Mallampalli Basin to the west lying unconformably on the EDC and the Albaka Basin in faulted contact with the Bastar craton to the east (Vaidyanadhan and Ramakrishnan, 2010). However, the separation of the stratigraphic

formations in these two basins are not universally agreed, so to avoid confusion over this issue we will refer to these two sub-parallel basins of Proterozoic sediments as the Eastern and Western Belts of the Godavari Supergroup.

The Cuddapah Basin, lying upon the EDC, is in southeastern India just south of Block-6. The Cuddapah Basin is filled with Proterozoic sedimentary rocks, including sandstones, shales, and limestones. The basin is known for its stromatolitic limestones and potential for hosting uranium deposits. The northern extremity of the Cuddapah Basin lies close to the southern extremity of the Pranhita-Godavari basin and is overthrust by the Eastern Ghats Mobile belt along a major fault on its east side and is folded parallel to this structure.

Kimberlite intrusions occur both within the Purana basins, and within the proximal Archaean cratons (Fareeduddin and Rao, 2007). Many occur within the Cuddapah Basin (Paul et al., 2006) in the Bastar Craton (Mainkar et al., 2008). To date none have been identified within Block-6.

The Gondwana Basins are distributed across Peninsular India and are associated with the late Palaeozoic to early Mesozoic eras. The Gondwana sediments are characterized by coal-bearing sequences, as seen in the Damodar Valley, Son-Mahanadi, and Godavari rift basins. These basins were formed during the breakup of the Gondwana supercontinent and contain extensive fluvial and lacustrine deposits. The main basin discussed in this report is a Godavari Graben.

The Deccan Traps are a major continental flood basalt located in west-central India, representing one of the largest volcanic provinces in the world. Large volumes of basalt were extruded in the late Cretaceous period covering an estimated 500,000 square kilometres associated with the breakup of Gondwana supercontinent, resulting in significant anorogenic mountains (Vaidyanadhan and Ramakrishnan, 2010). The Deccan Traps occur within the northwest part of Block-6.

The main orogenic belt of India is the Himalayan Orogenic Belt formed by the collision between the Indian Plate and Eurasian Plates. This is an ongoing orogeny beginning about 50 million years ago. The other major orogenic belt in India is the much older, Proterozoic age Aravalli-Delhi Orogenic Belt in the northwest of India that resulted from the collision of the Bundelkhand craton and the Marwar craton (Mishra et al., 2013). Neither orogenic belt has a direct influence on the geology within Block-6.

3.2 Geologic overview of Block-6

3.2.1 Archaean Eastern Dharwar Craton

The eastern margin of the Eastern Dharwar Craton (EDC) occurs within Block-6 where it is bounded by the sediments of the Pranhita-Godavari Basin. Parts of the northwest edge of the EDC is comprised of the Karimnagar Granulite Belt. The gneissic rocks of the EDC are unconformably overlain by or in fault contact with the Proterozoic sediments of the Godavari Supergroup.

A number of greenstone belts occur within the EDC. In general, the greenstones are dominated by volcanics over sediments, and are surrounded by younger granites, so that boundaries are intrusive contacts (Vaidyanadhan and Ramakrishnan, 2010). None of the greenstone belts occur within Block-6, but a belt of older supracrustal rocks known as the Warangal Group lies within the EDC adjacent to the Karimnagar Granulite. Included within the Warangal Group are pillow basalts and iron stone formations.

Palaeoproterozoic age basaltic dykes occur across much of the Dharwar Craton. In the northwest extremity of the EDC, proximal to the Pranhita-Godavari Basin, the dykes strike between 51° and 60° from north. These dykes were formerly known as the Karimnagar dyke swarm but more recently are described as part of the Dharwar giant dyke swarm (Kumar et al., 2012). These dykes preserve significant magnetic remanence which can be expected to influence the associated magnetic anomalies.

3.2.2 Archaean Bastar Craton

The Bastar Craton is predominantly a gneissic complex, enclosing rafts of Amgaon Group supracrustal sediments including banded iron stones and ultramafic rocks (Vaidyanadhan and Ramakrishnan, 2010).

The western margin of the Bastar Craton occurs within Block-6 where it is bounded by the Proterozoic and Phanerozoic sediments of the Pranhita-Godavari Basin. The southeast edge of the Bastar Craton includes the 30 to 40 km wide Bhopalpatnam Granulite Belt, in fault contact with the Proterozoic sediments of the Godavari Supergroup and the younger Gondwana sediments.

East of the Bhopalpatnam Granulite belt is the approximately north trending Kotri-Dongargarh Orogen, consisting of three Palaeoproterozoic age supracrustal sediment and volcanic cycles becoming younger from south to north: the Bailadila Group, the Nandgoan Group and the Khairagarh Group respectively (Vaidyanadhan and Ramakrishnan, 2010). Of these, the Bailadila is conspicuously present within Block-6 forming a south verging arcuate ridge that wraps around the south edge of the Dongargarh Granite. The southwest tip of a separate northeast trending ridge occurs within Block-6 just a little further south. The Bailadila Group includes significant haematite rich banded ironstone formations (BIF) that are extensively mined, as well as associated extrusive meta-volcanics and meta-sediments.

The Bastar Craton is conspicuously intruded by younger granites (Vaidyanadhan and Ramakrishnan 2010). In particular, the Dongargarh granite-granodiorite intrusion (Ramachandra and Roy 1998) occurs within the northeast corner of Block-6. Further north outside of Block-6 is the Malanjkhanda Granite that hosts the important hydrothermal Malanjkhanda copper deposit.

Amphibolite and dolerite dykes trending north-northwest, parallel to the regional structural trends, are common within the Bastar Craton (Srivastava et al., 1996). These dykes are younger than the host granitic gneisses, but younger than the later intrusive granites such as the Dongargarh granite.

In addition, a suite of east-northeast dykes has been observed near Chhura, just to the east of Block-6, that have Palaeoproterozoic ages similar to the basaltic dykes of the Dharwar giant dyke swarm and are probably part of the same swarm (Srivastava et al. 2021).

3.2.3 Eastern Ghats Mobile Belt

The Eastern Ghats Mobile Belt (EGMB) follows the east coast of India for much of its length along the Bay of Bengal and impinges on the southeastern extremity of Block-6. The EGMB is characterized by ultra-high grade granulitic metamorphic rocks that have undergone multiple phases of deformation and metamorphism, (Misra et. al., 2015). The northwest boundary of the EGMB where it is in contact with the EDC and Bastar cratons is marked by a wide transition zone. The northeast trending structural trends of the EGMB are strongly discordant with the southwest structural trends of the EDC at the boundary. The boundary between the EGMB and the EDC to the northwest is marked by the 30 to 130 km wide greenstone Nellore-Khammam schist belt (NKSb) (Okudaira et al., 2000), bounded on both sides by shallow southeast dipping faults with the high-grade granulite of the Eastern Ghats to the east (Figure 3.3). The NKSb was probably accreted to the EGMB during the late Mesoproterozoic to early Neoproterozoic. The NKSb is split into upper and lower units, with lower and higher grades of metamorphism. In Block-6 it is the lower unit, comprising of high-grade metabasaltic rocks that are in contact with the Archaean cratonic rocks.

The transition zone boundary between the EGMB and the Bastar Craton is marked by the Jeypur Province. West-northwest structural trends in the granulite and schists of the Bastar Craton are deflected to the northeast trend of the EGMB, with a gradual transition to the high-grade metamorphism associated with the western part of the EGMB (Vaidyanadhan and Ramakrishnan, 2010).

3.2.4 Pranhita-Godavari Basin Proterozoic Sediments

The Pranhita-Godavari Basin includes both Mesoproterozoic age and Phanerozoic age sediments. The Proterozoic age sediments occur in two, non-continuous sub-parallel Sub-Basins, both trending to the north-northwest, separated by the later Palaeozoic age Gondwana sediments of the Godavari Graben that are discussed below (Vaidyanadhan and Ramakrishnan, 2010). Overall, the basin has a half graben geometry deepening to the east: the basin on the east side has clear faulted contact with the Bastar Craton, in contrast to the basin on the west side which lies either non-conformably upon the high-grade metamorphic rocks of the EDC (Burhanuddin 2017) or is in contact along low throw faults (Dasgupta 2007). Both Sub-Basins include several outliers on the nearby surrounding Archaean rocks, and inliers within the Gondwana sediments, illustrated in Figure 3.4.

The Proterozoic sediments of the Pranhita-Godavari Basin, including both Sub-Basins, are termed the Godavari Supergroup (Chaudhuri 2003). In both Sub-Basins the stratigraphy has been sub-divided into four main groups (Vaidyanadhan and Ramakrishnan, 2010), shown in Figure 3.4 and Figure 3.5, although the equivalency of the groups in each Sub-Basin is open to interpretation. For simplicity in this report, we refer to the basins on either side of the Godavari Graben as the East Belt and the West Belt after Ramakrishnan and Vaidyanadhan (2010). Dasgupta (2007) suggests that the Godavari Supergroup sediments lie beneath and form the “basement” to the later Phanerozoic age Gondwana Sediments.

The Godavari Supergroup sediments generally dip toward the northeast, and in the West Belt they are faulted and folded prior to the deposition of the youngest of the four groups: The Sullavai Group, which lies unconformably over the older sediments. Southwest verging folds and stratigraphic repetition related to thrusting, is observed in the northern part of the West Belt, as well as fold structures in the fault bounded Kaddam outlier of the West Belt. Tight folds and thrust related imbrication occur in the southern parts of the West Belt, and structural trends are deflected from northwest to northeast due to the influence of the Eastern Ghats Mobile Belt at the southern end of the Belt. Likewise, in the East Belt, the older sediments are folded and imbricated by thrusting with northwest trending axes, although in this instance the oldest Usur Group sediments of the East Belt are co-folded with the underlying sediments, underlining the difference in the equivalent sub-groups of the two Sub-Basins. Metamorphic grade generally increases toward the Eastern Ghats Mobile belt to the southeast.

Based on stratigraphic studies, Chaudhuri (2002) concluded that the Pranhita-Godavari Basin subsided at a greater rate toward the southwest end during the Proterozoic, resulting in thicker and wider sediment deposition (Figure 3.6). A more detailed map of the units within the Eastern and Western Belts is provided in Figure 3.7.

3.2.5 Gondwana Godavari Graben

The Godavari Graben is a Phanerozoic age north-northwest trending rift that lies between the EDC and the Bastar Craton, dividing the Proterozoic age sedimentary rocks within the Pranhita-Godavari Basin. Clearly both the Proterozoic and Phanerozoic sedimentation occurred due to extension across the boundary of the cratons, but periods of both extension and compression have occurred across the cratonic boundary over time (Vaidyanadhan and Ramakrishnan, 2010).

Up to 5000 m of syn-rift sediments accumulated in two periods of rifting in the Phanerozoic, one from the Early Permian to Early Jurassic related to the breakup of the Gondwana supercontinent, followed by another in the Early Cretaceous related to the breakup of India from Antarctica (Biswas 2003). The graben is bounded by two north northwest trending master faults, which are disrupted and show both normal and reverse faulting in different locations. The main boundary faults are crosscut by northwest trending intra-rift faults that propagate into the surrounding cratons and follow the main structural trends of the EDC, suggesting they are controlled by earlier structures. The intra-basin faults break up the main rift into Sub-Basins and ridges, with different degrees of extension accommodated by strike-slip faulting. The main Sub-Basins are, from south to north, the Chintalapudi, Kothagudem, Godavari, and Chandrapur Sub-Basins (Dasgupta and Jain, 2007).

At its northwestern end the Godavari Graben is partially covered by the Deccan Trap volcanics. At its southeastern end, the Godavari Graben is almost truncated by the Eastern Ghats Ridge, but the Chintalapudi Sub-Basin apparently continues beneath the Krishna-Godavari Basin to the southeast (Biswas 2003) (see section 3.2.6).

A general cross section of the Pranhita-Godavari Basin including the Godavari Graben is constructed from modelling of magnetic and gravity data by Sarma & Krishna Rao (2005) (Figure 3.8). Their model shows that while the combination of Proterozoic and Gondwana sediments occupies an asymmetric basin which is steeper on the northeast side, the Gondwana age rift alone is more or less symmetric, and it appears that the main formation of

the graben post-dates the Proterozoic sediments. Dasgupta (2007) presents a different model from both gravity and seismic data, in which the Proterozoic sediments continue beneath the Phanerozoic sediments within a half Graben structure. A review of the Gondwana age sedimentary fill of the Godavari Graben is given by Sengupta (2003), and their outcrop is illustrated in Figure 3.9.

3.2.6 Krishna-Godavari Basin

The southeast extremity of Block-6 impinges upon the northeast trending Krishna-Godavari coastal basin that cuts across the south-southeast trending Pranhita-Godavari Basin (Vaidyanadhan and Ramakrishnan, 2010). Sedimentary fill of the Krishna-Godavari basin commenced in the Cretaceous as Antarctica rifted away from India, crosscutting the Pranhita-Godavari Basin that probably continued into Antarctica (Biswas 2003). Sedimentation within the Krishna-Godavari Basin continued into the Holocene. Similar to the Godavari Graben, the Krishna-Godavari Basin includes fault bound Sub-Basins and ridges with consequent varying thicknesses of sediment. Whilst the Krishna-Godavari Basin represents successful rifting between India and Antarctica, the Godavari Graben, whilst it underwent significant extension, is a failed rift. But nonetheless, activity along the Pranhita-Godavari Rift and similarly trending structures is believed to have triggered the eruption of the lavas that formed the Deccan Traps (Vaidyanadhan and Ramakrishnan, 2010).

3.2.7 Deccan Traps

Parts of the northwest of Block-6 are covered by thick layers of volcanics known as the Deccan Traps, a huge outpouring of mostly tholeiitic basaltic lavas that accumulated during the breakup of Gondwana right around the time of the Cretaceous – Tertiary boundary (Vaidyanadhan and Ramakrishnan, 2010), although rare alkalic mafic lavas and carbonatites also occur (Huff and Owen 2015). The layers are virtually flat lying, and individual layers range from 10 to 15 cm in thickness (Halder 2017). The Deccan Traps are believed to have been generated by a mantle-plume, and the lavas contain a large amount of crustal contamination which if high enough can result in high sulphur content and the formation of volcanic sulphides (Halder 2017).

Whilst copper and epithermal gold and silver deposits are known to occur within flood basalts, so far none have been identified in the Deccan Traps (Vaidyanadhan and Ramakrishnan, 2010). However, bauxite that arises from surface erosion under tropical conditions does occur as caps on tops of hills and can be a source of economic grade aluminium ore.

In some locations, “inter-trappen” formations of fossiliferous sediments occur within the layers of basaltic flows (Vaidyanadhan and Ramakrishnan, 2010). This includes Maastrichtian age ostracod bearing sediments at Asifabad in the northwest part of Block-6.

3.2.8 Geology Map of Block-6

Figure 3.10 shows a simplified geology map of Block-6, including the elements discussed above. This map was constructed by the Geological Survey of India and made available to Sander Geophysics prior to the findings of this report but is generally in accordance and provides a useful reference for the rest of this document.

3.3 Known Mineral occurrences and deposit types on Block-6

3.3.1 Gadchiroli Mining district (Surjagarh Iron Ore Mine)

The Surjagarh Iron Ore Mine is located in the Wooria Hills within the Surjagarh hill range in the Gadchiroli district, Maharashtra at coordinates 19°37′01.2″N / 80°21′00″E. It is owned by Lloyds Metals and Energy Limited, and has been operated since 2021 by Thriveni Earthmovers Pvt. Ltd. The original publicly available proven resources of the mine were estimated in the 1970s to be 73.6 MMT. Currently a new study is being conducted by Tata Steel Industrial Consulting which is estimating that the resource is likely much larger than previously indicated.

There is very little publicly available data on the geology of the Surjagarh Iron Ore mine deposit. Preliminary geological mapping of the region (Topo Sheet 65A/06) was subsequently carried out by the Saxena, Das, Zaheer and Sengupta of the GSI during the field season of 1978-79, and by Jain and Pattanaik also during the field season of 1978-79. Legacy publicly available GSI geophysical datasets do not cover the region of this deposit.

Gemco Kati, under contract from Lloyds Metals and Energy Limited, the parent company of the mine, is currently (2022-present) conducting exploration over a nearby region ~15 km to the northwest of similar geologic units and structures. A southerly portion of the region of new exploration is located in Block-6. According to the GSI's geologic mapping, this new region of exploration is in the same units/group as the Surjagarh Iron Ore mine. Due to the similarities in the lithology, unit, deposit type, and proximity of the new exploration to the existing mine, and due to the lack of publicly available data on the existing mine, it may be possible to use this new exploration as an example of what may be seen over the existing deposit. This exploration program is using similarities in stratigraphy between the Surjagarh mine and the prospective location, pre-existing low-resolution airborne magnetic data, and Sentinel 2B multispectral imagery analysis to determine prospective banded ironstone formation (BIF) mineralized zones.

The Surjagarh Iron Ore Mine and the prospective localities belong to the BIFs of the Palaeoproterozoic Bailadila Group, which are known to contain large iron ore resources. However, while the Surjagarh, Damkodwadvi, and Bhamragarh Hill Ranges all are comprised of the Bailadila Group, only Wurera Hill in the Surjagarh hill range is developed (the existing deposit in question in Block-6). The Bailadila group is a greenschist belt comprised of schists, ferruginous phyllite, banded hematite quartzite (which contains the iron ore deposits), and quartzite. The highest-grade ore bodies are related to supergene enrichment and leaching of iron oxides from the banded haematite quartzite (BHQ). There is also some indication of haematite leaching from the ferruginous phyllite associated with the BHQ. Thus, the highest grades are generally altered regions of the BHQ located along structural traps (fold closures).

Ground geophysical surveys were conducted in the region of the current mine in 1982-83 by Sengupta and Das (the data is no longer publicly available). These surveys were conducted in Topo Sheets 65A/06 (where the current mine is located) and 65A/10 (where the new exploration is located) using electromagnetic (EM), spontaneous potential (SP), induced polarization (IP), and magnetic methods. An EM survey in the Khothi area delineated shear zones in an echelon pattern with out of phase anomalies. The same shear zones are encompassed by a broad SP low bounded by 140 mv contours. Some of these negative regions extend over a 1 km strike length. The IP surveys of the same area outlined zones with high chargeability. Sulphide mineralization was deemed to occur where the high resistivity zones discovered with the SP methods fell within the EM anomaly zones. The SP anomaly zones which followed the strike of the shear zones were determined to be due to the presence of graphite along the shear zones.

Element composite analysis maps from Sentinel 2B multispectral imaging can map out the BIFs in the new exploration zone where they are exposed at the surface, and the same is likely true for any BIFs in the 65A/06 region, though there is currently no direct analysis of the 65A/06 region.

A magnetic analytical signal map of the 65A/10 region indicates positive anomalies over areas deemed to be of possible exploration potential. These magnetic highs do not seem directly correlate with the entire length of the BIF, and so are believed to be correlated with mineralized locations. However, the data in question is low resolution, and is not available for the 65A/06 region of interest for this survey block.

In Topo Sheet 65A/06 (where the current mine is located), small but prominent SP, EM, and IP anomalies were observed over the mineralized quartzite (SP 130mv, IP 30ms). However, these anomalies do not extend along strike.

3.3.2 Mailaram Mining District (Copper)

The Mailaram Copper District is in the Kinnerasani region of Telangana (Topo Sheet 65C/10). This district is comprised of three known copper occurrences which are available in the public record. The coordinates of these occurrences are 17°42'53.2"N / 80°40'27.2"E, 17°39'36.6"N / 80°39'12.3"E, and 17°42'30.3"N / 80°35'41.6"E. Previous copper workings were reported at the first occurrence by Mahadevan in 1943, and subsequent prospecting program which included geochemical analyses, geological mapping, and geophysical surveys, was initiated by the Andhra University and the GSI in 1957. Further development of this mine was conducted by the Andhra Pradesh Mining Corp. Ltd. and by the Mineral Exploration Corp. Ltd. Public records of mines and exploration in this region are sparse, and there are no public records of mines in this region after subsurface geophysical surveys were conducted in 1981.

Copper deposits in this district are classified as quartz reefs, which are of hydrothermal origin and occur due to granite plutonism attributed to the Peninsular Gneissic Complex II (PGCII) (note, Vaidyanadhan and Ramakrishnan, 2010 prefer that the term Peninsular Gneiss be restricted to the WDC, but here is employed in the EDC). The known occurrences occur where the PGC II intrudes the Bijapur Gneissic Complex or where they intrude

the Bollapalli shales of the Mallampalli group. This indicates the mineralization is connected to the intrusive PGCI suite itself, not the host rocks. Mineralization occurs as chalcopryite, malachite, and other copper oxides in blue-grey quartz veins which intrude quartz-chlorite schists in the Khammam Group. Mineralization is largely contained to two major parallel ore shoots (the main/central ore shoots and the northern ore lens). At one occurrence, reserves were estimated at 0.812 MT with a grade of 1.07%.

The geophysical survey conducted in 1957 included SP, IP, and magnetic methods. The SP survey concluded that negative potential anomalies (up to 200 mV) coincided with known historical workings, and it was determined that the negative SP anomalies could be used to indicate ore zones. The results of the IP survey are not publicly available. The magnetic survey determined that the area had no positive or negative anomalies, indicating no magnetic correlation to this deposit.

In 1981, a Turam-type EM survey was conducted over the third listed deposit which was undergoing exploratory mining. Prior Slingram-type EM surveys had been conducted over the deposit by the GSI, however they were not able to penetrate deep enough through the overburden to illicit a geophysical response. This Turam-type EM survey was able to delineate the known ore zones, and to determine other potential ore zones, with EM anomalies.

In 1982, a subsurface gravity-based density mapping program was conducted in the Mailaram Copper Mines. It was found that a decrease in density coincided with poor or barren subsurface zones, likely indicating sericite or quartz schists, or regions of lower-grade chalcopryite in the quartz-chlorite schists. It was also found that zones of increased density corresponded to known high-grade ore zones, and thus increased density was used as an indication of the presence of high-grade ore.

The Mailaram Copper Belt is also covered by legacy GSI magnetic and gravity data. While the third listed occurrence occurs on the edge of a positive magnetic anomaly, the other occurrences are not correlated with any anomalous magnetic signature. This is consistent with the findings of the GSI's magnetic survey completed in 1957. The legacy gravity surveys (other than the one conducted in 1957 directly over an occurrence) are too low resolution to be able to draw any conclusions from in regard to these specific deposits.

3.3.3 Thanewasna, Dubarpeth, and Ghot-Chamorsi Cu-Au Deposits

The Thanewasna and neighbouring Dubarpeth copper deposits are located 60 km to the southeast of Chandrapur in Maharashtra within GSI Toposheet 56M/09. The surface level ore of the Thanewasna deposit was historically mined prior to the middle of the 18th century. Initial geological mapping of the region was carried out in 1877 by Hughes and then by Hallows in 1923. More in depth mapping was conducted by B.N. Sinha of the GSI during the 1955-1956 field season. Exploratory drilling of the Thanewasna site was conducted by the Government of Maharashtra from 1961 to 1963. Further mapping of the region was conducted by Kulkarni of the GSI over the 1963-1964 field season.

A subsequent report on the deposit, which covered the geochemical work done between 1971-1979, was published by the GSI in 1979. This report highlighted the potential for similar mineralization along the parallel shear zones at Dubarpeth and Ghot-Chamorsi. The Thanewasna and Dubarpeth deposits were studied during the 2014-2015 field season by the GSI, and continued to be studied by the general public until the deposits were auctioned to Vedanta Ltd. in 2019. The Thanewasna deposit has a grade of 0.5%-1% copper, with an estimated 8.02 MT of reserves. The Dubarpeth deposit has a grade of 0.5-1% copper, with an estimated 1.343 MT of reserves. Some surveys have found gold grades of up to 0.34 ppm at the Thanewasna deposit.

Both deposits are classified as quartz reef epithermal vein type deposits. The mineralization occurs in quartz-chlorite veins restricted to brittle-ductile shear zones within granitoids (granites and tonalite-quartz diorites) as chalcopyrite, arsenopyrite, and pyrite. The granitoids were emplaced along the northern section of the Pranhita-Godavari Basin. This emplacement was likely the major ore-forming event, causing intense chloritisation along the Thanewasna shear zone. The formation of chlorite has been genetically connected to the copper-gold mineralization, indicating the mineralization is directly related to the alteration seen along the shear zone.

SP, IP, and magnetic surveys were conducted over the deposits during the 1963-1964 field season. Slingram and Turam EM surveys were conducted, and only marginally delineated the shear zone as a poor conductor. The SP survey failed to delineate any major anomalies, only indicating mild positive values over the quartzite of the veins. The IP survey was unable to detect the deposits all together. The magnetic survey was able to delineate the shear zone itself due to the contact between the quartzite and gneiss along it. It was also found that the ore bodies present at depth produced large positive magnetic anomalies.

Legacy GSI magnetic and gravity data also cover these deposits. The magnetic data indicates these deposits are associated with positive magnetic anomalies which occur along the known shear zones, which is consistent with the findings of the 1963-1964 geophysical surveys. Legacy gravity data in the region is generally able to delineate major lithology changes and faults. However, the resolution is too low to be able to directly correlate it with the known ore bodies.

3.3.4 Godavari Valley and Wardha Valley Coal Fields

Extensive deposits of coal occur at or near the surface in the Gondwana sediments of the Godavari Graben. The deposits occur mostly along the western margin of the rift in the Godavari Valley and Wardha Valley and generally occur in the Lower Gondwana formations such as the Barakar and Lower Kamthi (or Raniganj) formations (GSI 2024). A map of the Godavari deposits in the Godavari and Chintalapudi Sub-Basins is provided by Aggarwal et al. (2022), whereas the Wardha Valley coal field occurs further to the north-northwest in the Chandrapur Sub-Basin, just west of the town of Chandrapur. The Geological Survey of India (GSI 2024) state that the coal is High Volatile Bituminous C, High Volatile Bituminous B to Sub-Bituminous coal in type, with a grade of G1 (the highest) to G14 (where G17 is the lowest).

Much of the coal mining in the Godavari and Wardha valleys is shallow or open cast, but deeper mining to depths of 600 m is under consideration (Subrahmanyam et al., 2020).

The presence or absence of coal is not directly detectable by the aeromagnetic or gamma-ray data, but the lithology of the sediments of the coal bearing formation may have distinguishing geophysical characteristics. Within the Gondwana Supergroup, the coal bearing Barakar formation is stratigraphically below the Barren Measures formation, the former with coal and the latter without. Neither formation has a strong magnetic signature, but together they have a reasonably distinctive gamma-ray signature, best described as “neutral” in that potassium, uranium and thorium are all relatively equally represented compared to adjacent formations, albeit with local variations within the formations. An example of the gamma-ray signature that corresponds to an area of mapped Barakar formation is shown in Figure 3.11. In areas where the coal has been exploited, the open cast mining operations have disturbed the characteristic signature and may even expose underlying rocks of a different character. The lithotectonic map (see section 11) includes areas where the mapped boundaries of the Barakar and/or Barren Measures formations have been modified using the gamma-ray data to refine the boundaries.

4. MAGNETIC DATA AND DERIVATIVES

4.1 Introduction

The anomalous magnetic field (AMF) gives the closest representation of the intensity of the Earth's magnetic field arising from the geology as recorded during a magnetic survey. It is the main result of magnetic survey data processing. A detailed description of the magnetic data processing is given in the Data Processing Report, but a summary of the processing steps is provided here:

- Data corrected for aircraft manoeuvre related interference ("compensation").
- Data position adjusted for the offset in location between the magnetic sensor and the GPS antenna on the aircraft ("lag correction").
- Diurnal variations in the magnetic field subtracted based on static measurements at a reference station ("diurnal correction").
- Residual diurnal variations corrected via tie-line levelling ("levelling").
- Survey line data interpolated rendered on to a two-dimensional grid of points equally spaced at 60m in UTM X and Y directions based on a minimum curvature algorithm ("gridding").
- Further residual diurnal variations corrected by identification and removal of line related artifacts in the grid ("micro-levelling").
- Enhancement of short wavelength signal mainly in the direction perpendicular to the survey lines using magnetic gradient data from the wing tip sensors.
- Data converted to the anomalous magnetic intensity by subtraction of the International Geomagnetic Reference Field ("IGRF correction").

To extract pertinent geological information from the observed magnetic data an analysis of a suite of transformation products is carried out. The processes allow for an enhanced selective visualization of specific characteristics of the data including the amplitude or wavelength which allow for inference of geological characteristics. This section gives a description of the transformation processes and products employed on this interpretation.

4.2 Anomalous Magnetic Field

Subtracting the International Geomagnetic Reference Field (IGRF) from the Total Magnetic Intensity leaves primarily the crustal contribution, the Anomalous Magnetic Field (Figure 4.1). This represents the component of local anomalies in the direction of the geomagnetic field.

4.3 Magnetic Anomaly Reduction to the Pole

The reduction to the pole (RTP) transformation removes anomaly asymmetry caused by inclination of the Earth's magnetic field and transforms anomalies as if they were located above Earth's magnetic north pole where the inducing field is vertical. The transformation assumes that magnetic anomalies arise from purely induced magnetization. Where magnetic remanence exists, this assumption will not be valid and therefore anomalies will be incorrectly transformed. Reduction to the pole allows for the direct comparison of anomaly shapes from different magnetic latitudes, and if the assumptions hold true the anomaly will be symmetrically located about the causative body. It therefore simplifies magnetic data interpretation.

Reduction to pole is essentially a phase shift filter applied in the frequency domain, and is described by:

$$F(k_x, k_y) = \frac{1}{[\sin(I) + i \cos(I) \cos(D - \theta)]^2}$$

where

θ is the angle in the $k_x k_y$ plane

I is the local magnetic inclination

D is the local magnetic declination

i is the square root of -1

For ease of calculation, this transformation can be performed through filtering in the frequency domain using a constant (average/central) inclination and declination which can be considered valid throughout the entire grid. An inclination and declination of 27.1° and -0.5° were employed.

The reduction the pole of the anomalous magnetic field is shown in Appendix Figure 4.2.

4.4 Vertical Derivatives of Magnetic Anomaly

Vertical derivatives act as high pass filters that enhance the high frequency/short wavelength content of the data and suppress low frequency/ long wavelength signal. The first vertical derivative ($n=1$) enhances rapid changes in the magnetic field at the edges of anomalies, and therefore it is useful for delimiting the extents of causative bodies. The second vertical derivative ($n=2$) further enhances high frequency signal variations and can be used to delimit domains of a specific geophysical character based on textural characteristics.

The n^{th} vertical derivative of a potential field can be defined in the Fourier domain as follows:

$$F(k_x, k_y) = (-k)^n \text{ where } k = \sqrt{(k_x^2 + k_y^2)}$$

Where k_x and k_y are the wavenumbers in the two-dimensional frequency domain.

The first vertical derivative of the anomalous magnetic field is shown in Appendix Figure 4.3 and second vertical derivative in Appendix Figure 4.4.

4.5 Total Horizontal Gradient of the Magnetic Anomaly

Horizontal gradient grids are used primarily for edge detection of causative bodies (contacts and faults with a large vertical displacement) but can also be useful for trend analysis and depth to source calculations. For RTP data, the horizontal gradient exhibits a symmetric peak with a maximum over the contact edge (Pilkington and Keating 2004).

Horizontal gradients are most conveniently calculated in the space domain. The total horizontal gradient of a potential field “ f ” is calculated from the gradients in the horizontal x and y plane as follows:

$$THG = \sqrt{\left[\frac{\partial f}{\partial x}\right]^2 + \left[\frac{\partial f}{\partial y}\right]^2}$$

The total horizontal derivative of the anomalous magnetic field reduced to the pole is shown in Appendix Figure 4.5.

4.6 Amplitude of the Total Gradient of the Magnetic Anomaly (Analytic Signal)

The total gradient amplitude (TGA), commonly referred to as the amplitude of the 3D analytic signal, is an especially powerful tool for interpreting magnetic data sets, particularly in areas of low magnetic latitude (inclination <20°). The total gradient amplitude will produce peaks which are symmetric and centred over the middle of narrow bodies and the edges of wide bodies irrespective of the inducing field direction. While the total gradient amplitude is not completely independent of magnetization strength and geologic strike, it is more easily dealt with during the interpretation than with pole-reduced data, especially in areas of low magnetic latitude (MacLeod et al. 1993). For this reason, the TGA is computed from magnetic intensity that is not reduced to the pole.

The total gradient amplitude of a potential field “ f ” is defined as:

$$|(A(x, y))| = \sqrt{\left[\frac{\partial f}{\partial x}\right]^2 + \left[\frac{\partial f}{\partial y}\right]^2 + \left[\frac{\partial f}{\partial z}\right]^2}$$

where $|A(x, y)|$ is the amplitude of the total gradient and f is the magnetic intensity at a point (x, y) . The horizontal derivatives are easily calculated in the space domain, whilst the vertical derivative is calculated as described above.

The total gradient amplitude of the anomalous magnetic field is shown in Appendix Figure 4.6.

4.7 Hanning Convolution Filter

A moving average filter operates by working out a weighted average of several points from the input data to produce each point in the output data. The Hanning convolution filter in one dimension (1D) produces an output which is the scaled average of three successive inputs with the centre point weighted twice as heavily as its two adjacent neighbours. In two dimensions, the $[3 \times 3]$ coefficient matrix for the Hanning convolution filter defined as:

$$\begin{bmatrix} 0.06 & 0.1 & 0.06 \\ 0.1 & 0.36 & 0.1 \\ 0.06 & 0.1 & 0.06 \end{bmatrix}$$

Application of the filter once produces practically no noticeable change on the magnetic data, therefore recursive applications are commonly applied to smooth the data. The convolution residual is obtained by subtracting the smoothed data from the original data set or one with fewer filter iterations applied. Pole-reduced magnetic data with 100 and 12800 Hanning convolution filter passes applied, and their residuals are shown in Figures 4.7, 4.8, 4.9 and 4.10.

4.8 Upward Continuation

The upward continuation transformation alters a potential field measured at one observation level to the field that would be measured on another surface farther away from the source. This has the effect of attenuating anomalies with respect to wavelength. Higher frequency, short wavelength signal is smoothed more than low frequency, long-wavelength signal as the continuation height is increased. It is therefore useful at masking shallow short wavelength anomalies. No information or assumptions of the source bodies are required when computing upward continuation.

The upward or downward continued field can be calculated convolving the frequency response with:

$$e^{h(u^2 + v^2)^{1/2}}$$

where h is the level above or below the original observed field.

Subtracting the upward continued field from the original field gives a residual which preferentially highlights the shallower sourced contribution to the field. The upward continued fields and their corresponding residuals for heights 100 m and 1 km are shown in Figures 4.11, 4.12, 4.13 and 4.14.

4.9 Power Spectrum Analysis

The two dimensional power spectrum of the magnetic anomaly data is determined by the Fourier Transform of the data, and can be represented by a contour plot of power versus wave-number in the two dimensional (u, v) frequency plane. The low frequencies have the highest power levels, generally dropping off to low powers at high frequencies. The shape of the drop off in power with frequency is different in two dimensions, but the overall pattern for the entire data set is represented by the Radial Averaged Power Spectrum (RAPS). This is determined by calculating the average power for a given radius from the centre of the power spectrum plot (the radial frequency $r = (u^2 + v^2)^{1/2}$), so that the power ascribed to each frequency is equal to the average power for that frequency in two-dimensions (Syberg 1972). The highest frequencies are characterized by an uneven RAPS; this is because of the Nyquist frequency, which is the highest frequency that can be correctly modelled by the grid. The Nyquist frequency is equal to twice the grid cell size.

The RAPS of the anomalous magnetic intensity after reduction to the pole is shown in Figure 4.15.

Analysis of the RAPS is based upon the work of Spector and Grant (1970); the authors developed a model for natural magnetic bodies, approximated as vertical sided prisms, which can be used to predict the power spectrum they would generate. The model has several terms related to the geometry, size and distribution of the prisms, but it was found that the dominant term is related to the depth to the top of the magnetic source, such that for an ensemble of prisms,

$$\ln \langle E(r) \rangle = \ln \langle P(r) \rangle + \text{other minor terms}$$

where

"< >" denotes ensemble average,

"r" is the radial frequency in radians/km,

"E" is the power

"P" is the function of wavenumber with respect to depth to source "h" such that

$$\langle P(r) \rangle = e^{-2hr}$$

(Cowan and Cowan 1993).

Therefore, any given ensemble of sources at a given depth will generate a RAPS with a constant slope such that

$$\ln E = -2hr$$

and therefore,

$$h = \ln E / -2r = \ln E / -4\pi f = \text{gradient} / 4\pi$$

where

"f" is the radial frequency in cycles/km

"gradient" is the slope of the RAPS

h is depth to source in km

Linear segments of the RAPS which correspond to depths to different ensembles of magnetic sources may be recognized on the RAPS, and the depth may be determined using the formula given above. Because of the assumptions built into the model, the value "h" will not be exact. In particular, the finite thickness of prisms means that the value is probably an over-estimate. A RAPS may be continually curved, in which case there are no levels of sources that can be interpreted using the model. Nevertheless, it may be possible to recognize multiple ensembles, and their relative depths determined. Kivior and Boyd (1998) show an example in which they recognize six separate ensembles. The shallowest ensemble is often equal to the flying height, i.e. the "depth" is actually the distance between the detector and the surface, and the shallow ensemble relates to surface sources.

Although the model does not directly apply to the gravity data, linear segments may still be recognized, and the overall principles applied. However, the depths so determined are unreliable except in the relative sense.

Once the power spectrum of the data has been analyzed, separation filters are designed. Superior separation of long, intermediate and short wavelength components of the signal is achieved by employing second order Butterworth band pass filters. The filters cut off limits are derived from the RAPS by determining the frequency at which the linear segments of the RAPS intersect. High frequency data relating to shallow features are separated using a high pass filter. Low frequency data relating to deep features are separated using a low pass filter, and the intermediate frequency features are separated using a band pass filter with cut off limits equal to the high and low pass filters.

The parameters used to separate the magnetic data are as follows:

- For shallow sources → 195 m high pass filter.
- For deep sources → 13.67 km low pass filter.
- For Intermediate sources, band pass between the two limits above.

Results of the separation filtering are in Figures 4.16, 4.17 and 4.18.

5. MAGNETIC SOURCE PARAMETER ESTIMATIONS

5.1 Introduction

There are several procedures available that convert magnetic data into mappable source body characteristics. For depth to source on gridded data, two methods are implemented in this interpretation: Grid Euler Deconvolution and Trend Analysis. The results and implications of these procedures is presented below.

5.2 Euler Deconvolution

Euler deconvolution (Reid et al. 1990) is a widely used inversion method for estimating the location and depth to the source of a magnetic anomaly. The implementation of the technique entails selecting a small data window and inverting for the source location assuming a specific source type. Different sources are identified using a source parameter, the structural index, which describes the field decay rate for different source models e.g. contacts, dykes, cylindrical pipes and point sources whose fields are known to be homogeneous and are listed in Table 1. The conventional approach inverts for a single source per data window i.e. the most dominant source, with the other sources contributing to noise in the inversion. The windowing process is repeated until the whole map is covered and normally with a high degree of overlap in the windows to allow for multiple source location estimations.

Table 1. Structural indices used in 3D Euler deconvolution

Structural Index	Geological Structure
0	contact, high throw fault
1	dyke, sill, sheet edge, limited throw fault
2	vertical pipe, thin offset
3	spherical body

In addition to the above, an index of 0.5 is also used. In theory all structural indices are integers, related to specific magnetic body geometries, but a non-integer index is a recognition that many magnetic sources will not be well represented by any single geometric shape, and so it is a compromise between the two most commonly appropriate indices. A display of the source location as dots in map form is the most common way of displaying Euler deconvolution results. The solutions are either colour-coded or size-scaled to indicate source depths. Linear clustering of solutions is usually taken as an indication that the appropriate structural index has been selected. The size of the data window can be used to focus the inversion to sources at different depths. Small windows tend to focus towards smaller, shallower sources while large windows focus on large sources that may be deep or shallow.

The gradient enhanced anomalous magnetic field without reduction to the pole (RTP) was used as the input for Euler deconvolution. RTP is often recommended, but is in fact not required, and is best avoided at low latitudes where distortions may occur that could impact the results. The data grids have a cell size of 60 m. An Euler moving sub-window of 11 x 11 grid points (660 m x 660 m) was selected as appropriate for investigating magnetic sources at depths of just over a kilometre whilst retaining reasonable resolution of smaller

anomalies. Thresholding and application of a Laplacian XY filter (Fairhead et al. 1994) removes spurious solutions and those not associated with significant positive curvature in the total horizontal gradient grid. Further rejection criteria are applied as follows:

Solutions deeper than two times the window size (1320m) are rejected

Solutions shallower than two times the cell size (120m) are rejected

Solutions with a standard deviation of more than a certain threshold are rejected (the tolerance)

Solutions that are in the air above the surface of the ground are rejected

Of these parameters, the tolerance can be varied to obtain the most coherent pattern of more reliable solutions available whilst trying to obtain solutions that describe most of the significant anomalies. For this survey tolerance of 20 nT was selected as a good compromise.

The resultant cleaned out solution space is provided which still includes solution reliability parameters allowing for an even tighter trimming of the solutions if need be. This might be necessary when viewing the solutions for smaller subsets. The results from Euler deconvolution with a structural index of 0 are presented (Figures 5.1 and 5.2) as they are the most broadly applicable to the structures across the entire area. The Archaean age cratonic rocks are dominated by contacts whilst the dominant features within the sedimentary basins are relatively significant faults. But the results from all the indices are provided so that they can be leveraged when interpreting local features that are better described by higher indices. The solutions presented show estimates of the depths to tops of magnetic sources from the surface and relative to mean sea level.

5.3 Trend Analysis

Trend analysis uses the horizontal gradient grid of the anomalous magnetic field to estimate strikes and depths to thick and thin edges, respectively (Phillips et al. 2007). The method relies on the general principle that shallow sources produce anomalies with steep gradients, whereas deep sources produce anomalies with broad gradients. The program uses a 5 by 5 grid cell (300 m x 300 m) window to locate both the crests of maxima and determine strike direction. Once a crest is located and the strike direction known, data within the window and within a belt perpendicular to the strike can be used to determine the depth of the contact by performing least squares fit to the theoretical shape of the horizontal gradient over a contact. The procedure is normally applied to data that is reduced to the pole. In this instance it is applied to the enhanced magnetic field without reduction to the pole to avoid issues with distortions of short wavelengths at low latitudes. This means that the locations of the crests may not be accurate, but the trends will be reliable.

All the depth estimates tend to be shallow and can be inferred to represent the minimum depth to top of the magnetic sources. Applying trend analysis on upward continued data can be used to give a crude estimate of the dip direction of a source contact or dyke as the location of the inverted source drifts in the down dip direction in the upward continued data.

5.4 Tilt Derivative

The tilt-angle derivative of magnetic data is most commonly used for structural mapping (Verduzco et al. 2004) falling among the suite of tools focusing on shallow structures. The tilt-angle θ of the magnetic field M reduced to the pole is defined as:

$$\theta = \tan^{-1} [\delta M / \delta z / \delta M / \delta h]$$

where,

$$\delta M / \delta z = [(\delta M / \delta x)^2 + (\delta M / \delta y)^2]^{-1/2}$$

For a simple vertical fault model, the zero contour of the tilt-angle is located on the edge of the causative contact body, and thus it can be used to outline the magnetic sources (Salem et al. 2007). In addition, the width between the $\pm 45^\circ$ contours provides a rough estimate to the top of the fault. These properties are of particular use in mapping the Sub-Basin structures within the Godavari Graben.

Figures 5.3 and 5.4 show the tilt angle contours of $\pm 5^\circ$ and $\pm 45^\circ$. The former was used to map fault locations, the latter to estimate the depth to the top of the fault.

5.5 Keating Coefficients

Possible kimberlite targets are identified from the gradient enhanced residual magnetic intensity data, based on the identification of roughly circular anomalies. This procedure is automated by using a known pattern recognition technique (Keating 1995, Keating and Sailhac 2004) which consists of computing, over a moving window, a first-order regression between a vertical cylinder model anomaly and the gridded magnetic data. Note that the data is not reduced to the pole, the local magnetic declination and inclination are accounted for by the model. Only the results where the absolute value of the correlation coefficient is above a threshold of 75% were retained. On the magnetic maps, the results are depicted as circular symbols, scaled to reflect the correlation value. The most favourable targets are those that exhibit a cluster of high- amplitude solutions. Correlation coefficients with a negative value correspond to reversely magnetized sources.

Two different sets of model parameters were used as follows (one parameter shown only where it is the same in both cases:

- Cylinder radius: 100 m or 200m
- Cylinder length: infinite
- Overburden thickness: 0 m
- Magnetic inclination: 27°N
- Magnetic declination: 0°W
- Magnetic intensity: 44102 nT
- Window size: 1000 m x 1000 m or 2000 m x 2000 m
- Susceptibility: 0.005

An example of the model's magnetic response is shown in Figure 5.5.

It is important to be aware that other magnetic sources may correlate well with the vertical cylinder model, whereas some kimberlite pipes of irregular geometry may not. The user should study the magnetic anomaly that corresponds with the Keating symbols, to determine whether it does resemble a kimberlite pipe signature, reflects some other type of source or even noise in the data, e.g., boudinage (beading) effect of the minimum curvature gridding. All available geological information should be incorporated in kimberlite pipe target selection.

Results are shown in Figure 5.6 and listed in Table 2. Only anomalies that yield a 0.8 out of 1.0 fit to the model are selected. Where the same anomaly is identified multiple times, the location with the best fit is selected. There are many localized magnetic anomalies that are the result of cultural effects, such as from towns, factories, mines or bridges. Those anomalies that are clearly associated with cultural effects have been labelled as "Suspect" in Table 2 and are not shown in Figure 5.6. In all cases the anomalies marked as suspect occur within the otherwise magnetically subdued area of the Gondwana Supergroup sediments that fill the Godavari Graben. The prospective anomalies are discussed further in section 12.9.

Table 2. Coordinates of magnetic anomalies identified as potential kimberlites by the Keating coefficient method.

Latitude dd:mm:ss.ssss	Longitude ddd:mm:ss.ssss	X m	Y m	Radius m	Fit	Suspect
18:16:28.7061	080:28:40.2799	444810	2020650	200	0.885	Yes
16:43:16.3722	080:51:38.8342	485160	1848720	100	0.862	
19:49:55.5672	080:00:11.3371	395610	2193210	200	0.859	
19:48:08.9329	079:56:35.4823	389310	2189970	200	0.858	
16:40:39.2607	080:19:17.2485	427650	1844010	200	0.852	
17:38:58.8376	079:53:45.4944	382890	1951770	200	0.842	
16:57:10.6455	080:44:04.8020	471750	1874370	200	0.838	
17:07:42.7105	080:38:10.5831	461310	1893810	500	0.836	
16:51:58.1328	080:42:46.1551	469410	1864770	200	0.826	
19:49:49.2208	079:18:10.2716	322260	2193600	100	0.821	Yes
16:55:21.5808	080:18:19.3469	426030	1871130	200	0.821	
17:39:32.7320	079:50:09.4532	376530	1952850	200	0.82	
17:50:32.3135	080:57:14.1958	495120	1972740	100	0.819	
19:35:00.6298	080:26:19.9560	441150	2165490	200	0.819	
16:59:28.1404	080:42:09.9627	468360	1878600	100	0.818	
19:59:15.5836	079:17:19.8501	320970	2211030	200	0.815	Yes
17:18:14.4129	080:19:45.7079	428730	1913310	200	0.809	
16:39:53.3945	080:54:23.0613	490020	1842480	100	0.809	
17:54:13.9059	080:57:07.0013	494910	1979550	200	0.807	
19:48:02.0107	079:59:08.1205	393750	2189730	200	0.805	
18:23:01.7084	080:57:16.7529	495210	2032650	200	0.804	
19:54:15.9314	079:20:31.8408	326460	2201760	100	0.804	Yes
20:22:36.0244	080:20:50.0414	431880	2253300	100	0.804	
16:42:27.8226	080:20:18.6589	429480	1847340	100	0.803	
17:48:34.6386	079:27:11.5001	336060	1969800	100	0.802	
18:20:58.4983	080:25:16.0561	438840	2028960	100	0.801	Yes
19:47:12.6018	080:03:11.7389	400830	2188170	200	0.801	

6. RADIOMETRIC DATA AND RATIOS

6.1 Introduction

The radioelement concentration grids of potassium, uranium and thorium are the main result of the gamma-ray survey data processing. A detailed description of the gamma-ray data processing is given in the Data Processing Report, but a summary of the processing steps is provided here:

- Data corrected for a constant radioactive contribution from the survey aircraft ("aircraft background").
- Data corrected for the impact of gamma-rays created by the impact of cosmic radiation in the upper atmosphere ("cosmic background").
- Data corrected for the impact of gamma-rays from radon gas ("radon background").
- Data corrected for scatter of gamma-rays from higher energy to lower energy ("stripping").
- Data corrected for the impact of distance from the ground ("attenuation").
- Data corrected for residual background and/or changes in conditions over the period of the survey via various levelling and Microlevelling techniques ("levelling").
- Data converted to equivalent concentrations of the radioelements at the Earth's surface ("sensitivity").
- Survey line data interpolated rendered on to a two-dimensional grid of points equally spaced at 60m in UTM X and Y directions based on a minimum curvature algorithm and also on a cosine weighted algorithm ("gridding").

Since gamma-rays are very effectively absorbed by solid substances, the gamma-ray signal detected in the airborne survey comes from no more than the top metre of the Earth's surface, often less depending on the composition of the material. Therefore, gamma-ray surveys are essentially surveys of the surface of the Earth, with no effective "penetration". This means that only where bedrock is exposed will it directly affect the gamma-ray signature. In the majority of circumstances, the gamma-ray signal will be directly affected by the overburden, such as soil or sand, which covers the bedrock. It can also be used to infer a bedrock source. Therefore, a gamma-ray survey may reasonably be expected to provide information on the surface extent of geological units that may be used to modify or confirm the boundaries of such units, and to study the erosional and depositional processes that lead to the formation and distribution of the overburden.

The typical concentrations of the three principle radioactive elements are given in Figure 6.1. However, when looking for anomalous amounts of radioactive elements that may be related to mineralization, the concentrations of the radioactive elements must be considered against the background levels due to each particular bedrock and/or overburden type within the survey area. Therefore, it is appropriate to sub-divide a survey into regions of similar radiometric signature to be assigned different background values. Anomalies can be identified within each region. This approach is employed in this interpretation.

Water is a very effective absorber of gamma-rays, and the moisture content of the overburden will affect the amount of gamma radiation detected. An increase in soil moisture of 10% will lead to a 10% reduction in gamma-ray radiation. Therefore, areas of similar geological character may have weaker signal if in a low lying, damp area for example. The thickness and type of overburden may have a similar effect. A 2 cm thick overburden of non-radioactive material can reduce radiation by as much as 35%. Trees and vegetation can

have much the same effect. For this reason, it is often better to look at relative ratios of the radioelements than to look directly at the concentrations. In this way, gross variations in concentration are removed and relative enrichment of one radioelement over another is highlighted. Care must be taken when interpreting ratio information, as low numbers in the denominator due to wet ground for example, may cause artificially high ratios. Since potassium is abundant and common, it is appropriate to use its presence to monitor the general levels of radiation, and to discard results from areas of low radiation as unreliable; 0.2% ^{40}K is the standard cut off.

6.2 Radiometric Data

Gamma-ray data is fully corrected during processing for the effects of cosmic radiation, aircraft background radiation, radon radiation, Compton scattering, and attenuation with increasing effective height. Data for potassium, equivalent thorium, and equivalent uranium are then converted to ground concentrations using system sensitivities and the results are presented in Figures 6.2, 6.3 and 6.4.

Ratio grids of $e\text{Th}/K$, eU/K and $eU/e\text{Th}$ are generated and presented in Figures 6.5, 6.6 and 6.7. Note that cells with a potassium concentration less than 0.2% are considered insignificant and given a null value.

Potassium, uranium and thorium grids are combined to make a ternary map. The ternary map captures the relative and absolute levels of radiation. A histogram for normalized concentrations of each of the three input grids and a weighted sum of the three grids is calculated using the following formula:

$$\text{Weighted Sum} = K + eU + eTh$$

The total radioactivity is split into five levels that together span the full range of values from zero to the maximum total radioactivity encountered. The intensity of the colours used increases for each higher level of total radioactivity. The choice of how the colours are rendered varies, and two different versions are presented here. The ternary map presented in Figure 6.8., generated using SGL's proprietary software, employs a cyan-magenta-yellow (CMY) colour scheme for uranium, potassium and thorium respectively, with increasing intensity indicated by increasing vibrancy of the colours. The ternary map presented in Figure 6.9., generated using Geosoft Oasis montaj® software, employs a red-green-blue (RGB) for potassium, thorium and uranium respectively, with increasing intensity indicated by a change from dark (low) to light (high).

7. REGOLITH MAP

Regolith refers to lithospheric material that overlies un-weathered bed rock. For the most part the presence of regolith is a hindrance to geological exploration. In particular, since almost all the terrestrial gamma-ray signal picked up by an airborne spectrometer comes from the top 20 cm of the ground, the relationship of the regolith or “overburden” to the underlying geology is important when interpreting the data. Therefore, understanding and categorizing the nature of the regolith in the survey area is an aid to interpretation.

There are many variations on how to go about creating a regolith map. SGL has adopted a method based on the approaches described by Caruso et al. (2018) and Metelka et al. (2018). The technique involves deriving a relationship between the concentrations of the three main radioelements detected in airborne survey, potassium, uranium and thorium, and a parameter known as the Topographic Position Index (TPI), that captures the local nature of the landform.

TPI is simply the difference between the altitude of a digital elevation model (DEM) at a point, and the mean of the surrounding DEM values (Guisan et al. 1999). If the value is positive the point in question is on a ridge or hill, negative it is in a valley, whilst a TP near zero is on flat or constantly sloping ground. The determination is highly scale dependent, the choice of the size of the area represented by the central point, and the surrounding area, will make a difference in the result. The input DEM used to calculate the TPI for this project is COP30 (Copernicus GLO-30 Digital Elevation Model from the European Space Agency) at 30m resolution. TPI was calculated using the General Data Abstraction Library built into QGIS.

An important step is to screen out areas where outcrop is significant, where there are more or less permanent bodies of water, and where there are open pits due to mining activity. To achieve this, the geomorphological mapping data of Block-6 provided by the GSI was used. Of 127 geomorphological categories mapped, 68 were found to correspond to areas of significant outcrop (often hilly and/or rugged), 3 to open pit mines, and 5 to bodies of water. A colour of deep blue was assigned to the water bodies, and the other two were assigned light grey. The data were then clipped to remove all these categories, leaving areas where significant regolith is likely to dominate the near surface characteristics.

Four variables, the TPI, concentration of potassium (%), concentration of equivalent uranium (ppm) and concentration of equivalent thorium (ppm) were each normalized to a value between zero and one using the following formula:

$$x' = (x - \mu) / (x_{\max} - x_{\min})$$

where x is each 60m cell of the data, and μ is the sample mean.

The values for each of the four variables are then clustered by K-means with “hill climbing” (Rubin 1967), performed using QGIS software. This approach identifies from a minimum of two to a maximum of twenty clusters. The clusters are analysed visually to see at what point the change in the mapped clustering becomes

negligible. This point is well defined at seven for this project. Each of the seven clusters is assigned a colour, and the resultant regolith map is illustrated in Figure 7.1.

Each cluster needs to be classified related to the nature of the regolith that it coincides with. The classification used for this project are as follows:

- | | |
|----------------|---|
| 1. Black: | High in uranium and thorium, low in potassium. |
| 2. Light Blue: | Low gamma-ray signal. |
| 3. Aquamarine: | Very high thorium, uranium low relative to thorium, low potassium. |
| 4. Green: | High potassium, uranium and thorium not significant. |
| 5. Orange: | Weak uranium, relatively high uranium to thorium. |
| 6. Red: | Reasonably high thorium, uranium low relative to thorium, very low potassium. |
| 7. Brown: | Weak potassium, uranium and thorium not significant. |

8. LEGACY GRAVITY DATA

Gravity data covering parts of Block-6 is provided by the GSI to SGL to assist in the interpretation of the newly aeromagnetic and gamma-ray data. The data is of insufficient resolution to be used for direct detection of economic deposits but does provide regional contextual information.

The data is presented “as is”, with no additional reprocessing. It is assumed that the Bouguer data was derived from the Free Air data using a standard crustal density of 2.67 g/cc. Two versions of the data are made available by the GSI. Bouguer (terrain corrected) gravity data at a resolution of 5 mGal is published under a collaborative project by the GSI, NGRI, ONGC, SOI and OIL (2006), which provides full coverage of Block-6. 1 mGal Bouguer gravity data is provided under the National Geophysical Mapping Program (NGPM), which provides only partial coverage of Block-6.

The 5 and 1 mGal versions of the gravity data in Block-6 are illustrated in Figures 8.1. and 8.2.

9. SENTINEL-2 SATELLITE DATA

The European Space Agency (ESA) Copernicus Sentinel-2 satellite data is used as a supplement to the geophysical data in the creation of the litho-tectonic boundaries, and to a lesser extent in the identification of areas of interest. The Sentinel-2 web site describes the specifications of the instrument as follows. "Multispectral imager (MSI) covering 13 spectral bands (443 nm–2190 nm) with a swath width of 290 km and spatial resolutions of 10 m (4 visible and near-infrared bands), 20 m (6 red-edge/shortwave-infrared bands) and 60 m (3 atmospheric correction bands).

A Sentinel-2 false colour image is generated using the following spectral bands:

- Red Band 12 Short Wavelength Infrared wavelength 2.190 μm
- Green Band 11 Short Wavelength Infrared wavelength 1.610 μm
- Blue Band 4 "Red" 0.665 μm

This particular combination is found to provide the best definition of lithological boundaries. Although satellite data has been used to find areas of alteration (Mahboob et al. 2019) it depends on local conditions and works best where there is plentiful rock exposure which is not the case in Block-6. No anomalies of interest were identified using this data.

RGB-bands 12:11:4 are employed to make a single RGB image as shown in Figure 9.1.

10. MINERALIZATION AND GEOPHYSICAL DATA

Figure 10.1 shows a chart presented by Airo (2015), adapted from Ford et al. (2007) showing the general utility of different geophysical techniques toward direct or indirect detection of various types of mineral deposit.

The relationship between various forms of mineralization and geophysical data is complicated (Ford et al. 2007). The effects of alteration, weathering and lithological variation means it is not possible to make simple correlations. Nevertheless, there are many examples of mineralization associated with anomalous aeromagnetic and gamma-ray signatures. Some legacy gravity data is available but is of insufficient resolution to be directly associated with mineral deposits (the highest density is a data point every 1 km), and no electromagnetic or seismic data is made available for this report. Therefore, the following brief synopsis covers the most probable types of deposit that may occur in Block-6 and how they may be manifest in gamma-ray and magnetic data only.

10.1 GAMMA-RAY SIGNATURES OF MINERAL DEPOSITS

10.1.1 Uranium Mineralization

One of the most straight forward means of using gamma-ray data to detect mineralization is in the exploration for uranium. Deposits of uranium generally have the following gamma-ray characteristics (from IAEA 2003):

- a) Elliptical dispersion halos from 70 by 80 m to 80 by 350 m,
- b) Anomalous uranium concentrations of 4 to 20 ppm eU,
- c) Associated thorium anomalies of 5 to 40 ppm,
- d) Radioelement ratios in the following ranges: $eU/eTh > 1$, $eU/K > 5$ to 10, eTh/K of 4 to 5.

Skarn deposits that normally form during regional or contact metamorphism of carbonate rocks may have associated uranium anomalies, and may contain economic concentrations of REEs and uranium, for example the Mary Kathleen deposit of Queensland, Australia contains sufficient uranium and thorium to be detected by airborne survey (Kwak and Abeysinghe 1987).

Tin, molybdenum, fluorine and uranium and other incompatible elements are associated with fractionated granites and may be deposited in late-stage pegmatites, quartz veins and greisens (altered granite).

10.1.2 Potassium Alteration and Mineralization

Potassium alteration, leading to anomalously high potassium concentrations and low eTh/K ratios are known to be associated with several different types of mineralization, including volcanic-hosted massive sulphides, magmatic hydrothermal deposits and porphyry copper-gold deposits (Shives et al. 1997). In particular, strong potassium anomalies with low eTh/K ratios less than 2.5 (ppm eTh/K) are a particularly good indicator of potassium alteration (Shives et al. 1997) as opposed to normal crustal ratios of the order of 5 (Galbraith and Saunders 1983).

eTh/K ratio lows may also occur in association with polymetallic hydrothermal deposits. For example, Gandhi et al. (1996) identified hydrothermal alteration of bismuth, copper, cobalt, gold and arsenic bearing arsenopyrite-pyrite-magnetite veins, identified by potassium enrichment and coincident high magnetic anomaly over a 3 x 4 km area that was detected by airborne survey.

10.1.3 Thorium Mineralization

Commercially significant Thorium occurs in the mineral monazite, but thorium also occurs in the minerals thorite and thorianite. Monazite is an ore composed of several rare earth metals including thorium, cerium and lanthanum, all of which are commercially important. Monazite is formed in granitic and phosphatic pegmatites, carbonatites and other alkaline igneous rocks, but also occurs as a trace element in common igneous and metamorphic rock and in veins. Monazite is dense (4.6 to 5.7 g/cm³) and is normally resistant to breakdown and as such can occur in placer deposits from erosion of original source rocks.

Thorium bearing veins may be associated with carbonatites (that may or may not contain Monazite). Carbonatites are known to contain a large number of industrially important rare earth elements (Wang et al 2020).

10.2 Magnetic signatures of Mineral Deposits

Magnetic signatures may be directly associated with mineral deposits, sometimes the host rock, and sometimes (Ford et al. 2007, Gunn and Dentith 1997).

Kimberlites may or may not have a magnetic anomaly associated with them due to the presence of magnetite and ilmenite and may or may not have strong magnetic remanence. If a magnetic anomaly is present, it is typically a simple circular bullseye magnetic high with a lower surrounding magnetic low, if the field is near vertically oriented.

Carbonatites and alkali complexes also generate round anomalies, but they may be more irregular in shape and complex in character with rings of high and low intensity.

Indirect detection of hydrothermal gold deposits may be performed by targeting areas of low magnetization along shear zones or faults related to alteration of magnetitic minerals in the host rocks. Similarly, unconformity related uranium deposits that occur at the boundary of the Proterozoic and Archaean have no direct magnetic signature, but associated pelitic rocks in the Archaean basement are low in magnetization.

Conversely, types of deposit may (but not always) include the formation of magnetic minerals, in particular magnetite and especially pyrrhotite which can have very strong magnetic remanence. This includes Volcanic Massive Sulphides, where the deep feeder pipe, main tabular lens, and the broad thin cap may all be significantly magnetic. Both Sedimentary exhalative (SEDEX) and Mississippi Valley Type (MVT) Lead-Zinc deposits may have associated pyrrhotite and so have a magnetic signature. Copper porphyries may have both

magnetic highs and lows, where the alteration in the vicinity of a felsic intrusion results in destruction of magnetic minerals in the surrounding country rocks, but a high-level cap of volcanics can generate a field of very strong and chaotic magnetic anomalies, whilst the central core may or may not include magnetite and consequently an associate central magnetic high.

Olympic Dam type deposits may generate magnetic anomalies due to deposition of magnetite and/or haematite in varied settings, including in breccias, veins, massive bodies, and disseminated in the country rocks. The underlying granite or granodiorite may also generate a broad regional gravity high, with regional highs due to the shallower deposits superimposed upon them.

In some cases, both the host rock and the ore body may be magnetic. For example, pyrrhotite bearing magmatic nickel-copper-PGE deposits occur within mafic or ultramafic intrusions and flows. Similarly, chromite bodies usually occur within ultramafic intrusions, in either stratiform or podiform bodies, and both are magnetic. Some possibility of locating the chromite may be afforded by associated with serpentinization of the host rock, resulting in an increase in the already strong magnetic anomaly, but this may be hard to distinguish. Nickel sulphides with associated pyrrhotite and magnetite are also hosted in magnetic ultramafic and mafic rocks, so again direct detection may be difficult despite the strong magnetism associated with the ore.

In the case of banded iron formations (BIF), the original host rock may contain variable amounts of both magnetite and haematite, with associated strong magnetization that includes a high contribution from remanence and also an anisotropic response of induced magnetization due to the strong banding. But relative lows in the magnetization may indicate areas of alteration of magnetite to haematite leading to supergene enrichment to potentially ore grade levels at a stratigraphically higher level.

Lateritic bauxite occurs as a result of tropical weathering alteration of silicate rocks such as granite, gneiss, basalt, syenite, and shale in areas of good drainage such as hill tops. Iron oxides such as goethite and haematite are formed (Amosun et al. 2020), and so typically have a magnetic signature. The degree to which they stand out will depend on the magnetism of the unaltered rock.

Skarn mineralization occurs as a result of contact metamorphism of carbonates due to igneous intrusions. This can result in magnetic minerals being formed, but the process is complex and does not always occur. Magnetic aureoles in carbonates around intrusive rocks may be indicative of the presence of a skarn.

Placer deposits in riverbeds do not generally have a magnetic signature associated with them but under certain circumstances palaeochannels may be identified if they contain detrital magnetic material such as magnetite or maghemite, or if the palaeochannel happened to erode through a magnetic layer.

Potential for many but not all of the types of deposit mentioned in this section have been identified within Block-6, as discussed in Section 12.

11. LITHO-TECTONIC INTERPRETATION

11.1 Introduction

The methodology for the creation of the litho-tectonic interpretation map is presented below. The results of the interpretation are made available as an ArcPRO project with select copies from the map presented below. The compilation and processing of the different data sets required for the interpretation have been presented in previous chapters. These include a range magnetic data transformations (e.g. reduction to the pole), derivatives (e.g. first vertical derivative) and residuals (e.g. upward continuation residual). The radiometric data were also prepared in a range of styles that included ratios of different elements and ternary maps of elements and of ratios. The primary remote sensing data utilized was Sentinel-2 with a range of spectral band combinations generated.

All interpreted data and mapped geological data, made available by the GSI were all brought together on to the same platform for consolidation.

Block-6 has a reasonable degree of magnetic interference from man-made “cultural” interference. This includes a number of power lines, and local anomalies due to frequent settlements or industrial sites. Rather than attempt to remove these features, which can be problematic and time consuming, the approach taken is to leave them in but cross reference with satellite imagery to check their provenance. Likewise, there are features in the gamma-ray data that are clearly related to human activity, in particular in the vicinity of the coal mines that occur in the lowest formations of the Gondwana Sediments. Cultural elements are not marked on the litho-tectonic map as they have no geological significance.

11.2 Lithology mapping

The unadjusted pre-survey lithology mapping is illustrated in Figure 11.1, using the Unified Legend Colours and Litho-codes for India, as provided by the GSI.

The geophysical signature characterization presented in Chapter 12 is the primary basis of the mapping of the lithological units. Lithological units are interpreted from their magnetic signature/fabric and or their radiometric signature with the magnetic anomaly edges defined with the assistance of the peaks of the total magnetic horizontal derivatives, and radiometric data when applicable.

In creating the litho-tectonic interpretation map, previously mapped geological boundaries were honoured where supported by the magnetic data and adjusted where deviations were observed. Small or isolated units from the geology map which did not impact other neighbouring units and had no discernible magnetic or radiometric response were not marked. When a mapped unit was large with a boundary that impacted neighbouring units but had no discernible geophysical signature, the boundary was honoured.

Figure 11.2 illustrates the litho-tectonic map with only the lithological units shown, but with all units where new codes were required are shown in grey. Unit codes (litho-codes) from the existing geological map were amended to allow for further subdivisions of lithologic units presenting systematic variations in their geophysical signatures. A unique number was appended to the litho-code to represent any unit subdivision split based on a distinguishing geophysical signature. The sub-unit must be large enough to likely represent a separate geological structural lithology. Sub-units with the same geophysical signature will have the same number appended. A list of all the new codes employed is provided in Appendix I. Figure 11.3 illustrates the litho-tectonic map with only the lithological units shown, updated to use the new codes. Figure 11.4 illustrates the litho-tectonic map using the new codes, with all other elements added.

11.3 Faults, fractures, dykes, and lineaments

Structural features were interpreted from the magnetic data as follows:

- a) Known faults interpreted from linear magnetic lows associated with noticeable lateral displacement of magnetic or radiometric features.
- b) Inferred faults interpreted from linear magnetic lows without obvious magnetic or radiometric feature displacement but long enough to stand out as anomalous.
- c) Unknown faults interpreted from previously mapped faults with no geophysical signature.
- d) Fractures from linear magnetic lows.
- e) Dykes interpreted from long narrow linear magnetic high anomalies.
- f) Lineaments from topographic data were manually digitized.

The linear features are presented in Figure 11.5. Faults are easiest to map in magnetic terranes where they disrupt or displace anomalies. Faulting is discussed in section 12.1.1. Fractures are linear magnetic lows with no discernible offset. It is apparent that there are many more fractures in the EDC compared to the Bastar Craton within Block-6. The Bastar Craton's gneissic terrain appears to be highly sheared, often subparallel to the Godavari basin, so the deformation regime in the Bastar is more ductile compared to the more brittle deformation in the EDC.

Dykes are marked by linear magnetic highs which stand out and are easily mapped when intruded into the less magnetic units like sedimentary units or into non-magnetic granites. They have subtle and less obvious associated signature when intruded into the magnetic granitoids and often become negative when reduced to the pole indicating significant remanence.

Lineaments are other linear features apparent in the topographic data that are not identified as faults, fractures or dykes.

11.4 Areas of Significant Change in the Map

Whilst much of the re-drawing of boundaries within the litho-tectonic map are a matter of refining the existing map, there are areas where significant alterations have occurred. These are described below.

Figure 11.6 shows changes in the litho-tectonic mapping in the northern part of the Bastar Craton, where bands of newly interpreted supracrustal areas have been added. These areas probably consist of metasediments and metavolcanics and are described in Section 12.3.

Figure 11.7 shows changes in the litho-tectonic mapping in the eastern part of the Bastar Craton, where areas of folded supracrustal areas have been updated and more areas added. These areas probably consist of metasediments and metavolcanics with mostly quartzite in the core of the folds and are described in Section 12.3.

Figure 11.8 shows changes in the litho-tectonic mapping in the Eastern Ghats Mobile Belt, as follows, with newly interpreted granulite area located by analogy with a previously mapped and well exposed granulite with similar geophysical signature and is described in Section 12.4.

Figure 11.9 shows changes in the litho-tectonic mapping in the northern part of the Bastar Craton, with a newly interpreted formation of enigmatic origin with a distinctive gamma-ray signature, described in Section 12.3.

11.5 Buried Geologic Boundaries

Buried geologic boundaries, mainly but not exclusively within the Godavari Graben, are apparent in the magnetic data. In some instances, the boundaries are extended under recent cover by extrapolation of the geophysical response, and some fully buried geophysical contacts are also included. The buried boundaries are illustrated in Figure 11.10.

11.6 Areas of high mineral potential and zones of alteration

The potential mineral and deposit occurrences are used to identify the areas of potential mineralization based on deposit type and or the tectonic setting. The geophysical data are used to address and define additional geological aspects related to the known areas or of other areas which might be identified as additional geochemical data becomes available.

Direct detection of mineralization with the available data is limited to detection of high magnetite concentrations or high concentrations of radioactive elements. Mapping zones of alteration particularly those that occur within belts of mineralization was done to identify areas of interest as likely targets. The radiometric data was utilized to map alteration zones by mapping areas with anomalous gamma-ray concentrations and ratios. These were initially tagged as of interest if they had a magnetic anomaly associated with the interpreted alteration zone. The sites were also further evaluated based on the interpreted geology and their location in mineralization zones or relation to mafic and ultramafic rocks and regional faults of interest. The results of the target selection are presented in Section 12.9.

12. GEOPHYSICAL CHARACTERIZATION OF DOMAINS

12.1 Overview of the geophysical signature

For the purpose of analysis of the geophysical data, Block-6 is broken into geological domains as illustrated in Figure 12.1.1. These domains correspond to well established geological terranes.

12.1.1 Magnetic Trends and Graben Related Structures

Plots of the dominant structural trends for each domain are extracted from the magnetic data using the trend analysis method described in section 5.4, individually presented in Figure 12.1.2, and an overview of the trends for Block-6 is provided in Figure 12.1.3. These charts are referred to below in each section as appropriate. The trends identified by the trend analysis are based on short wavelength signature. Major structures are captured too but are often less statistically significant than the pervasive fabric of any given area.

Figure 12.1.3. shows that apart from in the south, the dominant trends are in the west-northwest direction, varying either side of 65°W by about $\pm 10^\circ$. This includes the sediments of the Godavari Graben, the Proterozoic age sediments in Sub-Basins on both flanks of the rift, and both cratons. It also includes the Deccan Trap volcanics, which appear to be disorganized but clearly are not. The main axis of the Godavari Graben runs at approximately 35°W, at 30° to the dominant trends, and in most areas a subsidiary but significant trend parallel to the rift axis can be identified. Only the inlier of Bastar Craton shows three equally significant trends, the two as described plus another at 55°W.

The southernmost areas, including the EGMB, the Proterozoic sediments at the south end of the main Godavari Rift, and the Krishna-Godavari Basin, all have dominant trends that are either westerly or close to it. The Krishna-Godavari trends are mostly derived from the magnetic fabric of the underlying EGMB basement, with subsidiary northeast trends associated with folding of the overlying sediments superimposed.

The trends that are parallel to the main Godavari Graben axis are not surprising, they are probably related to the long history of tectonic activity of extension and compression across the cratonic boundary that would be dominantly perpendicular to the axis. The pervasive dominant trends at 65°W are sub-parallel to a number of major faults that offset the western margin of the Pranhita-Godavari Rift and could be related. The tilt derivatives of the magnetic field suggest that some of these faults persist into the rift (Figure 12.1.4). Only those faults that are seen to pass from the cratons into the basin are marked in the figure, other intra-basement faults may also occur related to the magnetic boundaries indicated by the tilt derivative, but there is relatively little disruption of the sedimentary layers obviously associated with these structures. In addition, where the higher resolution gravity data partially covers the Godavari Graben, a prominent local gravity high can be seen that is sub-parallel to the graben's long axis (Figure 12.1.4). This same feature appears as a relatively strong magnetic high, best isolated in the intermediate filtered reduced to pole magnetic intensity (Figure 12.1.4). The presence of the uplift is also marked in the radiometric data as an inlier of Godavari Supergroup sediments at the surface surrounded by Gondwana Sediments (Figure 12.1.4), except for

a narrow band that connects to the main Godavari Supergroup outcrops of the Western Belt at the northwest extremity. The obvious interpretation of this feature is that there is a basement uplift here, either in an anticline as shown by Dasgupta and Jain (2007) (Figure 12.1.5) or it is a faulted horst, suggested by the blocky outline of the magnetic anomaly, and is termed the Chinnur Inliers by Burhanuddin (2017). But many other well defined magnetic anomalies, sometimes blocky in nature and sometimes not, occur in areas where the higher resolution gravity does not show any indication of an uplift of denser rocks. This, combined with the general lack of associated offsets in the basin sediments, suggests that these anomalies arise due to magnetic contrasts within the basement to the Pranhita-Godavari Rift, either across fault lines or due to lithological variations such as local intrusions. Therefore, apart from the anomaly that is associated with the uplift the apparent depths of these anomalies from the tilt derivatives give an approximate depth to the bottom of the sedimentary basin. Using the distance between the $\pm 45^\circ$ contours of the tilt, a map of depths is provided in Figure 12.1.6. Since the method assumes that reduction to pole is valid and accurate, and the source results from a vertical contrast in magnetic properties, not too much emphasis should be placed on the exact depths, but a general pattern is evident. The shallowest sources have been omitted for clarity, and inspection of the rest shows that the basin deepens from the 1 to 2km depth range along its margins, especially on the west side, and there are three locations where the deeper solutions up to 4km or more occur. One coincides with the Sironcha Depression, another occurs in the Kothagudem Sub-Basin, and the third occurs within the Chintalapudi Sub-Basin; see Figure 12.1.5. for the location of these areas. The fact that the Eturanagram Depression does not show up is not indicative that it is not deep, only that there are no magnetic anomalies in that location by which to judge its depth. So overall it appears the basin deepens toward its axis but is generally deeper towards the east side and towards its southern end, more or less in agreement with the gravity data. Improved gravity for the entire basin data would permit a joint inversion on magnetic and gravity to give a well constrained model of the basement to the Pranhita-Godavari Rift.

Confirmation or otherwise of this concept would be greatly assisted by improved resolution of gravity data across the entire graben. Dasgupta and Jain (2007) have assessed potential for hydrocarbons in the graben, and a better understanding of the potential hydrocarbon structural traps could prove very beneficial. If the magnetic features are due to basement uplift, these structures could be extensional or compression related, potentially as reactivated normal faults, the geophysical data does not preclude either of these possibilities.

A 2.5D cross section of the Pranhita-Godavari Basin is presented in Fig 12.1.7. Coordinates of the profile end points are as follows:

D 331480 / 1977836, 17°52'54.78"N / 79°24'33.65"E
D' 481225 / 2076719, 18°46'55.30"N / 80°49'18.65"E

The shape of the combined Proterozoic and Gondwana sedimentary basin is dominated by the gravity data profile, taken from the 5 mGal resolution data. Unfortunately, the 1 mGal resolution gravity data does not provide a complete cross section of the data in the main Godavari rift, being confined to the western side only.

The magnetic data provides subsidiary constraints on the model, although the susceptibilities required to model variations in the marginal granulite and gneissic terrains are at the high limits of what is probable, indicating that remanence may be important in these rocks. The shape of the Gondwana age Godavari Rift within the Pranhita-Godavari Basin is not resolved due to a lack of contrast between the lithologies or the Godavari Supergroup and the Gondwana sediments, and two possible contrasting options are shown in the figure. In the first option, the Godavari Supergroup sediments are restricted to the margins of the Basin, with Gondwana sediments filling the centre of the rift all the way to the basement. Another second option shows the Godavari Supergroup sediments passing continually beneath the Gondwana sediments from one side of the rift to the other. Either of these, or a hybrid of the two, are all compatible with the magnetic, gravity and gamma-ray data. Based on additional seismic data, Dasgupta (2007) shows option two, with continuous Godavari Supergroup sediments, as mentioned earlier in Section 3.2.5.

West trending dykes that can be traced running through the Bastar Craton in the north (see section 12.3), under shallow Proterozoic age Godavari Supergroup sediments and in the inlier of Bastar Craton in the north of Block-6, also appear to run under the deeper Gondwana age sediments of the Godavari Graben (see Section 12.6). Where the dykes occur under the Gondwana Supergroup sediments, they appear to be distinctly deflected in a dextral sense as they approach the principle Godavari Graben fault on the east side of the graben, along the edge of the Bastar Inlier. Against this, a shallow, distinctly potassic, sedimentary formation that appears to sit on underlying Bastar Basin (see section 12.3) has what appears to be sinistral offset across a fault that appears to branch off the eastern bounding fault of the Graben.

A 20 km by 20 km embayment of Proterozoic sediments occurs in the eastern side of the Godavari Graben centred at coordinates 395500 / 2122300, 19°11'29".92N / 80°00'21.68"E (Figure 12.1.8). The southwest margin is in contact with the younger Gondwana Supergroup sediments of the Graben, but the main Graben boundary fault can still be seen in the magnetic data beneath the sediments. The southeast margin appears to be an unconformable contact with the Bastar Craton, with the magnetic data indicating gradual deepening of the sediments in the northwest direction. The arcuate boundary on the northeast and northwest sides is sharp against the more magnetically active Bastar Craton indicating that it is probably fault bound. Therefore, this appears to be a small half graben of Proterozoic sediments to the side of the later Godavari Graben.

12.1.2 Potential Kimberlites from Magnetic Data

Keating coefficients have been calculated across the entirety of Block-6, as described in Section 5.5 and illustrated in Figure 5.5. This method searches for the specific magnetic signature expected to be generated by a kimberlite pipe, which in turn may or may not be diamond bearing, although the anomaly may be generated by other features. Apart from those identified within the Godavari Graben that all appear to be related to cultural effects, all the identified locations are worthy of further investigation. However, two areas stand out in particular. The likelihood that the identified anomalies are actually kimberlites is increased where they occur in clusters. One such group of four identified anomalies occurs in the Bastar Craton some 18 km north-northwest

of the town of Mulchera, as shown in Figure 12.1.9. It can be seen that there are a number of other dipolar anomalies in the area that were not picked up by the Keating Coefficient method, but these too may be of interest especially if one or more of the four identified bodies turn out to be a positive identification of a kimberlite.

The second grouping of interest is in the Eastern Ghats Mobile Belt (EGMB) (Figure 12.1.10). A total of ten identified anomalies occur in two lines. Three occur in an approximately north to south line along the axis of the Munera River and could potentially be extended to a fourth some distance to the north 20 km east northeast of the town of Khammam. As noted in section 12.4, a large group of probably detrital diamonds occurs just to the southeast of the southmost of the potential kimberlites, and downstream along the Minera and Krishna Rivers. It is possible that this line of identified anomalies represents a suite of kimberlites that have exploited a line of weakness in the crust. The presence of the diamond occurrences in a location close to the confluence of two rivers makes these targets particularly attractive. Another line of identified anomalies runs from the southeast corner of Block-6 up to the north-northwest, totalling seven in total, possibly eight if the anomaly close to Khammam is included in this line. The two to the southeast are within the Krishna-Godavari Basin, but the anomalies are almost certainly from the underlying EGMB basement. Once again it seems possible that a line of kimberlites has occurred along a line of weakness. Of particular interest is the anomaly identified close to the town of Tiruvuru. A prominent group of diamond occurrences occurs on the side of the valley of the Kaltale River that runs south southwest from Tiruvuru, just northwest of the village of Gosaveedu. No potential kimberlite pipe was identified close to this cluster of occurrences, so they may be detrital in origin from the occurrence at Tiruvuru, although they are to the side of the river and the magnetic signature in the area is more complex, so that a kimberlite like anomaly may not be so easily detected in this location.

12.1.3 Baseline Gamma-Ray Statistics

The anomalous gamma-ray data can only be understood in the context of the regional averages for each of the different geological domains within the survey area. Tables 3 and 4 tabulate the basic statistics for each of the areas described below.

Table 3. Radio-element statistics of geological domains.

Geological Zone	Potassium (%)			Equivalent Uranium (ppm)			Equivalent Thorium (ppm)		
	Min	Max	Avg	Min	Max	Avg	Min	Max	Avg
Deccan Traps	0.12	4.97	0.75	0.05	6.45	0.98	1.29	94.12	6.17
Krishna-Godavari Basin	0.07	2.64	1.02	0.03	11.93	2.55	1.02	102.17	34.10
Godavari Graben	0.00	4.52	0.85	0.00	13.45	2.16	0.08	88.44	19.33
Pranhita-Godavari Basin West	0.01	6.11	1.40	0.00	8.75	2.07	0.23	70.73	13.87
Pranhita-Godavari Basin East	0.00	4.04	0.92	0.00	7.52	2.03	0.35	78.99	11.49
Eastern Ghats Mobile Belt	0.00	3.75	0.99	0.00	12.17	1.76	0.14	138.08	17.82
Eastern Dharwar Craton	0.00	6.26	2.53	0.00	20.55	2.27	0.08	265.60	26.80
Bastar Craton	0.00	5.24	1.37	0.00	17.78	2.02	0.00	97.67	13.64

Table 4. Radio-element ratio statistics of geological domains.

Geological Zone	eU/eTh			eTh/K			eU/K		
	Min	Max	Avg	Min	Max	Avg	Min	Max	Avg
Deccan Traps	0.02	0.79	0.17	1.97	75.54	9.50	0.12	29.81	1.73
Krishna-Godavari Basin	0.00	0.38	0.07	8.33	371.84	40.15	0.09	44.91	3.06
Godavari Graben	0.00	1.11	0.12	2.11	772.06	39.26	0.04	92.59	4.27
Pranhita-Godavari Basin West	0.01	2.53	0.16	1.00	261.02	11.95	0.07	30.36	1.85
Pranhita-Godavari Basin East	0.01	1.30	0.19	1.47	614.82	16.48	0.07	65.40	2.98
Eastern Ghats Mobile Belt	0.00	4.63	0.10	1.03	185.29	19.11	0.04	24.32	1.92
Eastern Dharwar Craton	0.00	1.11	0.10	0.94	223.25	12.16	0.01	22.92	1.01
Bastar Craton	0.01	0.85	0.15	1.01	303.80	11.69	0.04	49.23	1.80

Of particular note in the statistics above are:

- Generally high thorium concentrations across the entire survey area, with the notable exception of the Deccan Traps.
- Low potassium concentrations in both the Godavari Graben and the Krishna-Godavari Basin relative to uranium and thorium.
- Relatively high potassium and thorium relative to uranium in the Eastern Dharwar Craton, and generally high radioelement concentrations, in contrast the Bastar Craton (apart from some local granitic intrusions).
- High maximum uranium relative to thorium in the Eastern Ghats Mobile Belt, and to a lesser extent in the Pranhita-Godavari Basin West.
- Low radioelement concentrations in the Deccan Traps.

12.2 Geophysical character and anomalies of the Archaean Eastern Dharwar Craton

The part of the Eastern Dharwar Craton (EDC) within Block-6 is mostly mapped as either grey biotite granite in the north or alkali feldspar granite in the south, roughly divided along an east west line at UTM Y 1987000, but both belonging to the so-called Peninsular Gneiss. This north south divide is not apparent in either the magnetic or the gamma-ray data.

Magnetic sources determined by Euler deconvolution are dominantly of shallow original across the entire EDC (<150 m below ground based on a structural index of zero, appropriate for contacts, Figure 5.1). Locally deeper sourced magnetic anomalies are scattered throughout the craton, some of which have interesting anomalies associated with them.

The part of the EDC that falls within Block-6 can be split into three broad areas of different magnetic and gamma-ray character. The boundaries are gradational in character but is clearly seen in both the magnetic and gamma-ray data (Figure 12.2.1). The southwest has a low amplitude magnetic character and a strong mainly potassium gamma-ray character and is designated as Alkali Feldspar Granites based on the existing mapping. The area to the north has much higher magnetic amplitudes and a much lower thorium character and is designated as Grey Biotite Gneiss. The area to the southeast is characterized by strong curvilinear magnetic anomalies that are subparallel to the margin of the craton with relatively strong horizontal gradients probably reflecting lithological variations within the highly deformed Archaean age rocks, but nonetheless have a definable overall strike of approximately 115°. In addition, the southwest area is high in thorium, has bands of high uranium, but is generally low in potassium, and is designated as Migmatite Gneiss. According to current mapping, the Karimnagar Granulite is restricted to the northern part of the Grey Biotite Gneiss in a 35 km long by 5 km wide band parallel to and just south of a major 120° bearing structural break, where the low potassium gamma-ray signature is locally more similar to the Migmatite Gneiss, and the magnetic amplitudes are lower than the adjacent gneisses. If this gamma-ray signature is characteristic then the granulite is more extensive than currently mapped, and bands of Karimnagar Granulite are extended to the south in the litho-tectonic map. On the other hand, there is no immediate evidence of any volcano-sedimentary rocks in the vicinity of the Karimnagar Granulite, such as the Warangal Supracrustal rocks mentioned in section 3.2.1., but outcrop is generally limited in this area which may explain why they are not apparent in the geophysical data.

In the Alkali Feldspar Granites, the short wavelength magnetic data is similar to that further east with many short curvilinear features, but they are generally lower in amplitude and less organized. The western area includes sub-areas of much lower gradient magnetic signature, but these are a drop in resolution due to the aircraft flying higher above the ground due to various obstructions or legal requirements and are of no geological consequence. The Alkali Feldspar Granites potassium concentrations range from 2% to just over 5% which is not unusual for granitic rocks. Although there are areas of higher potassium within the EDC, the ratios of potassium to thorium or uranium are not elevated in those places, indicating that the local potassic highs are mostly related to a greater degree of exposure, primarily over the area of higher relief in the west of the EDC. This western part of the EDC is however crossed by distinctive bands of high uranium with a broad

curvilinear trend of 150° (as noted in the magnetic data as well) (Figure 12.2.1) which includes areas of mapped leucogranite, indicating a magmatic-hosted deposit. The mapped leucogranite in the south clearly coincides with the bands of well-defined high uranium concentration, with relatively elevated eU/eTh and eU/K ratios up to 0.7 and 9 and uranium concentrations of as much as 20 ppm in places, especially in a series of granitic outcrops that form two distinctive lines of hills that flank the broad ridge that is formed by the leucogranite. Further north the leucogranite is not mapped, but the gamma-ray data shows that it continues for a distance of over 150 km within Block-6 from coordinates 365553 / 1880764, 17°00'25.24N / 79°44'13.03"E to 288787 / 2013432, 18°11'58.99"N / 79°00'10.46"E and extends beyond the boundaries of the block at both ends. This distinctive band of lithologies also coincides with a broad gravity low for its entire length, which is almost certainly related. For most of its length there are two distinct bands of high uranium on either side, with an area of lower gamma-ray signature in the middle. At one place a second sub-parallel band appears centred on coordinates 340410 / 1960739, 17°43'41.05"N / 79°29'41.68"E, with the same pattern, and an isolated single sub-parallel band of very high uranium occurs at coordinates 319280 / 2005675, 18°07'56.72"N / 79°17'30.51"E with a concentration of over 12 ppm. Neither of these flanking bands are mapped as leucogranite, but it seems likely that they are the same lithology, and both coincide with areas of lower magnetic signature. Leucogranites are known to sometimes host uranium deposits (McKeechie et al. 2009, Chen et al. 2021), and these outcrops reach the required concentrations and ratios to potassium, albeit that there are no associated thorium highs. The pattern of the uranium highs suggest that the elevated uranium levels occur at the margins of the granite. There are other areas mapped as leucogranite nearby, but they are not linear in aspect and lack any distinctive gamma-ray signature.

The area of Migmatite Gneiss is illustrated in (Figure 12.2.2). The relatively low potassium and high thorium and uranium character is apparent, and thorium and uranium occur together in curvilinear bands that parallel the margins of the EDC and the Pranhita-Godavari Basin, with some locally very high concentrations and ratios to potassium, often close to but not coincident with local topographic highs. These features do not have coincident magnetic anomalies. The strongest thorium anomaly is over 250 ppm thorium, located at coordinates 388650 / 1965700, 17°46'33.11"N / 79°56'58.32"E with an eTh/K ratio of 190, and an associated uranium anomaly of 12 ppm. Thorium deposits are known to occur in vein type bodies that may represent the feeder systems to now eroded alkali intrusive, possibly carbonatite intrusions, and can be polymetallic containing base metals, rare metals, uranium, thorium and rare earth elements (IAEA 2019).

The Migmatite Gneiss area terminates along a 40° boundary along its northwest edge. Northwest of this boundary, the gamma-ray signature of the Grey Biotite Gneiss is totally different, being mainly potassic but higher in relative uranium than the EDC further to the west. There are magnetic lineaments that are parallel and close to this boundary, but they are no more prominent than many others. There is a topographic ridge that is broadly coincident, but it too does not appear to control the pattern of exposure. The conclusion is that the Migmatite Gneiss area is depleted in potassium due to alteration, with local highs of thorium in vein structures running through it. As such it is generally an area of interest for exploration, with the anomalously thorium rich veins being potential targets.

On the eastern side of the EDC, the short wavelength anomalies of the Archaean age basement gradually diminish in amplitude to the east-northeast over a distance of approximately 10 km reflecting increasing depth of burial of the basement below relatively less magnetic Proterozoic sediments of the Western Belt of Godavari Supergroup sediments in the Pranhita-Godavari Basin. Along or at least close to the boundary of the EDC and the Pranhita-Godavari Basin there is a narrow topographic ridge that is high in uranium and also relatively high in thorium, but less so than in other lineations, are low in potassium, and that have associated strong magnetic anomalies that appear to extend to sources dipping to the east below the basin sediments (Figure 12.2.2). The Godavari Supergroup sediments lie non-conformably upon the EDC (Burhanuddin 2017), although Biswas (2003) and DasGupta (2007) indicate that the boundary is faulted, albeit the throws of the faults along the boundary do not seem high. Note that the ridge is mapped in the north as Khammam ironstone and chlorite schist and continues further southeast down to a more clearly fault bound embayment of Pranhita-Godavari Basin rocks protruding south into the Archaean rocks by around 10km. Where the boundary changes from unconformity and/or low throw fault to clearly fault bound, the character of the gamma-ray anomalies along the contact changes. In particular, the magnetic anomalies are not present. High eTh/K ratios occur just west of the embayment at coordinates 409180 / 1947420, 17°36'41.74"N / 80°08'38.31"E with thorium concentrations of 90 ppm. The boundary to the east of the embayment has the highest eU/K ratios just under 30, U concentrations of 7 ppm at coordinates 419333 / 1945672, 17°35'46.27"N / 80°14'23.04"E. In between, around the west and south edges of the embayment, the boundary is marked by potassium enrichment, mapped as either quartzite or biotite-gneiss with local concentrations up to 6% at coordinates 411570 / 1941160, 17°33'18.41"N / 80°10'00.34"E. High grade uranium deposits are known to occur along the Archaean basement to Proterozoic sediment unconformity in the Athabasca Basin of Canada (Tschirhart et al. 2022). The deposits are often irregular in shape and localized around faults. There are parallels to be drawn with the geology of the EDC to Pranhita-Godavari Basin unconformity which identify this location as an area of potential economic interest.

Strong linear magnetic features cross the full extent of the EDC. The most prominent of these are widely spaced asymmetric magnetic highs that trend at around 70° and sometimes display an echelon pattern along their length. The anomalies gradually increase on the northwest side and are steep and more sharply defined on the southeast side. There is no apparent offset of other magnetic features across these lineaments, and they are interpreted to generated by dolerite dykes that belong to the Dharwar giant dyke swarm (formerly known as the Karimnagar dyke swarm). These dykes do not have symmetric anomalies when reduced to the pole, but in fact become negative linear features, meaning they have significant magnetic remanence, which is known to be the case for the Dharwar dykes and is typical of Proterozoic age dolerite dykes in general. The asymmetry of the anomaly cannot be modelled by a dyke plane dipping toward the northwest, and the way the dykes cut across topography in a linear fashion indicates that they are either vertical or steeply dipping. So, the asymmetry is more likely due to the angle of the magnetism of the dyke which will be a combination of induced and remanent magnetism. Where these dykes pass eastward closer to the edge of the craton, an interesting phenomenon occurs; the magnetic highs now appear as magnetic lows, often quite clearly in continuation with the magnetic high anomalies further west. Whilst it is possible that this is the result of a

change in polarity of the magnetic remanence in the dyke either in depth or horizontally, the negative anomalies are generally narrower, more symmetric, and generally less prominent than the positive ones, and also appear offset the boundary of the EDC with the Pranhita-Godavari Basin in a few locations by as much as 5 km. These negative anomalies are interpreted as fractures associated with the dyke intrusion further west.

Another set of slightly less prominent but still significant magnetic high lineaments have a trend of approximately 30°, crosscutting the Dharwar dykes mostly without obvious offsets of either. These linear anomalies are also but less obviously asymmetric, being more sharply defined on the southwest side and are also interpreted as dykes. When reduced to the pole they become prominent lows which suggests that magnetic remanence is significant. Parallel to the 30° dykes is a prominent magnetic low lineament that clearly offsets the EDC to Pranhita-Godavari Basin boundary and is therefore considered a significant fault line. This fact underlines how the trend of many of the dykes are structurally controlled by possibly preexisting fractures.

Within the EDC there are a number of prominent local magnetic anomalies of particular interest, some of which also have associated gamma-ray signatures.

In the south, a high magnetic anomaly occurs at coordinates 318230 \ 1888820, 17°04'35.61N / 79°17'30.64"E which, as well as the main dipolar anomaly, also appears to have a weaker superimposed ring structure of magnetic highs and lows apparent in the first vertical derivative of the magnetic anomaly (Figure 12.2.3). There is another more subtle ring like magnetic feature a little further northwest, with an egglike shape centred at coordinates 308450 \ 1902950, 17°12'12.33"N / 79°11'55.47E. Both of these intrusions become very prominent and symmetric when reduced to the pole (Figure 12.2.3) suggesting that neither has significant remanence. Of the two, the southern magnetic anomaly is about 9 km in diameter and has an associated uranium high of up to nearly 6 ppm in the core. Some apparent high ratios of uranium and thorium to potassium in the rings are in fact due to local potassium lows, but the west side of the ring structures appear to have a topographic expression. The northern of the two magnetic anomalies also has a central magnetic anomaly and has locally enriched uranium in a small hill of 17 ppm, eU/K over 5. Although weak, the ratio eTh/K mimics the outer ring of the magnetic anomaly (Figure 12.2.3). Despite the lack of strong thorium anomalies, the ring like magnetic anomalies and associated uranium highs mark these two locations as potential alkali intrusions, possible carbonatites of significant size.

Models of the two intrusions discussed above based on the reduced to pole magnetic anomaly data are provided in Figure 12.2.4. The lines of cross section are shown in Figure 12.2.3, and Coordinates of the profile end points are as follows:

A	299443 / 1899255, 17°10'09.39"N / 79°06'51.89"E
A'	316441 / 1906405, 17°14'07.08"N / 79°16'24.85"E
B	313541 / 1885630, 17°02'50.49"N / 79°14'53.03"E
B'	323119 / 1893791, 17°07'18.68"N / 79°20'14.55"E

In both cases a layer of non-magnetic overburden is included. The Euler solutions of structural index zero that trace the edge of these bodies indicate that this layer is around 50 to 100m thick, so the bodies may not be exposed at the surface. This certainly appears to be the case from the satellite imagery of the area. But it must be kept in mind that the magnetic solutions may reflect the depth at which relatively unaltered rock occurs, and weathered remnants of the intrusions may occur at shallower depths. The Phillips trend solutions show that the contacts of these bodies are essentially vertical or slightly dipping inward in some places. The models employ the following parameters:

- Magnetic Declination/Inclination 0°/90° (reduced to the pole)
- Magnetic Intensity 44102 nT

The background magnetic susceptibility of the gneissic country rocks is set to 0.002 SI as employed by Sarma & Krishna Rao (2005). The models were constructed in 2.5 D using GM-SYS profile modelling operating under Geosoft Oasis montaj®. Magnetic remanence is considered to be negligible given that the bodies become so distinct and symmetric when reduced to the pole. The line of section A-A' was chosen to be as close to 2.5D as possible, which is not entirely the case given that the body is a ring structure. However, the model was found to be relatively insensitive to variations in the Y dimension and the 2.5D approximation appears to be more or less valid. The various rings of the intrusion are modelled by vertical bands of rock with of different magnetic susceptibility. The susceptibility values required are high, varying from 0.01 to 0.028 SI. The steep sides of the body are confirmed by the modelling, and the body is modelled to a depth of 10 km although there is no significant control on how deep the body actually goes.

Line of section B-B' runs through a more homogenous body that fits the 2.5D approximation well. In this case a single high magnetic susceptibility of 0.05 SI was employed, and a local small high on one side was modelled using a branch of the intrusion. As with the previous model, the depth of the body extends to 10km below the surface but is not well constrained. In both models the dimensions of the reduced to pole anomalies closely match the dimensions of the bodies used to model the data.

Reduced to pole magnetic anomaly data also highlights a smaller magnetic anomaly further to the northwest at 294200/1908600 17°15'11.62"N / 79°03'51.34"E that has an associated eTh/K anomaly too, with a value of 14. Other scattered high ratios nearby are due to localised lows in the potassium, but potassium is if anything locally quite high at just under 5%, meaning the high relative thorium is significant.

An isolated very prominent hill at coordinates 329420 / 1994370, 18°01'51.99"N / 79°23'18.80"N has a low uranium character but a strong magnetic high (one of the strongest in the entire survey area) and has been mapped in detail as deformed banded quartzite and ultramafic rocks of Karimnagar granulite. Given the strength of the magnetization, this hill is of obvious interest for possible alteration and mineralization.

A strong magnetic high over 11,000 nT occurs at coordinates 291450 / 2067280, 18°41'10.97"N / 79° 01' 21.05"E in the northern part of the EDC in Block-6 centred on a small hill. This magnetic anomaly is low in gamma-ray radiation similar to the previously described feature. As such it too could be an area of ultramafic rocks of Karimnagar granulite.

Further north, where the major 120° trending fault occurs, a distinctive line of isolated but elongate hills are scattered along the north side of the fault line. The Godavari River valley is associated with this fault, although the fault runs along the southern slope of the valley. There are gamma-ray highs associated with the isolated hills, but they seem to be mostly due to exposure and the ratios are not particularly noteworthy. Neither are there any local magnetic highs associated with this fault line. However, just north of this structure, and south of the Deccan Traps, within the valley associated with the fault, there is a subtle ring structure in the magnetic data at coordinates 295220 / 2102043, 19°00'02.71"N / 79°03'16.68"E (Figure 12.2.5) partially obscured by the magnetic anomaly created by the fault, that is interpreted as a possible alkali intrusion. The ring structure is approximately 10 km by 8 km and appears to have been distorted by shear in the vicinity of the fault line and along its northeast side. There is an associated gamma-ray signature with a central potassium high, with outer rings of uranium and thorium separated by a narrow ring of higher potassium. eTh/K is as low as 2 in the central core and over 32 in the outer rings. eU/K is less than 0.1 in parts of the core, and up to 3 in the rings. The potassium in the core shows evidence of subtle ring structures too. The topography of the valley includes a low curving ridge that follows the outer rings on the west side of the intrusion, at one point intersecting with the river where there are shallows evident in the bed of the Godavari River that look like rock exposures in the Sentinel-2 satellite image.

12.3 Geophysical character and anomalies of the Archaean Bastar Craton

The vast majority of the Bastar Craton within Block-6 is mapped as Bengpal Gneiss the only other major units being the Bhopalpatnam Granulite belt that lies close to the western edge of the craton in the south, and the extensive Dongargarh Granite in the northwest. Whilst the granulite belt is hard to distinguish from the Bengpal Gneiss in either the magnetic or gamma-ray data, the Dongargarh Granite is quite distinct, as discussed below.

Magnetic sources determined by Euler deconvolution are dominantly of shallow origin, mostly less than 200m below ground, across the entire Bastar Craton. Deeper solutions of over 400m occur in association with the Bhopalpatnam granulite along the eastern margin of the craton, as well as associated with specific local features within the craton.

The overall magnetic character of the Bastar Craton along its western side where it is in fault contact with the Pranhita-Godavari Basin, and incorporates the Bhopalpatnam Granulite belt, is similar to the EDC on the opposite side to the rift. The magnetic signature is dominated by short wavelength curvilinear anomalies within which various trends can be determined. Along much of the boundary with the Eastern Belt of the Proterozoic Godavari Supergroup sediments in the south the magnetic fabric within the Bastar Craton is strongly parallel to the boundary, but at coordinates 427440 / 2088770, 18°53'23.10"N / 80°18'39.81"E on the boundary this relationship changes. At this point a prominent 160° trending fault or shear zone runs through the Bastar craton. Northwest of this fault, the magnetic trends in the Bastar Craton are initially poorly defined adjacent to a continuation of the Eastern Belt of Godavari Supergroup sediments. But further northwest the Bastar Craton is in direct contact with the much younger Gondwana Supergroup sedimentary fill along a clearly faulted boundary. In this part of the boundary between the craton and the younger sediments the trends in the magnetic data whilst still not exactly linear are at a high angle to the boundary, truncated at the fault.

Continuing further north the Pranhita-Godavari Basin divides either side of an inlier of Bastar Craton. The west side of the inlier is in direct contact with the Gondwana Supergroup sediments, and although the dominant magnetic trends in the inlier are more closely parallel to the boundary and show some curvature towards it at the southern tip of the inlier, the overall impression is still very much of a clean faulted break. The part of the Pranhita-Godavari Basin that lies between the Bastar Craton inlier and the main exposure of the Craton to the East is almost all Eastern Belt Proterozoic age Godavari Supergroup formations. The boundaries between the Godavari Supergroup sediments and the outcrops of the Bastar Craton on both sides are more gradational in nature and appear to be an unconformity and/or low throw faults in the same way the Western Belt Godavari Supergroup sediments are related to the eastern margin of the EDC.

So, while the Bastar Craton is in fault contact with both generations of sedimentary basin, the nature of the fault contact is quite different. The earlier faulting appears to include a significant degree of shear or compression within the Bastar Craton in the south, whereas the later fault contacts with the Gondwana Supergroup sediments shows no such impact and appears like a clean brittle break. And in the north the brittle break with the Gondwana Supergroup persists whilst by contrast the contact with the Eastern Belt of the Godavari Supergroup is more gradual and lacks the strong shearing seen further south.

Further east from the Bastar Craton edge, the magnetic data changes in character, becoming less like the EDC in nature. The amplitude of the short wavelength magnetic anomalies becomes generally less, with areas of stronger or weaker anomalies separated by structural breaks, probably faults, that have a general north-northwest trend. Overall, the west margin of the Bastar Craton is much more tectonically disturbed than the east margin of the EDC.

The gamma-ray signature of the Bengpal Gneiss also contrasts to that of the granitic gneisses of the EDC. Overall, the intensity of the signal is much weaker, which could be due to thicker over burden, but this is

unknown. The gamma-ray signature is mainly potassic and has a weakly defined fabric that follows the same general north-northeast trends as the structural features described above.

The most prominent feature in the Bastar Craton within Block-6 is the Dongargarh Granite. It is worth paying extra attention to this body in the light of the similar aged Malanjkhand Granite further to the north outside of Block-6 that hosts an important hydrothermal copper deposit that has many of the characteristics of a copper porphyry deposit or deep hydrothermal type deposit. The southern part of the Dongargarh Granite exposure in Block-6 comprises an elongate approximately ovoid shaped pluton that is very well defined by high potassium (Figure 12.3.1) mostly in the 3 to 4% range. The character of the granite is clear enough that other areas currently mapped as the same unit to the south and southwest are probably not the same. Uranium is also generally slightly elevated, but thorium is generally low. Further north the boundaries of the granite are less clear. The granite wraps around an embayment of Bengpal Gneiss that itself encloses a roughly north to south trending range of hills mapped as phyllitic quartzite that are distinctly weak in gamma-ray signal and relatively weakly magnetic too. North of the embayment the areas of mapped Dongargarh Granite show the same general pattern of gamma-ray data as in the south but is less consistently high in potassium. Magnetically the Dongargarh Granite sits on a large regional magnetic dipolar anomaly which covers the entirety of the outcrop. All of the magnetic high of the dipole in the south is present, but only about half the equivalent magnetic low to the north is within Block-6. The magnetic data reveals a suite of closely spaced northwest trending dykes crosscutting the granite (Figure 12.3.1), and are described below, as well as a few much larger dykes that cut across the granite in the north in and east to west direction. Some local magnetic highs are observed along the fringes of the granite, in particular at coordinates 424800 / 2206425, 19°57'10.27"N / 80°16'52.81"E but they do not coincide with gamma-ray anomalies. On the other hand, there are a number of interesting gamma-ray anomalies on the fringes of the granite that are clearly structurally controlled. Whilst at first glance the ovoid pluton appears quite uniform in potassium and weak in thorium, a close examination of the eTh/K ratio (Figure 12.3.1) reveals that it is distinctly banded, with concentric rings of slightly higher or lower potassium and thorium. Ford et al. (2007) state that elevated potassium relative to thorium is a good way to distinguish potassic alteration from simply higher potassium lithology, and although the eTh/K ratio varying between about 6 and 8 is not particularly low by general standards, it shows clearly as a low in the context of the surrounding lithologies. So, it is possible that potassium alteration, known to be associated with Olympic Dam and Copper Porphyry deposits has broadly effected the Dongargarh Granite. A notable feature is that local thorium and uranium highs occur at two locations along the west side of the southern part of the granite at the ends of two faults that pass through the granite at a trend of approximately 115° and are picked out as relative highs in the eTh/K ratio, low in potassium (hence the ratio) and lows in the magnetic data. Along each fault the highest eTh/K ratios occur at the point where they meet the country rocks on the west side, with ratios of over 40 eTh/K, 80 ppm thorium, as well as 12 ppm uranium occurring in the vicinity of coordinates 420600 / 2193000, 19°49'52.96"N / 80°14'30.40"E. The magnetic anomalies noted on the fringe of the granite above actually occur in a gap in the elevated eTh/K ratios, between where the two fault lines emerge from the granite. So, whether or not the high potassium in the granite is inherent to the lithology or later due to alteration, as suggested by the ratio to thorium, it appears that there has been a period of

alteration along two fault lines that may have resulted in elevated thorium and uranium in the adjacent country rocks.

Wrapping around the southern edge of the Dongargarh Granite is a prominent ridge of the Surjagarh Hills formed by the banded ironstone formations (BIF), ultramafic rocks and phyllites of the Bailadila Formation. Clearly this formation has been disrupted and folded by the intrusion of the granite. There is a strong magnetic anomaly associated with this formation whereas all of potassium, uranium and thorium appear as lows. The Surjagarh Iron Ore Mine is located in the nose of the fold at coordinate 433400 / 2170600, 19°37'45.98"N / 80°21'53.29"E close to a strong magnetic high, but as noted in the description of this deposit the highest grades are generally altered regions of the Banded Hematite Quartzite due to supergene enrichment resulting in concentrations within structural traps, and consequent local magnetic lows within the generally high magnetic formation. So, the proximity of the magnetic high to the mine may be coincidental, or indicative that originally highly magnetic rocks generate the highest grades when altered. Based on the new airborne magnetic data, the next most prominent magnetic high occurs just 4km east of the known deposit along the ridge at coordinates 437600 / 2171400, 19°38'12.50"N / 80° 24'17.40"N at a prominent point on the ridge line. The magnetic anomaly at this point is over 3100 nT, compared to just over 2000 nT at the Surjagarh Iron Ore, but it is the areas of lower magnetization along strike to the west and the northeast of this anomaly that may be where supergene enrichment has occurred.

A second ridge of Bailadila Formation rock including BIF occurs south of the Surjagarh Hills which is also folded such that the nose of the fold is just within Block-6 at coordinates 446150 / 2160800, 19°32'28.56"N / 80°29'12.06"E but there is little magnetic expression of these hills. Bailadila Formation BIF also occurs in some isolated hills further south. In this case there is a small but significant over 3000 nT magnetic anomaly at coordinates 444800 / 2140200, 19°21'18.26"N / 80°28'27.89"E that is part of a small north verging apparently folded band of higher magnetization. The area along strike just to the east of the high anomaly may be the nose of the fold, and is of lower magnetization, so is of interest.

The Thanewasna and Dubarpeth quartz reef epithermal vein type deposits with significant copper mineralization are present on the northern part of the Bastar Craton as described in Section 3.3.3. In both cases the mineralization occurs within shear zones but only one fracture that starts at the Dubarpeth deposit is apparent in the magnetic data (Figure 12.3.2). There are no strong magnetic anomalies located at the sites of the ore bodies. The Dubarpeth lies close to newly identified probable green stone belts described later in this section, just to the east, and may be related. The sinusoidal gamma-ray anomaly that passes through the Thanewasna deposit is due to river sediments only. Investigations along the fracture that appears associated with the Dubarpeth deposit, and parallel fractures nearby, is suggested.

An approximately 5 km wide circular magnetic anomaly with a high of 1300 nT occurs at coordinates 409200 / 2250600, 20°21'04.79"N / 80°07'48.19"E mapped as meta-gabbro in the far north of Block-6. There is a cluster of topographic features in the area that are centred on the anomaly. In addition, potassium, uranium

and thorium are all distinctly low relative to the surrounding area where this anomaly occurs. Just further west at coordinates 400200 / 2245200, 20°18'07.52"N / 80°02'38.88"E there is a north-northwest trending ridge of the same unit that also creates a locally strong magnetic high and has the same low gamma-ray signature. It is therefore reasonable to assign these anomalies to the lithology alone.

Another roughly circular magnetic anomaly occurs along the western margin of the Bastar Craton at coordinates 395300 / 2138400, 19°20'12.61"N / 80°00'11.67"E (Figure 12.3.3). The first vertical derivative of the magnetic anomaly indicates ring like structures occur, suggesting a possible alkaline complex. In a similar fashion to the two prominent magnetic anomalies described from the southwest part of the EDC in Block-6, this anomaly becomes a distinct high when reduced to the pole, indicating that magnetic remanence is not a factor. The magnetic anomaly is coincident with an area of low potassium but is otherwise unremarkable in the gamma-ray data. An area of slightly increased uranium on the southwest side appears more due to deposition of river sediments than anything to do directly with the intrusion.

A distinctive geological unit, centred on coordinates 35800 / 2207800, 19°54'41.06"N / 76°34'05.73"E measuring some 20 by 13 km in size, occurs on the western margin of the Bastar Craton, at the point where eastern branch of the sedimentary basin starts to bifurcate either side of an outlier of the Bastar Craton (Figure 12.3.4). The sediments of the eastern branch are mapped as mostly Proterozoic in age and are discussed below in relation to prominent west trending dykes that appear to run under the sediments. The unit is strong in all radioelements, but is particularly potassic in nature, with some pockets of different character that appear to be small, isolated pockets of mapped Proterozoic sediment. Despite being mapped as Bengpal Gneiss in continuation with the rest of the craton, it is much less magnetic, and it also appears to be offset by approximately 6km in a sinistral sense along the main basin bounding fault, which it straddles. The possibility that this is a fairly recent normal fault is discussed in Section 12.1.1. The western margin of the unit also appears to be fault bounded where it meets the Godavari Graben. The magnetic trends of the Bastar Craton can be seen weakly continuing beneath the formation, forming the basement. Therefore, the formation appears to be relatively thin, and probably sedimentary in origin.

In the northern part of the Bastar Craton in Block-6, west of the Dongargarh Granite, there are major structures that trend at approximately 150° that are apparent in the magnetic data. Interesting anomalies occur in two locations associated with these structures. Running from coordinates 382000 / 2198900, 19°52'57.86"N / 79° 52' 22.22"E to 390800 / 2171400, 19°38'05.19"N / 79°57'30.60"E there is an approximately 32 km long curvilinear feature in the gamma-ray data, in which all three elements are higher than the surroundings (Figure 12.3.5). This band of higher radiation follows the curving line of the westmost of the group of magnetic lineations that run through this area and truncate the magnetic fabric of the Bengpal Gneiss. Banding along the length of this feature is observed in the ratios. The first band on the west side is about 5 km wide and is relatively high in potassium, with the highest concentration at over 5%. Adjacent to this is a similar width band that is higher in both uranium and thorium, followed by a thin weak band of relatively high potassium around 1km wide, and another similar width band of high uranium and thorium again. These

appear to be bands of metasediments of metavolcanics within the generally granitic terrain, much like ironstones that occur near the Dongargarh Granite, but of different character with a generally much lower amplitude magnetic character (Figure 12.3.5). Further south along this same structure, there is a distinctive potassium high of 5% that in this instance correlates with a strong magnetic anomaly at coordinates 411900 / 2147000, 19°24'55.24"N / 80°09'39.11"E. Uranium and thorium are also a little elevated in this location, but both eTh/K and eU/K ratios are low with respect to their surroundings in this location, and there is no eU/eTh ratio anomaly. There is some suggestion that the potassium high stretches out to the north and south along the line of the structure. The magnetic data shows that the anomaly actually sits within a 3 km wide band of low magnetism which is part of the major structural trends in this area. The body has the general character of a VMS but is on the large size for this sort of deposit, and it may just be an isolated area of different lithology. On the other hand, in some examples the central ore body of a VMS may be capped by an associated laterally extensive magnetic layer (Gunn and Dentith 1997), with both local and dispersed potassic alteration. Regardless, the litho-tectonic mapping has identified a number of probably areas of un-recognized metasediments and/or metavolcanics which could be so called "greenstone belts" as found in many Precambrian terranes in the world. Greenstones are known to host deposits of base metals such as gold, silver, copper, lead and zinc, and therefore should be the focus of more detailed geological mapping.

South of the anomaly described above, the proposed metasediments and metavolcanics pinch out into the major 160° degree trending structure that appears to be a fault or narrow shear zone, described at the beginning of this section. Where the shear approaches the edge of the Bastar Craton, a significant area of high potassium rocks with concentrations of up to 4% occurs along the east side (Figure 12.3.6). This area is centred on coordinates 428200 / 2105400, 19°02'24.23"N / 80°19'03.59"E and is 30km long parallel to the shear and 8km wide perpendicular to the fault. Magnetically it does not stand out strongly from the adjacent cratonic rocks but falls within the currently mapped extents of the Bhopalpatnam granulite. The boundary can be seen in the magnetic data but is not strongly marked, and the edge of the unit does have slightly higher uranium and thorium character, with up to 44 ppm thorium in places. This unit may be a local area of more granitic rock within the granulite. Beyond the south tip of this unit, the shear widens and turns to trend southeast along the Bastar Craton margin. Here the shear displays a strong local thorium and uranium character and appears to be a continuation of the metasediment/metavolcanic belt from further north, that initially wraps around the granitic body and appears to be highly deformed. The magnetic anomalies in this area are parallel to the craton edge, and relatively strong magnetic lineaments occur coincident with banding in the gamma-ray data along the faulted contact with the Eastern belt Godavari Supergroup sediments. This feature continues all along the edge of the Bastar Craton, generally becoming narrower toward the south, before widening again somewhat just before pinching out altogether where it meets the EGMB.

A small but strong magnetic anomaly of over 2000 nT occurs at coordinates 375000 / 2238000, 20°14'08.01"N / 79°48'11.91"E and is elongate with a trend of 115°. The anomaly occurs close to east-west trending dykes described below, which are also magnetic, but differ from them in that the dykes have no gamma-ray signature. On the other hand, this magnetic anomaly has a coincident uranium anomaly, with

eU/eTh and eU/K ratios of 0.7 and 17 respectively, and >16 ppm of uranium. There is no unit mapped where the anomaly occurs, it is all assigned as Bengal gneiss. An outcrop of ultramafic rock is a possible explanation.

As noted above, there are sets of dykes that are seen within the Bastar Craton in Block-6. Neither of these dyke swarms are shown in the mapped lithology. Both are apparent in the magnetic data picked out by asymmetric (high and low) linear anomalies, one set trending at around 140° ("NNW") (Figure 12.3.1) and the other around 80° (approximately east-west) (Figure 12.3.7). The NNW dykes occur as a dense swarm, most apparent within the ovoid shape of the southern exposure of the Dongargarh granite and appear to be restricted to the northeast corner of Block-6. The magnetic anomalies are obscured by the strong magnetic signature of the Bailadila Formation south of the Dongargarh Granite, but weaker anomalies south of the Bailadila Formation suggest that they do continue to the south southeast although perhaps at greater depth. Much further south there are some curvilinear magnetic anomalies of a similar trend, but these appear to be more related to the structural fabric of the Bengal Gneiss. To the north the relationship to the west trending dykes is ambiguous. In many places the NNW dykes appear to truncate at the west trending dykes, but in one location they appear to offset the west trending dykes. Field observations and/or dating would help to resolve this issue.

The west trending dykes are fewer in number, but the associated magnetic signal is much stronger than the NNW dykes and they are more continuous, albeit that they are occasionally broken and offset in an en echelon fashion. These dykes may be a continuation of the Dharwar giant dyke swarm as suggested by Srivastava et al. (2021). The East-West dykes only occur in the north part of Block-6 and are notable for the fact that they continue under the Proterozoic age basin rocks that occupy the eastern branch of the Pranhita-Godavari Basin in the north of Block-6. The magnetic anomalies of the dykes become less sharp as they are buried beneath the East Belt Godavari Supergroup sediments but at least one of the dykes shows no signs of disruption as it crosses the Bastar Craton to Pranhita-Godavari Basin divide meaning it must post date any significant tectonic activity along that boundary. Since the Proterozoic basin sediments overlay and almost certainly post-date the dykes, this indicates that the basin formed by sagging along this part of the boundary as observed along much of the western margin of the Pranhita-Godavari Basin where the Basin meets the EDC, and unlike the boundary between the Proterozoic basin and the Bastar Craton further south. This observation is supported by the fact that some of the Bastar Craton related magnetic anomalies appear to be seen continuing beneath the Proterozoic basin where the dykes occur, although the presence of the strong dyke anomalies obscures this observation. On the western side of the eastern branch of the Pranhita-Godavari Basin the northmost dyke appears to continue into the Bastar Craton inlier, supporting the concept that this transition is an unconformity too. Within the area of the Proterozoic basin the signature of the dykes becomes lower in amplitude toward the south, suggesting the sediments are deepening in that direction up to the margin of the Godavari Graben.

There are four east-west trending broad anomalies that are consistent with the general continuation of the East-West dykes beneath the Gondwana basin sediments in the main Godavari Graben to the west of the Bastar Inlier. If so, they are not continuous into the Bastar Craton, supporting the concept that the west side of the Bastar Craton inlier is fault bounded in the same fashion as the boundary of the main rift further south.

Furthermore, the dykes appear to be deflected in a fashion consistent with sinistral shear along the margin of this fault, as discussed in Section 12.1.1.

There is an isolated hill at coordinates 476000 / 2097300 18°58'04.73N / 80°46'19.25"E that has a high magnetic anomaly >400 nT, elevated eU/eTh, but the concentrations of all the radioelements is low. The unit is clearly mapped as calcareous quartzite, and therefore the anomaly is probably entirely due to the local lithology.

A number of fold structures are apparent in the magnetic data within the Bengpal Gneiss in the eastern part of the Bastar Craton in Block-6 (Figure 12.3.8). In each case the fold is marked by a band of relatively high magnetism that closes towards the north-northwest or south southeast in the direction of the major structural trends. The folds are open toward the south southwest, although the southern extent of the most northerly example is outside the block coverage. The closures of four folds are located at coordinates 492500 / 2047600, 18°31'08.12"N / 80°55'44.20"E, 478300 / 2074200, 18°45'33.24N / 80°47'38.83"E, 488700 / 2071000, 18°43'49.42"N / 80°53'34.11"E and 490500 / 2112900, 19°06'32.71"N / 80°54'34.85"E. The first of these, the most southerly, is the least prominent in the magnetic data and is not mapped as anything different within the Bengpal Gneiss. But seen in the RTP data (Figure 12.3.9) it appears to close to south-southwest, and forms part of the same fold structure as the second fold that closes to the north-northwest but slightly offset in the centre of the fold. The second is mapped as having a core of quartzite, that is essentially non-magnetic, rimmed by a band of grunerite magnetite quartzite which generates the curving anomaly. The third is small, lies just to the east of the second, also closes to the north-northwest, also has a quartzite core, but its' south-southeast closure is not well defined. The last of the four, further north, is partially mapped, with the rim generated by a combination of grunerite magnetite quartzite and gabbro. The south-southwest close of the fourth fold structure is outside the survey boundary. Of these folds, only the fourth in the north has a gamma-ray signature; the magnetic anomaly around the rim is coincident with slightly elevated thorium and uranium with respect to potassium, whilst the core has relatively high potassium, up to nearly 4%, with eTh/K of around 4. This does not indicate particularly high concentration of potassium, but it is higher than most of the surrounding Bengpal Gneiss. Only this fact and the observation that similar structures nearby lack elevated potassium, suggests potassium alteration may have occurred in the core of this fold at coordinates 489600 / 2114200, 19°07'14.99"N / 80°54'04.02"E. These structures are of general interest as they are probably folded synclines of metasediments and/or metavolcanics lying upon the Bengpal gneissic basement, and as such are areas of possible mineralization, even though they mostly lack strong anomalies.

A relatively large area of elevated thorium and uranium relative to potassium occurs in the east part of the Bastar Craton within Block-6, approximately 22 km north to south by 9 km east to west. The highest eTh/K ratio of 1022 occurs at coordinates 482300 / 2096000, 18°57'22.66"N / 80°49'54.74"E in one locality within the generally higher ratio. At this point uranium reaches 4 ppm and thorium 36 ppm. This entire area is relatively weakly magnetic and corresponds to a flat valley bottom, suggesting we are looking at surficial deposits only.

Kimberlites are known to occur within the Bastar Craton further east of Block-6 as previously discussed, see Section 12.1.2.

12.4 Geophysical character and anomalies of the Eastern Ghats Mobile Belt

The southeast part of Block-6 is within the Eastern Ghats Mobile Belt. A large part of this area to the west of the Chintalapudi Sub-Basin of the Godavari Graben is mapped as “Peninsular gneiss”, a general term for the gneisses of the EDC, but has undergone complex deformation in this area. Most of this part of Block-6 can be thought of as occupying the transition zone between the EGMB and the two cratons described above. Only further to the southwest in Block-6 where units of the EGMB itself are mapped do we see a distinct northeast trend to the magnetic anomalies reflecting the north-westward compression associated with the development of the EGMB.

Within this complicated area, two strong local magnetitic anomalies stand out. The first one is a large anomaly centred on coordinates 448300 / 1845500, 16°41'29.71"N / 80°30'54.31"E coincident with a group of hills, which is roughly circular in aspect, about 25 km wide, and has a poorly defined short wavelength ring magnetic anomaly around the edge that includes occurrences of chromite along the eastern side (Figure 12.4.1). So, the margins of this intrusion could be of significant economic importance. This anomaly falls within an area mapped as Eastern Ghat charnockite, a high grade metamorphic rock. There is a suggestion of an inner ring of very weak magnetism, but there is also a hint of a local magnetic high in the centre. The most prominent gamma-ray anomalies are a low eTh/K (Figure 12.4.1) and eU/K ratios, mainly due to low thorium and uranium with some locally high potassium on the west side in the vicinity of the chromite occurrences. The large hill in the centre of the magnetic anomaly has a notably higher eU/eTh ratio just below 0.7 in places, which is in fact due to locally even weaker thorium not elevated uranium, both being low in concentration within the area of the anomaly. A cluster of diamond occurrences occur just to the southwest of this feature. However, this is an area of active Meghalayan age alluvial deposits near the confluence of the Krishna and Munneru Rivers, so they are probably detrital in origin. The possible origins of these diamonds are discussed above in Section 12.1.2.

This pattern repeats further north within the same geological unit where a group of smaller hills centred on 455200/1871300 all have the same ratio anomalies associated with them, as well as a local magnetic anomaly. The rim of this anomaly would be worth further investigation in the light of the observations above.

Another cluster of diamond occurrences occurs at coordinates 444000 / 1874200, 16°57'03.29"N / 80°28'26.55"E but other than an unremarkable small uranium and thorium high in the area, there is nothing of note to link the occurrences at this location to the local geology. There is certainly no evidence of a magnetic anomaly associated with a potential kimberlite pipe.

The second of the two strong magnetic anomalies occurs at coordinates 449700 / 1911500, 17°17'17.54"N / 80°31'36.20"E. This anomaly is also located over a prominent topographic feature that is also mapped as Eastern Ghat charnockite and khondalite. A strong dipolar magnetic anomaly occurs in association with this feature, and the entire area of the body where it is exposed in the hills has a slightly increased

potassium level compared to the surrounding rocks, especially on its southern side, but there are distinct eTh/K and eU/K ratio lows. The entire body is surrounded by an area of low eU/eTh and a less distinctive high eTh/K ratio with a variable width, but generally of the order of 5km wide. The highest local thorium concentration is 37 ppm in this contact region, at the west end of the charnockite. The inference is that there has been alteration in the surrounding gneiss that resulted in higher thorium levels, possibly at the same time the metamorphism that created the charnockite occurred.

A band of alkali granite outcrops occur in a broad and discontinuous band running south southeast and centred on coordinates 427434 / 1889957, 17°05'34.37"N / 80°19'04.59"E. These rocks have a high gamma-ray signature, being highest in uranium which is up to 12 ppm and thorium that reaches over 100 ppm, but no significant associated magnetic anomaly. So, this feature is mainly of interest because of the elevated uranium and thorium.

Further north there is another prominent hill trending west-southwest at coordinates 441800 / 1932600, 17°28'43.45"N / 80°27'6.57"E that marks the location of the mapped Chimalpahad Complex, a layered igneous complex of basic and ultrabasic rocks believed to represent the chamber of an island arc (Dharma Rao et al. 2011). The main mapped body has no related strong magnetic short wave anomalies (Figure 12.4.2) but does have a clear strong eU/eTh ratio of over 2. Uranium levels are in fact not high, thorium levels are low, as too is potassium. The increased eU/eTh ratio and distinct areas of low thorium and potassium extend further south than the mapped extent of the complex (Figure 12.4.2) onto a southwest trending ridge that includes a cluster of chromite occurrences centred at coordinates 434317 / 1917003, 17°20'15.19"N / 80°22'54.56"E. The area to the south of the Complex is generically mapped as Peninsular Gneiss, but this same area has been described as Khammam Schist by Banothu and Babu (2022) whilst admitting that the schists only occur as "sporadic enclaves" within the gneiss. The fact that it is on a ridge adjacent to the main outcrop diminishes the possibility that the gamma-ray signature has been transported from the main mapped areas. Smaller patches of the complex are indeed mapped in this same area, but the low magnetic intensity of the complex does not extend into this area. Rather, the character of the data is more like elsewhere in the Peninsular Gneiss. There is a sharp change in the short wavelength magnetic data along the southeast side of the mapped Chimalpahad Complex, and the boundary is also marked by deeper magnetic anomalies with the same trend, which are offset in one location by a northwest trending fault. The persistence of the gamma-ray signature associated with the complex to the south and east, the change in shallow magnetic anomalies, and the presence of the deeper sourced anomalies all suggest that the complex extends in this direction but changes in magnetic character in the same areas where the chromite occurs. It has been suggested that the complex was thrust to the northwest during the formation of the EGMB (Dharma Rao and Santosh 2011), so that the igneous complex may be tilted, and we are looking at the chamber at least partially in its side. In this scenario chromite occurrences could be sourced from the more magnetic layers of the complex in this area.

Close by the Chimalpahad Complex, just to the east, a distinctive gamma-ray anomaly marks the location of a small area of mapped Khammam staurolite, kyanite mica schist, located at coordinates 454200 / 1927850,

17°26'09.92N / 80°34'07.38"E that has elevated uranium at 12 ppm, elevated thorium at 46 ppm thorium, but only slightly high potassium at 1.5%. So, this unit is of interest as a source of the actual radioelements of uranium and thorium.

At the southern end of the Bastar Craton within Block-6, where it transitions into the EGMB, the contact with the younger basin-fill sediments swings from north-northwest to southwest, reflecting the dramatic impact of the Eastern Ghats Mobile Belt (EGMB) that was thrust toward the northwest in the Mesoproterozoic. The structural trends seen in the magnetic data swing into this same trend, forming a narrowing tongue of EGMB metamorphic rocks in direct contact with the Gondwana Supergroup sediments on the southeast side and mostly with West Belt Godavari Supergroup sediments on the northwest side. At its southwestern extremity there is a narrow band of Gondwana sediments, clearly marked by its less active magnetic signature that is a narrow neck of the Godavari Graben that links the main area of the rift to the Chintalapudi Sub-Basin to the southeast. Some local magnetic highs occur in association with minor outcrops of banded magnetite quartzite within the gneiss, for example at coordinates 498400 / 1987600, 17°58'35.87"N / 80°59'05.60"E. Recently this area within the EGMB to the east of the Chintalapudi Sub-Basin has been described as part of the EDC (Burhanuddin et al. 2024) suggesting that the EDC underlies the entire Pranhita-Godavari Basin. The gravity data indicates that the basin is deepest along its eastern side, suggesting the EDC to Bastar suture may well be located along that side of the basin, but the character of the gamma-ray and magnetic signature within the EGMB is different from both the Bastar Craton and the EDC. Therefore, the new geophysical data does not support or refute the assignment of the Archaean rocks east of the Chintalapudi Sub-Basin to the EDC but underlines the impact of the EGMB deformation on the earlier cratonic rocks.

In the part of the EGMB to the east of the Chintalapudi Sub-Basin, at one location a linear feature is apparent in both the magnetic and gamma-ray data, running from coordinates 477100 / 1956800, 17°41'53.22"N / 80°47'02.57"E to 481900 / 1960000, 17°43'37.51"N / 80°49'45.43"E. This short lineation has a higher uranium and potassium signature, which could potentially be due to a small area of uncorrected radon in the data but does coincide with a low magnetic lineation in the magnetic data that cuts across the general trends in the magnetic data. There is a possibility that uranium enrichment has occurred along a fracture in this location. It could also be a sliver of unmapped potassium altered Proterozoic Mallampalli Shale that occur not far away to the north as described later in the section on the Proterozoic Basins. In this same general area, another short lineation of distinctive uranium signature gamma-ray data occurs from coordinates 472300 / 1950600, 17°38'31.28"N / 80°44'19.91"E to 478700 / 1952100, 17°39'20.34"N / 80°47'57.06"E coincident with a weak magnetic linear anomaly that follows the general trend in this area. There are also some small patches of the same signature close by to the west, but these appear to be due to the settling ponds of a mine site. The known Mailaram copper deposit at coordinates 463200 / 1952600, 17°39'35.88"N / 80°39'10.94"E falls very close to the edge of the Bastar Craton where it meets highly deformed sediments of the West Belt of the Godavari Supergroup. The deposits are known to occur within quartz reefs through hydrothermal alteration, and a weak and of west-southwest trending potassium alteration occurs at this location. The Mailaram copper deposit is known to be hydrothermal in origin (see Section 3.3.2), so its location may be structurally controlled.

The deposit occurs on a gently curving fracture trending at approximately 80° apparent in the magnetic data that cuts across the magnetic and geological fabric in this location (Figure 12.4.3). Further investigation along this fracture is recommended.

A thin band of Godavari Supergroup sediments are mapped along the western edge of the EGMB, termed the Sharnavala Outliers by Burhanuddin (2017). The gamma-ray data is only faintly different from the adjacent gneisses of the EDC and EGMB to the west and east, mainly because the outliers are very thin, although a thin band of distinctly weak uranium character extending south from the main outcrop of Godavari Supergroup sediments in the southernmost part of the Kothagudem Sub-Basin corresponds to the northernmost of the outliers. The presence of the outliers is only subtly apparent in the magnetic data with a slight reduction in the amplitude of the magnetic anomalies, best seen in the second vertical derivative of the magnetic anomaly (Figure 12.4.4) results from burial below what is probably only a relatively thin layer of sediments.

12.5 Geophysical character and anomalies of the Proterozoic Basins

The various Sub-Basins of the West Belt of the Godavari Supergroup can be readily distinguished in the gamma-ray data from the adjacent EDC to the west and Gondwana sediments to the east. These Proterozoic age sediments are weak in gamma-ray signal, unlike the EDC. The character of the signal is either weak potassium, weak uranium, or both, unlike the Gondwana sediments that have relatively consistent low potassium signature. In the far south of Block-6 the mapped extents of the thin north-south trending Sharnavala outlier of the Western Basin is not distinguishable from the EDC. In the north the northeast trending Kaddam outlier can be distinguished from the adjacent EDC because it occurs as some hills located on top of the Archaean basement, and its magnetic signature is strong enough to obscure the Archaean age magnetic trends beneath so that they appear truncated. The gamma-ray signature of the Kaddam outlier is similar to the EDC as a whole, but locally different because in the immediate vicinity the EDC shows the same potassium depletion as seen further south and described in the section on the EDC above only to a much lesser extent.

The West Belt sediments are for the most part only weakly magnetic. The magnetic anomalies that occur within the Sub-Basin are mostly deep and related to structures beneath the basin that pass into the Pranhita-Godavari Rift, and in places offset the margin with the EDC as well.

There is little correspondence between these deep magnetic features and the patterns in the gamma-ray data that are in places related to boundaries in the different aged sedimentary formations. There are very few local magnetic anomalies of note in the West Belt. A number of small anomalies occur within the West Belt in the far north, but they are all either due to outliers of the Deccan Trap basalts, or due to man-made infrastructure.

The more interesting gamma-ray features of the West Belt occur in the main basin that lies to the east of Warangal. This part of the Western Belt has a weak uranium character, but there are some bands of slightly

stronger uranium signature, and some areas of stronger potassium and uranium signature. The areas of somewhat stronger uranium character correspond to areas of mapped Jakkaram Arkose, the largest of these areas being centred on coordinates 38480 / 2002900, 18°03'56.37"N / 76°38'31.88"E. This appears to be a characteristic of the lithology. On the other hand, the areas of increased potassium signature overprinting the uranium character of the rocks in this area fall within parts of the mapped Laknavaram Shale which for the most part does not have elevated potassium (Figure 12.5.1). Furthermore, these areas correspond to one of the few locations within the West Belt where there are short wavelength magnetic anomalies that are somewhat chaotic in nature but correspond to a distinct area of low eU/K and even lower eTh/K centred at 427800/1973800, 17°51'02.54"N / 80°19'06.85"E. The western edge of this area, which is about 8 km by 5 km in dimension, is sharp where it meets the probably fault bound Gondwana sediments but is less distinct on the other boundaries where it grades into more normal areas of Laknavaram Shale. Therefore, this looks like an area of potassic alteration with local magnetic anomalies that suggest it may host mineralization of interest in proximity to the magnetic anomalies.

Another larger area of potassic alteration approximately 11 km by 14 km in size occurs centred on coordinates 419400 / 1991100, 18°00'24.37"N / 80°14'19.05"E (Figure 12.5.1) but in this case the magnetic anomalies are restricted to the edges. There are also smaller areas of potassic alteration associated with local magnetic anomalies within the Laknavaram Shale a little further south, some of which are wrapped around a promontory of the EDC. All of these areas warrant further investigation.

The geological description of the Western Belt describes significant thrust faulting and folding, but for the most part this is not apparent in the magnetic data due to the low magnetic character of the lithologies. There is one location that does appear to show patterns that can be explained by repetitions due to fault imbrication. This occurs in a small area in the Sullavai Sandstone, the highest formation in the Western Belt, located at coordinates 408156 / 2010000, 18°10'37.67"N / 80°07'53.68"E. High frequency linear anomalies trending 110° occur, sub-parallel to similar fold and fault related magnetic anomalies in the adjacent Gondwana Supergroup.

On the Eastern side of the Godavari Rift, in the north of Block-6, the Pranhita-Godavari Basin divides either side of an inlier of the Bastar Craton, as described in Section 12.3. Most of the eastern branch of the rift is occupied by Proterozoic age Godavari Supergroup sediments that have been mapped as belonging to the Penganga Formation. For the most part the Penganga Formation is only very weakly magnetic, with the main anomalies generated from features beneath the sediments. This includes the east-west dykes described in the section on the Bastar Craton above. Euler solutions of structural index 1, suitable for dykes, can be used to determine the depth to the top of the underlying dykes. The solutions may occur where the dykes are unaltered, so they may be deeper than the pre-sediment palaeo-surface, but the solutions do prove a maximum depth of the sediments at any given point and relative depths of sediments within the basin. A cross section in Figure 12.5.2 shows that the thickness of the Godavari Supergroup sediments in this area is not great, with an estimated maximum of just over 700m in the middle of the basin, becoming thinner to the

north and the south. This contrasts to the much thicker sequence of Gondwana sediments in the Godavari Graben. Coordinates of the profile end points are as follows:

C 338026 / 2257152, 20°24'20.84"N / 79°26'51.71"E

C' 349088 / 2231723, 20°10'37.15"N / 79°33'20.93"E

Within the area of the Penganga Formation exposure there are some local but broad and low amplitude magnetic highs that either represent relative basement highs or locally more magnetic material in the basement beneath the sediments. The gamma-ray data is mostly weak, with a uranium character. However, there are places within the uniformly mapped Penganga Formation which are a little higher in potassium concentration, and ratios of eTh/K and eU/K are distinctly lower. There is a poorly defined north to south band of increased potassium that also coincides with three of the deep source magnetic anomalies, suggesting a causal link resulting in potassic alteration (see from coordinates 336500 / 2249000, 20°19'55.27"N / 79°26'01.75"E to 335100 / 2234500, 20°12'03.32"N / 79°25'18.26"E), but there are no short wavelength magnetic anomalies that would suggest an economic deposit at or close to the surface. Upon closer inspection this area of increased potassium is associated with a north to south running stream, and the feature is almost certainly due to deposition of more potassium rich sediments derived from the Bastar Craton. The same pattern is observed further north at coordinates 324100 / 2259100, 20°25'19.71"N / 79°18'50.71"E where the relationship is clearer, since the stream that feeds the sediments in the valley can be traced by its higher potassium signature within the Bastar Craton itself. Rivers that carry the gamma-ray signature of upstream lithologies are in fact a common occurrence within Block-6.

The main Sub-Basin of East Belt occurs on the east side of the main Pranhita-Godavari Basin as a strong topographic feature. As with other exposures of Proterozoic age sediments, this area lacks strong magnetic anomalies and has a weak gamma-ray signal with a mainly uranium character. An area mapped as Sullavai Sandstone on the east side forms the highest hills, with a particularly steep drop off to the adjacent Bastar Craton, has a particularly low potassium and uranium gamma-ray signal. The majority of the Sub-Basin is mapped as Albaka sandstone and orthoclase quartzite, with a low uranium character. The north and south tips of the Sub-Basin are mapped as Lakanavaram shale, which also has a low uranium character, but as with the same formation (at least by name) mapped in the West Belt, there are patches of what could be potassic alteration centred at coordinates 423400 / 2077300, 18°47'09.42"N / 80°16'23.33"E in the north and 477200 / 2010200, 18°10'50.81"N / 80°47'03.86"E, in the south (Figure 12.5.1). But unlike their counterparts in the west, there are no coincident magnetic anomalies that might indicate associated economic deposits.

Further south, another area of East Belt rocks occurs along the northwest side of the EGMB. Once again, areas of what could be potassic altered shale occur, albeit mapped as Mallampalli Shale (Figure 12.5.1). The two main areas are centred on coordinates 471500 / 1970300, 17°49'12.27"N / 80°43'51.80"E and 478100 / 1976000, 17°52'18.02"N / 80°47'35.80"E. Of these two, the second appears non-magnetic but the first has weak but distinct magnetic anomalies that run approximately north to south and coincide with the areas of highest

uranium in particular within the areas of locally higher potassium. Therefore, these magnetic anomalies are probably more related to the original lithology than with any subsequent potassic alteration.

12.6 Geophysical character and anomalies of the Phanerozoic Godavari Graben

The Godavari Graben is the most prominent macro-scale geological feature within Block-6 and has a very distinct geophysical signature. The magnetic data is mostly devoid of strong, short wavelength features, reflecting the weakly magnetic Gondwana sediments that fill the graben. In this regard it is very similar to the adjacent Godavari Supergroup sediments that fall to either side, but very different from the cratons. But the graben's magnetic data is not devoid of interest. There are broadly two categories of magnetic anomaly, broad anomalies of significant amplitude that reflect the deep basin structure and basement rocks, already discussed in section 12.1.1, and much lower amplitude, short wavelength curvilinear anomalies that are mostly sub-parallel to the margins of the graben, with a north-northwest trend. The lower amplitude linear anomalies are pervasive, and probably mostly related to subtle changes in the magnetic properties of dipping sedimentary layers where they are truncated at the surface. But in other places somewhat stronger anomalies reflect structural breaks that probably occurred as a result of syn-sedimentary faulting that may also have generated local growth folds (Figure 12.6.1). Whether any of these faults were reactivated as later thrusts is not resolved in the data but discussed as a possibility in Section 12.1.1.

Because of the overall low amplitude of the magnetic anomalies in the Godavari Graben, the effects of cultural interference from man made infrastructure is more apparent than elsewhere in Block-6. The most obvious feature is a power line related linear anomaly that crosses the survey area from the north northeast toward the southwest. This particular anomaly is strong enough that it is easily traced through the stronger amplitude anomalies of the adjacent cratonic rocks. But there are many other sources of interference, including towns, villages, other power lines, bridges, dams and mine sites. In general, the flat land around the course of the Godavari River is highly populated and is characterized by many small, disorganized low amplitude magnetic features in addition to the more obvious anomalies associated with the bigger clusters of buildings and man-made structures. Cross checking the anomalies with the Sentinel-2 Satellite imagery helps to eliminate these sorts of feature from further analysis.

Two particularly strong local magnetic anomalies occur at coordinates 298400 / 2235600, 20°12'26.47"N / 79°04'13.78"E that is 5.5 km long, and another at coordinates 297500 / 2240100, 20°14'52.43"N / 79°03'40.97"E that is 3.5km long, located in the northwest corner of Block-6. Initially these look like cultural interference, and the northern one does occur in the vicinity of a village. Local potassium lows also occur, although they are not particularly definitive in this location. The satellite imagery over the southern one shows only one area of buildings at the west end of the southmost of these two features, as well as a small hill at the east end, confirmed by video. However, the geological mapping indicates that Deccan Trap volcanics occur as an outlier in this location. Similar occurrences of Deccan Trap outliers occur mostly in the area just east of the main exposures of the Traps. In this instance the two anomalies sit upon longer wavelength, lower amplitude

east-west anomalies that are ascribed to continuations of dyke anomalies beneath the sediments in the description of the Bastar Craton magnetic data in Section 12.3, so the juxtaposition seems coincidental. But an alternative explanation is that these are dykes, at least where they underlay the Gondwana sediments in this location, are of Deccan Trap age and connected to the lava flows. Shrivastava et al. (2017) state that based on other studies the flows were fed by a dyke system that allowed flow along them for approximately 1000 km elsewhere and concluded that the dykes could have acted as feeders to the lava flows. So, this alternate explanation is a possibility but not preferred. Unlike the situation in the East Belt Godavari Supergroup in the north, the possibly dyke related anomalies at this location are too deep to generate anomalies that can be analysed for depth below surface and hence the thickness of the sediments. That the Gondwana sediments are much thicker in this location is however apparent.

Other than anomalies associated with the deeper parts of the graben (discussed in section 12.1.1 and below), and cultural anomalies, there are relatively few significant short magnetic anomalies in the Chintalapudi Sub-Basin to the east of the western front of the EGMB deformation. There is one small but prominent anomaly at coordinates 490200 / 1901600, 17°11'57.31"N / 80°54'28.20"E that does coincide with a small town, but it does not have the characteristics of cultural interference. There is no gamma-ray anomaly at this location. This anomaly has the characteristics of a possible kimberlite pipe, but it is too large to be identified using the Keating coefficient parameters employed that targeted smaller bodies of 100 m to 200 m width. A relatively large area of stronger magnetic signal occurs on the eastern edge of the basin within Block-6, apparently due to an exposure of Bijapur Granulite. The granulite is at the surface as seen in the Sentinel-2 satellite data but appears to extend to the southeast beneath the relatively thick Gondwana Sediments of the Chintalapudi Sub-Basin

Unlike the magnetic data, the gamma-ray data does clearly distinguish the Gondwana sediments from the Proterozoic Godavari Supergroup sediments, and also from the surrounding cratonic rocks. Mostly the sediments have a relatively weak gamma-ray signature and are distinctly low in potassium, whilst being more or less even in uranium and thorium. This contrasts with the cratonic rocks that have generally high gamma-ray signatures often high in potassium (although not everywhere), and the Godavari Supergroup sediments that have a more uranium character with local potassium highs from alteration. It is noticeable that bands of slightly stronger radiation tend to occur close to mapped internal contacts between units of the Gondwana sedimentary sequence. This could be related to processes occurring on palaeosurfaces during breaks in sedimentation and periods of potential erosion. In one particular place a low ridge of sediments at coordinates 449000 / 2009000, 18°10'10.02"N / 80°31'04.07"E is entirely of uranium character and distinct from the surrounding thorium-uranium sediments. Whether this is a primary or secondary characteristic of the lithology at this location is not known, but this location may warrant further investigation.

Within the Gondwana sediments, some areas have noticeably stronger uranium-thorium, and low potassium character compared to the rest. One such place occurs near the tip of the Bastar Craton inlier, where a ridge that trends approximately east to west, but appears folded to some extent around the inlier, straddles a

reservoir. The ridge extends from coordinates 310600 / 2233100, 20°11'09.66"N / 79°11'14.91"E to 32990 / 2233400, 20°08'28.92"N / 76°32'05.90"E, a distance of approximately 21 km when the fold is accounted for. eTh/K and eU/K are both high, up to 50 and 6 respectively. For the most part this ridge is not differentiated from the area of mapped Kamthi Sandstone, so it appears that the higher levels of uranium and thorium at this location are simply down to more bedrock exposure in the ridge. This pattern is repeated throughout the length of the graben, where the highest concentration of thorium and uranium coincide with physical features, often ridge lines that are sub-parallel to the graben boundaries.

Some formations of the Gondwana sediments do have a more potassic gamma-ray signature than the rest. In particular, outcrops of the lower most formations of the sediments that occur along the west side of the graben, including the Talchir, Barakar, Barren Measures, Kamthi and Maleri formations all have a more balanced gamma-ray signature. Other formations have significantly higher eU/K and eTh/K ratios. The Barakar formation is of particular interest since it hosts well known and highly exploited coal deposits. The Barakar formation is similar in all regards to the overlying Kamthi formation, but the distribution of the gamma-ray character of these two units does not suggest that there are any significant outcrops of the Barakar that are not already known and mapped.

In the Chhattisgarh Basin to the northeast of Block-6, the Barakar formation sits directly upon the Archaean basement. In a similar fashion as described for the Godavari Supergroup sediments to EDC contact in Section 12.2, uranium enrichment has occurred along the unconformity at the base of the Barakar in this basin. In the Godavari Basin, for the most part the Barakar does not sit directly upon the Archaean Basement but has the Godavari Supergroup in between. In the one location where it is directly in contact, for a distance of approximately 14 km centred on coordinates 349800 / 2061700, 18°38'27.52"N / 79°34'33.83"E there is no immediate evidence that the uranium is particularly high along the contact.

A number of potassium highs, with somewhat elevated thorium and uranium as well, occur where coal mining has stripped the Gondwana sediments away (Figure 12.6.2), probably exposing underlying granitic rocks or otherwise being contaminated by human activity. Likewise, a facility located at coordinates 313800 / 2218300, 20°03'09.55"N / 79°13'10.57"E has high uranium of over 7 ppm, somewhat elevated thorium of 24 ppm, and low potassium compared to the surroundings.

12.7 Geophysical character and anomalies of the Krishna-Godavari Basin

A small part of the Krishna-Godavari Basin occurs in the extreme southeast of Block-6. Overall, the magnetic data is lower in intensity than the exposed EGMB to the northwest, but the boundary between these two areas of contrasting age and lithology is not as clear as between the Gondwana Sediments and the EGMB for example. The area of mapped Krishna-Godavari sandstones has low magnetic amplitudes and a gamma-ray signature that is weak in potassium, not unlike the Gondwana sediments. However, these characteristics extend further to the northwest than the edge of the mapped basin, albeit that the magnetic data in particular becomes increasingly strong. The impression is of a thin layer of non-magnetic sediment that is gradually

becoming thinner as it onlaps onto the EGMB metamorphic rocks. However, the outcrops defined in the regolith map indicate that much of this area should have significant rock exposure, so that the mapping of the area as Peninsular Gneiss within the EGMB should be reliable. Therefore, the presence of a larger area with the gamma-ray signature similar to the younger sediments accompanied by lower amplitude magnetic data could either be due to a relatively thin and discontinuous layer of Krishna-Godavari sediments along the edge of the basin, possibly remnants of erosion, or it could be due to transported detritus from the sedimentary rocks. The litho-tectonic map retains a modified version of the original mapped boundary.

Whatever the actual extent of the Krishna-Godavari sediments, the stronger magnetic features within or adjacent to the sediments are almost certainly from EGMB rocks either at the surface or below a thin later of detritus and/or sedimentary rocks. The basin's northwest margin is marked by a number of well-defined northeast trending lineaments sub-parallel to magnetic lineaments definitively within the EGMB just to the northwest at coordinates 485300 / 1884600, 17°02'44.01"N / 80°51'42.71"E.

There is the suggestion of a potential ring complex in the magnetic data at coordinates 486000 / 1850400, 16°44'11.06"N / 80°52'07.17"E about 10km across, but there is no obvious gamma-ray feature associated with the magnetic anomaly. Possibly this feature is buried beneath the Krishna-Godavari sediments.

As with the Gondwana sediments that fill the Godavari Graben, the gamma-ray signature is weak in potassium, stronger in thorium and uranium. The eU/eTh ratio shows some southwest to northeast trending wide banding, probably reflecting changes in the lithology of the sediments and/or basement rocks in the basin. There are no strong gamma-ray anomalies of interest in the basin within Block-6.

12.8 Geophysical character and anomalies of the Deccan Traps

The basalts of the Deccan Traps occur toward the north-northwest of Block-6 and extend for a great distance further to the west. The basalts overtop all other geology where they occur within the block, forming topographic highs. Within Block-6 there are two main areas where the traps occur, separated by a valley in which East Belt Godavari Supergroup sediments and some Archaean basement are still mapped at the surface, and there are several outliers to the east of these main exposures too, isolated by erosion. The traps are strongly magnetic, with many chaotic short wavelength anomalies from the near surface geology, typical of lava flows. In a couple of locations these anomalies are truncated by lineaments defined by magnetic lows that trend 120°, parallel to a major fault that offsets the EDC further south. These lineaments do appear to offset the boundary of the Deccan Traps as well, suggesting that they are faults and if they are related to the major fault further south this would indicate that it is a relatively late feature, post Deccan Trap, or at least was reactivated at a late stage.

The gamma-ray signature of the Deccan Traps is very low in all elements. The Traps have a very weak uranium character, slightly potassic, and very little thorium. There are some local higher uranium and thorium features, also obvious in the ratios eU/K and eTh/K, that occur mostly in the more northern of the two major

exposures. These clearly relate to mapped laterites that have formed at the tops of hills due to tropical alteration in well drained sites, which have the potential to be bauxites with associated aluminum. Although the laterites are known, the uranium and thorium help define their extents more precisely. The strongest anomalies occur in two clusters close together, centred at coordinates 301700 / 2175200, 19°39'43.83"N / 79°06'30.86"E and 309200 / 2167300, 19°35'29.61"N / 79°10'51.18"E.

Although the Deccan Traps are magnetic, for the most part there are no particularly high local magnetic anomalies. However, there is an exception. A large regional magnetic anomaly occurs right on the western edge of Block-6 with its centre around coordinates 289800 / 2159400, 19°31'05.69"N / 78°59'48.78"E (Figure 12.8.1). Most of the anomaly is actually outside Block-6, so the true centre is probably further to the west. The centre of this anomaly falls more or less in between the two main exposures of Deccan basalts where older rocks are mapped as described above, but the high and low anomaly pair extend into the area where the Deccan Traps occur, especially to the north. The magnetic high, within Block-6, reaches over 5,584 nT, whereas the associated low goes down to -1,700 nT. The mapped units here are Neoproterozoic Penganga limestones and Takallapalli shales, neither of which seem to be the source of the anomaly. The inference is that there is a deep-seated body, probably an igneous intrusion at this location that is not exposed. The low magnetic anomaly is superimposed on the high frequency magnetic anomalies from the overlying Deccan Trap basalts, but there is one local high low magnetic anomaly pair within the low of -320 nT (+1.380 nT with respect to the low it occurs within) at coordinates 292600 / 2166600, 19°35'00.85"N / 79°01'21.94"E which is stronger and different in character to those associated with the basaltic flows, being larger in extent and more equidimensional in shape. This may be the location of a shallower body related to the deeper inferred intrusion and therefore is a location of interest. The fact that this feature has no associated gamma-ray anomaly is not surprising as it is most likely wholly or mostly buried beneath the Deccan Basalts.

12.9 Summary of Anomalies of Potential Economic Interest

Table 5 summarizes the locations and characteristics of the most prospective areas identified within Block-6 based on the interpretation of the newly acquired aeromagnetic and spectrometric data in Block-6. Estimates of depths below ground to the tops of the various bodies are provided in Table 5 based upon Euler deconvolution results. The structural index upon which the depth estimate is based is provided in parentheses. Where a body is expected to have a specific geometry, such as a cylindrical body for a kimberlite pipe, the appropriate index for that body was selected. Typically, it is expected that the correct index for any given body will be manifest as the most coherent set of solutions, but this is not always definitive. Nevertheless, that approach was employed as much as was possible in selecting the solutions from which to estimate depths for the other targets with less definite expected geometries. In cases where the identification of the target included the gamma-ray signature, with or without a subsidiary magnetic anomaly, this is indicated by "Yes" under the column "Gamma-Ray Anomaly". Under these circumstances it can be anticipated that either exposed bedrock, or the overlying regolith, reflecting geology that is the source of the anomaly.

Table 5. Locations of mineral prospects in Block-6 (Datum WGS-84, UTM coordinates in Zone 44 North). The first column lists the anomaly number plus a letter relating to the target area, which are referenced in the text. Not all numbered anomalies are included in a target area.

Target areas A-E are high priority.

Target areas F-N are medium priority.

Target areas O-R are low priority.

1,2: these are coordinates at either end of a long band of leucogranite.

†: this depth solution was rejected as unreliable, see text.

‡: part of the body appears to be exposed within the bed of the Godavari River.

Geological Domains as follows: EDC - Eastern Dharwar Craton, BC - Bastar Craton EGMB - Eastern Ghats Mobile Belt, PGW - Pranhita-Godavari Basin Western Belt, PGE - Pranhita-Godavari Basin Eastern Belt, GG - Godavari Graben, KGB - Krishna-Godavari Basin.

SI: Structural Index used for Euler deconvolution depth estimate.

No.	Latitude N dd:mm:ss.ss	Longitude E dd:mm:ss.ss	UTM X m	UTM Y m	Potential Deposit Type	Mineral Potential	Geological Domain	Gamma Ray Anomaly	Depth Below Ground in m (SI)
1 C	16:43:16.37	80:51:38.83	485160	1848720	Kimberlite	Diamonds	KGB	No	218 (2)
2 A	19:49:55.57	80:00:11.34	395610	2193210	Kimberlite	Diamonds	BC	No	265 (2)
3 A	19:48:08.93	79:56:35.48	389310	2189970	Kimberlite	Diamonds	BC	No	188 (2)
4 B	16:40:39.26	80:19:17.25	427650	1844010	Kimberlite	Diamonds	EGMB	No	383 (2)
5	17:38:58.84	79:53:45.49	382890	1951770	Kimberlite	Diamonds	EDC	No	199 (2)
6 C	16:57:10.65	80:44:04.80	471750	1874370	Kimberlite	Diamonds	EGMB	No	238 (2)
7 C	17:07:42.71	80:38:10.58	461310	1893810	Kimberlite	Diamonds	EGMB	No	45 (2)†
8 C	16:51:58.13	80:42:46.16	469410	1864770	Kimberlite	Diamonds	EGMB	No	278 (2)
9 B	16:55:21.58	80:18:19.35	426030	1871130	Kimberlite	Diamonds	EGMB	No	325 (2)
10	17:39:32.73	79:50:09.45	376530	1952850	Kimberlite	Diamonds	EDC	No	221 (2)
11	17:50:32.31	80:57:14.20	495120	1972740	Kimberlite	Diamonds	BC	No	271 (2)
12	19:35:00.63	80:26:19.96	441150	2165490	Kimberlite	Diamonds	BC	No	283 (2)
13 C	16:59:28.14	80:42:09.96	468360	1878600	Kimberlite	Diamonds	EGMB	No	265 (2)
14	17:18:14.41	80:19:45.71	428730	1913310	Kimberlite	Diamonds	EDC	No	394 (2)
15 C	16:39:53.39	80:54:23.06	490020	1842480	Kimberlite	Diamonds	KGB	No	230 (2)
16	17:54:13.91	80:57:07.00	494910	1979550	Kimberlite	Diamonds	BC	No	321 (2)
17 A	19:48:02.01	79:59:08.12	393750	2189730	Kimberlite	Diamonds	BC	No	287 (2)
18	18:23:01.71	80:57:16.75	495210	2032650	Kimberlite	Diamonds	BC	No	286 (2)
19	20:22:36.02	80:20:50.04	431880	2253300	Kimberlite	Diamonds	BC	No	291 (2)
20 B	16:42:27.82	80:20:18.66	429480	1847340	Kimberlite	Diamonds	EGMB	No	187 (2)
21	17:48:34.64	79:27:11.50	336060	1969800	Kimberlite	Diamonds	EDC	No	241 (2)
22 A	19:47:12.60	80:03:11.74	400830	2188170	Kimberlite	Diamonds	BC	No	201 (2)
23	17:11:57.31	80:54:28.20	490200	1901600	Kimberlite	Diamonds	GG	No	300 (2)
24 F	17:00:25.24	79:44:13.03	365553	1880764	Magmatic Hosted (Leucogranite) ¹	Uranium, REEs	EDC	Yes	N/A
25 F	18:11:58.99	79:00:10.46	288787	2013432	Magmatic Hosted (Leucogranite) ²	Uranium, REEs	EDC	Yes	N/A
26 F	17:43:41.05	79:29:41.68	340410	1960739	Magmatic Hosted (Leucogranite)	Uranium, REEs	EDC	Yes	200 (0)
27 F	18:07:56.72	79:17:30.51	319280	2005675	Magmatic Hosted (Leucogranite)	Uranium, REEs	EDC	Yes	Not Resolved
28 G	17:46:33.11	79:56:58.32	388650	1965700	Alkaline dyke	Thorium, REEs,	EDC	Yes	Not Resolved

No.	Latitude N dd:mm:ss.ss	Longitude E dd:mm:ss.ss	UTM X m	UTM Y m	Potential Deposit Type	Mineral Potential	Geological Domain	Gamma Ray Anomaly	Depth Below Ground in m (SI)
					intrusions	Polymetallic			
29 H	17:04:35.60	79:17:30.64	318230	1888820	Alkaline Complex	Thorium, Uranium, REEs	EDC	Yes	230-500 (0)
30 H	17:12:12.33	79:11:55.47	308450	1902950	Alkaline Complex	Thorium, Uranium, REEs	EDC	Yes	200-400 (0)
31 I	19:00:02.71	79:03:16.68	295220	2102043	Alkaline Complex	Thorium, Uranium, REEs	EDC	Yes	0 ⁺
32 J	16:41:29.71	80:30:54.31	448300	1845500	Alkaline Complex	Thorium, Uranium, REEs	EGMB	Yes	350-450 (0)
33 D	17:36:41.74	80:08:38.32	409180	1947420	Unconformity- Type	Thorium, Uranium	EDC	Yes	450-700 (0)
34 D	17:35:46.27	80:14:23.04	419333	1945672	Unconformity- Type	Uranium	EDC	Yes	150-200 (1)
35 O	17:05:34.37	80:19:04.59	427434	1889957	Alkaline Granite	Thorium, Uranium, REEs	EGMB	Yes	125-170 (0.5)
36 P	18:01:51.99	79:23:18.80	329420	1994370	Ultramafic Intrusion	Uranium, Iron	EDC	Yes	Surface
37 K	19:49:52.96	80:14:30.40	420600	2193000	Magmatic Hosted (Granite)	Polymetallic	BC	Yes	150-200 (1)
38 L	19:24:55.24	80:09:39.11	411900	2147000	VMS	Polymetallic	BC	Yes	190-220 m (0.5)
39	17:39:35.88	80:39:10.95	463200	1952600	Hydrothermal Alteration	Copper (known)	BC	No	Not Resolved
40 E	17:20:15.19	80:22:54.56	434317	1917003	Magmatic Chamber	Chromium, PGMs	EGMB	Yes	140-160 (0.5)
41 R	19:07:14.99	80:54:04.02	489600	2114200	Hydrothermal Potassic Alteration	Polymetallic	BC	Slight	350-600 (1)
42 M	17:51:02.54	80:19:06.85	427800	1973800	Hydrothermal Potassic Alteration	Polymetallic	PGW	Yes	130-170 (0)
43 M	18:00:24.37	80:14:19.05	419400	1991100	Hydrothermal Potassic Alteration	Polymetallic	PGW	Yes	Not Resolved
44	19:37:45.98	80:21:53.29	433400	2170600	Iron Stone Formation	Iron (known)	BC	No	450-500 (1)
45 N	19:38:12.50	80:24:17.40	437600	2171400	Iron Stone Formation	Iron	BC	No	450-500 (1)
46 Q	19:21:18.26	80:28:27.89	444800	2140200	Iron Stone Formation	Iron	BC	No	168 (1)
47	19:39:43.83	79:06:30.86	301700	2175200	Bauxite	Aluminium	DT	Yes	Surface
48	19:35:29.61	79:10:51.18	309200	2167300	Bauxite	Aluminium	DT	Yes	Surface

Mapped areas of the Barakar Formation include the main coal deposits, not all of which has been exploited, although no new areas of this formation have been identified.

For one of the kimberlites, target number 7, the depth estimate was in fact rejected due to a lack of sufficient curvature in the magnetic field. Nevertheless, this particular potential kimberlite is of particular interest due to the close proximity of diamond occurrences, and the apparently shallow depth, shallower than all the other possible kimberlites, is still worth noting.

Regarding the location of these anomalies of interest, it is important to keep in mind that while some of the anomalies are essentially point locations, such as the potential kimberlites, in many cases the coordinate provided are just the centre of an area that is described under Section 12 of this report. All such descriptions can be found by searching the report text for the UTM coordinates provided in Table 5. In one example, anomalies 24 and 25, these are the end points of a long curvilinear band of apparent leucogranite with high uranium.

Details of the main target areas A to R recommended for follow up investigation are described below and the locations of these areas of interest are included on the litho-tectonic map, illustrated in Figure 12.9.1. Potential kimberlite anomalies 5, 10, 11, 12, 14, 16, 18, 19, 21 and 23 are individually as indicative of a possible kimberlite as the others but are more scattered, compared to the others that occur within a cluster or in linear arrays, so they are not included in the immediate priorities regarding this type of target. Other anomalies are not listed as targets since the deposits are already known or obvious, including anomaly 39 the Mailaram Mining District copper deposit, anomaly 44 the Surgagarth iron deposit, and two potential bauxites anomalies 47 and 48 at the surface on the top of the Deccan Traps.

12.9.1 High Priority Target Area A: Northern Bastar Craton Potential Kimberlites

High priority Target Area A (Table 6, Figure 12.9.2) includes four identified potential kimberlite pipes, anomalies 2, 3, 17, and 22, occurring in a cluster in this part of the Bastar Craton, along with other similar magnetic anomalies that also have the potential to be kimberlites.

Table 6: Coordinates of Target Area A (WGS-84, UTM Zone 44N).

X (m)	Y (m)
383800	2183400
383700	2195100
402700	2195000
402700	2183200

12.9.2 High Priority Target Area B: Eastern Ghats Mobile Belt Potential kimberlites

High priority Target Area B (Table 7, Figure 12.9.3) includes three identified potential kimberlite pipes, anomalies 4, 9, and 20, occurring in a line in this part of the Eastern Ghats Mobile Belt.

Table 7: Coordinates of Target Area B (WGS-84, UTM Zone 44N).

X (m)	Y (m)
425200	1841000
425100	1873000
431600	1872800
431600	1840800

12.9.3 High Priority Target Area C: Eastern Ghats Mobile Belt Potential kimberlites

High priority Target Area C (Table 8, Figure 12.9.4) includes six identified potential kimberlite pipes, anomalies 1, 6, 7, 8, 13, and 15, occurring in a line in this part of the Eastern Ghats Mobile Belt.

Table 8: Coordinates of Target Area C (WGS-84, UTM Zone 44N).

X (m)	Y (m)
485443	1833899
450448	1892149
461962	1899261
496383	1840813

12.9.4 High Priority Target Area D: Eastern Dharwar Craton/Godavari Supergroup Unconformity

High priority Target Area D (Table 9, Figure 12.9.5) is the unconformable contact between the Eastern Dharwar Craton and the Godavari Supergroup on the western side of the Godavari Graben, including anomalies 33 and 34.

Table 9: Coordinates of Target Area D (WGS-84, UTM Zone 44N).

X (m)	Y (m)
393492	1983901
395524	1977692
402298	1966742
406362	1954663
414038	1947212
418441	1951163
425891	1939875
417425	1935698
408281	1943035
402072	1951841
397330	1958614
393944	1974644
389767	1980176
389993	1988078
377011	2005463

12.9.5 High Priority Target Area E: Eastern Ghats Mobile Belt Magmatic Chamber

High priority Target Area E (Table 10, Figure 12.9.6) is the known Chimalpahad Complex and the area immediately to the south and southeast which may be a continuation of the complex but with higher magnetic character, in an area where chromite minerals have been found, anomaly 40.

Table 10: Coordinates of Target Area E (WGS-84, UTM Zone 44N).

X (m)	Y (m)
433263	1889937
431251	1928490
454048	1945615
463881	1933518

X (m)	Y (m)
459747	1924690
444549	1915918
442203	1889825

12.9.6 Medium Priority Target Area F: Eastern Dharwar Craton Leucogranite

Medium priority Target Area F (Table 11, Figure 12.9.7) are extensive bands of uranium rich rocks, mapped as leucogranite in their southern extent, running in between anomaly coordinates 24 and 25 and including anomalies 26 and 27.

Table 11: Coordinates of Target Area F (WGS-84, UTM Zone 44N).

X (m)	Y (m)
287823	2000160
288056	2022395
318907	2010026
325597	2003336
326480	1993112
339084	1976420
354320	1951954
348789	1936714
374067	1880657
356685	1881044
320344	1944812
304649	1981869

12.9.7 Medium Priority Target Area G: Eastern Dharwar Craton Alkaline Potential Intrusive Dykes

Medium priority Target Area G (Table 12, Figure 12.9.8) is a broad area of the Eastern Dharwar Craton designated in this report as migmatite, that is low in potassium and has sub-linear features that are high in thorium and uranium. The area selected includes the highest local concentrations of thorium within the broader area of this character and includes anomaly 28.

Table 12: Coordinates of Target Area G (WGS-84, UTM Zone 44N).

X (m)	Y (m)
356400	1967800
393900	1968000
394900	1948700
357000	1948200

12.9.8 Medium Priority Target Area H: Eastern Dharwar Craton Potential Alkaline Intrusions

Medium priority Target Area H (Table 13, Figure 12.9.9) are a group of intrusions in the Eastern Dharwar Craton that show ring like structure and may be alkaline in nature, including anomalies 29 and 30.

Table 13: Coordinates of Target Area H (WGS-84, UTM Zone 44N).

X (m)	Y (m)
289635	1914700
312439	1914023
318422	1906573
324630	1899686
324405	1884334
309164	1884605
289522	1907814

12.9.9 Medium Priority Target Area I: Eastern Dharwar Craton Potential Alkaline Intrusion

Medium priority Target Area I (Table 14, Figure 12.9.10) is an intrusion in the Eastern Dharwar Craton that shows a ring like structure and may be alkaline in nature, anomaly 31.

Table 14: Coordinates of Target Area I (WGS-84, UTM Zone 44N).

X (m)	Y (m)
288700	2096400
302600	2096400
302600	2109600
288700	2109600

12.9.10 Medium Priority Target Area J: Eastern Ghats Mobile Belt Potential Alkaline Intrusion

Medium priority Target Area J (Table 15, Figure 12.9.11) is a possible intrusion in the Eastern Ghats Mobile Belt, poorly defined in the magnetic data, that if confirmed may be alkaline in nature, anomaly 32.

Table 15: Coordinates of Target Area J (WGS-84, UTM Zone 44N).

X (m)	Y (m)
441400	1853200
455400	1853200
455400	1840100
441400	1840100

12.9.11 Medium Priority Target Area K: Bastar Craton Potential Magmatic Hosted Alteration

Medium priority Target Area K (Table 16, Figure 12.9.12) are fractures within and the margins of the Dongargarh Granite of the Bastar Craton that show indications of alteration evidenced by higher thorium, anomaly 37.

Table 16: Coordinates of Target Area K (WGS-84, UTM Zone 44N).

X (m)	Y (m)
416301	2187661
429864	2213023
441281	2207577
427905	2181529

12.9.12 Medium Priority Target Area L: Bastar Craton Potential VMS

Medium priority Target Area L (Table 17, Figure 12.9.13) is a relatively magnetic anomaly within a newly interpreted supracrustal belt of the Bastar Craton that may relate to a volcanogenic massive sulphide (VMS). The anomaly is probably too large to be directly related to a sulphide body but may related an apron of exhalative magnetic minerals. The anomaly is designated as number 38.

Table 17: Coordinates of Target Area L (WGS-84, UTM Zone 44N).

X (m)	Y (m)
407800	2152300
416000	2152300
416000	2141200
407800	2141200

12.9.13 Medium Priority Target Area M: Godavari Supergroup Potential Potassium Alteration

Medium priority Target Area M (Table 18, Figure 12.9.14) are two areas of potential potassic alteration of Godavri Supergroup sediments on the west side of Godavari Graben including anomalies 42 and 43. There are other areas of similar character around the margin of the rift, but this location includes magnetic as well as gamma-ray anomalies.

Table 18: Coordinates of Target Area M (WGS-84, UTM Zone 44N).

X (m)	Y (m)
411081	1993442
415104	1998694
419574	2001935
423038	1997242
424156	1993331
426279	1989308
426167	1986290
424714	1984726
425161	1981709
429072	1976233
431643	1972546
432648	1970087
429743	1969529
428067	1965394
426167	1970422
423262	1974557
421697	1976904
424044	1982379
424156	1984279
421474	1984950
418345	1982268
416445	1979586
413540	1986290

12.9.14 Medium Priority Target Area N: Bastar Craton Ironstone

Medium priority Target Area N (Table 19, Figure 12.9.15) is a segment of the Bailadila Formation ironstone of the Bastar Craton, just along strike from an existing iron ore mine, including anomaly 45. The area includes the highest magnetic anomaly observed within the formation, similar in magnitude to the anomaly associated with the mine, although any ore body will likely lay just to the south of the anomaly where supergene enrichment of iron may have occurred. As with the iron ore site, the Bailadila formation is disrupted within the marked zone, and therefore structural traps where enrichment may occur exist in this area.

Table 19: Coordinates of Target Area N (WGS-84, UTM Zone 44N).

X (m)	Y (m)
437384	2172118
438026	2172719
439046	2173808
440261	2175442
441448	2174716
441085	2174115
440135	2172607
439213	2171252
438571	2170442
437481	2169799
436112	2169785

12.9.15 Low Priority Target Area O: Eastern Ghats Mobile Belt Alkaline Granites

Low priority Target Area O (Table 20, Figure 12.9.16) is a line of previously mapped alkaline granites in the Eastern Ghats Mobile Belt, designated as anomaly 35. These granites are generally high in uranium and thorium but are otherwise not remarkable.

Table 20: Coordinates of Target Area O (WGS-84, UTM Zone 44N).

X (m)	Y (m)
412834	1914668
421330	1914744
439532	1872440
429563	1872863

12.9.16 Low Priority Target Area P: Eastern Dharwar Craton Ultramafic outlier

Low priority Target Area P (Table 21, Figure 12.9.17) is an outlier of mapped Karimnagar granulite within the Eastern Dharwar Craton, anomaly 36, that is already mapped in detail and has a very high magnetic anomaly, the highest in the survey area, and is of interest for that reason alone. The outlier is also very low in gamma-ray signature despite being largely exposed as a hill, reflecting its ultra-mafic character.

Table 21: Coordinates of Target Area P (WGS-84, UTM Zone 44N).

X (m)	Y (m)
412834	1914668
421330	1914744
439532	1872440
429563	1872863

12.9.17 Low Priority Target Area Q: Bastar Craton Ironstone

Low priority Target Area Q (Table 22, Figure 12.9.18) is a small area of previously mapped Bailadila Formation including banded ironstone that locally has a high magnetic intensity, anomaly number 46, and appears folded, much like the situation proximal to the Surjagarh Iron Ore further north.

Table 22: Coordinates of Target Area Q (WGS-84, UTM Zone 44N).

X (m)	Y (m)
447500	2144500
447500	2135000
442000	2135000
442000	2144500

12.9.18 Low Priority Target Area R: Bastar Craton supracrustal Rock

Low priority Target Area R (Table 23, Figure 12.9.19) is a folded area of supracrustal rocks, one of four in the eastern part of the Bastar Craton, but the only one with a slightly higher potassium gamma-ray signature, anomaly 41.

Table 23: Coordinates of Target Area R (WGS-84, UTM Zone 44N).

X (m)	Y (m)
485587	2119025
499867	2111520
499874	2092340
485265	2092482

13. FOLLOW UP RECOMMENDATIONS

The focus going forward on all areas of interest is to obtain additional data to supplement that already available.

The following geophysical methods are recommended to further investigate the various identified targets listed in Table 5, mainly drawn from the recommendations of Ford et al. 2007.

1. Kimberlites – Increased density of airborne aeromagnetic survey lines (e.g. 100 m spacing), to better detect and define smaller kimberlites that may be missed by the current 300 m line spaced survey. Resistivity survey (target has high conductivity) airborne or on the ground. Ground gravity survey (target has low density) to map the geometry of the body. This includes anomalies 1 to 23, and target areas A, B and C.
2. Intrusive Hosted – Resistivity and induced polarity (IP) methods to locate areas of mineralization may be applicable. Either airborne survey for resistivity, or on the ground for both resistivity and IP. This includes anomalies 24 to 27, and 37, and target areas F and K.
3. Alkaline Dykes and Complexes – Gravity survey to map the shape of the body (target has high density), either airborne or on the ground. This includes anomalies 28 to 32 and target areas G, H, I and J.
4. Unconformity-Type - Gravity survey to detect areas of mineralization (target has high density). Resistivity survey to identify associated graphitic metapelites. This includes anomalies 33 and 34, and target area D.
5. Ultramafic Intrusion - Ground gravity survey to map the shape of the body (lithology has high density). Resistivity survey (highly conductive) to define the shape of the body. This includes anomaly 36 and target area P.
6. Hydrothermal Alteration – Possibly resistivity or IP to detect faults, veins, contacts, and/or alteration) or IP to detect resistive shear/fault hosted deposits. Gravity may be helpful, both airborne or on the ground, mainly to better understand the geological framework. This includes anomalies 39, 42 and 43, and target area M.
7. Magmatic Chamber – Gravity to detect the dense chromite since both chromite and a possible serpentinite host are usually magnetic so they cannot be distinguished (Gunn & Dentith, 1997), but serpentinitization decreases density. This includes anomaly 40 and target area E.
8. Volcanogenic Massive Sulphide – Ideal resistivity targets (target is highly conductive), both resistivity for the main body and IP for the stockwork or alteration halo (Morgan, 2010), plus gravity for the geological framework, by airborne survey or on the ground. This includes anomaly 38 and target area L.

9. Iron Stone Formation – Local low intensity anomalies within the overall high anomaly of the lithology results from supergene enrichment of BIF with magnetite altered to hematite (Gunn and Dentith, 1997). Alteration occurs nearer the surface but can penetrate >100m. Gravity can help model the shape of the ironstone formation as modelling of the magnetic signature can be complex due to alteration and high susceptibility, plus remanence, self-demagnetization and anisotropy of magnetic susceptibility. Resistivity, spontaneous potential (SP), and IP have all been previously employed. This includes anomalies 44, 45 and 46, and target areas, and target areas N and Q.
10. Bauxite – Resistivity tomography (target has low resistivity), on the ground. This includes anomalies 47 and 48.
11. Supracrustal rocks & granites– Surface mapping and or sampling of potential and previously mapped supracrustal rocks of the Bastar Craton is recommended. This includes both newly identified areas, and previously mapped but better defined areas such anomalies 41 and target area R. The same is recommended for the previously mapped alkaline granites of anomaly 35, target area O in the Eastern Ghats Mobile Belt.

The scope of these investigations should be focused on the deposit scale, so in many cases ground based surveys will suffice. Where airborne resistivity surveys are proposed, focused rotary (helicopter) time domain electromagnetics (TEM) using relatively low powered systems for near surface investigations are recommended. Frequency domain electromagnetics (FEM) are only likely to be of use for very shallow (<150 m depth) deposits, but under those circumstances FEM will probably be superior to TEM.

Sub-surface modelling based on magnetic data alone, especially for bodies with the potential for magnetic remanence, is generally ambiguous. Combining additional geophysical data to the magnetic data is likely to provide the required constraints for meaningful two or three dimensional modelling of specific bodies.

Whether the top of a body is expected to be close to the surface or buried beneath significant overburden indicates whether additional ground mapping and/or sampling for geochemical analysis is likely to be successful in assessing and of the potential targets. Extra surface mapping and/or sampling of buried bodies where no gamma-ray anomaly is present is unlikely to yield any additional information on the possible body. Under these circumstances the emphasis is on the additional geophysical techniques listed above. For those with associated gamma-ray anomalies, surface mapping and/or sampling to determine geophysical properties such as density, magnetic susceptibility and magnetic remanence, all of which will help to constrain modelling, may prove useful. In particular, any density contrast between the Godavari Supergroup and the Gondwana sediments would be particularly helpful for modelling gravity data (see below). For any positively identified deposit, the approach should be to understand the mineral system by which the deposit was generated. By doing so, the chances of finding the full extent of a deposit, or other related deposits, is greatly enhanced.

Hydrocarbon potential has been identified within the rift (Dasgupta and Jain 2007). The current gravity coverage of the Pranhita-Godavari Rift does not lend itself to complete modelling of the basin sub-structure. An airborne gravity survey with a target anomaly amplitude resolution of 0.5 mGal (0.3 mGal target noise level) and a spatial resolution of 1 km half wavelength can be achieved with an airborne survey performed with a line spacing of 250 m using an SGL AIRGrav system flown on a fixed wing (Airplane) platform for example. The rift is probably too large an area for a cost-effective helicopter borne gravity survey, but if undertaken the resolution achievable would drop to 700 m half wavelength using the SGL AIRGrav system. Any such survey should be flown preferably perpendicular to the long axis of the rift (i.e. approximately N°80E). Together with the newly available high resolution magnetic data, high resolution gravity data will result in improved basin modelling that will help identify possible hydrocarbon traps. In addition, it will help to resolve the nature of the edges of the basin where the craton meets the sediments and should there be a sufficient density contrast between the Godavari Supergroup and the Gondwana sediments, which is unknown at this time, it could also help to constrain the nature of the boundary between those two sedimentary sequences as well.

Gravity gradiometry would not greatly help in improving the basin modelling but could be employed to better determine near surface gravity variations and to help model any deposits that are expected to have a significant gravity signature as described above.

14. SUMMARY AND CONCLUSION

Sander Geophysics Limited (SGL) conducted a fixed-wing high resolution magnetic gradient and gamma-ray survey over Block-6 in central India, part of the ongoing National Airborne Geophysical Mapping Program (NAGMP) funded by National Mineral Exploration Trust (NMET). The 300 m survey line spacing and the 80 m nominal flying height allows for a high-resolution imaging of the near surface bedrock geological features. The primary deliverable from the survey is the anomalous magnetic field and radiometric data, which are directly related to the local geology.

The primary objective of the qualitative integrated structural interpretation of the magnetic and radiometric data is to extract pertinent geological information. For this study, the structural interpretation outlines the general geophysical signature of the area and identifies prominent geophysical features and maps dominant structural domains and elements such as faults and lineaments.

With much of the survey covering near surface Archaean and Proterozoic basement, data derivatives that highlight the short wavelength signature in the magnetic data and image shallow sources were used. Longer wavelength derivatives of magnetic data were mainly employed for interpretation of the central Godavari Graben where structures are generally deeper. Radiometric data generally detects sources at the surface. Counts, concentrations and ratios have been supplied. To help the interpretation, a number of techniques were available to convert the data into mappable source body characteristics. Grid Euler deconvolution and trend analysis were implemented, focusing on both near surface features and deeper features depending on the geological terrain.

Using pre-existing boundaries between mapped geological units as a reference, a litho-tectonic map was generated based on boundaries determined from the aeromagnetic and gamma-ray geophysical data acquired for this purpose, supplemented by pre-existing gravity data and satellite imagery. The resultant litho-tectonic map provides guidance for re-evaluation of existing geological mapped boundaries and for future geological mapping.

An interpretation of a number of interesting geophysical anomalies has been performed, with eighteen areas of economic potential recommended for suggested follow up work, summarized in Table 24.

Table 24: Summary of target areas. Target areas A-E are high priority; Target areas F-N are medium priority; Target areas O-R are low priority.

Zone no.	Area (Km ²)	Geological feature	Economic Importance	Follow-up Survey
A B C	223 206 899	potential kimberlite pipes	Diamonds, ilmenite, spinel, REEs	magnetic gravity
D	617	uranium enriched unconformity	unconformity related U deposits	resistivity gravity
E	870	magmatic chamber	Base metals like Cu-Ni-Zn, PGEs, REEs, Fe, Cr, Ti, U	gravity
F	3770	uranium rich leucogranite	U, REEs	resistivity IP
G	734	alkaline intrusive dykes	PGEs, Ni, Cr, Cu	gravity
H I J	723 183 183	alkaline intrusive	REEs, phosphate, carbonatite, magnesite, zircon, Ti, nepheline, apatite	gravity
K	374	magmatic hosted	Ni-Cu-PGE, Cr, Au, Fe, Ti	resistivity IP
L	91	VMS	Cu, Zn, Pb, Fe, Au	resistivity IP gravity
M	273	hydrothermal potassic alteration	K-feldspar, biotite, muscovite, chlorite (Cu-Au)	IP gravity
N Q	13 52	ironstone	(BIF) hematite, magnetite, goethite, limonite	gravity SP IP resistivity
O	385	alkaline granite	REEs, U	mapping
P	154	ultramafic intrusion	Cr-Ni, PGMs, magnesite, Co	resistivity gravity
R	331	supracrustal rocks	Precious-base metals, industrial mineral, REEs, kimberlite	mapping

15. INTERPRETATION PRODUCTS

15.1 Digital Grids

Digital grids are provided in the following formats:

- Geosoft Binary (.grd)
- GeoTiff (.tif)

The grids have the following properties:

- Datum: WGS-84
- Projection: UTM 44N
- Cell Size: 60 m

A list of all digital grids delivered can be found in Table 25.

Table 25: Digital Grids

Grid File Name	Units	Description
Block-6_1VD	nT/m	Anomalous Magnetic Field First Vertical Derivative
Block-6_2VD	nT/m ²	Anomalous Magnetic Field Second Vertical Derivative
Block-6_RTP	nT	Anomalous Magnetic Field Reduced to Pole
Block-6_RTP_HP	nT	Anomalous Magnetic Field Reduced to Pole high pass filtered
Block-6_RTP_BP	nT	Anomalous Magnetic Field Reduced to Pole band pass filtered
Block-6_RTP_LP	nT	Anomalous Magnetic Field Reduced to Pole low pass filtered
Block-6_RTP_UC100	nT	Anomalous Magnetic Field Reduced to Pole residual after upward continuation of 100m
Block-6_RTP_UC100-Res	nT	Anomalous Magnetic Field Reduced to Pole after upward continuation of 100m
Block-6_RTP_UC1000	nT	Anomalous Magnetic Field Reduced to Pole residual after upward continuation of 1000m
Block-6_RTP_UC1000-Res	nT	Anomalous Magnetic Field Reduced to Pole after upward continuation of 1000m
Block-6_RTP_Han100	nT	Anomalous Magnetic Field Reduced to Pole residual after 100 passes of a 3x3 Hanning Filter
Block-6_RTP_Han100-Res	nT	Anomalous Magnetic Field Reduced to Pole after 100 passes of a 3x3 Hanning Filter
Block-6_RTP_Han12800	nT	Anomalous Magnetic Field Reduced to Pole residual after 12800 passes of a 3x3 Hanning Filter
Block-6_RTP_Han12800-Res	nT	Anomalous Magnetic Field Reduced to Pole after 12800 passes of a 3x3 Hanning Filter
Block-6_RTP_TILT_ANGLE	degree	Anomalous Magnetic Field Reduced to Pole Tilt Angle

Grid File Name	Units	Description
Block-6_RTP_TILT_ANGLE_05	degree	Anomalous Magnetic Field Reduced to Pole Tilt Angle limited to +/- 5 degrees
Block-6_RTP_TILT_ANGLE_45	degree	Anomalous Magnetic Field Reduced to Pole Tilt Angle limited to +/- 45 degrees
Block-6_EULER_SI0	m	Euler solution depths below ground Structural Index 0
Block-6_EULER_SI0.5	m	Euler solution depths below ground Structural Index 0.5
Block-6_EULER_SI1	m	Euler solution depths below ground Structural Index 1
Block-6_EULER_SI2	m	Euler solution depths below ground Structural Index 2
Block-6_EULER_SI3	m	Euler solution depths below ground Structural Index 3
Block-6_MAGBASE	m	Euler solution heights above Mean Sea Level Structural Index 0
Block-6_GRAVITY_BOUGUER-1	mGal	Legacy Bouguer Gravity Anomaly 1mGal resolution
Block-6_GRAVITY_BOUGUER-5	mGal	Legacy Bouguer Gravity Anomaly 5mGal resolution

15.2 Euler Solutions

Results of classic 2D Euler deconvolution of the anomalous magnetic field (Reid et al. 1990) are provided. Tolerance is set low to allow all solutions to pass, but the data can be screened by the tolerance value so as to only employ the more reliable results at a level of the user's discretion. The files provided are simple ASCII text, which can be imported into most geophysical and GIS software packages. The files provided are as follows:

- Euler_Solutions_SI_0.txt Euler solutions from anomalous magnetic intensity, Structural Index 0
- Euler_Solutions_SI_0.5.txt Euler solutions from anomalous magnetic intensity, Structural Index 0.5
- Euler_Solutions_SI_1.txt Euler solutions from anomalous magnetic intensity, Structural Index 1
- Euler_Solutions_SI_2.txt Euler solutions from anomalous magnetic intensity, Structural Index 2
- Euler_Solutions_SI_3.txt Euler solutions from anomalous magnetic intensity, Structural Index 3

The format of the files is provided in Table 26.

Table 26: Euler Solution Data Format

Column Name	Column Width Size	Units	Description
TOL	13	nT	solution tolerance
EX	11	m	solution X coordinate WGS-84 UTM 44N
EY	11	m	solution Y coordinate WGS-84 UTM 44N
EZ_BA	10	m	solution depth below aircraft (positive down)
EZ_BG	10	m	solution depth below ground (positive down)

Column Name	Column Width Size	Units	Description
EZ_MSL	10	m	solution height w.r.t. Mean Sea Level (positive up)
AC_Z_MSL	10	m	aircraft height w.r.t. Mean Sea Level (positive up)
DEM-MSL	10	m	digital elevation model height w.r.t. Mean Sea Level

15.3 Philips Trend Data

Results of running Philips analysis (Phillips et al. 2007) are provided. Traditionally this analysis is run on reduced to pole data, but distortion of the short wavelength data due to the relatively low latitude results in the introduction of false trends. Therefore, this analysis was run on the anomalous magnetic field without reduction to the pole. For this reason, the depths are not considered reliable and are not reported. For depths to magnetic source, refer to the Euler deconvolution and/or the tilt angle results. The files provided are as follows:

- Trends-0.txt Trends from anomalous magnetic field, 0m upward continuation
- Trends-50.txt Trends from anomalous magnetic field, 50m upward continuation
- Trends-100.txt Trends from anomalous magnetic field, 100m upward continuation
- Trends-250.txt Trends from anomalous magnetic field, 250m upward continuation
- Trends-500.txt Trends from anomalous magnetic field, 500m upward continuation
- Trends-1000.txt Trends from anomalous magnetic field, 1000m upward continuation
- Trends-2000.txt Trends from anomalous magnetic field, 2000m upward continuation

The format of the files is provided in Table 26.

Table 27: Format of Philips trend data.

Column Name	Column Width Size	Units	Description
SD	12	nT	solution standard deviation
TX	12	m	solution X coordinate WGS-84 UTM 44N
TY	12	m	solution Y coordinate WGS-84 UTM 44N
STRIKE	12	degree	strike of trend clockwise from North

15.4 Tilt Depth Estimates

The results of estimating depth to magnetic source using the distance between the $\pm 45^\circ$ tilt angle contours (Verduzco et al. 2004) are provided. These values were extracted from the grid of the tilt angle using a tool built into Geosoft Oasis montaj® software. The file provided is as follows:

- Tilt_Depth.Txt

The format of the file is provided in Table 26.

Table 28: Format of tilt depth estimates data.

Column Name	Column Width Size	Units	Description
X	12	m	solution X coordinate WGS-84 UTM 44N
Y	13	m	solution Y coordinate WGS-84 UTM 44N
DEPTH	10	degree	strike of trend clockwise from North

15.5 ArcPro Project

Final interpretation maps are supplied as an ArcGIS project for Block-6, incorporating geophysical and other geoscience data layers.

16. REFERENCES

- Airo, M.L., 2015. Geophysical signatures of mineral deposit types. Geological Survey of Finland, Special Paper 58, 144pp.
- Aggarwal, N., Mathews, Arif Husain Ansari, A.H., Thakur, B. and Agrawal, S., 2022. Palaeoenvironmental reconstruction for the Permian (lower Gondwana) succession of the Godavari Valley Coalfield in southern India based on a combined palynofacies, carbon isotope, and biomarker study. *Journal of Palaeogeography*, v.11, p.123-144.
- Air, M.L., 2015. Geophysical signatures of mineral deposit types in Finland. In *Geophysical Signatures of Mineral Deposit Types – Synopsis*, Edited by Airo, M.L., Geological Survey of Finland, Special Paper 58, 9–70. *Journal of Emerging Technologies and Innovative Research*, v.9, p.390-402.
- Amosun, J.O., Alagbe, O.A., Fagbemigun, T.S., Sanuade, O.A. and Olaseeni, O.G., 2020. Imaging lateritic bauxite bearing zones in Ekiti, Southwestern Nigeria, using magnetic and electrical resistivity tomography techniques. *SN Applied Sciences* v.2:2033.
- Banothu, V. and Babu, L.P., 2022. Field relationship and Geochemical characterization of Amphibolites from Khammam schist belt at the margin of the Eastern Dharwar Craton, South of Wyra, Khammam District, Telangana, South India.
- Biswas, S.K., 2003. Regional tectonic framework of the Pranhita–Godavari Basin, India. *Journal of Asian Earth Sciences*, v.21, p. 543-551.
- Burhanuddin, M., 2017. Deformed Mesoproterozoic Pakhal sequence in southeastern Pranhitha Godavari Basin along margin of Eastern Dharwar Craton: Interpreted as an outcome of Eastern Ghat Orogeny during India-East Antarctica amalgamation. *Indian Journal of Geosciences*, v.70/71, p.227–246.
- Burhanuddin M., Sreenivasa Rao, T. and Rama Murthy S., 2024. A note on the structurally controlled northeastern extension of Eastern Dharwar Craton and its relationship with Bastar Craton-Eastern Ghats Mobile Belt in Khammam-Bhadrachalam-Sabharai Region, South India. *SGAT Bulletin* v.25, p.30-38.
- Caruso, A.S., Clarke, K.D., Tiddy, C.J., Delean, S. and Lewis, M.M., 2018. Objective Regolith-Landform Mapping in a Regolith Dominated Terrain to Inform Mineral Exploration. *Geosciences*, v.8, 318.
- Chaudhuri, A.K., 2002. Stratigraphy and palaeogeography of the Godavari Supergroup in the south-central Pranhita-Godavari Valley, south India. *Journal of Asian Earth Sciences*, v.21, p. 595-611.
- Chaudhuri, A.K., Deb, G.K., Deb, S.P. and Sarkar, S., 2012. Paleo-geographic and tectonic evolution of the Pranhita-Godavari valley, central India: A stratigraphic perspective. *American Journal of Science*, v.312, p.766–815.
- Chen, J., Fan, H., Wang, S. and Gu, D., 2021. Sr-Nd Isotope Composition of Uraniferous Leucogranites in the Gaudeamus area, Central Damara Belt, Namibia. *IOP Conference Series: Earth and Environmental Science*, v. 783, 012009.
- Cowan, D.R. and Cowan, S., 1993. Separation filtering applied to aeromagnetic data. *Exploration Geophysics*, v.24, p.429-436.
- Dasgupta, U. and Jain, A.D., 2007. A surface geochemical survey over part of the Pranhita-Godavari Basin and its impact on the hydrocarbon prospects of the basin. *Journal of the Geological Society of India*, v. 70, p.187-193.

Dharma Rao, C.V. and Santosh, M., 2011. U–Pb zircon chronology of the Pangidi–Kondapalle layered intrusion, Eastern Ghats belt, India: Constraints on Mesoproterozoic arc magmatism in a convergent margin setting. *Journal of Asian Earth Sciences*, v.49, p.362-375.

Dharma Rao, C.V., Windley B.F. and A.K. Choudhary A.K., 2011. The Chimalpahad anorthosite Complex and associated basaltic amphibolites, Nellore Schist Belt, India: Magma chamber and roof of a Proterozoic island arc. *Journal of Asian Earth Sciences*, v.40, p.1027-1043.

Fairhead, J.D., Bennett, K.J., Gordon, D.R.H. and Huang, D., 1994. Euler: Beyond the “Black Box”. SEG Technical Program Expanded Abstracts 1994

Fareeduddin and Rao, M.S., 2007 (Editors). Kimberlites and related rocks of India. *Journal of the Geological Society of India*, v.69, p.413-670.

Ford, K., Keating, P. and Thomas, M.D., 2007. Overview of geophysical signatures associated with Canadian ore deposits. In W. D. Goodfellow (Ed.), *Mineral Deposits of Canada—A Synthesis of Major Deposit-Types, District Metallogeny, the Evolution of Geological Provinces, and Exploration Methods*, p. 939-970. Special Publication No. 5, St. John's, NL: Geological Association of Canada, Mineral Deposits Division.

Galbraith, J.H. and Saunders, D.F., 1983. Rock classification by characteristics of aerial gamma-ray measurements. *Journal of Geochemical Exploration*, v.18, p.49-73.

Gandhi, S.S., Prasad, N., and Charbonneau, B.W., 1996. Geological and geophysical signatures of a large polymetallic exploration target at Lou Lake, southern great Bear magmatic zone, Northwest Territories. In *Current Research 1996-E*; Geological Survey of Canada, p.147-158.

Guisan, A., Weiss, S.B. and Weiss, A.D., 1999. GLM versus CCA spatial modeling of plant species distribution. *Plant Ecology* v.143, p.107-122.

Geological Survey of India, 2024. Minerals in Telangana-Spotlights. Published by the order of the Government of India, 31pp.

Gunn, P.J. and Dentith, M.C., 1997. Magnetic responses associated with mineral deposits. *AGSO Journal of Australian Geophysics and Geology*, v.17, p.145-158.

Halder, S.K., 2017. Deposits of Asia. In *Platinum-Nickel-Chromium Deposits, Geology, Exploration and Reserve Base*, p.145-189.

Huff, W.D. and Owen, L.A., 2015. Volcanic Landforms and Hazards. *Treatise on Geomorphology*, v.5, p.148-192.

IAEA 2003. Guidelines for radioelement mapping using gamma ray spectrometry data. Technical Document 1363, 173pp.

IAEA 2019. World Thorium Occurrences, Deposits and Resources. IAEA TecDoc-1877, 120pp.

Keating, P., 1995. A simple technique to identify magnetic anomalies due to kimberlite pipes. *Exploration Mining Crc1.*, v. 4, p.121-125.

Keating, P. and Sailhac, P., 2004. Use of the analytic signal to identify magnetic anomalies due to kimberlite pipes. *Geophysics*, v.69, p.180–190.

Krishnamurthy, P., 2019. Carbonatites of India. *Journal of the Geological Society of India*, v.94, p.117-138.

Kumar, A., Hamilton, M.A. and Halls, H., 2012. A Paleoproterozoic giant radiating dyke swarm

in the Dharwar Craton, southern India. *Geochemistry Geophysics Geosystems*, v.13, p1-12.

Kivior, I. and Boyd, D., 1998. The contribution of high quality aeromagnetic survey data to hydrocarbon exploration. *Exploration Geophysics*, v. 29, p.462-466.

Kwak, T.A.P. and Abeysinghe, P.B., 1987. Rare earth and uranium minerals present as daughter crystals in fluid inclusions, Mary Kathleen U-REE skarn, Queensland, Australia. *Mineralogical Magazine*, v. 51 (Part 5), p. 665-670.

MacLeod, I., Jones, K. and Ting Fan Dai, 1993, 3-D analytic signal in the interpretation of total magnetic data at low magnetic latitudes, *Exploration Geophysics*, v.24, p.679-688.

Mahboob, M.A., Genc, B., Celik, T., Ali, S. and Atif, I., 2019. Mapping hydrothermal minerals using remotely sensed reflectance spectroscopy data from Landsat. *The Journal of the Southern African Institute of Mining and Metallurgy*, v.119, p.279-289.

Mainkar, D., Lehmann, B., Burgess, R. and Belyatsky, B., 2008. The Diamondiferous Behradih Kimberlite Pipe, Raipur District, Chhattisgarh, India. 9th International Kimberlite Conference Extended Abstract No. 9IKC-A-00009, 2008.

Metelka, V., Baratoux, L., Jessell, M.W., Barth, A., Ježek, J. and Naba, S., 2018. Automated regolith landform mapping using airborne geophysics and remote sensing data, Burkina Faso, West Africa. *Remote Sensing of Environment*, v. 204, p.964-978.

Mishra, D.C., and Kumar, M. Ravi., 2013. Proterozoic orogenic belts and rifting of Indian cratons: Geophysical constraints. *Geoscience Frontiers*, v. 5, p.25–41.

Mishra, V.P., Datta, N.K., Ramachandra, H.M., Bhattacharya, D., Das, D.P., Kumuran, K., Ramamurthy, S., Lakshmana, B.K. and Nageswara Rao, C., 1987. Geological history of the Abujhamar basin, Bastar District, Madhya Pradesh. *Geological Survey of India Memoir No.6.*, p.189-199.

Misra, S., Mohanta, A.K., Diwan, P. and Vishwakarma, N., 2015. Zonation of the Eastern Ghats Mobile Belt: A Review. *International Journal of Geology and Earth Science*, v.1, p.46-54.

McKechnie, L.C., Ansdell, K/M. and Annesley, I.R., 2009. Granitic pegmatite and leucogranite-hosted uranium mineralization adjacent to the Athabasca basin, Saskatchewan, Canada: A different target for uranium exploration. Conference Poster.

Mondal, M.E.A., Hussain, M.F. and Ahmad, T., 2006. Continental Growth of Bastar Craton, Central Indian Shield during Precambrian via Multiphase Subduction and Lithospheric Extension/Rifting: Evidence from Geochemistry of Gneisses, Granitoids and Mafic dykes. *Journal of Geosciences, Osaka City University* v.49, p.137-151.

Morgan, L.A., 2010. Geophysical Characteristics of Volcanogenic Massive Sulfide Deposits. 7 of 21, Volcanogenic Massive Sulfide Occurrence Model, Scientific Investigations Report 2010–5070–C, U.S. Department of the Interior U.S. Geological Survey, 131 pp.

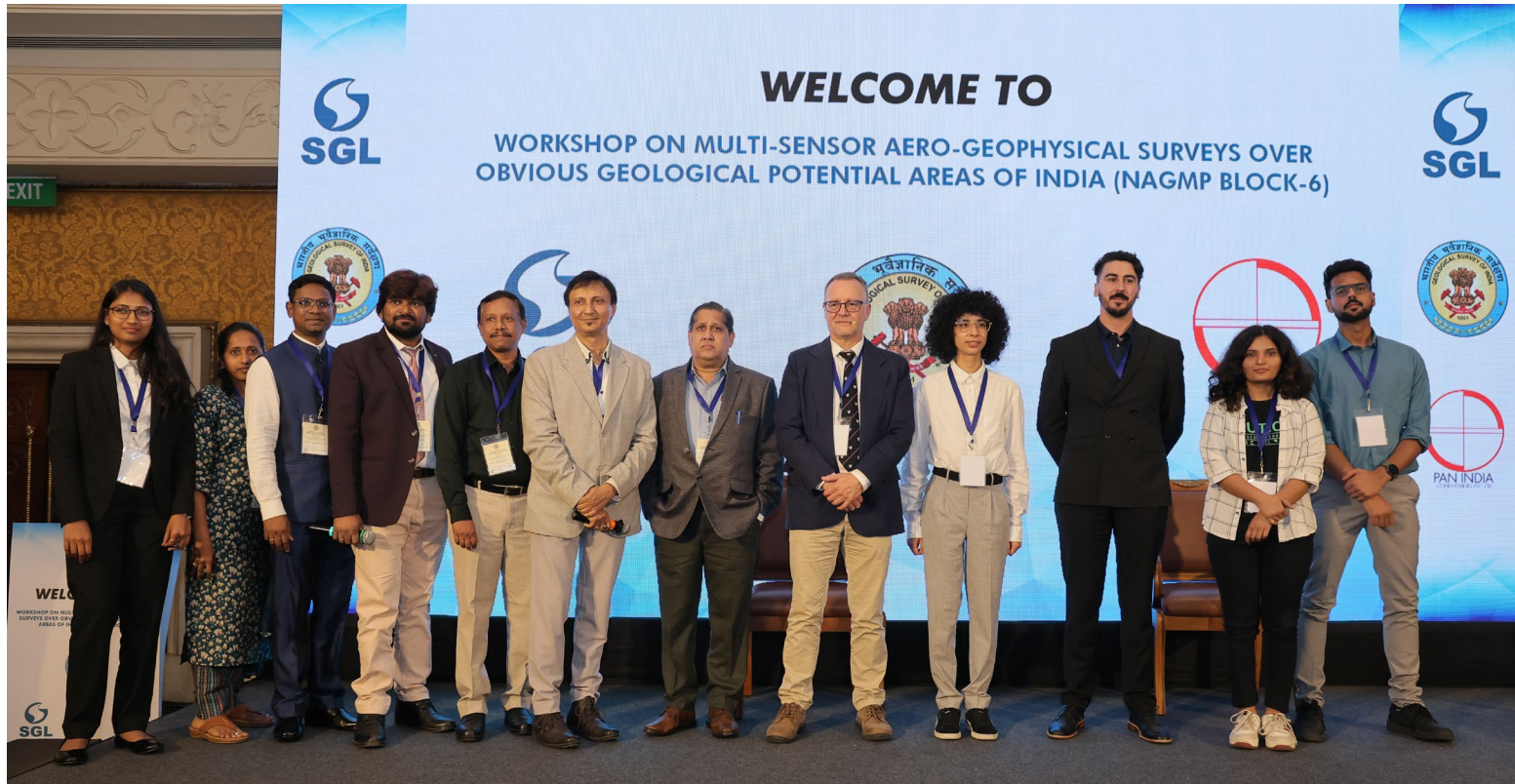
NGRI, OIL, GSI and SOI (2006). Bouguer gravity (5 mGal) map of India. National Geophysical Research Institute, India.

Okudaira, T., Hari Prasad, B. and Kumar, R., 2000. Proterozoic Evolution of the Nellore-Khammam Schist Belt in the Khammam district, SE India. *Journal of Geosciences, Osaka City University*, v.43, p.193-202.

- Patel, V.C., Jarial, A., Kumar, N., Rao, B. and Singh, A.P., 2023. Three-dimensional Moho depth model of the eastern Indian shield and its isostatic implications. *Journal of Earth System Science* v.132 69, p.1-20.
- Paul, D.K., Nayak, S.S. and Pant, S.C., 2006. Indian kimberlites and related rocks: Petrology and geochemistry. *Journal of the Geological Society of India*, v.67, p.328-355.
- Phillips, J.D., R. O. Hansen, R.O. and Blakely, R.J., 2007. The use of curvature in potential-field interpretation. *Exploration Geophysics*, v.38, p.111–119.
- Pilkington, M. and Keating, P.B., 2004. Contact Mapping from Gridded Magnetic Data – a Comparison of Techniques. *Exploration Geophysics* v.35, p.306-311.
- Shives, R.B.K., Charbonneau, B.W. and Ford, K.L., 1997. The detection of potassic alteration by gamma ray spectrometry - recognition of alteration related to mineralization in Geophysics and Geochemistry at the Millennium, Proceedings of the Fourth Decennial International Conference on Mineral Exploration (Exploration 97), 1100 pages.
- Subrahmanyam, D.S., Shyam, G., Vamshidhar, K. and Vikram, S., 2020. State-of-the-Art Technique to Conduct in situ Stress Measurements in Deep Proposed Coal-Mining Blocks of Singareni Collieries, India. *Current Science*, v. 119, p. 1027-1030.
- Ramachandra, H.M. and Roy, A., 1998. Geology of intrusive granitoids with particular reference to Dongargarh granite and their impact on the tectonic evolution of the Precambrian in central India. *Indian Minerals*, v.52, p.15-32.
- Rao, N.K., Dora, M.L., Baswani, S.R., Malpe, D.B. and Deshmukh, M.S., 2018. Petrography and geochemistry of the Proterozoic sandstones of Somanpalli Group from Pomburna area, Eastern Belt of Pranhita–Godavari Valley, central India: Implications for provenance, weathering and tectonic setting. *Journal of Earth Systems Science*, v.127:90, p.1-27.
- Reid, A.B., Allsop, J.M., Granser, H., Millett, A.J. & Somerton, I.W., 1990. Magnetic interpretation in three dimensions using Euler deconvolution, *Geophysics*, v.55, p.80-91.
- Rubin, J., 1967. Optimal classification into groups: An approach for solving the taxonomy problem. *Journal of Theoretical Biology*, v.15, p.103-144.
- Salem, A., Williams, S., Fairhead, J.D., Ravat, D. and Smith, R., 2007. Tilt-depth method: A simple depth estimation method using first order derivatives, *The Leading Edge* December 2007.
- Sarma, B.S.P. and Krishna Rao, M.V.R., 2005. Basement structure of Godavari basin, India – Geophysical modelling. *Current Science*, v.88, p.1172-1175.
- Sensarma, S. and Mukhopadhyay, D., 2014. Stratigraphy of ~2.5 Ga Dongargarh Belt, Central India: Key Observations and Suggested Revisions. *Gondwana Geological Magazine*, Special Volume No.16, p. 41-48.
- Sengupta, S., 2003. Gondwana sedimentation in the Pranhita–Godavari Valley: a review. *Journal of Asian Earth Sciences*, v.21, p.633-642.
- Sharma, U.P., Bidwai, R. and Roy, M.K. 2011. Uranium mineralization in Talchir Formation of Gondwana Supergroup, Surguja District, Chhattisgarh. *Current Science*, V.100, p.984-986.
- Shrivastava, J.P., Kumar, R., and Rani N., 2017. Feeder and post Deccan Trap dyke activities in the northern slope of the Satpura Mountain: Evidence from new ⁴⁰Ar–³⁹Ar ages. *Geoscience Frontiers* v.8 p. 483-492.

- Spector, A. and Grant, F.S., 1970. Statistical models for interpreting aeromagnetic data, *Geophysics* v. 35, p.293-302.
- Sreenivasa Rao, T., 1987. Thew Pakhal Basin – A perspective. *Geological Survey of India Memoir No.6*, pp.161-187.
- Srivastava, R.K., Hall, R.P., Verma, R. and Singh, R.K., 1996. Contrasting Precambrian mafic dykes of the Bastar Craton, central India: petrological and geochemical characteristics. *Journal Geological Society of India*, v.48, p.537-546.
- Srivastava, R.K., Söderlund, U., Ernst, R.E. and Gautam, C.G., 2021. A Ca. 2.25 Ga mafic dyke swarm discovered in the Bastar craton, Central India: Implications for a widespread plume-generated large Igneous Province (LIP) in the Indian shield. *Precambrian Research*, v.360.
- Syberg, F.J.R., 1972. A Fourier Method for the Regional-Residual Problem of Potential Fields. *Geophysical Prospecting*, v. 20, p.47-75.
- Tschirhart, V., Potter, E.G., Powell, J.W., Roots, E.A., & Craven, J.A., 2022. Deep geological controls on formation of the highest-grade uranium deposits in the world: Magnetotelluric imaging of unconformity-related systems from the Athabasca Basin, Canada. *Geophysical Research Letters*, v.49, p.1-11.
- Vaidyanadhan, R. and Ramakrishnan, M., 2010. *Geology of India*. Geological Society of India, 997pp.
- Verduzco, B., Fairhead, J.D., Green, C. and MacKenzie, C., 2004. New insights into magnetic derivatives for structural mapping, *The Leading Edge* 2004.
- Wang, Y.W., Fan, H.R., Zhou, L., Yang, K.F. and She, H.D., 2020. Carbonatite-Related REE Deposits: An Overview. *Minerals* 2020, v.10, 965.







Appendix I

Additional Litho-Codes



Table of new litho-codes employed for the litho-tectonic map of Block-6.

NOTATION	AGE	SUPER GROUP	GROUP NAME	FORMATION	LITHOLOGY
New lithology					
Adkh	Archaean	Dharwar	Khammam		Schist
θAcc4	Archaean			Chimalpahad Complex	Ortho-metamorphic Rock
ζPt ₂ i	Mesoproterozoic				Intrusive
AbnSC	Archaean		Bengpal		Supra-crustal
AbnSCS _k	Archaean		Bengpal		Supra-crustal
APtSC	Archaean - Palaeoproterozoic				Supra-crustal
APt ₁ bg	Archaean - Palaeoproterozoic				Granulite
APtMS _k	Archaean - Palaeoproterozoic	Bengpal			Basic Volcanic
P-Q	Permian – Quaternary				Sediment
Adkh7	Archaean	Dharwar			Intrusive
Group of lithologies in the same area					
Pt ₂ pm	Mesoproterozoic	Pakhal	Mallamoalli		Quartzite, Dolomite & Shale
APt ₁ kg	Archaean - Palaeoproterozoic		Karimnagar Granulite		Migmatite Gneiss
gug	Late Permian – Early Cretaceous	Gondwana	Upper Gondwana		Clay & Sandstone
P ₃ glg	Late Permian	Gondwana	Lower Gondwana		Clay & Calcareous Sandstone
Tgug	Early to Middle Triassic	Gondwana	Upper Gondwana		Mudstone, Clay & Ferruginous Sandstone
P ₃ glgblm	Late Permian	Gondwana	Lower Gondwana		Feldspathic, Ferruginous, Calcareous Sandstone
P ₃ glglm	Late Permian	Gondwana	Lower Gondwana		Calcareous Sandstone & Clay
C ₂ P ₁ glg	Late Carboniferous - Early Permian	Gondwana	Lower Gondwana		Tillite, Feldspathic Sandstone
C ₂ Pglg	Late Carboniferous - Late Permian	Gondwana	Lower Gondwana		Green Argillaceous, Ferruginous, Feldspathic, Calcareous Sandstone
Existing lithology with additional specification					
νAbg4mS _u	Archaean		Bengpal Gneiss		Granite Gneiss/Migmatite
νAbg4s	Archaean		Bengpal Gneiss		Granite Gneiss/Migmatite
Pt ₃ pt2S _k	Neoproterozoic		Penganga		Sandstone
Pt ₃ pt2S _{th}	Neoproterozoic		Penganga		Sandstone
P ₃ glgkmS _{th}	Late Permian	Gondwana	Lower Gondwana	Kamthi	Sandstone
νAbg4M	Archaean		Bengpal Gneiss		Granite Gneiss/Migmatite
νAbg4HF	Archaean		Bengpal Gneiss		Heavily Foliated Granite Gneiss/Migmatite
APtMS _k	Archaean-Palaeoproterozoic	Bengpal			Basic Volcanic
K ₁ gugcs _{th}	Early Cretaceous	Gondwana	Upper Gondwana	Chikiala	Sandstone
J ₁ gugk1S _u	Early Jurassic	Gondwana	Upper Gondwana	Kota	Calcareous Sandstone

NOTATION	AGE	SUPER GROUP	GROUP NAME	FORMATION	LITHOLOGY
vPt ₁ dng8s _k	Palaeoproterozoic				Granite
Existing code not previously mapped					
vPt ₁ ifg1	Palaeoproterozoic				Foliated Granite

For “Existing lithology with additional specification”, the following additional code letters are applied:

- S with subscript U, Th or K represents high counts of uranium, thorium or potassium.
- s with subscript U, Th or K represents low counts of uranium, thorium or potassium.
- S without subscript represents high counts of all of uranium, thorium and potassium.
- s represents low counts of all of uranium, thorium and potassium.
- M represents high magnetic amplitudes.
- m represents low magnetic amplitudes.
- HF represents heavily foliated.



Appendix II

Report Figures



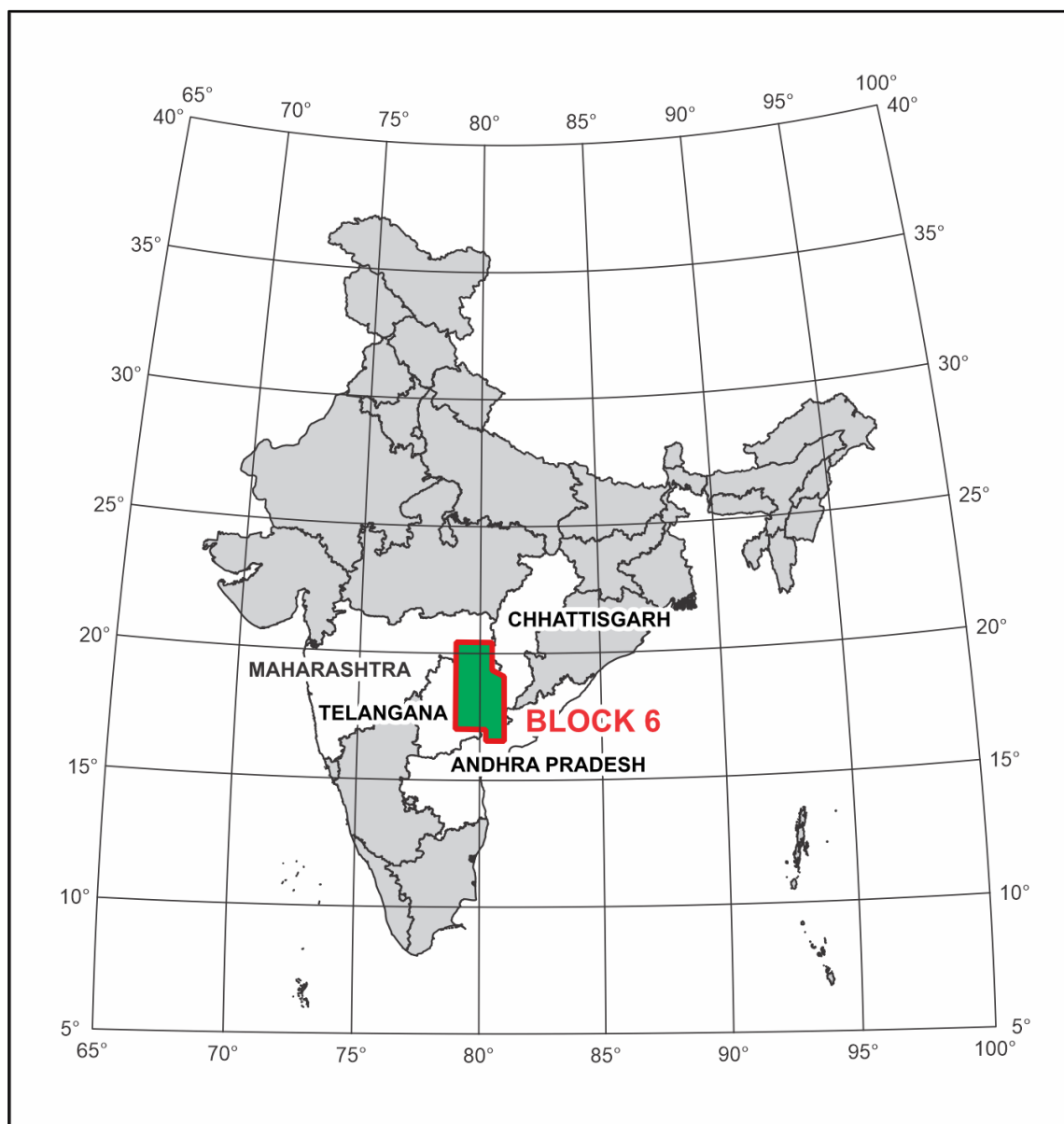


Figure 2.1: The location of National Airborne Geophysical Mapping Program (NAGMP) Block-6

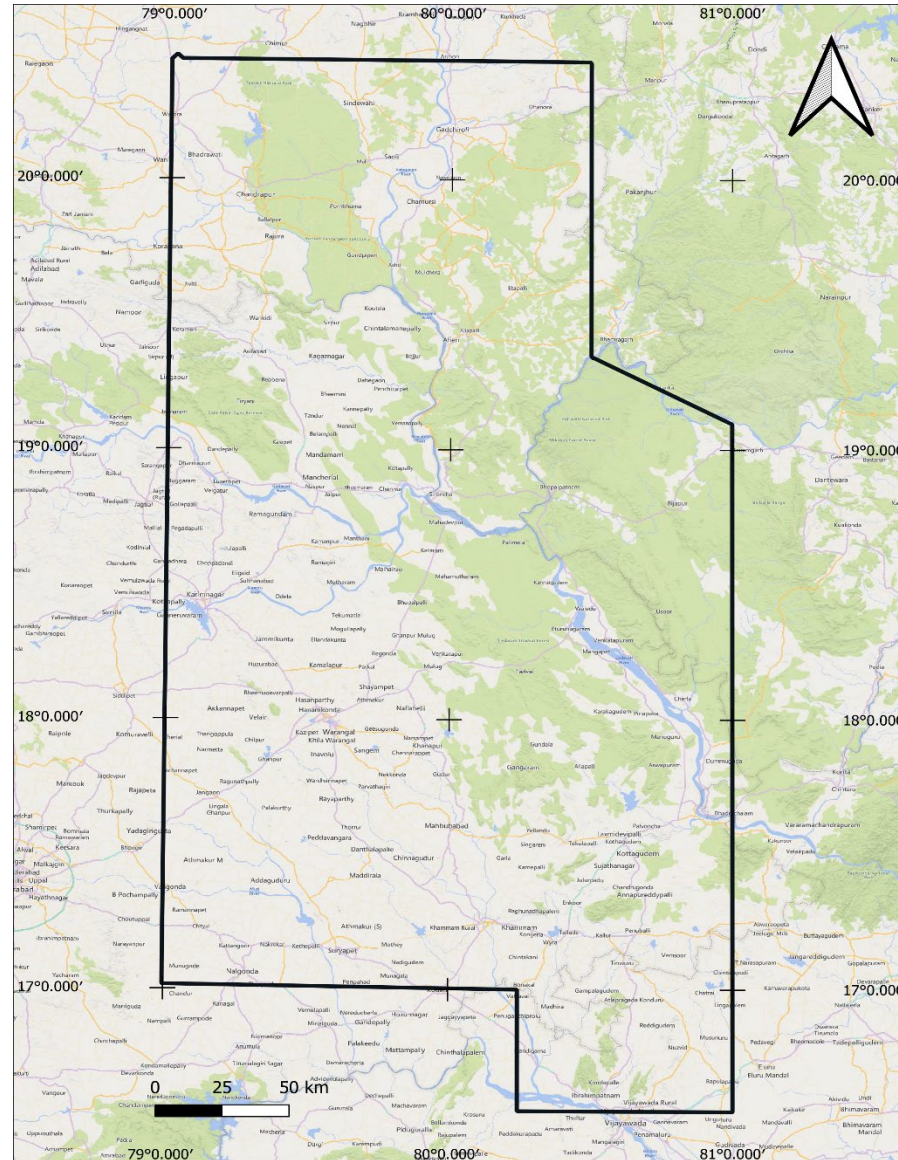


Figure 2.2: The geographic area of Block-6 (Microsoft® Bing™ Maps).

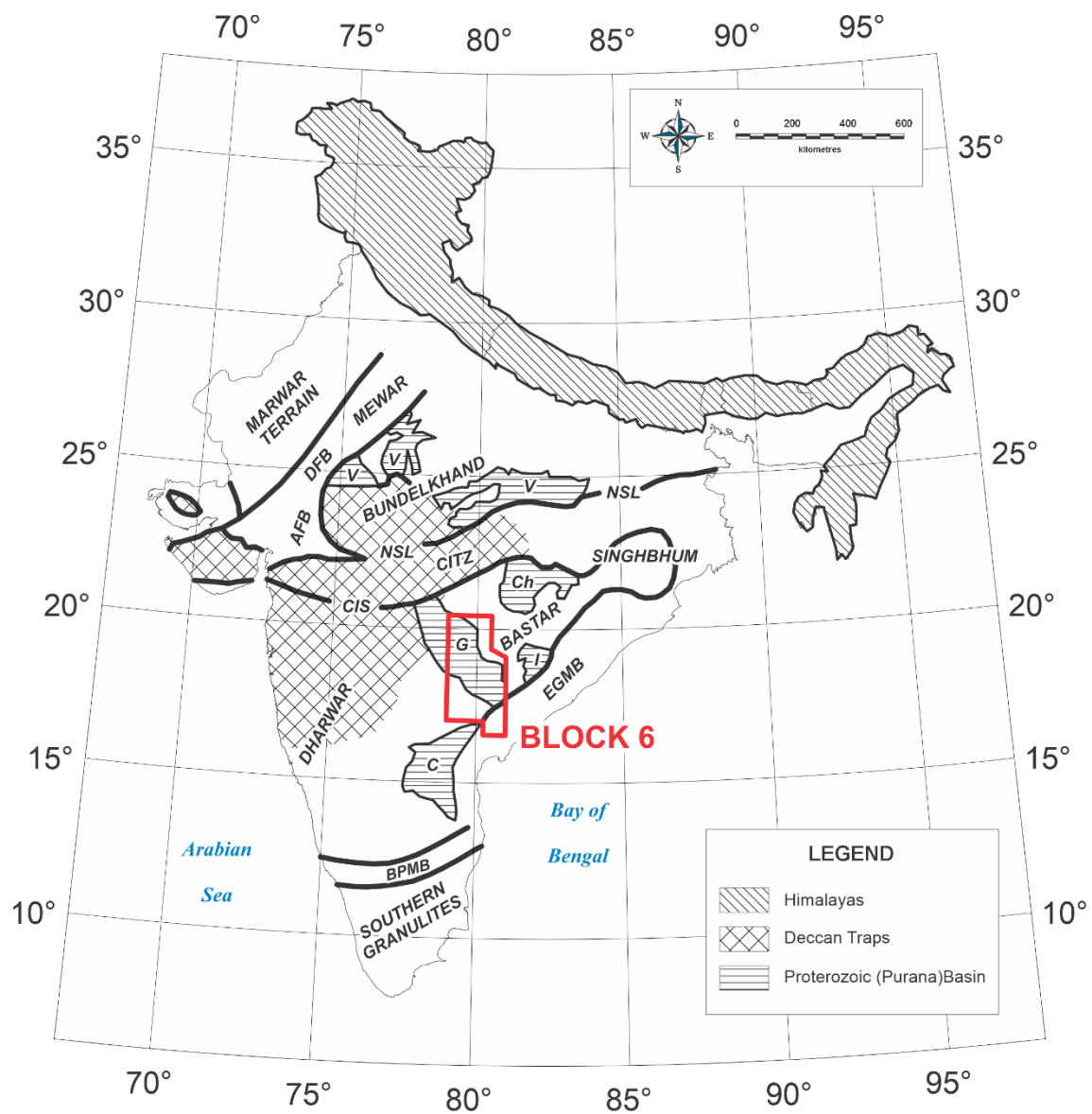
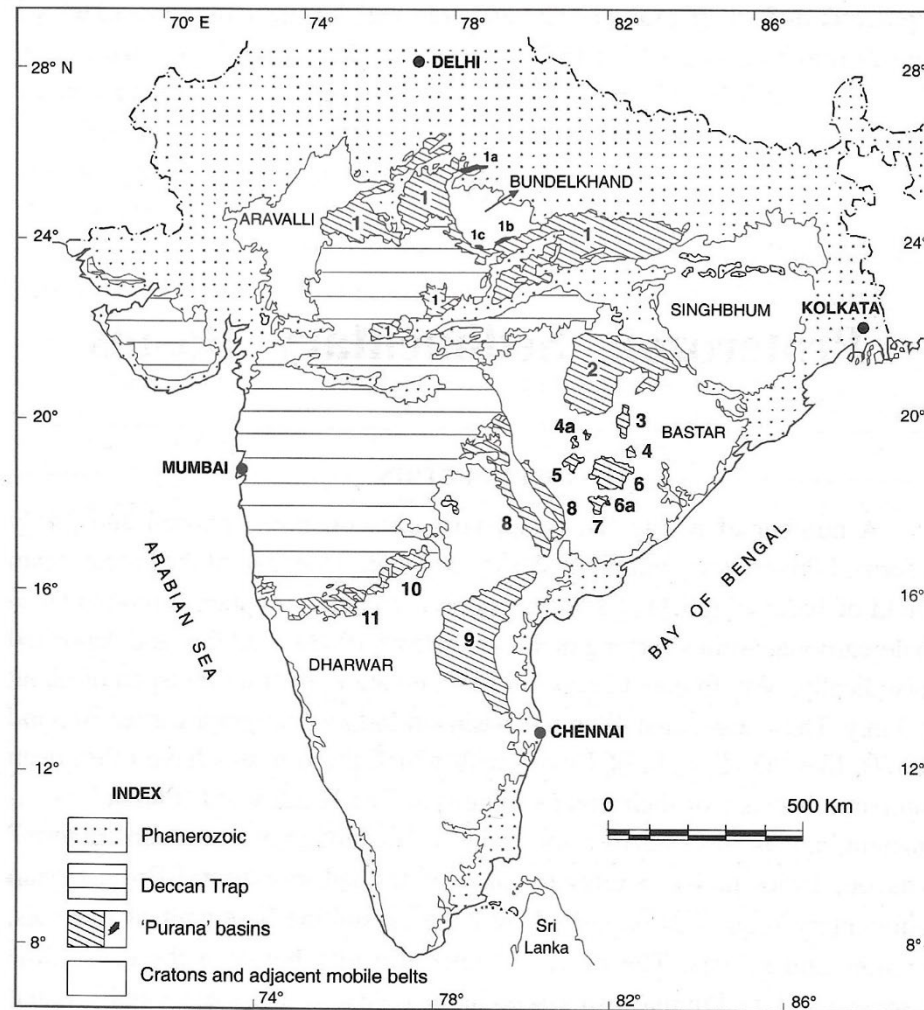


Figure 3.1: Tectonic map of India, modified from Chaudhuri *et al.* (2012), with the boundary of Block-6 shown.



Purana basins of Peninsular India within different cratons (after Kale, 1991). 1 - Vindhyan, 1a - Gwalior, 1b - Bijawar & 1c - Sonrai basins, 2 - Chhattisgarh basin, 3 - Khariar basin, 4 - Ampani basin, 4a - Keskal and Singanpur outliers. 5 - Abujhmar basin, 6 - Indravati basin, 6a - Chedrapal outlier, 7 - Sabari basin, 8 - Pranhita-Godavari basin, 9 - Cuddapah basin, 10 - Bhima basin, 11 - Kaladgi basin.

Figure 3.2: Distribution of the Proterozoic Age Purana Basins (from Ramakrishnan and Vaidyanadhan 2010).

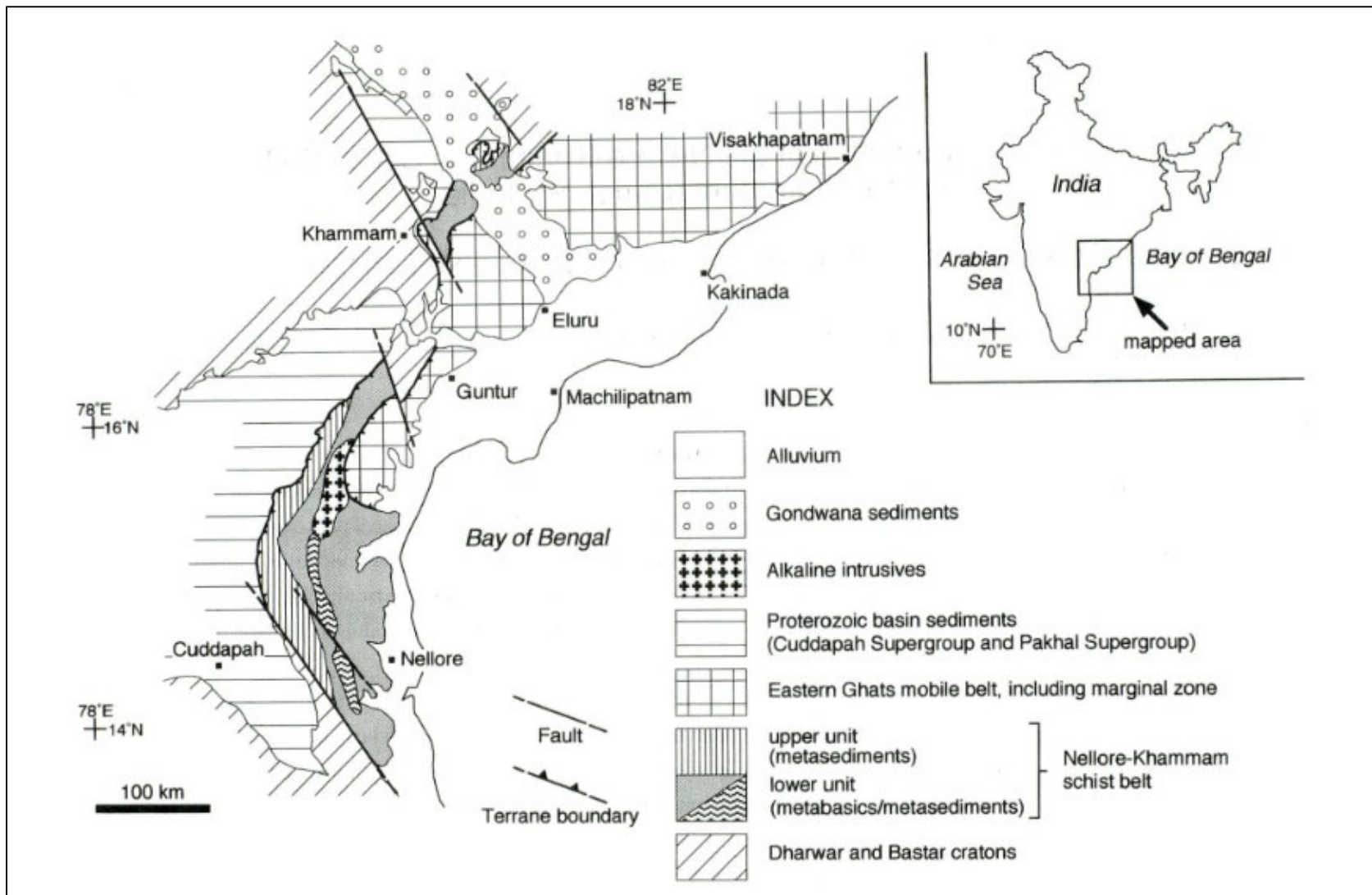


Figure 3.3: Geology of the Nellore-Khammam schist belt of the Eastern Ghats Mobile Belt (from Okudaira et al. 2000).

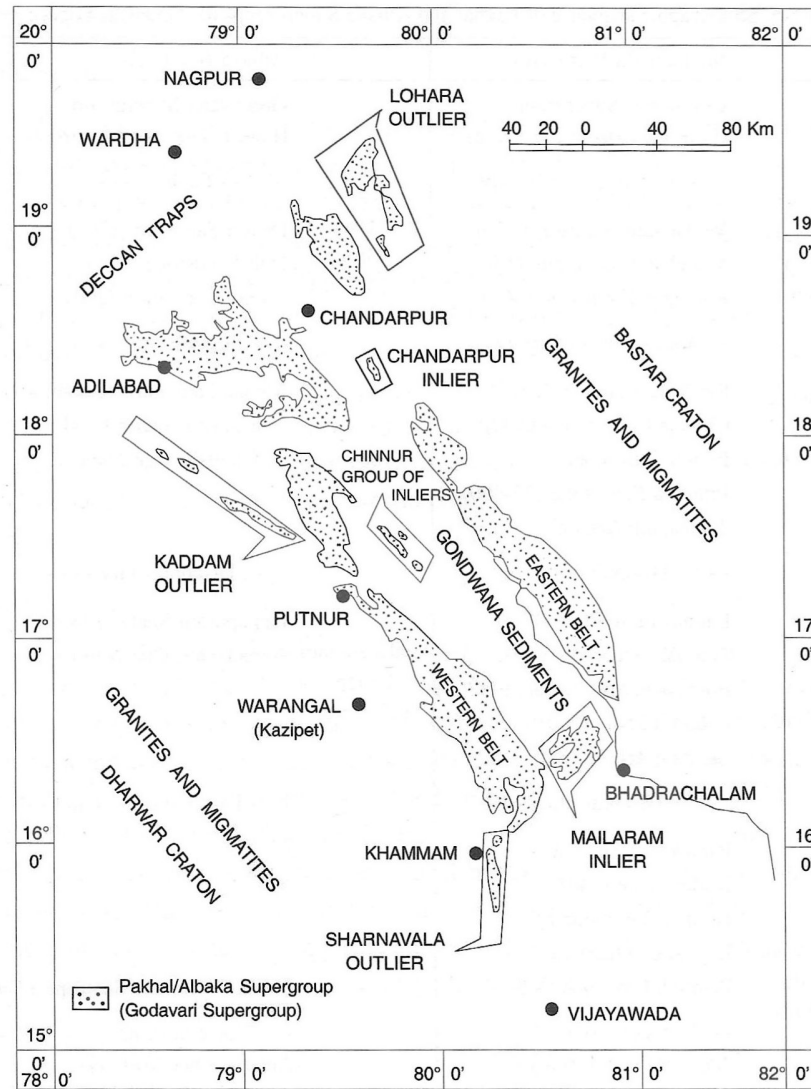


Figure 3.4: Map of the Pranhita-Godavari basin (from Ramakrishnan and Vaidyanadhan 2010).

Stratigraphic sequence of Pakhal and Albaka Supergroups (or Godavari Supergroup)			
Mallampalli Belt (SW)		Albaka Belt (NE)	
	Gondwana Supergroup (Late Palaeozoic-Mesozoic)		Gondwana Supergroup (Late Palaeozoic-Mesozoic)
	-- Angular Unconformity --		---- Fault ----
Sullavai Group (870 m)	Venkatapur Sandstone (50) Mancharial Quartzite (150) Ramagiri Formation (360)	Usur Group (1375 m)	Delam Sandstone (200) Doli Sandstone (975) Nambi Formation (200)
	-- Angular unconformity --		--- Disconformity ---
Penganga Group (2700 m)	Sat Nala Shale (200) Chanda Limestone / (300) Putnur Limestone Pranhita Sandstone (25-400) Takalapalli Arkose	(=Penganga Group) (1000 m)	Albaka/Pamanuru (Chelimala) Sandstone with basal Utlapalli Conglomerate
	--- Disconformity ---		---- Disconformity ----
Mulug Group (2830 m)	Laknavaram Shale (1500) Pattipalli Quartzite (300) Enchencheruvu Dolomite (300) Polaram Shale (500) Jakaram Arkose (230)	Venkatapuram Group (2250 m)	Tippapuram Shale (1340) Somadevara Quartzite (915)
	---- Disconformity ----		--- Disconformity/Fault ---
Mallampalli Group (825 m)	Pandikunta Shale / Karlai Shale (340) Gunjeda Dolomite / Bayyaram Quartzite Bolapalli Formation (185)		Cherla Formation / Somanpalli Gp
	-- Non-conformity / Angular unconformity --		--- Non conformity / Angular unconformity ---
	Crystalline basement (Dharwar craton)		Crystalline basement (Bastar craton)
Numbers in parenthesis denotes thickness in metres			

Figure 3.5: The stratigraphy of the Godavari Supergroup (from Ramakrishnan and Vaidyanadhan 2010).

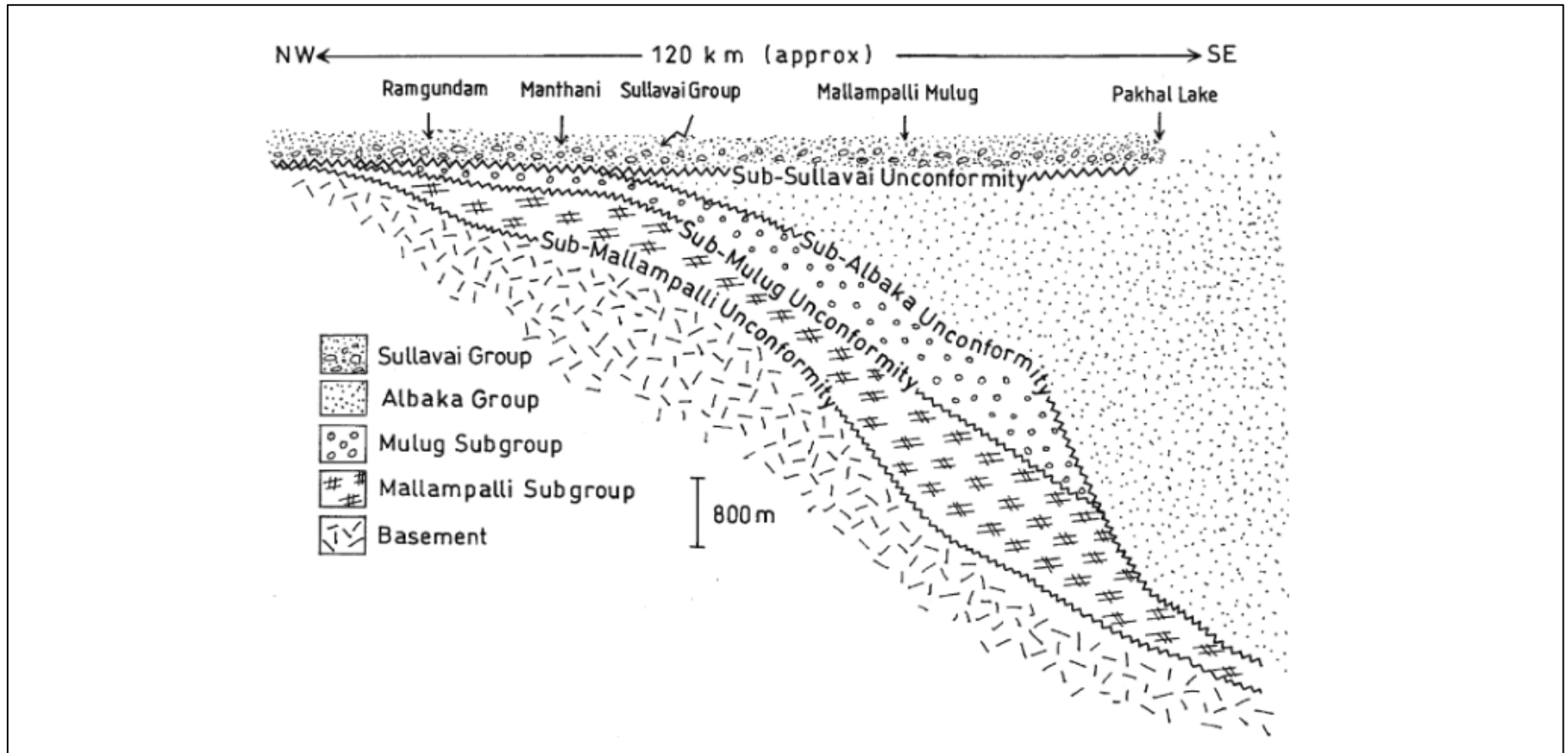


Figure 3.6: Schematic diagram of the stratigraphic relationships within the Godavari Supergroup along the long axis of the Pranhita-Godavari Basin (from Chaudhari 2003).

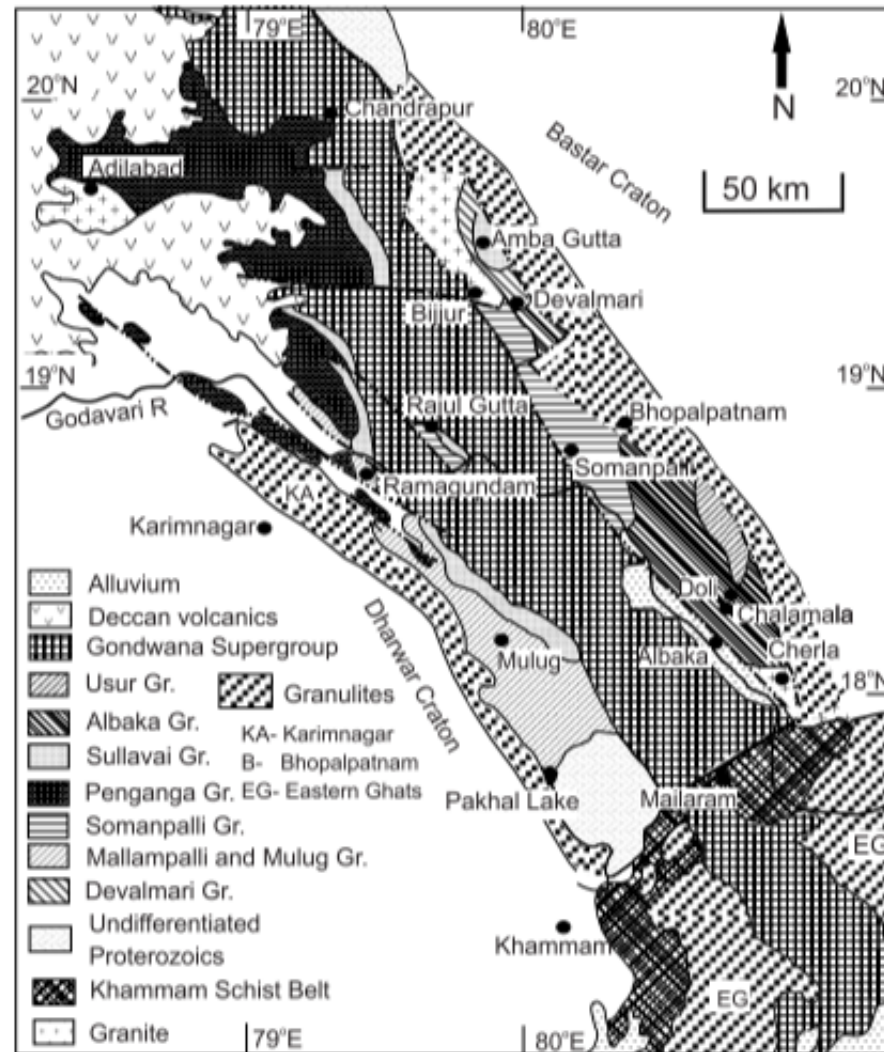


Figure 3.7: The geology of the Proterozoic age Pranhita-Godavari Basin from Chaudhuri et al. (2012). The various Proterozoic age units are shown between the Karimnagar Granulite Belt of the Eastern Dharwar Craton, the Bhopalpatnam Granulite Belt of the Bastar Craton, and the Eastern Ghats Mobile Belt, and either side of the younger Gondwana Supergroup.

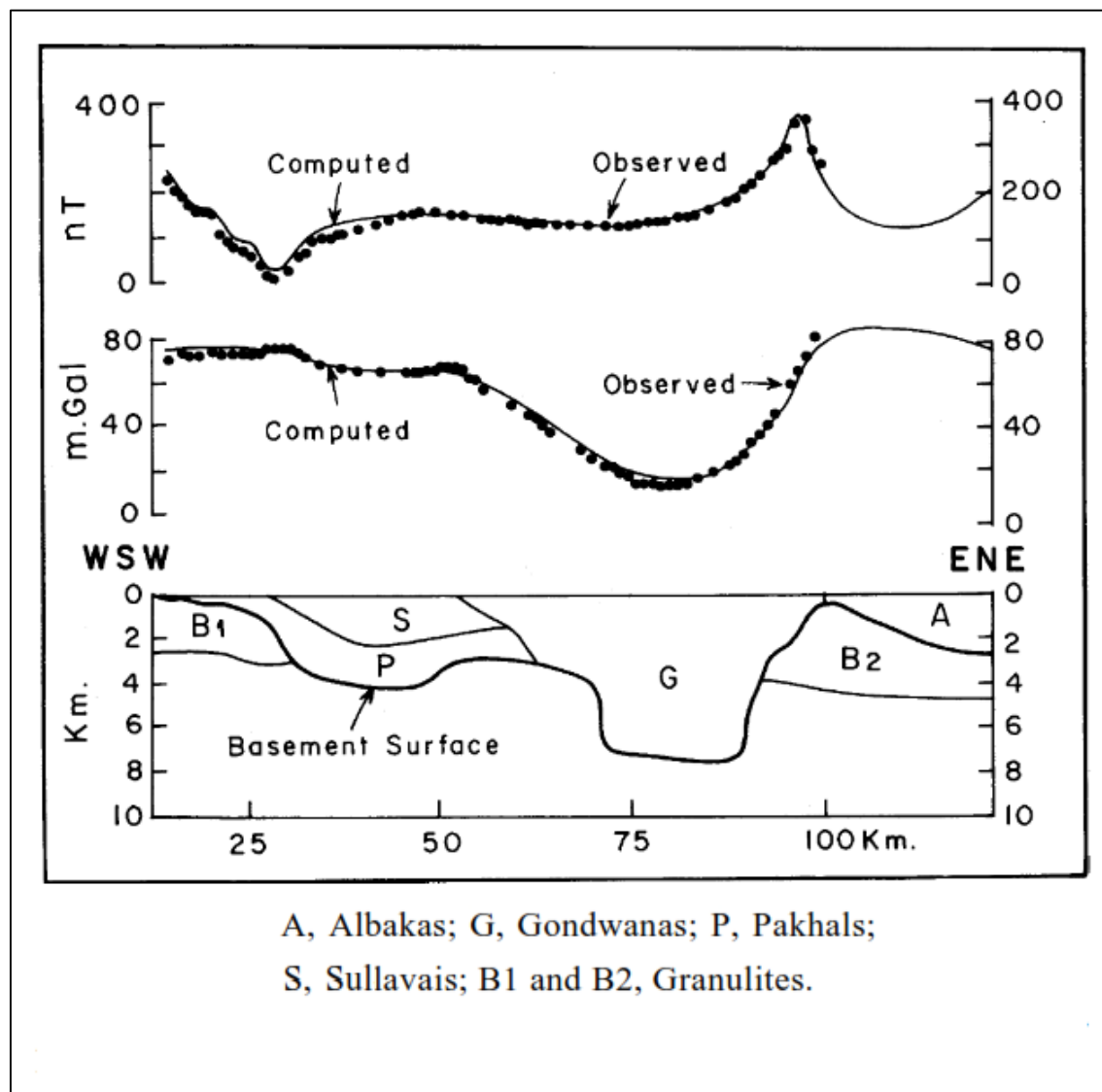


Figure 3.8: Cross section of the Godavari Rift based on regional gravity and magnetic data (from Sarma and Krishna Rao 2005).

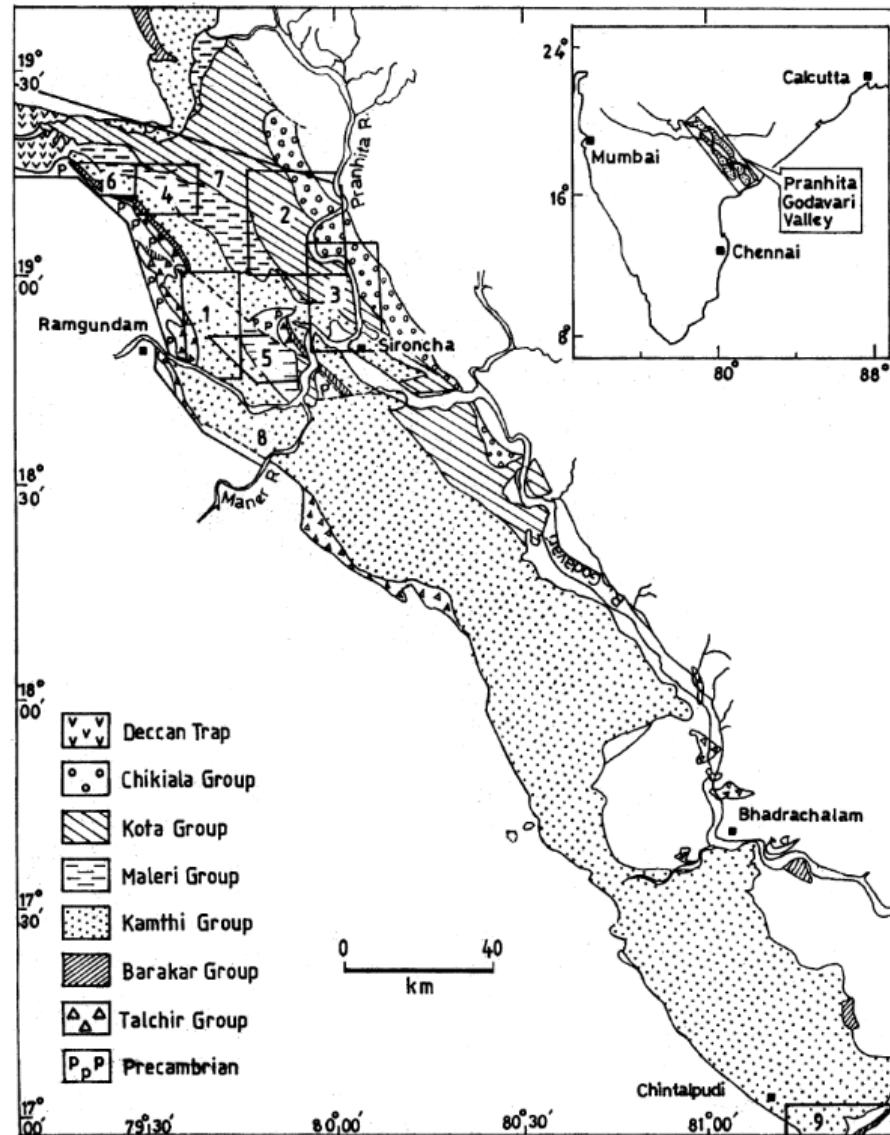


Figure 3.9: Formations of the Gondwana Supergroup (from Sengupta 2003).

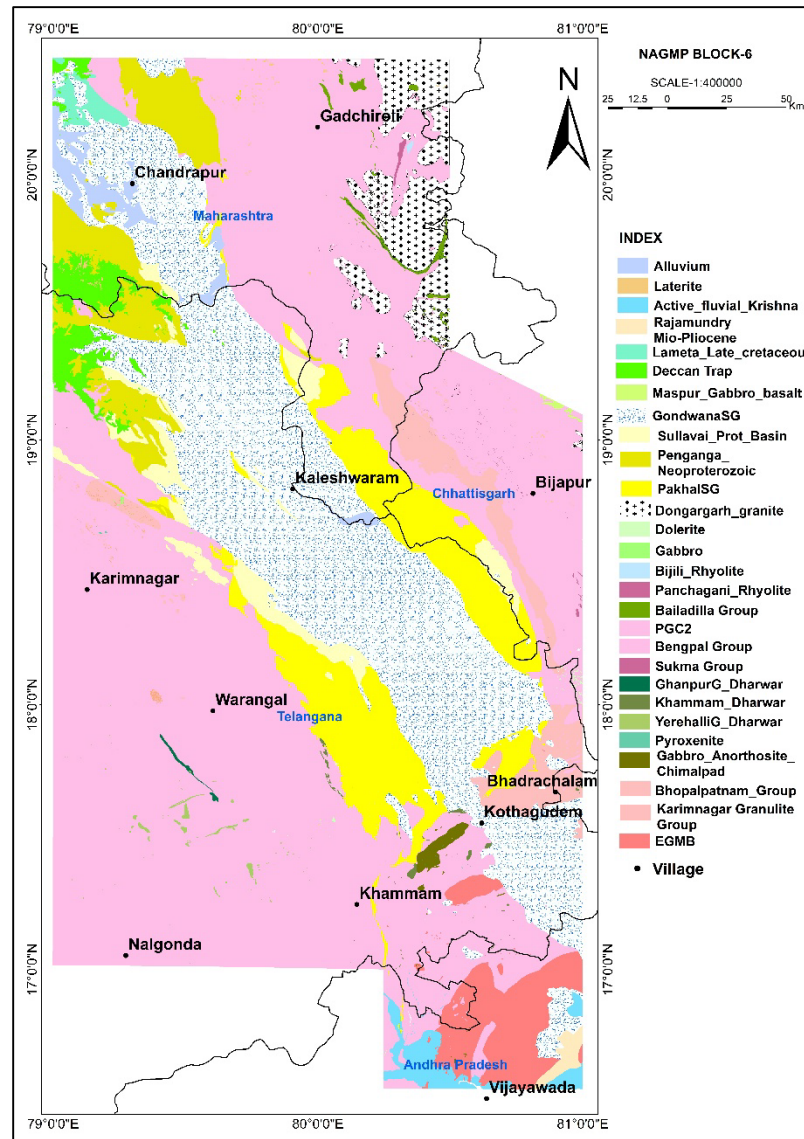


Figure 3.10: Simplified geological map of Block-6 provided by the Geological Survey of India prior to the findings of this report.

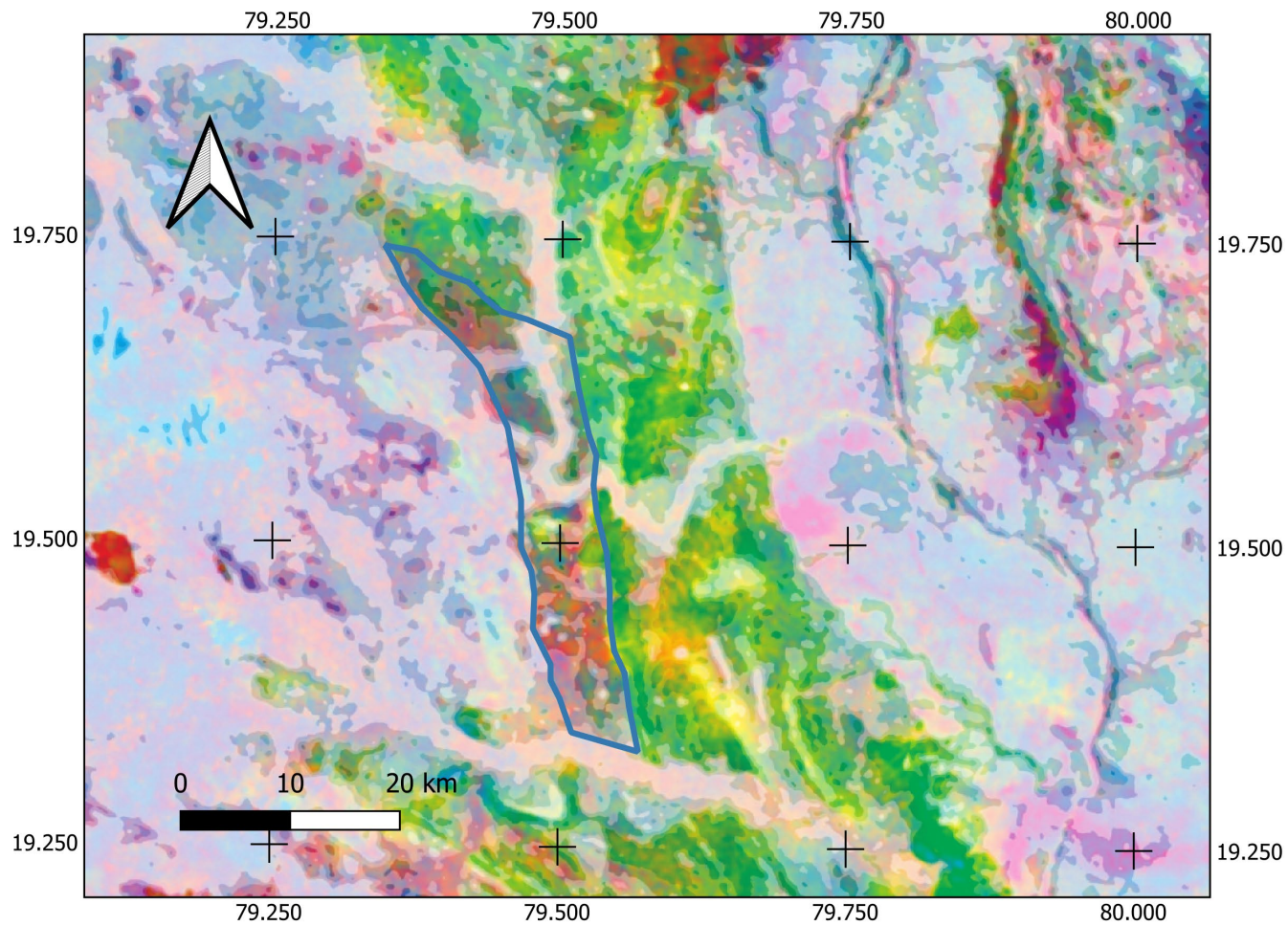


Figure 3.11: An area of mapped Barakar formation sediments from the Gondwana Supergroup, outlined in blue, illustrating the gamma-ray signature that is characteristic of this formation and also of the overlying Barren Measures formation.

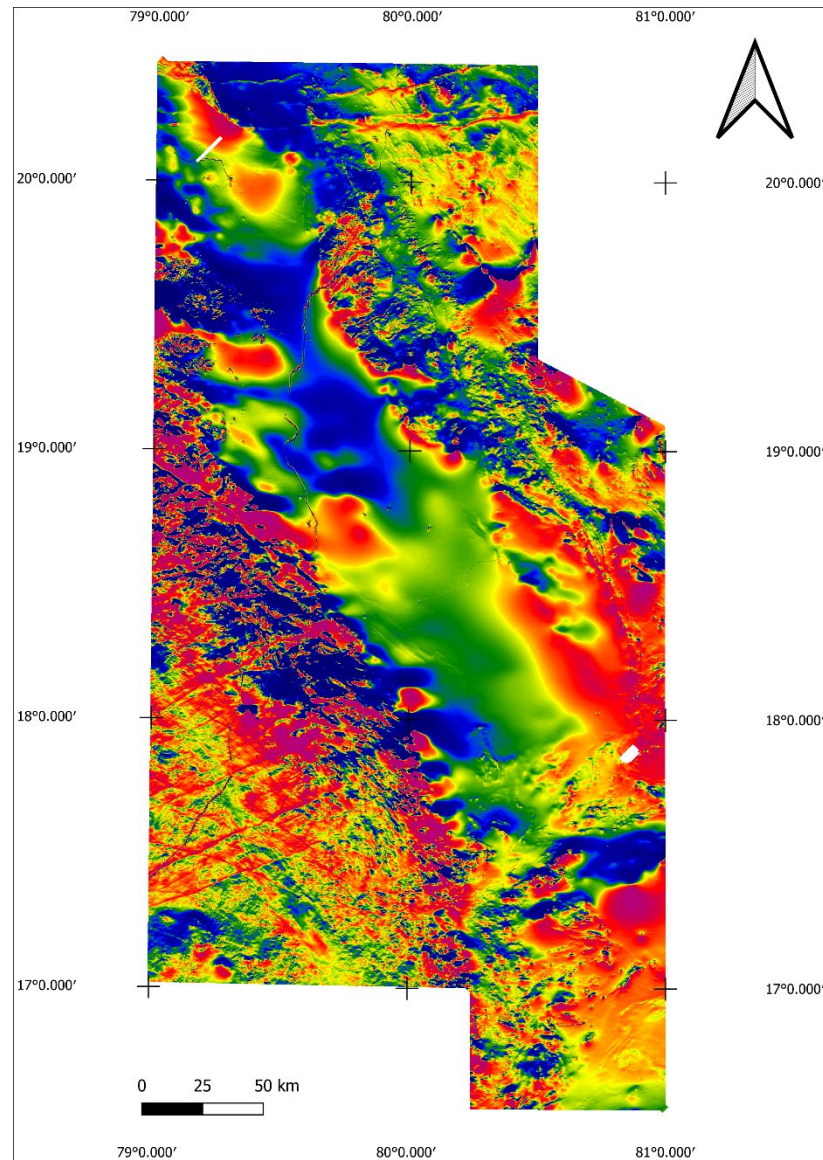


Figure 4.1: The anomalous magnetic field of Block-6.

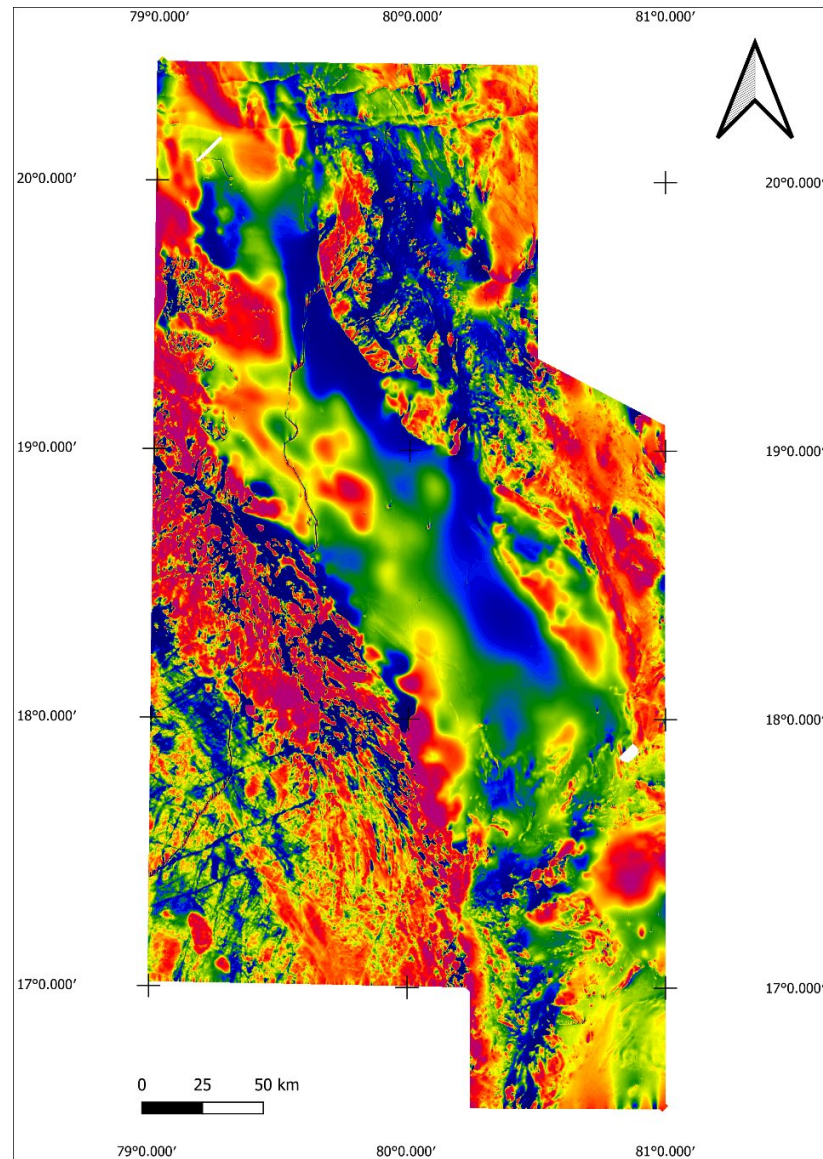


Figure 4.2: The anomalous magnetic intensity of Block-6 reduced to the pole.

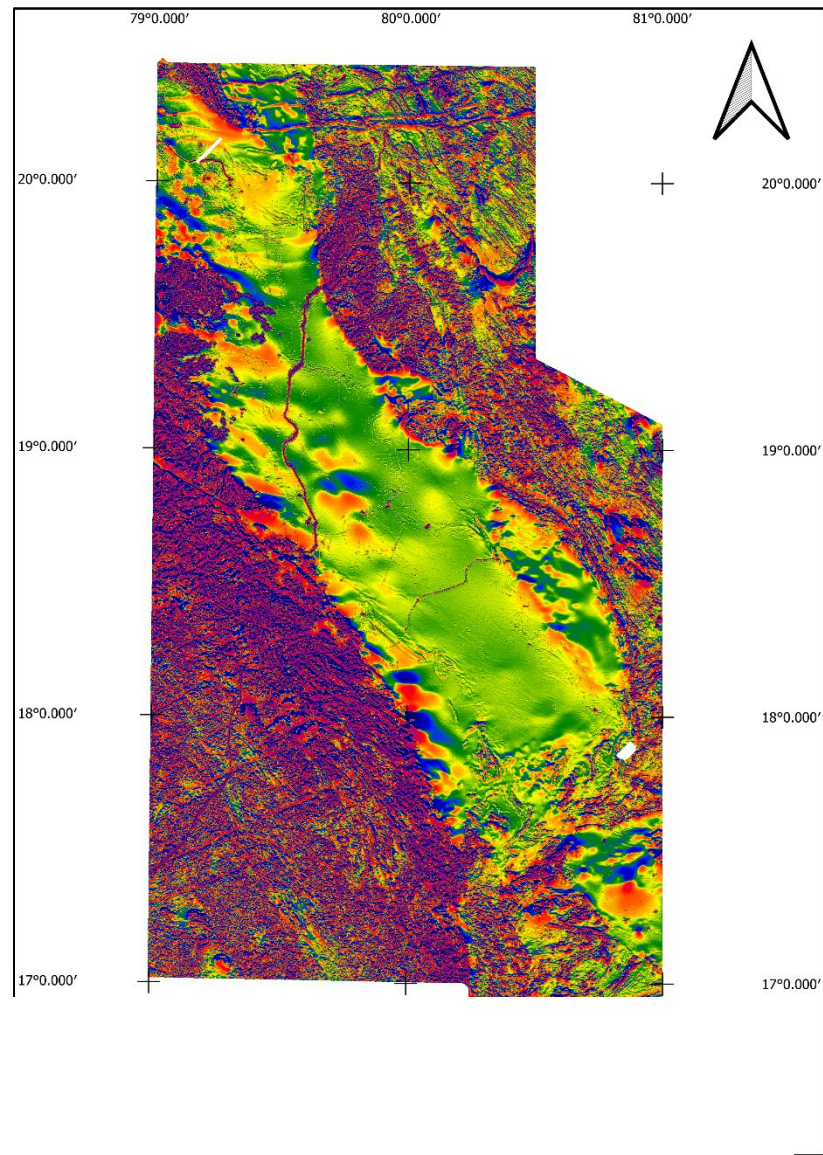


Figure 4.3: First vertical derivative of the anomalous magnetic field.

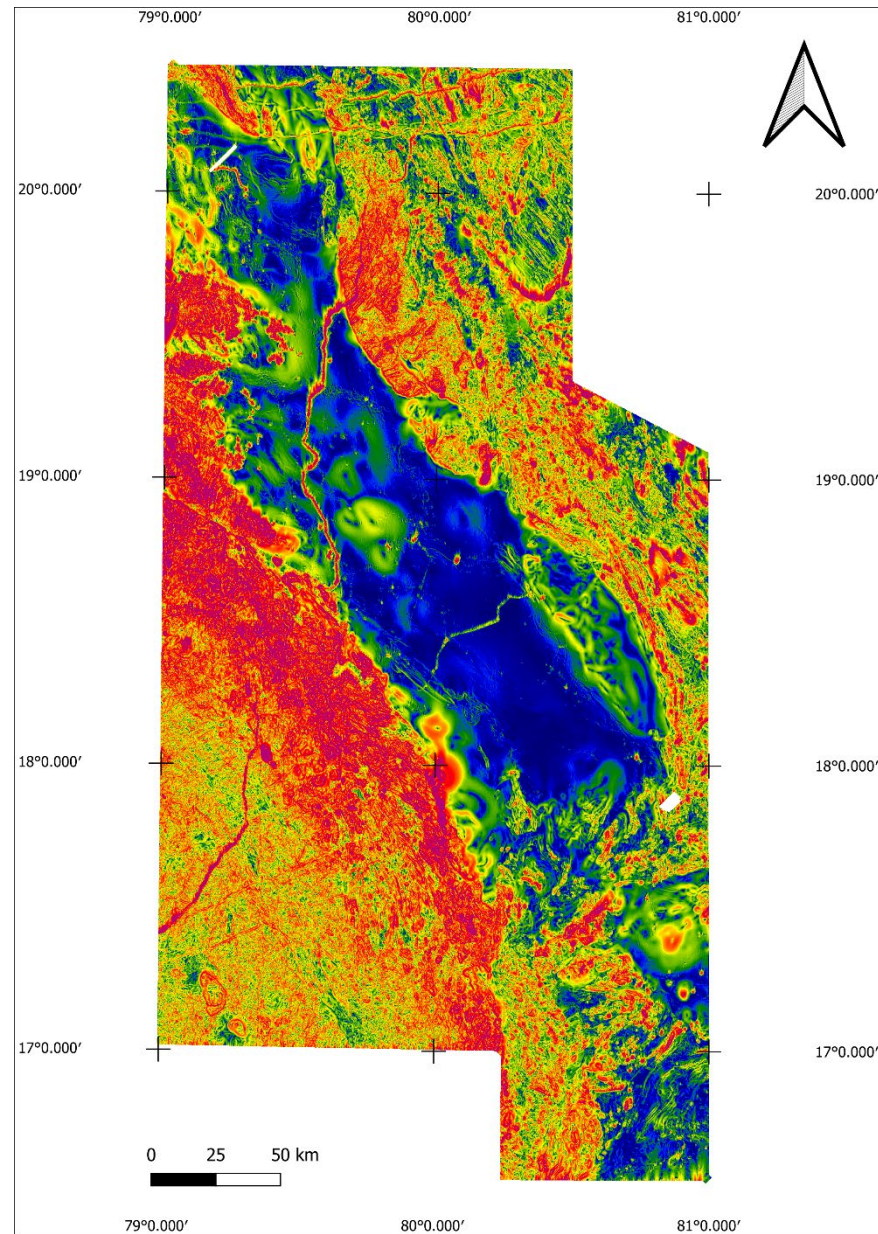


Figure 4.4: Second vertical derivative of the anomalous magnetic field.

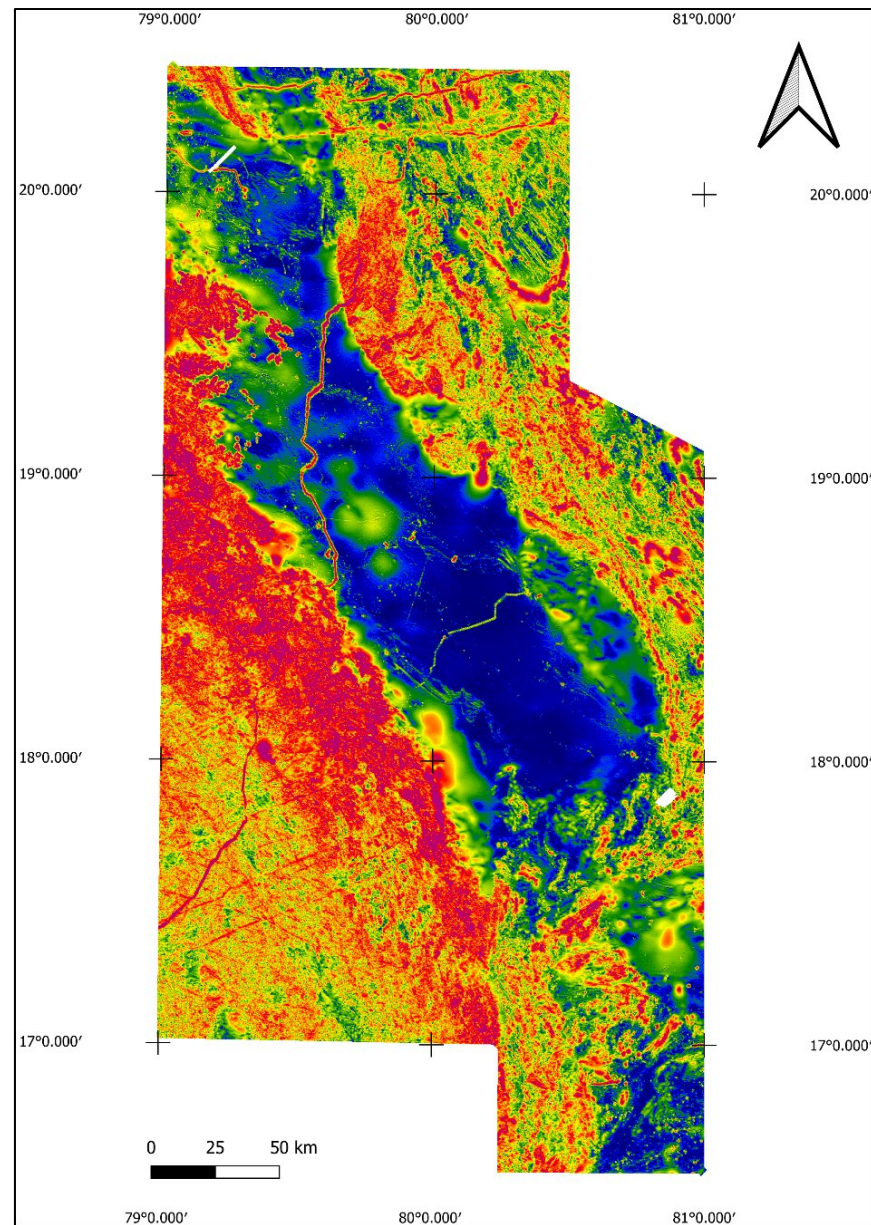


Figure 4.5: Total horizontal gradient of the anomalous magnetic field reduced to the pole.

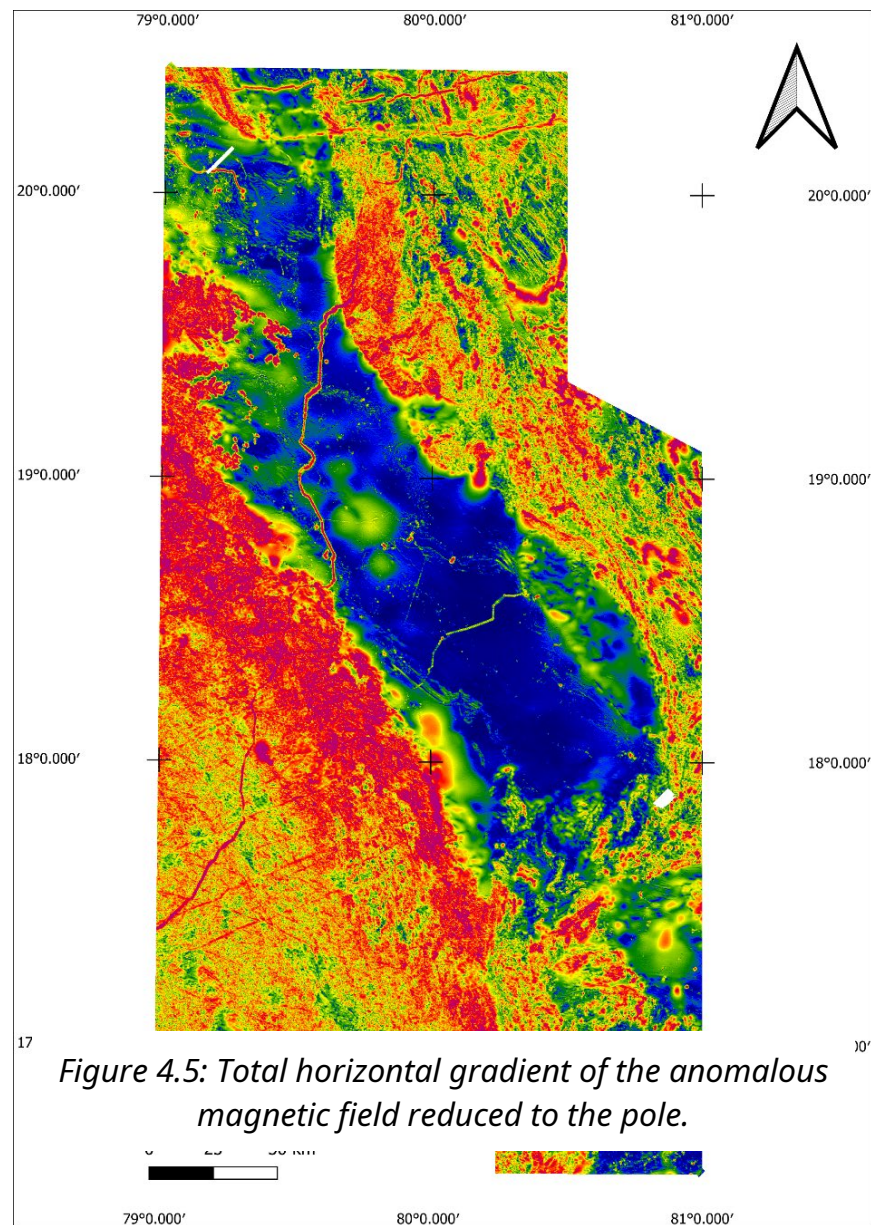


Figure 4.6: Analytic signal (total gradient) of the anomalous magnetic field.

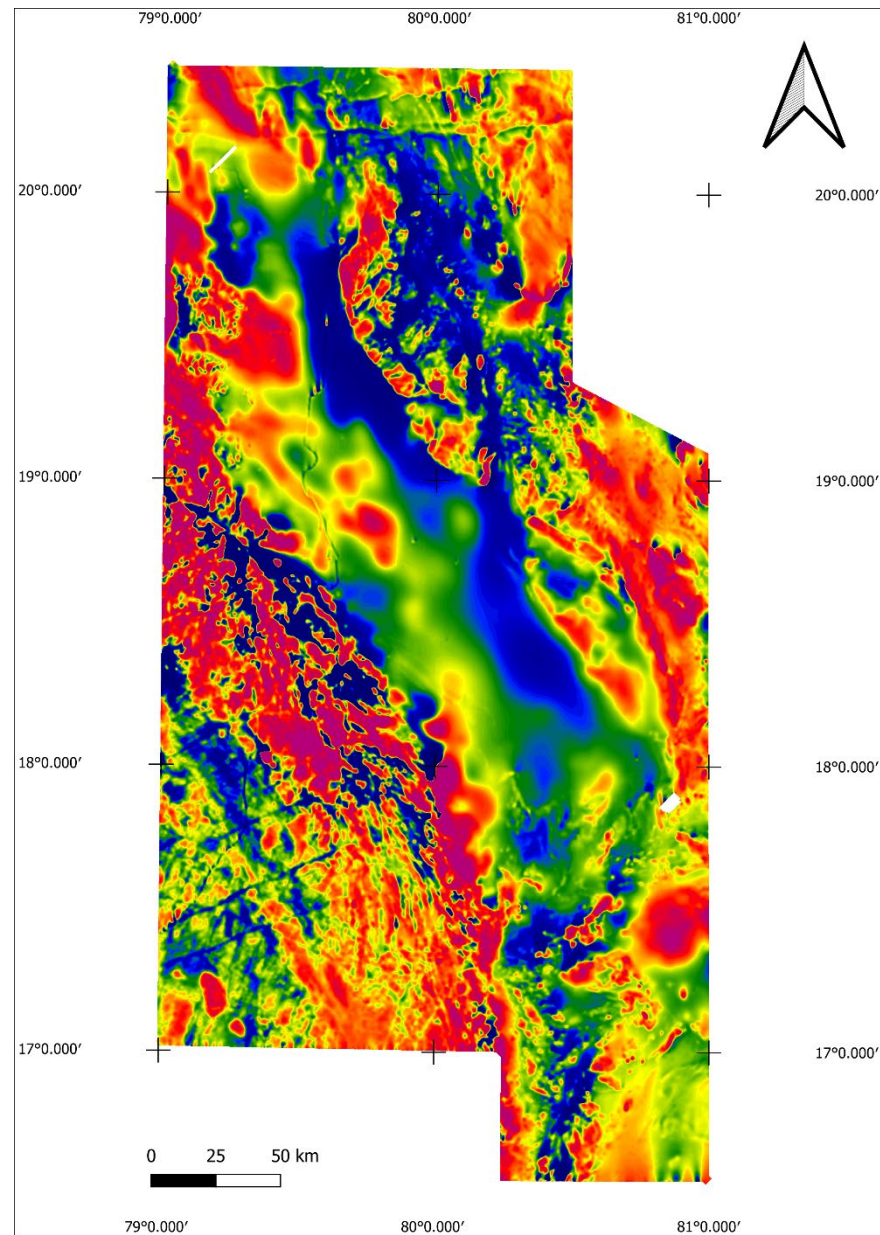


Figure 4.7: Low pass filtered anomalous magnetic field after 100 passes of a Hanning filter.

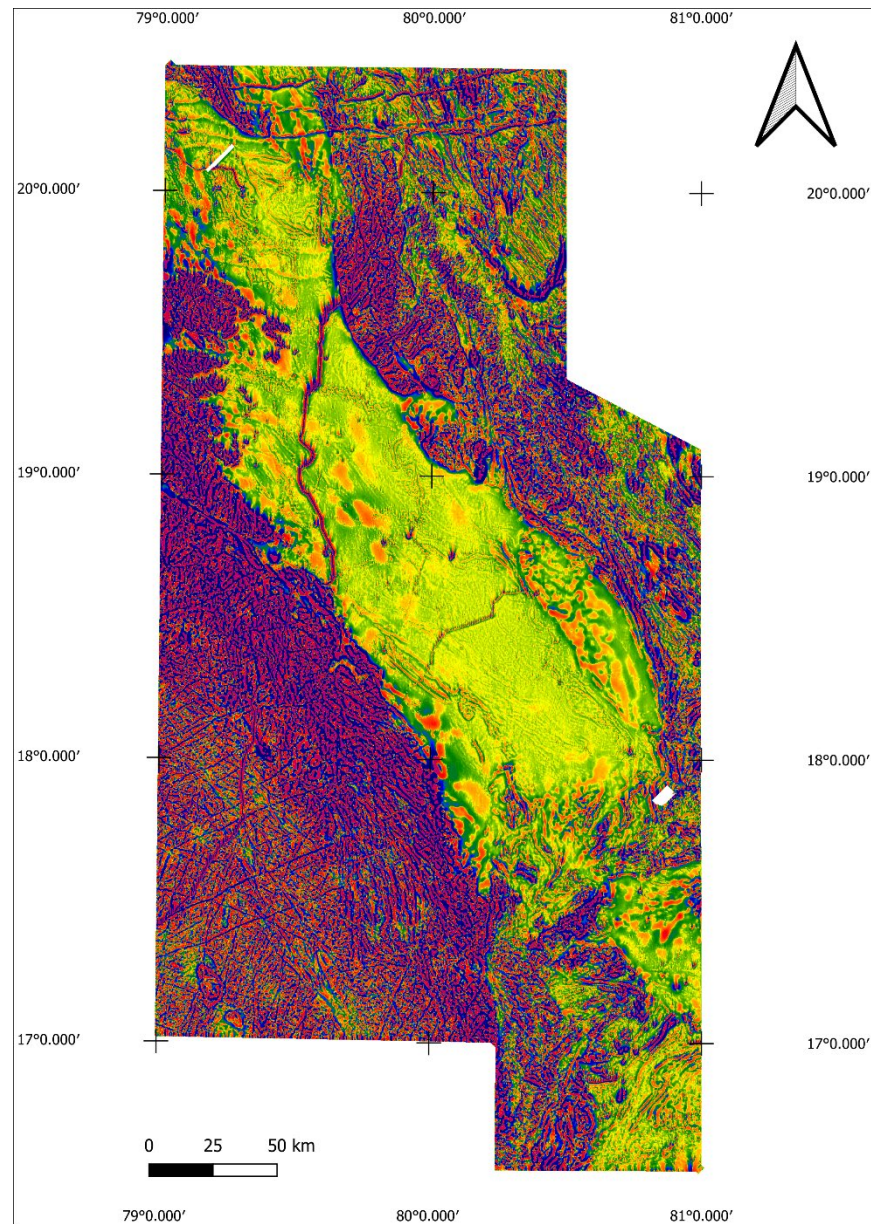


Figure 4.8: Residual high pass filtered anomalous magnetic field after 100 passes of a Hanning filter.

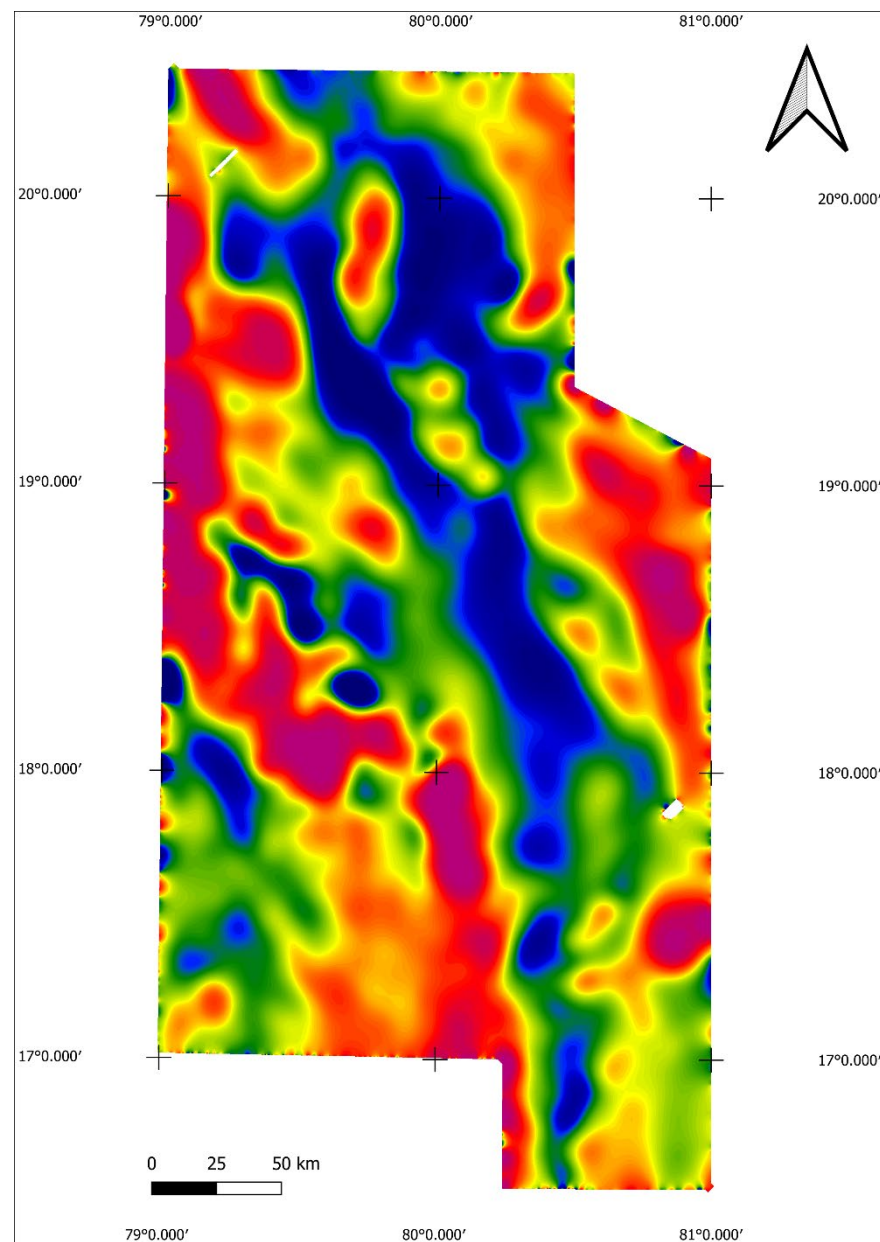


Figure 4.9: Low pass filtered anomalous magnetic field after 12800 passes of a Hanning filter.

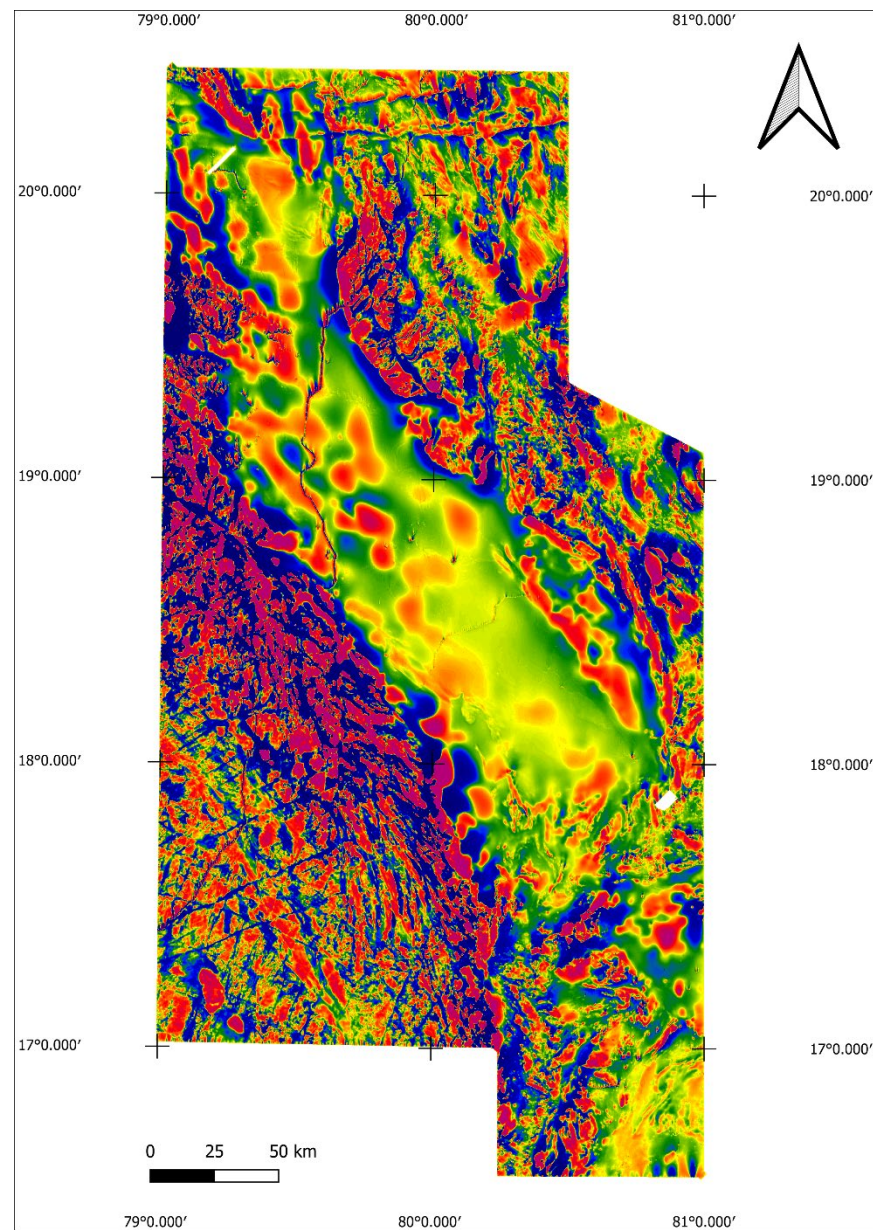


Figure 4.10: Residual high pass filtered anomalous magnetic field after 12800 passes of a Hanning filter.

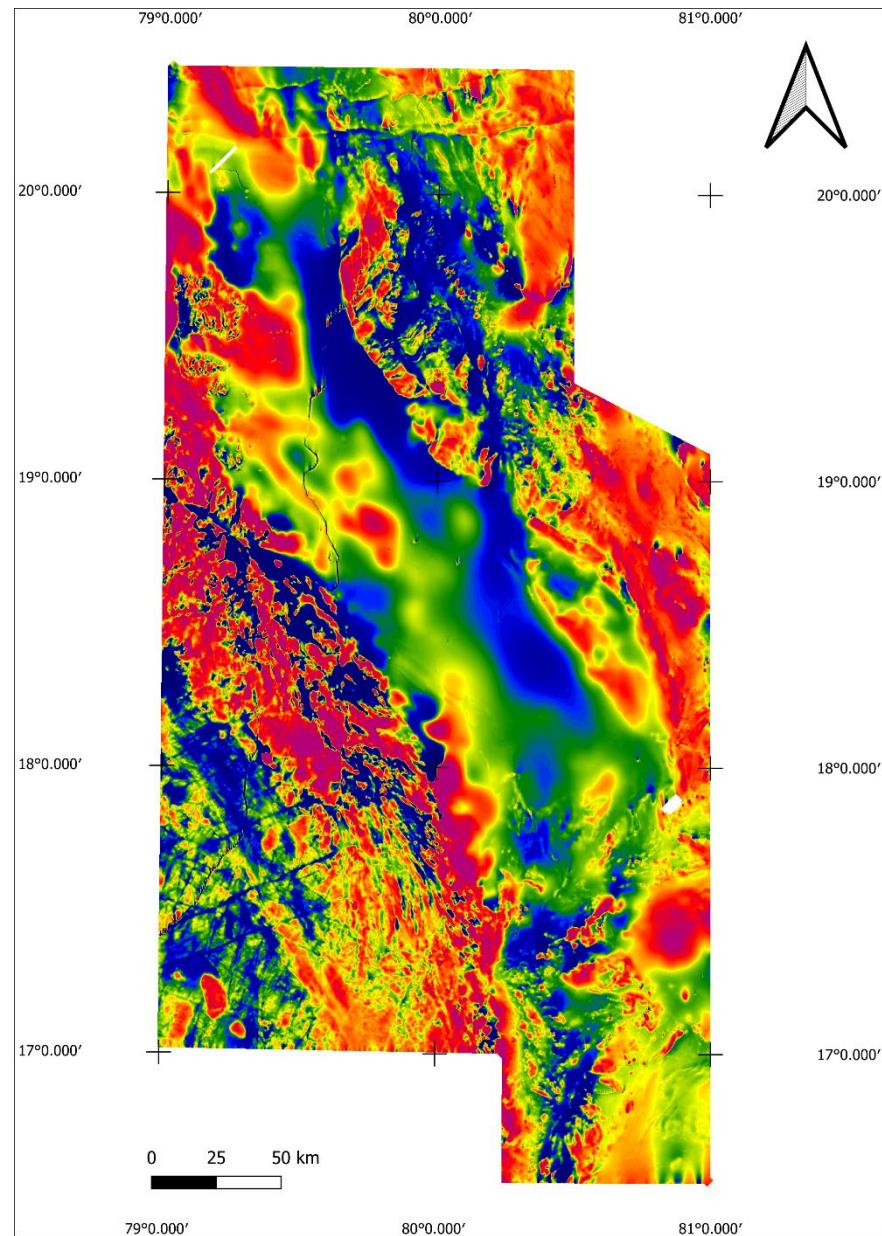


Figure 4.11: Anomalous magnetic field reduced to the pole and upward continued by 100m.

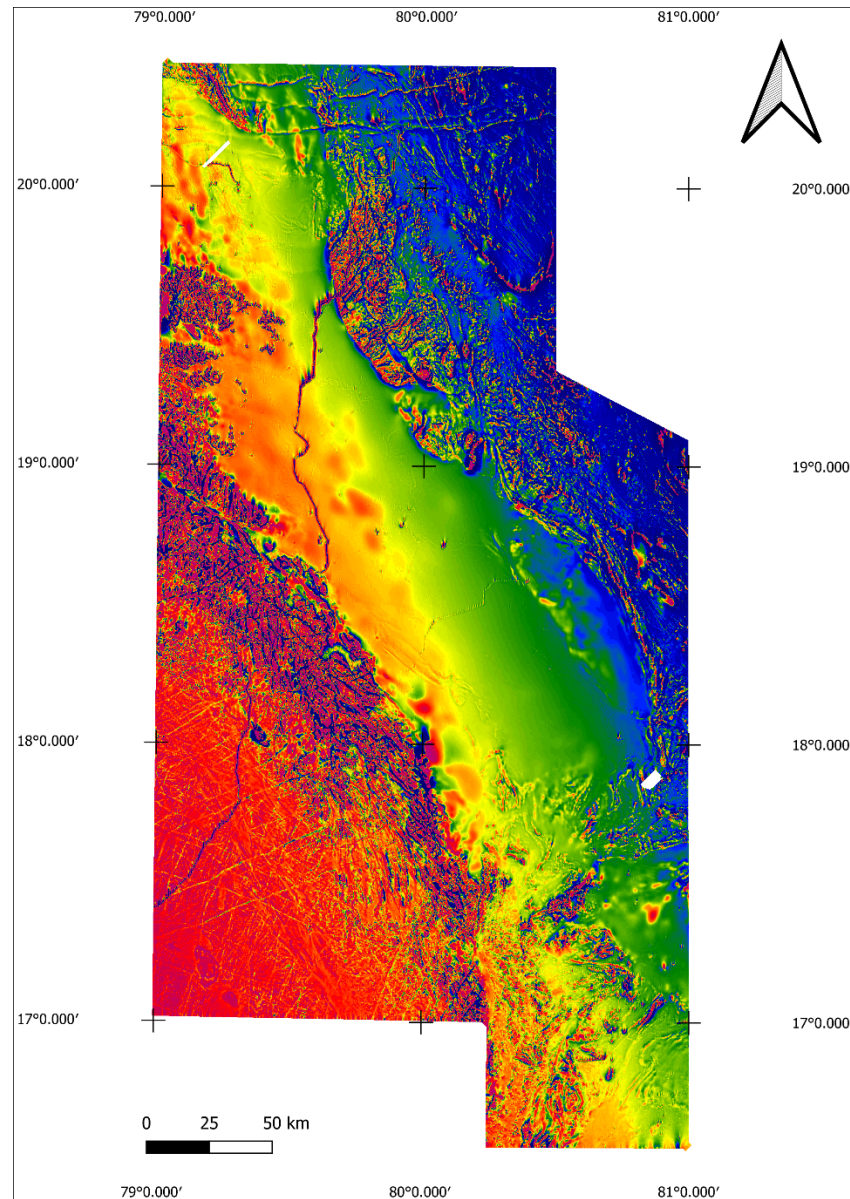


Figure 4.12: Residual of the anomalous magnetic field reduced to the pole and upward continued by 100m.

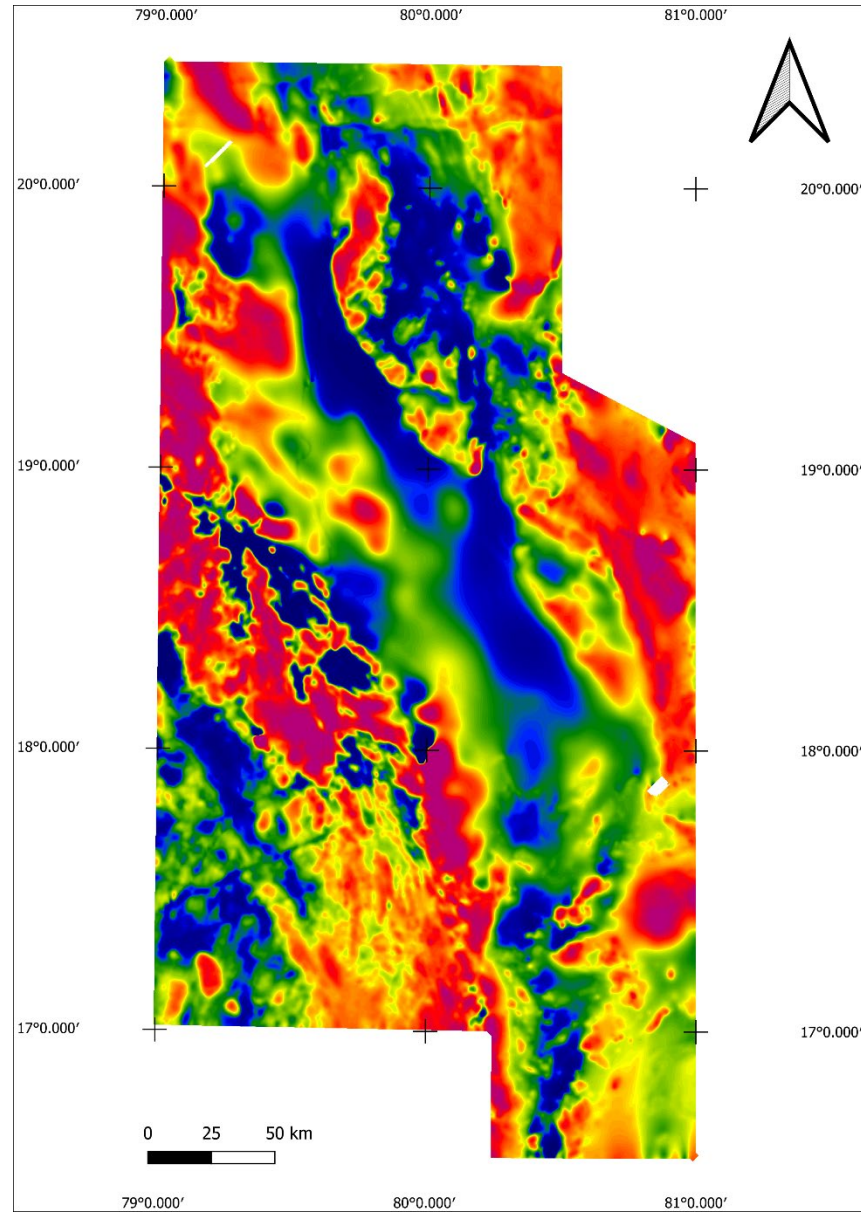


Figure 4.13: Anomalous magnetic field reduced to the pole and upward continued by 1000m.

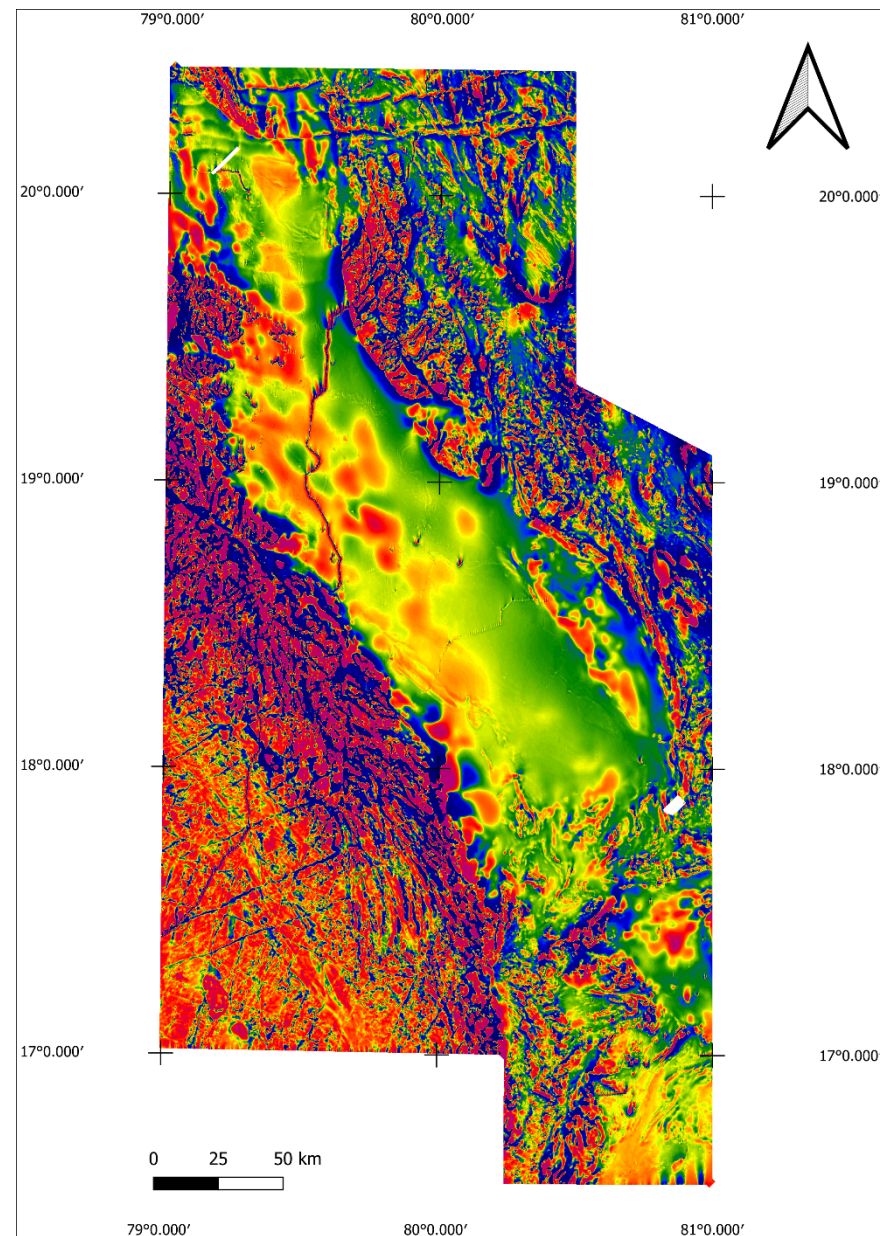


Figure 4.14: Residual of the anomalous magnetic field reduced to the pole and upward continued by 1000m.

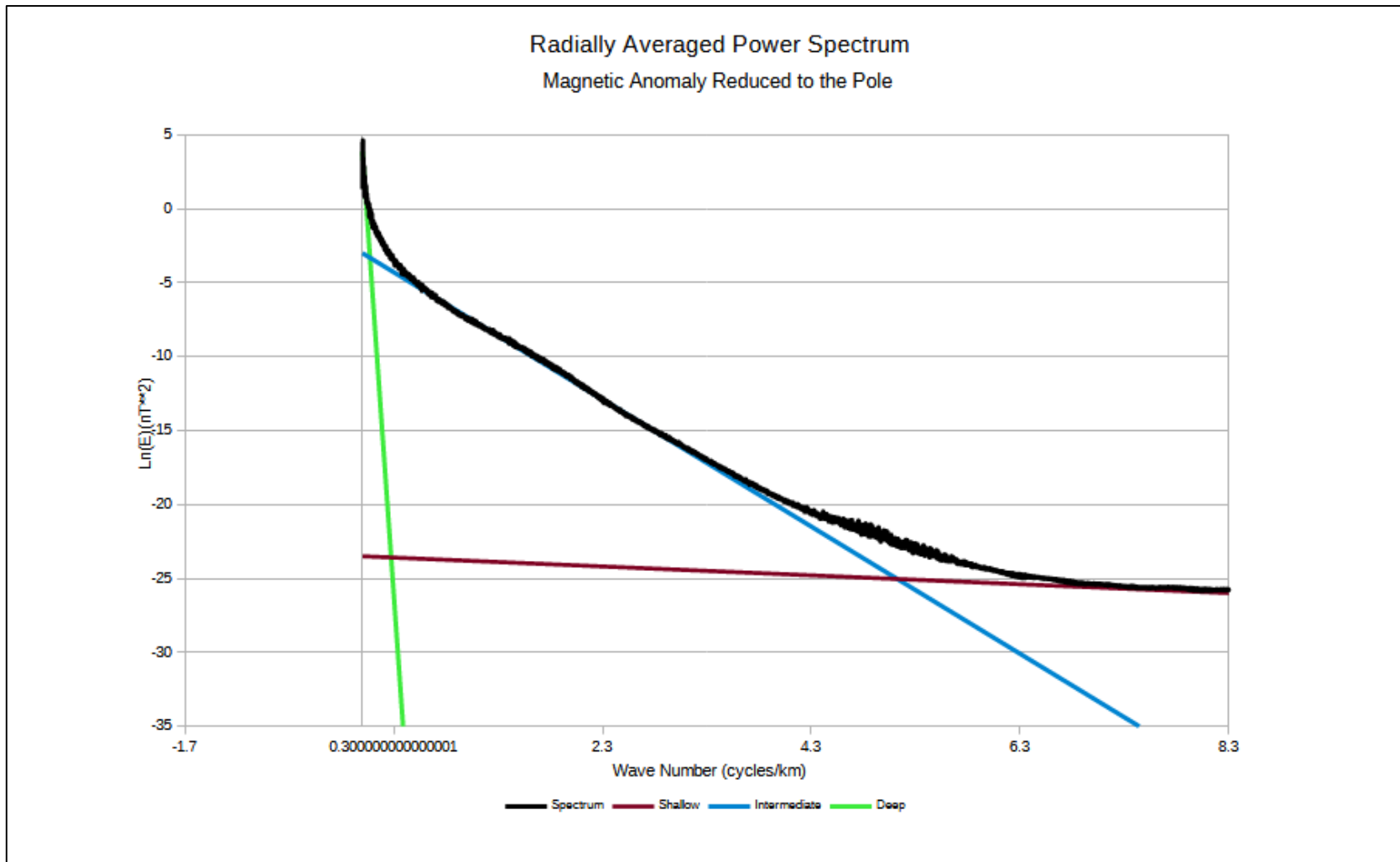


Figure 4.15: Radially averaged power spectrum of the anomalous magnetic field reduced to the pole. Linear fits to the spectrum correspond to low, intermediate and high frequency signal assemblages that are from deep, intermediate and shallow sources.

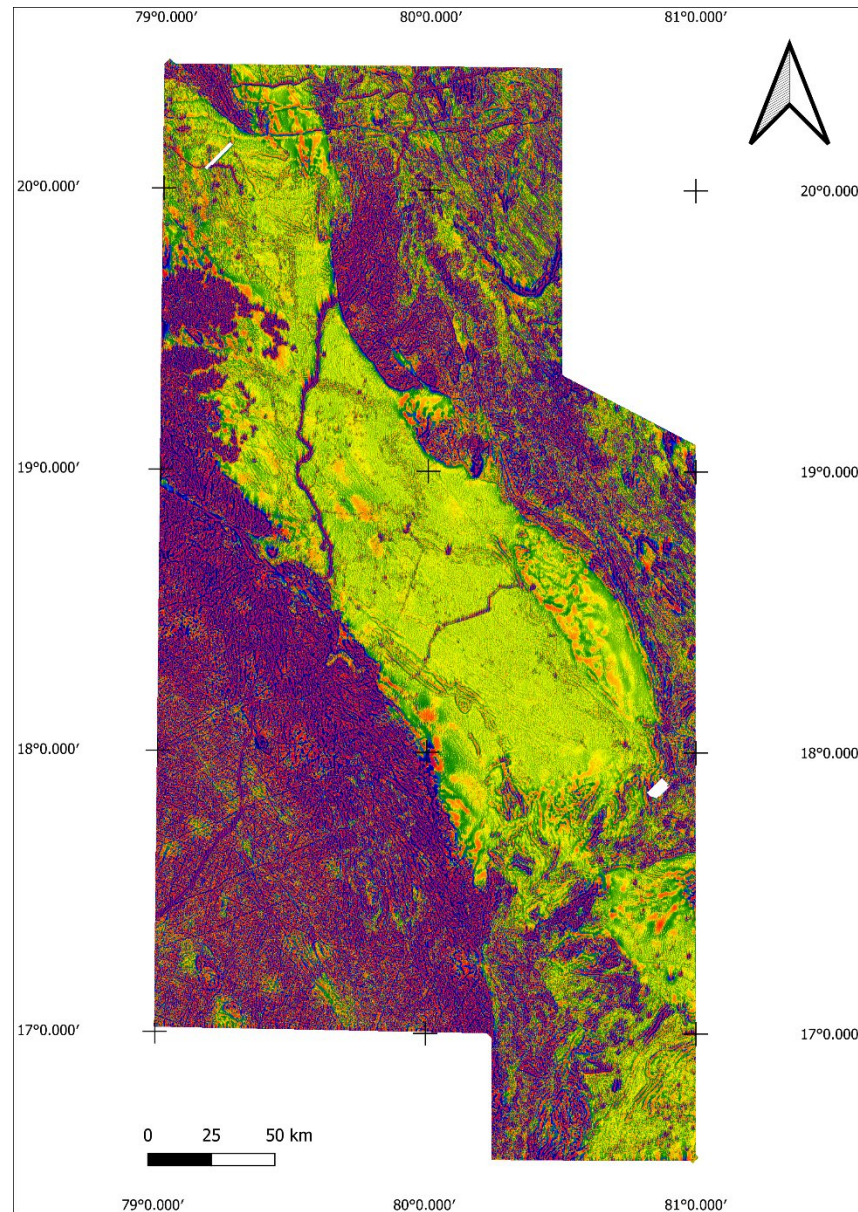


Figure 4.16: Shallow source depth magnetic intensity derived by high pass filtering based on power spectrum analysis.

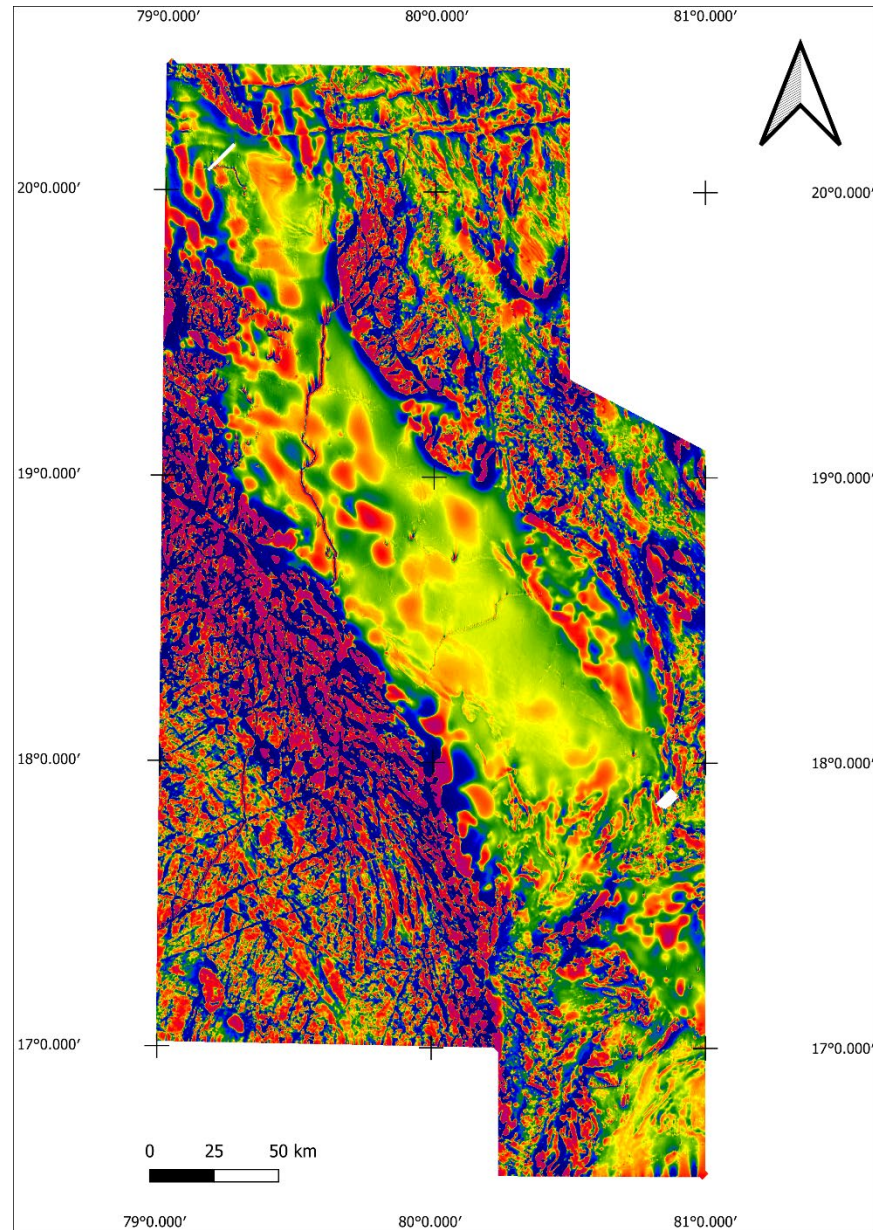


Figure 4.17: Intermediate source depth magnetic intensity derived by band pass filtering based on power spectrum analysis.

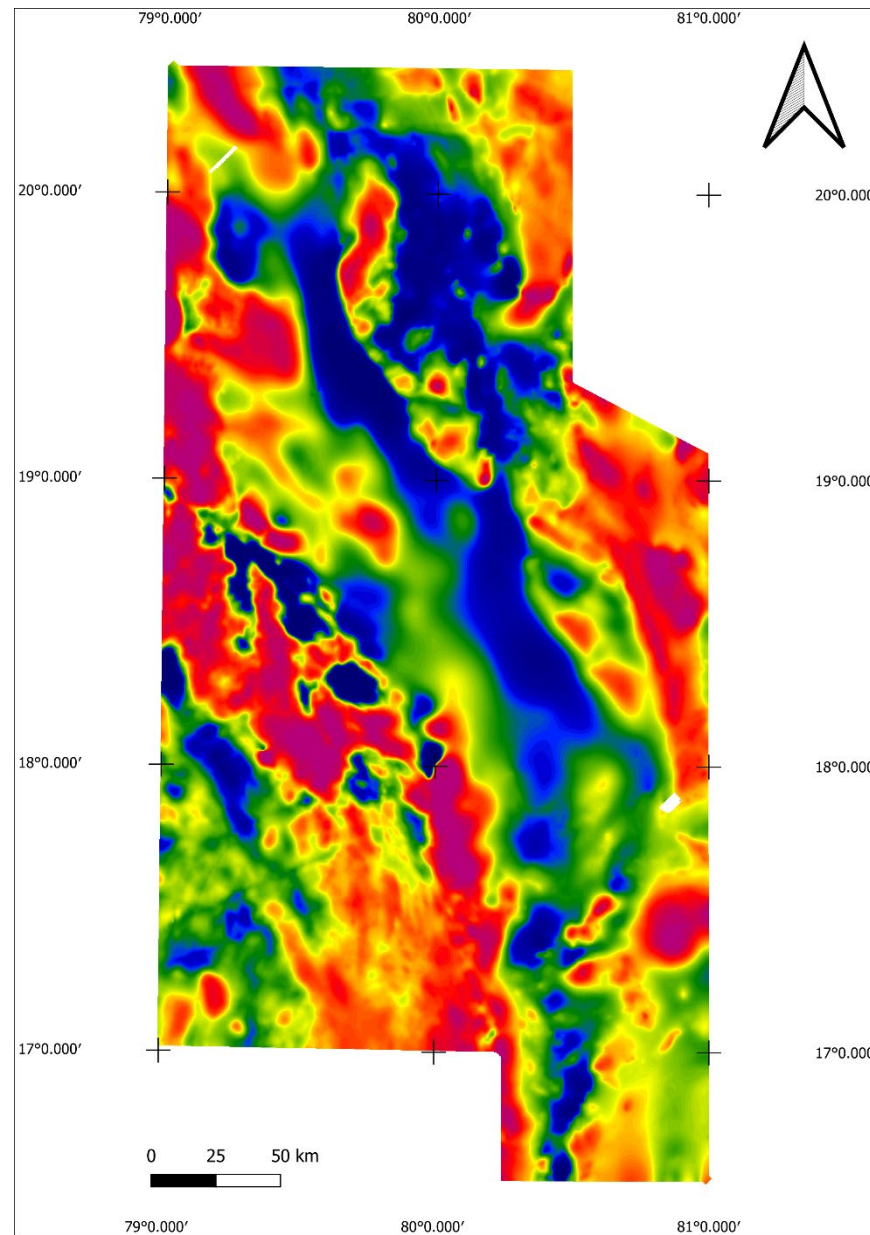


Figure 4.18: Deep source magnetic intensity derived by low pass filtering based on power spectrum analysis.

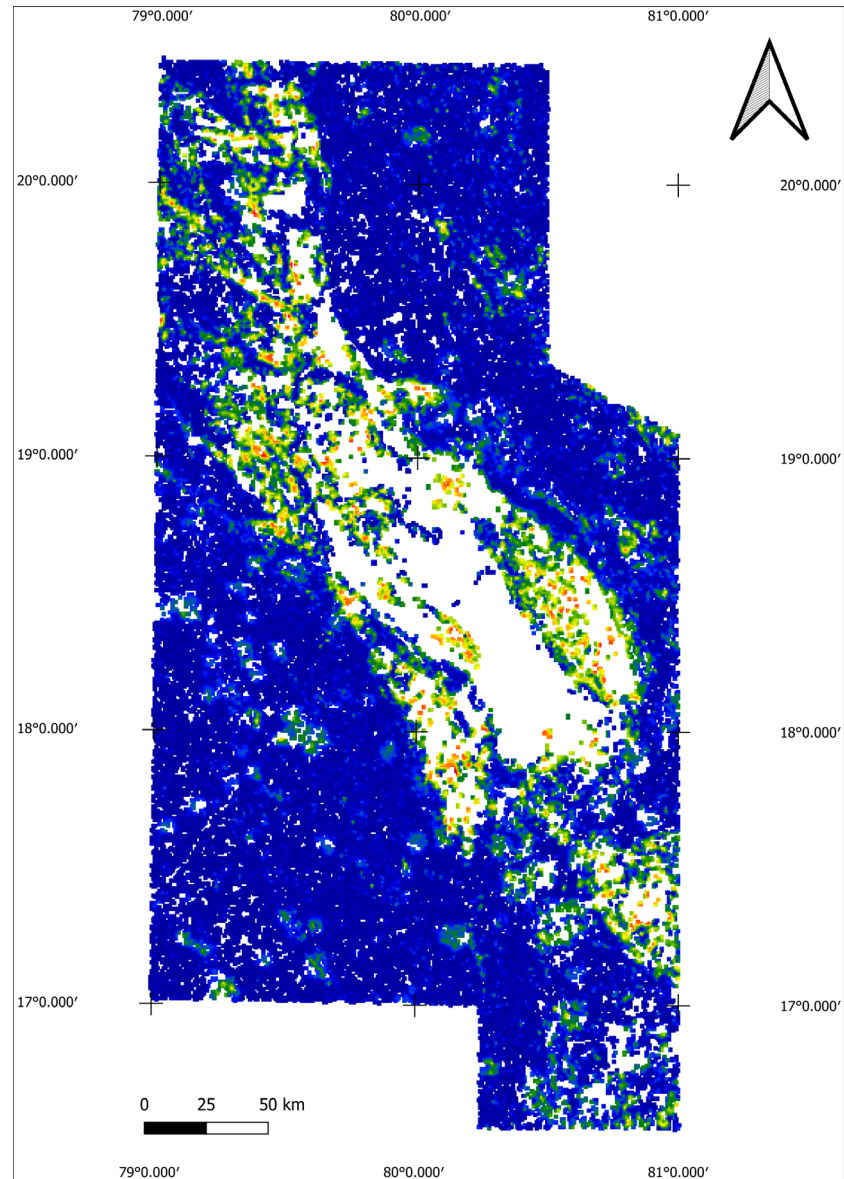


Figure 5.1: Depth to magnetic source below ground based on Euler deconvolution of the anomalous magnetic field reduced to the pole, with a structural index of zero.

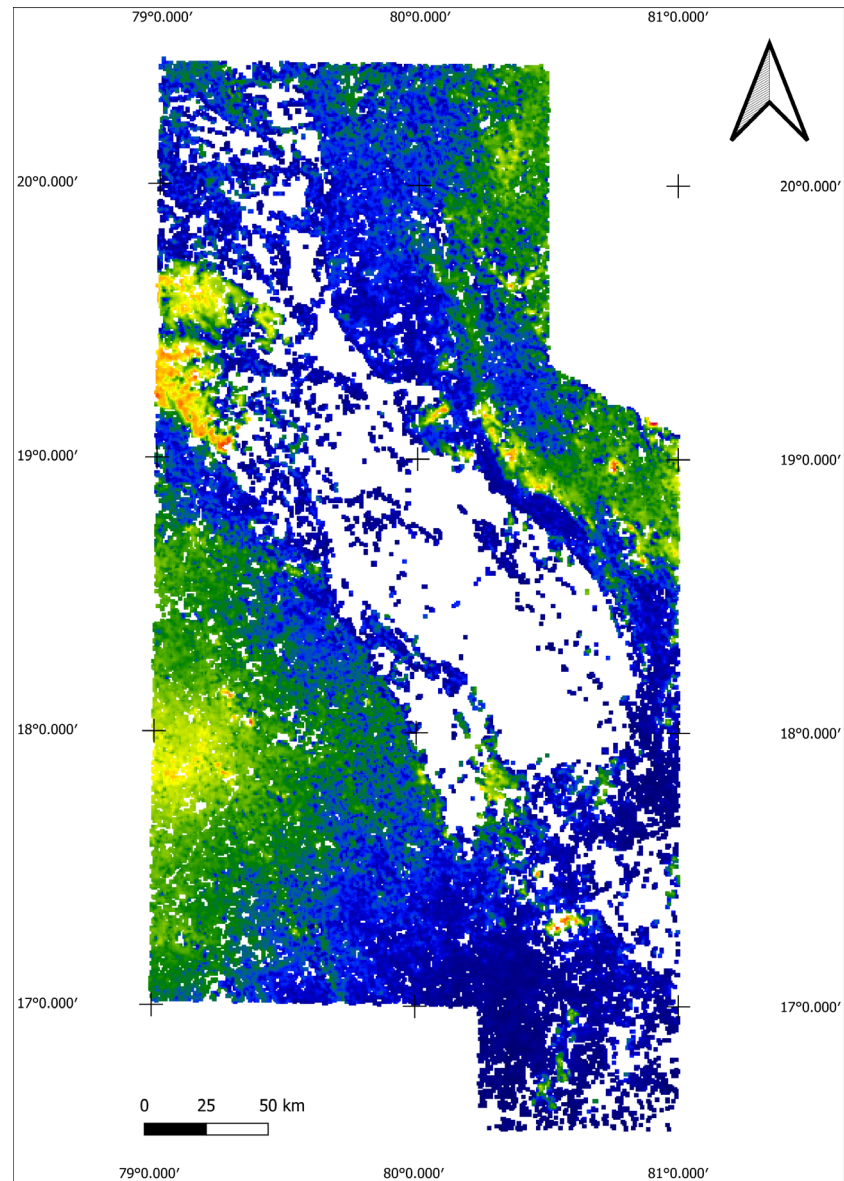


Figure 5.2: Height of magnetic source with respect to mean sea level based on Euler deconvolution of the anomalous magnetic field reduced to the pole, with a structural index of zero.

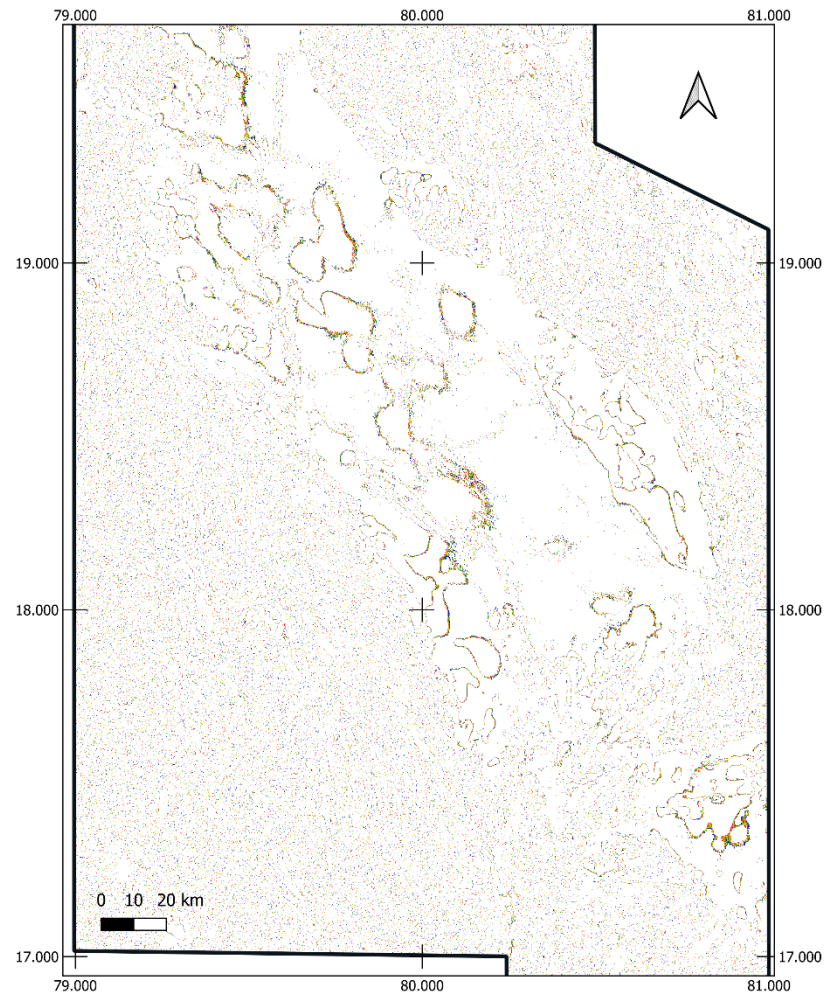


Figure 5.3: Tilt angle of the anomalous magnetic field reduced to the pole, restricted to $\pm 5^\circ$.

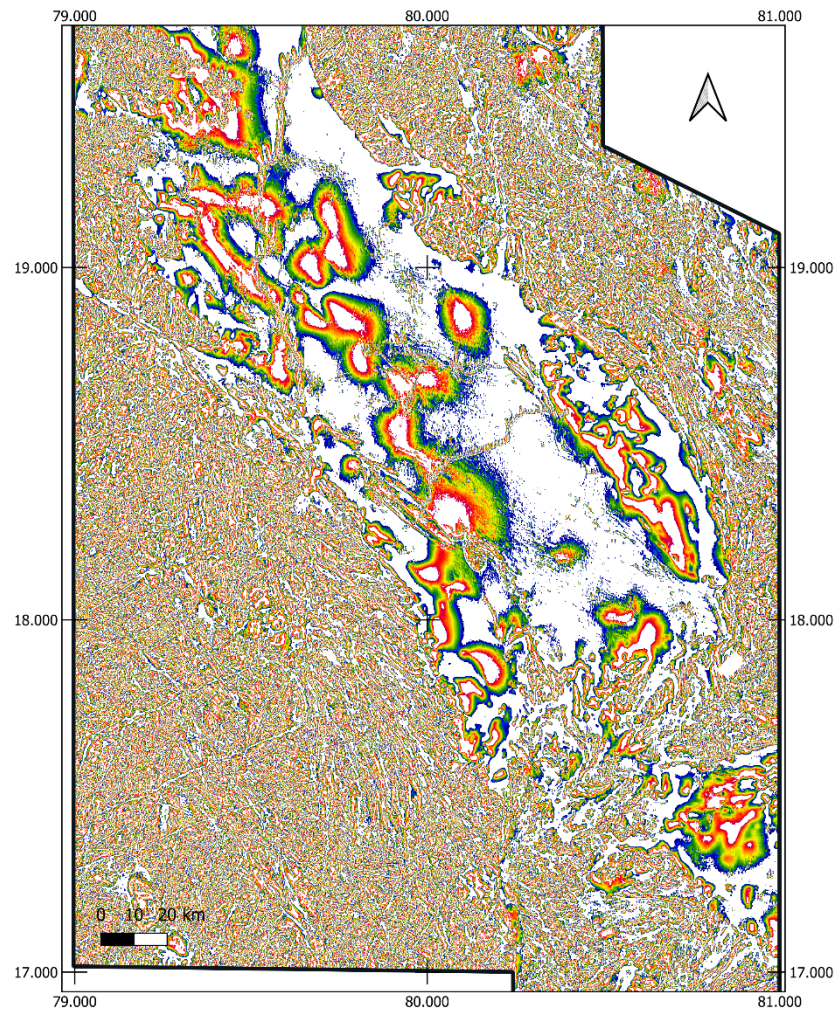


Figure 5.4: Tilt angle of the anomalous magnetic field reduced to the pole, restricted to $\pm 45^\circ$.

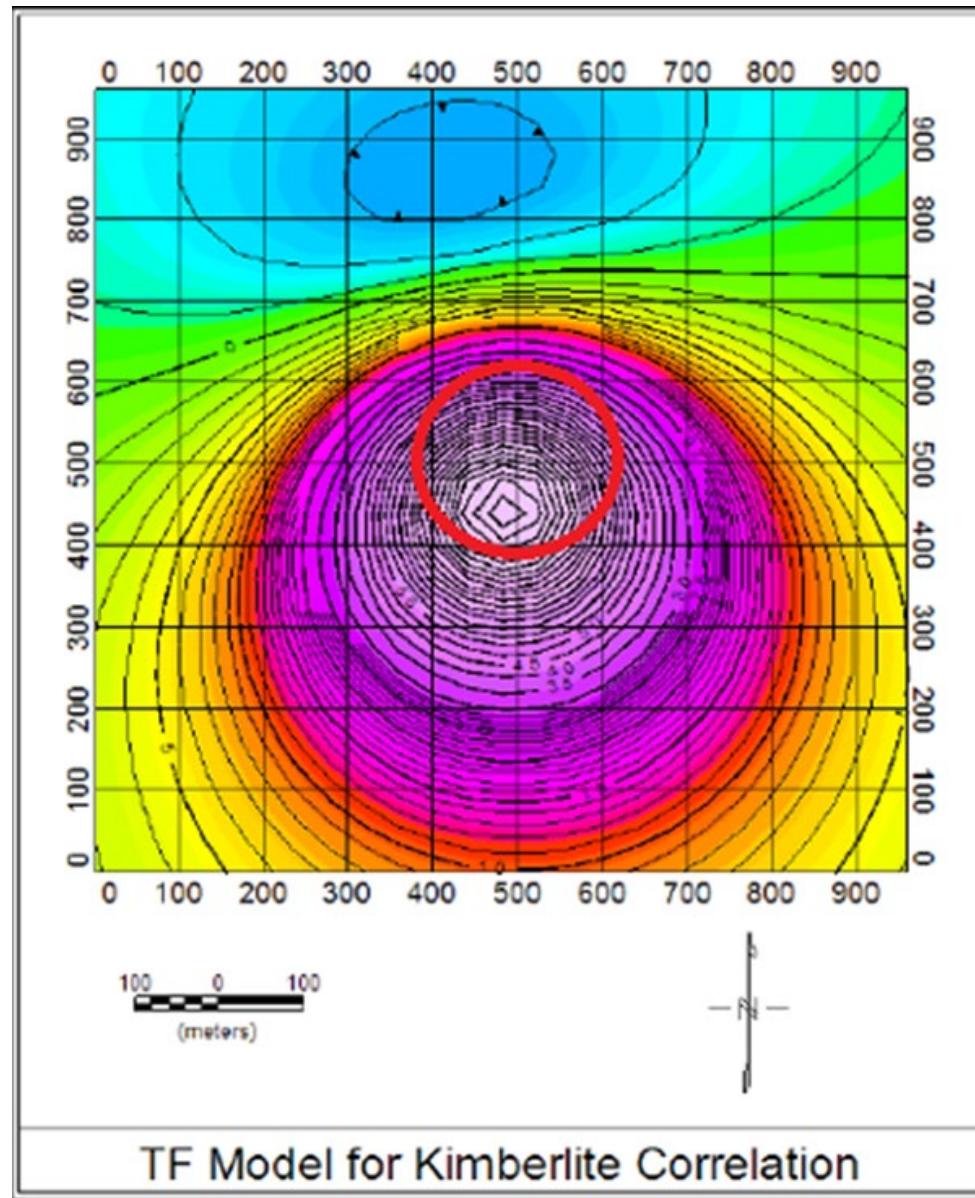


Figure 5.5: Example of a kimberlite model's magnetic response (after Keating 1995).

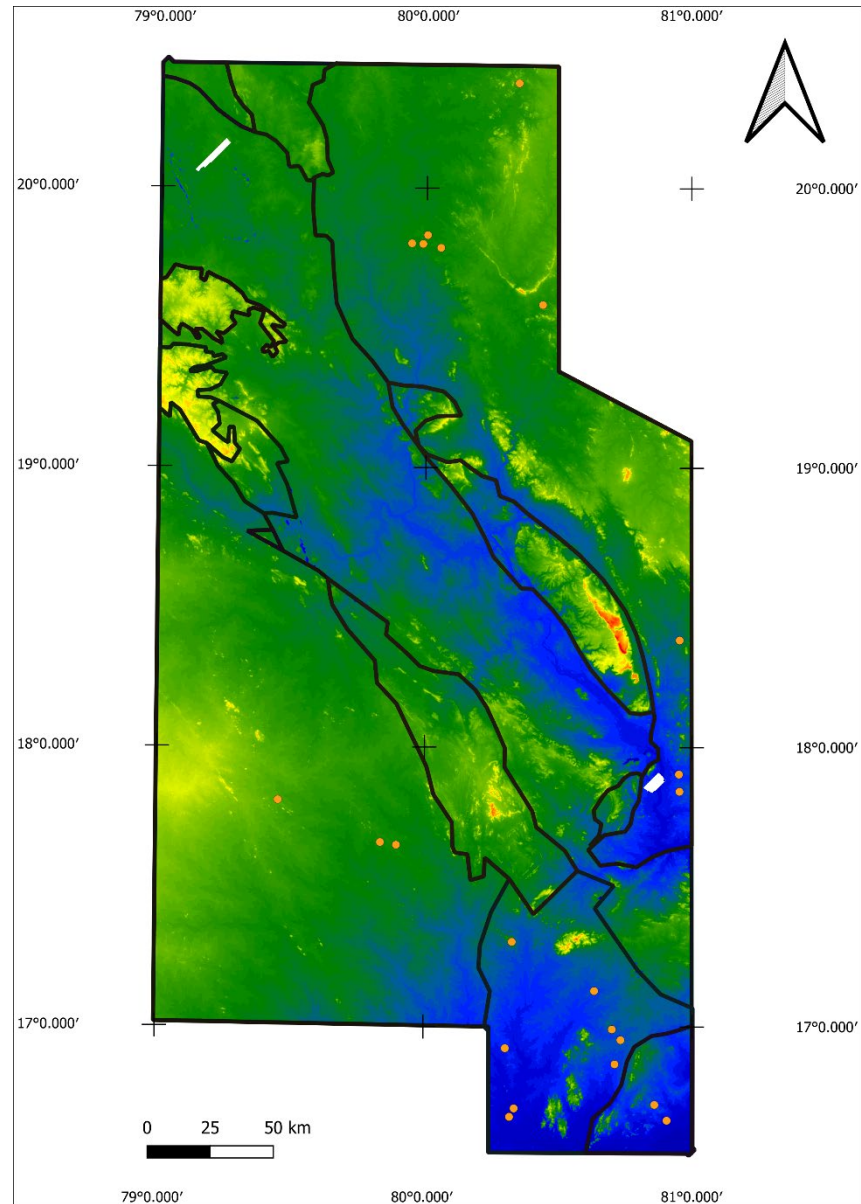


Figure 5.6: Keating coefficient results (orange dots) superimposed on a digital elevation model of Block-6.

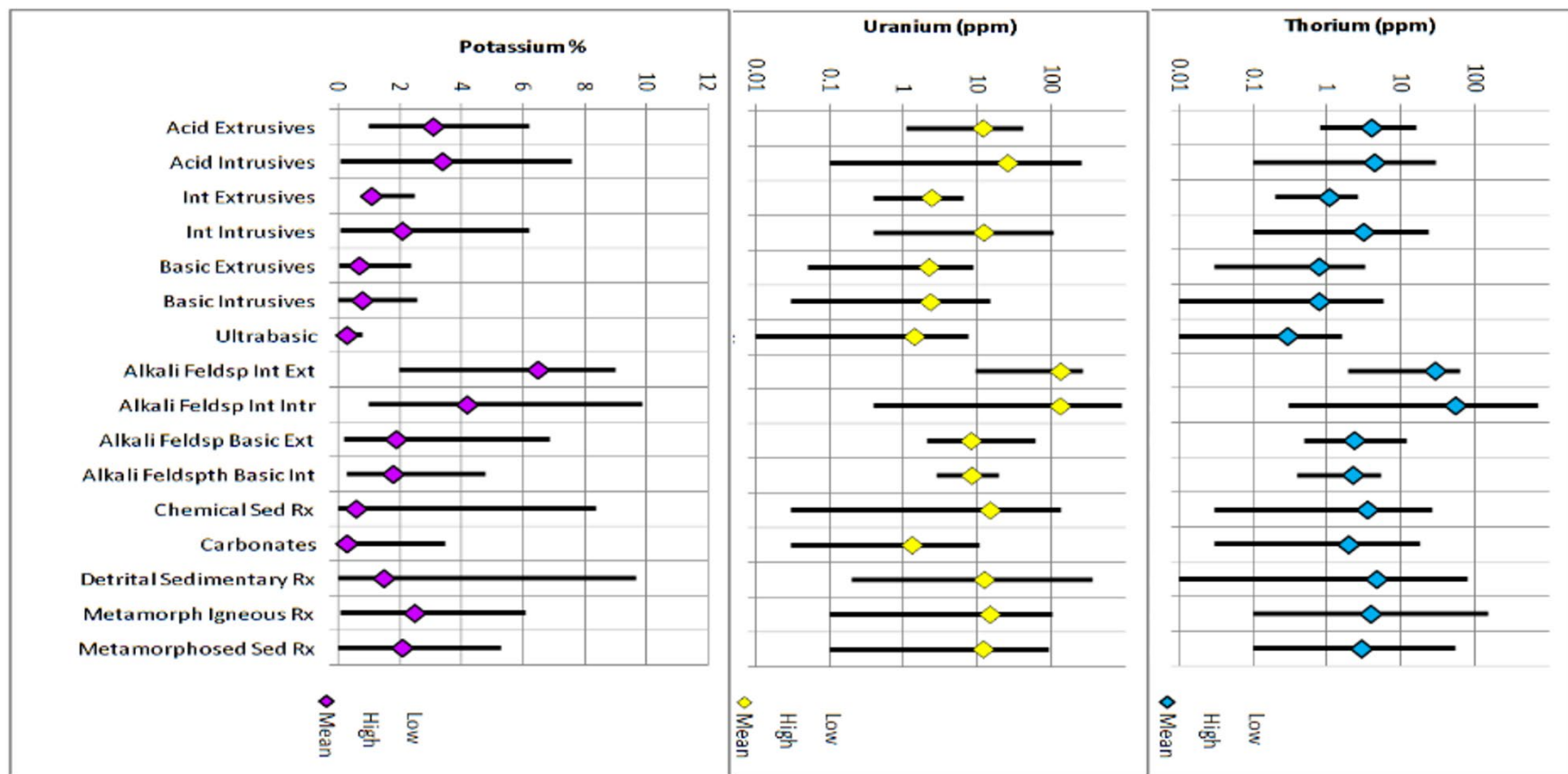


Figure 6.1: Ranges of radio-element concentrations for various lithologies (after Ford et al. 2007).

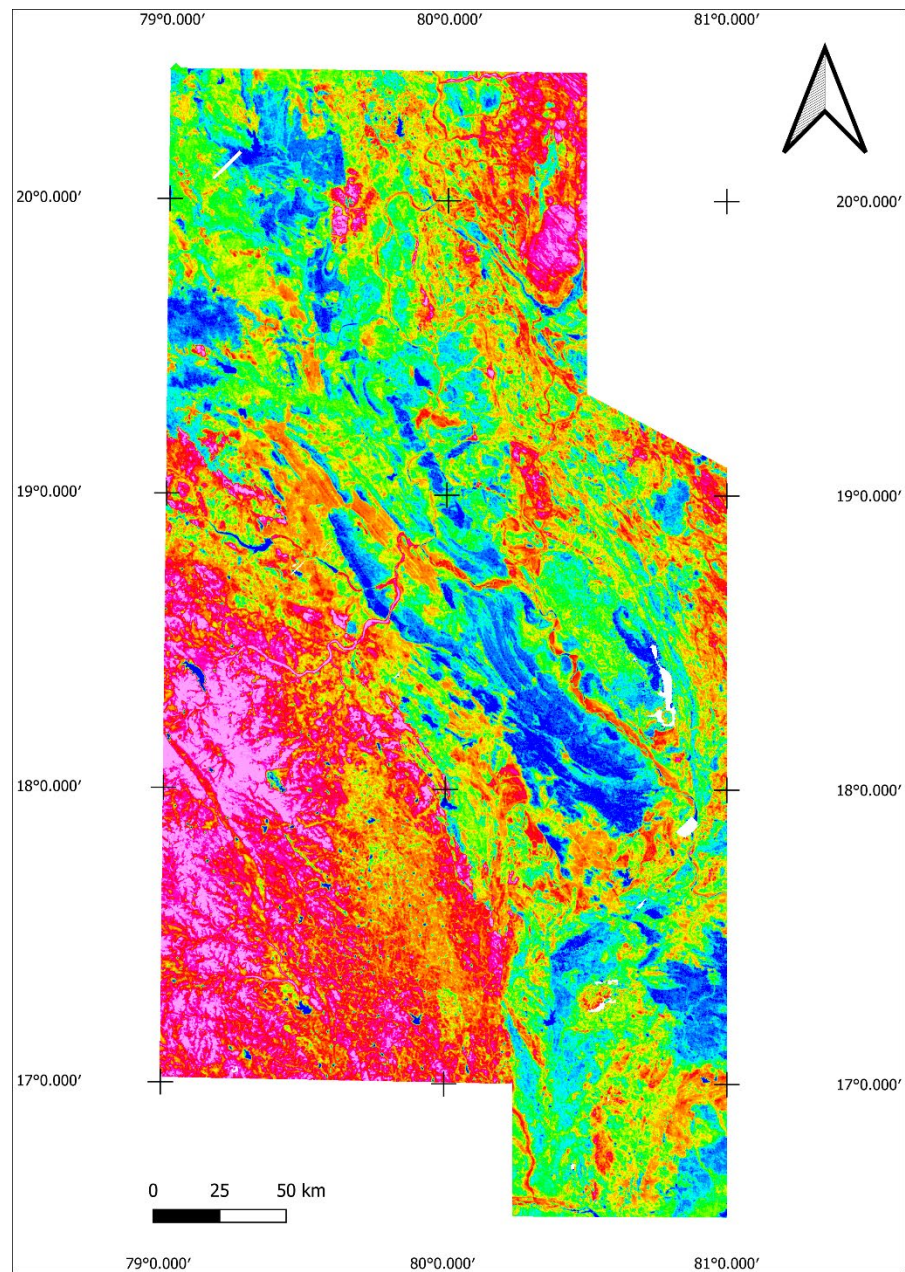


Figure 6.2: Potassium concentration.

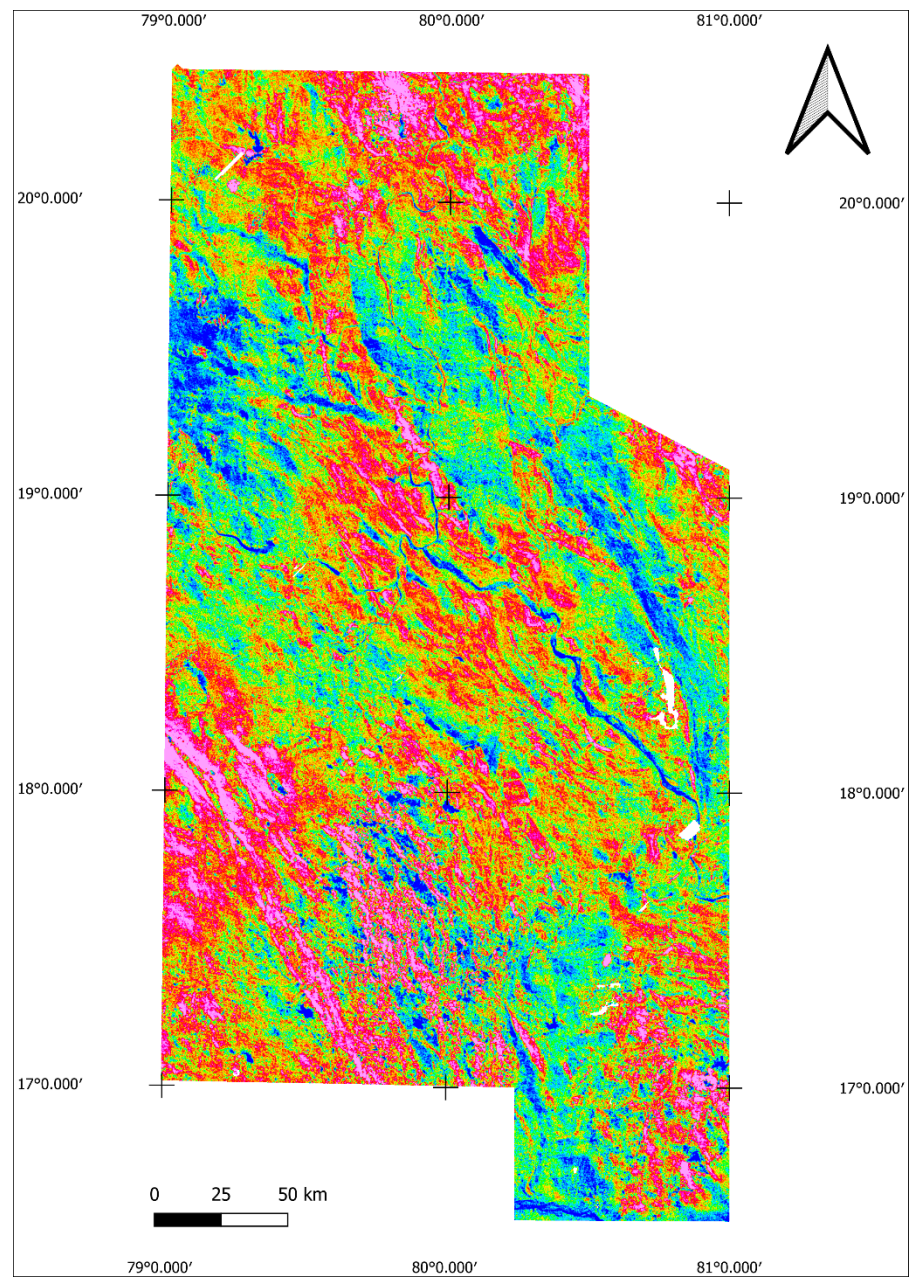


Figure 6.3: Equivalent uranium concentration.

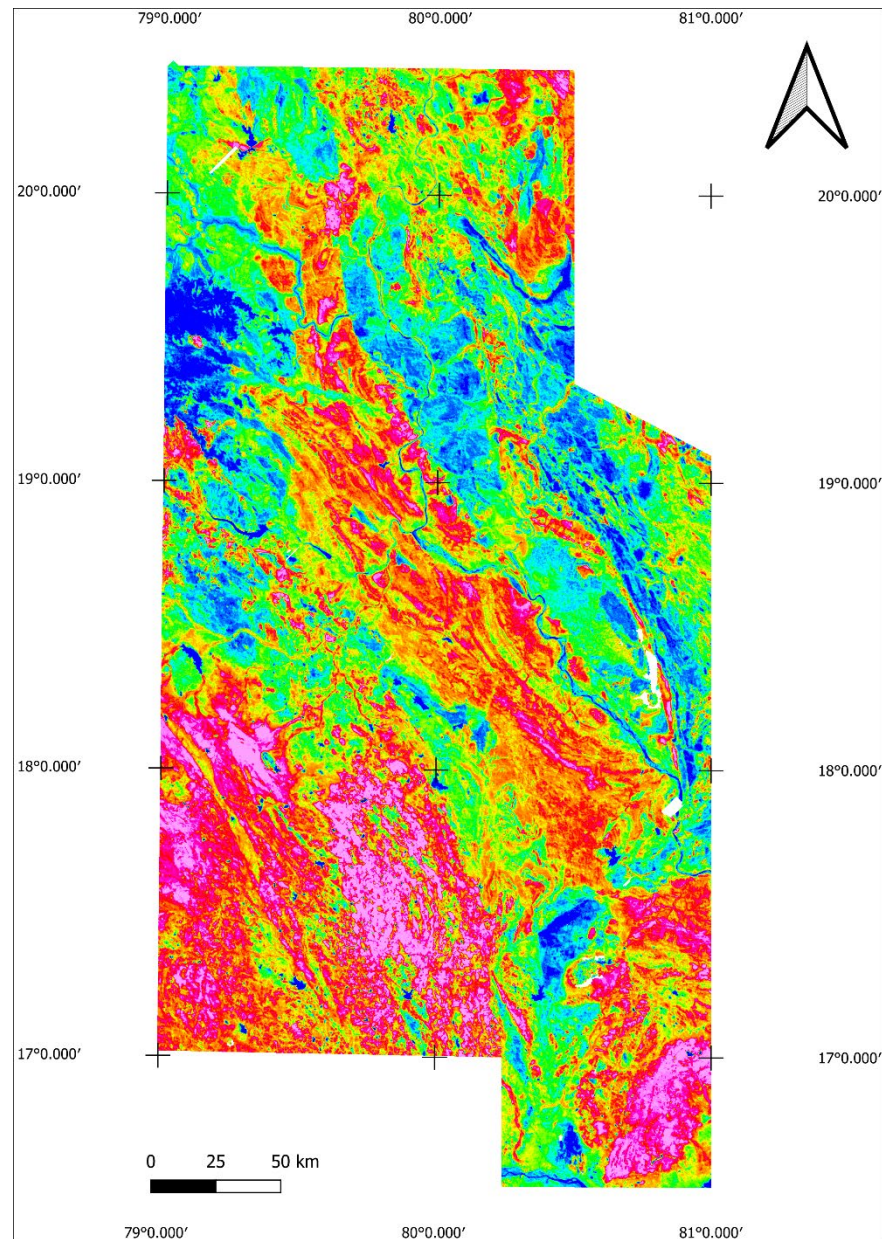


Figure 6.4: Equivalent thorium concentration.

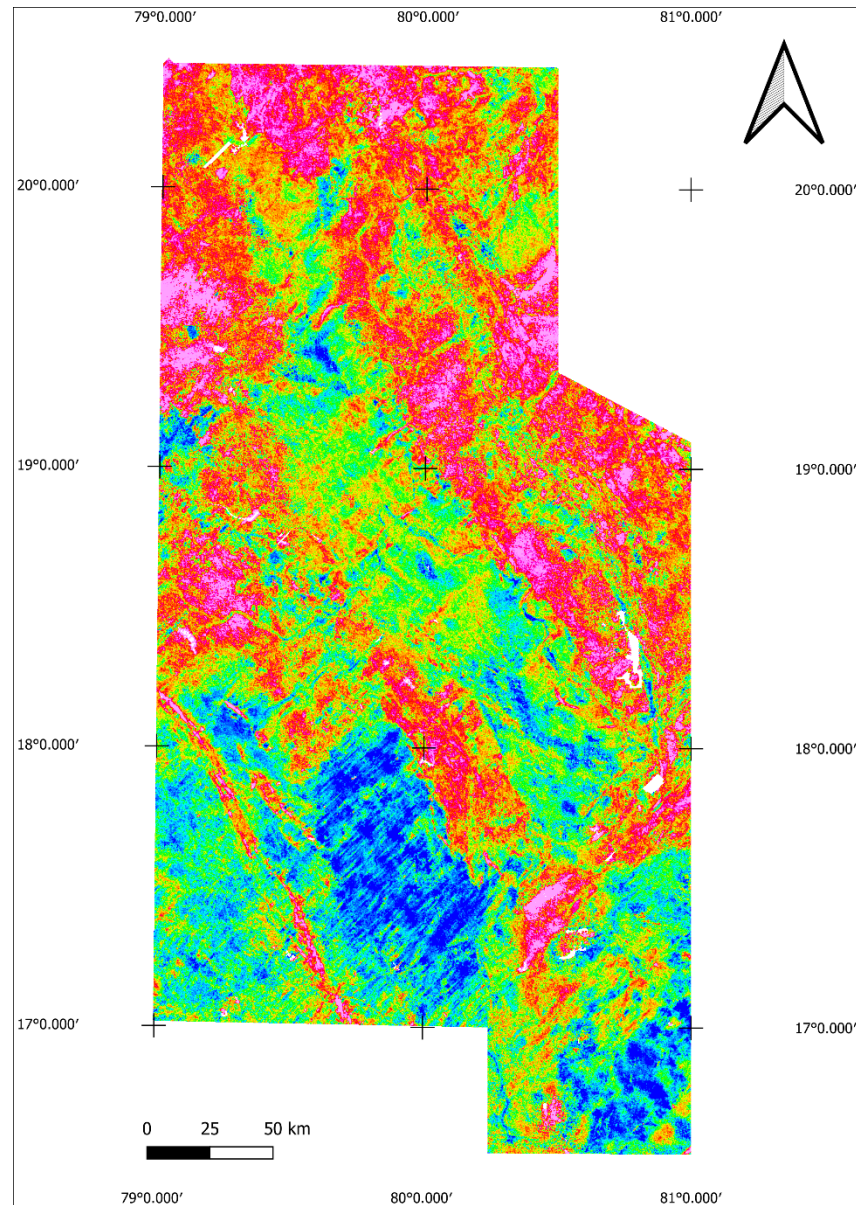


Figure 6.5: Ratio of equivalent uranium concentration to equivalent thorium concentration.

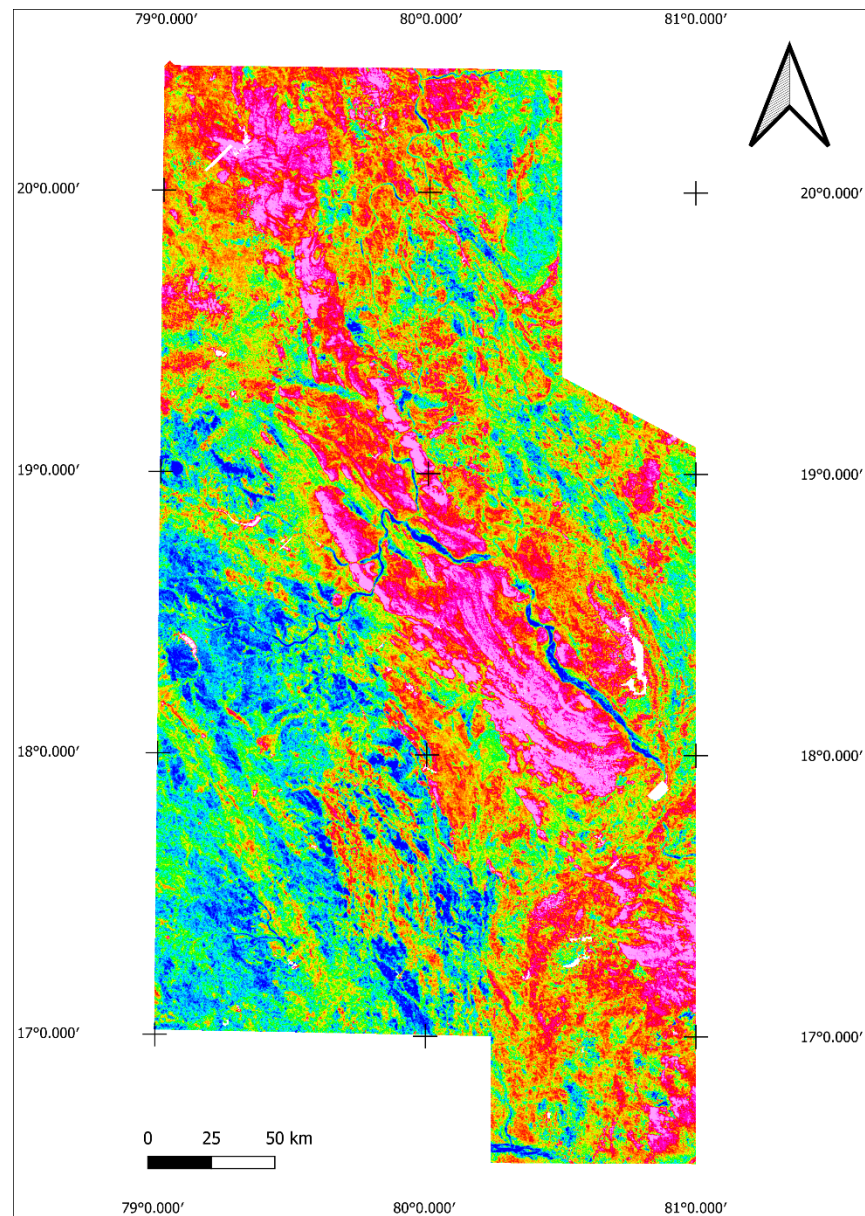


Figure 6.6: Ratio of equivalent uranium concentration to potassium concentration.

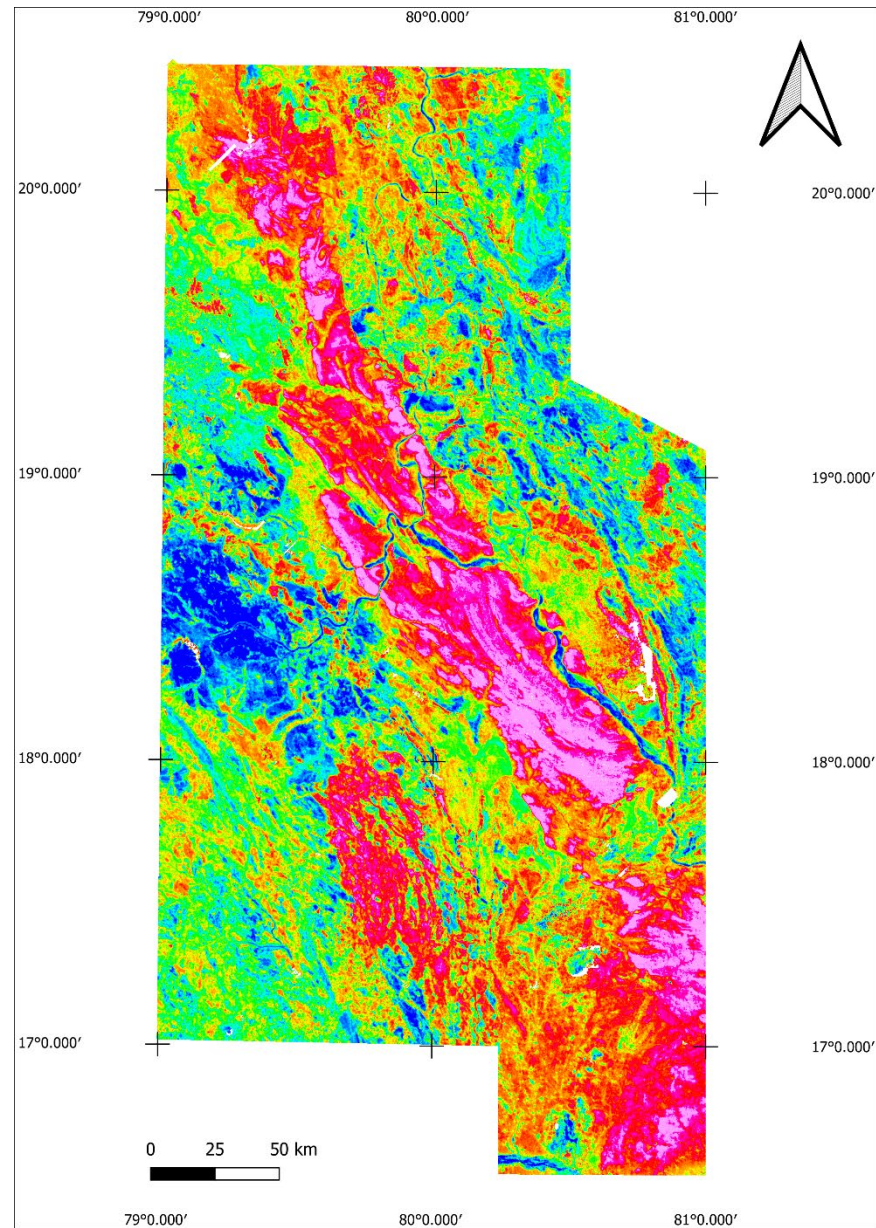


Figure 6.7: Ratio of equivalent thorium concentration to potassium concentration.

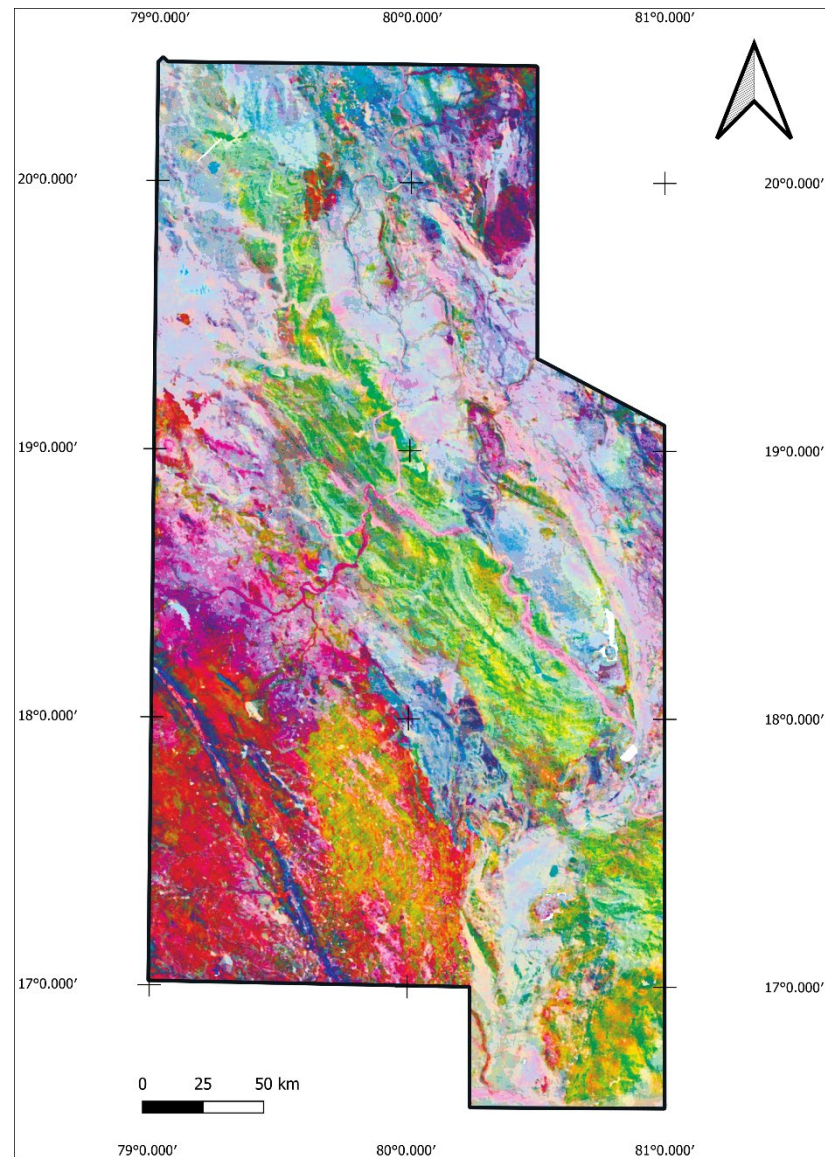


Figure 6.8: Radiometric ternary employing the following colour scheme: potassium – magenta, uranium – cyan, thorium – yellow. Higher intensity colour indicates higher concentrations of the elements.

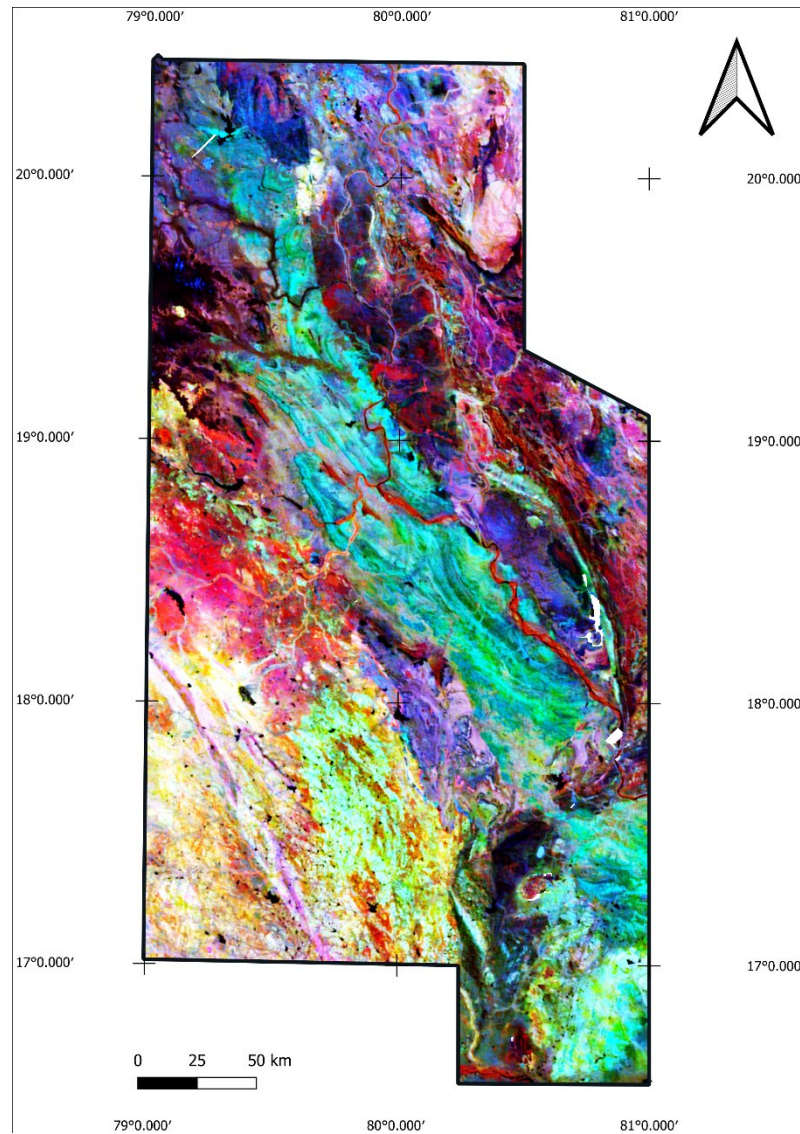


Figure 6.9: Radiometric ternary employing the following colour scheme: potassium – red, uranium – blue, thorium – green. Darker colour indicates lower concentrations of the elements, lighter colours indicate higher concentrations.

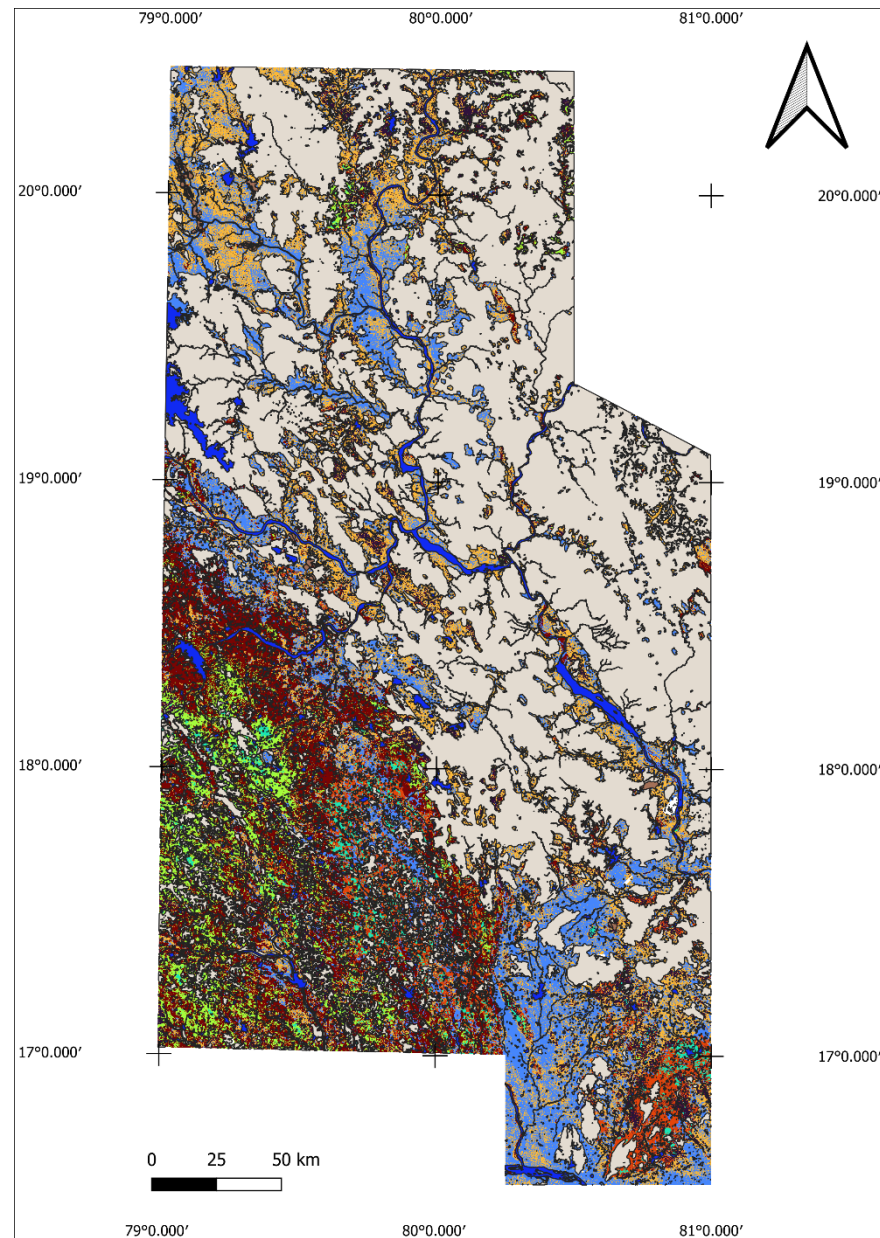
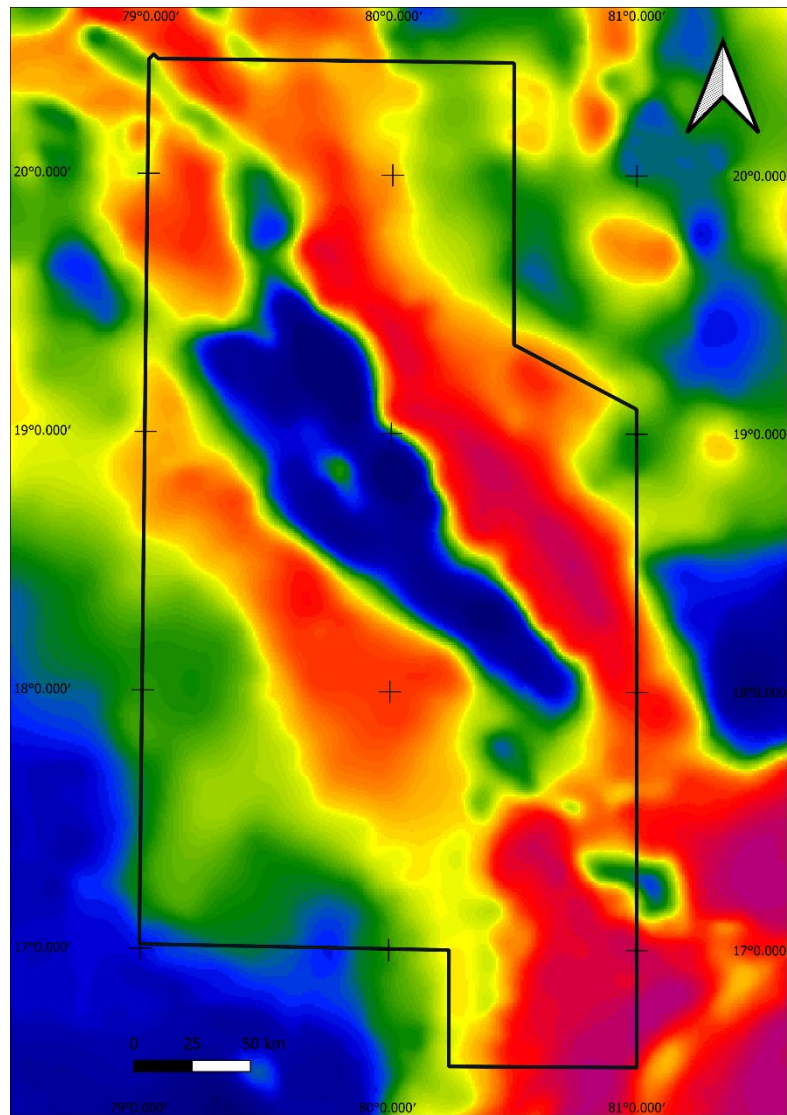


Figure 7.1: Regolith map based on gamma-ray signal and topographic index. See Section 7 for the meaning of the colours.



*Figure 8.1: Legacy gravity data at 5 mGal resolution
provided by the Geological Survey of India.*

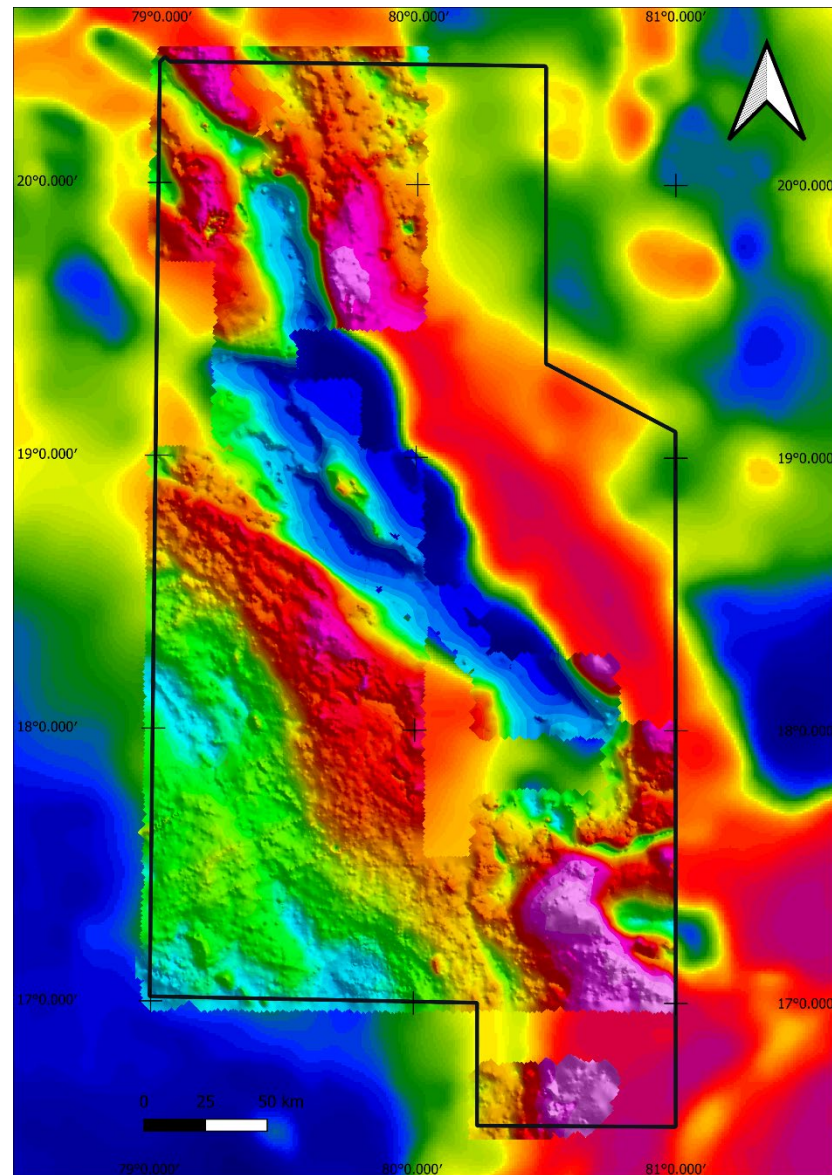


Figure 8.2: Legacy gravity data at 1 mGal resolution provided by the Geological Survey of India, superimposed on the 5 mGal resolution Bouguer gravity data.

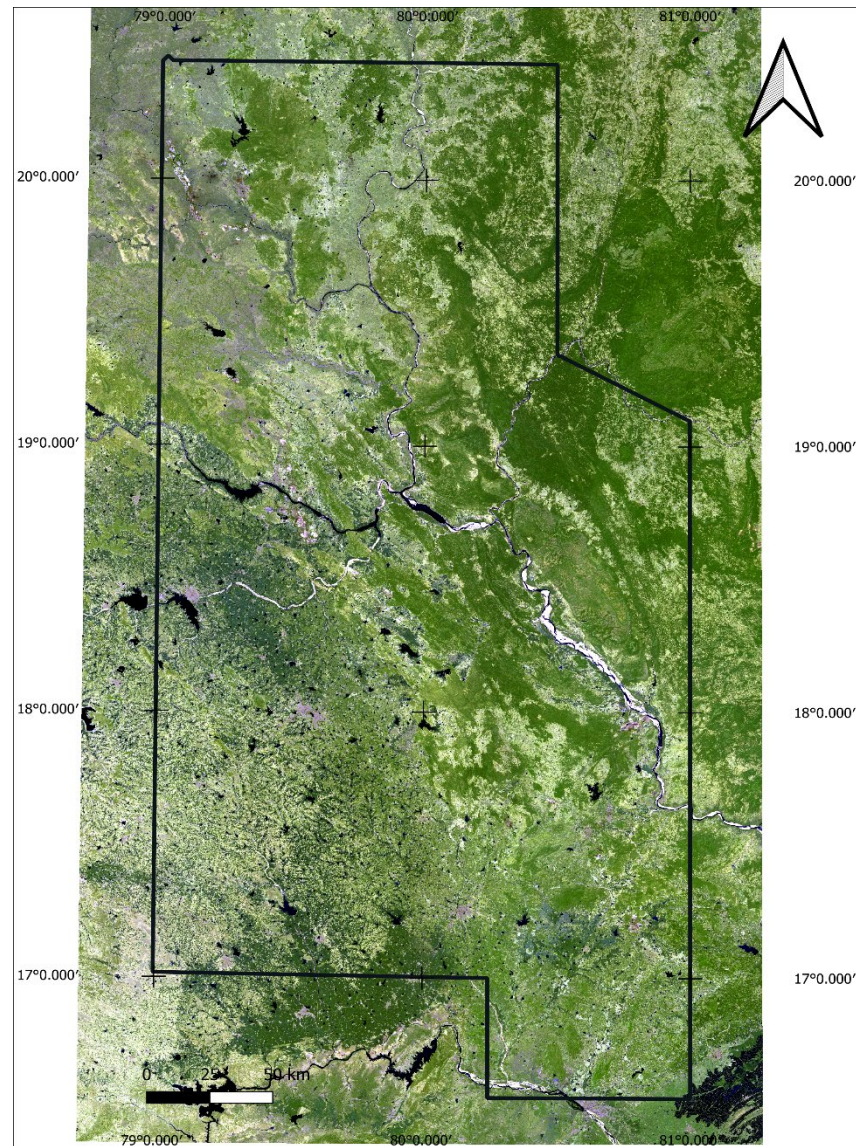


Figure 9.1: Sentinel-2 false colour image of Block6 using bands 12:11:4.

Table 1. Applicability of different geophysical methods in the exploration of various mineral systems (modified from Ford et al. 2007).

● Highly effective ● Moderately effective ● Generally ineffective

Geo-physical method	Air or ground	Application	Ni-Cu-PGE	Fe-Ti-BIF	Gold	VMS	Olympic Dam-type	SEDEX	Porphyry Cu	Pb-Zn	Diamonds
Magnetic	Air	Geological framework	●	●	●	●	●	●	●	●	●
		Direct targeting	●	●	●	●	●	●	●	●	●
	Ground	Geological framework	●	●	●	●	●	●	●	●	●
		Direct targeting	●	●	●	●	●	●	●	●	●
Electro-magnetic	Air	Geological framework	●	●	●	●	●	●	●	●	●
		Direct targeting	●	●	●	●	●	●	●	●	●
	Ground	Geological framework	●	●	●	●	●	●	●	●	●
		Direct targeting	●	●	●	●	●	●	●	●	●
Electric	Ground	Geological framework	●	●	●	●	●	●	●	●	●
		Direct targeting	●	●	●	●	●	●	●	●	●
Gravity	Air	Geological framework	●	●	●	●	●	●	●	●	●
		Direct targeting	●	●	●	●	●	●	●	●	●
	Ground	Geological framework	●	●	●	●	●	●	●	●	●
		Direct targeting	●	●	●	●	●	●	●	●	●
Radio-metric	Air	Geological framework	●	●	●	●	●	●	●	●	●
		Direct targeting	●	●	●	●	●	●	●	●	●
	Ground	Geological framework	●	●	●	●	●	●	●	●	●
		Direct targeting	●	●	●	●	●	●	●	●	●
Seismic	Ground	Geological framework	●	●	●	●	●	●	●	●	●
		Direct targeting	●	●	●	●	●	●	●	●	●

Figure 10.1: Applicability of different geophysical techniques to ore deposit exploration (from Aero 2015).

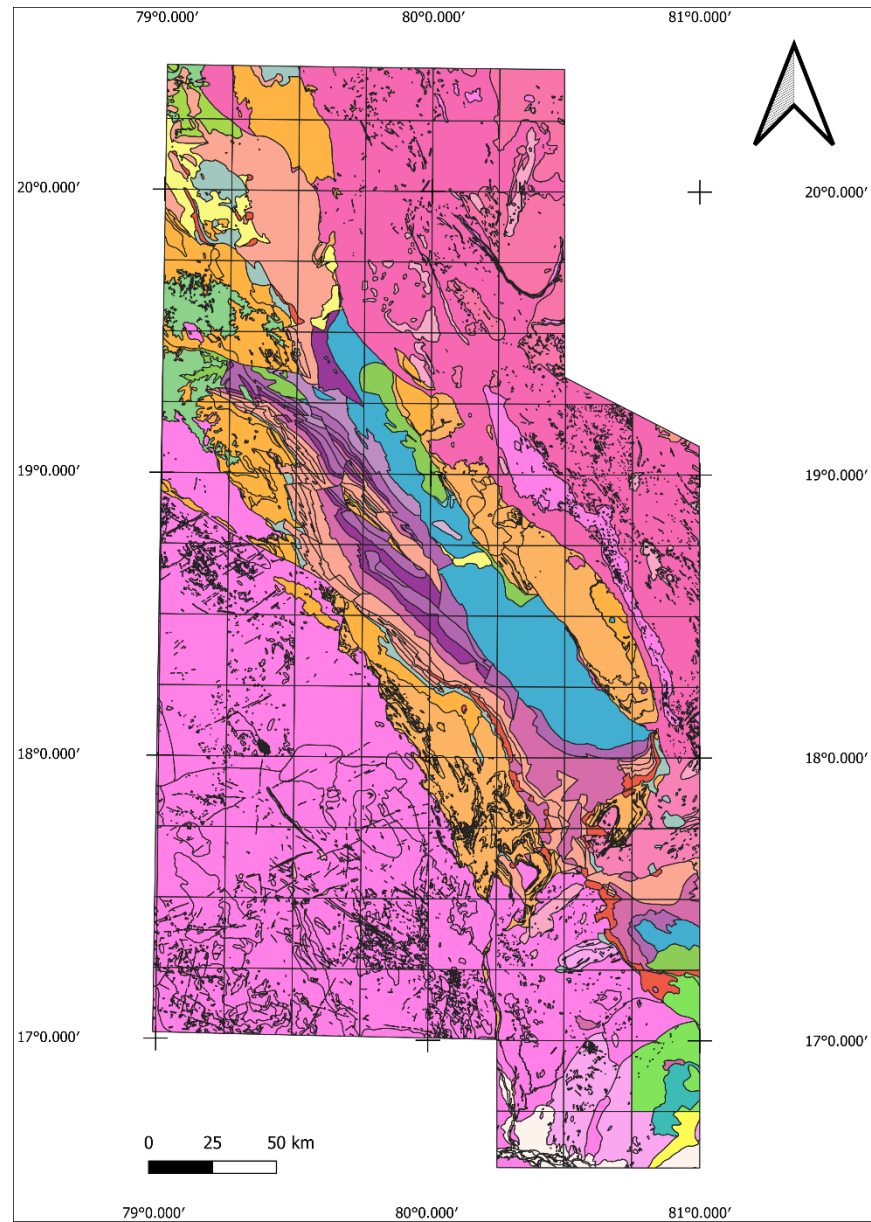


Figure 11.1: Pre-survey lithological map of Block-6, including linear elements in black.

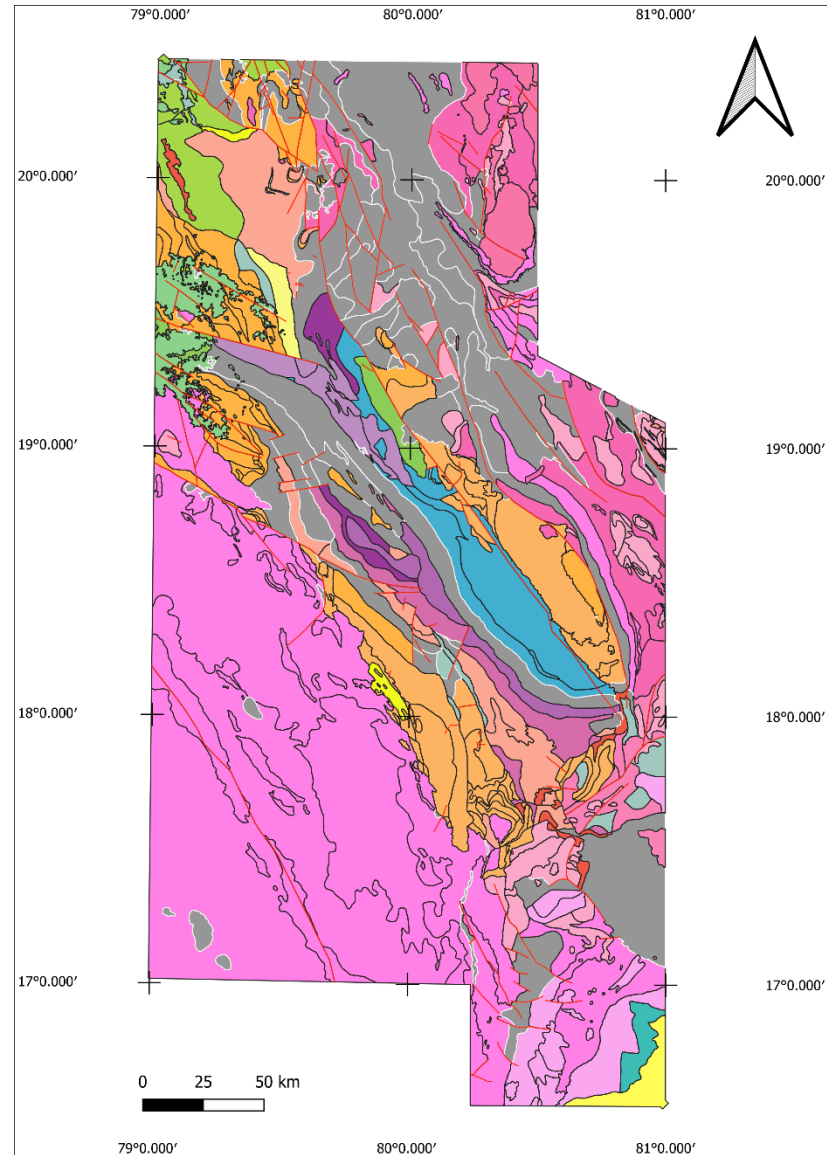


Figure 11.2: Litho-tectonic map of Block-6 with areas requiring new litho-codes coloured grey, fine black lines are lithological boundaries, grey lines are new lithological boundaries.

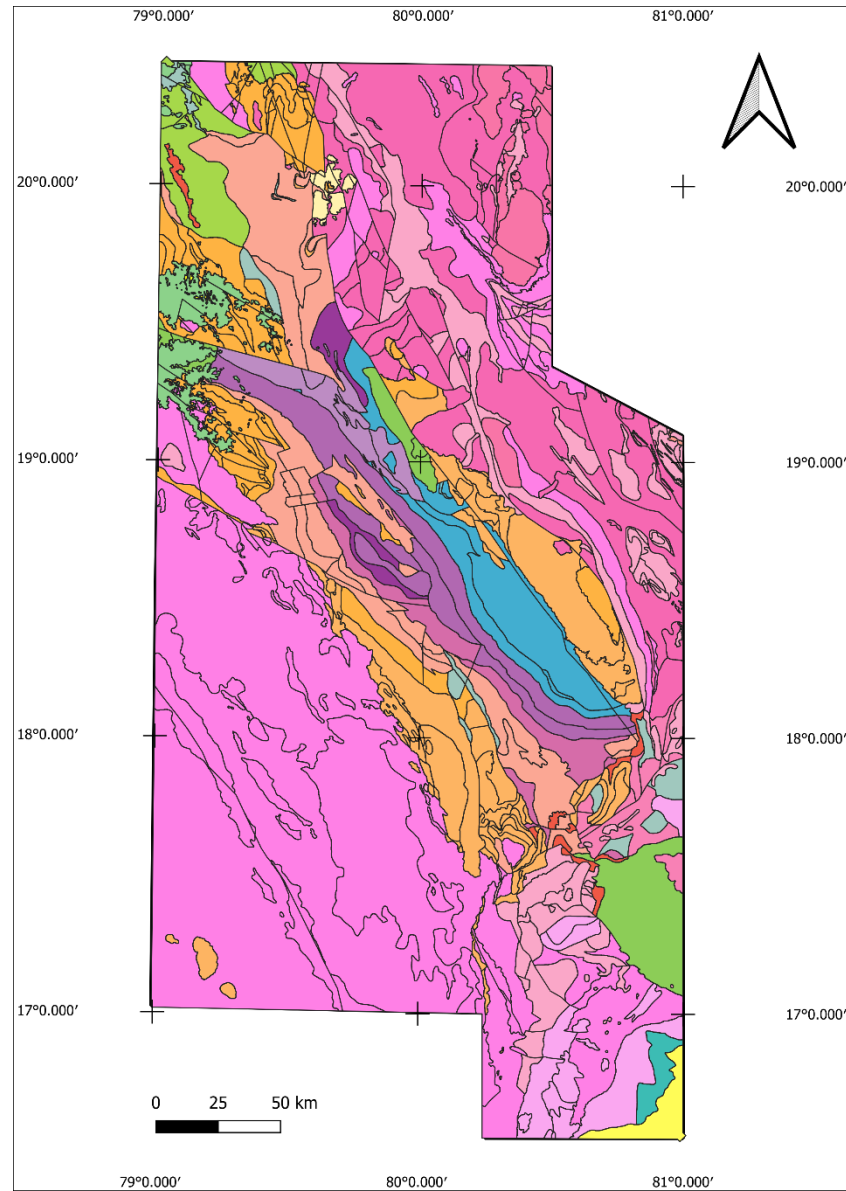


Figure 11.3: Litho-tectonic map of Block-6 with new litho-codes assigned, fine black lines are lithological boundaries.

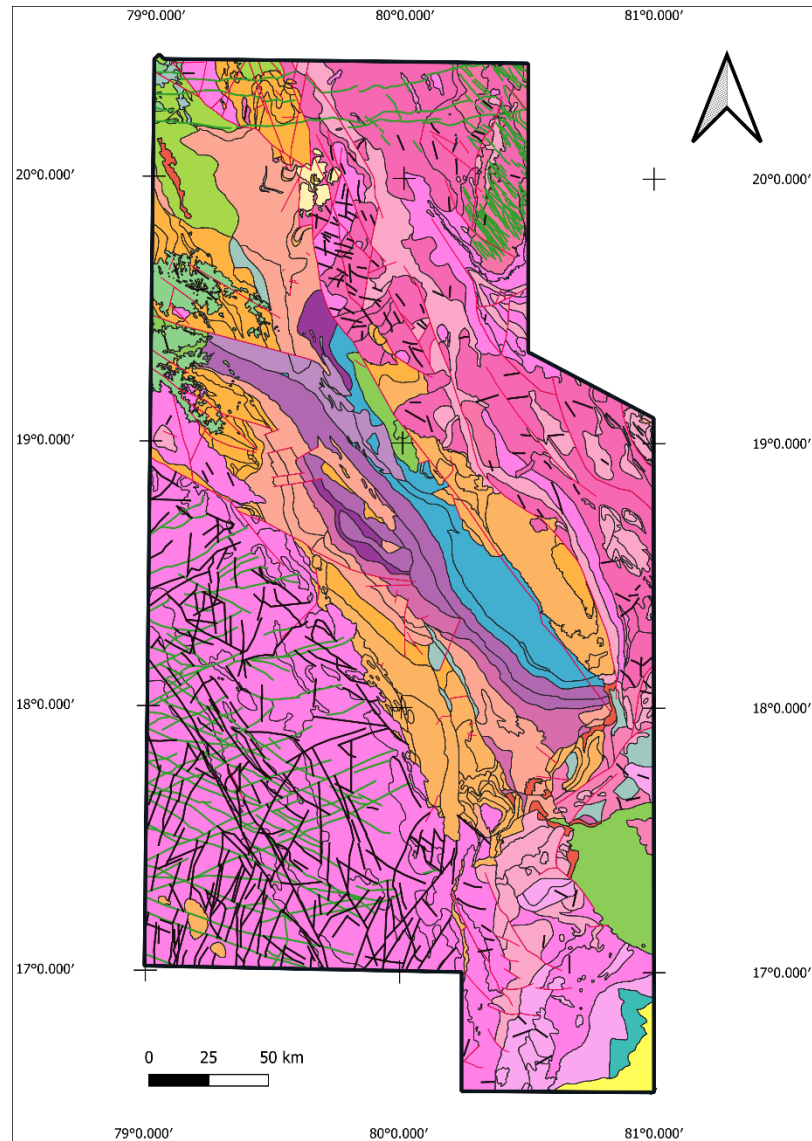


Figure 11.4: Litho-tectonic map of Block-6 with linear elements displayed, as follows: fine black lines are lithological boundaries, red lines are faults, black lines are fractures, green lines are dykes.

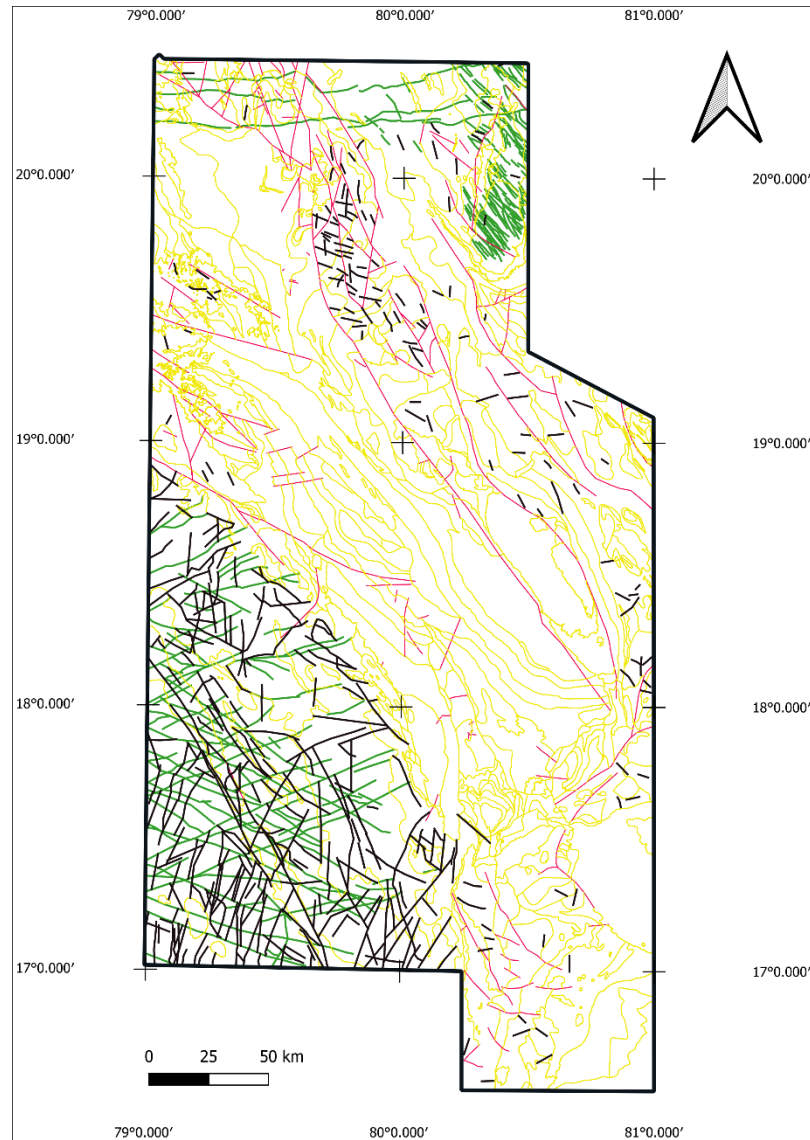


Figure 11.5: Linear elements of the litho-tectonic map of Block-6 as follows: red lines are faults, black lines are fractures, green lines are dykes, with lithological boundaries marked in yellow.

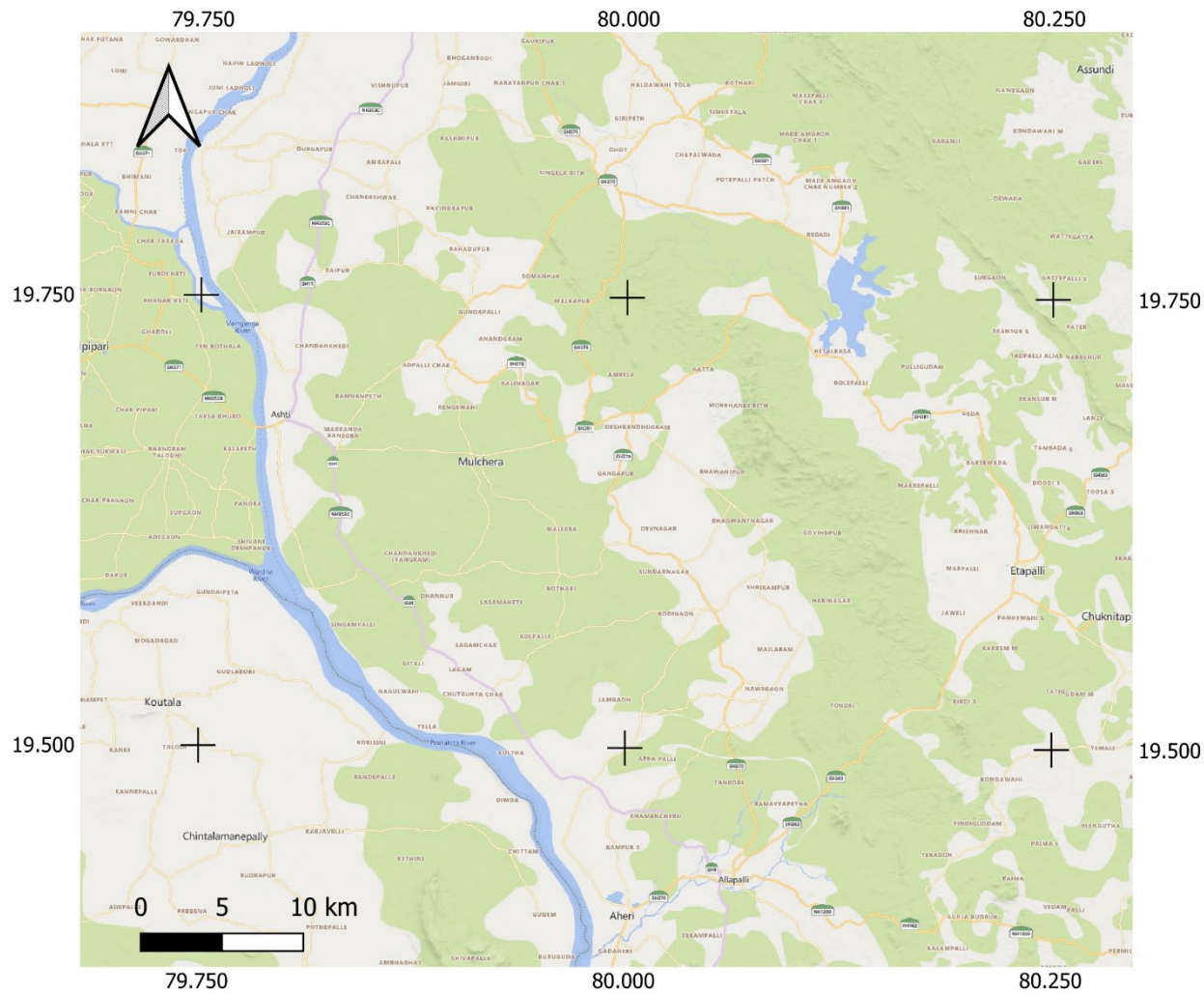


Figure 11.6a: Changes in the litho-tectonic mapping in the northern part of the Bastar Craton, as follows: a) geographic location (Microsoft® Bing™ Maps), b) original lithological mapping, c) updated lithological mapping, with newly mapped supracrustal areas marked by stars.

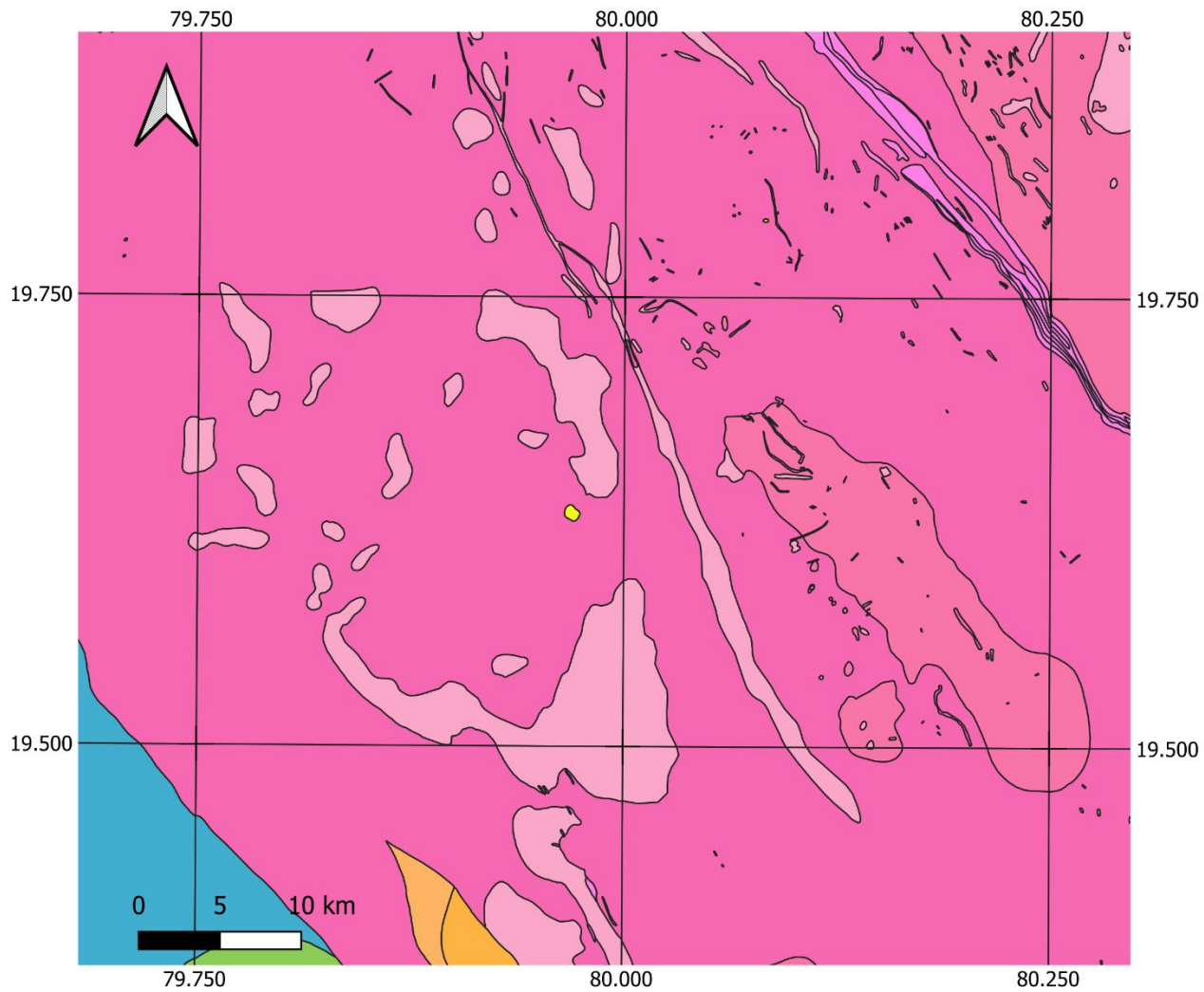


Figure 11.6b: Changes in the litho-tectonic mapping in the northern part of the Bastar Craton, as follows: a) geographic location (Microsoft® Bing™ Maps), b) original lithological mapping, c) updated lithological mapping, with newly mapped supracrustal areas marked by stars.

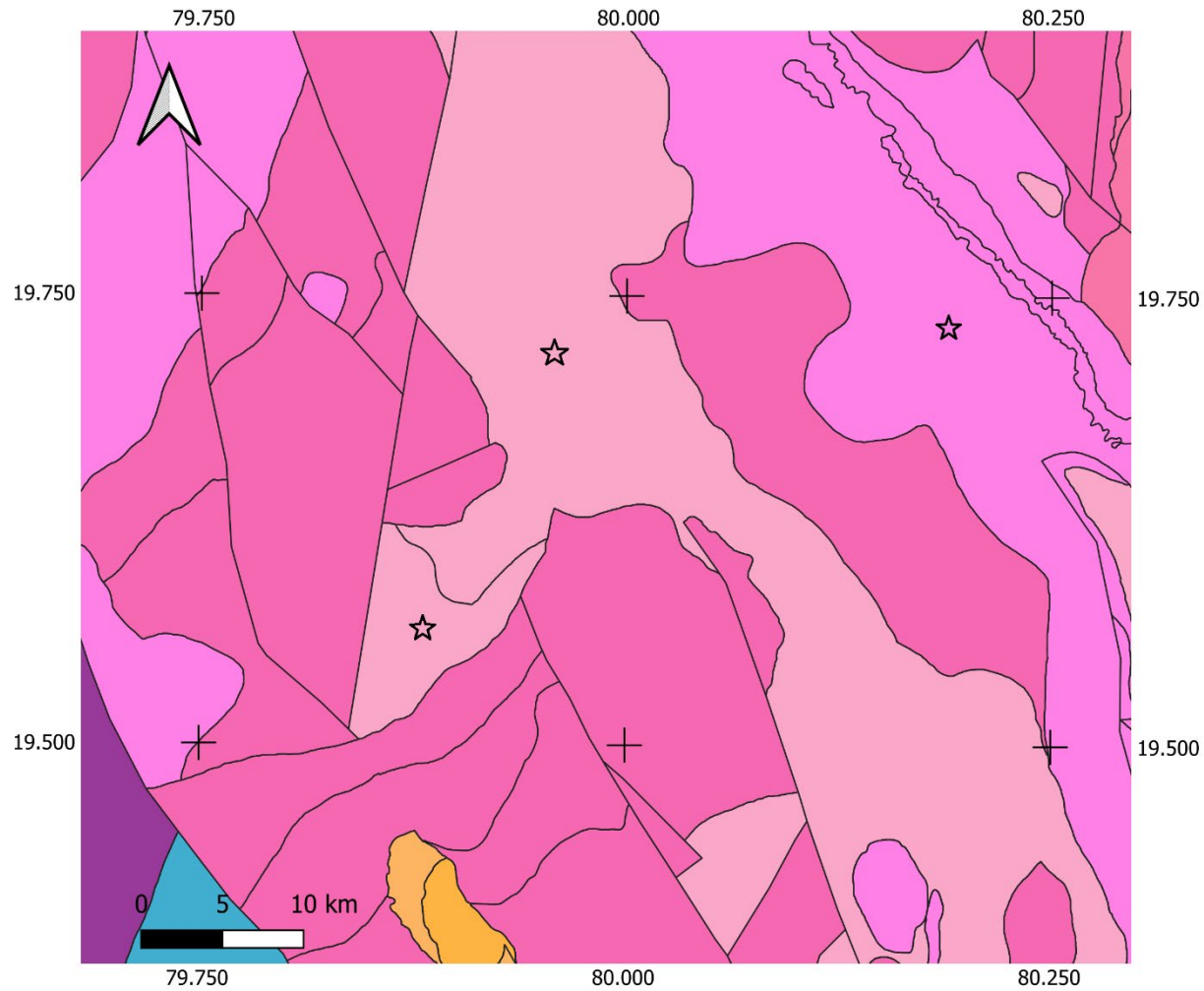


Figure 11.6c: Changes in the litho-tectonic mapping in the northern part of the Bastar Craton, as follows: a) geographic location (Microsoft® Bing™ Maps), b) original lithological mapping, c) updated lithological mapping, with newly mapped supracrustal areas marked by stars.

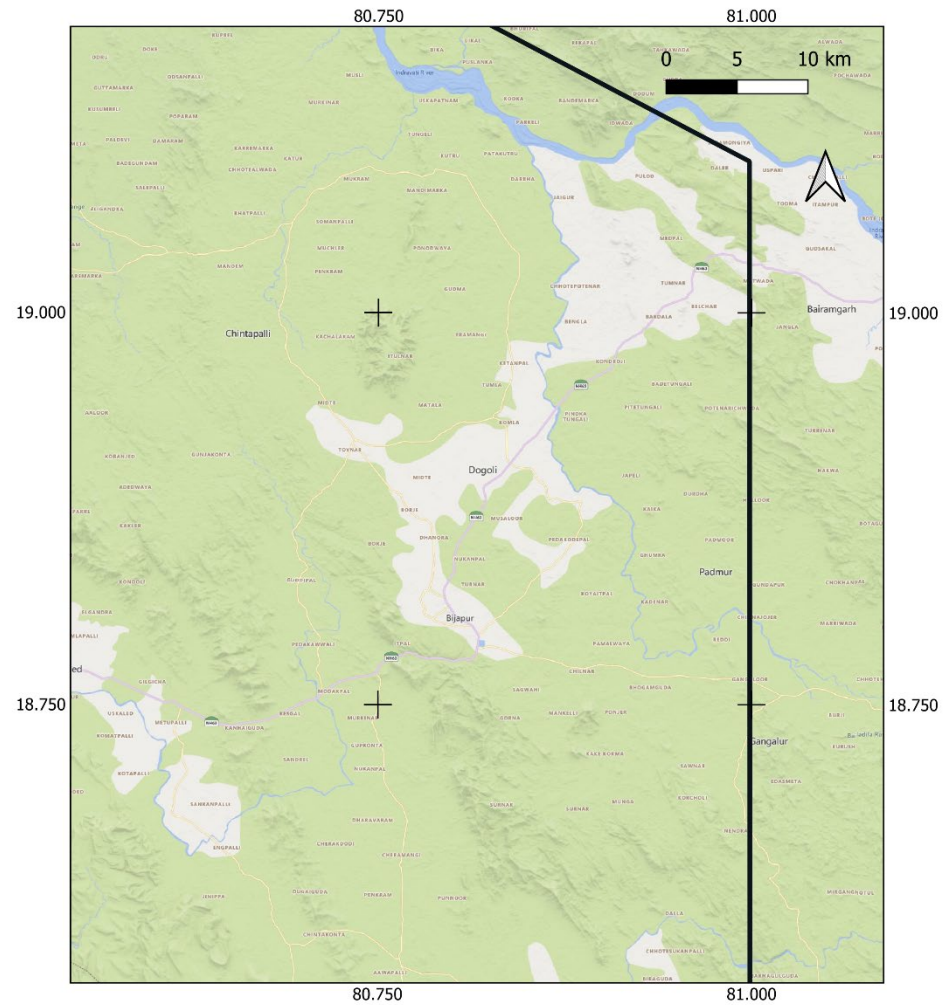


Figure 11.7a: Changes in the litho-tectonic mapping in the eastern part of the Bastar Craton, as follows: a) geographic location (Microsoft® Bing™ Maps), b) original lithological mapping, c) updated lithological mapping, with updated and newly mapped supracrustal areas marked

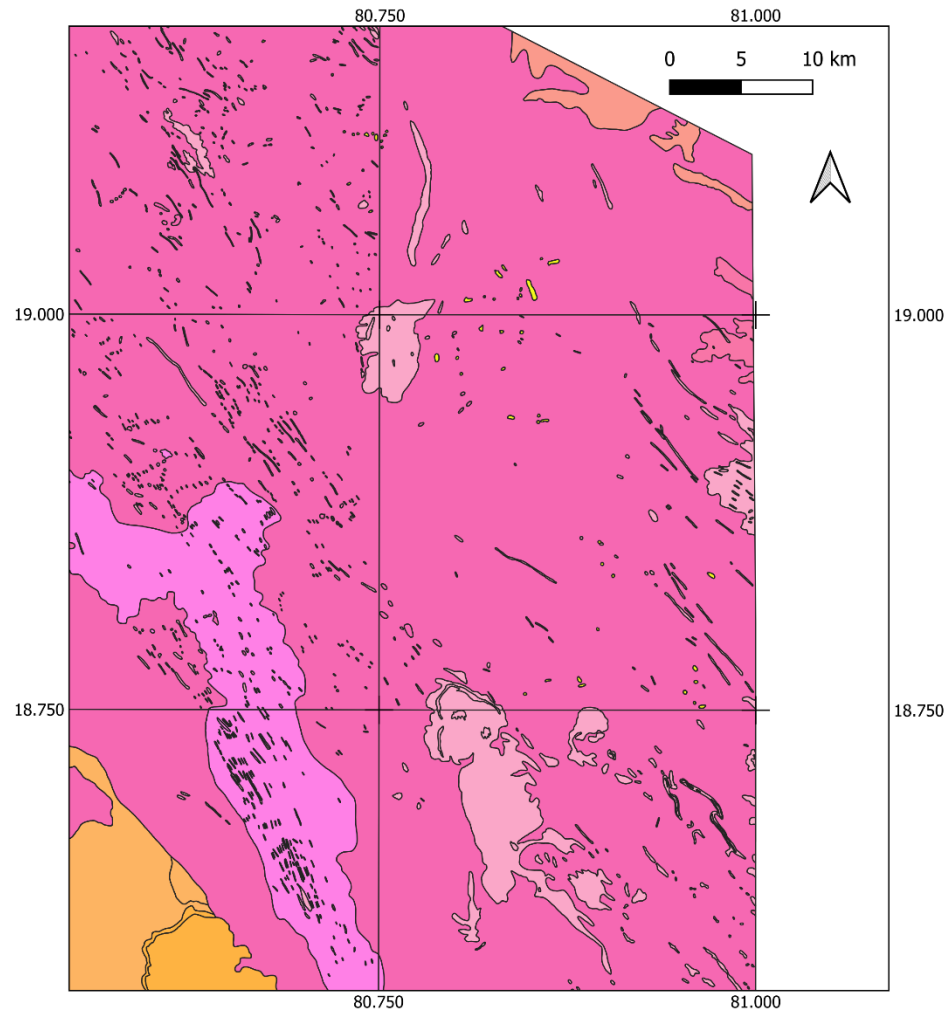


Figure 11.7b: Changes in the litho-tectonic mapping in the eastern part of the Bastar Craton, as follows: a) geographic location (Microsoft® Bing™ Maps), b) original lithological mapping, c) updated lithological mapping, with updated and newly mapped supracrustal areas marked

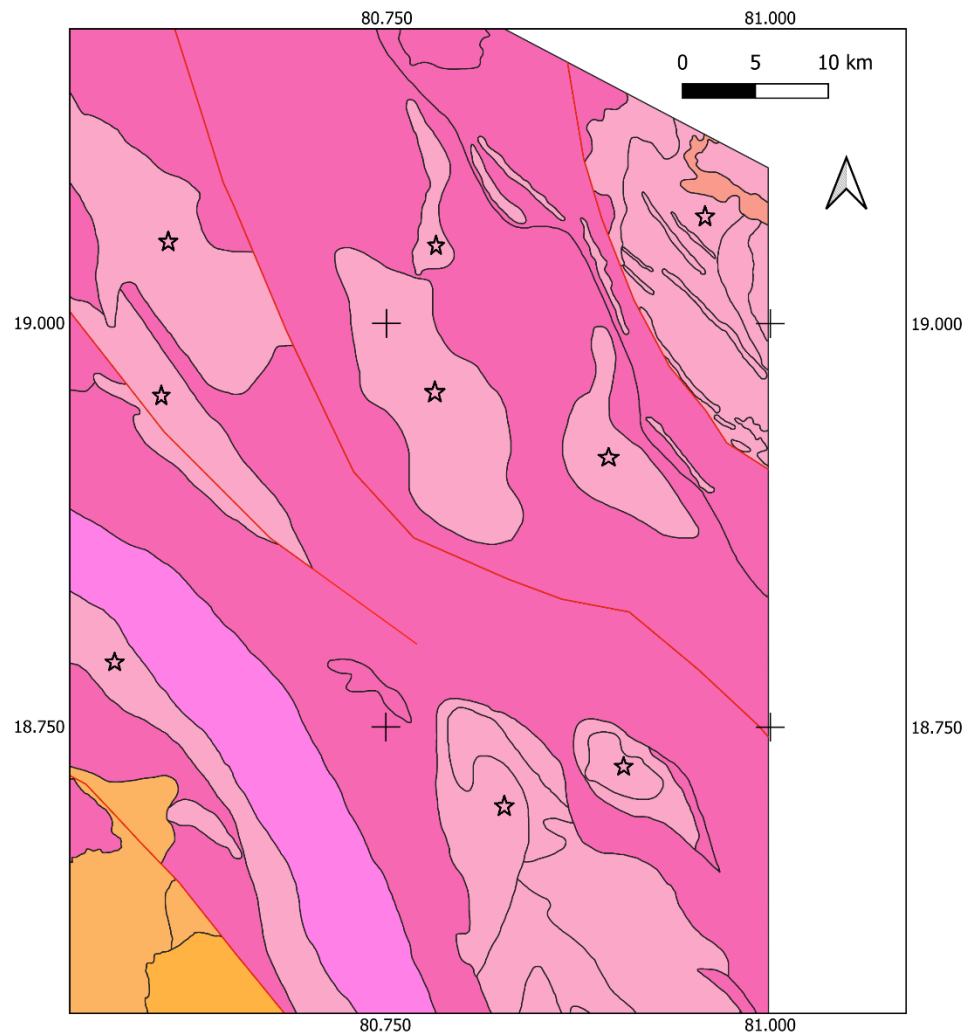


Figure 11.7c: Changes in the litho-tectonic mapping in the eastern part of the Bastar Craton, as follows: a) geographic location (Microsoft® Bing™ Maps), b) original lithological mapping, c) updated lithological mapping, with updated and newly mapped supracrustal areas marked



Figure 11.8a: Changes in the litho-tectonic mapping in the Eastern Ghats Mobile Belt, as follows: a) geographic location (Microsoft® Bing™ Maps), b) original lithological mapping, c) updated lithological mapping, with newly mapped granulite areas marked by a star.

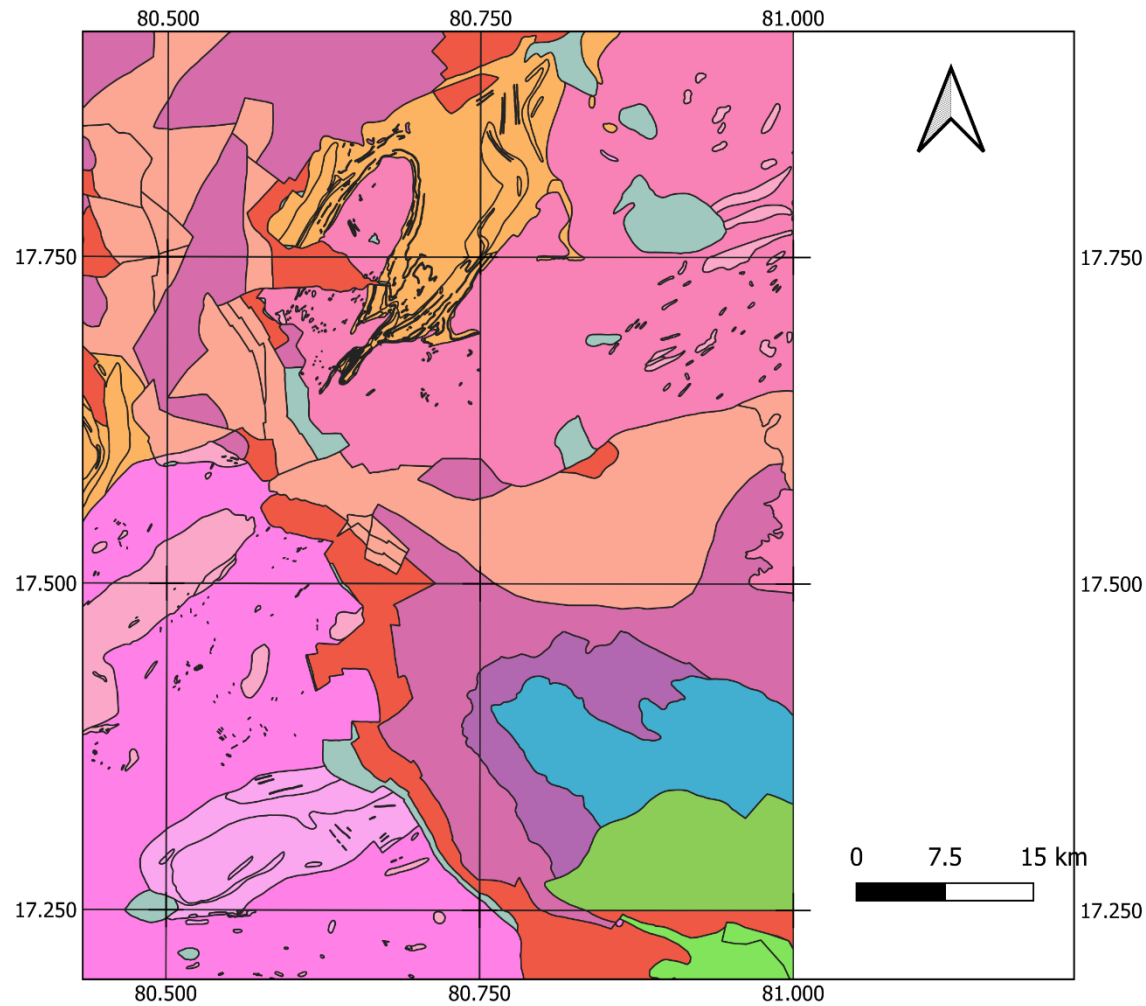


Figure 11.8b: Changes in the litho-tectonic mapping in the Eastern Ghats Mobile Belt, as follows: a) geographic location (Microsoft® Bing™ Maps), b) original lithological mapping, c) updated lithological mapping, with newly mapped granulite areas marked by a star.

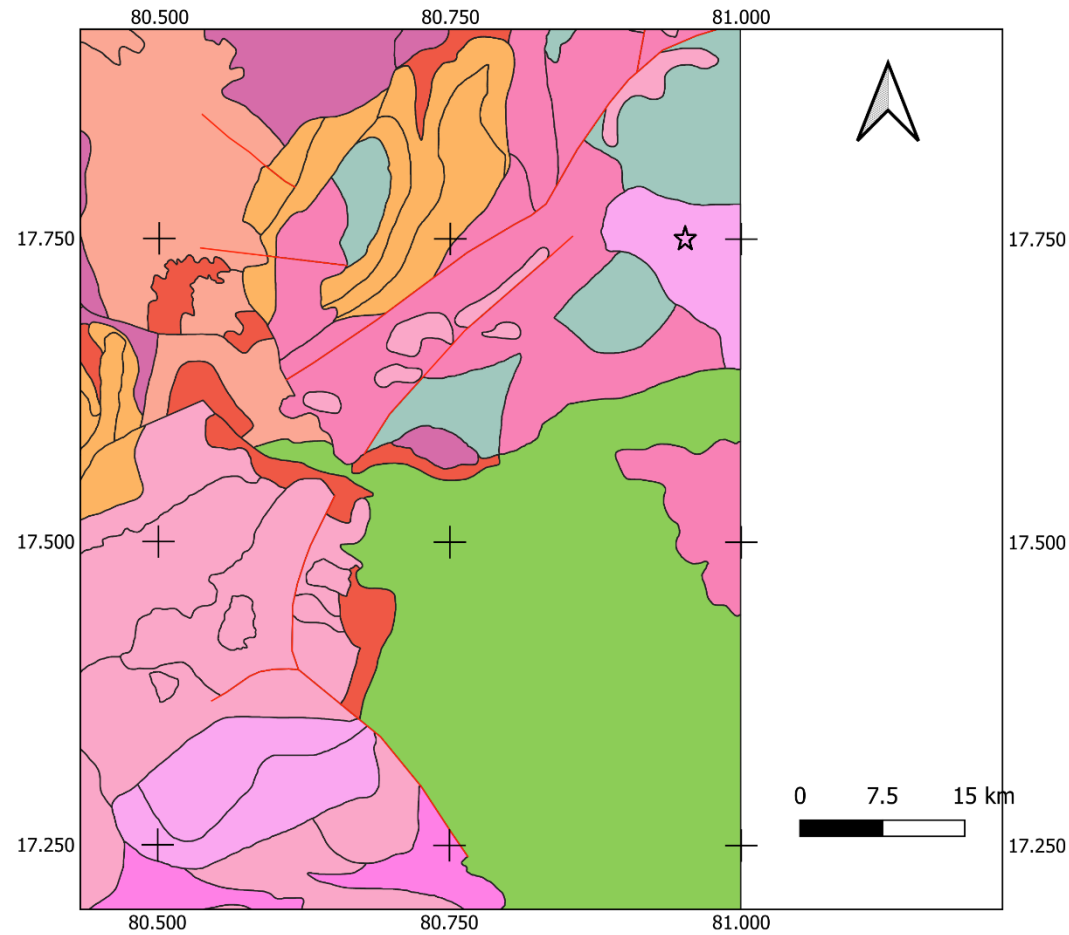


Figure 11.8c: Changes in the litho-tectonic mapping in the Eastern Ghats Mobile Belt, as follows: a) geographic location (Microsoft® Bing™ Maps), b) original lithological mapping, c) updated lithological mapping, with newly mapped granulite areas marked by a star.

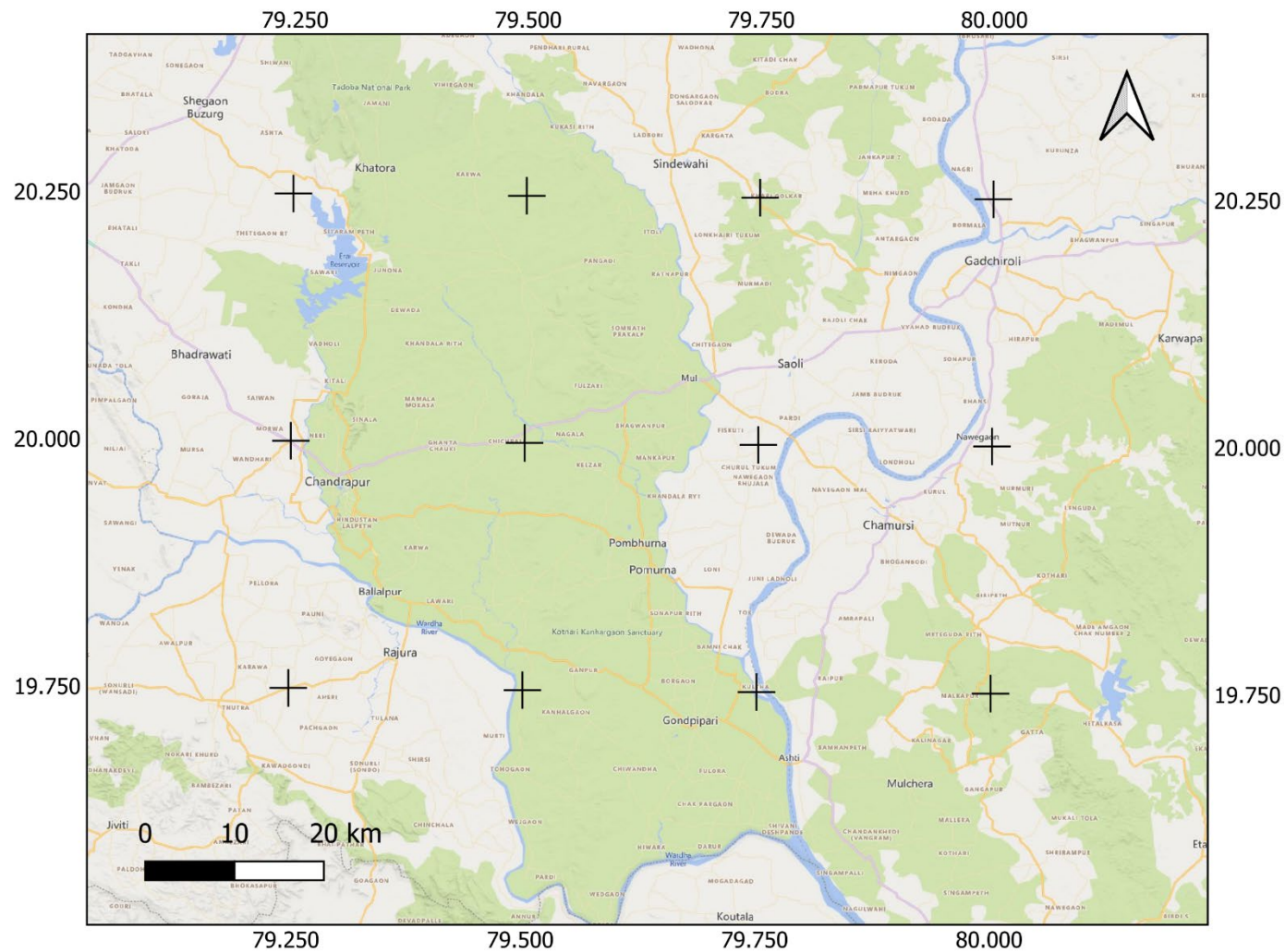


Figure 11.9a: Changes in the litho-tectonic mapping in the northern part of the Bastar Craton, as follows: a) geographic location, b) original lithological mapping (Microsoft® Bing™ Maps), c) updated lithological mapping, with a newly mapped formation marked by stars.

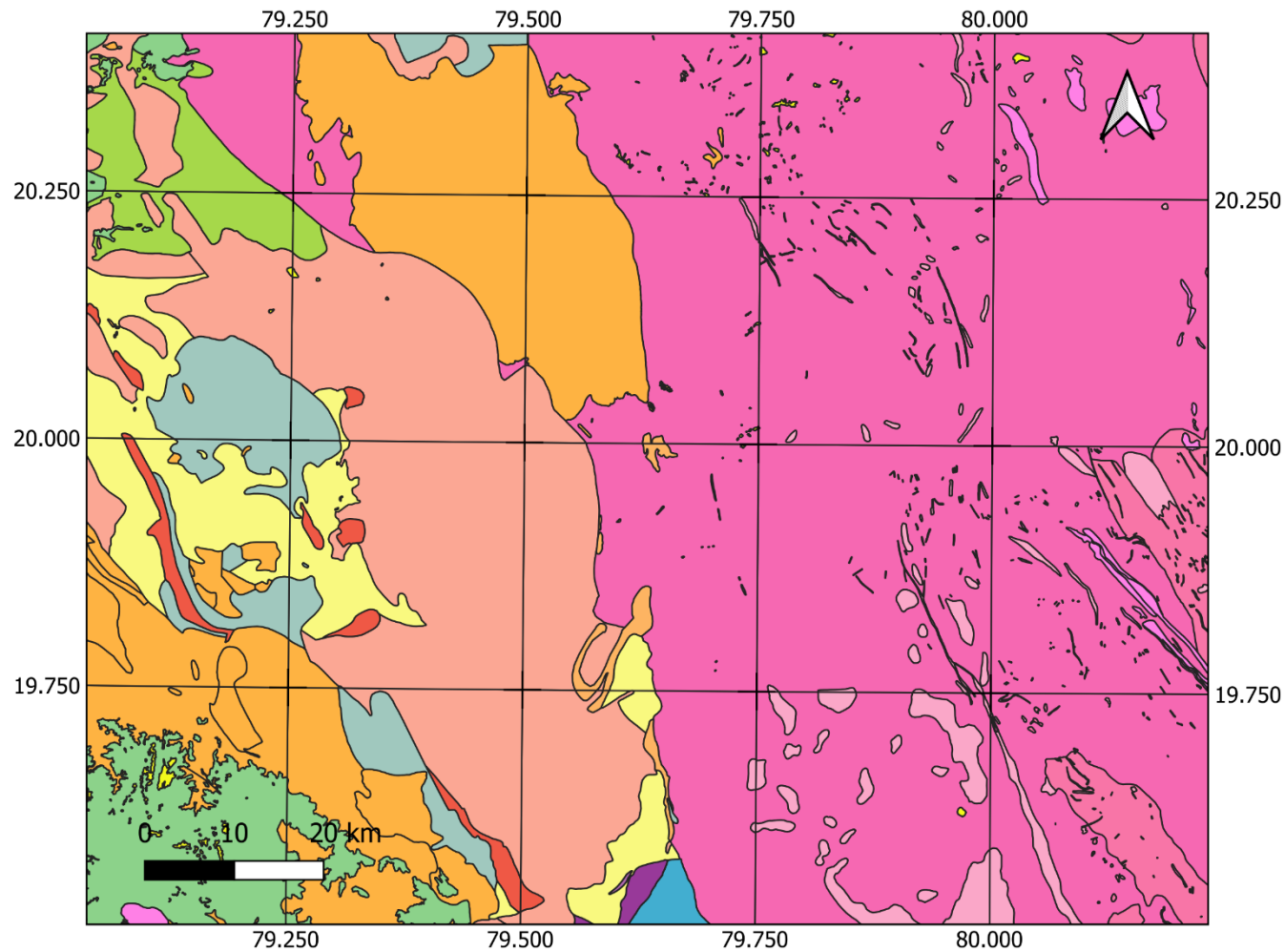


Figure 11.9b: Changes in the litho-tectonic mapping in the northern part of the Bastar Craton, as follows: a) geographic location (Microsoft® Bing™ Maps), b) original lithological mapping, c) updated lithological mapping, with a newly mapped formation marked by stars.

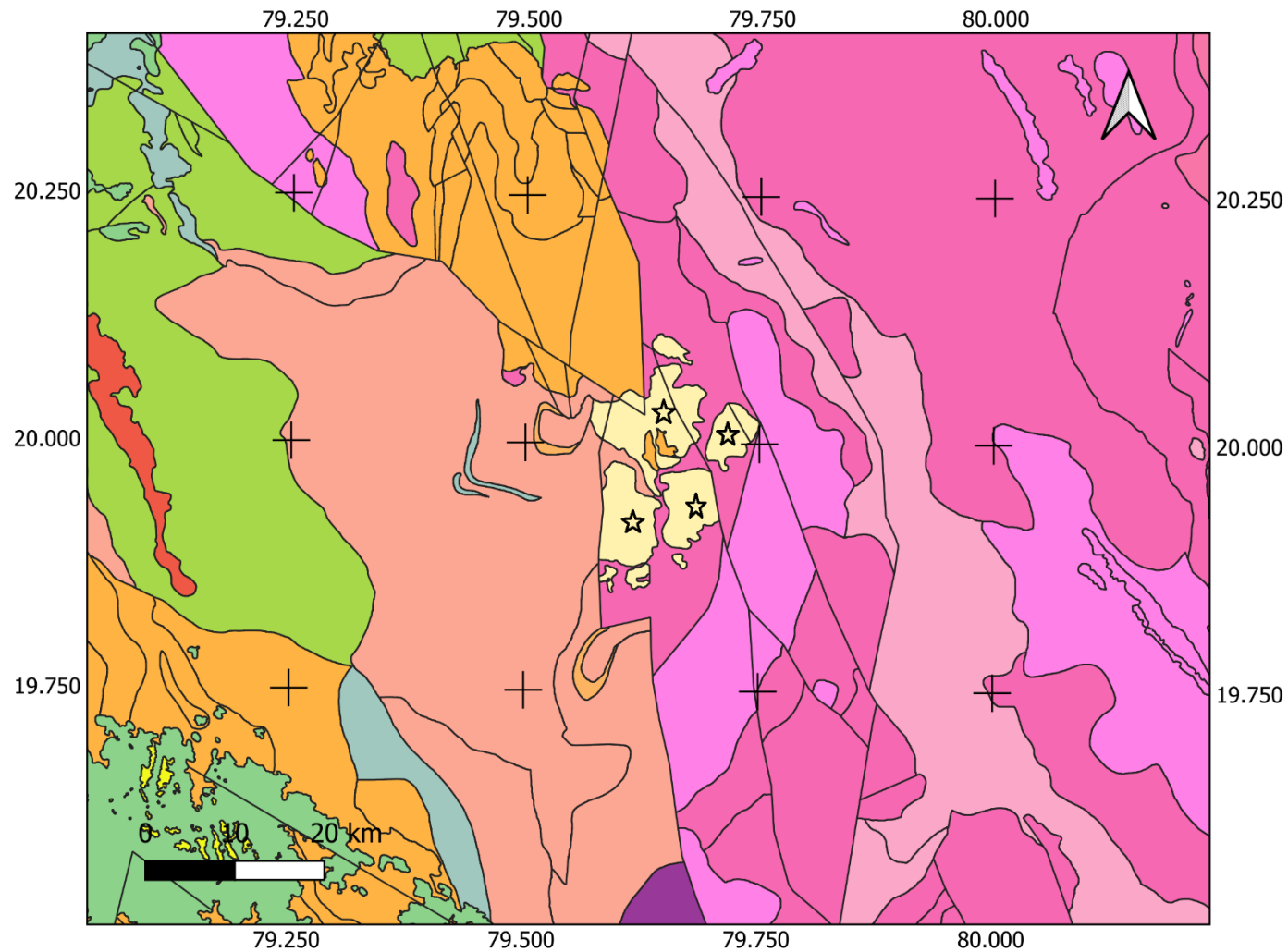
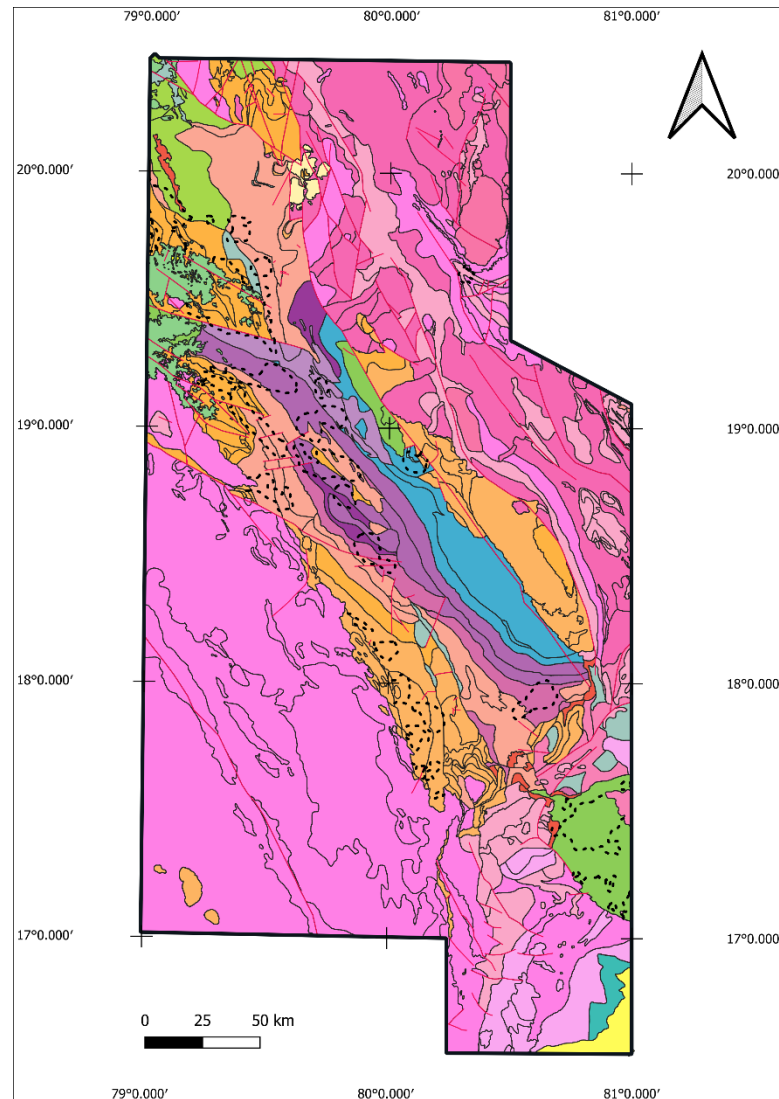


Figure 11.9c: Changes in the litho-tectonic mapping in the northern part of the Bastar Craton, as follows: a) geographic location (Microsoft® Bing™ Maps), b) original lithological mapping, c) updated lithological mapping, with a newly mapped formation marked by stars.



*Figure 11.10: Litho-tectonic map of Block-6 with boundaries of buried bodies shown as follows:
 red lines are faults, fine black lines are lithological boundaries, broken black lines are buried boundaries.*

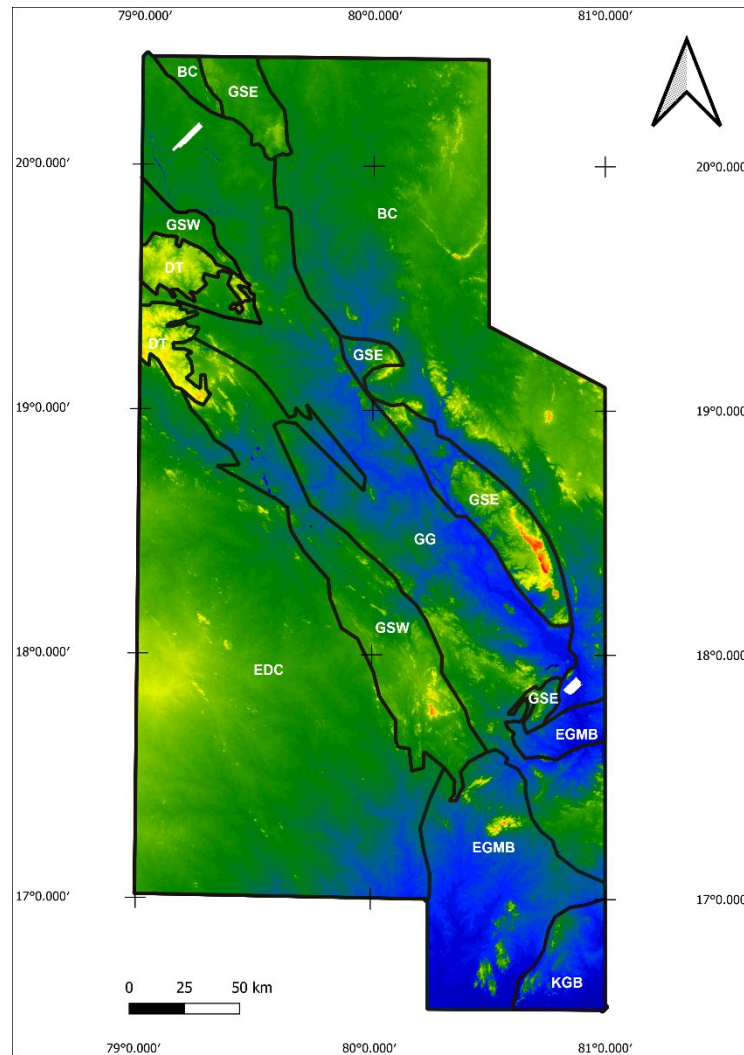


Figure 12.1.1: Major geological domains of Block superimposed on a digital elevation model of Block-6 as follows: EDC - Eastern Dharwar Craton, BC - Bastar Craton EGMB - Eastern Ghats Mobile Belt, GSW - Godavari Supergroup Western Belt, GSE - Godavari Supergroup Eastern Belt, GG – Gondwana Supergroup Graben, KGB – Krishna-Godavari Basin

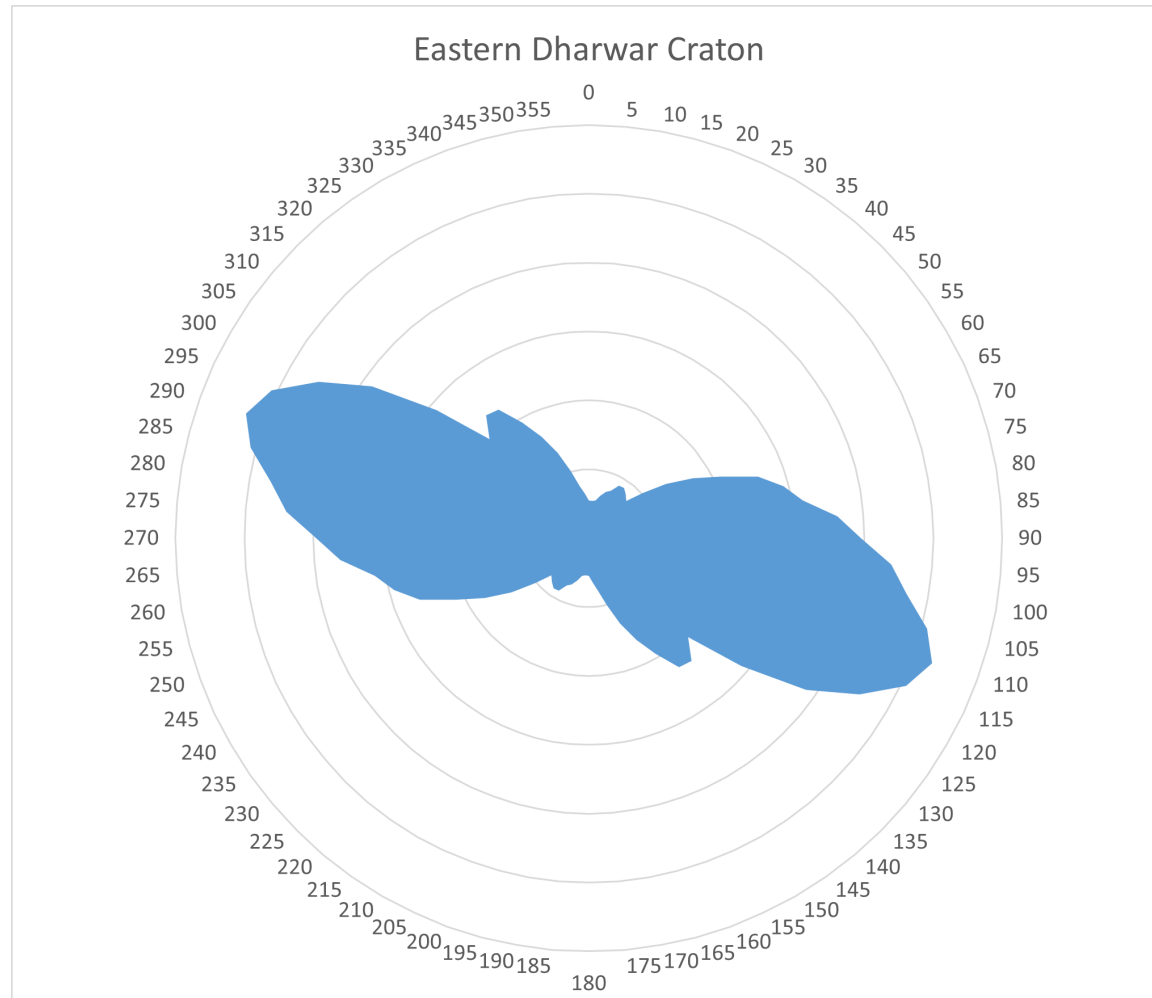


Figure 12.1.2a: Trends from short wavelength magnetic data lineaments for the main geological domains of Block-6. a) Eastern Dharwar Craton, b) Bastar Craton, c) Bastar Craton Inlier, d) Eastern Ghats Mobile Belt, e) Godavari Supergroup Western Belt south, f) Godavari Supergroup Western Belt north, g) Godavari Supergroup Eastern Belt south, h) Godavari Supergroup Eastern central, i) Godavari Supergroup Eastern north, j) Gondwana Supergroup Graben, k) Krishna-Godavari Basin, and l) Deccan Traps.

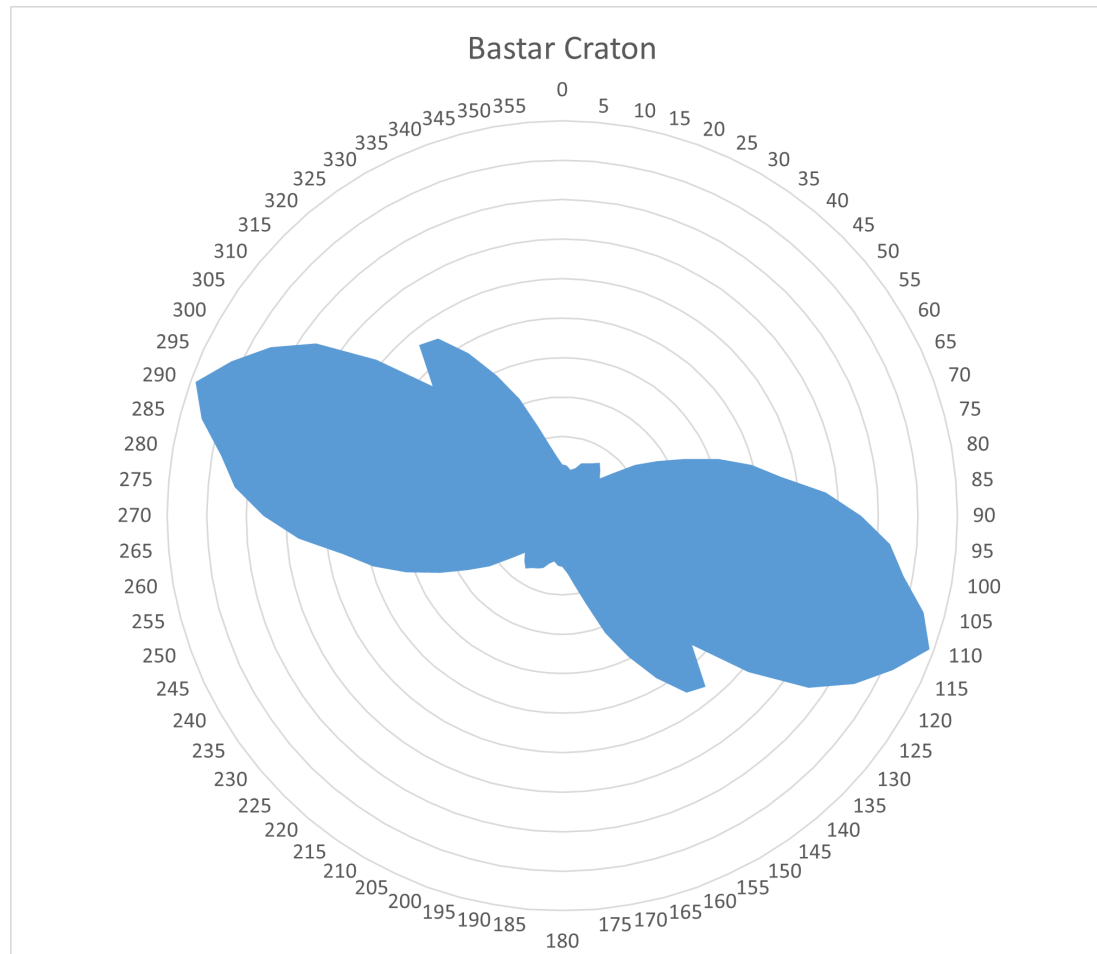


Figure 12.1.2b: Trends from short wavelength magnetic data lineaments for the main geological domains of Block-6. a) Eastern Dharwar Craton, b) Bastar Craton, c) Bastar Craton Inlier, d) Eastern Ghats Mobile Belt, e) Godavari Supergroup Western Belt south, f) Godavari Supergroup Western Belt north, g) Godavari Supergroup Eastern Belt south, h) Godavari Supergroup Eastern central, i) Godavari Supergroup Eastern north, j) Gondwana Supergroup Graben, k) Krishna-Godavari Basin, and l) Deccan Traps.

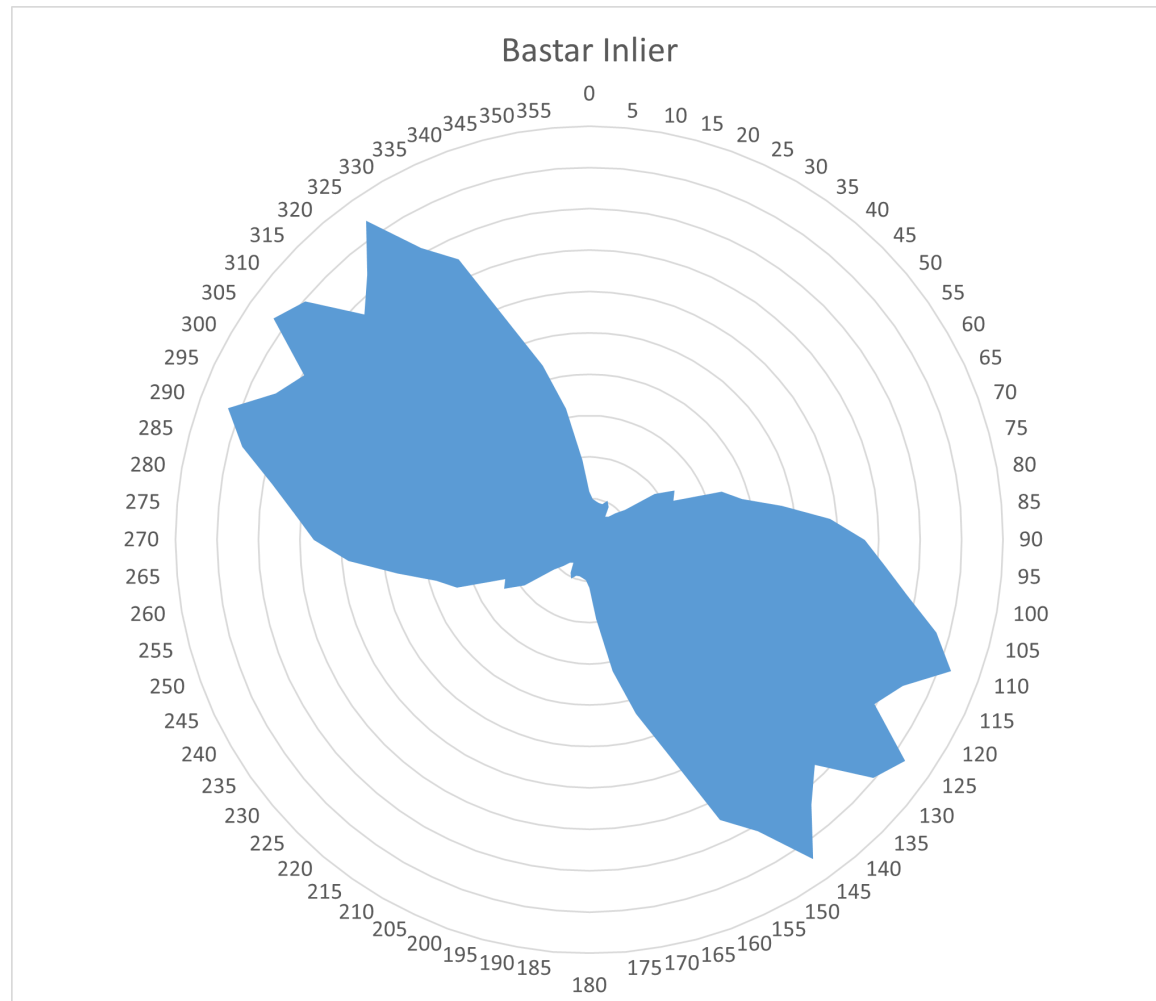


Figure 12.1.2c: Trends from short wavelength magnetic data lineaments for the main geological domains of Block-6. a) Eastern Dharwar Craton, b) Bastar Craton, c) Bastar Craton Inlier, d) Eastern Ghats Mobile Belt, e) Godavari Supergroup Western Belt south, f) Godavari Supergroup Western Belt north, g) Godavari Supergroup Eastern Belt south, h) Godavari Supergroup Eastern central, i) Godavari Supergroup Eastern north, j) Gondwana Supergroup Graben, k) Krishna-Godavari Basin, and l) Deccan Traps.

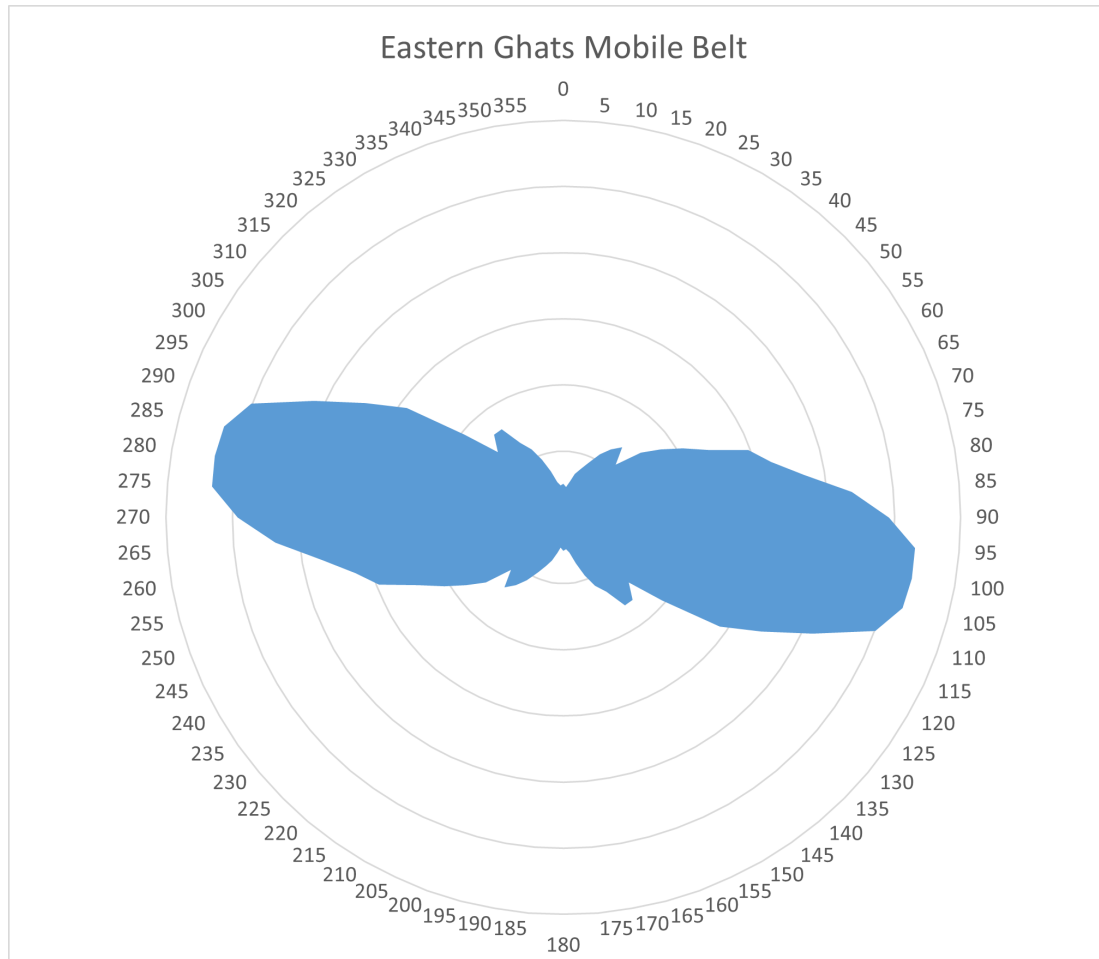


Figure 12.1.2d: Trends from short wavelength magnetic data lineaments for the main geological domains of Block-6. a) Eastern Dharwar Craton, b) Bastar Craton, c) Bastar Craton Inlier, d) Eastern Ghats Mobile Belt, e) Godavari Supergroup Western Belt south, f) Godavari Supergroup Western Belt north, g) Godavari Supergroup Eastern Belt south, h) Godavari Supergroup Eastern central, i) Godavari Supergroup Eastern north, j) Gondwana Supergroup Graben, k) Krishna-Godavari Basin, and l) Deccan Traps.

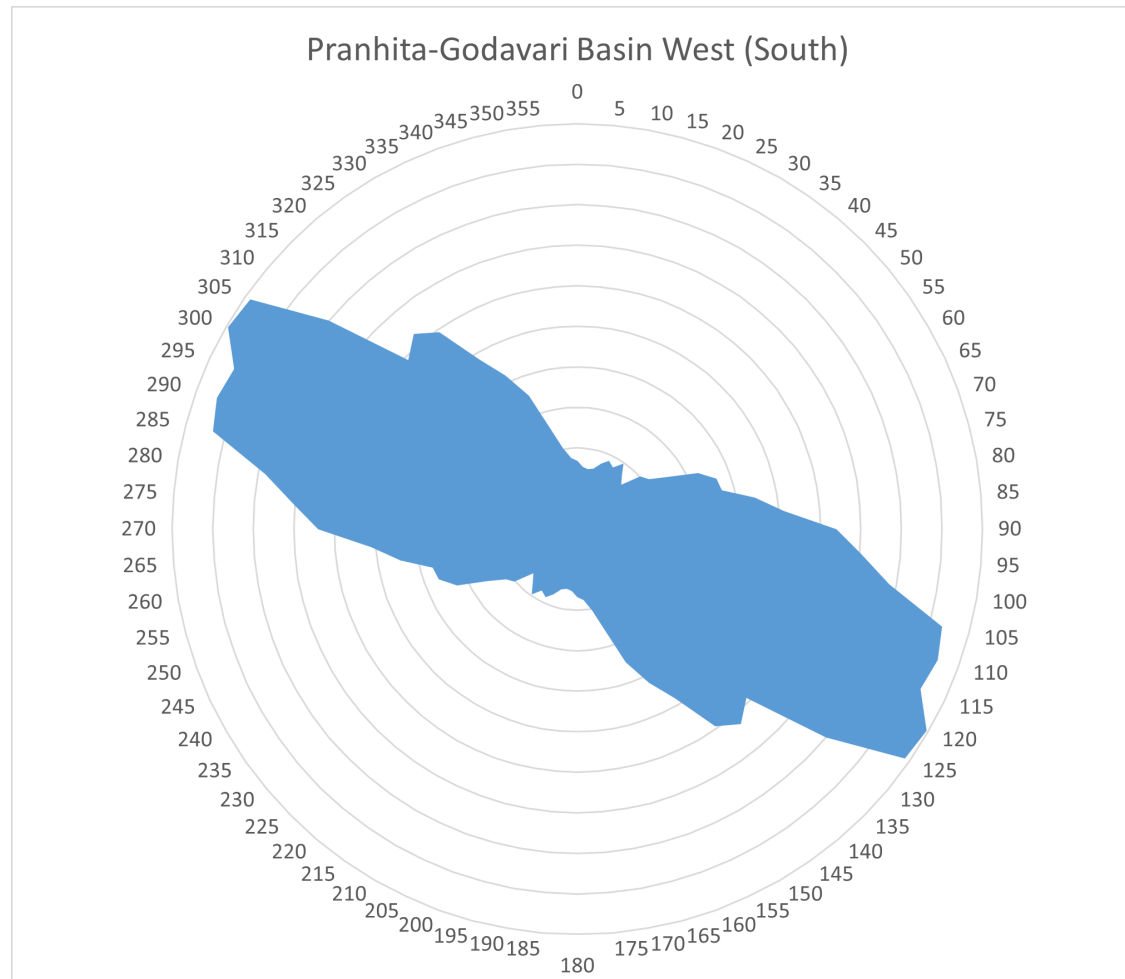


Figure 12.1.2e: Trends from short wavelength magnetic data lineaments for the main geological domains of Block-6. a) Eastern Dharwar Craton, b) Bastar Craton, c) Bastar Craton Inlier, d) Eastern Ghats Mobile Belt, e) Godavari Supergroup Western Belt south, f) Godavari Supergroup Western Belt north, g) Godavari Supergroup Eastern Belt south, h) Godavari Supergroup Eastern central, i) Godavari Supergroup Eastern north, j) Gondwana Supergroup Graben, k) Krishna-Godavari Basin, and l) Deccan Traps.

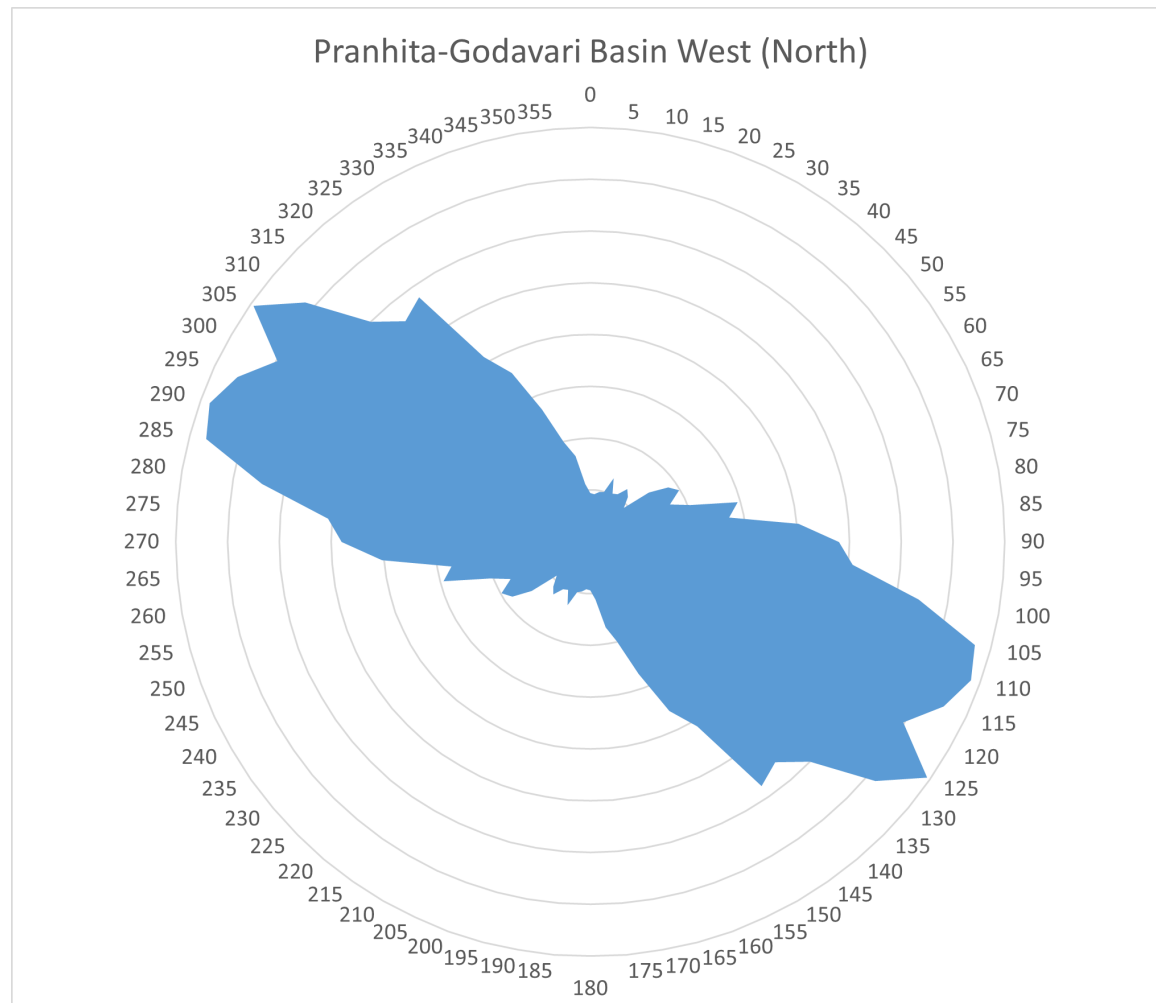


Figure 12.1.2f: Trends from short wavelength magnetic data lineaments for the main geological domains of Block-6. a) Eastern Dharwar Craton, b) Bastar Craton, c) Bastar Craton Inlier, d) Eastern Ghats Mobile Belt, e) Godavari Supergroup Western Belt south, f) Godavari Supergroup Western Belt north, g) Godavari Supergroup Eastern Belt south, h) Godavari Supergroup Eastern central, i) Godavari Supergroup Eastern north, j) Gondwana Supergroup Graben, k) Krishna-Godavari Basin, and l) Deccan Traps.

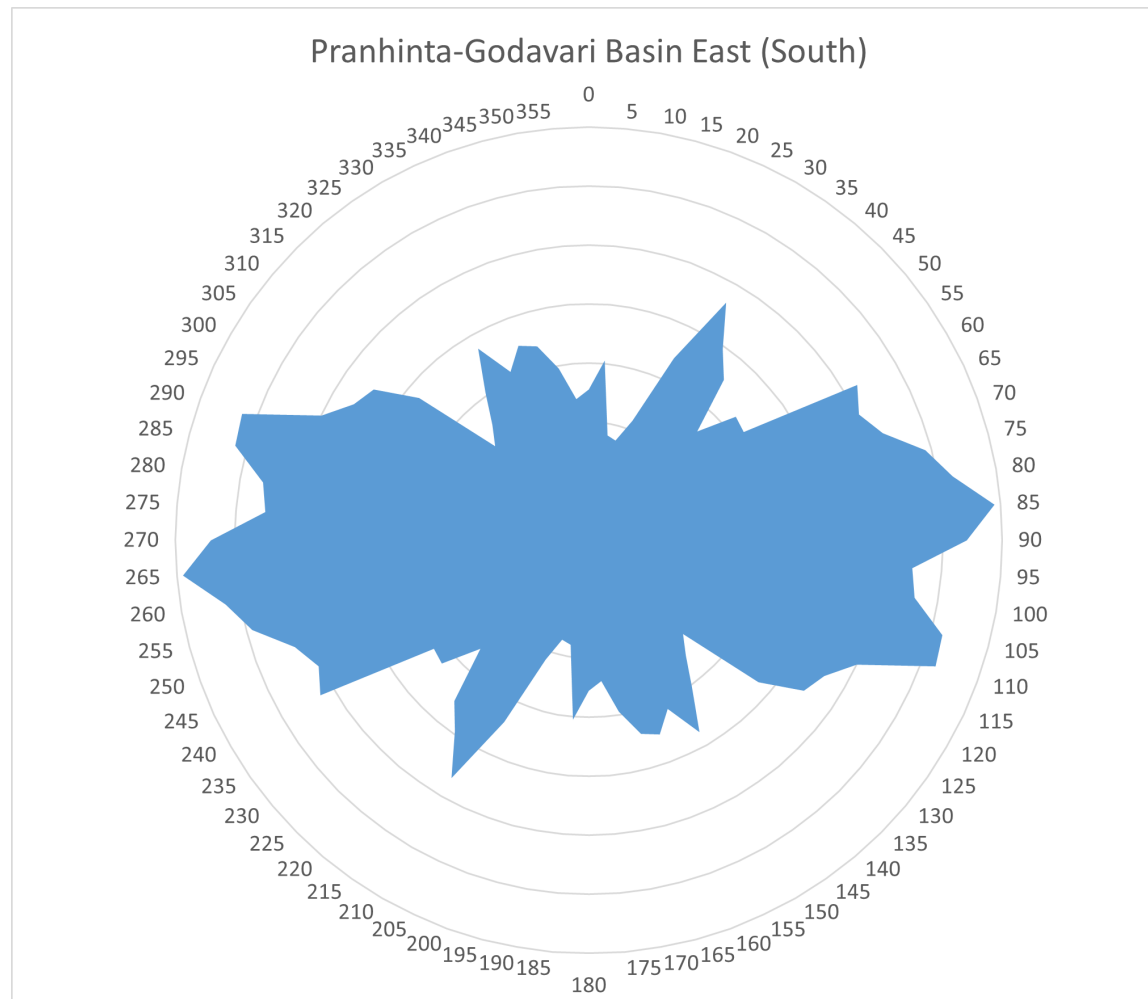


Figure 12.1.2g: Trends from short wavelength magnetic data lineaments for the main geological domains of Block-6. a) Eastern Dharwar Craton, b) Bastar Craton, c) Bastar Craton Inlier, d) Eastern Ghats Mobile Belt, e) Godavari Supergroup Western Belt south, f) Godavari Supergroup Western Belt north, g) Godavari Supergroup Eastern Belt south, h) Godavari Supergroup Eastern central, i) Godavari Supergroup Eastern north, j) Gondwana Supergroup Graben, k) Krishna-Godavari Basin, and l) Deccan Traps.

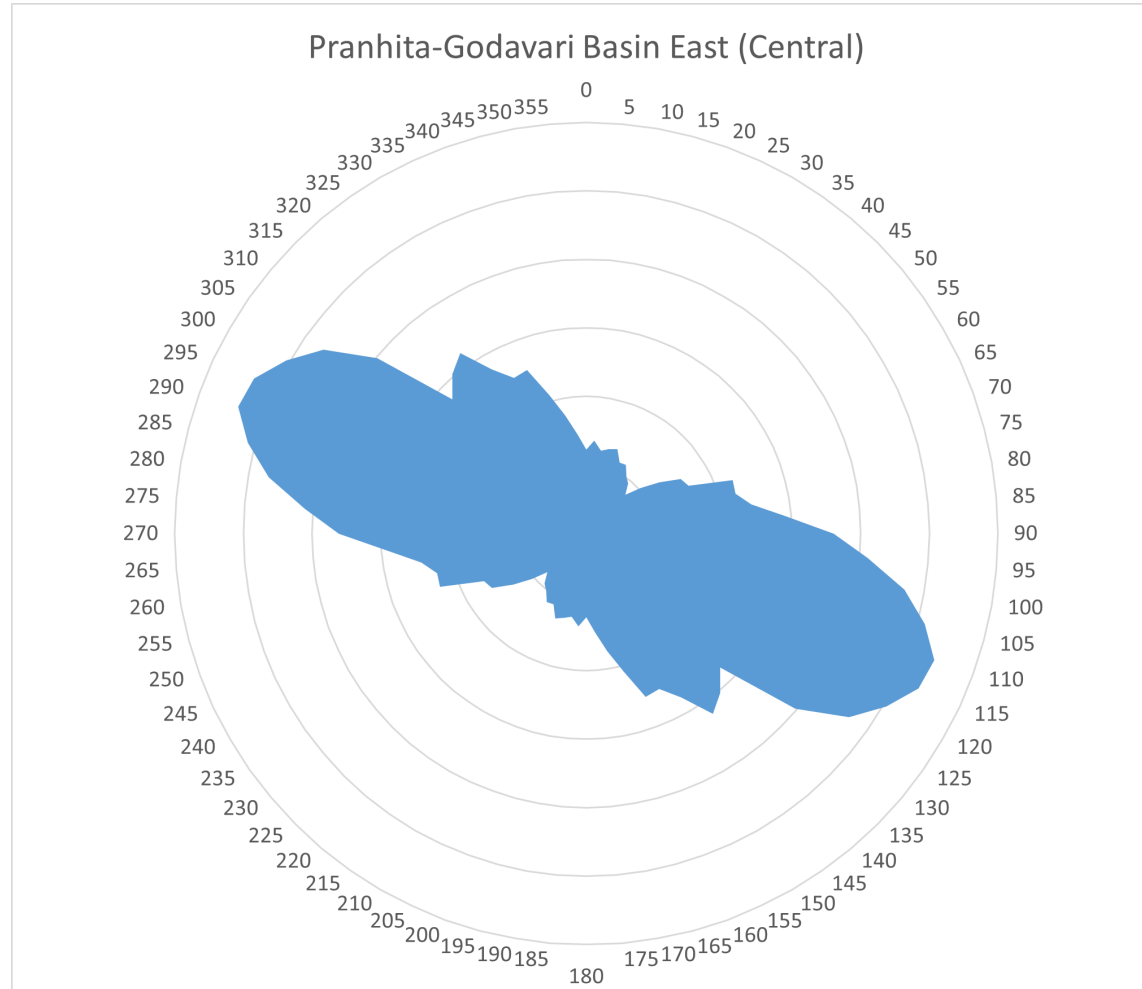


Figure 12.1.2h: Trends from short wavelength magnetic data lineaments for the main geological domains of Block-6. a) Eastern Dharwar Craton, b) Bastar Craton, c) Bastar Craton Inlier, d) Eastern Ghats Mobile Belt, e) Godavari Supergroup Western Belt south, f) Godavari Supergroup Western Belt north, g) Godavari Supergroup Eastern Belt south, h) Godavari Supergroup Eastern central, i) Godavari Supergroup Eastern north, j) Gondwana Supergroup Graben, k) Krishna-Godavari Basin, and l) Deccan Traps.

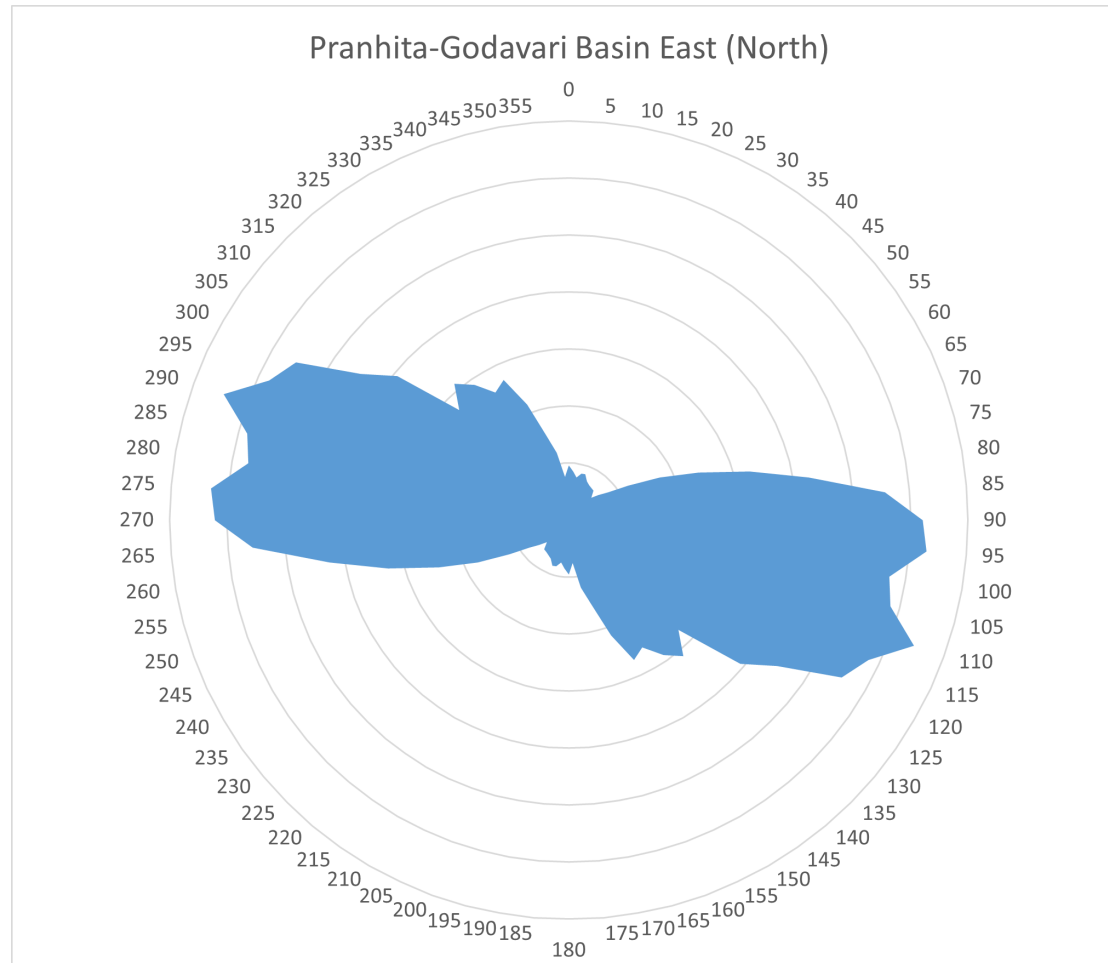


Figure 12.1.2i: Trends from short wavelength magnetic data lineaments for the main geological domains of Block-6. a) Eastern Dharwar Craton, b) Bastar Craton, c) Bastar Craton Inlier, d) Eastern Ghats Mobile Belt, e) Godavari Supergroup Western Belt south, f) Godavari Supergroup Western Belt north, g) Godavari Supergroup Eastern Belt south, h) Godavari Supergroup Eastern central, i) Godavari Supergroup Eastern north, j) Gondwana Supergroup Graben, k) Krishna-Godavari Basin, and l) Deccan Traps.

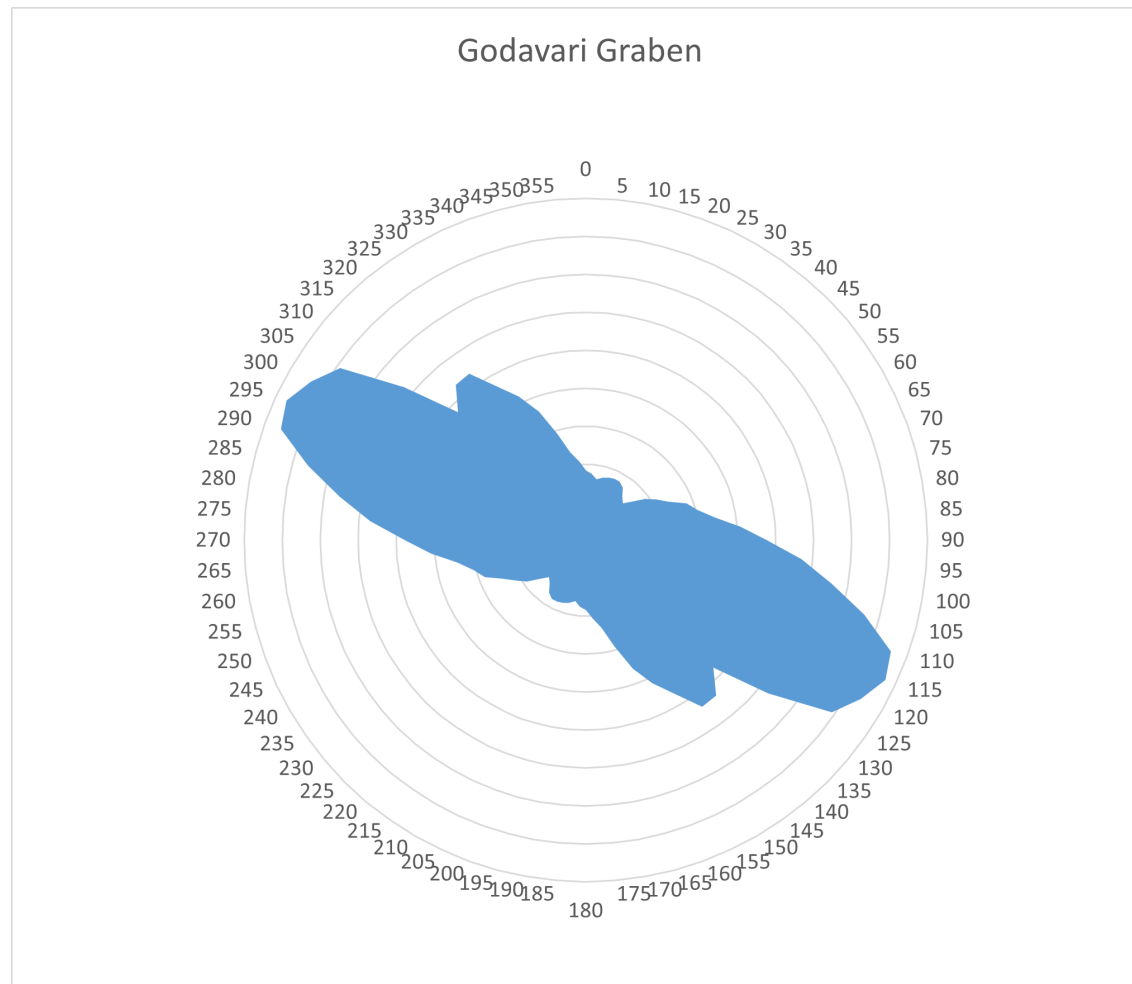


Figure 12.1.2j: Trends from short wavelength magnetic data lineaments for the main geological domains of Block-6. a) Eastern Dharwar Craton, b) Bastar Craton, c) Bastar Craton Inlier, d) Eastern Ghats Mobile Belt, e) Godavari Supergroup Western Belt south, f) Godavari Supergroup Western Belt north, g) Godavari Supergroup Eastern Belt south, h) Godavari Supergroup Eastern central, i) Godavari Supergroup Eastern north, j) Gondwana Supergroup Graben, k) Krishna-Godavari Basin, and l) Deccan Traps.

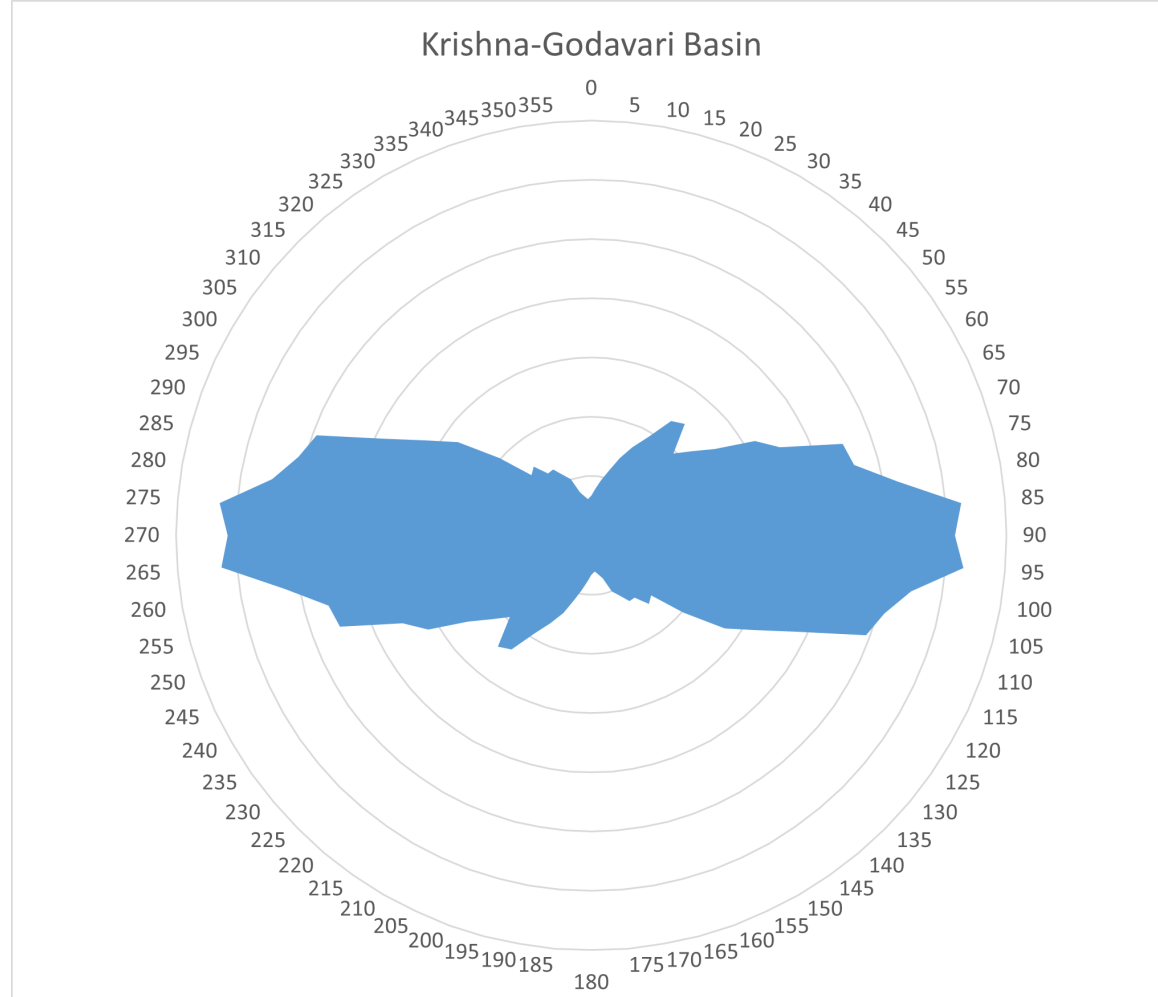


Figure 12.1.2k: Trends from short wavelength magnetic data lineaments for the main geological domains of Block-6. a) Eastern Dharwar Craton, b) Bastar Craton, c) Bastar Craton Inlier, d) Eastern Ghats Mobile Belt, e) Godavari Supergroup Western Belt south, f) Godavari Supergroup Western Belt north, g) Godavari Supergroup Eastern Belt south, h) Godavari Supergroup Eastern central, i) Godavari Supergroup Eastern north, j) Gondwana Supergroup Graben, k) Krishna-Godavari Basin, and l) Deccan Traps.

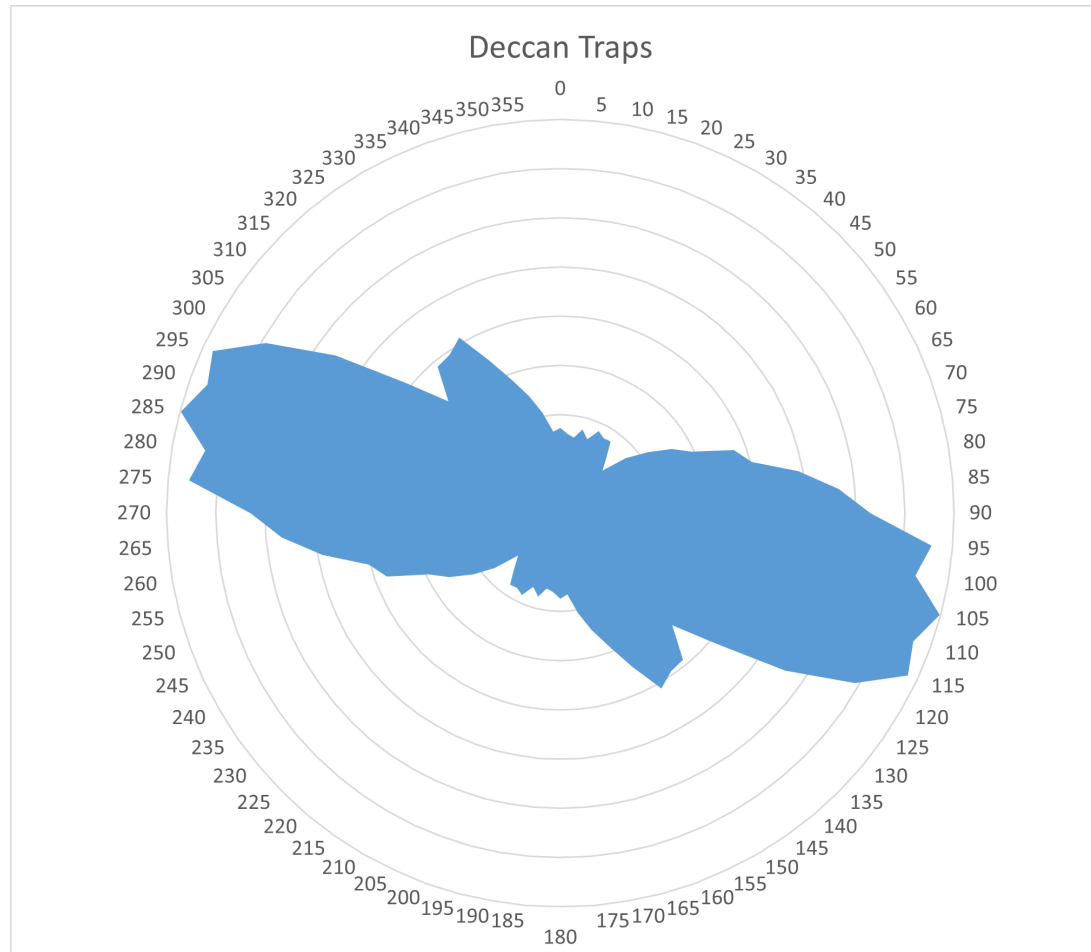


Figure 12.1.2l: Trends from short wavelength magnetic data lineaments for the main geological domains of Block-6. a) Eastern Dharwar Craton, b) Bastar Craton, c) Bastar Craton Inlier, d) Eastern Ghats Mobile Belt, e) Godavari Supergroup Western Belt south, f) Godavari Supergroup Western Belt north, g) Godavari Supergroup Eastern Belt south, h) Godavari Supergroup Eastern central, i) Godavari Supergroup Eastern north, j) Gondwana Supergroup Graben, k) Krishna-Godavari Basin, and l) Deccan Traps.

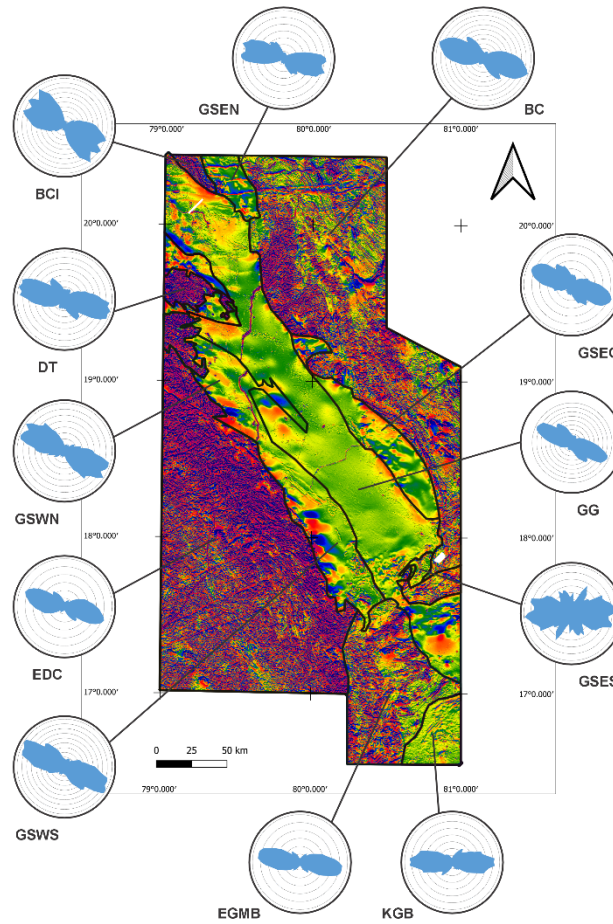


Figure 12.1.3: Trends from short wavelength magnetic data lineaments for the main geological domains of Block-6 located on the first vertical derivative of the magnetic anomaly. DC: Eastern Dharwar Craton, BC: Bastar Craton, BCI: Bastar Craton Inlier, D: Eastern Ghats Mobile Belt, GSWS: Godavari Supergroup Western Belt south, GSWN: Godavari Supergroup Western Belt north, GSES: Godavari Supergroup Eastern Belt south, GSEC: Godavari Supergroup Eastern Belt central, GSEN: Godavari Supergroup Eastern Belt north, GG: Gondwana Supergroup Graben, KGB: Krishna-Godavari Basin, and DT: Deccan Traps.

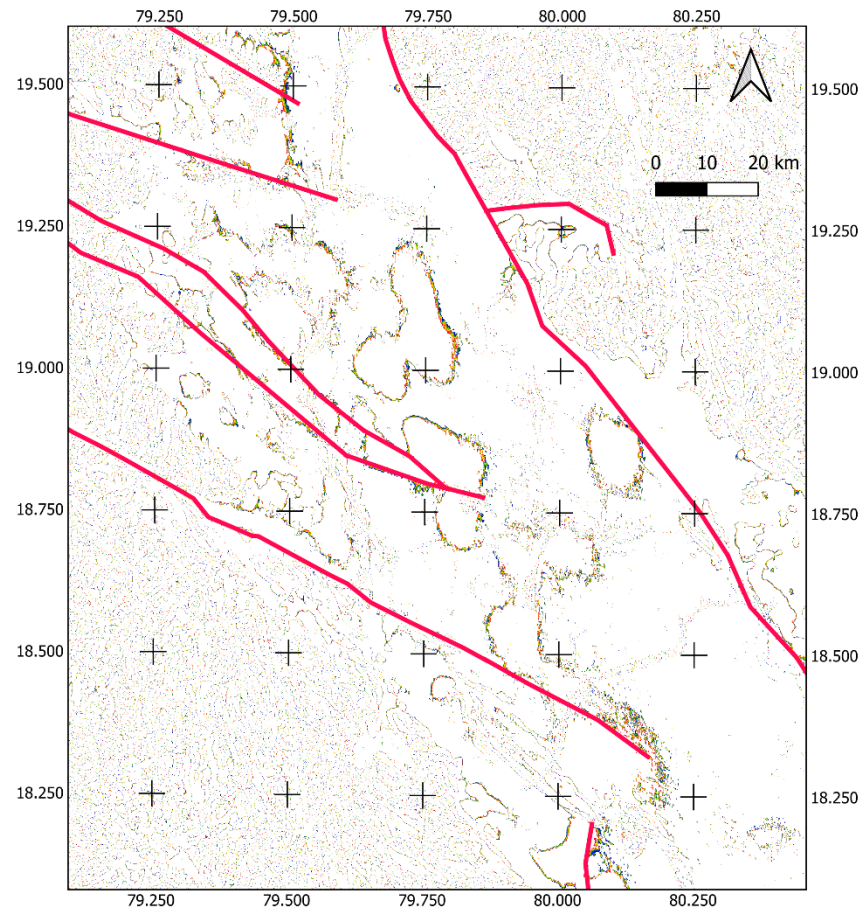


Figure 12.1.4a: The Chinnur Inliers of Godavari Supergroup sediments within the Gondwana sediments, as follows: a) magnetic tilt angles of $\pm 5^\circ$ and traces of major faults that pass from the craton into the Pranhita-Godavari Rift b) Bouguer Gravity c) band pass filtered Reduced to Pole magnetic anomaly d) gamma-ray ternary image e) geographic location (Microsoft® Bing™ Maps).

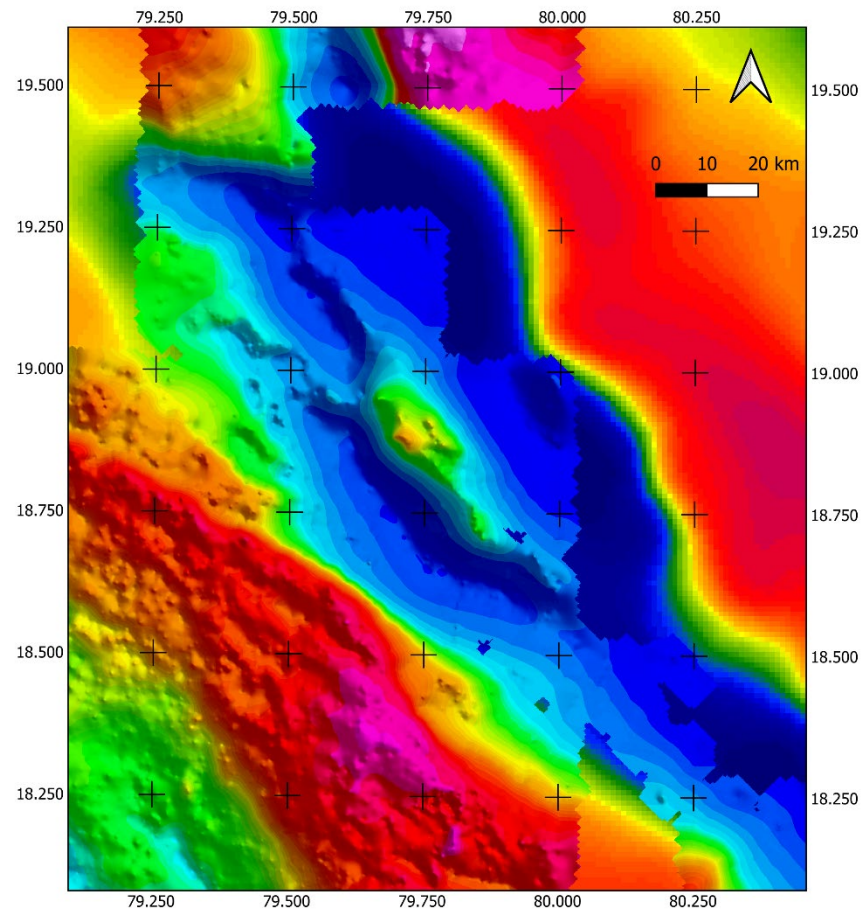


Figure 12.1.4b: The Chinnur Inliers of Godavari Supergroup sediments within the Gondwana sediments, as follows: a) magnetic tilt angles of $\pm 5^\circ$ and traces of major faults that pass from the craton into the Pranhita-Godavari Rift b) Bouguer Gravity c) band pass filtered Reduced to Pole magnetic anomaly d) gamma-ray ternary image e) geographic location (Microsoft® Bing™ Maps).

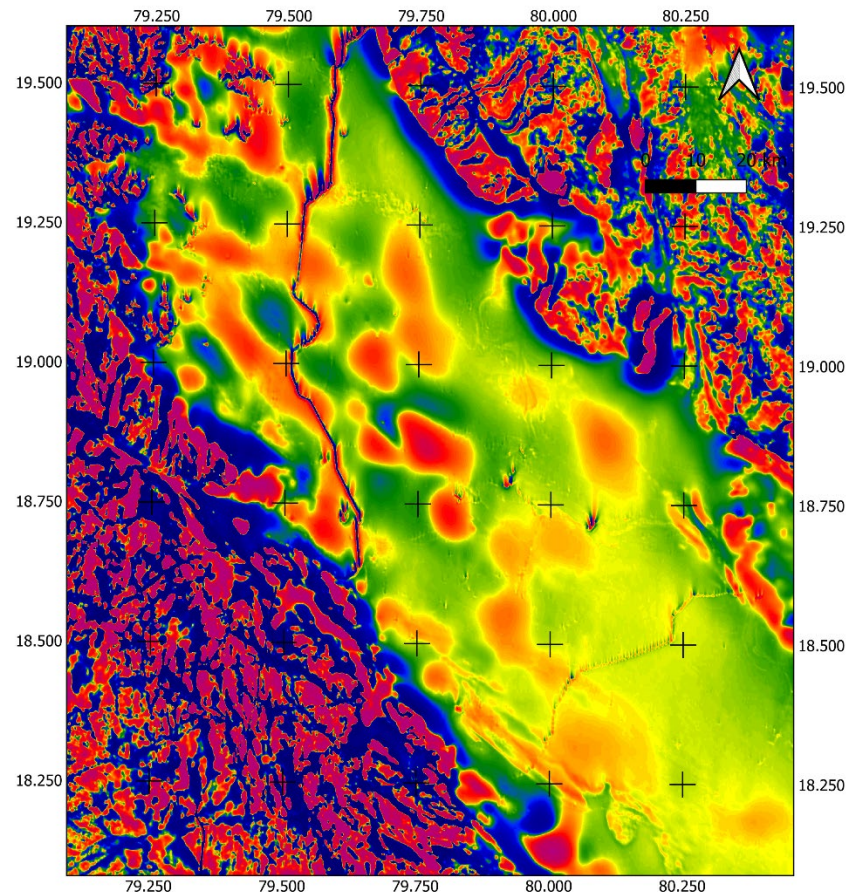


Figure 12.1.4c: The Chinnur Inliers of Godavari Supergroup sediments within the Gondwana sediments, as follows: a) magnetic tilt angles of $\pm 5^\circ$ and traces of major faults that pass from the craton into the Pranhita-Godavari Rift b) Bouguer Gravity c) band pass filtered Reduced to Pole magnetic anomaly d) gamma-ray ternary image e) geographic location (Microsoft® Bing™ Maps).

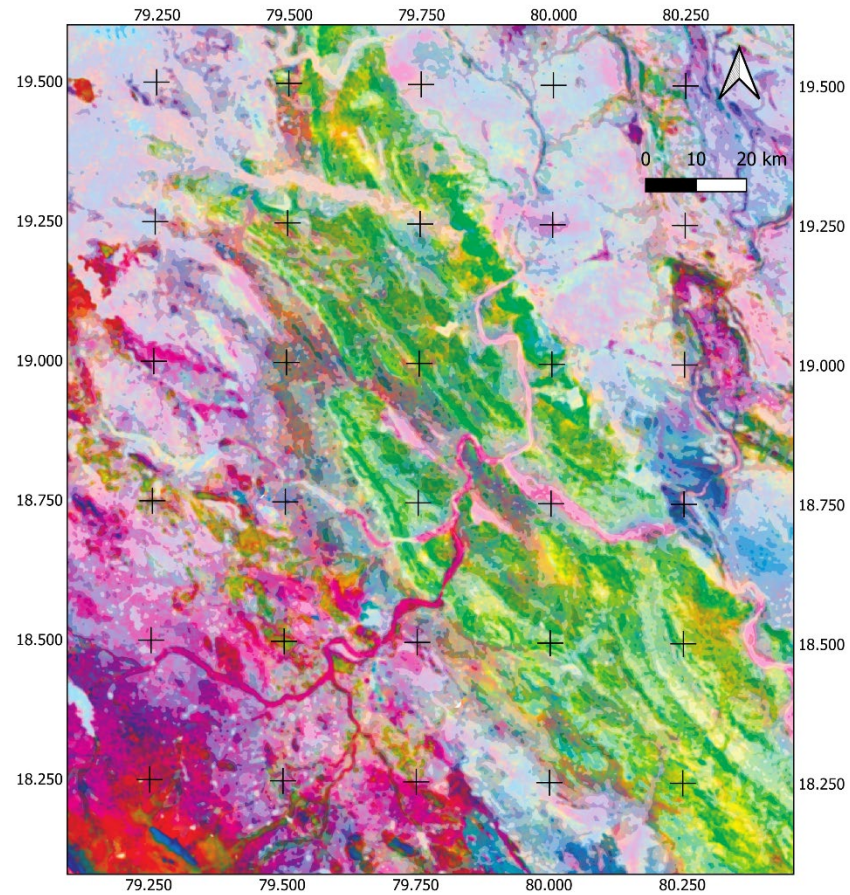


Figure 12.1.4d: The Chinnur Inliers of Godavari Supergroup sediments within the Gondwana sediments, as follows: a) magnetic tilt angles of $\pm 5^\circ$ and traces of major faults that pass from the craton into the Pranhita-Godavari Rift b) Bouguer Gravity c) band pass filtered Reduced to Pole magnetic anomaly d) gamma-ray ternary image e) geographic location (Microsoft® Bing™ Maps).

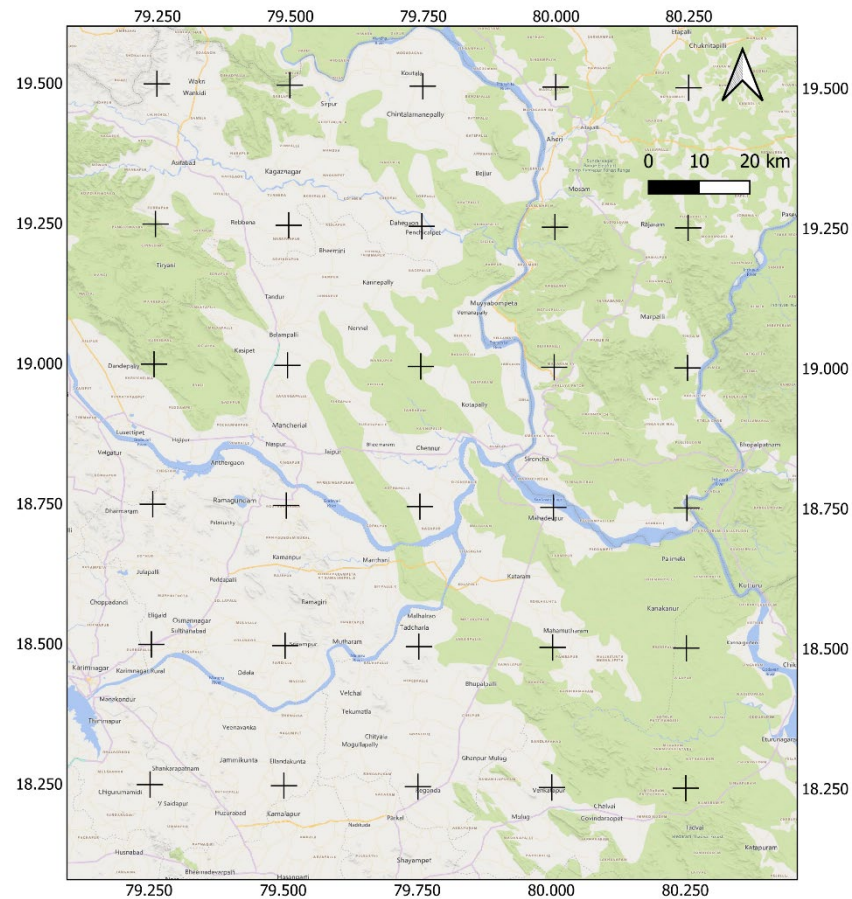


Figure 12.1.4e: The Chinnur Inliers of Godavari Supergroup sediments within the Gondwana sediments, as follows: a) magnetic tilt angles of $\pm 5^\circ$ and traces of major faults that pass from the craton into the Pranhita-Godavari Rift b) Bouguer Gravity c) band pass filtered Reduced to Pole magnetic anomaly d) gamma-ray ternary image e) geographic location (Microsoft® Bing™ Maps).

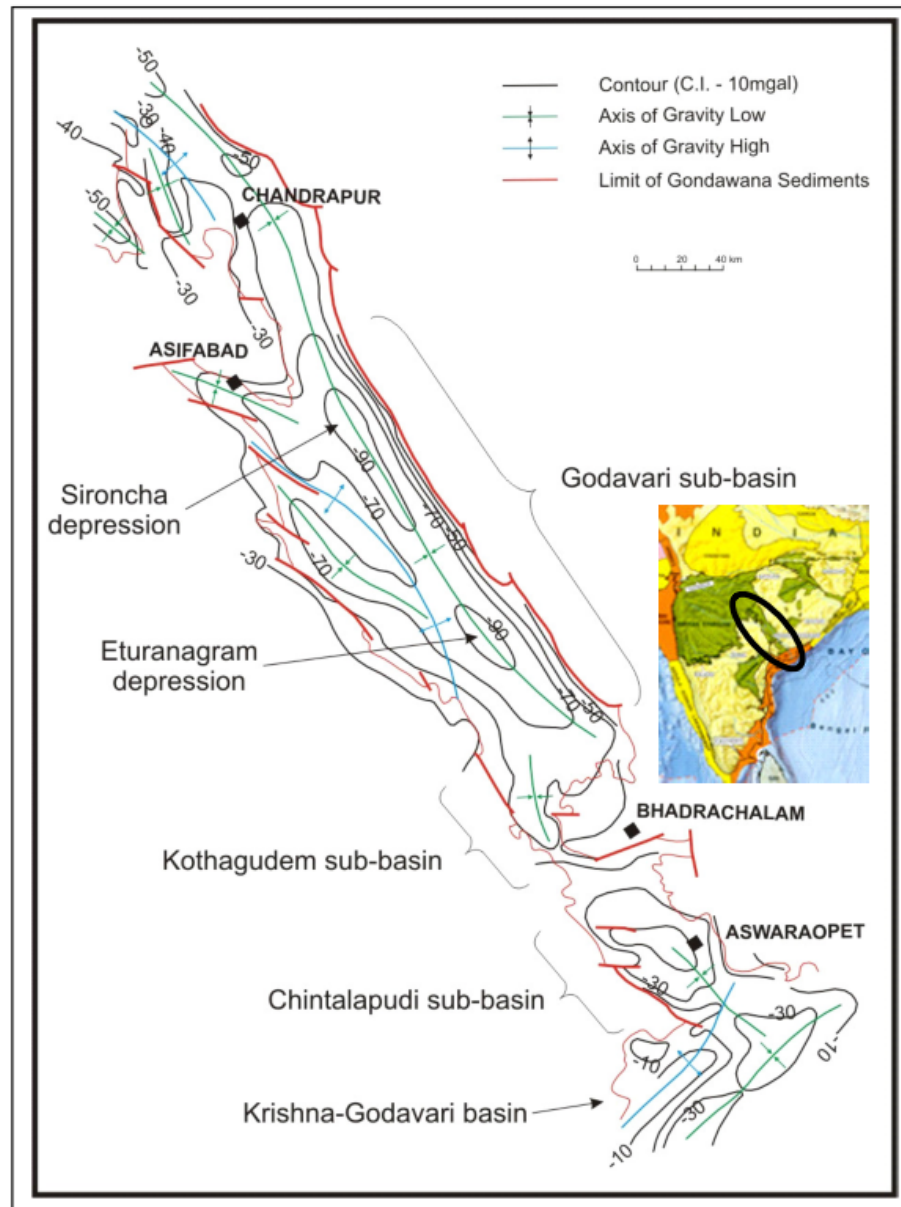


Figure 12.1.5: Bouguer gravity of the Pranhita-Godavari
Rift from Dasgupta and Jain (2007).

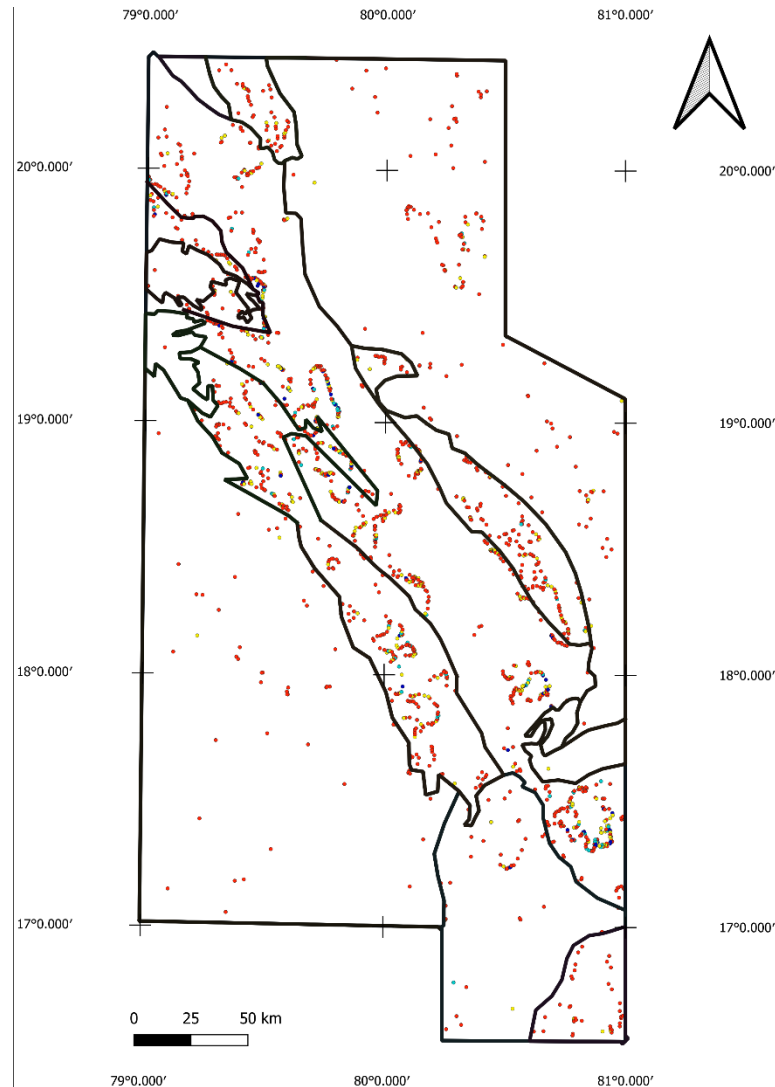


Figure 12.1.6a: Depths to magnetic source from $\pm 45^\circ$ tilt angle contours. Red symbols are for depths of 1-2 km, yellow symbols are for depths of 2-3 km, light blue symbols are for depths of 3-4 km, and dark blue are for depths of 4-10 km, as follows: a) all sources of 1 to 10 km depth, b) sources 1 to 2 km deep, c) sources 2 to 3 km deep, d) sources 3 to 4 km deep, e) sources 4 to 10 km deep.

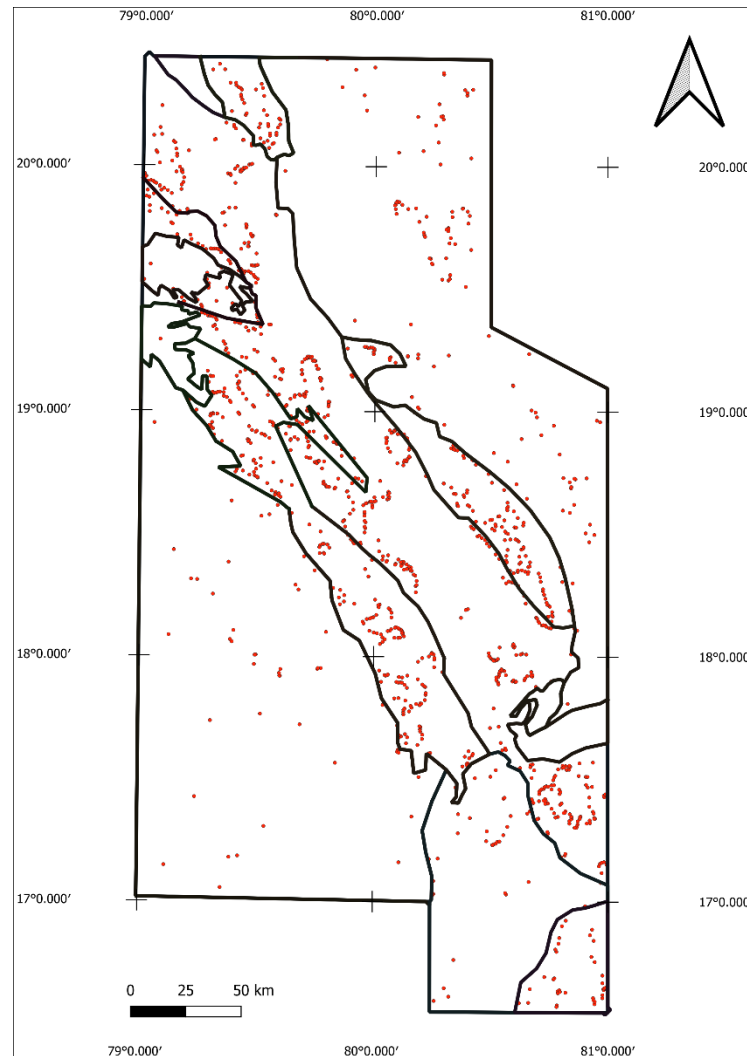


Figure 12.1.6b: Depths to magnetic source from $\pm 45^\circ$ tilt angle contours. Red symbols are for depths of 1-2 km, yellow symbols are for depths of 2-3 km, light blue symbols are for depths of 3-4 km, and dark blue are for depths of 4-10 km, as follows: a) all sources of 1 to 10 km depth, b) sources 1 to 2 km deep, c) sources 2 to 3 km deep, d) sources 3 to 4 km deep, e) sources 4 to 10 km deep.

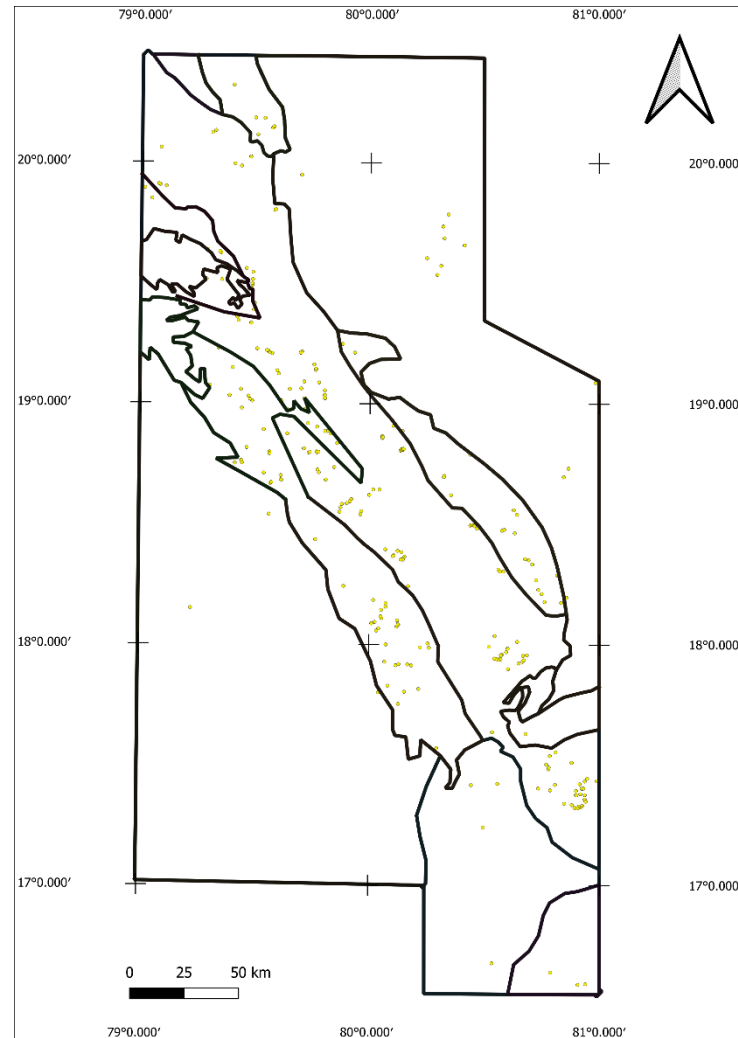


Figure 12.1.6c: Depths to magnetic source from $\pm 45^\circ$ tilt angle contours. Red symbols are for depths of 1-2 km, yellow symbols are for depths of 2-3 km, light blue symbols are for depths of 3-4 km, and dark blue are for depths of 4-10 km, as follows: a) all sources of 1 to 10 km depth, b) sources 1 to 2 km deep, c) sources 2 to 3 km deep, d) sources 3 to 4 km deep, e) sources 4 to 10 km deep.

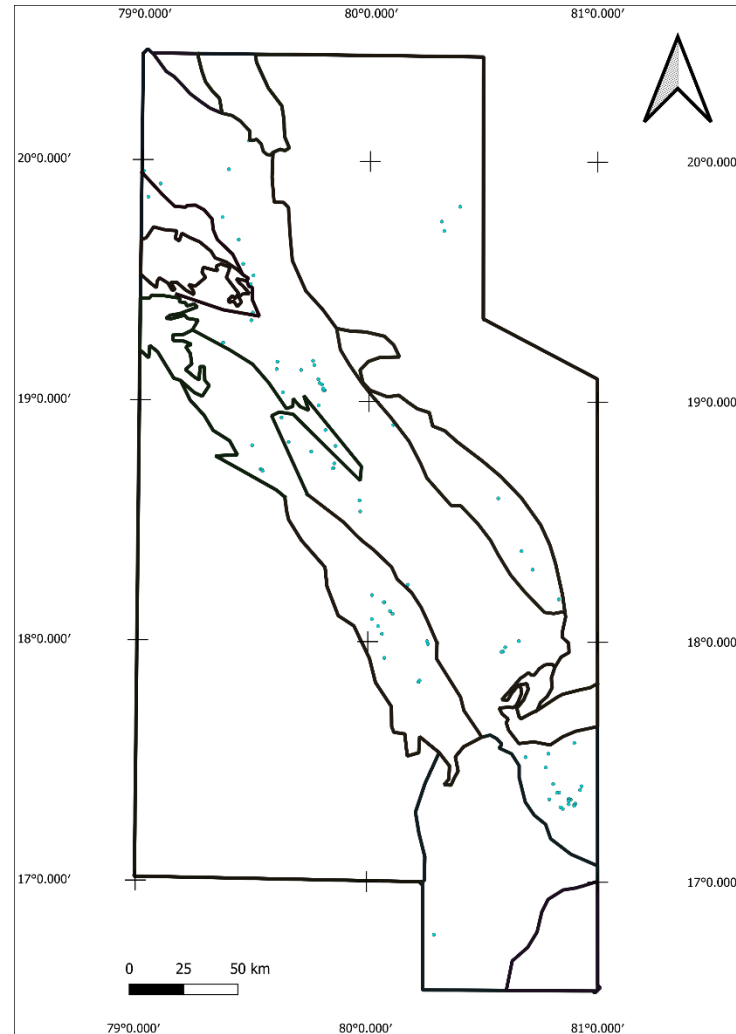


Figure 12.1.6d: Depths to magnetic source from $\pm 45^\circ$ tilt angle contours. Red symbols are for depths of 1-2 km, yellow symbols are for depths of 2-3 km, light blue symbols are for depths of 3-4 km, and dark blue are for depths of 4-10 km, as follows: a) all sources of 1 to 10 km depth, b) sources 1 to 2 km deep, c) sources 2 to 3 km deep, d) sources 3 to 4 km deep, e) sources 4 to 10 km deep.

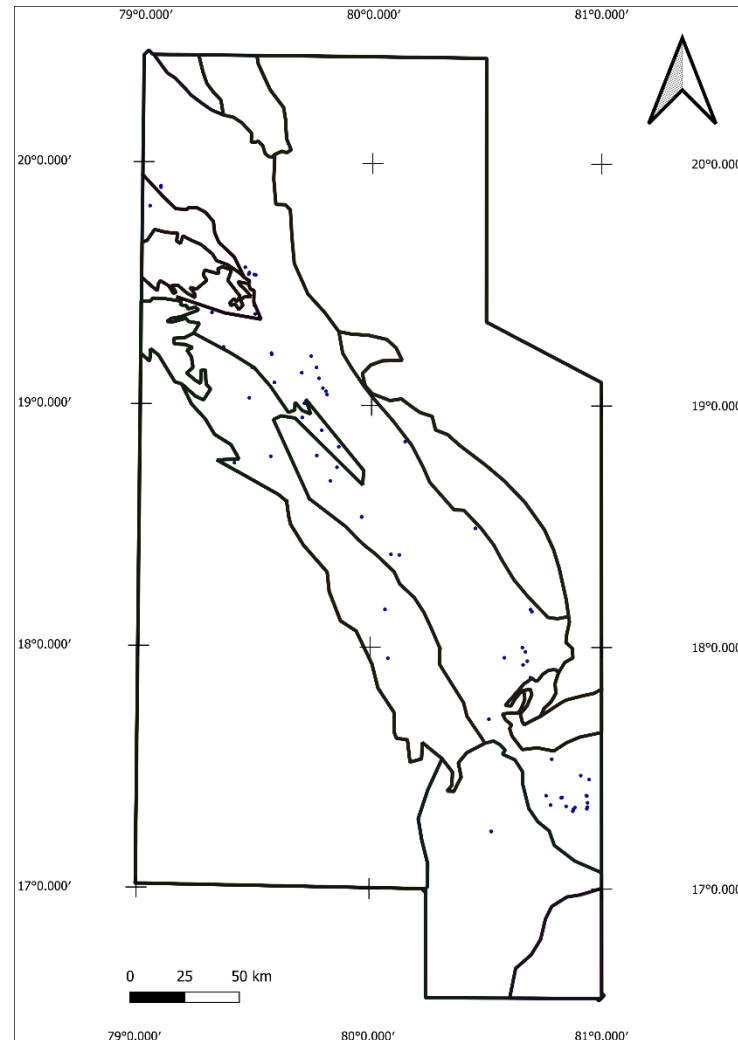


Figure 12.1.6e: Depths to magnetic source from $\pm 45^\circ$ tilt angle contours. Red symbols are for depths of 1-2 km, yellow symbols are for depths of 2-3 km, light blue symbols are for depths of 3-4 km, and dark blue are for depths of 4-10 km, as follows: a) all sources of 1 to 10 km depth, b) sources 1 to 2 km deep, c) sources 2 to 3 km deep, d) sources 3 to 4 km deep, e) sources 4 to 10 km deep.

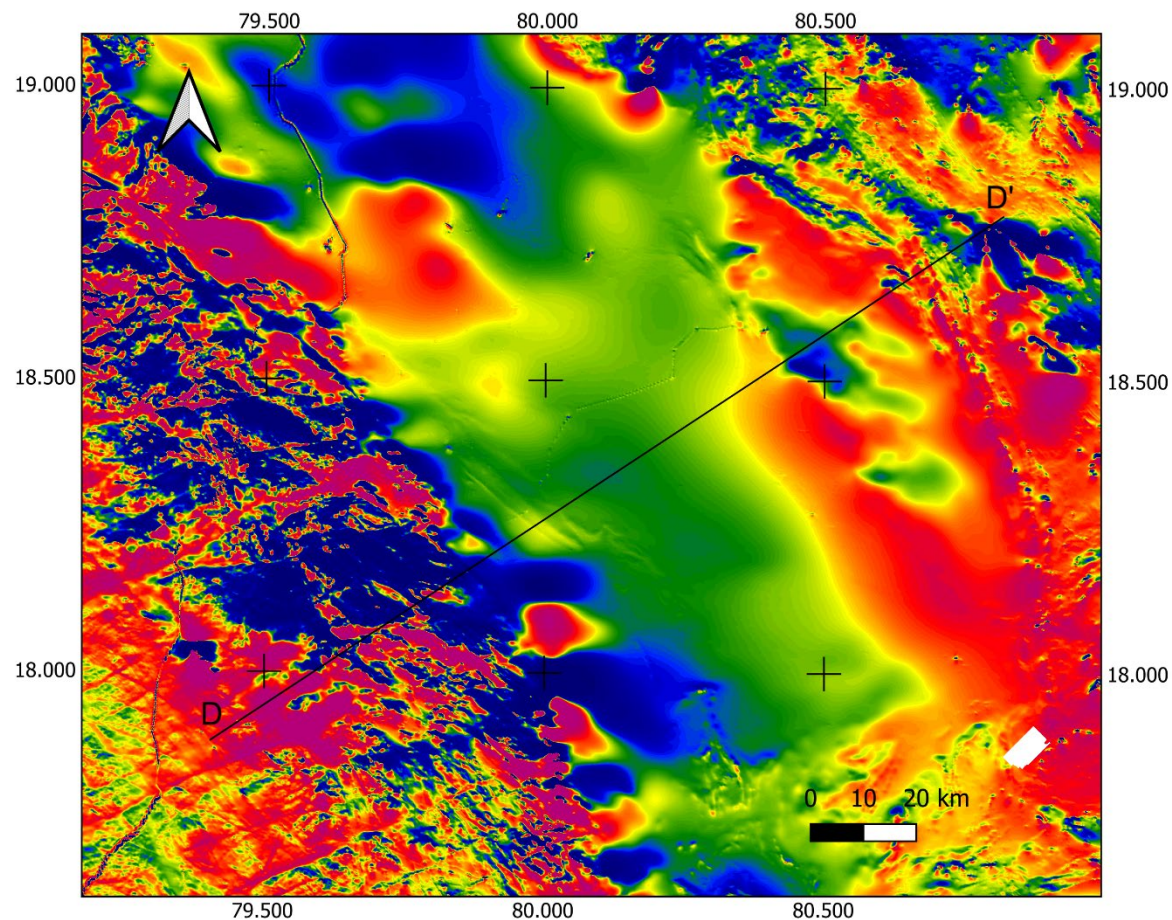


Figure 12.1.7.a: i-section of the Pranhita-Godavari Basin based on aeromagnetic and gravity data, as follows: a) line of the cross section shown on the anomalous magnetic field, b) 2.5D model of the magnetic and gravity data, PG for Peninsular Gneiss, BG for Bhopalpatnam Granulite, PGB for Pranhita-Godvari Basin, with generic Basement, c) model with a possible boundary of the Godavari Supergroup to Gondwana sediments shown d) model with an alternative boundary of the Godavari Supergroup to Gondwana sediments shown.

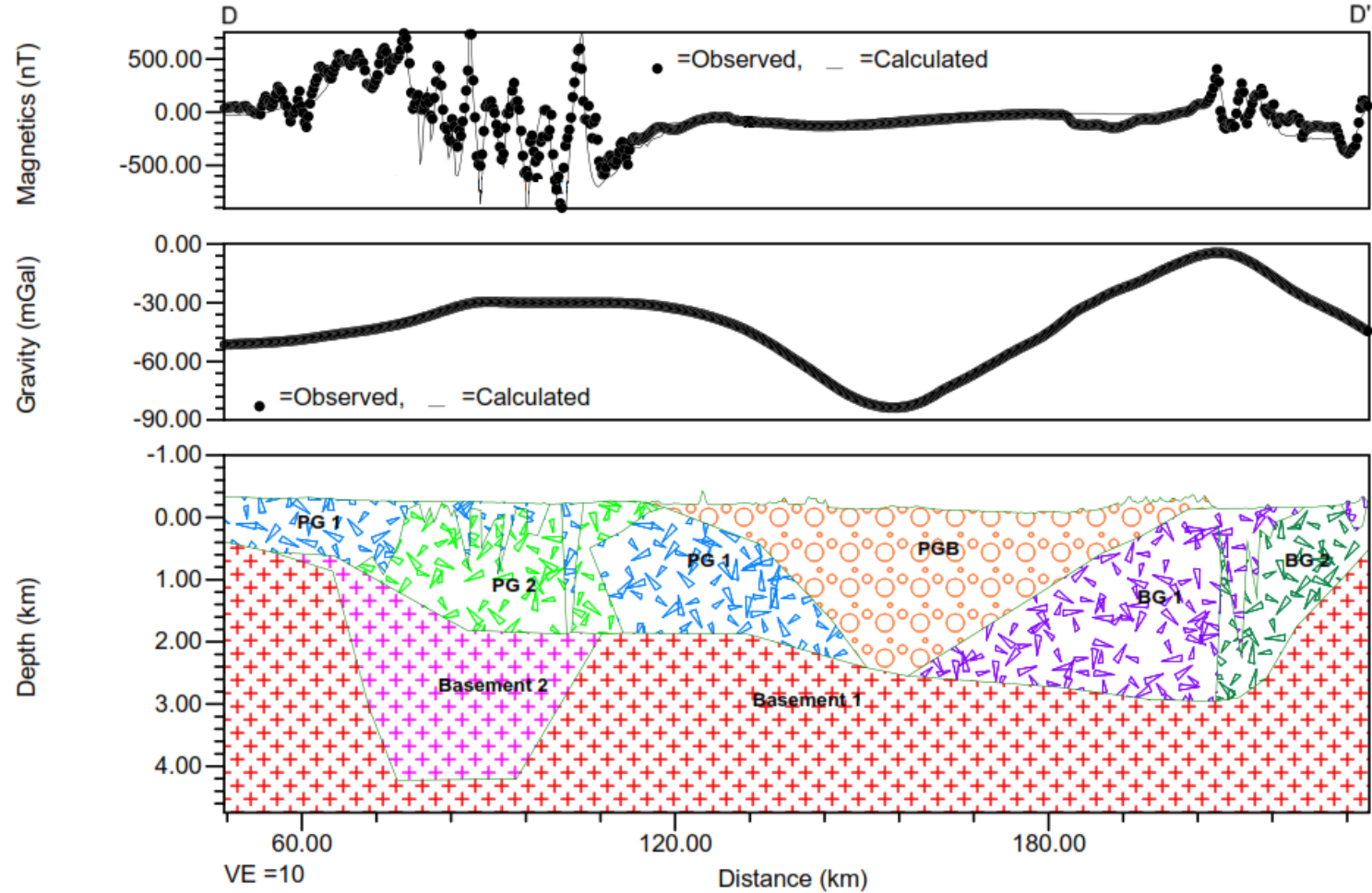


Figure 12.1.7.b: Cross-section of the Pranhita-Godavari Basin based on aeromagnetic and gravity data, as follows: a) line of the cross section shown on the anomalous magnetic field, b) 2.5D model of the magnetic and gravity data, PG for Peninsular Gneiss, BG for Bhopalpatnam Granulite, PGB for Pranhita-Godavari Basin, with generic Basement, c) model with a possible boundary of the Godavari Supergroup to Gondwana sediments shown d) model with an alternative boundary of the Godavari Supergroup to Gondwana sediments shown.

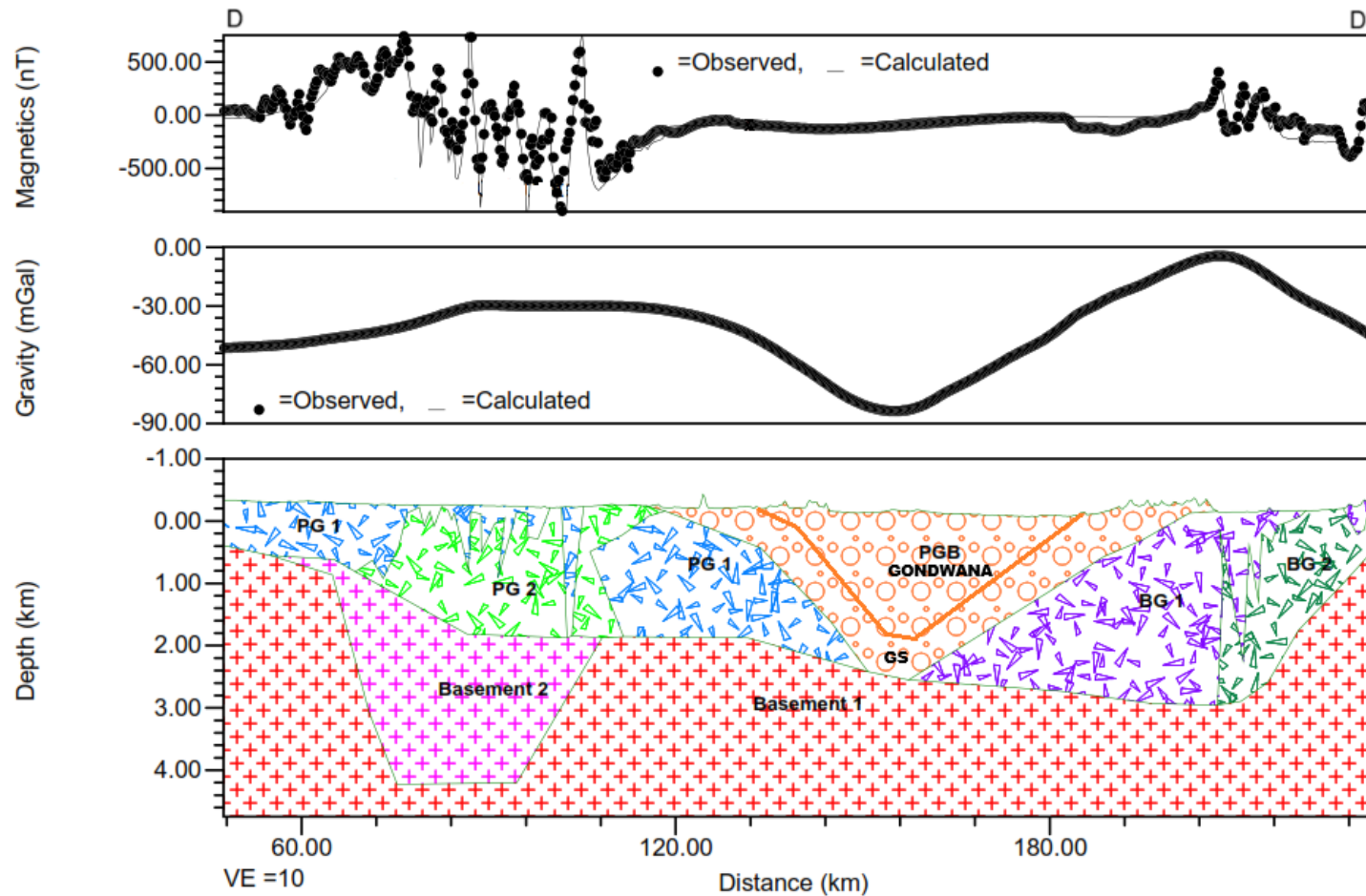


Figure 12.1.7.d: Cross-section of the Pranhita-Godavari Basin based on aeromagnetic and gravity data, as follows: a) line of the cross section shown on the anomalous magnetic field, b) 2.5D model of the magnetic and gravity data, PG for Peninsular Gneiss, BG for Bhopalpatnam Granulite, PGB for Pranhita-Godavari Basin, with generic Basement, c) model with a possible boundary of the Godavari Supergroup to Gondwana sediments shown d) model with an alternative boundary of the Godavari Supergroup to Gondwana sediments shown.

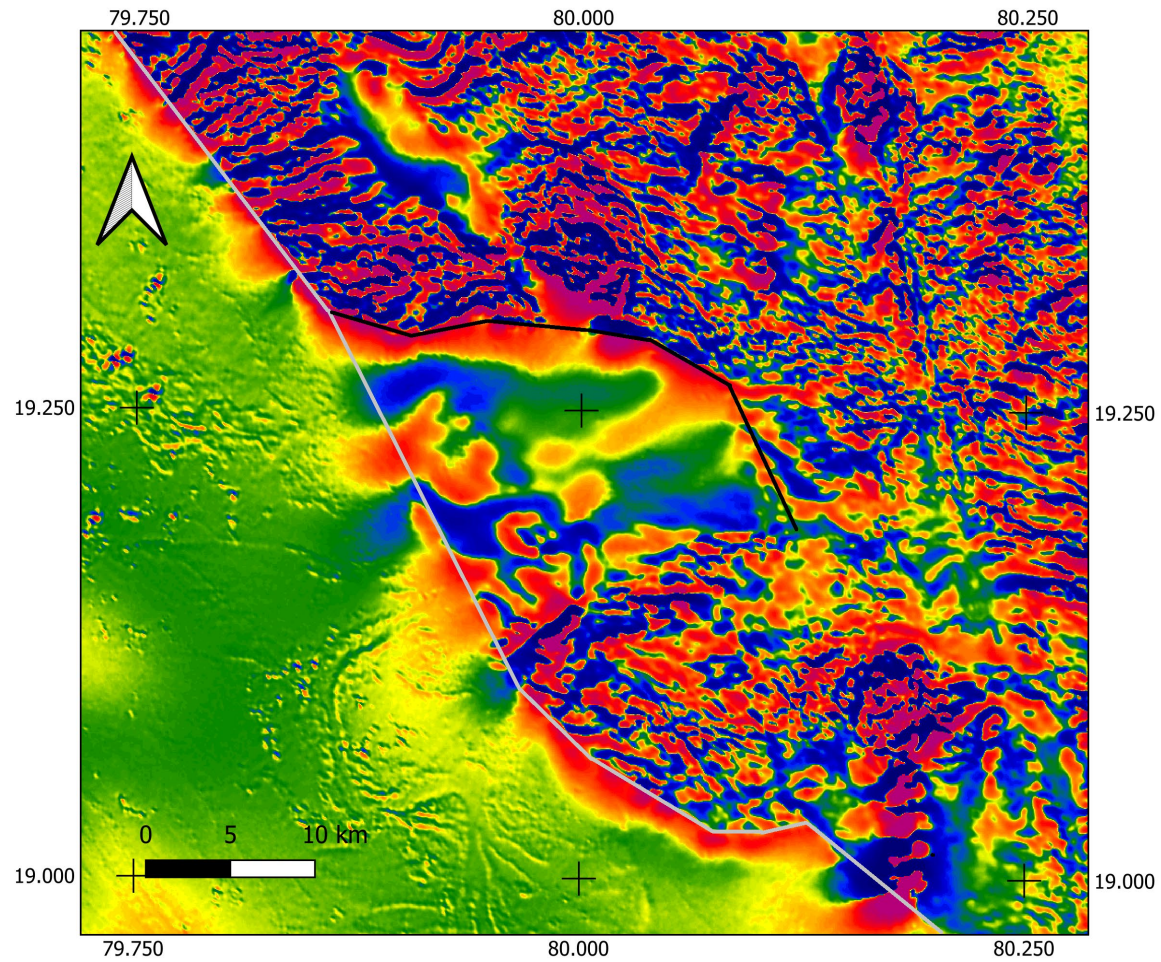


Figure 12.1.8.a: Half-graben of Godavari Supergroup sediments on the side of the main Godavari Graben, as follows: a) first vertical derivative of the anomalous magnetic field, b) geographic location (Microsoft® Bing™ Maps). The main east side bounding fault of the Godavari Grabens shown in grey. The half-graben fault is shown in black.

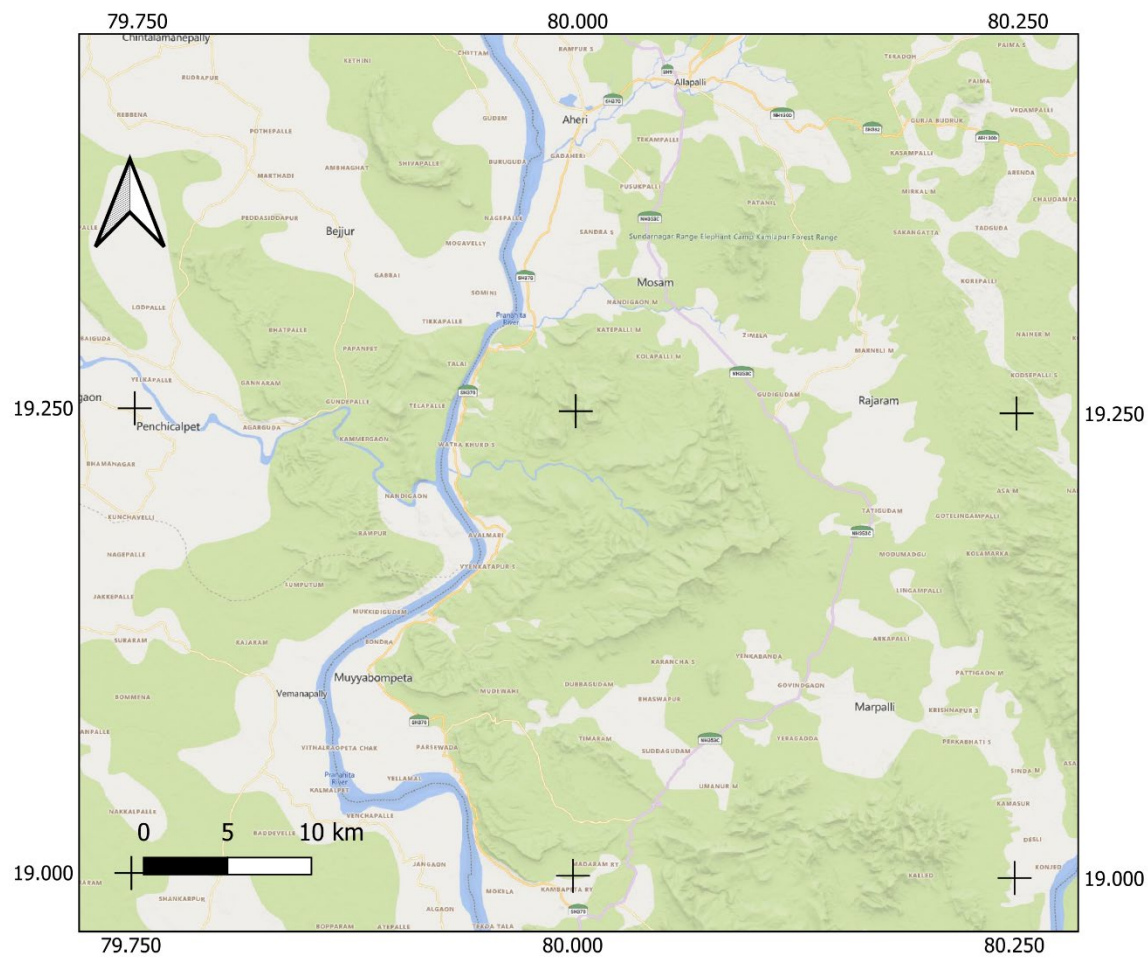


Figure 12.1.8.b: Half-graben of Godavari Supergroup sediments on the side of the main Godavari Graben, as follows: a) first vertical derivative of the anomalous magnetic field, b) geographic location (Microsoft® Bing™ Maps). The main east side bounding fault of the Godavari Grabens shown in grey. The half-graben fault is shown in black.

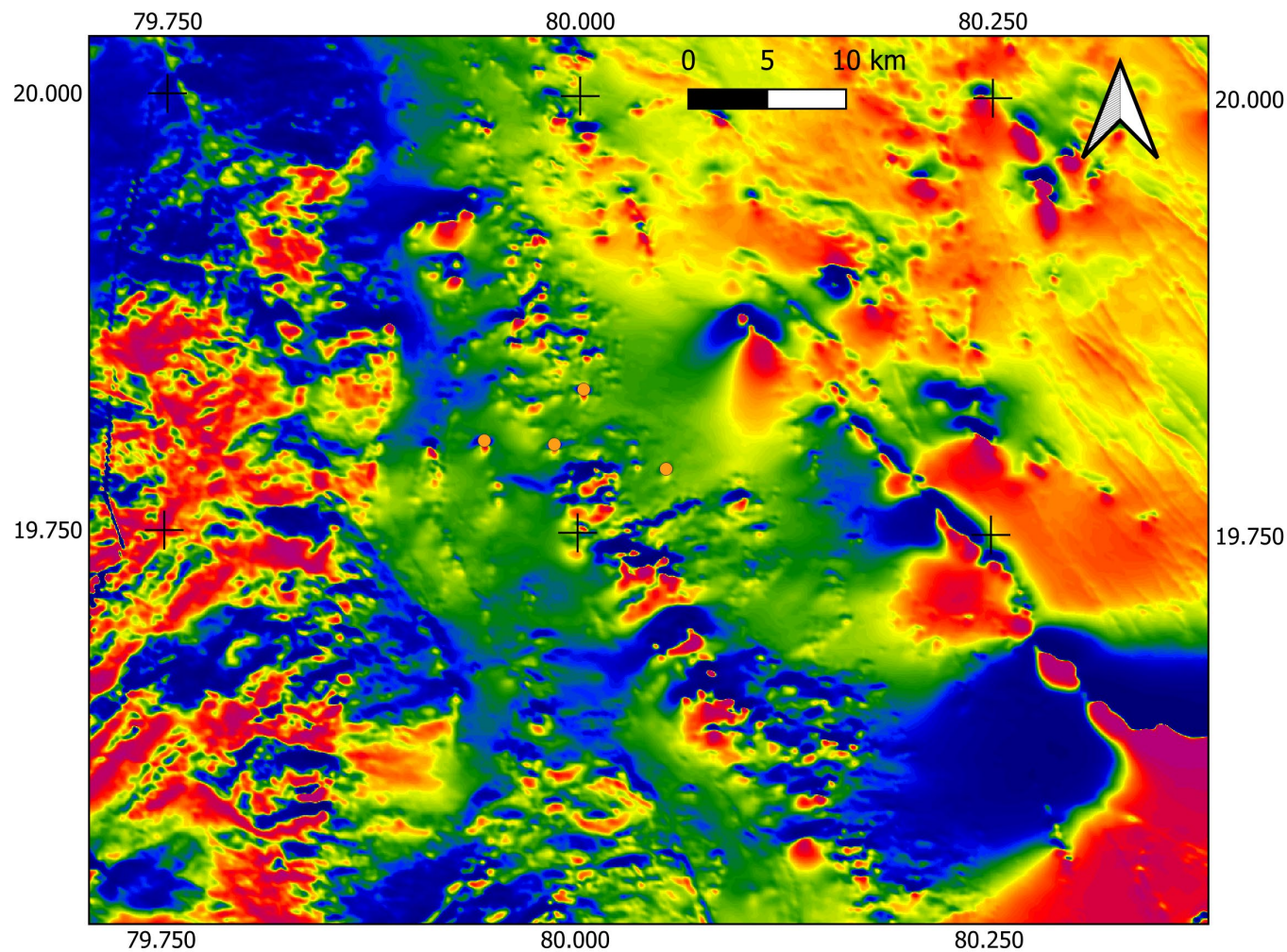


Figure 12.1.9.a: Potential kimberlite cluster marked by the orange circles in the Bastar Craton, as follows: a) anomalous magnetic field, b) geographic location (Microsoft® Bing™ Maps).

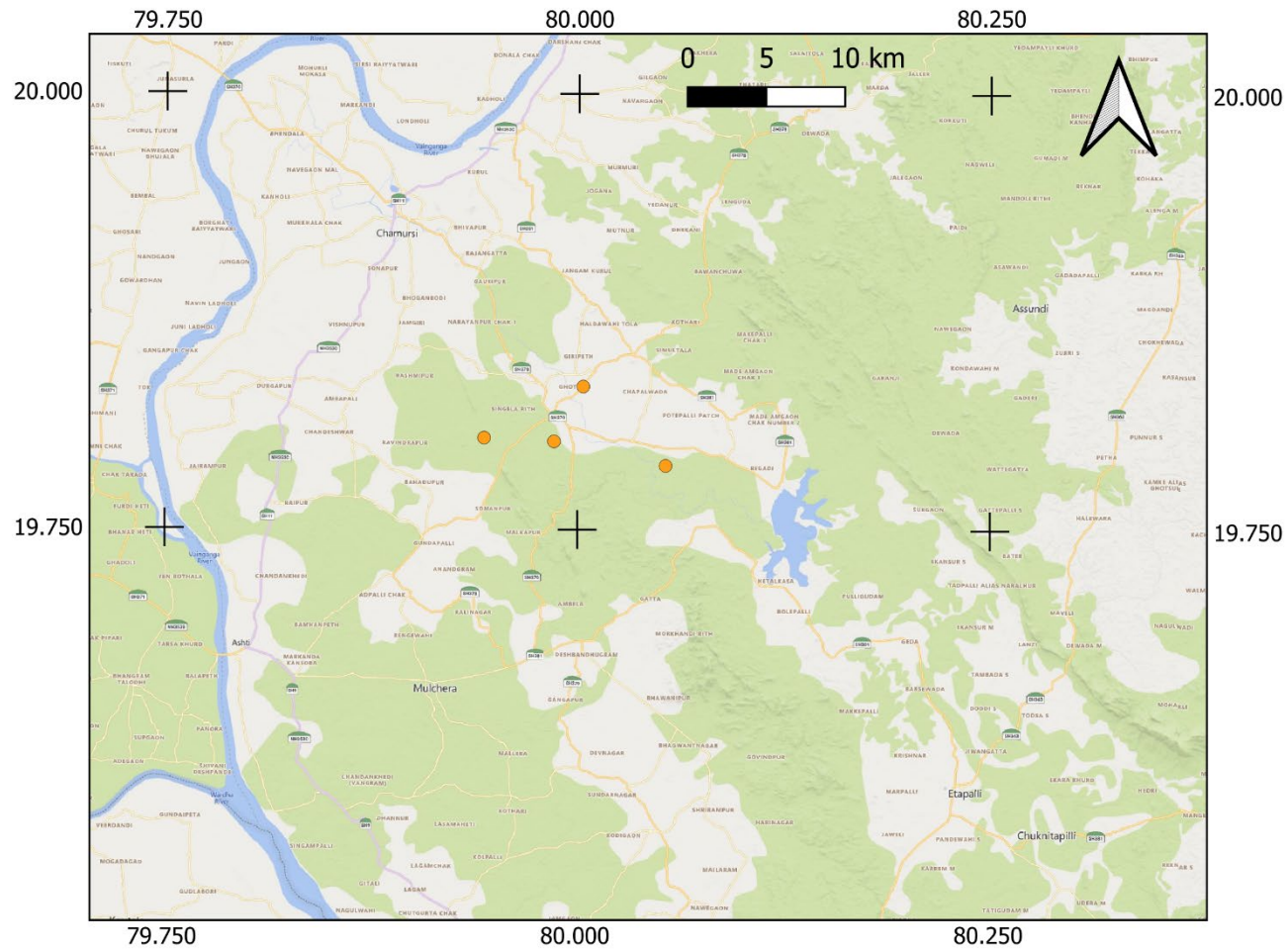


Figure 12.1.9.b: Potential kimberlite cluster marked by the orange circles in the Bastar Craton, as follows: a) anomalous magnetic field, b) geographic location (Microsoft® Bing™ Maps).

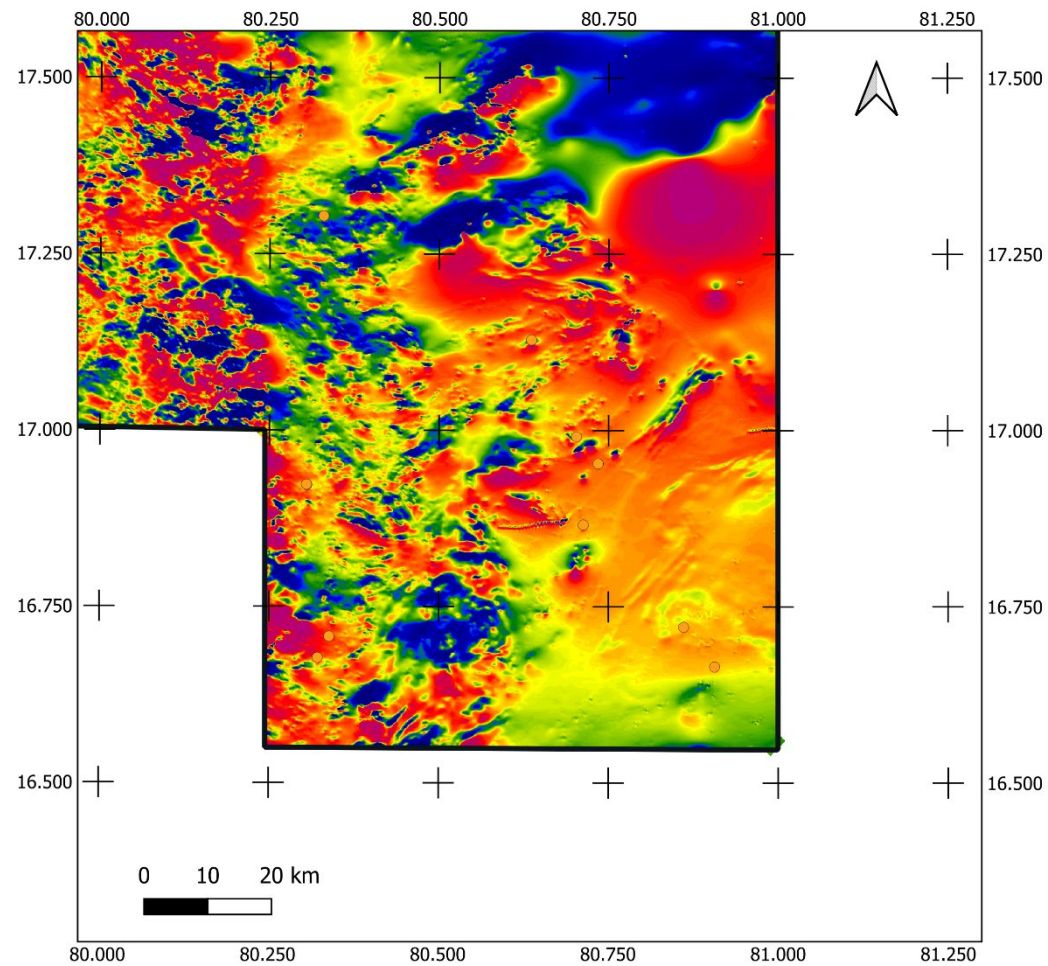


Figure 12.1.10.a: Potential kimberlite cluster marked by the orange circles in the Eastern Ghats Mobile Belt and the Krishna-Godavari Basin, as follows: a) anomalous magnetic field, b) geographic location (Microsoft® Bing™ Maps), with locations of diamond occurrences indicated by the black stars.

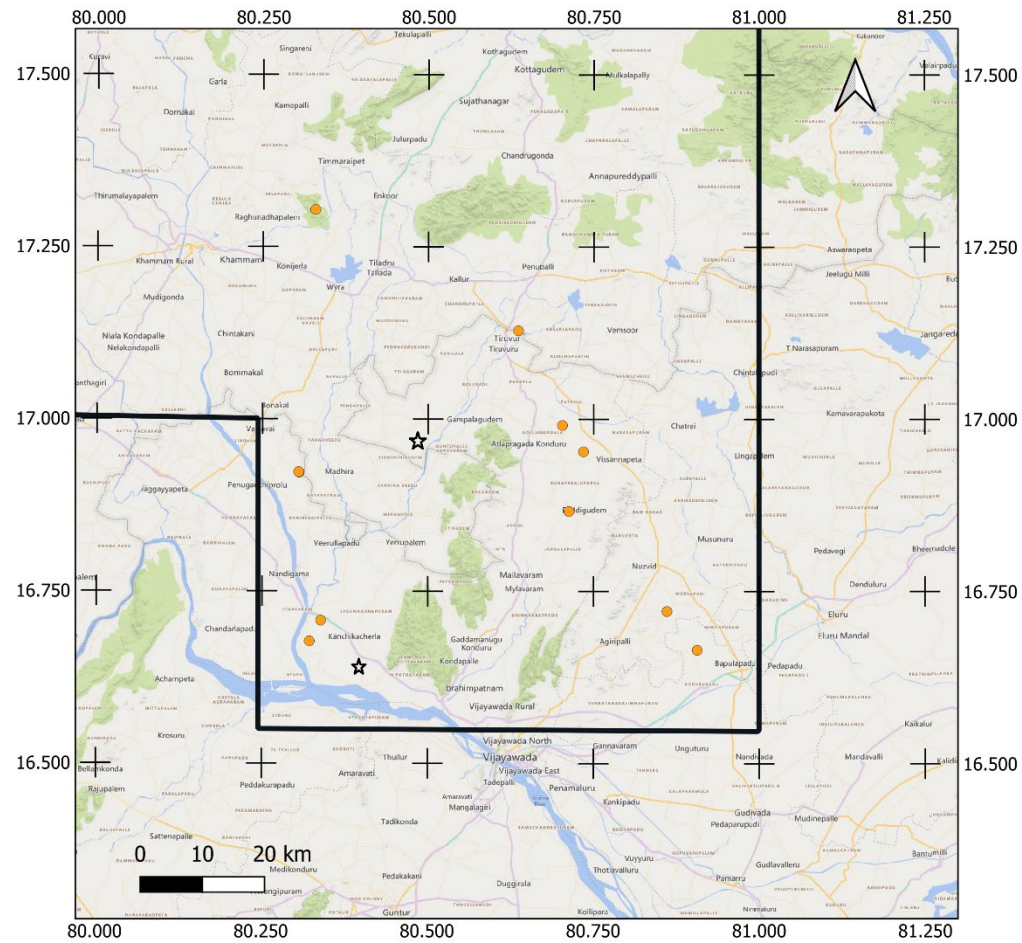


Figure 12.1.10.b: Potential kimberlite cluster marked by the orange circles in the Eastern Ghats Mobile Belt and the Krishna-Godavari Basin, as follows: a) anomalous magnetic field, b) geographic location (Microsoft® Bing™ Maps), with locations of diamond occurrences indicated by the black stars.

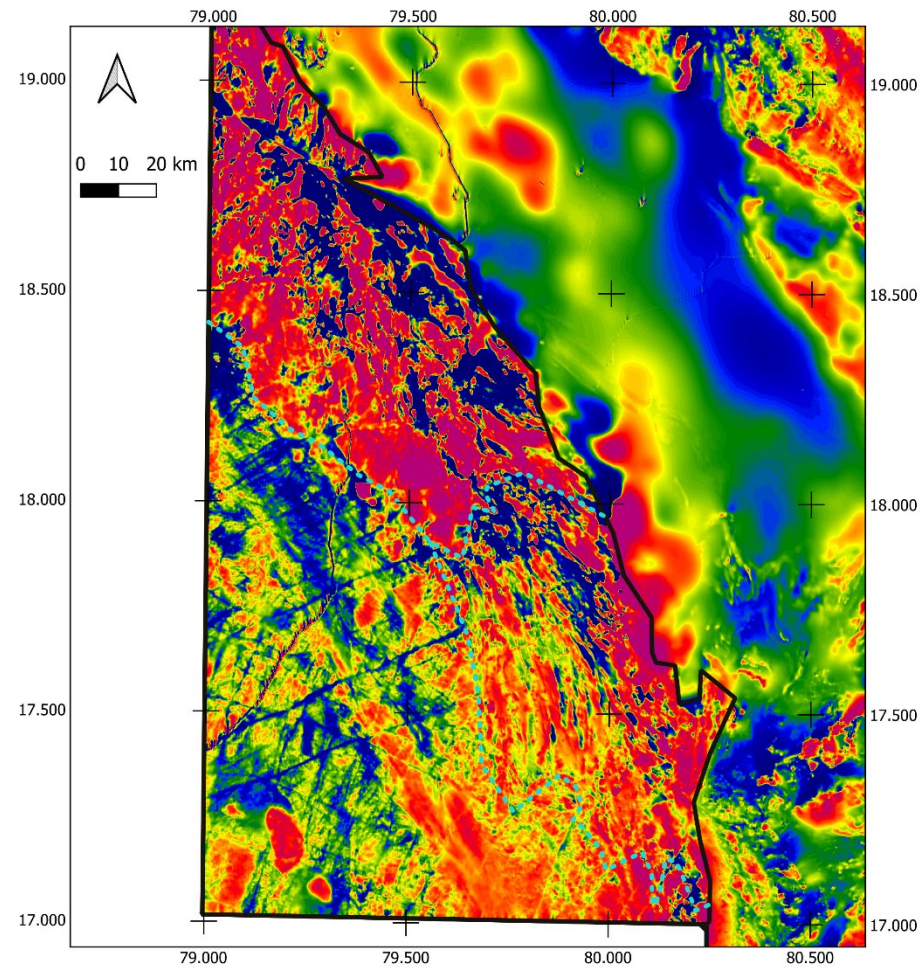


Figure 12.2.1.a: Southwestern part of the Eastern Dharwar Craton in Block-6 as follows: a) magnetic anomaly reduced to the pole, b) gamma-ray ternary image, c) geographic location (Microsoft® Bing™ Maps). Areas of Alkali Feldspar Granite (AFG), Grey Biotite Gneiss (GBG) and Migmatite Gneiss (MG) are demarked by the blue dashed line and labelled on the geographic location map.

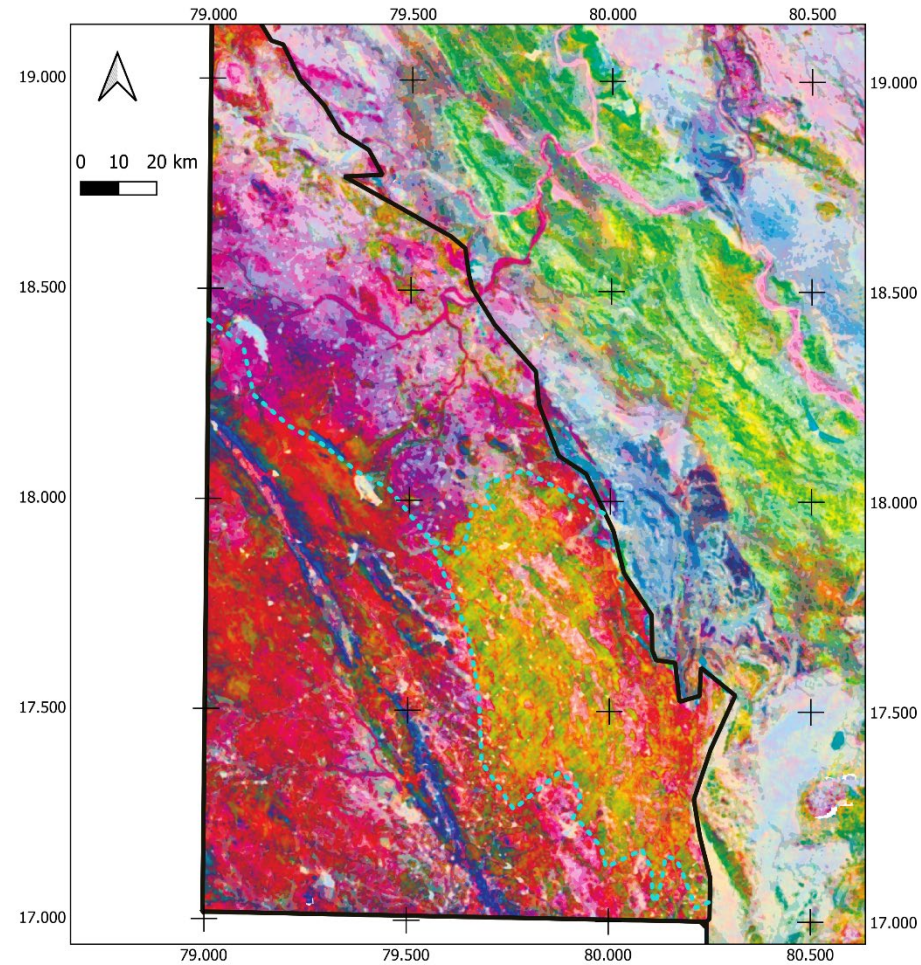


Figure 12.2.1.b: Southwestern part of the Eastern Dharwar Craton in Block-6 as follows: a) magnetic anomaly reduced to the pole, b) gamma-ray ternary image, c) geographic location (Microsoft® Bing™ Maps). Areas of Alkali Feldspar Granite (AFG), Grey Biotite Gneiss (GBG) and Migmatite Gneiss (MG) are demarked by the blue dashed line and labelled on the geographic location map.

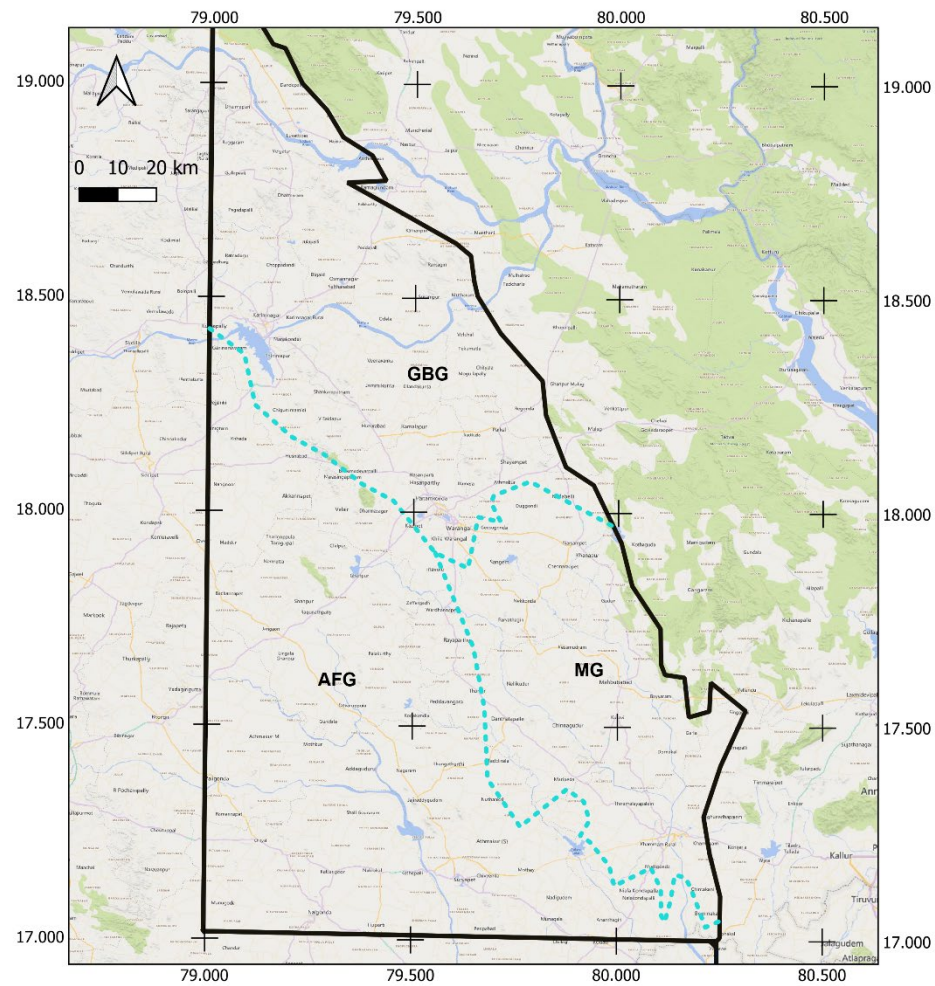


Figure 12.2.1.c: Southwestern part of the Eastern Dharwar Craton in Block-6 as follows: a) magnetic anomaly reduced to the pole, b) gamma-ray ternary image, c) geographic location (Microsoft® Bing™ Maps). Areas of Alkali Feldspar Granite (AFG), Grey Biotite Gneiss (GBG) and Migmatite Gneiss (MG) are demarked by the blue dashed line and labelled on the geographic location map.

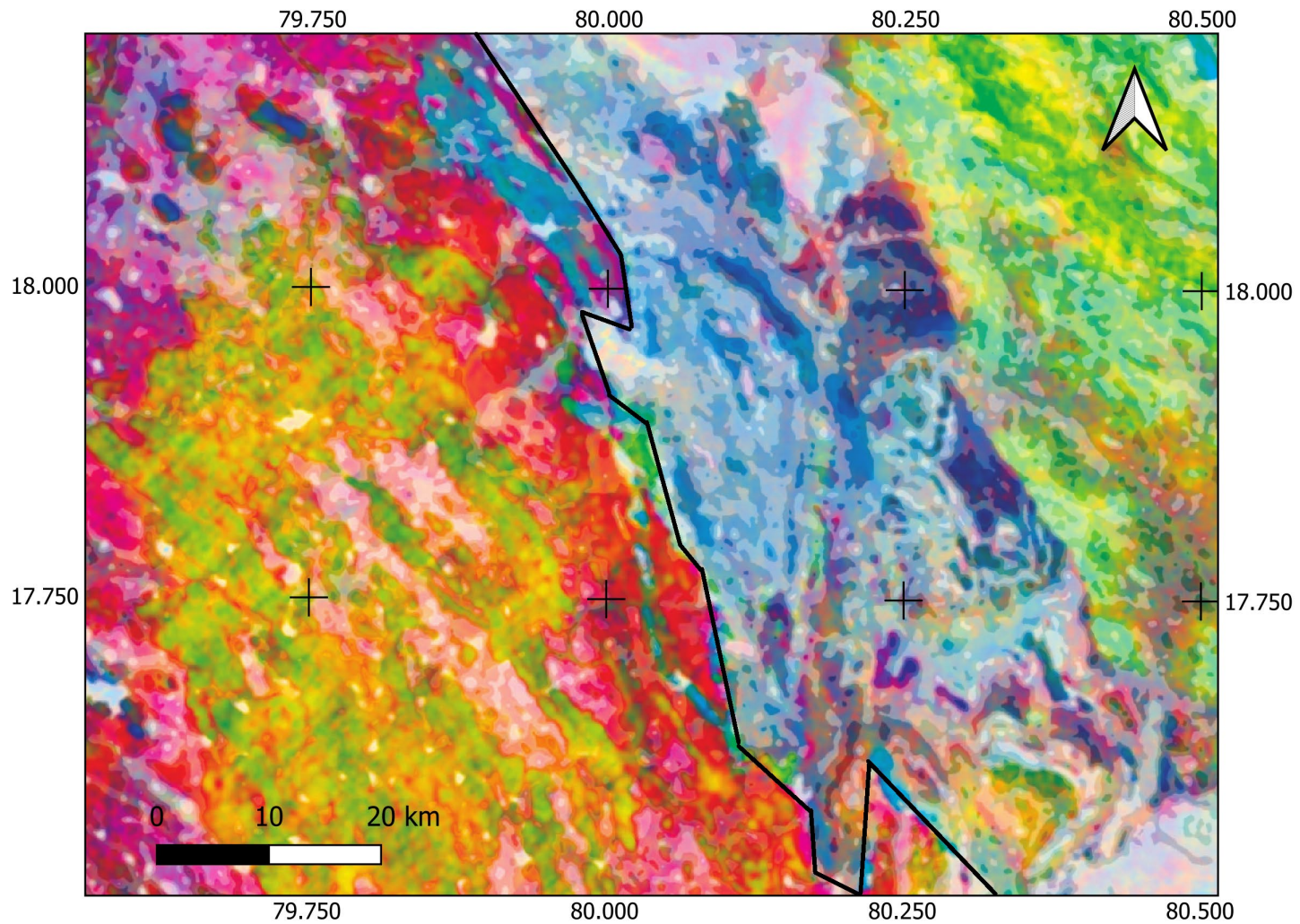


Figure 12.2.2.a: Boundary of the Eastern Dharwar Craton and the southern area of the Proterozoic age Pranhita-Godavari Basin Sediments of the Western Belt as follows: a) gamma-ray ternary image with the boundary marked, b) magnetic anomaly reduced to the pole, c) geographic location (Microsoft® Bing™ Maps).

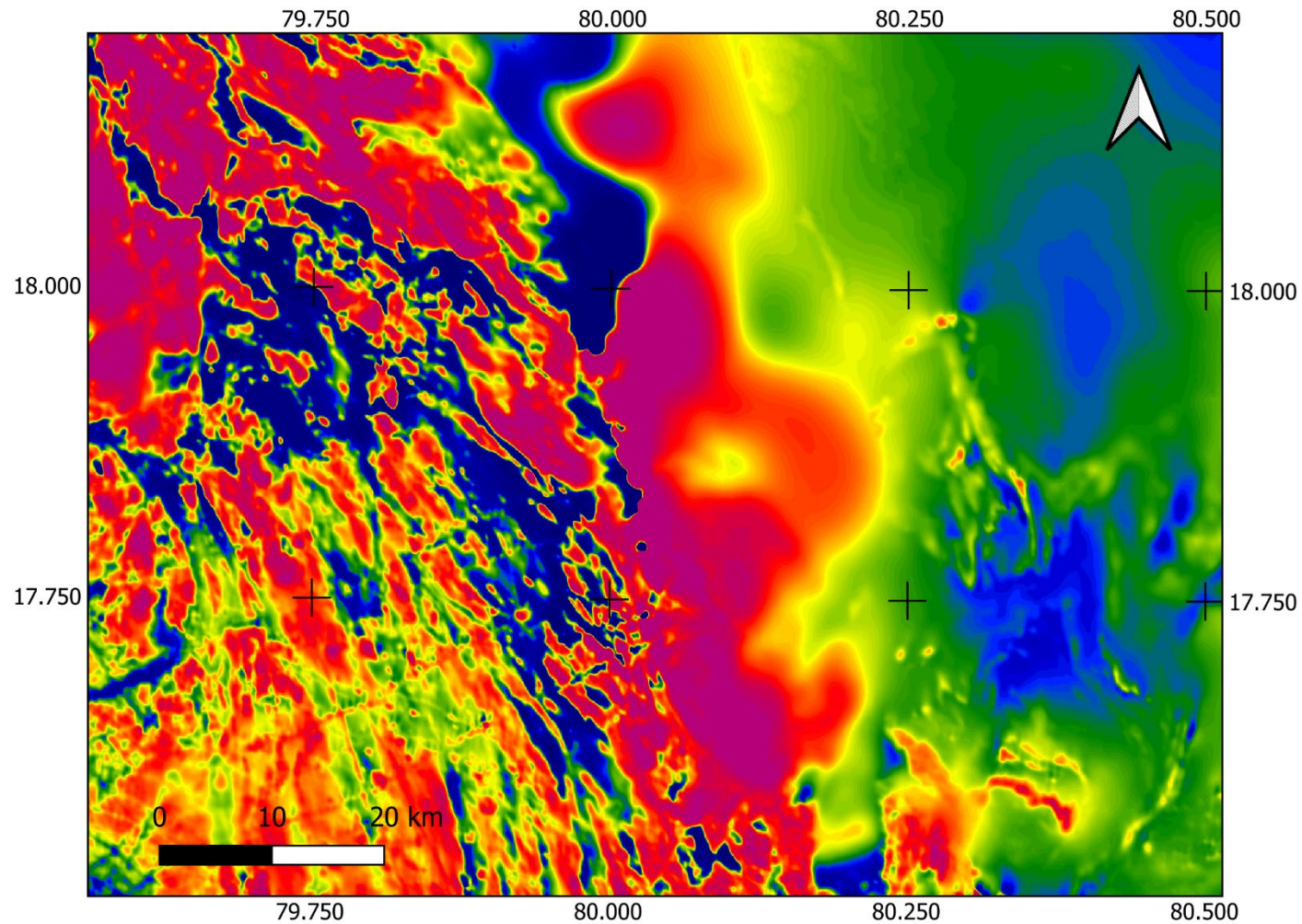


Figure 12.2.2.b: Boundary of the Eastern Dharwar Craton and the southern area of the Proterozoic age Pranhita-Godavari Basin Sediments of the Western Belt as follows: a) gamma-ray ternary image with the boundary marked, b) magnetic anomaly reduced to the pole, c) geographic location (Microsoft® Bing™ Maps).

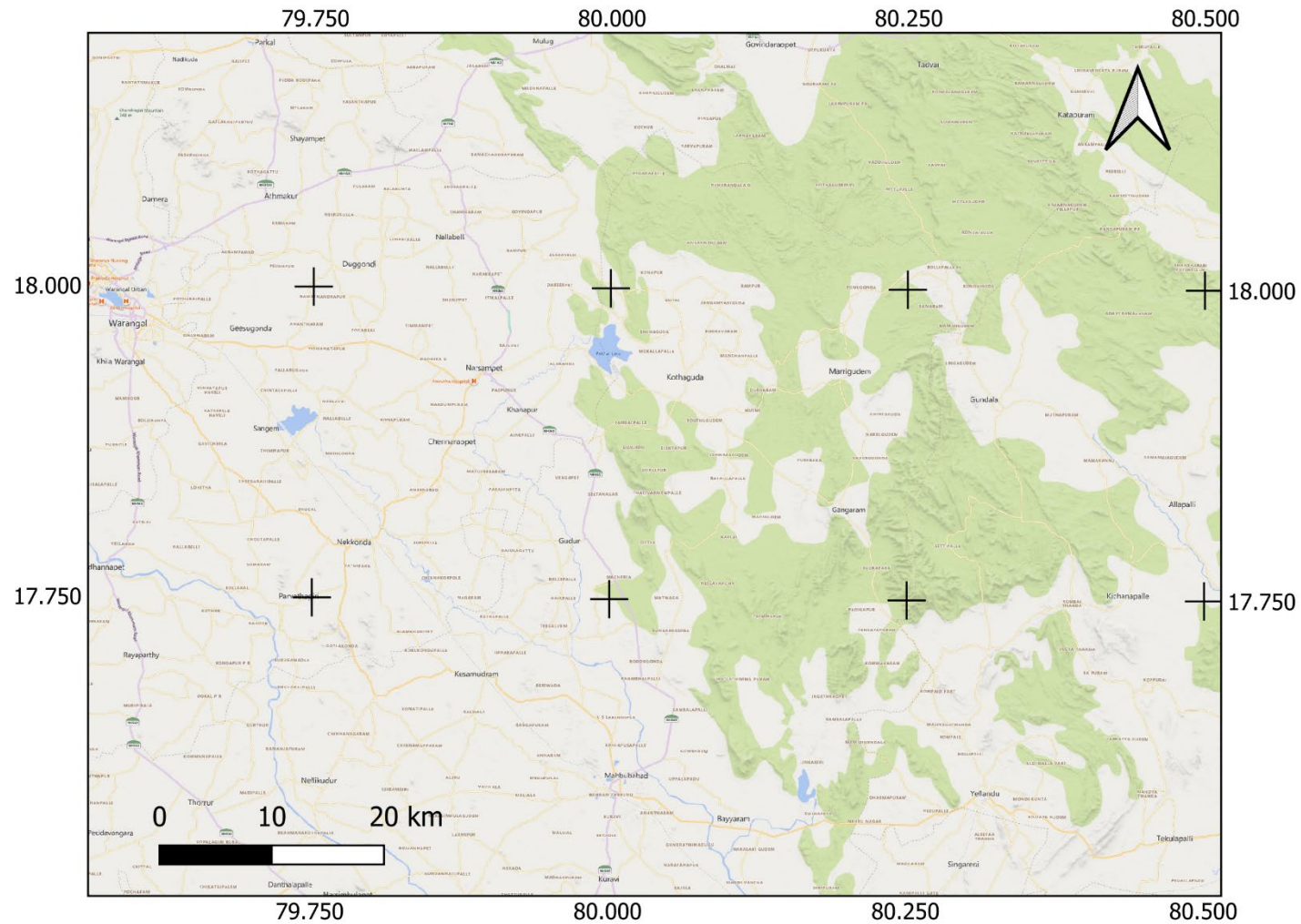


Figure 12.2.2.c: Boundary of the Eastern Dharwar Craton and the southern area of the Proterozoic age Pranhita-Godavari Basin Sediments of the Western Belt as follows: a) gamma-ray ternary image with the boundary marked, b) magnetic anomaly reduced to the pole, c) geographic location (Microsoft® Bing™ Maps).

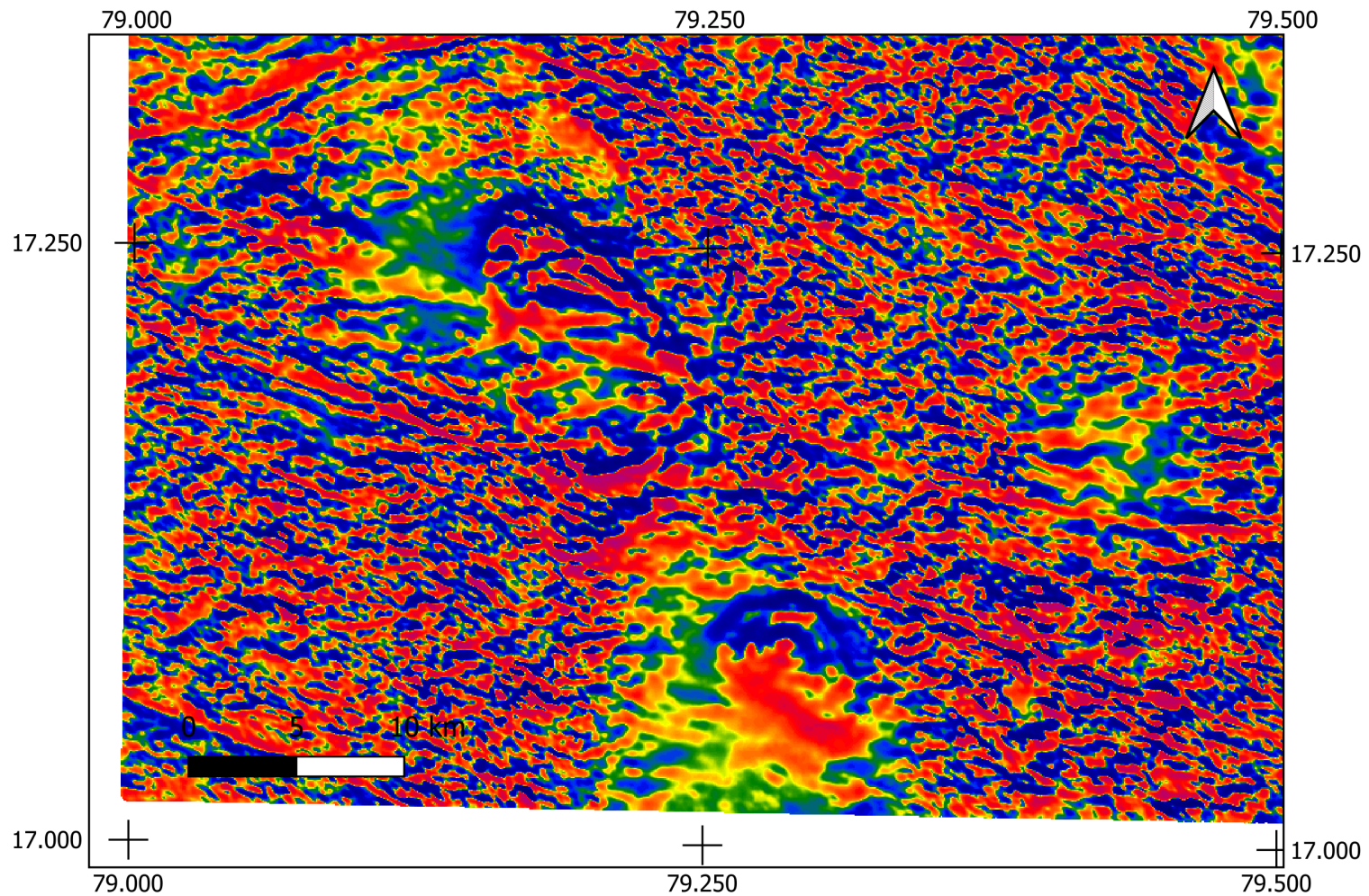


Figure 12.2.3.a: Igneous intrusions in the southwest extremity of the Eastern Dharwar Craton in Block-6 as follows: a) first vertical derivative of the magnetic anomaly, b) magnetic anomaly reduced to the pole with the three intrusions indicated by arrows and lines of cross-section shown, c) ratio of equivalent uranium to potassium, d) geographic location (Microsoft® Bing™ Maps).

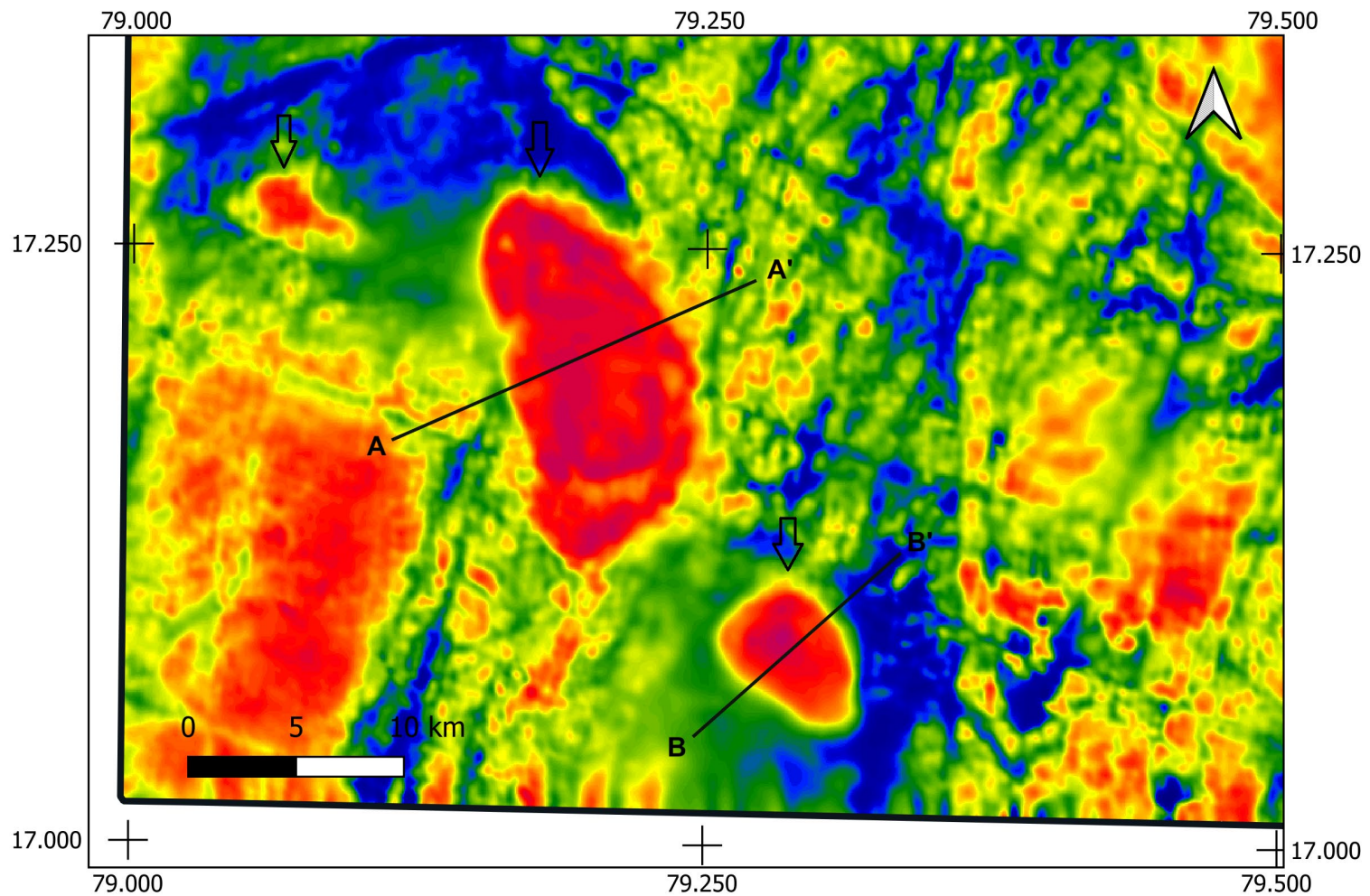


Figure 12.2.3.b: Igneous intrusions in the southwest extremity of the Eastern Dharwar Craton in Block-6 as follows: a) first vertical derivative of the magnetic anomaly, b) magnetic anomaly reduced to the pole with the three intrusions indicated by arrows and lines of cross-section shown, c) ratio of equivalent uranium to potassium, d) geographic location (Microsoft® Bing™ Maps).

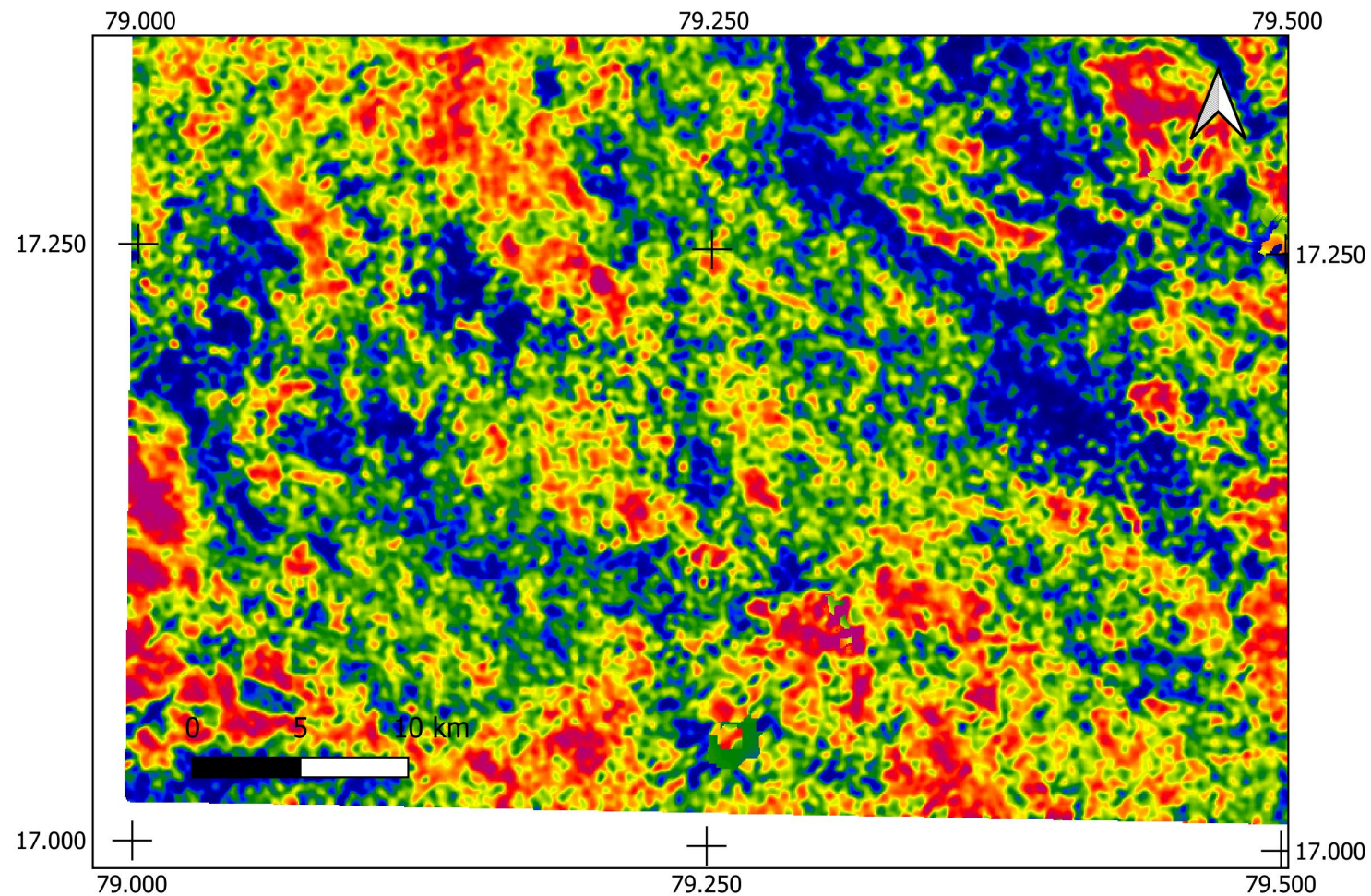


Figure 12.2.3.c: Igneous intrusions in the southwest extremity of the Eastern Dharwar Craton in Block-6 as follows: a) first vertical derivative of the magnetic anomaly, b) magnetic anomaly reduced to the pole with the three intrusions indicated by arrows and lines of cross-section shown, c) ratio of equivalent uranium to potassium, d) geographic location (Microsoft® Bing™ Maps).

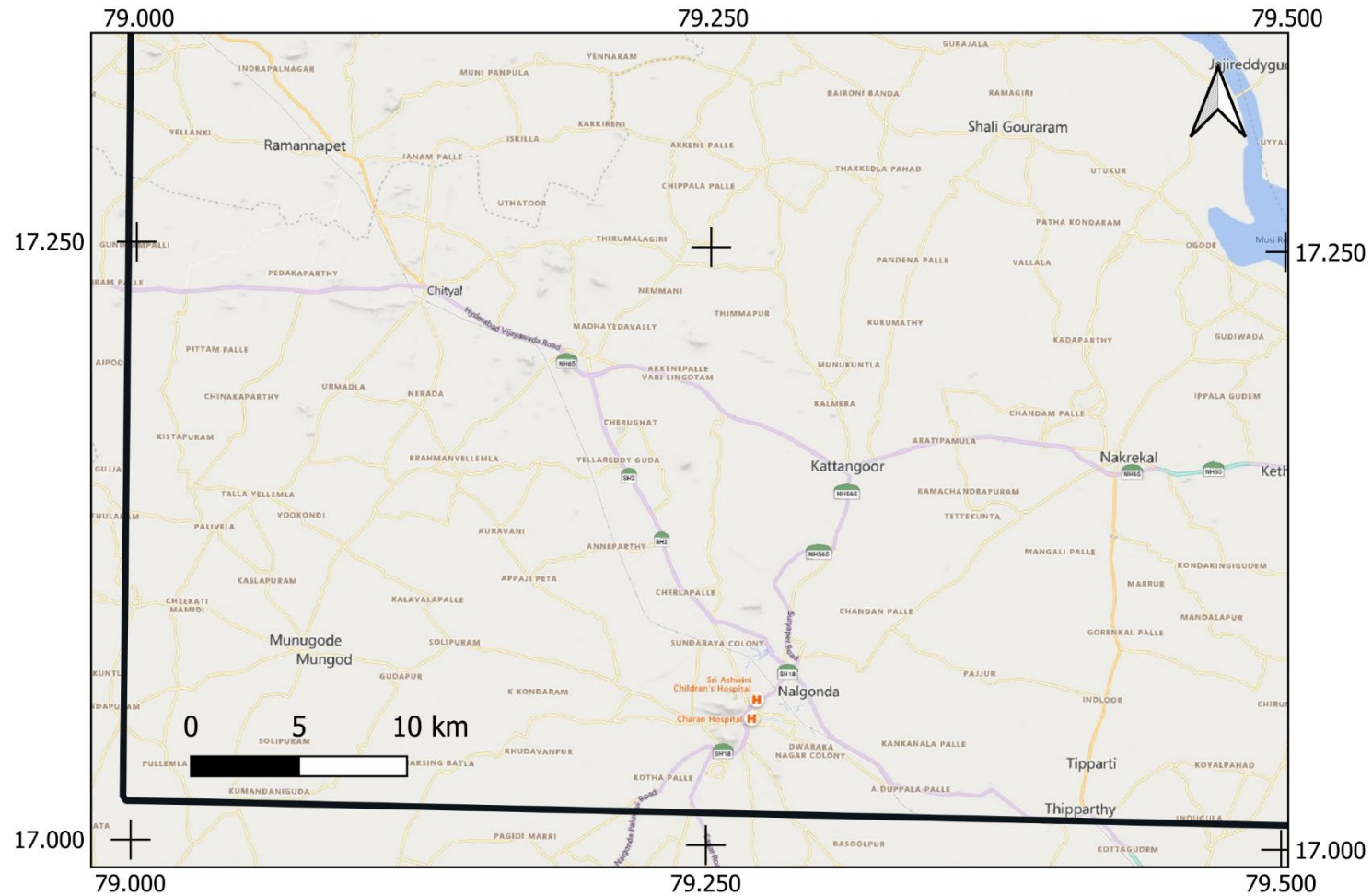


Figure 12.2.3.d: Igneous intrusions in the southwest extremity of the Eastern Dharwar Craton in Block-6 as follows: a) first vertical derivative of the magnetic anomaly, b) magnetic anomaly reduced to the pole with the three intrusions indicated by arrows and lines of cross-section shown, c) ratio of equivalent uranium to potassium, d) geographic location (Microsoft® Bing™ Maps).

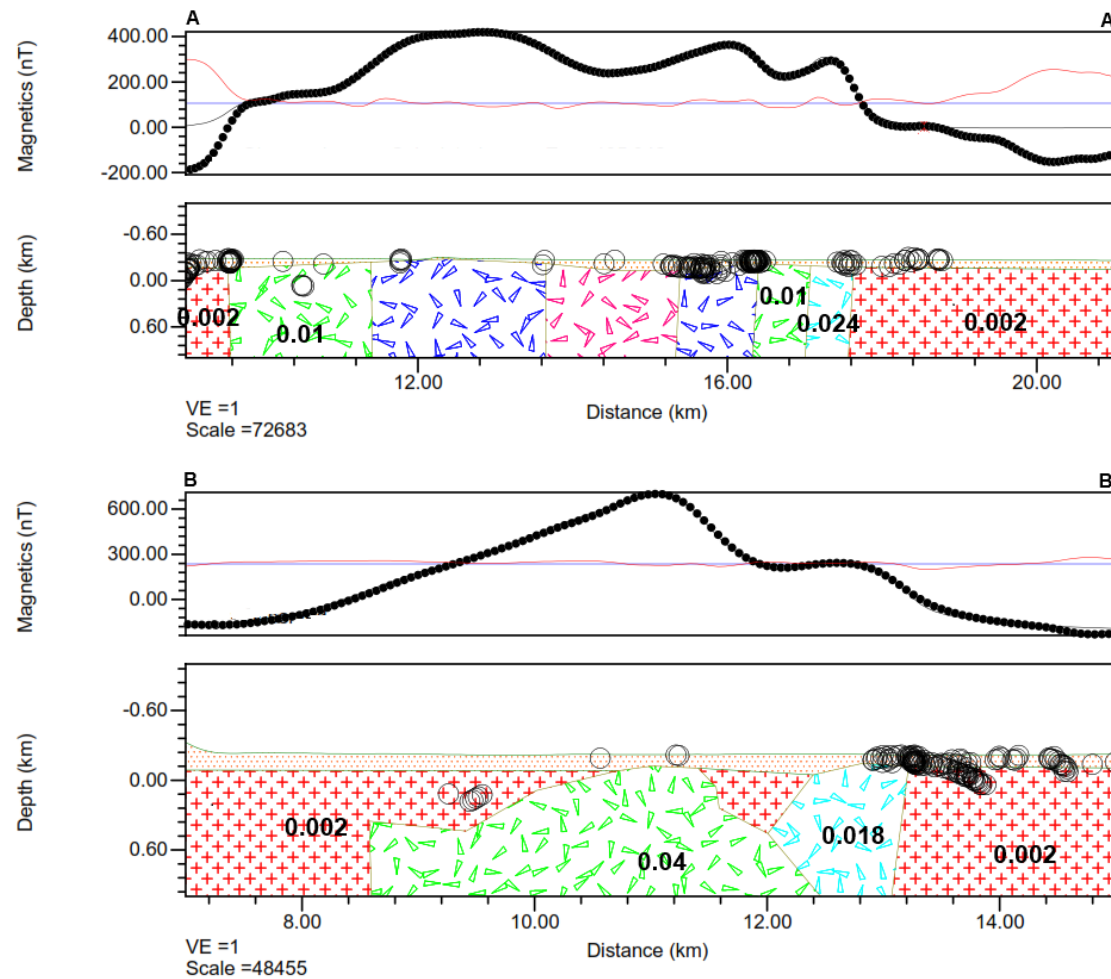


Figure 12.2.4: Cross sections of igneous intrusions modelled from the magnetic anomaly reduced to the pole. Lines of cross-sections are shown in Figure 12.2.3b. Vertical exaggeration is 1:1. Magnetic data lines are as follows: black spots are the observed profile, thin black line is the modelled profile, thin red line is the model misfit. Magnetic susceptibility values are shown over each unit (S.I. units). The surface layer is considered non-magnetic.

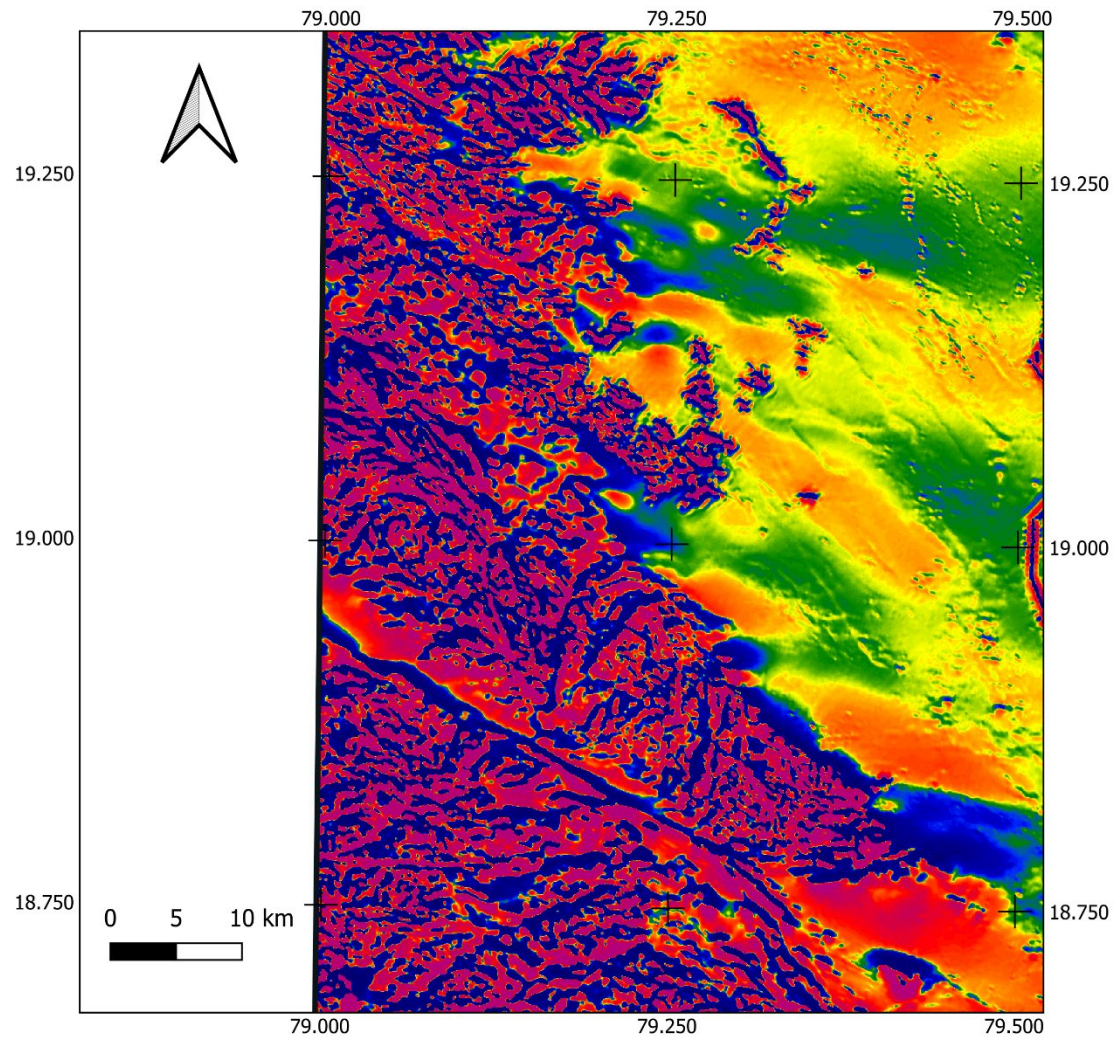


Figure 12.2.5.a: Ring structured igneous intrusion adjacent to the Godavari River in the Eastern Dharwar Craton in Block-6 as follows a) first vertical derivative of the magnetic anomaly, b) radiometric ternary image with the intrusion indicated, c) geographic location (Microsoft® Bing™ Maps).

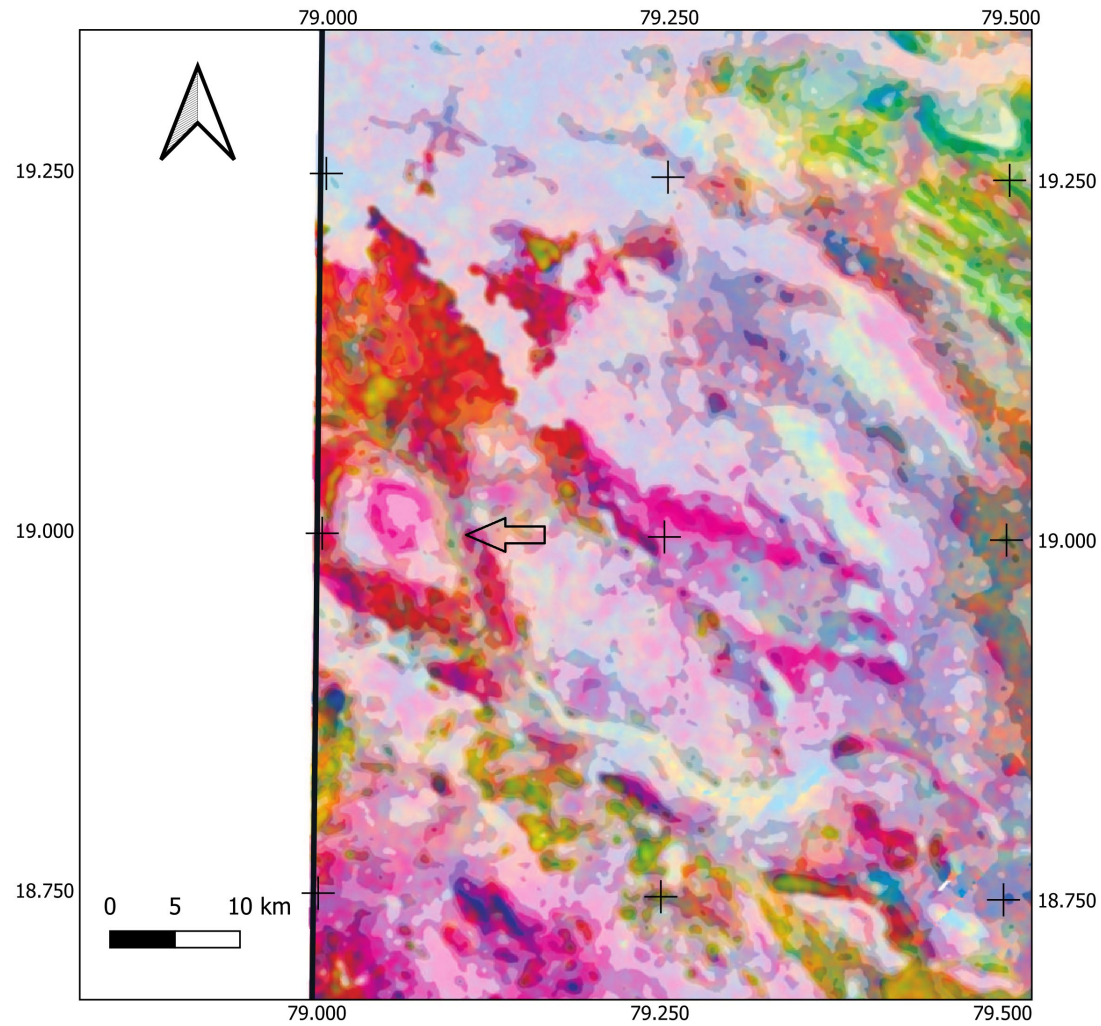


Figure 12.2.5.b: Ring structured igneous intrusion adjacent to the Godavari River in the Eastern Dharwar Craton in Block-6 as follows a) first vertical derivative of the magnetic anomaly, b) radiometric ternary image with the intrusion indicated, c) geographic location (Microsoft® Bing™ Maps).

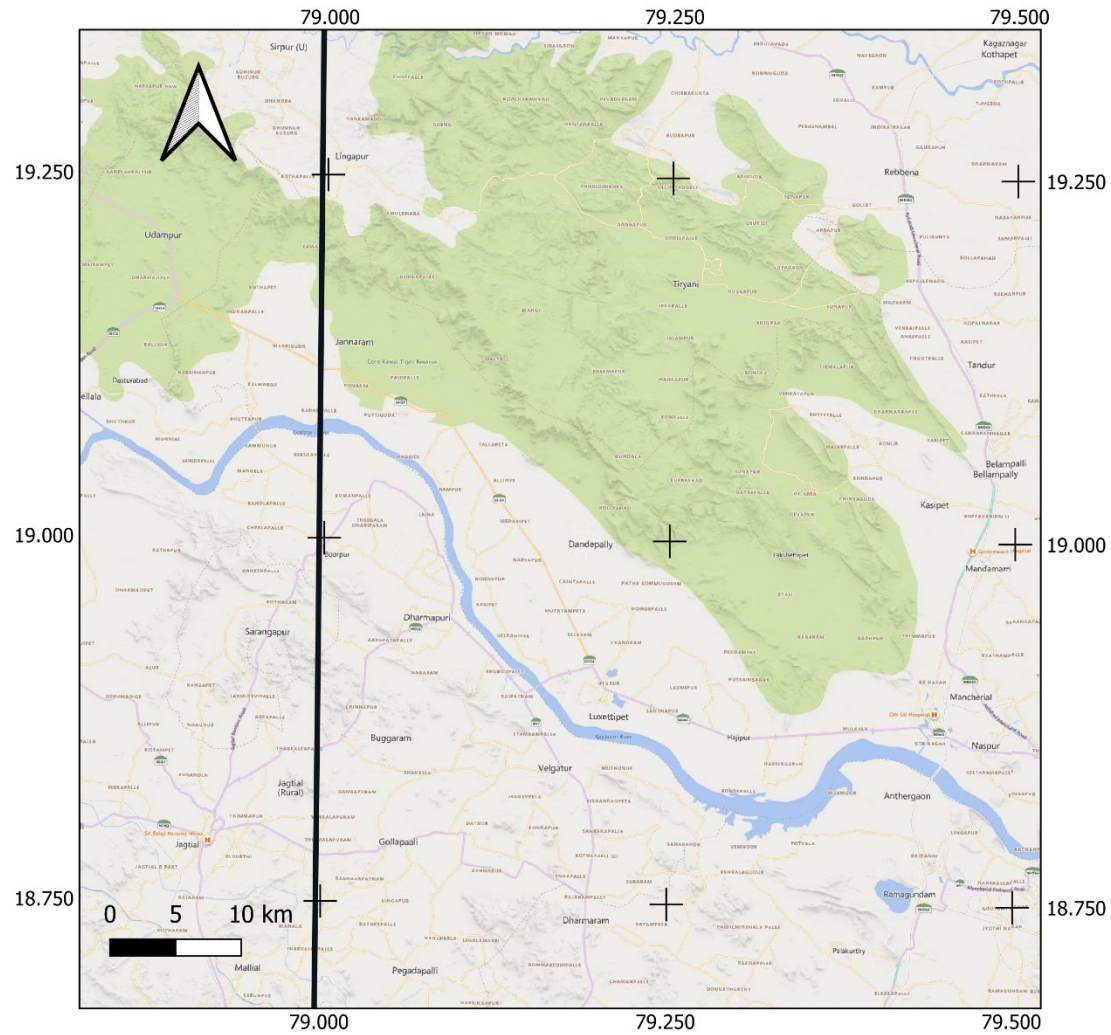


Figure 12.2.5.c: Ring structured igneous intrusion adjacent to the Godavari River in the Eastern Dharwar Craton in Block-6 as follows a) first vertical derivative of the magnetic anomaly, b) radiometric ternary image with the intrusion indicated, c) geographic location (Microsoft® Bing™ Maps).

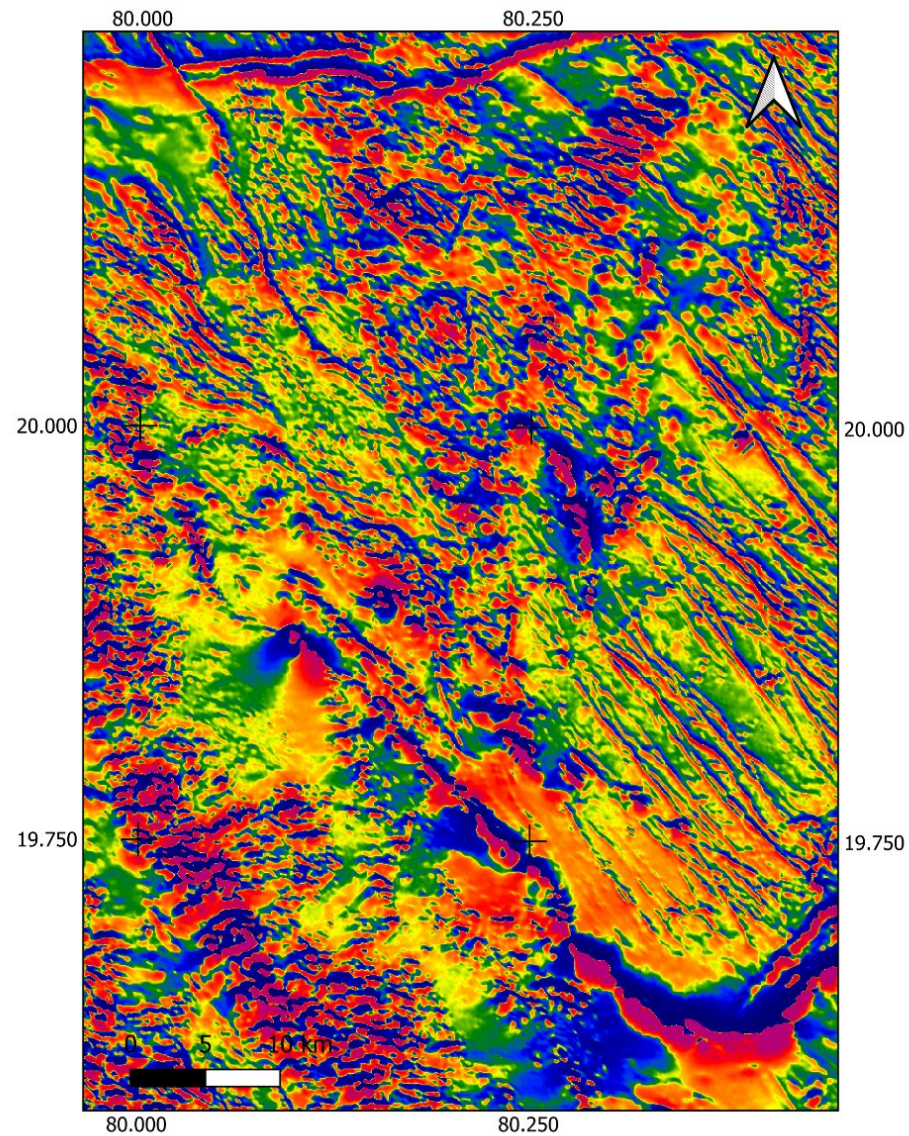


Figure 12.3.1.a: Dongargarh granite and surrounding area in the Bastar Craton, northeastern Block-6 as follows: a) first vertical derivative of the magnetic anomaly, b) potassium concentration, c) ratio of equivalent thorium to potassium with the altered fractures indicated, d) geographic location.

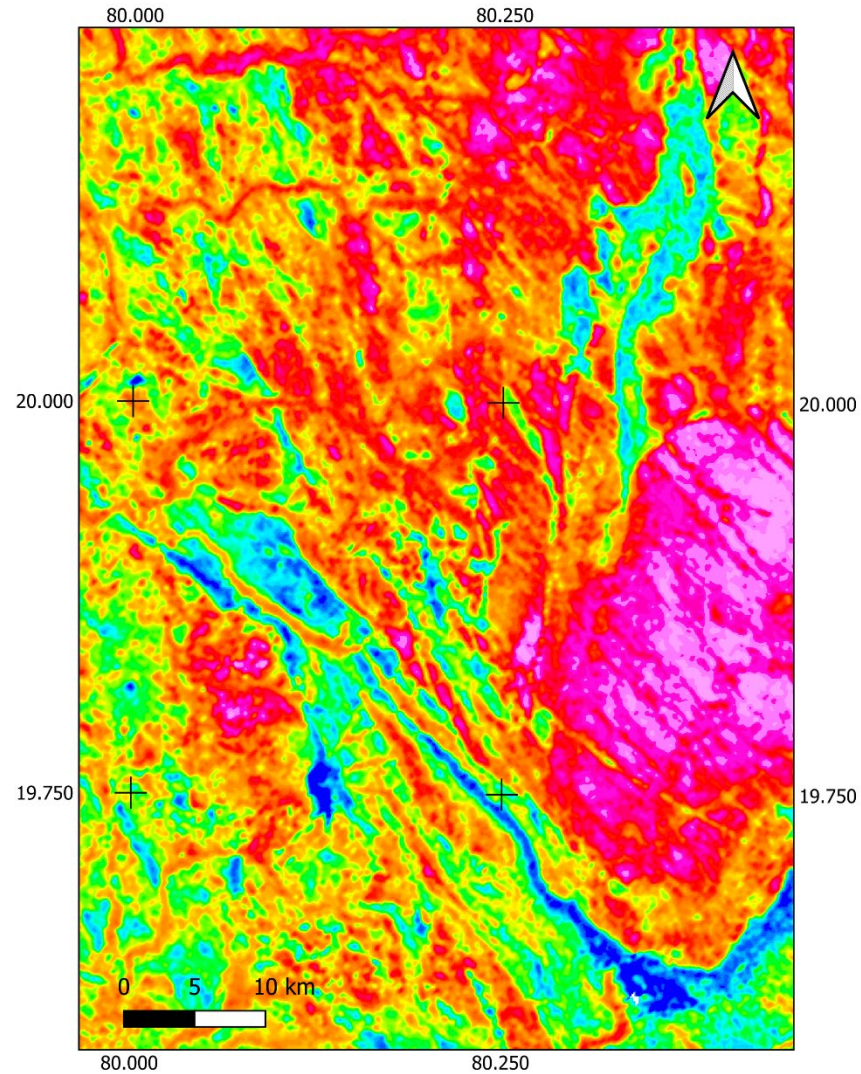


Figure 12.3.1.b: Dongargarh granite and surrounding area in the Bastar Craton, northeastern Block-6 as follows: a) first vertical derivative of the magnetic anomaly, b) potassium concentration, c) ratio of equivalent thorium to potassium with the altered fractures indicated, d) geographic location (Microsoft® Bing™ Maps).

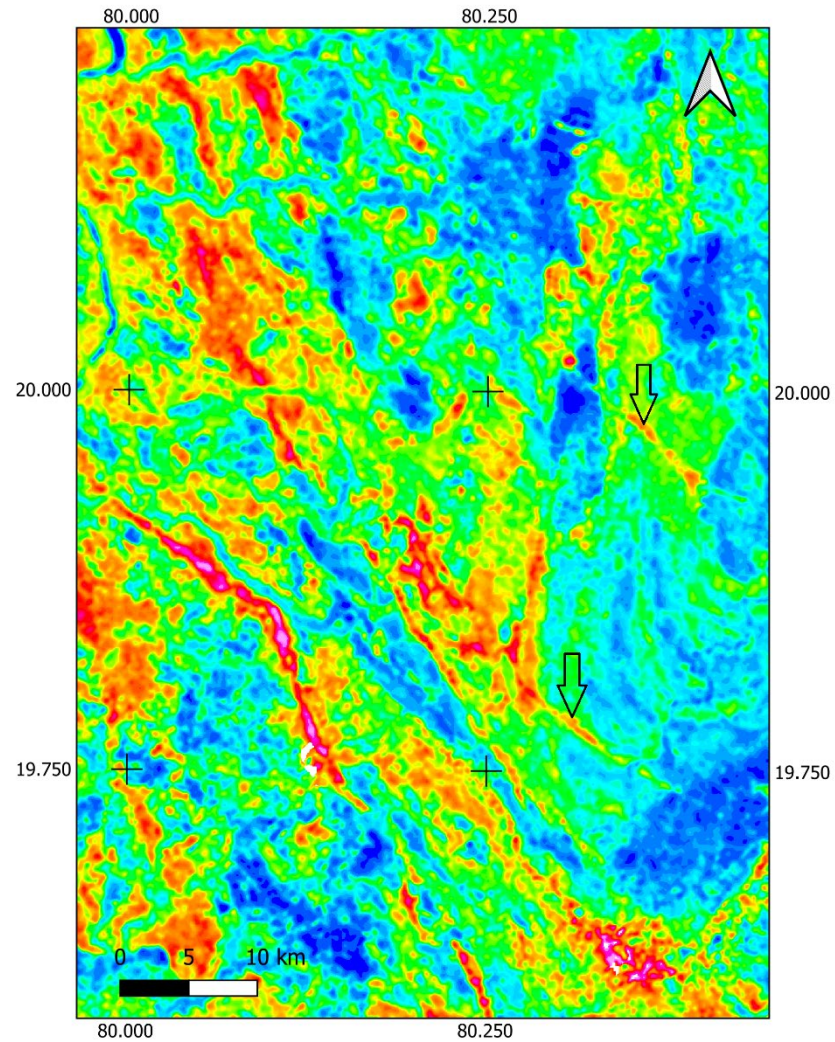


Figure 12.3.1.c: Dongargarh granite and surrounding area in the Bastar Craton, northeastern Block-6 as follows: a) first vertical derivative of the magnetic anomaly, b) potassium concentration, c) ratio of equivalent thorium to potassium with the altered fractures indicated, d) geographic location (Microsoft® Bing™ Maps).

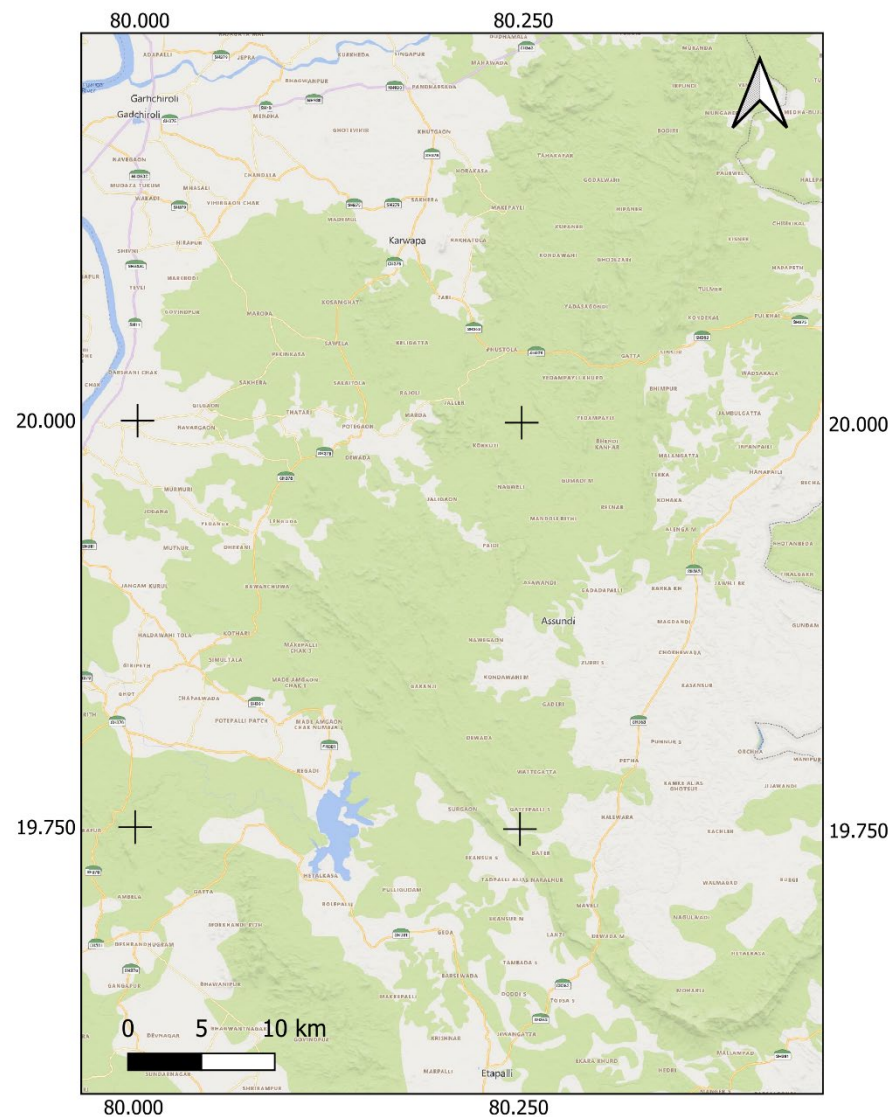


Figure 12.3.1.d: Dongargarh granite and surrounding area in the Bastar Craton, northeastern Block-6 as follows: a) first vertical derivative of the magnetic anomaly, b) potassium concentration, c) ratio of equivalent thorium to potassium with the altered fractures indicated, d) geographic location (Microsoft® Bing™ Maps).

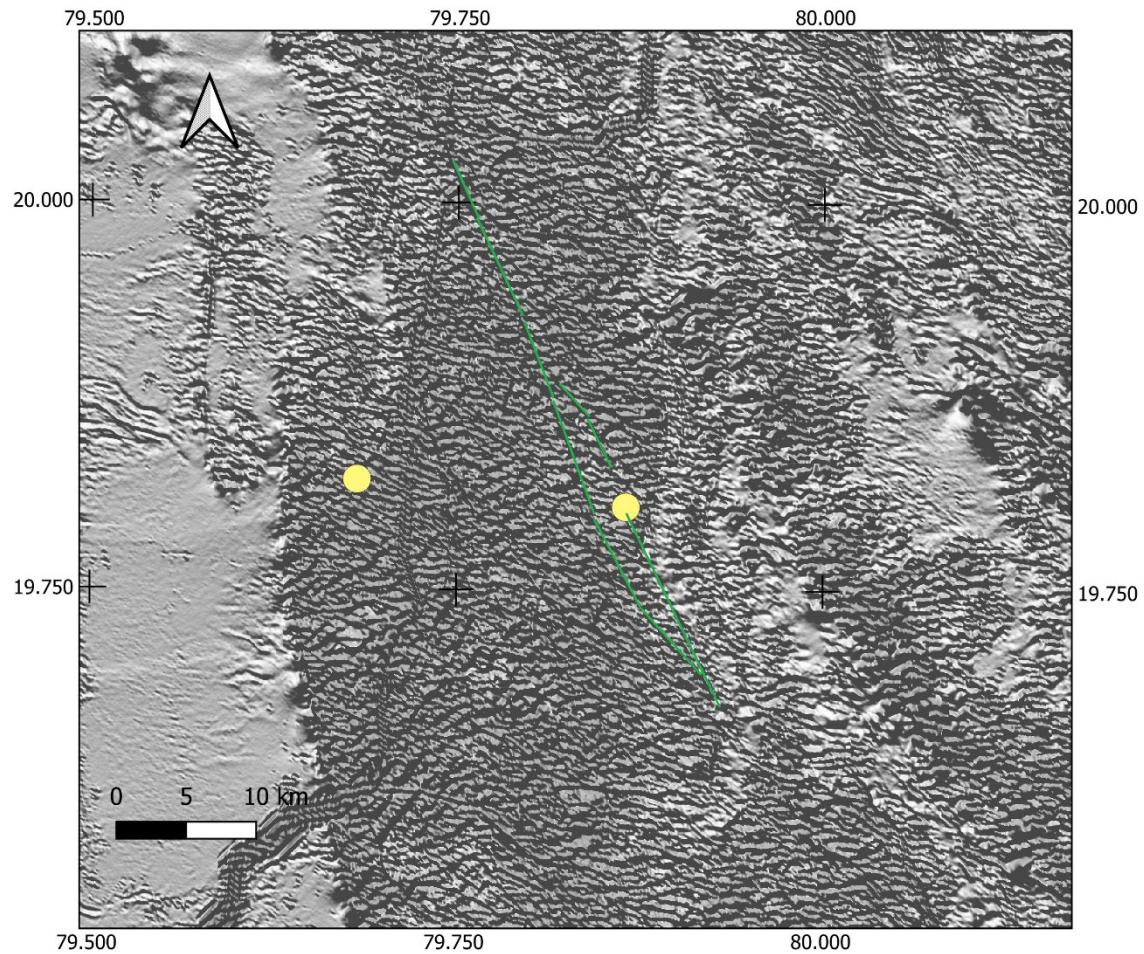


Figure 12.3.2.a: The location of the Thanewasna and Dubarpeth copper deposit locations, marked by the yellow circle, and the trends of fractures shown in the magnetic data that may exert structural control on the Dubarpeth deposit (the green line), as follows: a) first vertical derivative of the magnetic field shown with a monochrome shadow from the northeast, b) geographic location (Microsoft® Bing™ Maps).

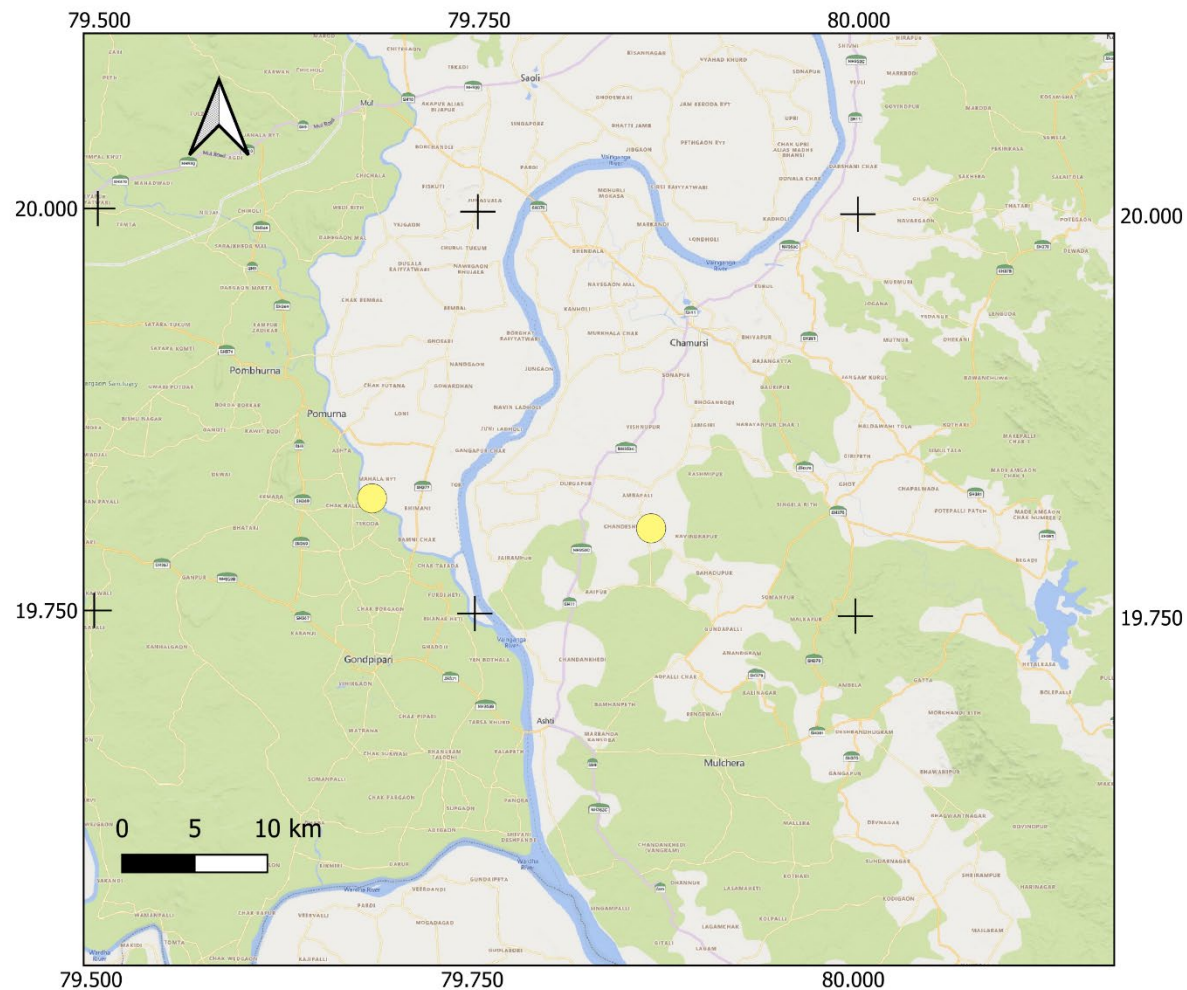


Figure 12.3.2.b: The location of the Thanewasna and Dubarpeth copper deposit locations, marked by the yellow circle, and the trends of fractures shown in the magnetic data that may exert structural control on the Dubarpeth deposit (the green line), as follows: a) first vertical derivative of the magnetic field shown with a monochrome shadow from the northeast, b) geographic location (Microsoft® Bing™ Maps).

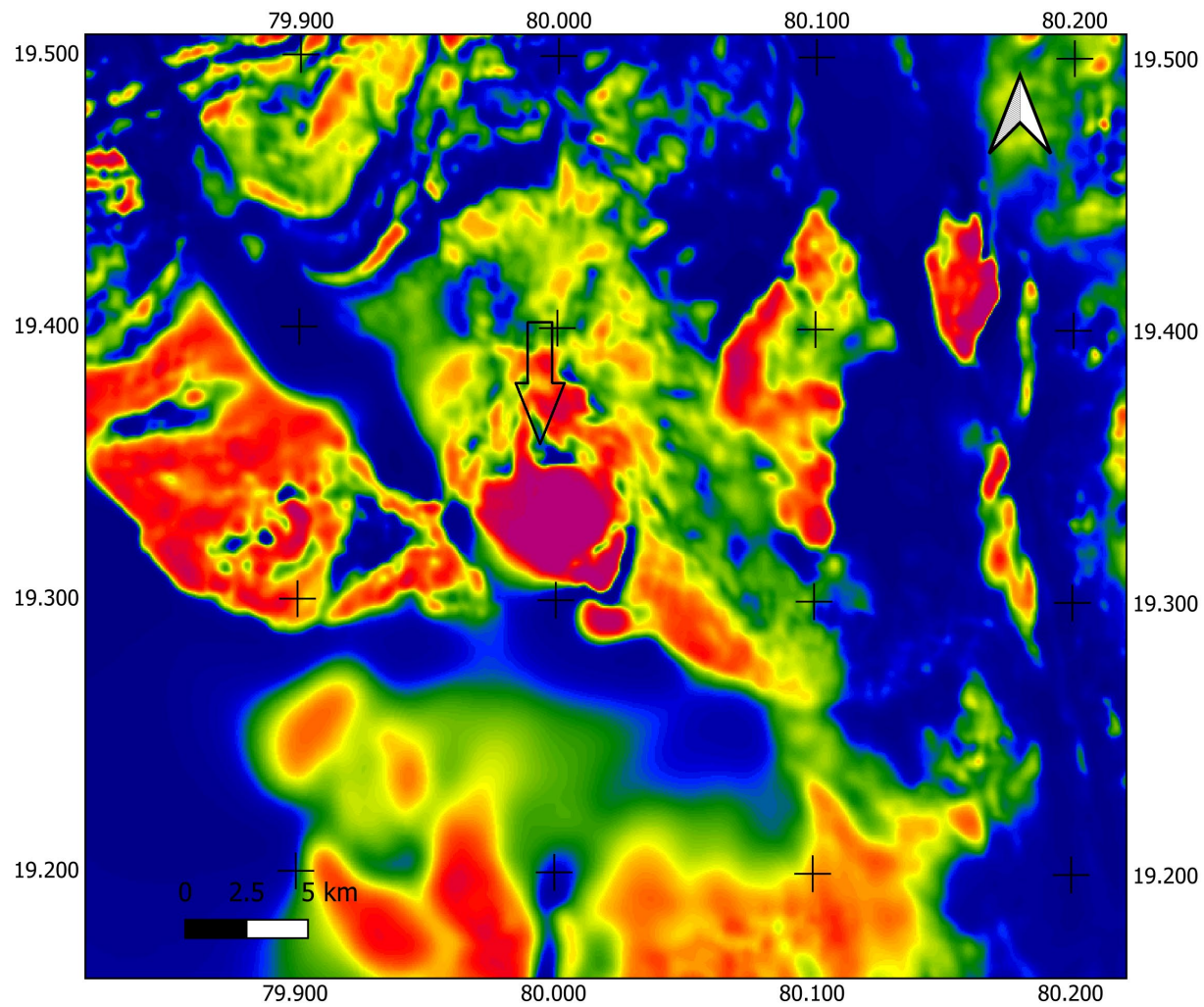


Figure 12.3.3.a: Magnetic intrusion with ring structure in the Bastar Craton, as follows: a) anomalous magnetic intensity reduced to the pole with the intrusion indicated, b) geographic location (Microsoft® Bing™ Maps).

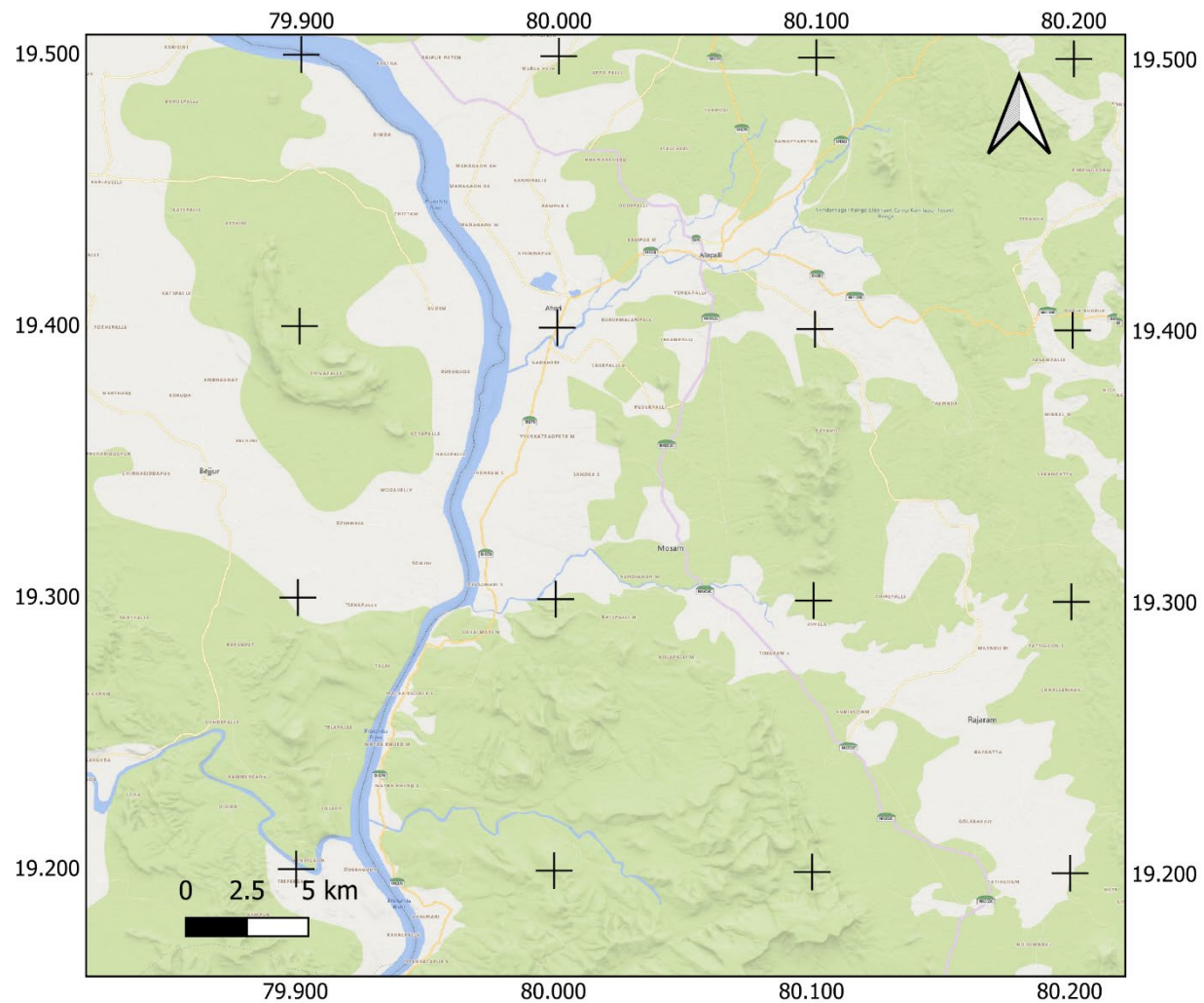


Figure 12.3.3.b: Magnetic intrusion with ring structure in the Bastar Craton, as follows: a) anomalous magnetic intensity reduced to the pole with the intrusion indicated, b) geographic location (Microsoft® Bing™ Maps).

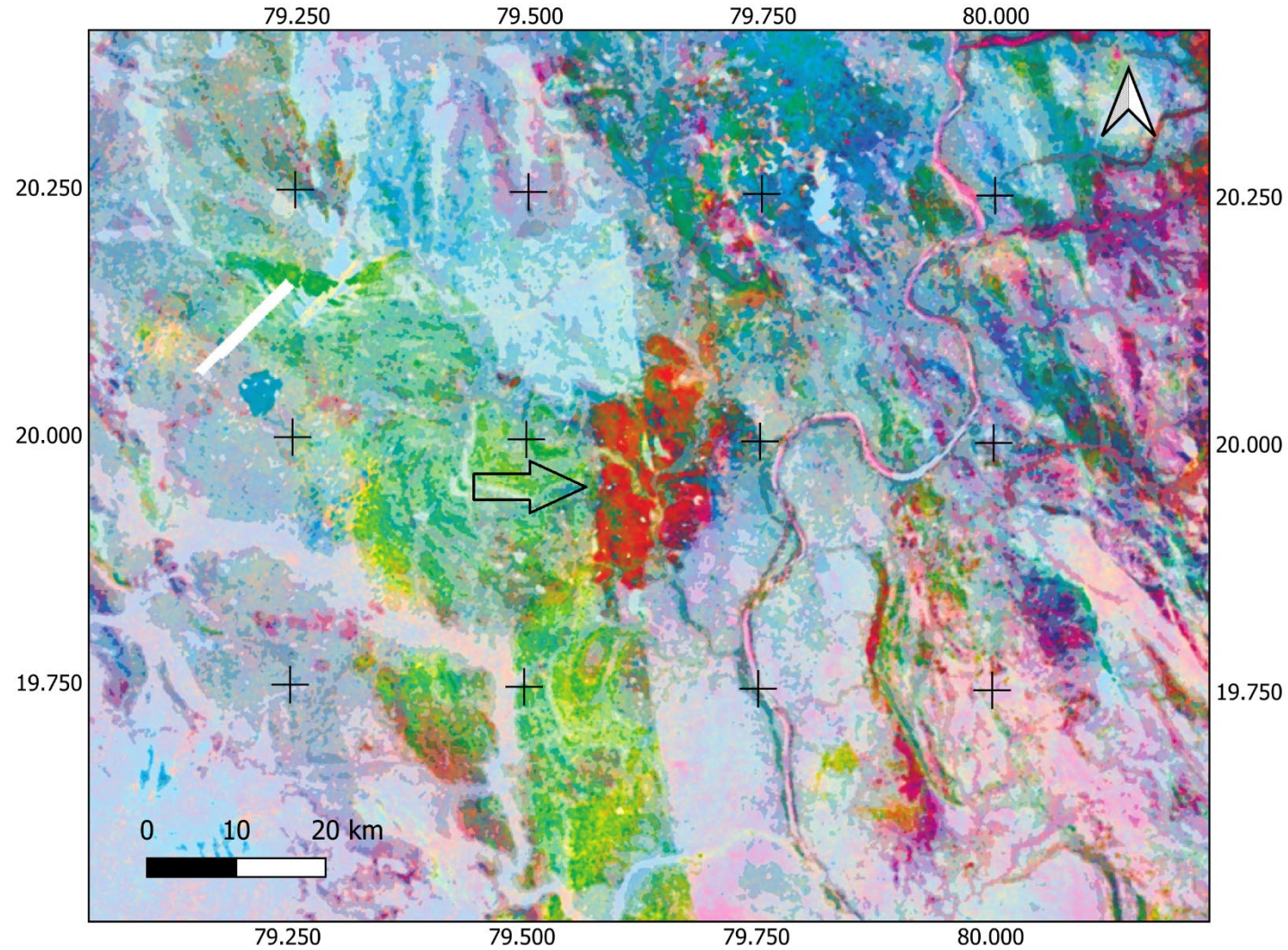


Figure 12.3.4.a: High potassium formation on the western margin of the Bastar Craton straddling and offset by the eastern boundary fault of the Godavari Basin as follows: a) radiometric ternary with the formation indicated, b) geographic location (Microsoft® Bing™ Maps).

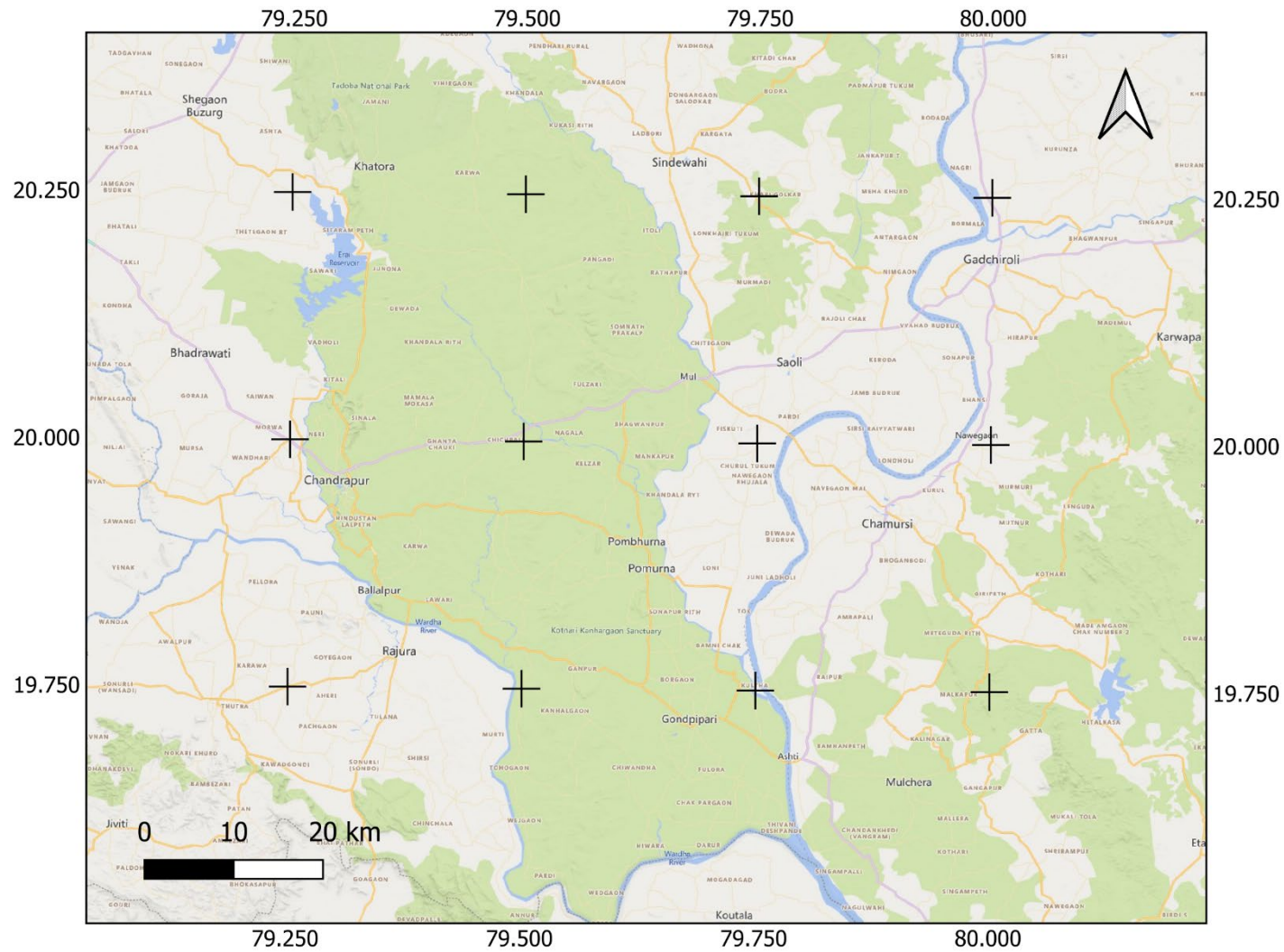


Figure 12.3.4.b: High potassium formation on the western margin of the Bastar Craton straddling and offset by the eastern boundary fault of the Godavari Basin as follows: a) radiometric ternary with the formation indicated, b) geographic location (Microsoft® Bing™ Maps).

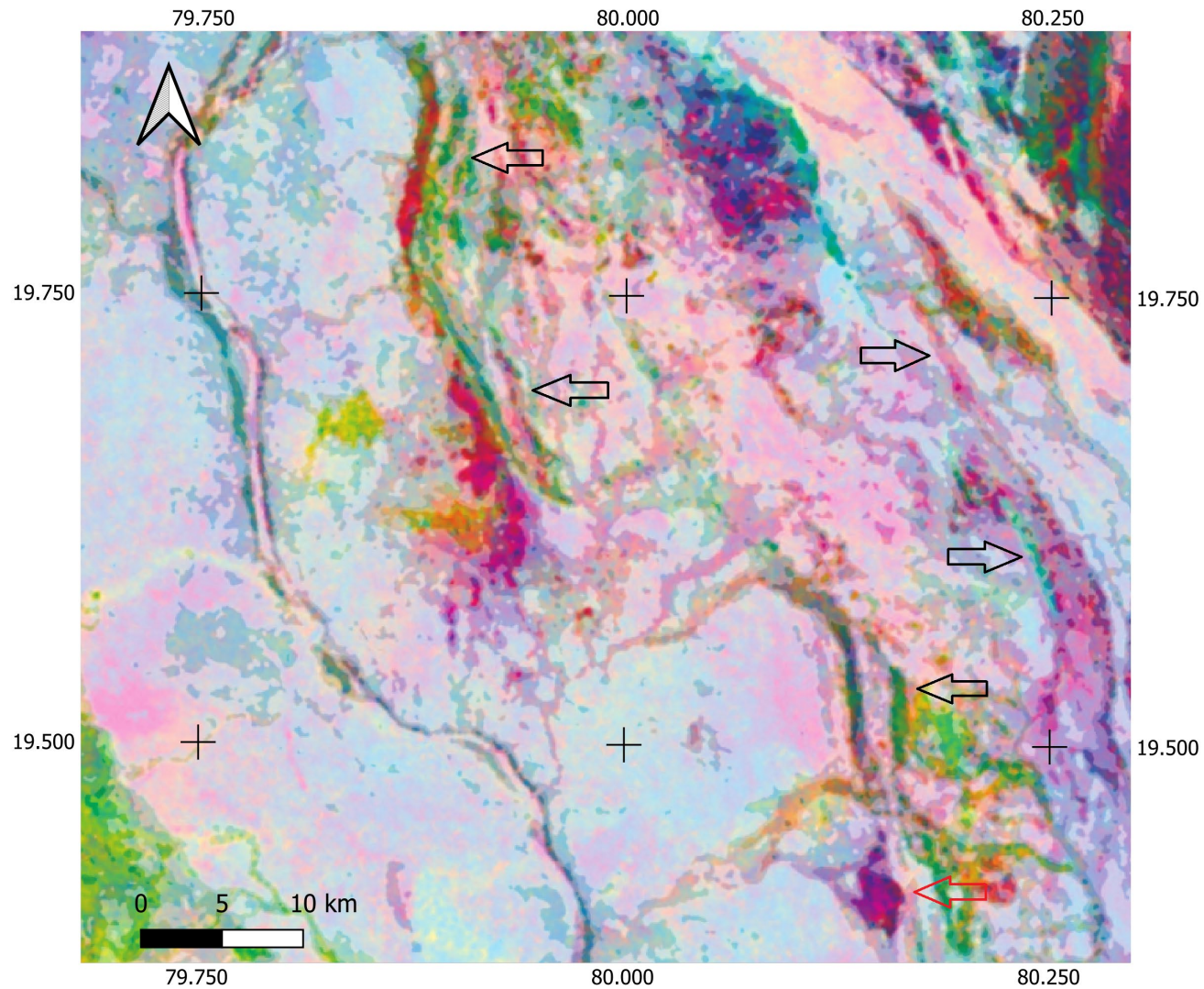


Figure 12.3.5.a: Meta-sedimentary and/or meta-volcanic bands within the gneisses of the Bastar Craton as follows: a) radiometric ternary image with bands indicated, and high coincident gamma-ray and magnetic anomaly shown with the red arrow, b) first vertical derivative of the magnetic anomaly, c) geographic location (Microsoft® Bing™ Maps).

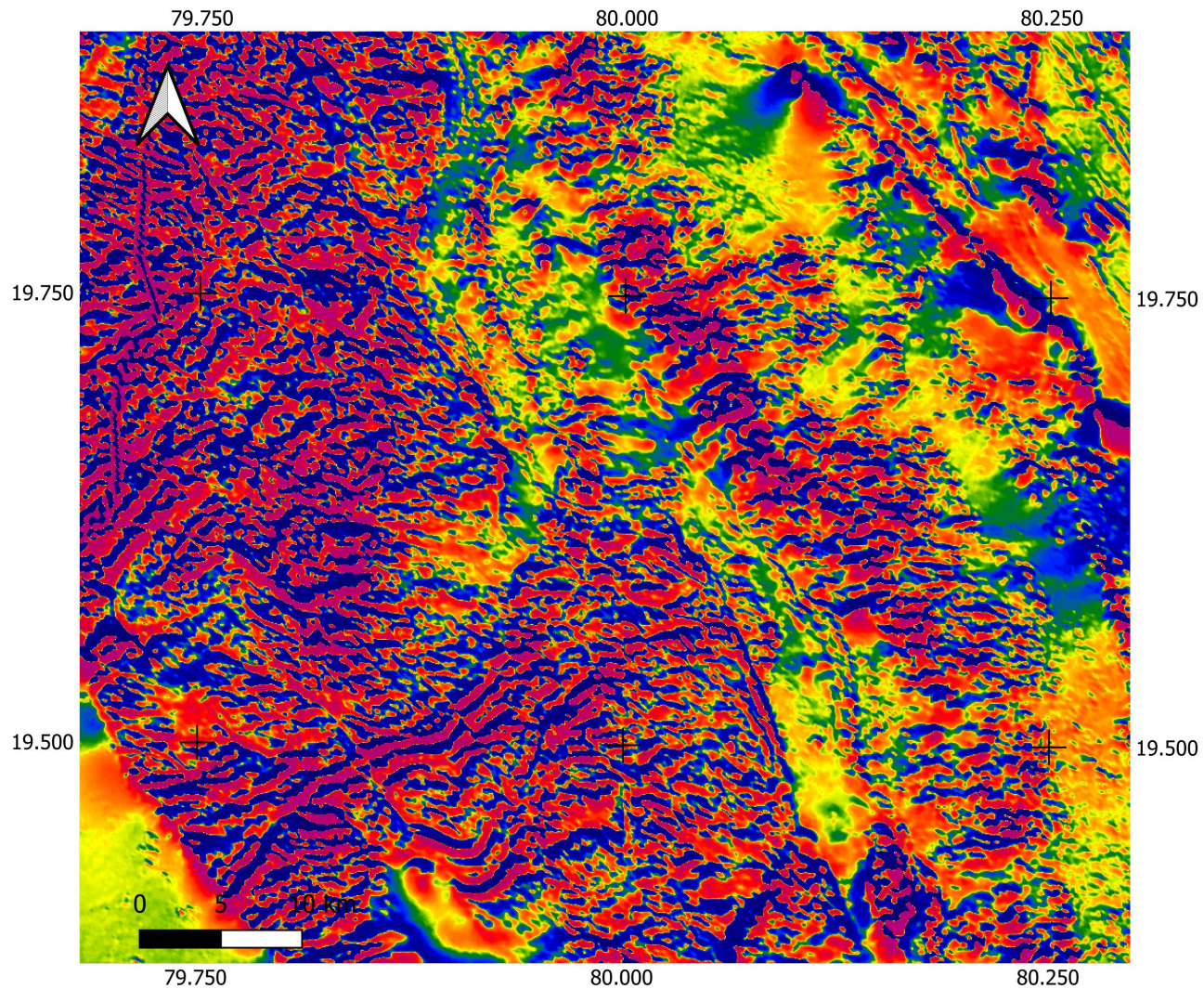


Figure 12.3.5.b: Meta-sedimentary and/or meta-volcanic bands within the gneisses of the Bastar Craton as follows: a) radiometric ternary image with bands indicated, and high coincident gamma-ray and magnetic anomaly shown with the red arrow, b) first vertical derivative of the magnetic anomaly, c) geographic location (Microsoft® Bing™ Maps).

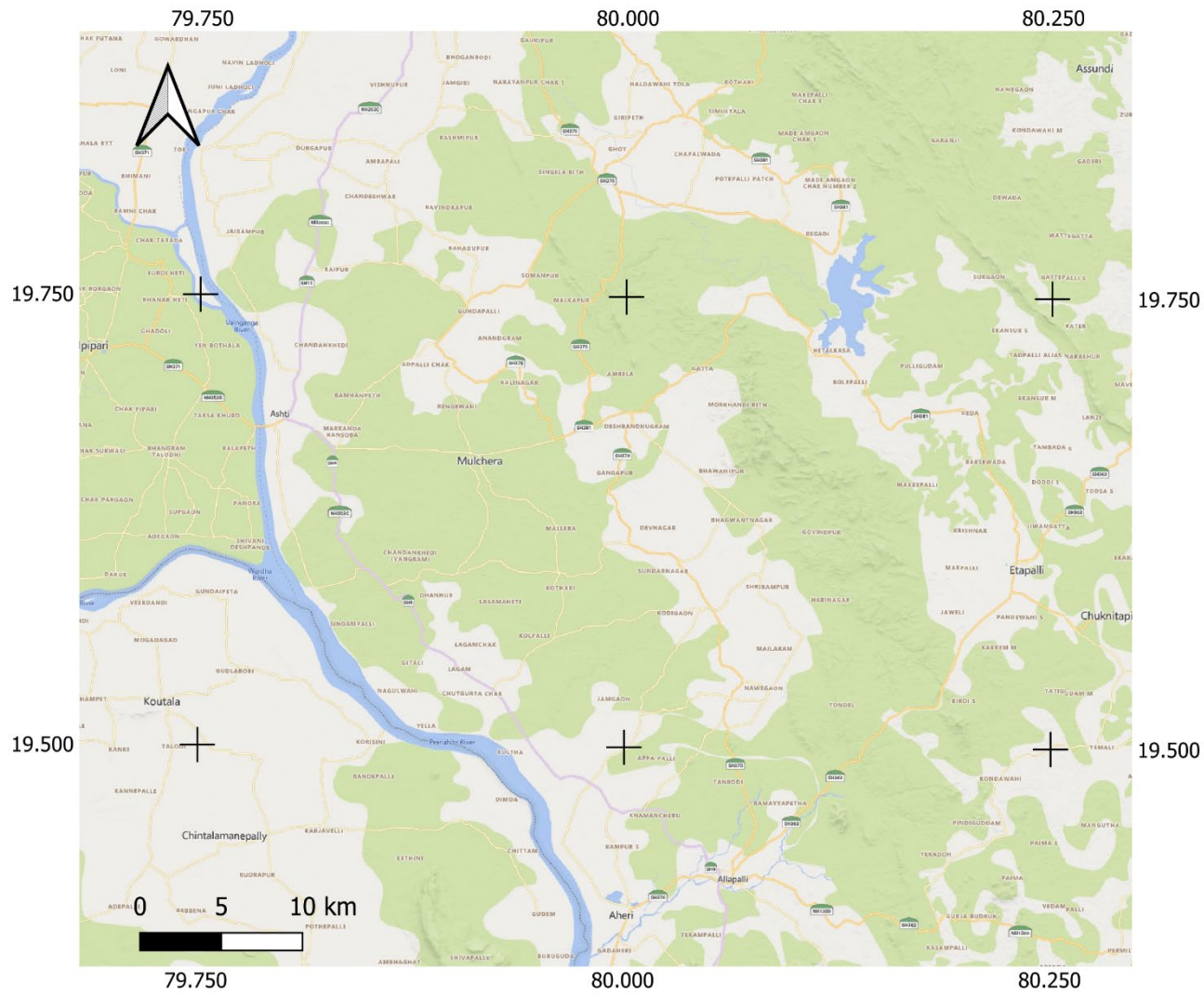


Figure 12.3.5.c: Meta-sedimentary and/or meta-volcanic bands within the gneisses of the Bastar Craton as follows: a) radiometric ternary image with bands indicated, and high coincident gamma-ray and magnetic anomaly shown with the red arrow, b) first vertical derivative of the magnetic anomaly, c) geographic location (Microsoft® Bing™ Maps).

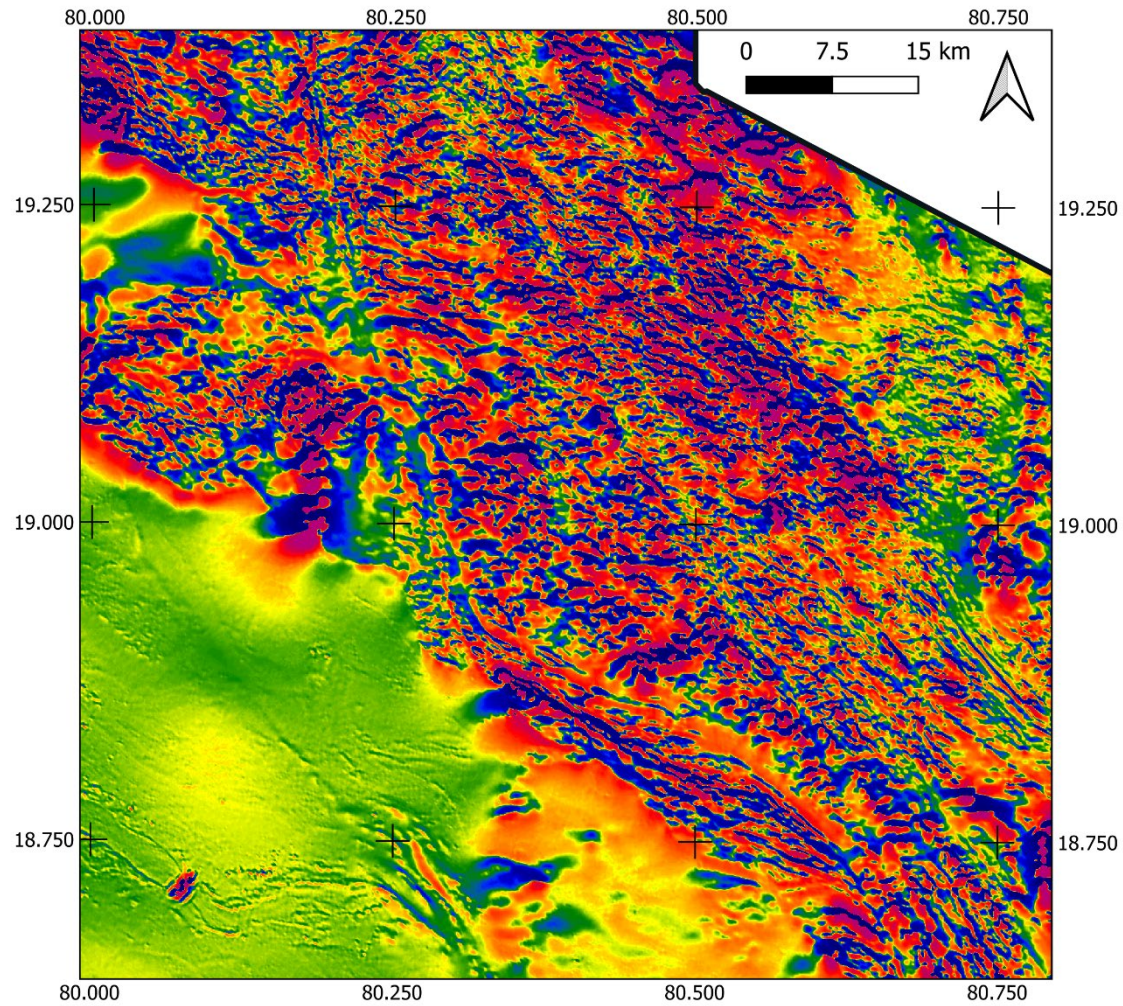


Figure 12.3.6.a: Possible granitic rocks within the Bhopalpatnam granulite, within a belt of deformed metasediments and metavolcanics, as follows: a) first vertical derivative of the magnetic anomaly, b) radiometric ternary with the granitic rocks indicated, c) geographic location (Microsoft® Bing™ Maps).

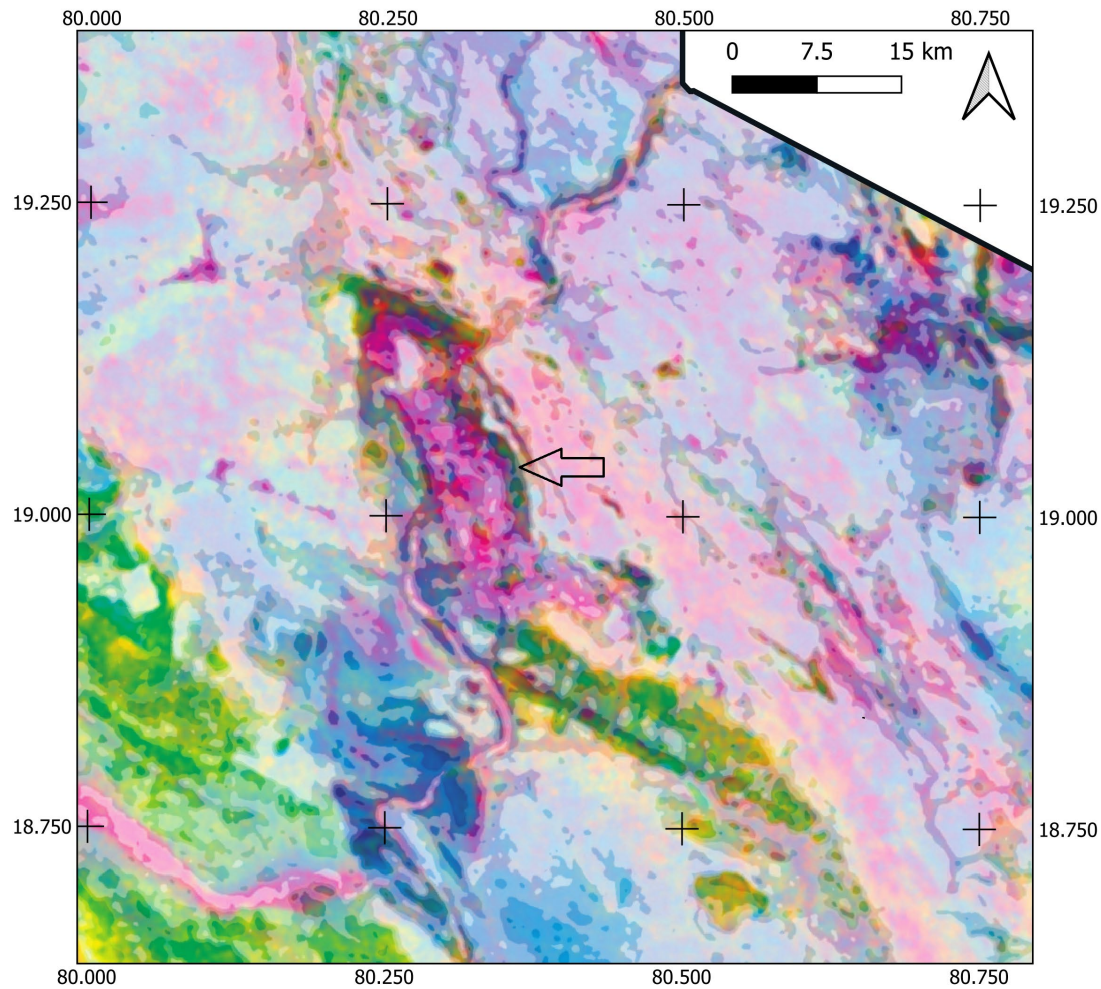


Figure 12.3.6.b: Possible granitic rocks within the Bhopalpatnam granulite, within a belt of deformed metasediments and metavolcanics, as follows: a) first vertical derivative of the magnetic anomaly, b) radiometric ternary with the granitic rocks indicated, c) geographic location (Microsoft® Bing™ Maps).

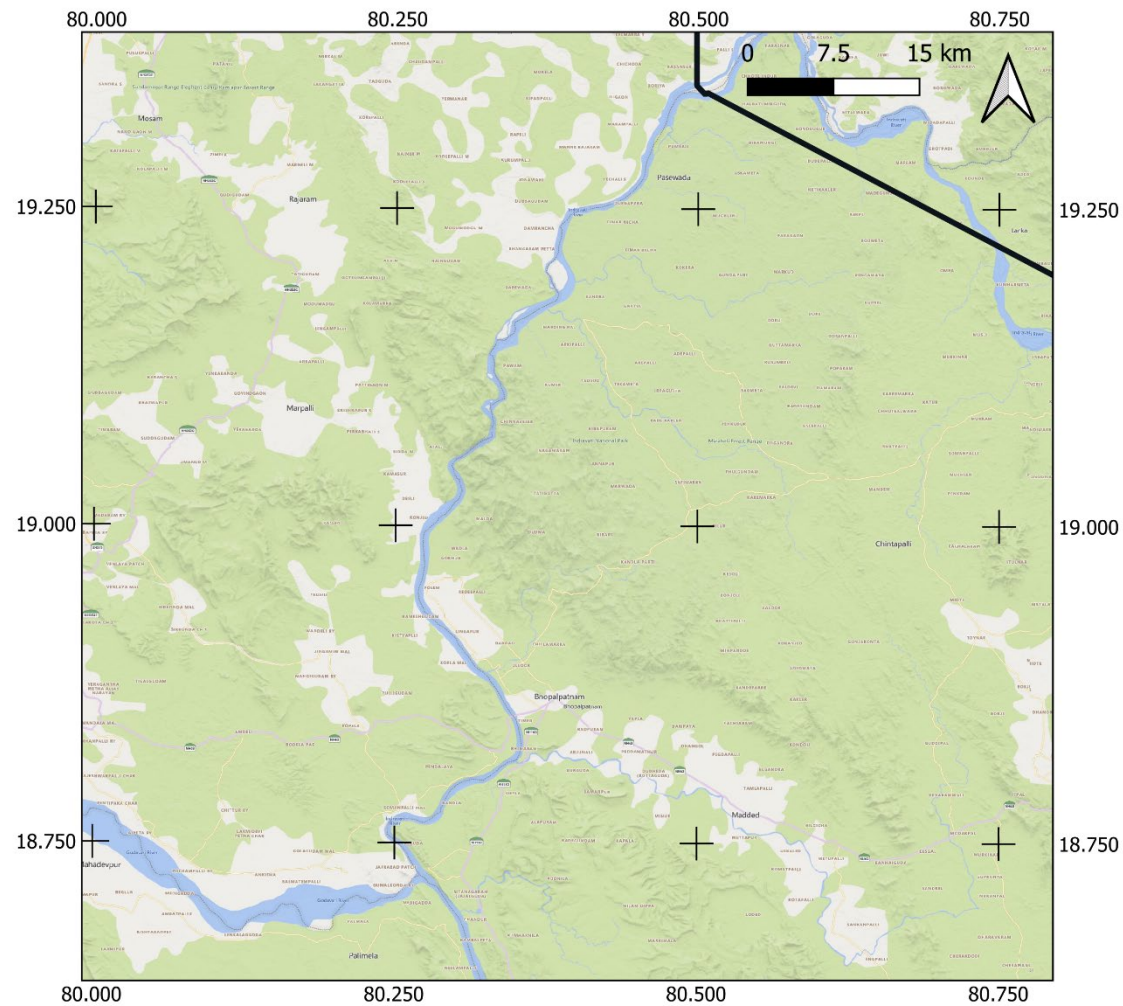


Figure 12.3.6.c: Possible granitic rocks within the Bhopalpatnam granulite, within a belt of deformed metasediments and metavolcanics, as follows: a) first vertical derivative of the magnetic anomaly, b) radiometric ternary with the granitic rocks indicated, c) geographic location (Microsoft® Bing™ Maps).

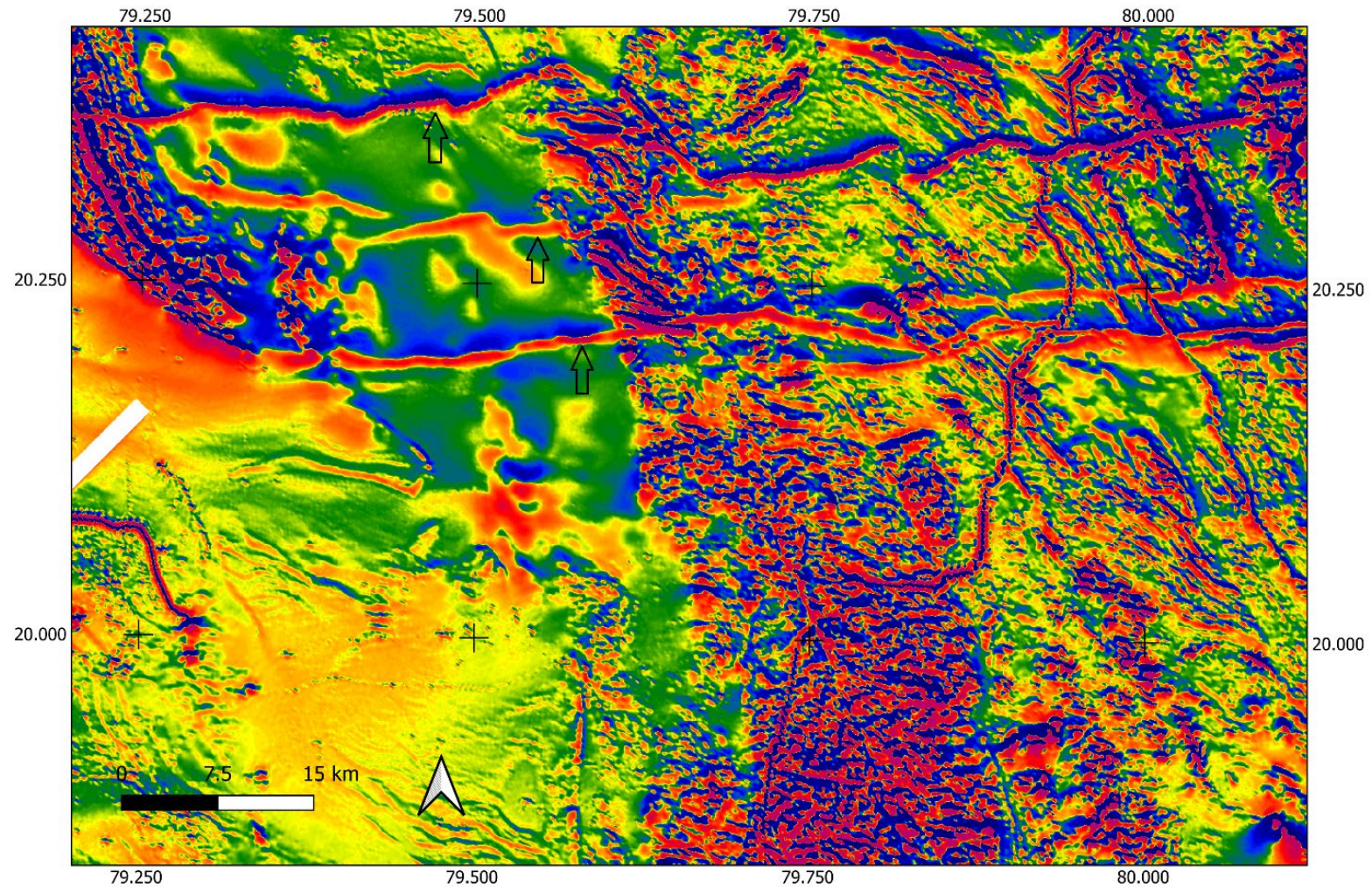


Figure 12.3.7.a: East to west trending dykes in the Bastar Craton in the north of Block-6 as follows: a) first vertical derivative of the magnetic anomaly with the three dykes indicated, b) geographic location (Microsoft® Bing™ Maps).

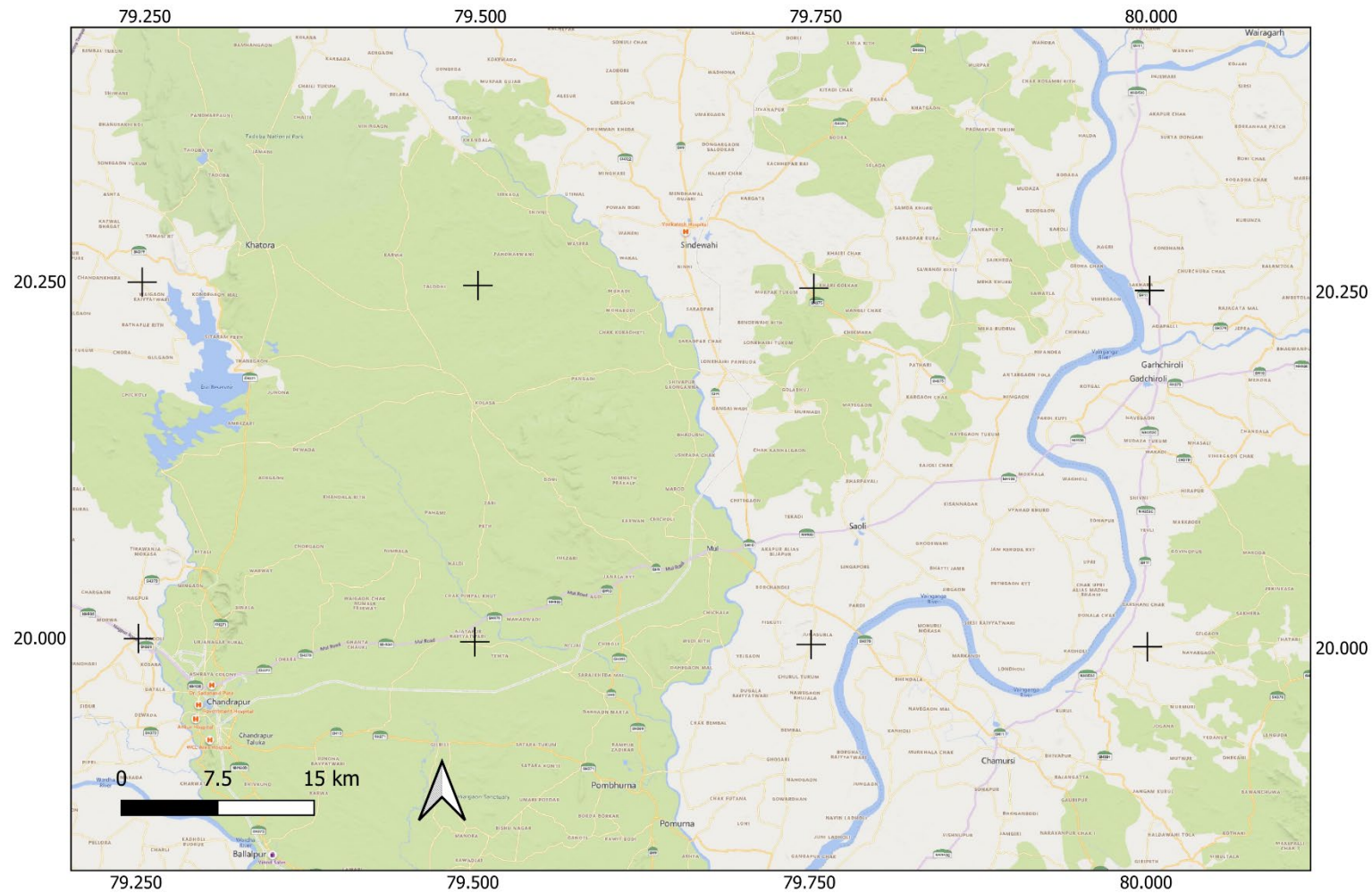


Figure 12.3.7.b: East to west trending dykes in the Bastar Craton in the north of Block-6 as follows: a) first vertical derivative of the magnetic anomaly with the three dykes indicated, b) geographic location (Microsoft® Bing™ Maps).

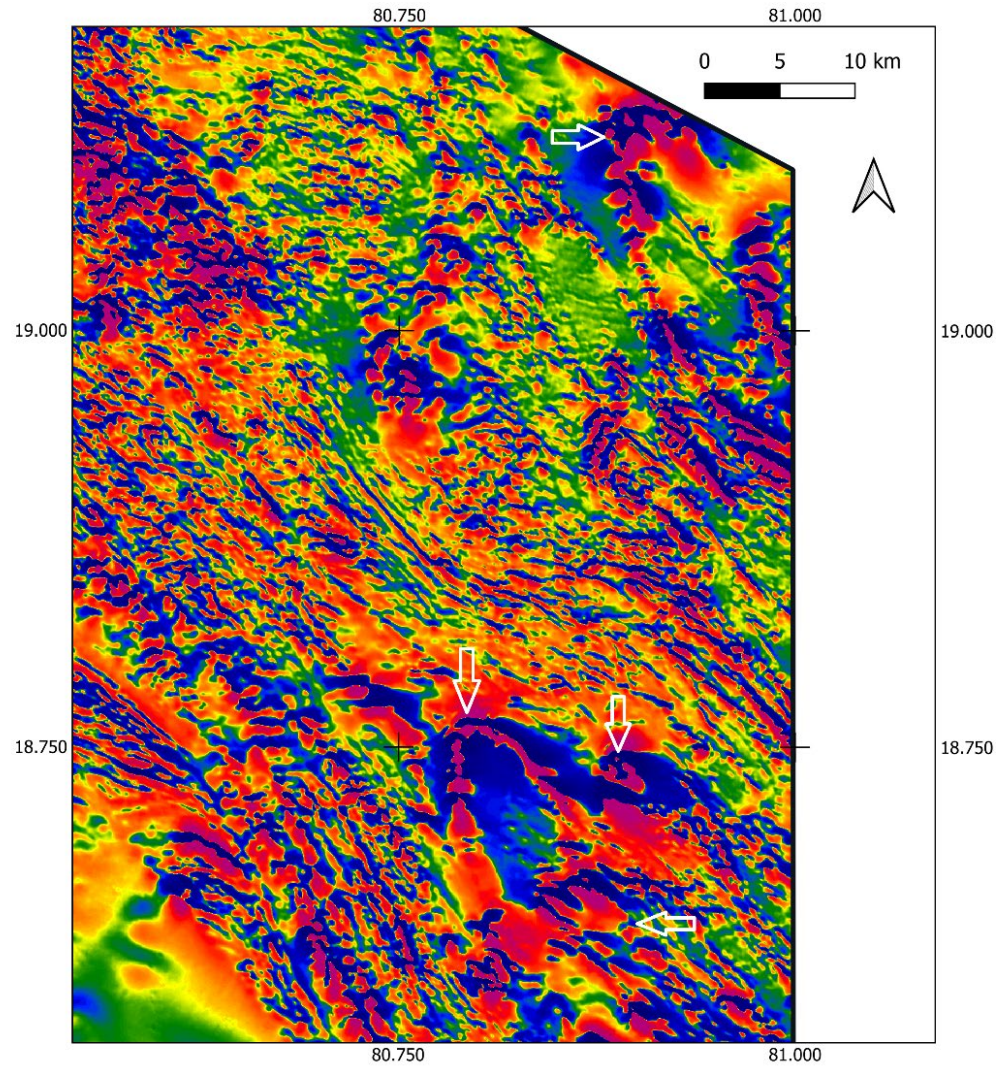


Figure 12.3.8.a: Folded meta sediments in the Bastar Craton, in the east of Block-6 as follows: a) first vertical derivative of the magnetic anomaly with the four folds indicated, b) Sentinel-2 VRT4 image, c) geographic location (Microsoft® Bing™ Maps).

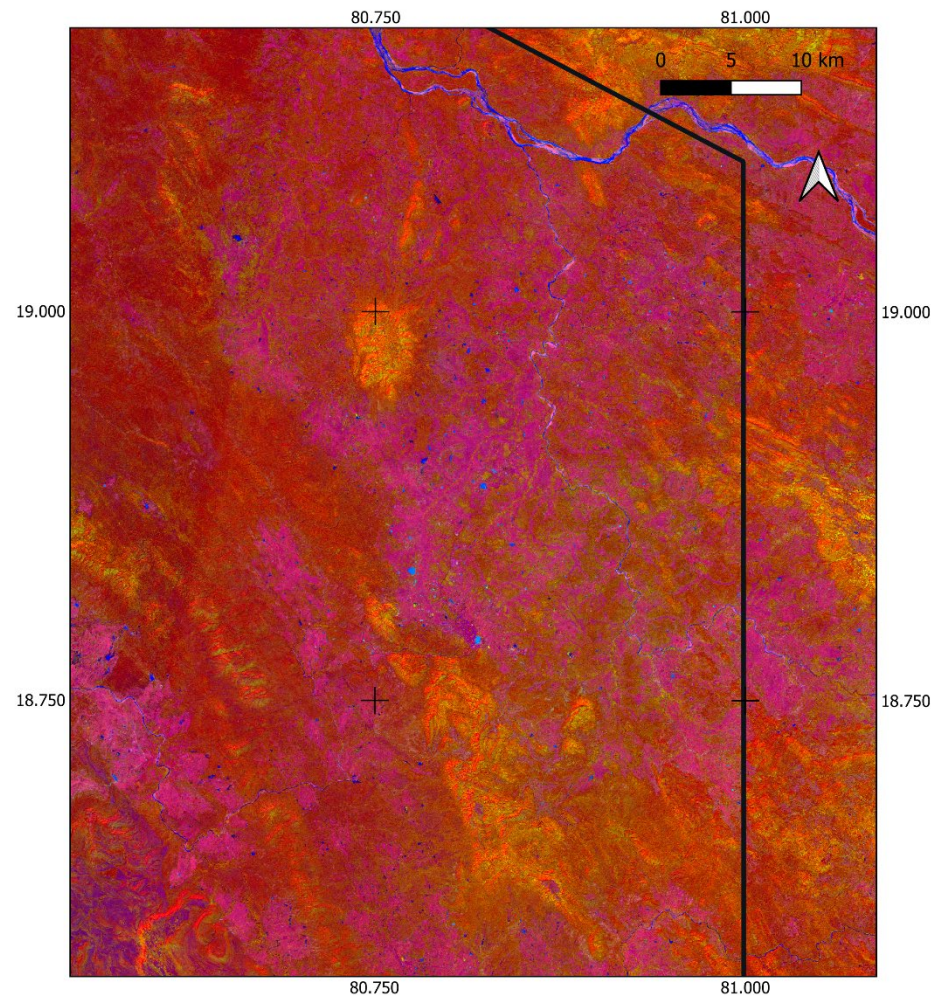


Figure 12.3.8.b: Folded meta sediments in the Bastar Craton, in the east of Block-6 as follows: a) first vertical derivative of the magnetic anomaly with the four folds indicated, b) Sentinel-2 VRT4 image, c) geographic location (Microsoft® Bing™ Maps).

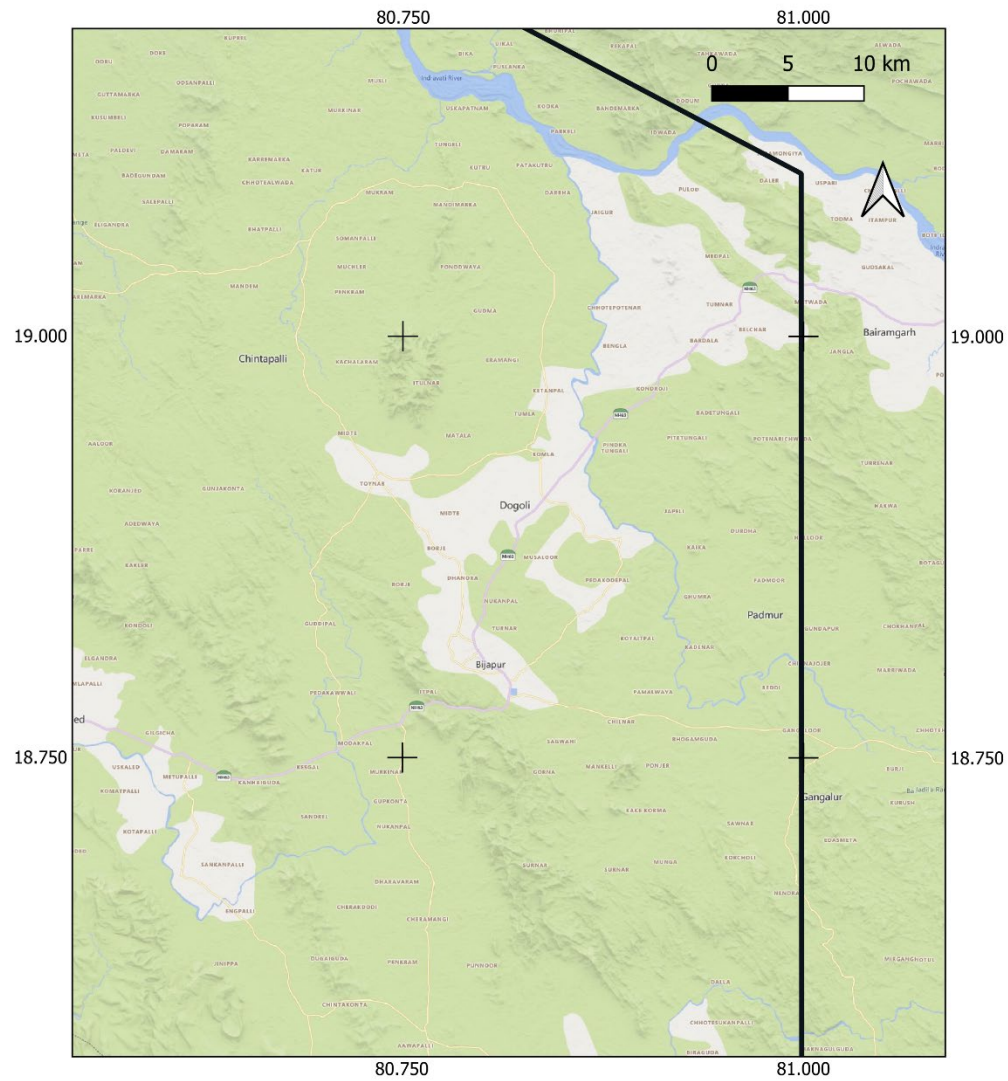


Figure 12.3.8.c: Folded meta sediments in the Bastar Craton, in the east of Block-6 as follows: a) first vertical derivative of the magnetic anomaly with the four folds indicated, b) Sentinel-2 VRT4 image, c) geographic location (Microsoft® Bing™ Maps).

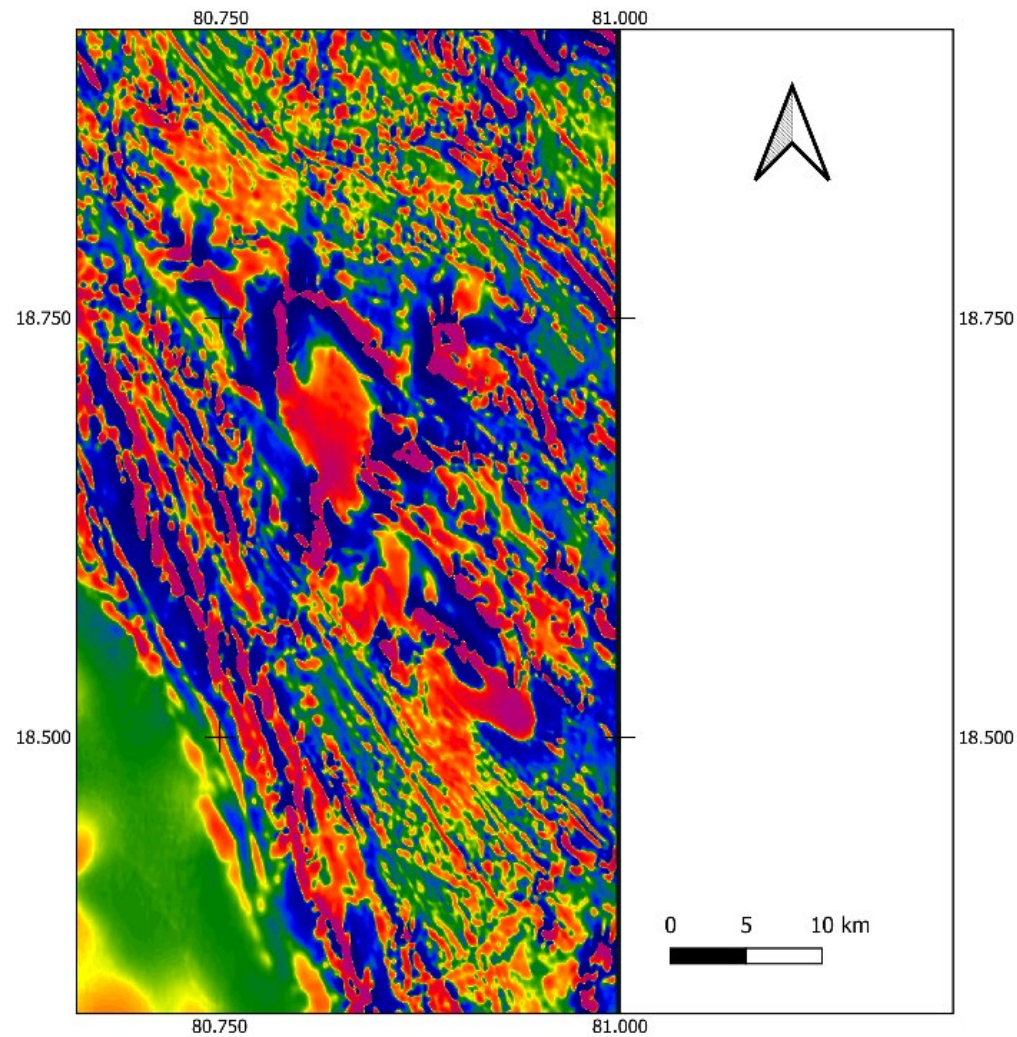


Figure 12.3.9.a: Close up of folded meta sediments in the Bastar Craton, in the east of Block-6 as follows: a) magnetic anomaly reduced to the pole, b) geographic location (Microsoft® Bing™ Maps).

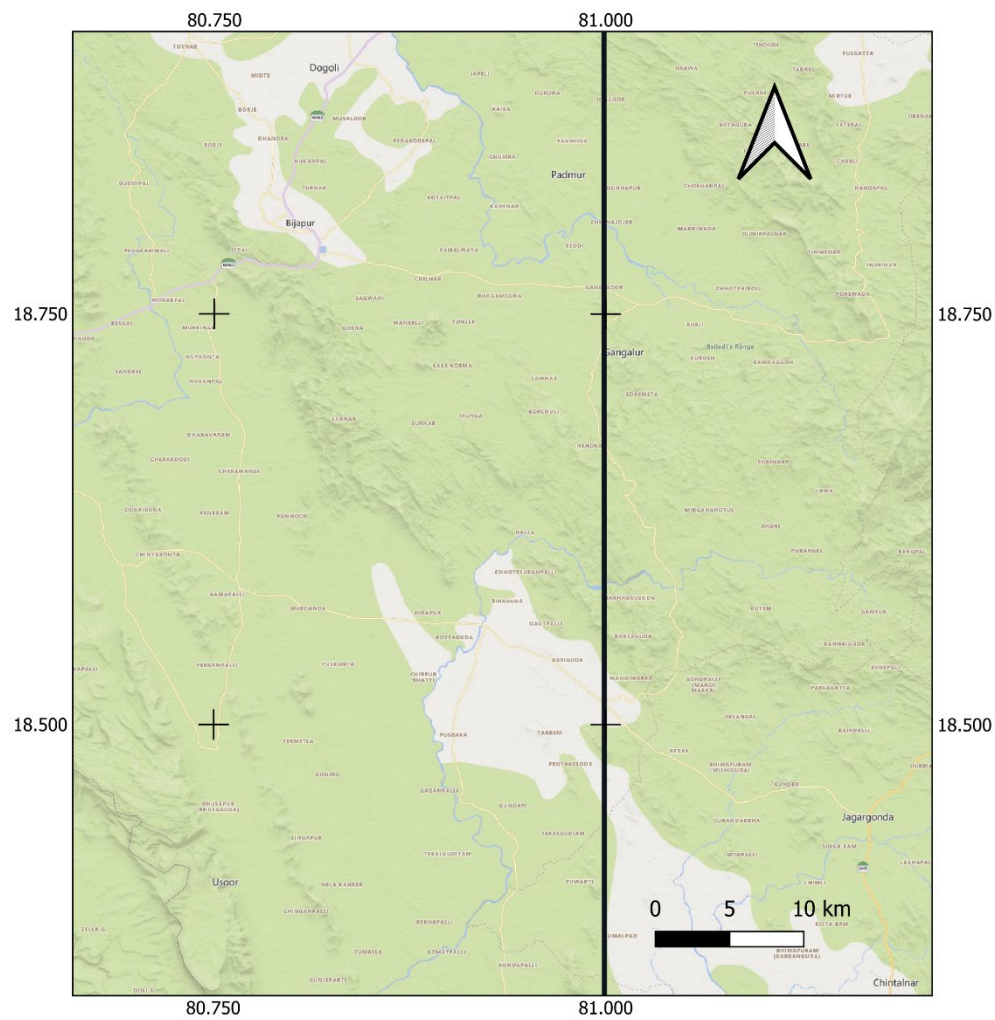


Figure 12.3.9.b: Close up of folded meta sediments in the Bastar Craton, in the east of Block-6 as follows: a) magnetic anomaly reduced to the pole, b) geographic location (Microsoft® Bing™ Maps).

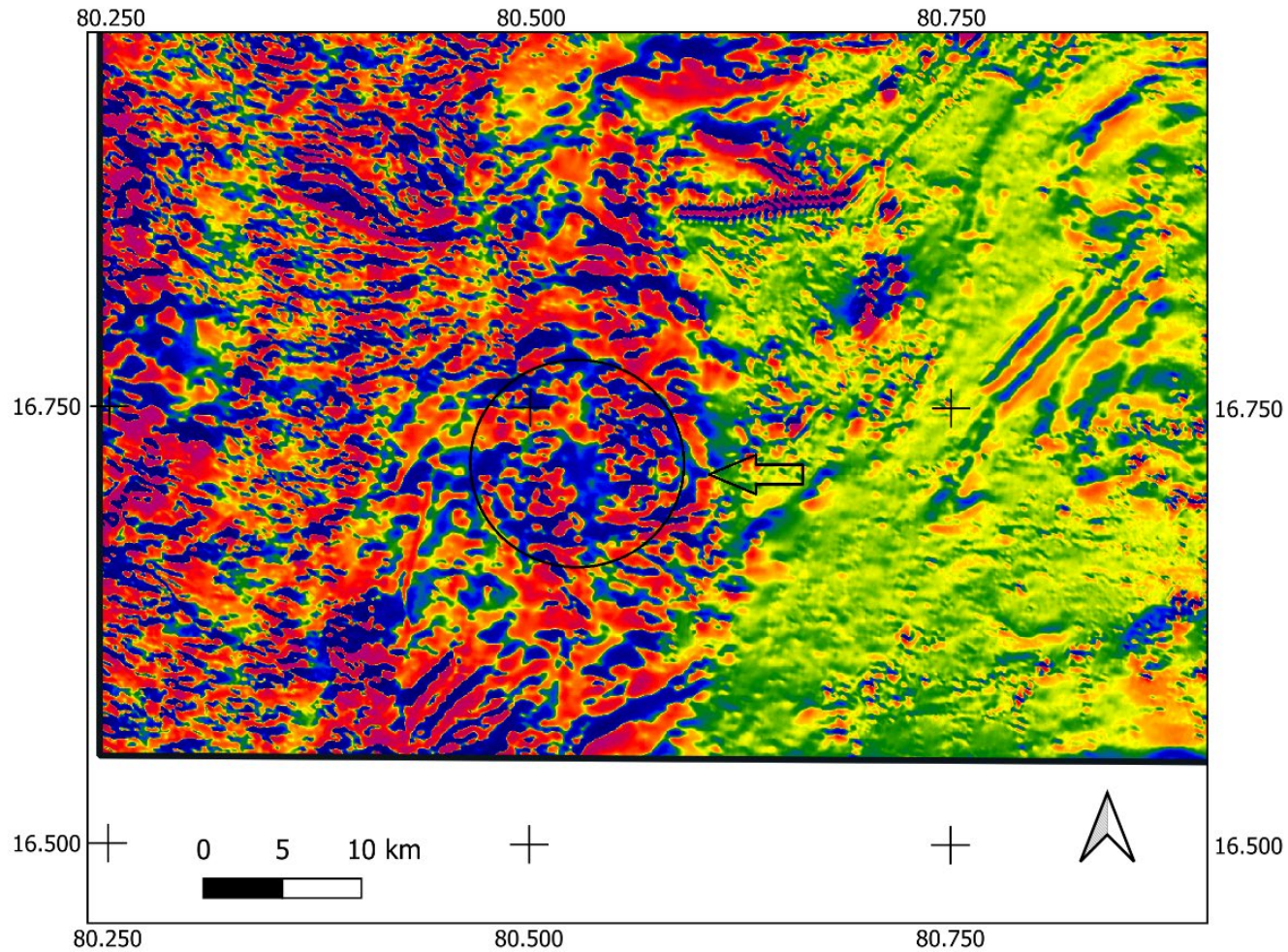


Figure 12.4.1.a: Large poorly defined magnetic ring structure in the Eastern Ghats Mobile Belt in the south of Block-6 as follows: a) first vertical derivative of the magnetic anomaly with the structure indicated and outlined, b) ratio of equivalent thorium to potassium, c) geographic location (Microsoft® Bing™ Maps).

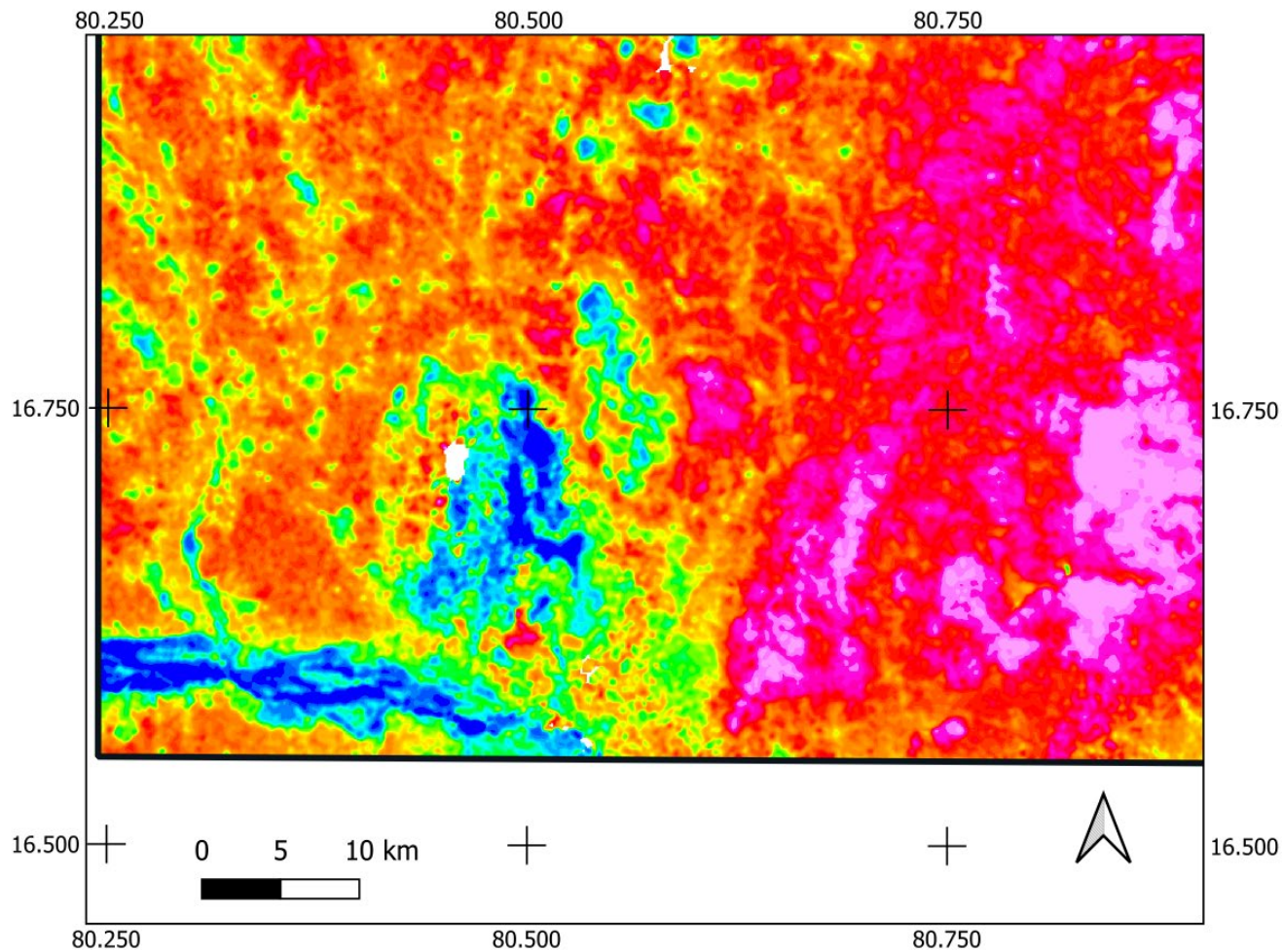


Figure 12.4.1.b: Large poorly defined magnetic ring structure in the Eastern Ghats Mobile Belt in the south of Block-6 as follows: a) first vertical derivative of the magnetic anomaly with the structure indicated and outlined, b) ratio of equivalent thorium to potassium, c) geographic location (Microsoft® Bing™ Maps).

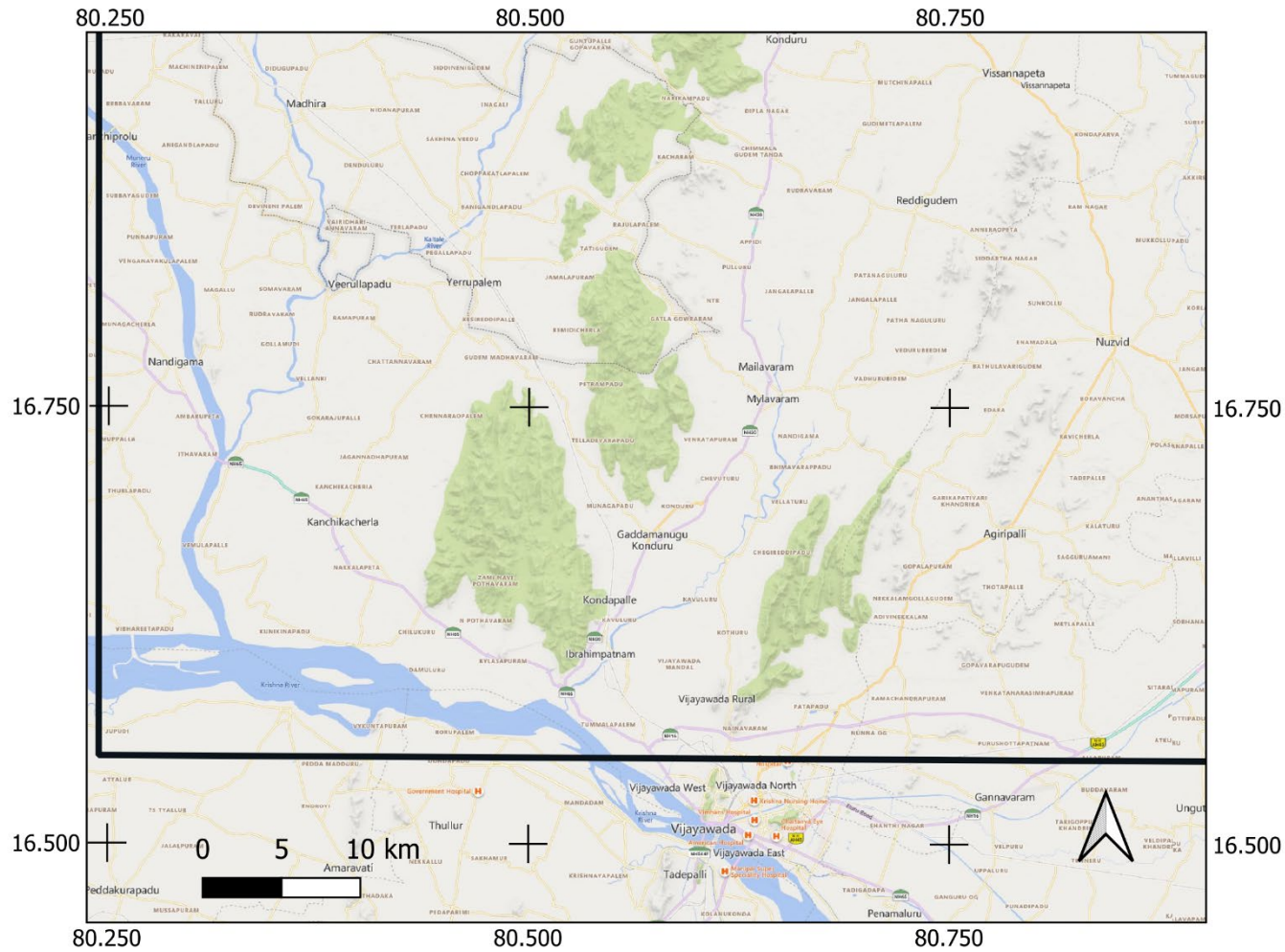


Figure 12.4.1.c: Large poorly defined magnetic ring structure in the Eastern Ghats Mobile Belt in the south of Block-6 as follows: a) first vertical derivative of the magnetic anomaly with the structure indicated and outlined, b) ratio of equivalent thorium to potassium, c) geographic location (Microsoft® Bing™ Maps).

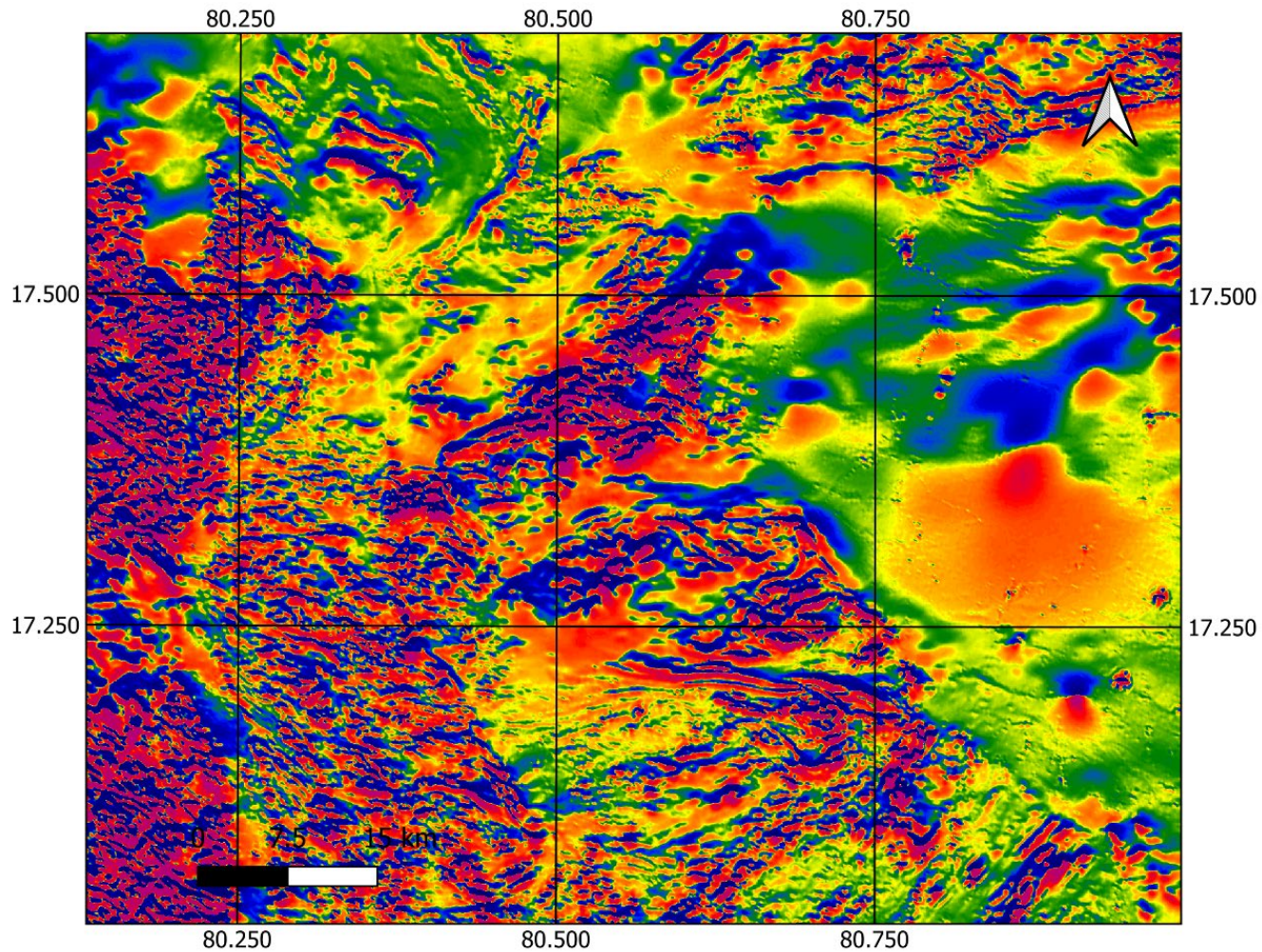


Figure 12.4.2.a: Anomalies associated with the Chimalpahad Complex in the Eastern Ghats Mobile Belt as follows: a) first vertical derivative of the magnetic anomaly, b) ratio of equivalent uranium to equivalent thorium, c) potassium concentration with the potassium low indicated, d) geographic location (Microsoft® Bing™ Maps).

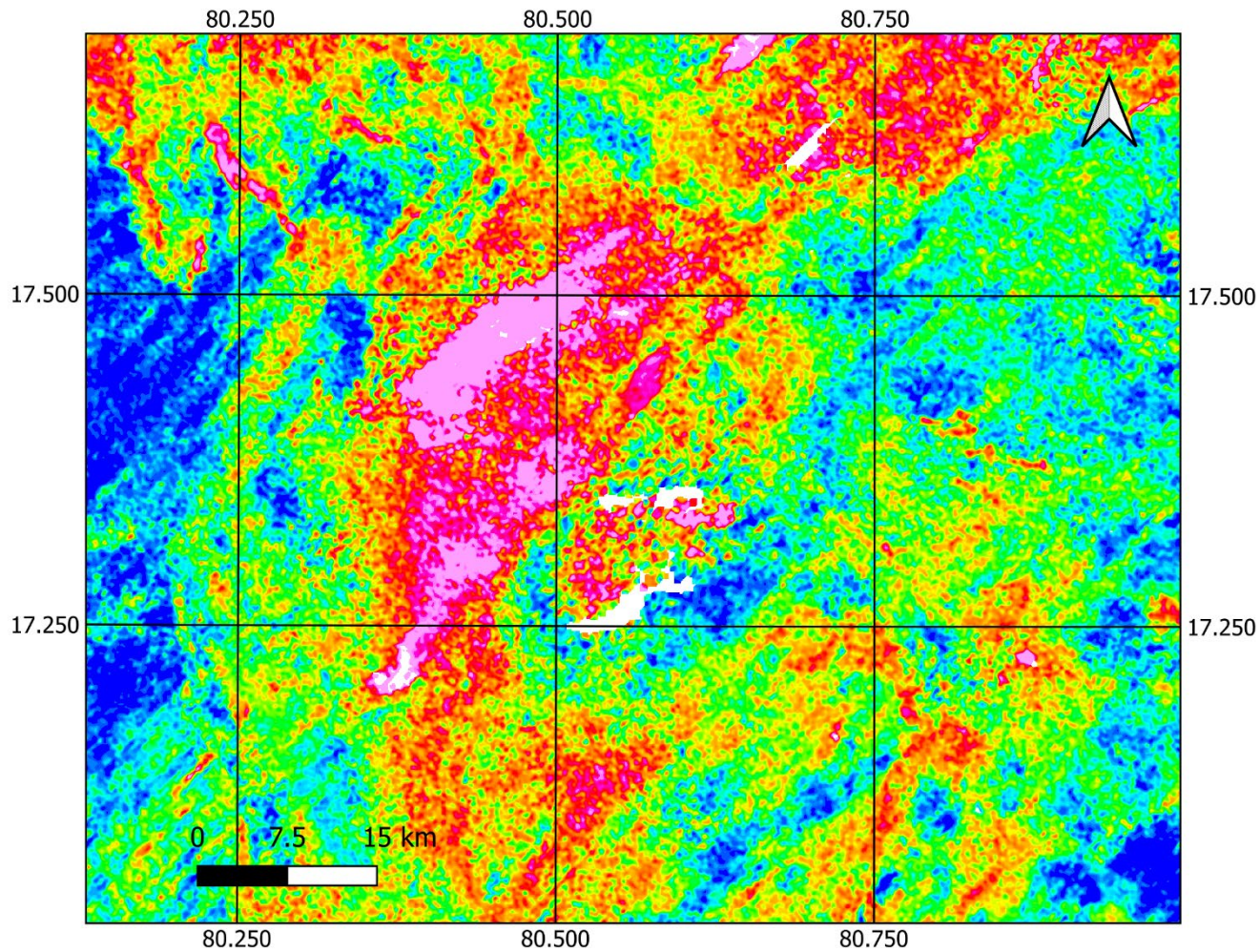


Figure 12.4.2.b: Anomalies associated with the Chimalpahad Complex in the Eastern Ghats Mobile Belt as follows: a) first vertical derivative of the magnetic anomaly, b) ratio of equivalent uranium to equivalent thorium, c) potassium concentration with the potassium low indicated, d) geographic location (Microsoft® Bing™ Maps).

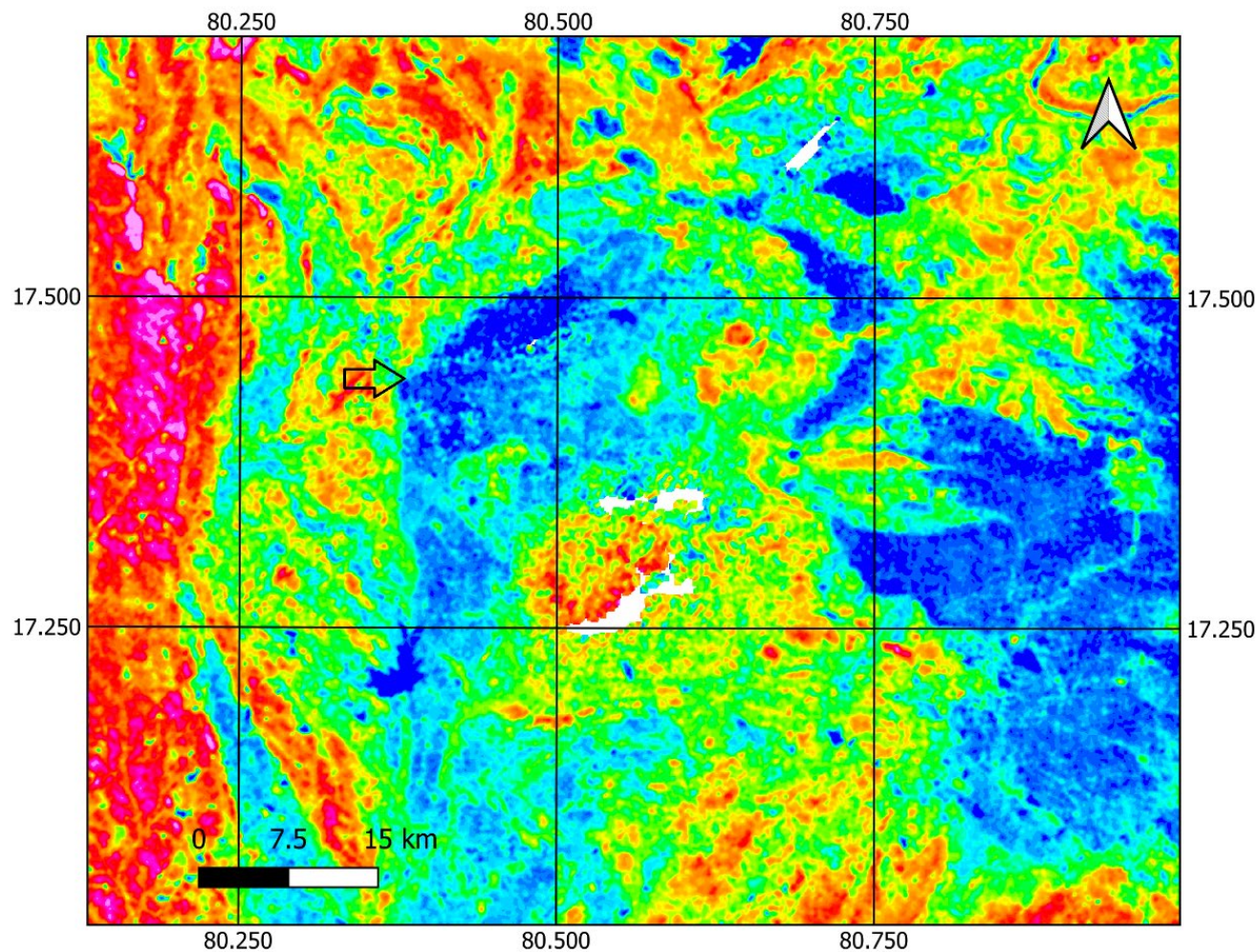


Figure 12.4.2.c: Anomalies associated with the Chimalpahad Complex in the Eastern Ghats Mobile Belt as follows: a) first vertical derivative of the magnetic anomaly, b) ratio of equivalent uranium to equivalent thorium, c) potassium concentration with the potassium low indicated, d) geographic location (Microsoft® Bing™ Maps).

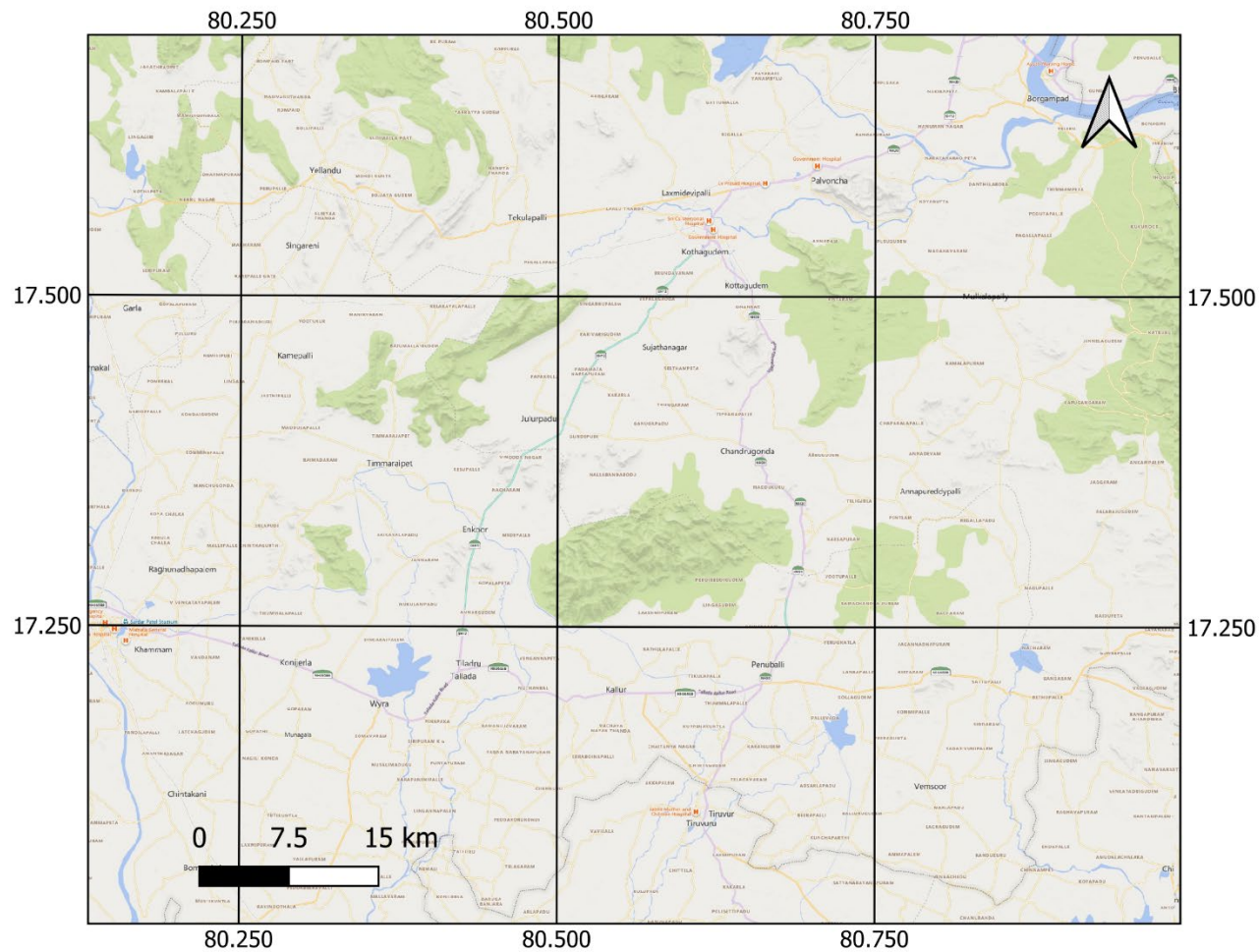


Figure 12.4.2.d: Anomalies associated with the Chimalpahad Complex in the Eastern Ghats Mobile Belt as follows: a) first vertical derivative of the magnetic anomaly, b) ratio of equivalent uranium to equivalent thorium, c) potassium concentration with the potassium low indicated, d) geographic location (Microsoft® Bing™ Maps).

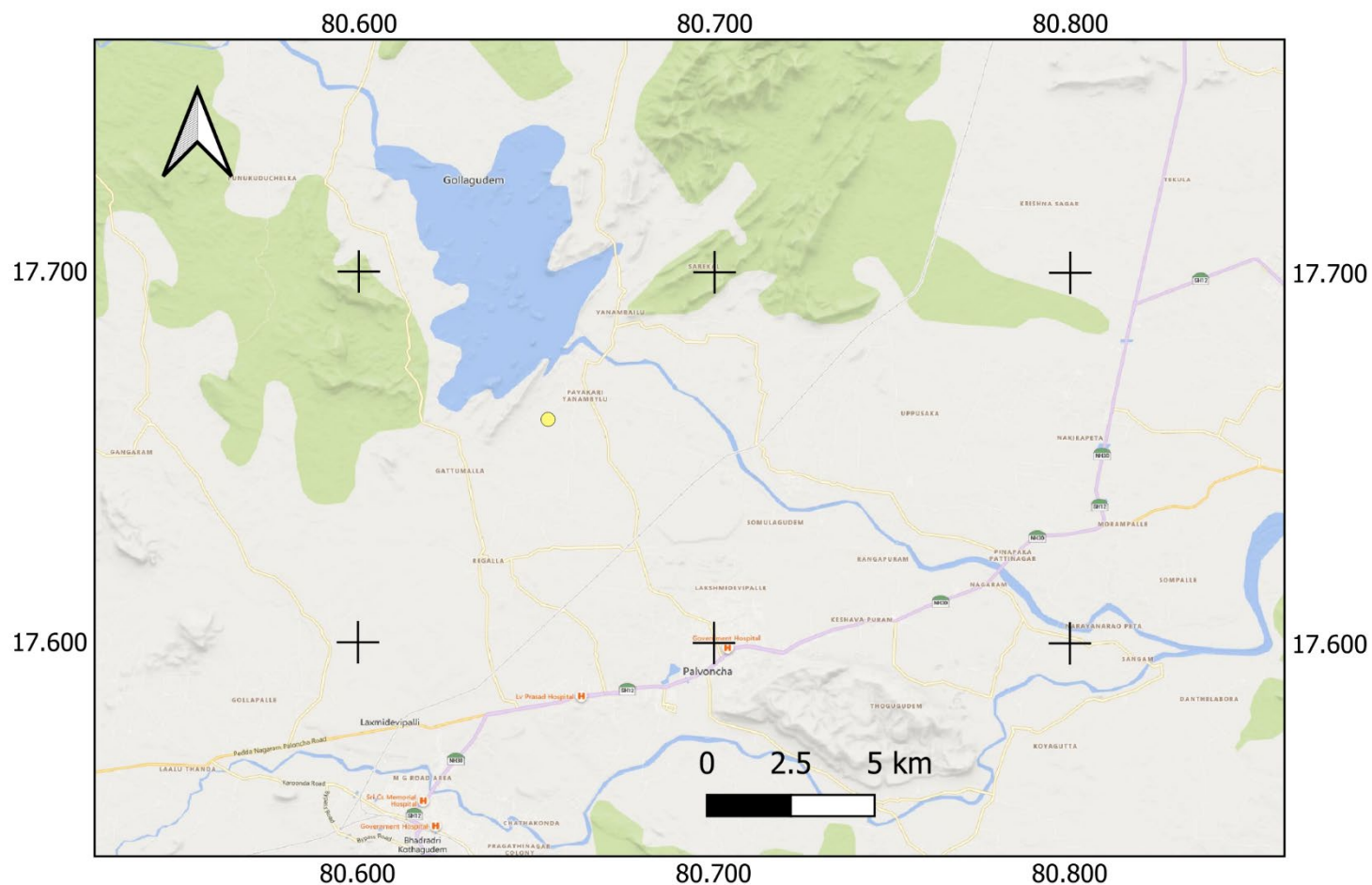


Figure 12.4.3.a: The Mailaram copper deposit location, marked by the yellow circle, and the trend of a fracture shown in the magnetic data that may exert structural control (the green line), as follows: a) first vertical derivative of the magnetic field shown with a monochrome shadow from the northeast, b) geographic location.

fracture shown in the magnetic data that may exert structural control (the green line), as follows: a) first vertical derivative of the magnetic field shown with a monochrome shadow from the northeast, b) geographic location (Microsoft® Bing™ Maps).

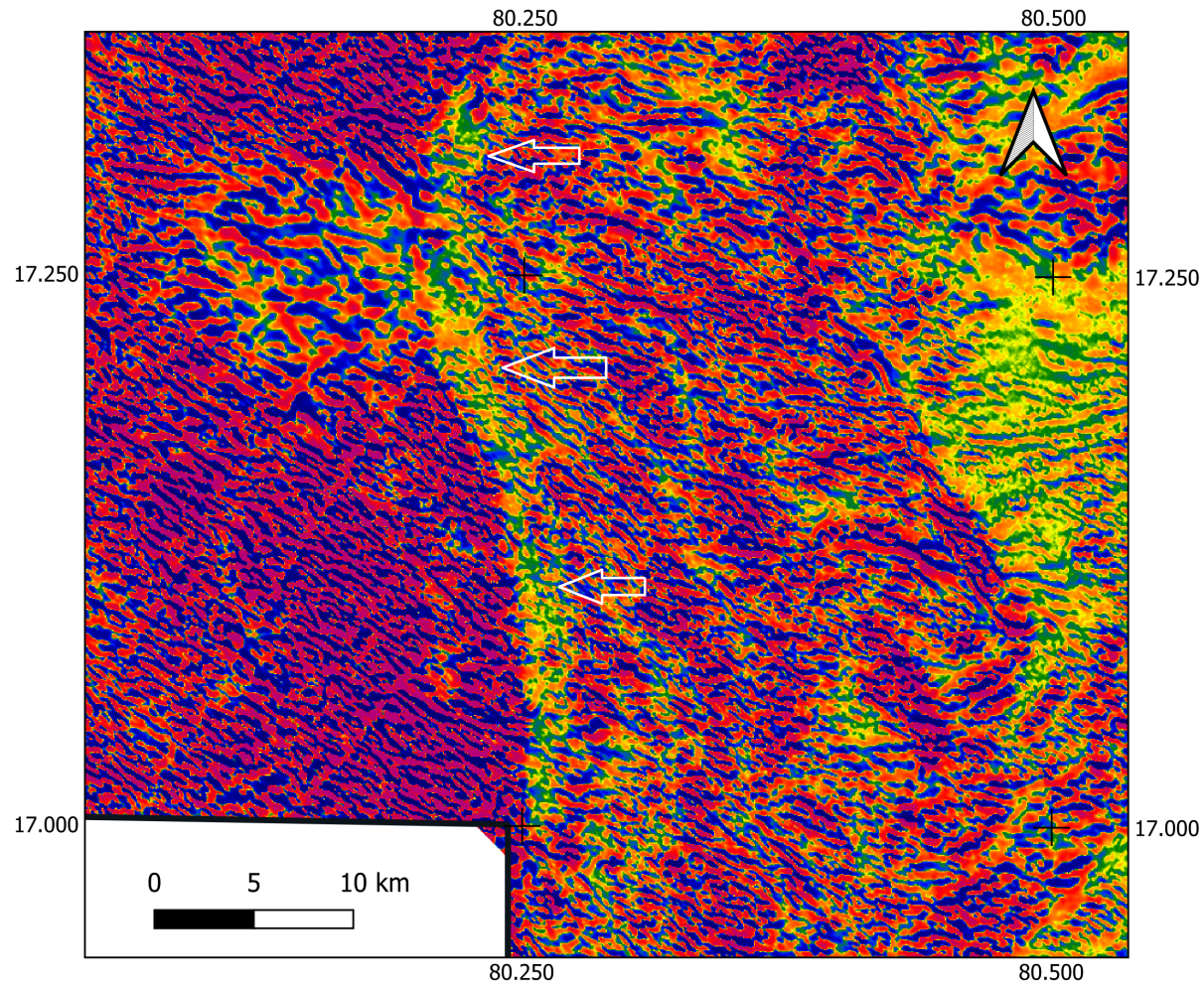


Figure 12.4.4.a: North to south trending Godavari Supergroup Shernawala Outliers between the EDC and the EGMB, marked by a band of lower amplitude magnetic anomalies, as follows: a) second vertical derivative of the anomalous magnetic field with the band of outliers indicated, b) geographic location (Microsoft® Bing™ Maps).

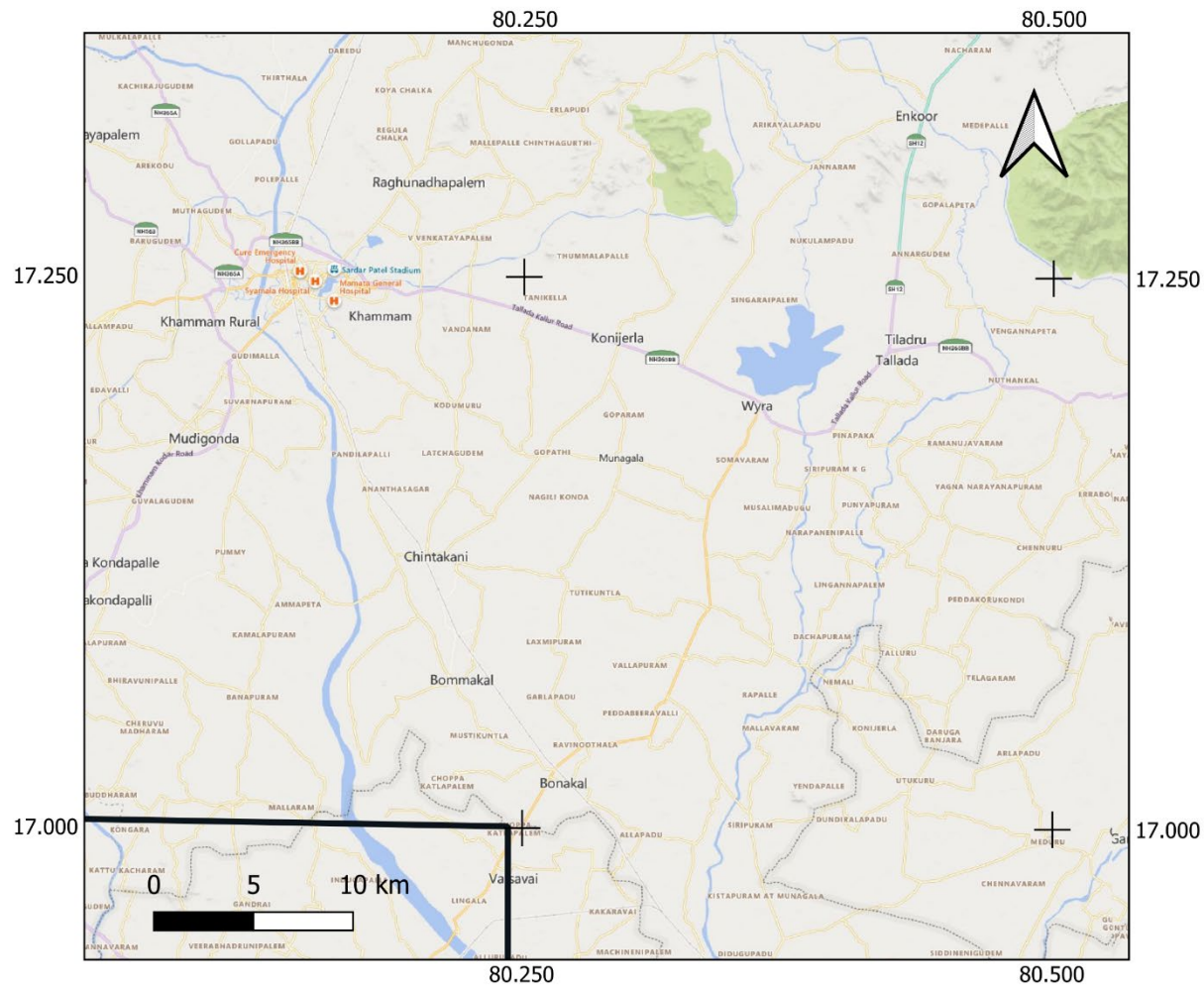


Figure 12.4.4.b: North to south trending Godavari Supergroup Shernawala Outliers between the EDC and the EGMB, marked by a band of lower amplitude magnetic anomalies, as follows: a) second vertical derivative of the anomalous magnetic field with the band of outliers indicated, b) geographic location (Microsoft® Bing™ Maps).

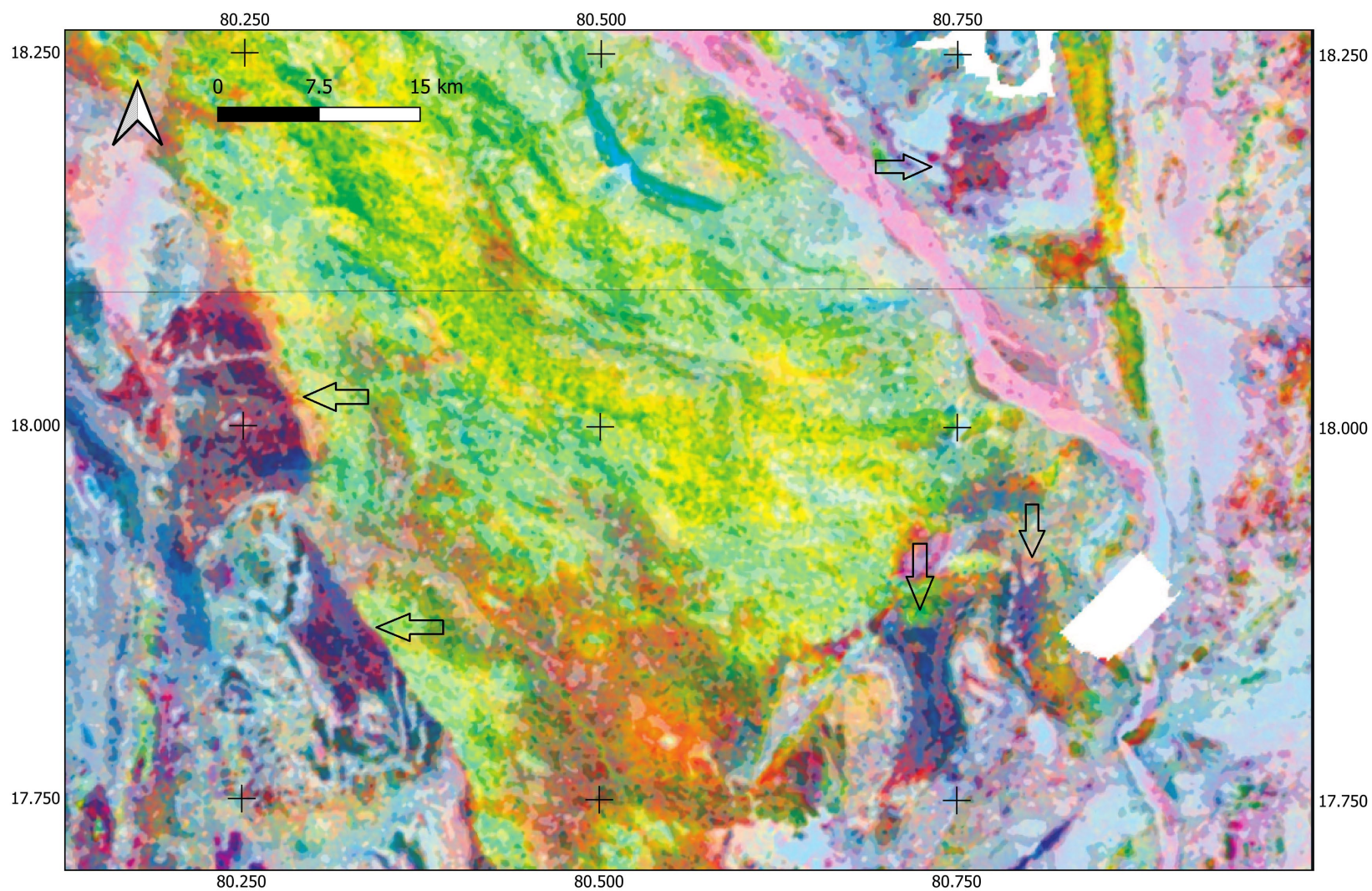


Figure 12.5.1.a: Potential potassic alteration apparent in Proterozoic age Godavari Supergroup sediments around the margins of the south end of the Godavari Graben, as follows: a) radiometric ternary image with areas of possible alteration indicated, b) geographic location (Microsoft® Bing™ Maps).

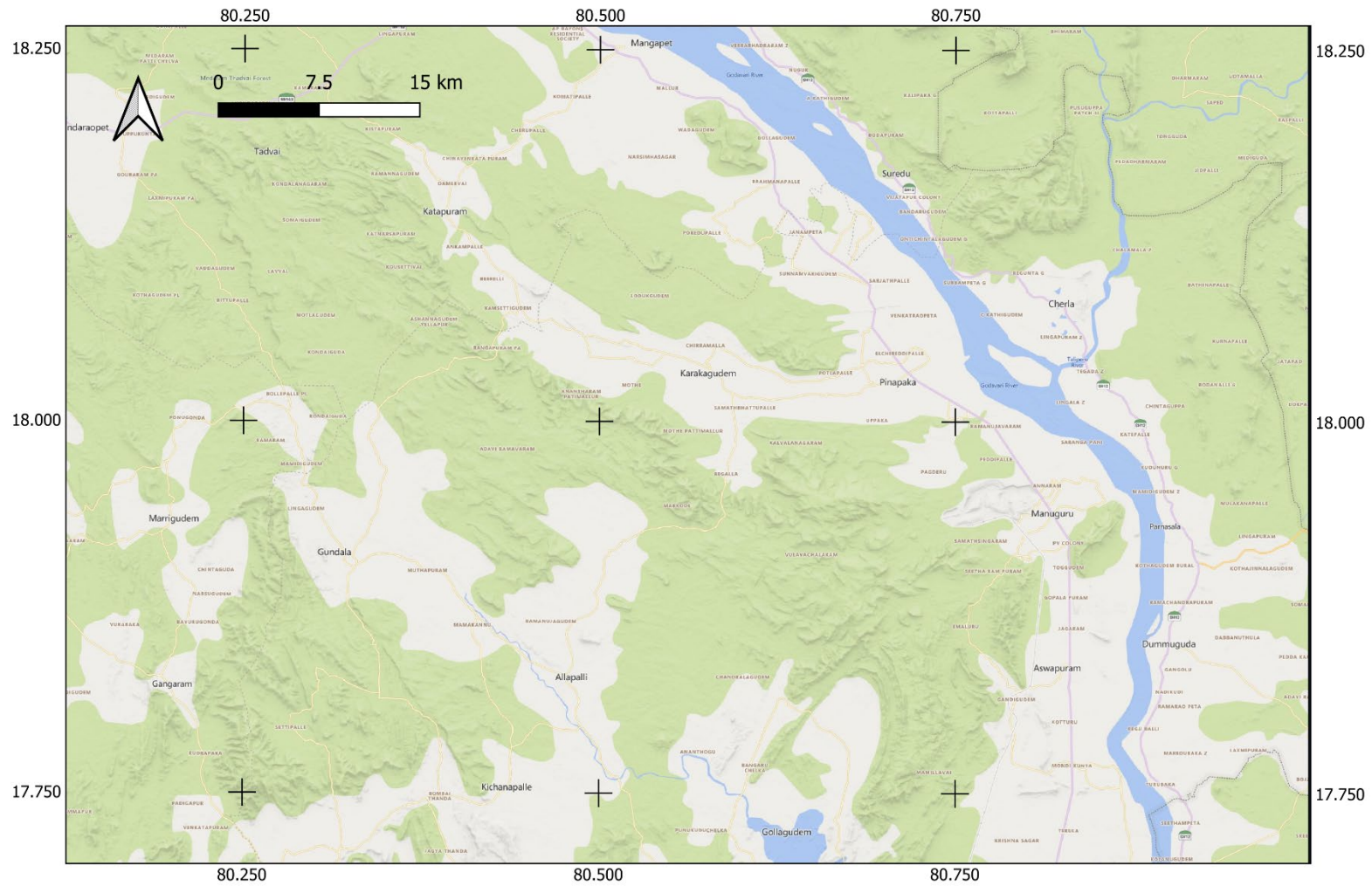


Figure 12.5.1.b: Potential potassic alteration apparent in Proterozoic age Godavari Supergroup sediments around the margins of the south end of the Godavari Graben, as follows: a) radiometric ternary image with areas of possible alteration indicated, b) geographic location (Microsoft® Bing™ Maps).

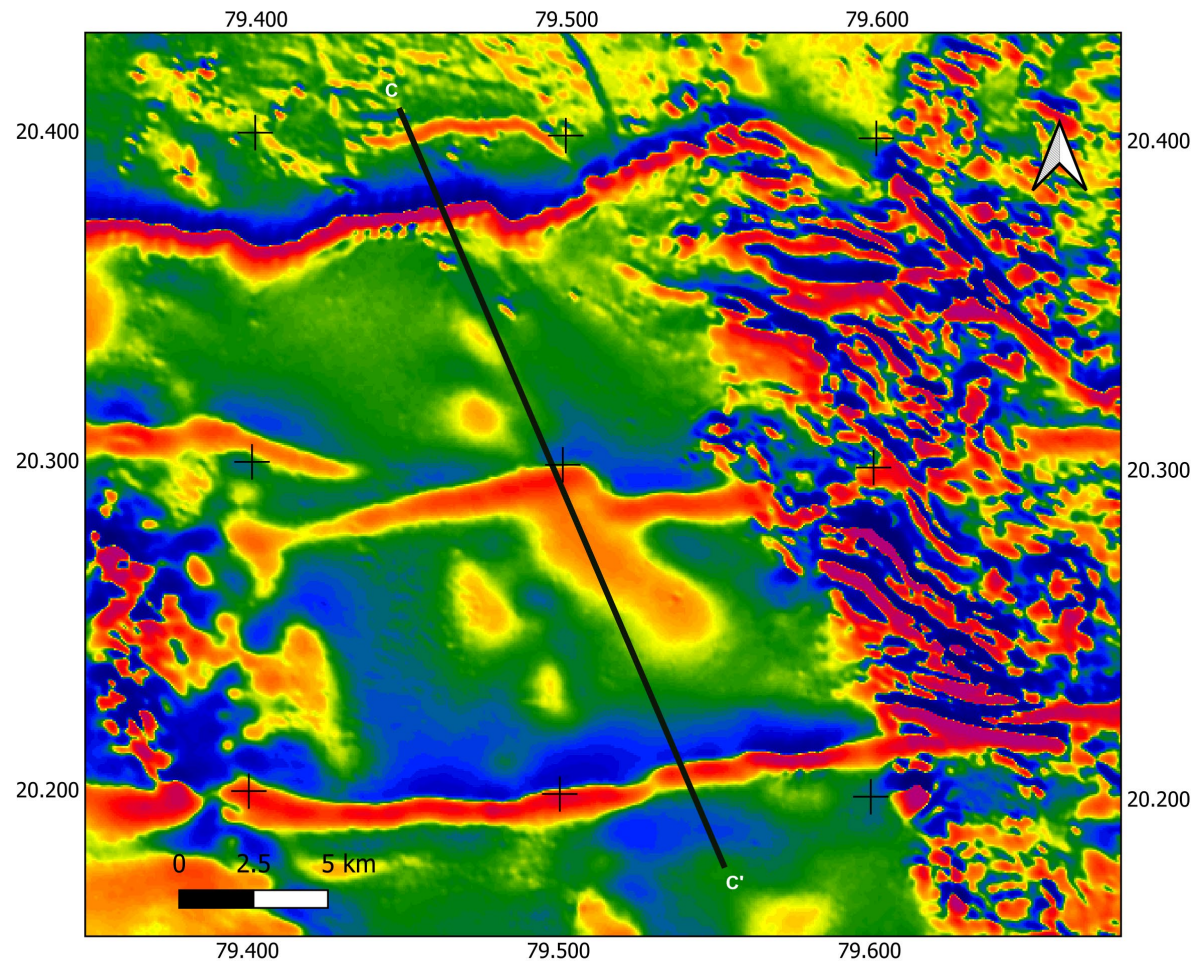


Figure 12.5.2.a: Cross section of the magnetic field in the north part of the East Belt Godavari Supergroup sediments, as follows: a) location of the cross section superimposed on the first vertical derivative of the anomalous magnetic field, crossing three east-west oriented linear magnetic anomalies ascribed to buried dykes, b) the magnetic field from the cross section, and the approximate depths of Euler solutions from the tops of the dykes below the surface of the sediments in metres.

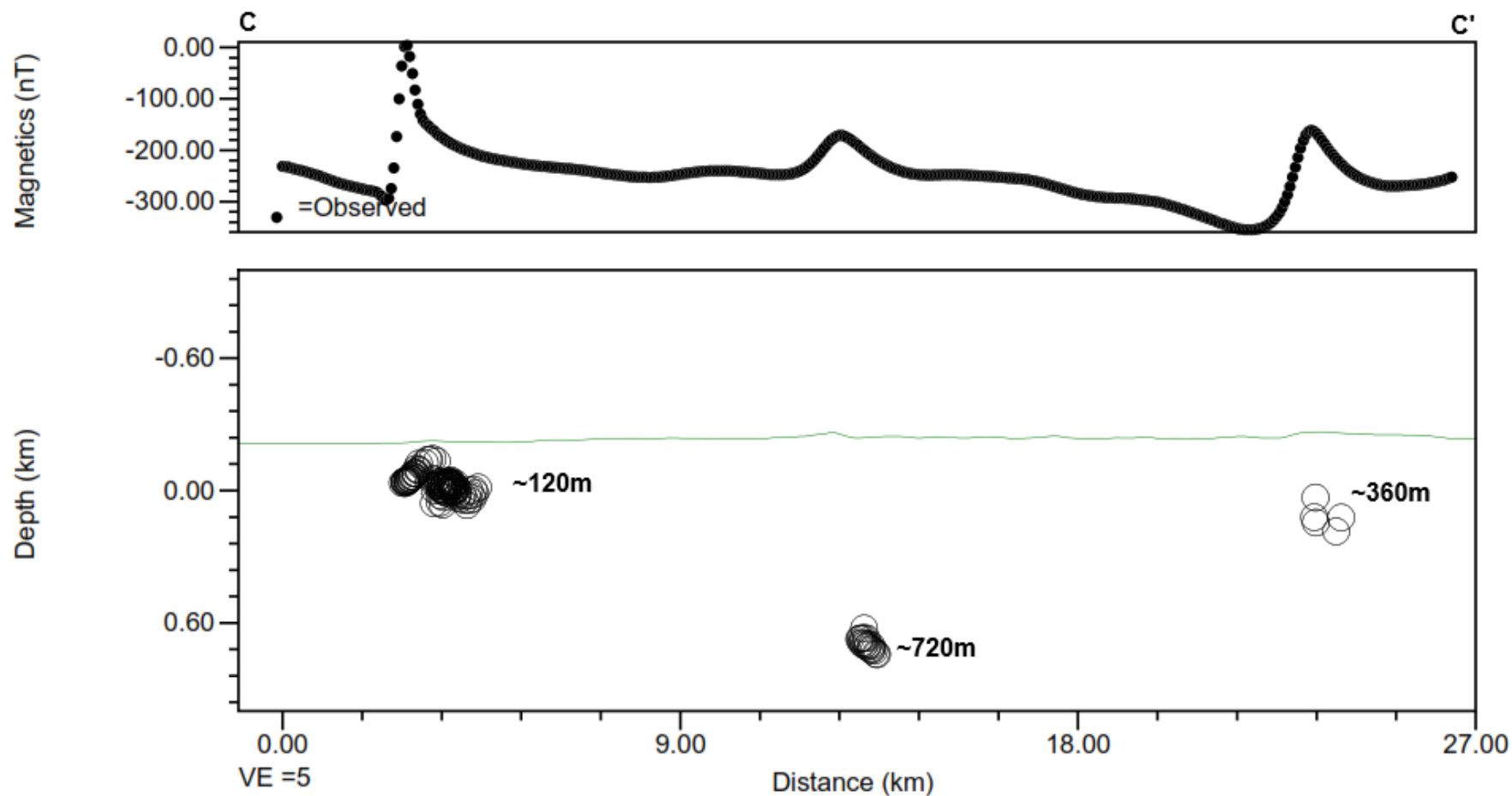


Figure 12.5.2.b: Cross section of the magnetic field in the north part of the East Belt Godavari Supergroup sediments, as follows: a) location of the cross section superimposed on the first vertical derivative of the anomalous magnetic field, crossing three east-west oriented linear magnetic anomalies ascribed to buried dykes, b) the magnetic field from the cross section, and the approximate depths of Euler solutions from the tops of the dykes below the surface of the sediments in metres.

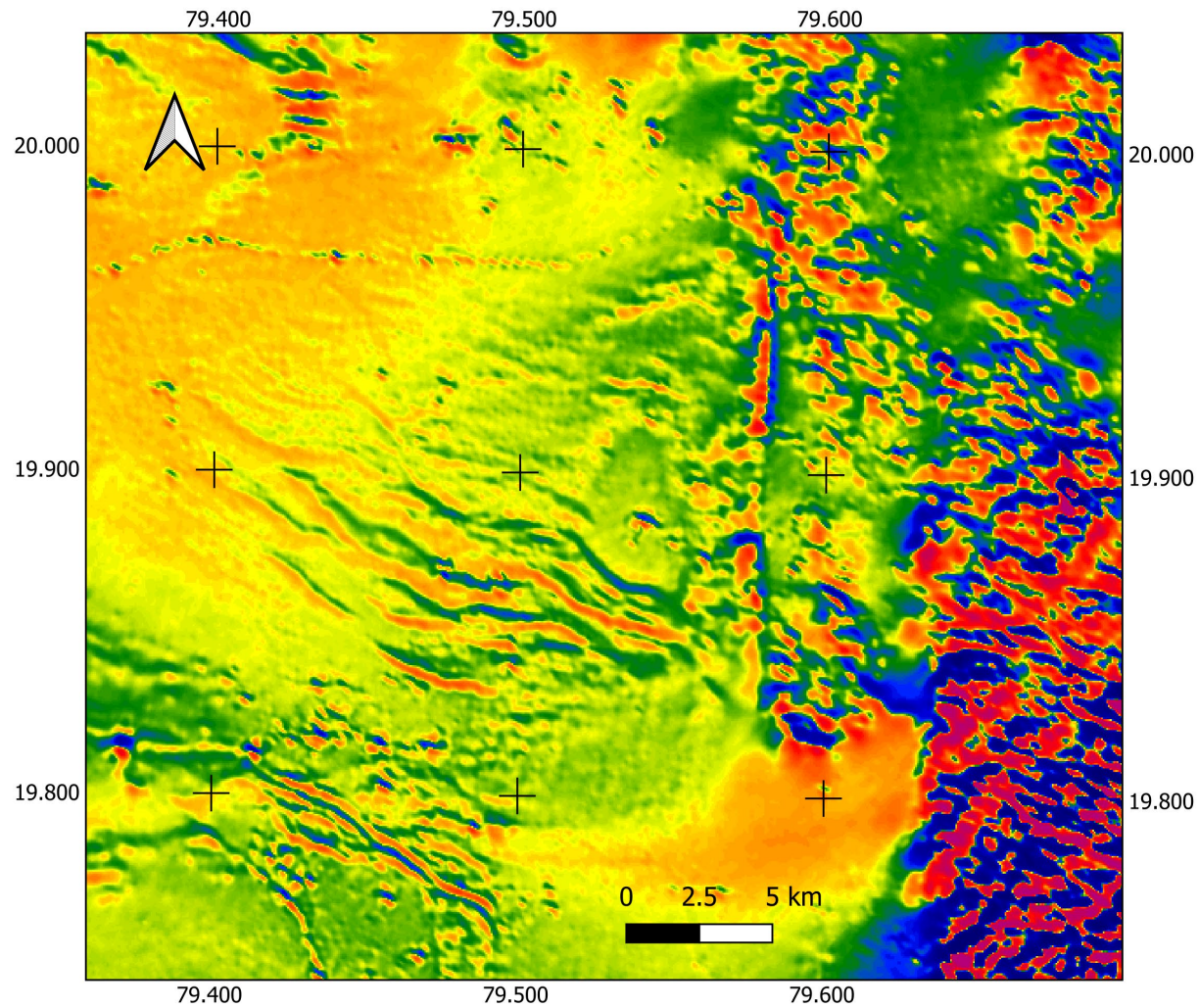


Figure 12.6.1.a: Fold structures in the sediments of the Godavari Supergroup in the northern part of the Godavari Rift, reflected in the magnetic data, as follows: a) first vertical derivative of the magnetic anomaly, b) geographic location (Microsoft® Bing™ Maps).

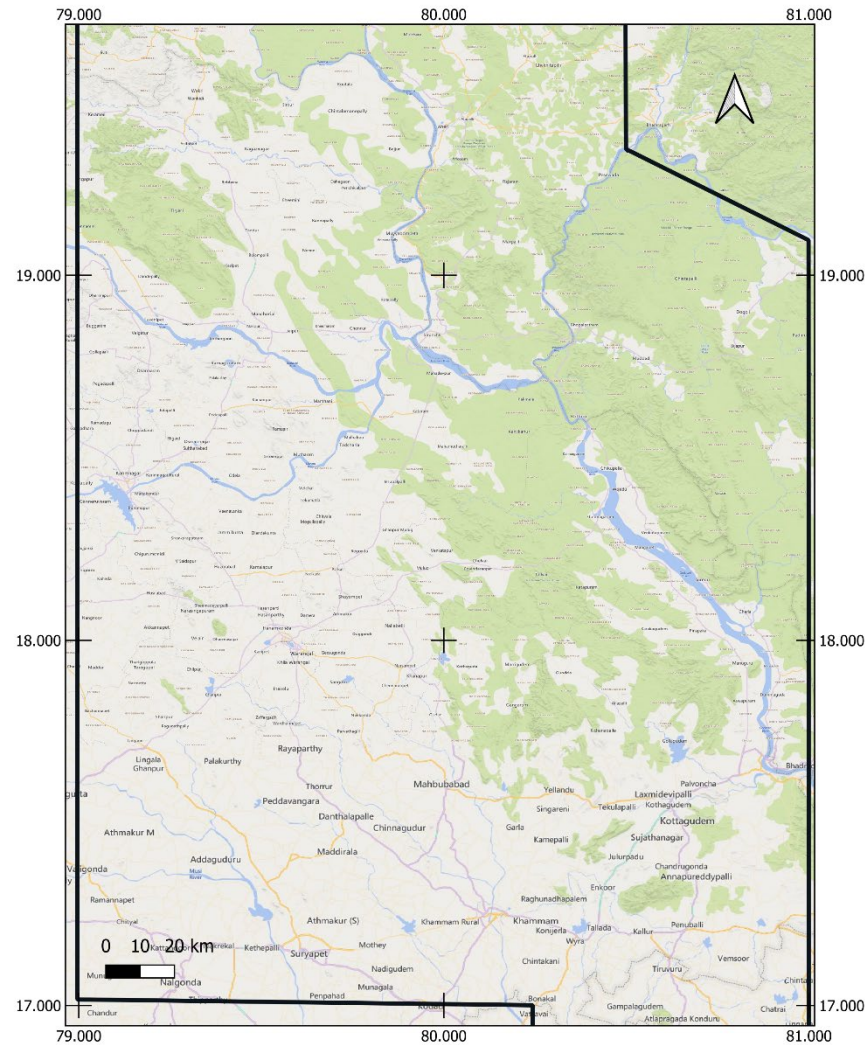


Figure 12.6.1.b: Fold structures in the sediments of the Godavari Supergroup in the northern part of the Godavari Rift, reflected in the magnetic data, as follows: a) first vertical derivative of the magnetic anomaly, b) geographic location (Microsoft® Bing™ Maps).

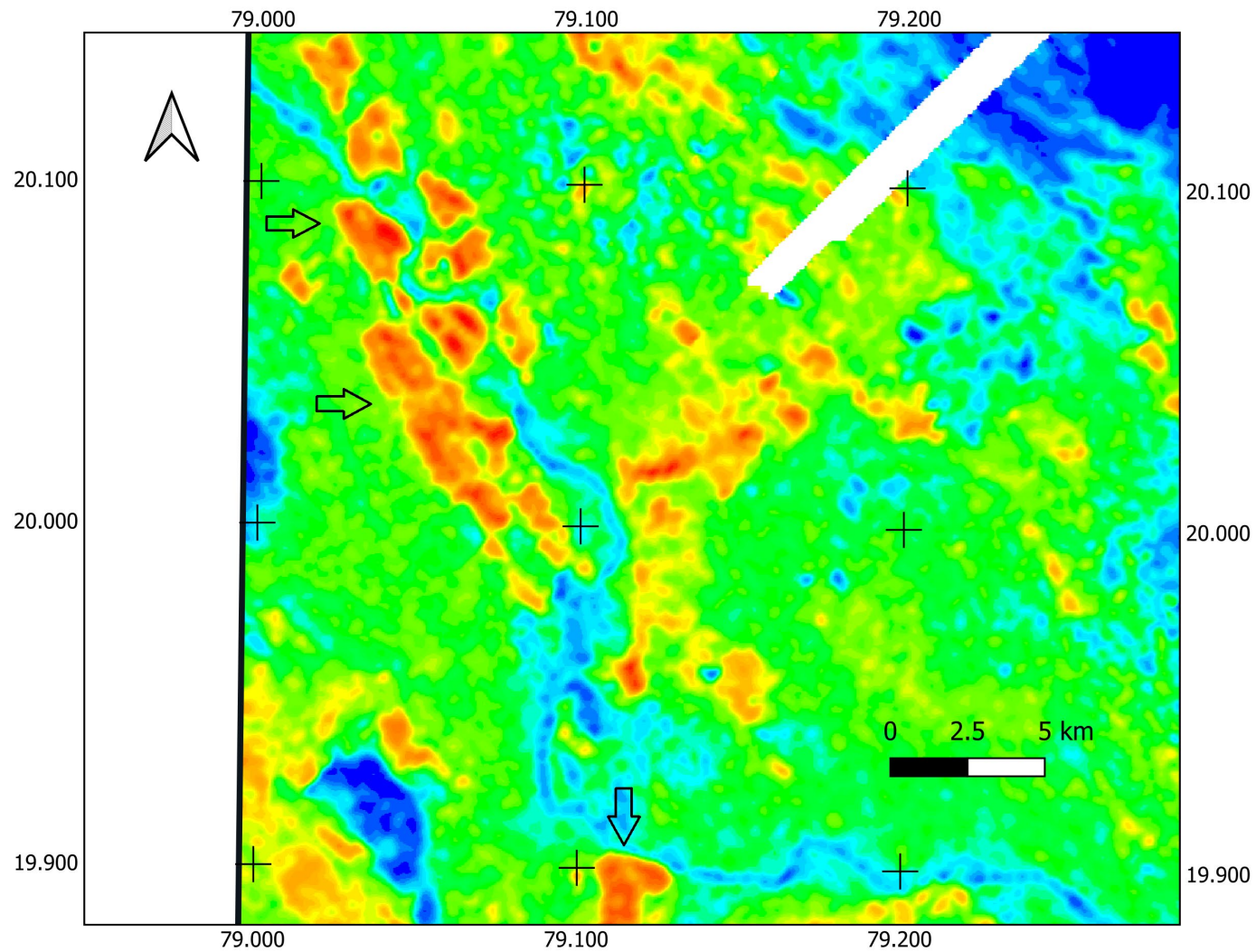


Figure 12.6.2.a: Gamma-ray anomalies associated with open coal mines in the lower formations of the Godavari Supergroup near Chadrapur, in the north of Block-6, as follows: a) potassium concentration with open pits indicated, b) geographic location (Microsoft® Bing™ Maps).

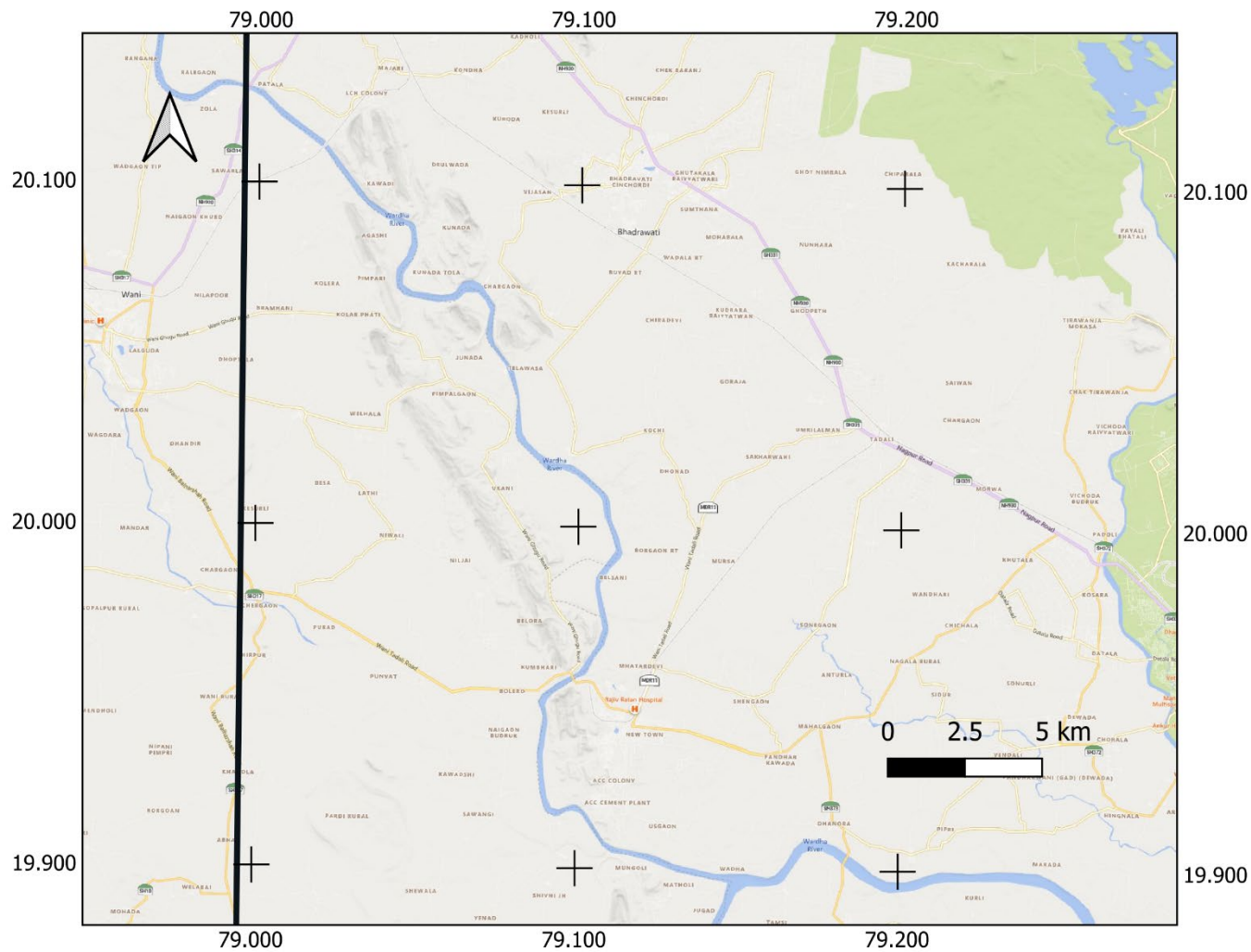


Figure 12.6.2.b: Gamma-ray anomalies associated with open coal mines in the lower formations of the Godavari Supergroup near Chadrapur, in the north of Block-6, as follows: a) potassium concentration with open pits indicated, b) geographic location (Microsoft® Bing™ Maps).

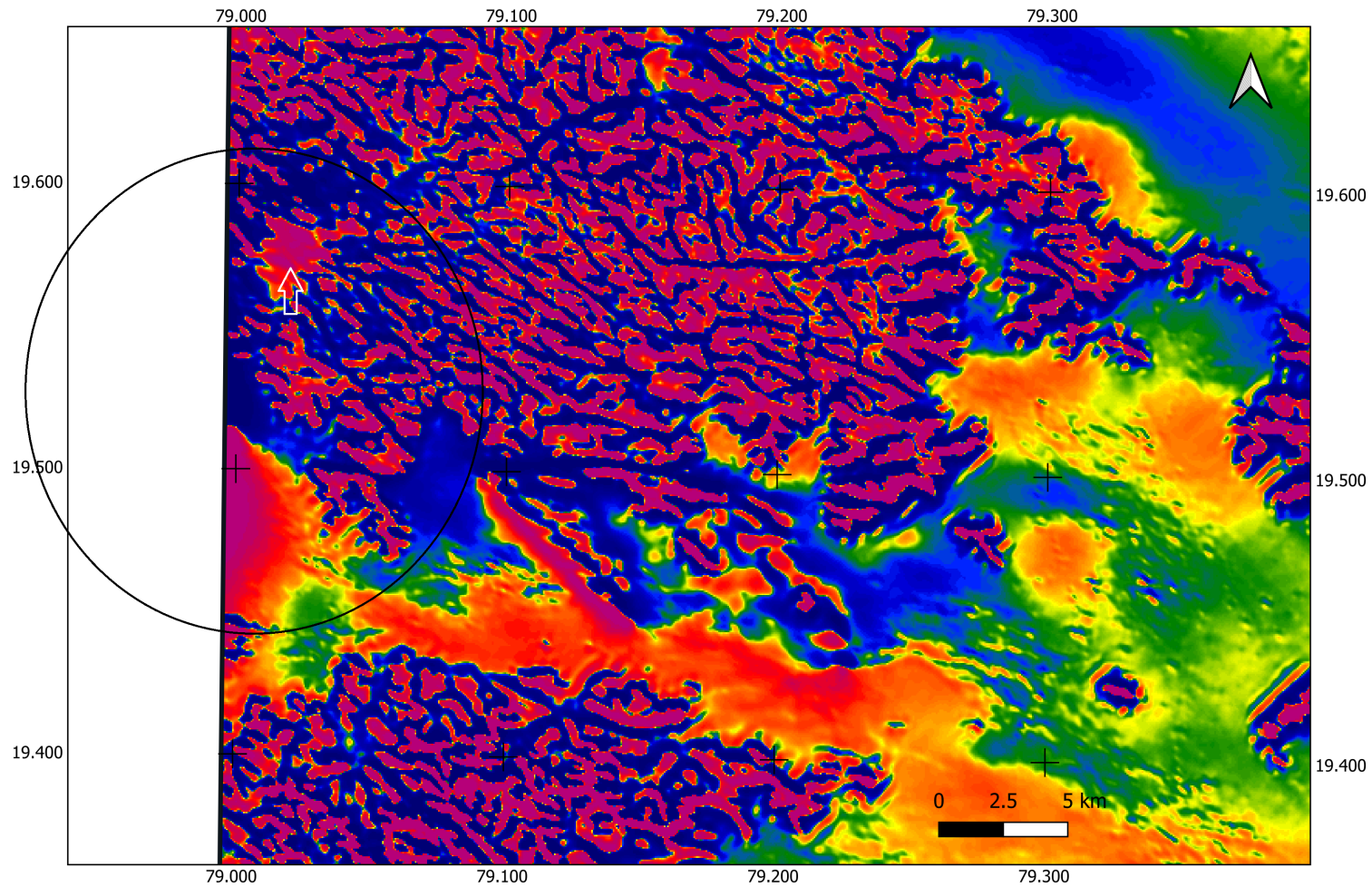


Figure 12.8.1.a: Dipolar magnetic anomaly in the Eastern Dharwar Craton, partially obscured by strong short wavelength magnetic anomalies due to the Deccan Traps basaltic lava flows, as follows: a) first vertical derivative of the magnetic anomaly with the dipolar anomaly outlined in black and a local magnetic high indicated, b) geographic location (Microsoft® Bing™ Maps).

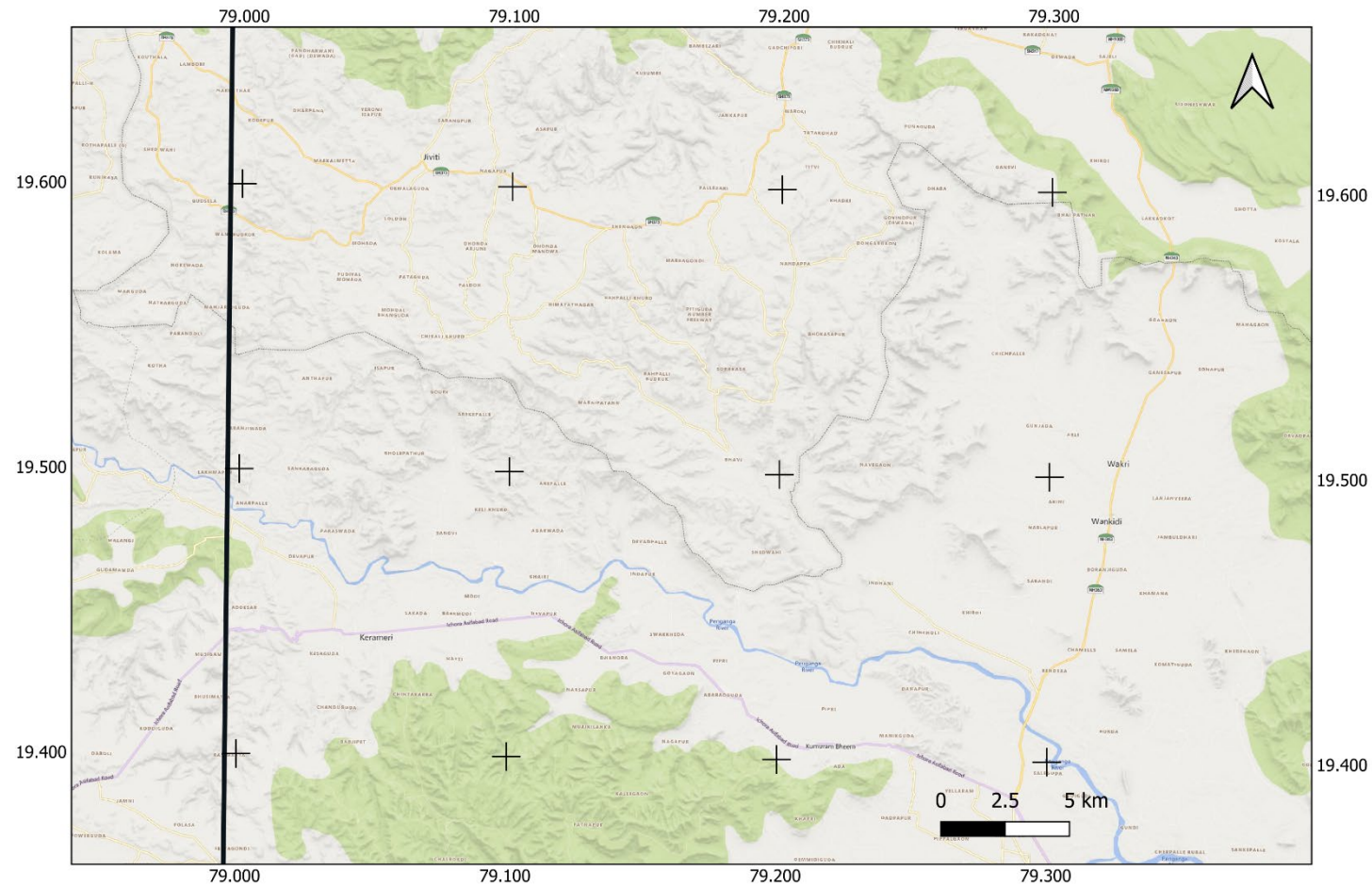


Figure 12.8.1.b: Dipolar magnetic anomaly in the Eastern Dharwar Craton, partially obscured by strong short wavelength magnetic anomalies due to the Deccan Traps basaltic lava flows, as follows: a) first vertical derivative of the magnetic anomaly with the dipolar anomaly outlined in black and a local magnetic high indicated, b) geographic location (Microsoft® Bing™ Maps).

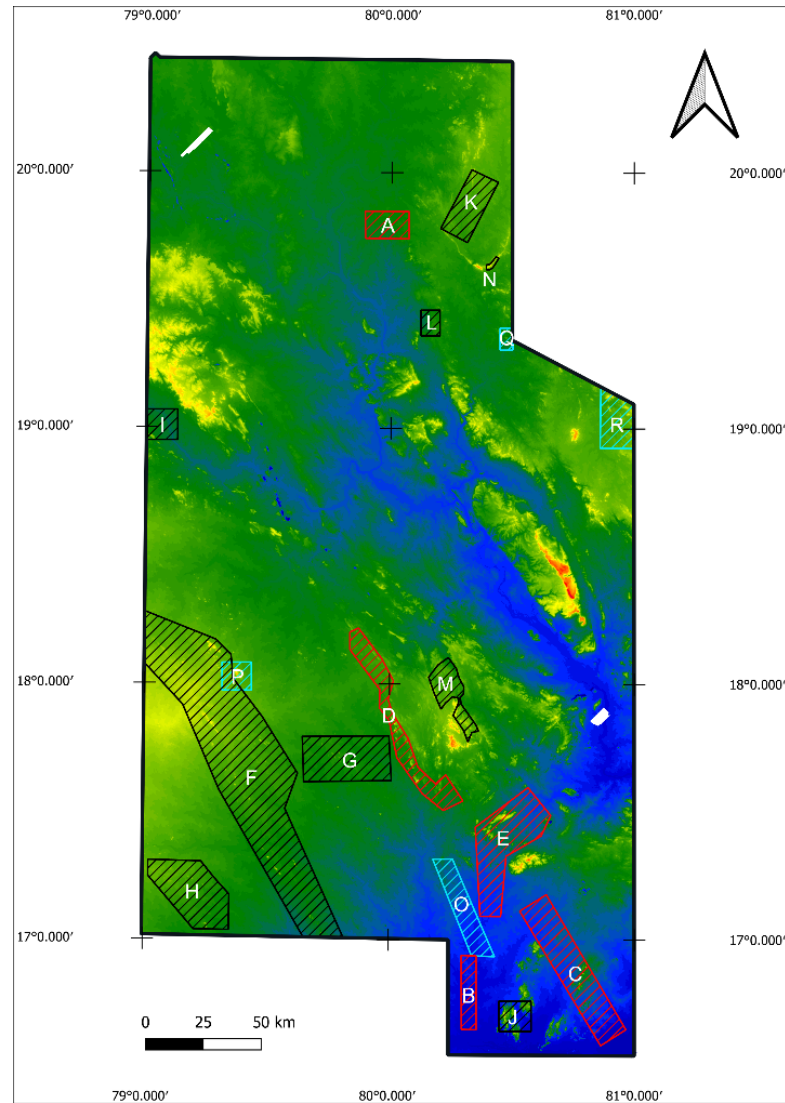


Figure 12.9.1: Main target areas for follow up exploration for potential economic targets in Block-6, superimposed on the digital elevation model, as follows: high priority areas A-E shown in red, medium priority areas F-N shown in black, low priority areas O-R are shown in blue.

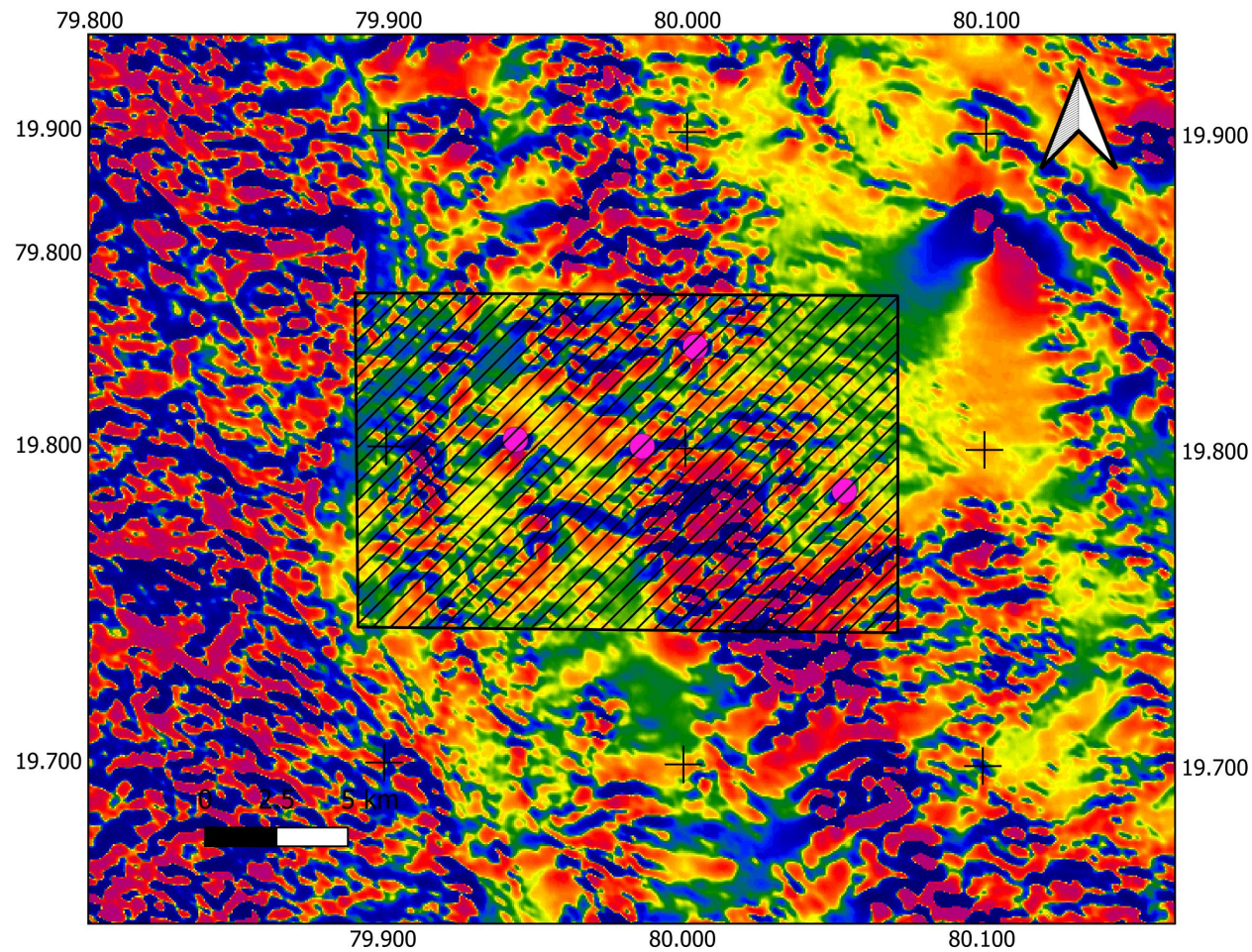


Figure 12.9.2: High priority Target Area A with four identified potential kimberlite pipes, anomalies 2, 3, 17, and 22, shown on the anomalous magnetic field of the Bastar Craton.

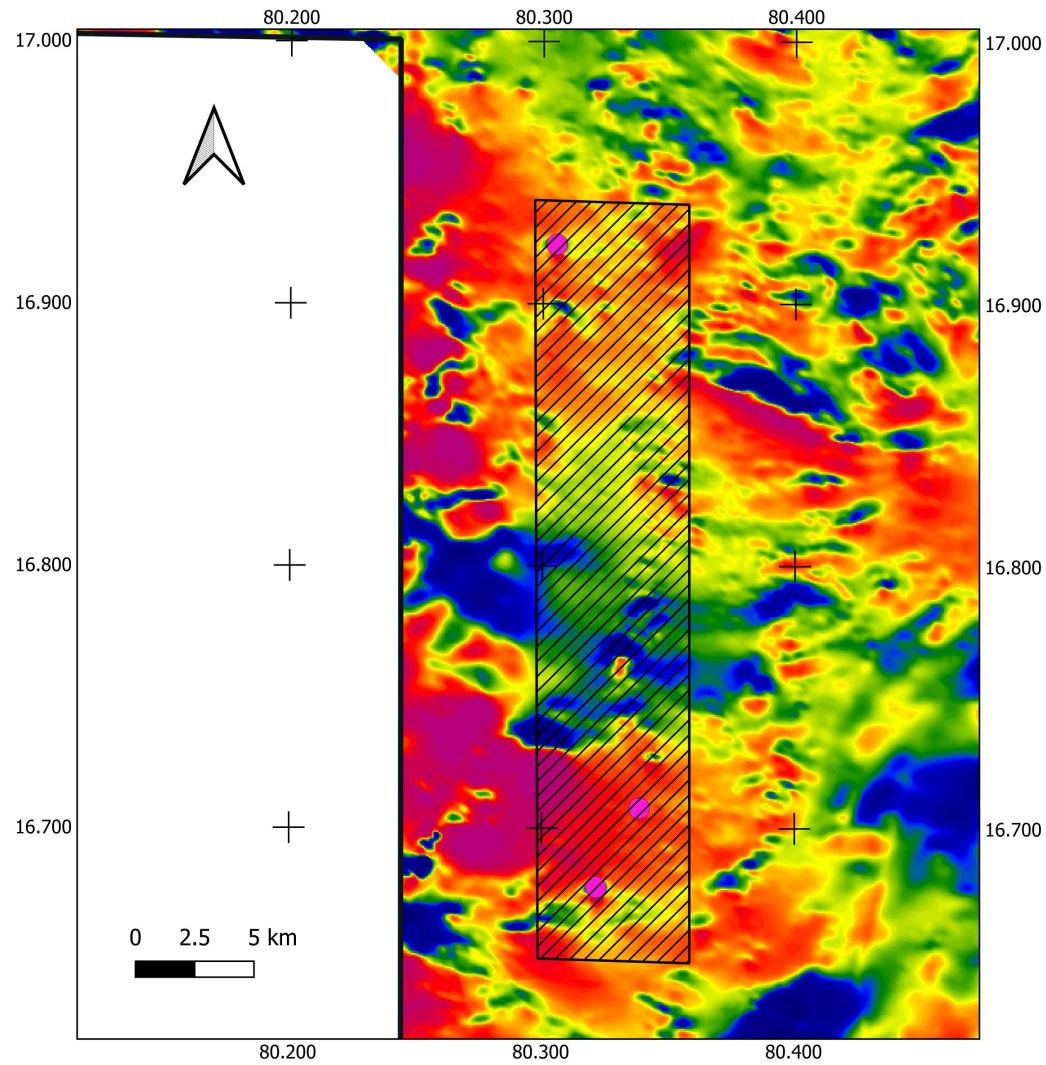


Figure 12.9.3: High priority Target Area B with three identified potential kimberlite pipes, anomalies 4, 9, and 20, shown on the anomalous magnetic field of the Eastern Ghats Mobile Belt.

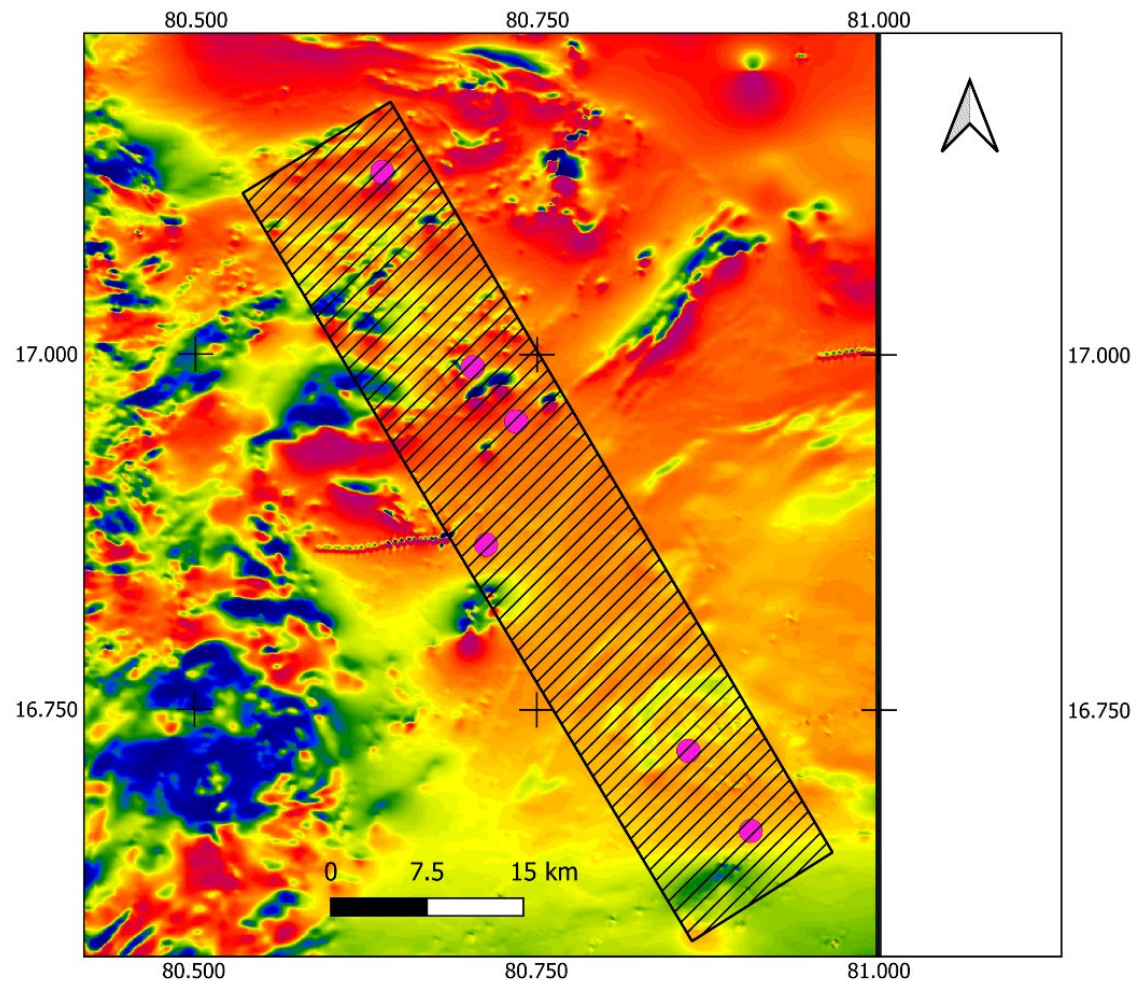


Figure 12.9.4: High priority Target Area C with six identified potential kimberlite pipes, anomalies 1, 6, 7, 8, 13, and 15, shown on the anomalous magnetic field of the Eastern Ghats Mobile Belt.

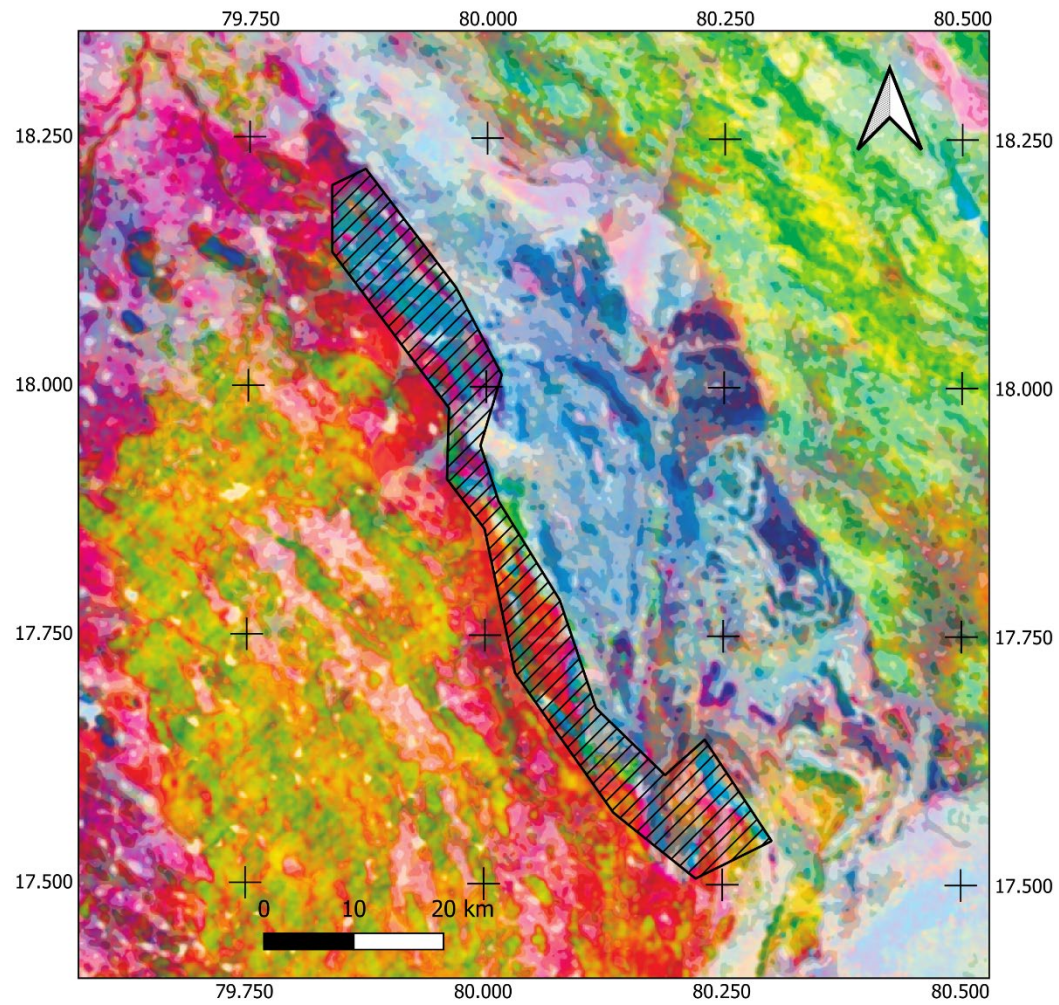


Figure 12.9.5: High priority Target Area D, the unconformity between the Eastern Dharwar Craton and the Godavari Supergroup, shown on the radiometric ternary image.

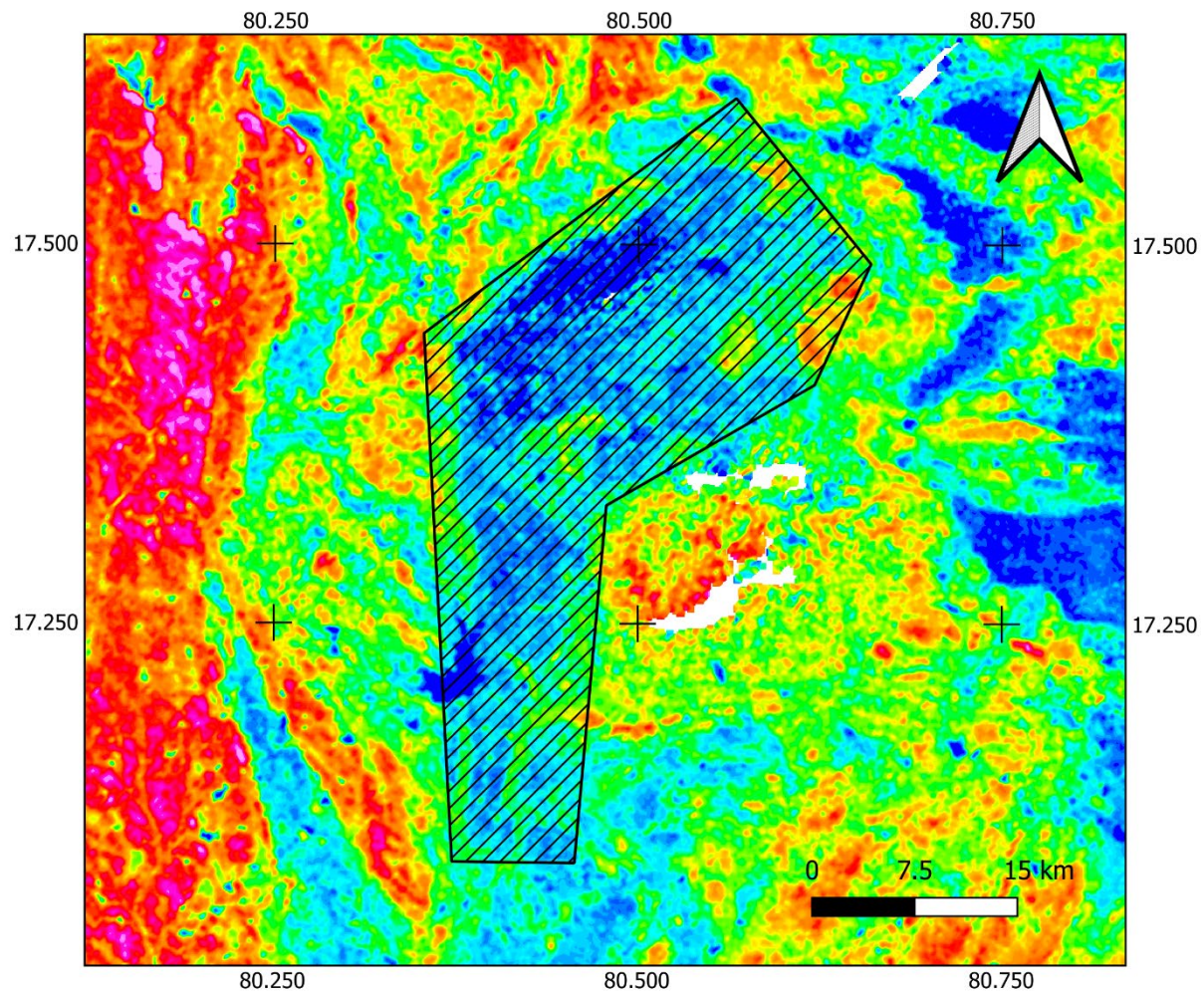


Figure 12.9.6: High priority Target Area E, the Chimalpahad Complex, shown on the potassium concentration of the Eastern Ghats Mobile Belt.

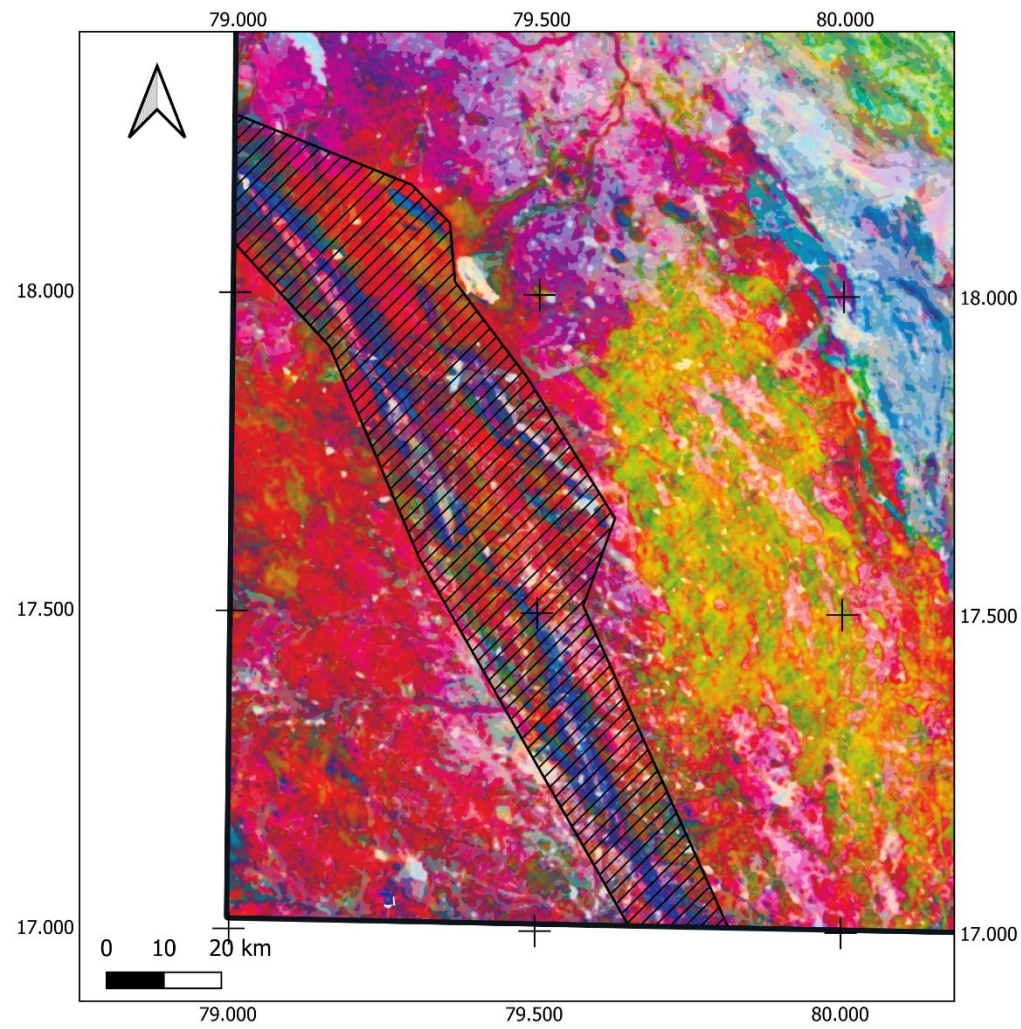


Figure 12.9.7: Medium priority Target Area F, bands of leucogranite, shown on the radiometric ternary image of the Eastern Dharwar Craton.

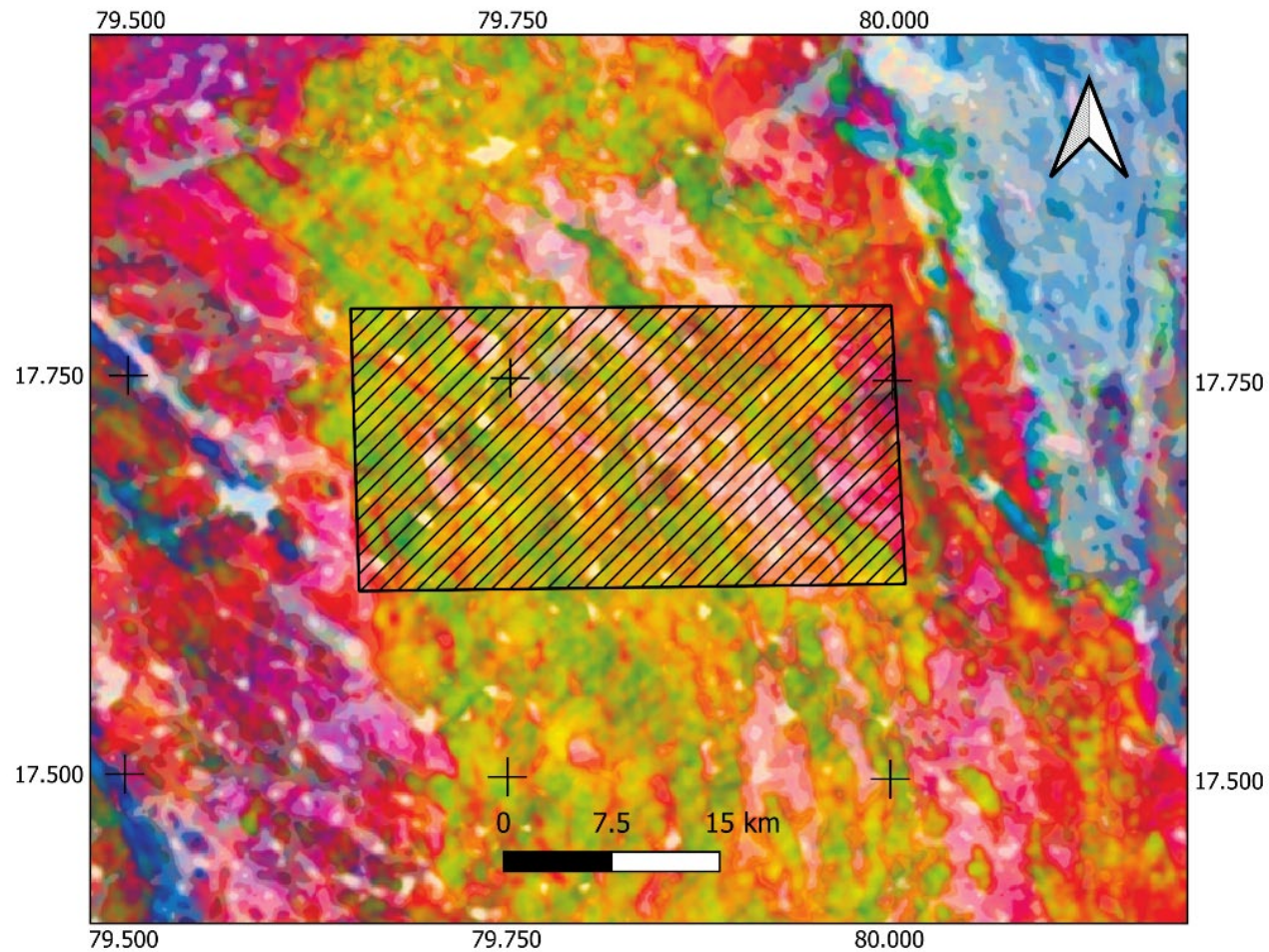


Figure 12.9.8: Medium priority Target Area G, sub-linear features high in uranium and thorium, shown on the thorium concentration of the Eastern Dharwar Craton.

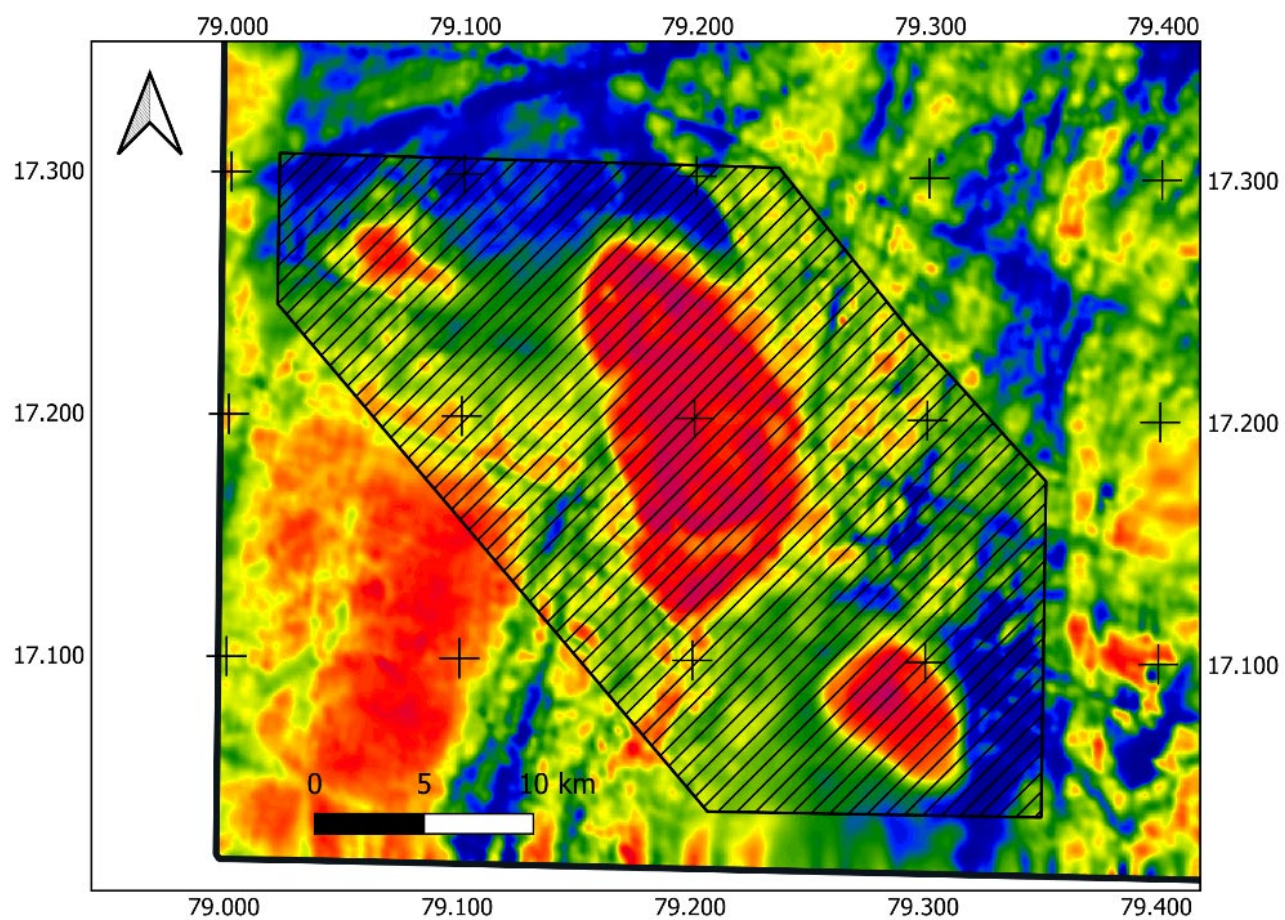


Figure 12.9.9: Medium priority Target Area H, intrusions of a potentially alkaline nature, shown on the magnetic anomaly reduced to the pole of the Eastern Dharwar Craton.

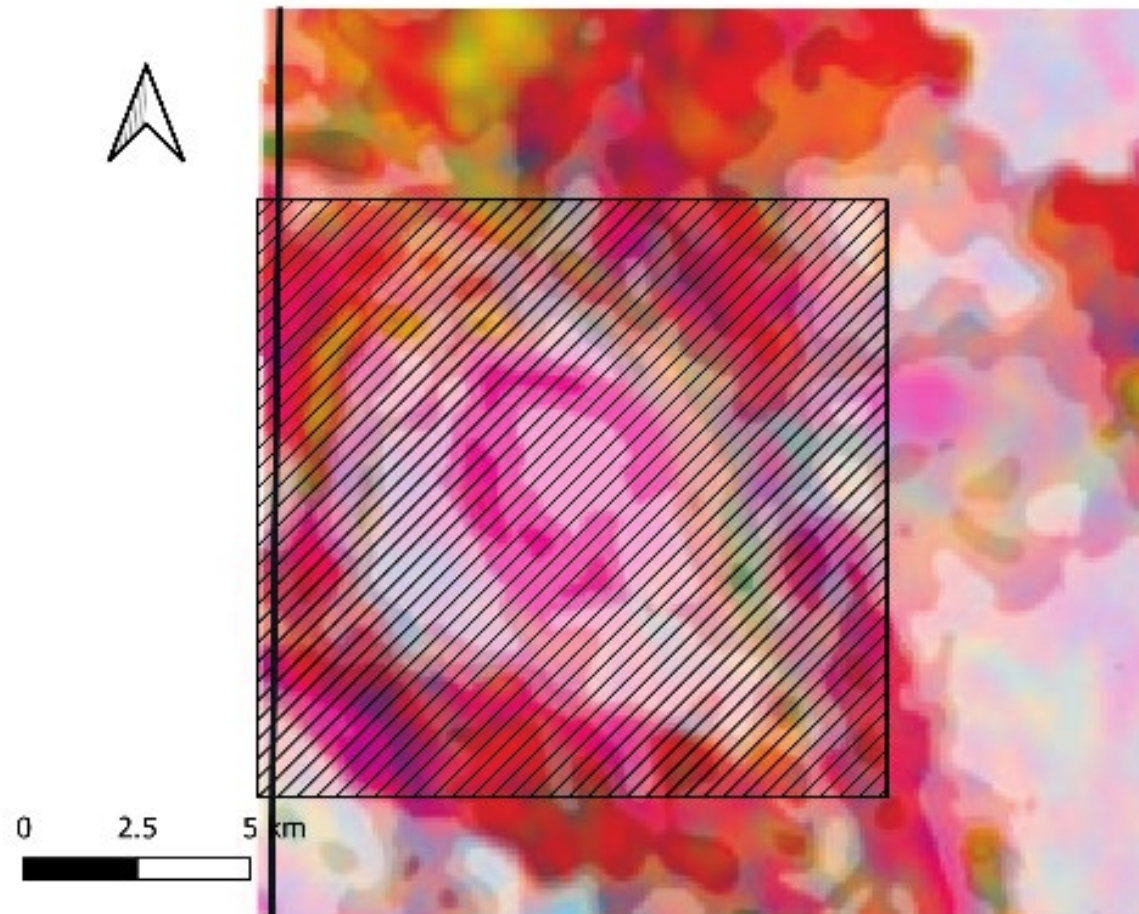


Figure 12.9.10: Medium priority Target Area I, intrusion of a potentially alkaline nature, shown on the radiometric ternary image of the Eastern Dharwar Craton.

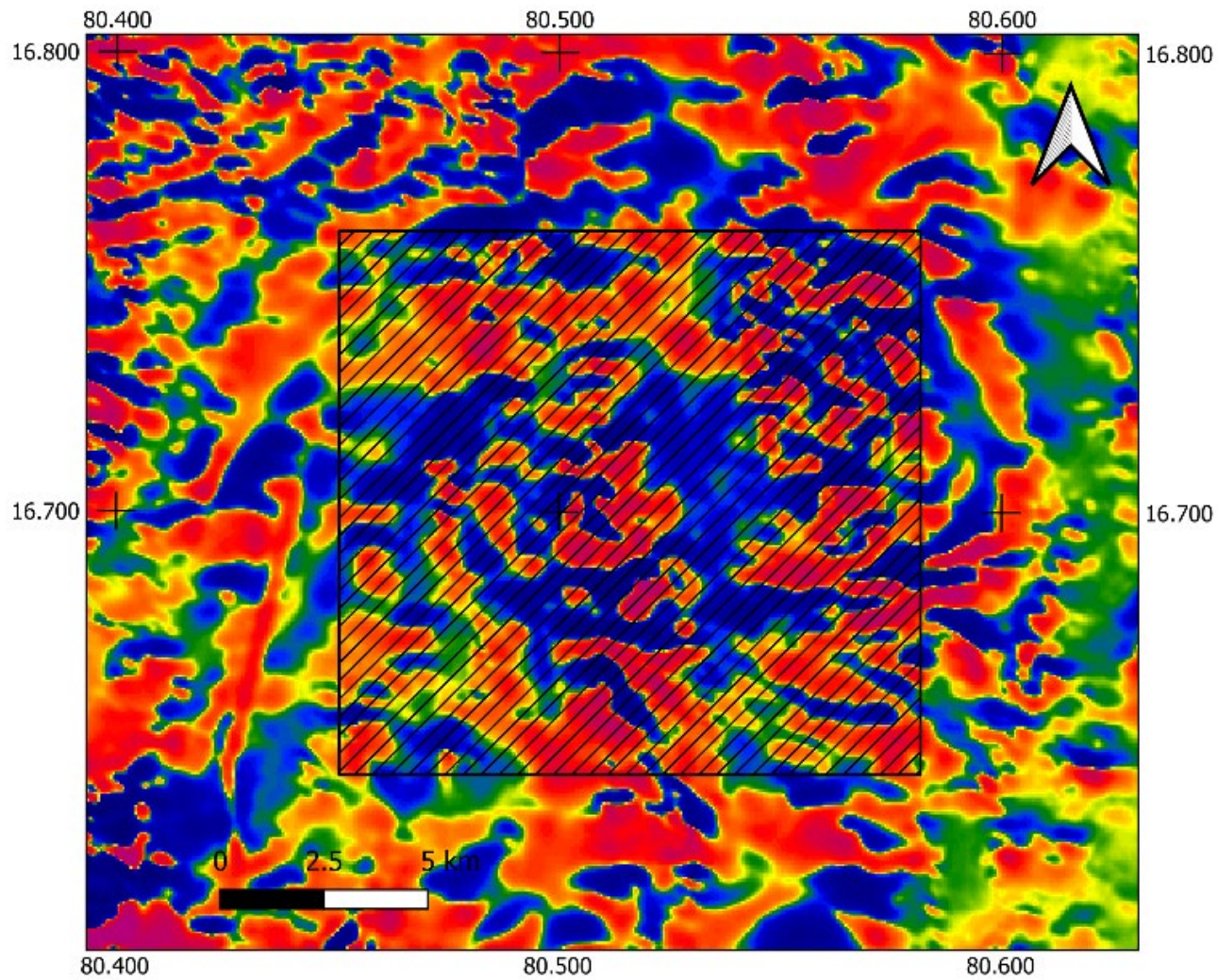


Figure 12.9.11: Medium priority Target Area J, possible intrusion of a potentially alkaline nature, shown on the magnetic anomaly of the Eastern Ghats Mobile Belt.

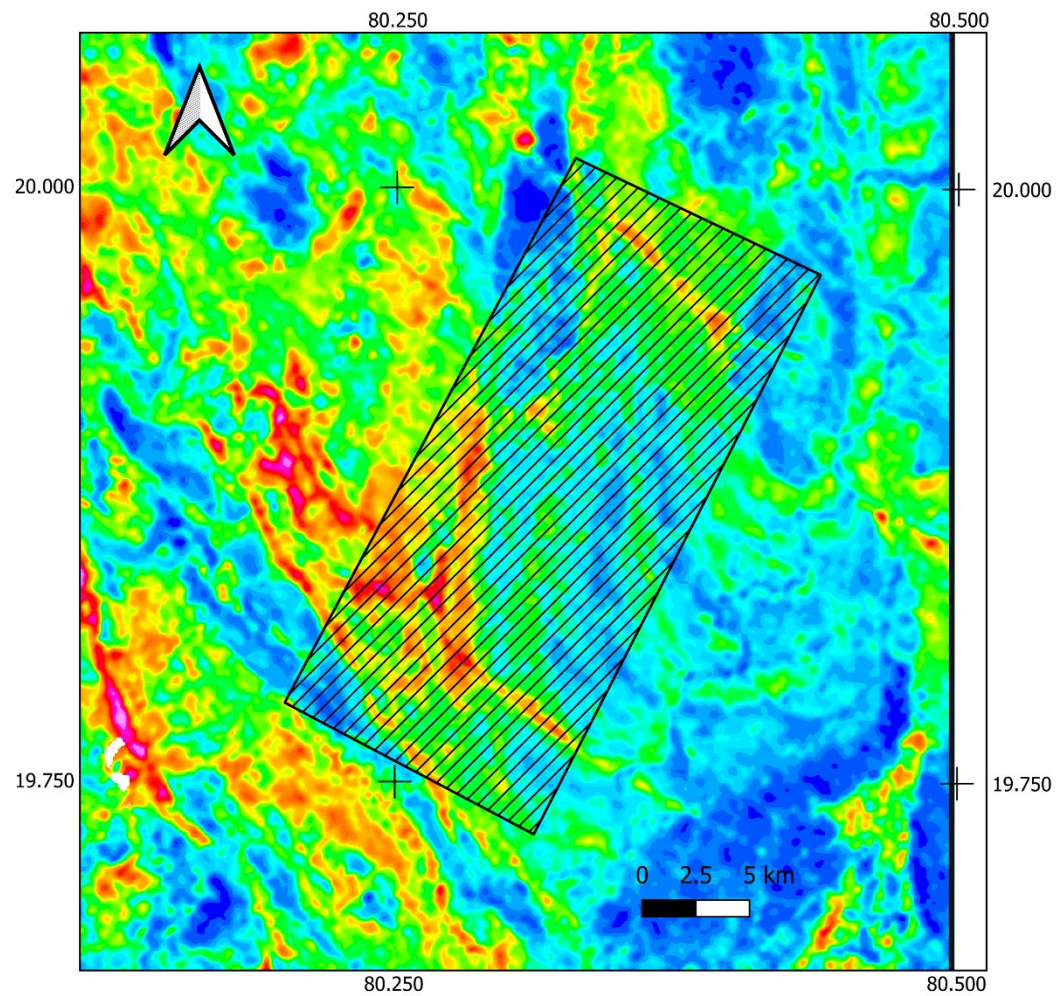


Figure 12.9.12: Medium priority Target Area K, alteration along fractures and the margins of the Dongargarh Granite, shown on the thorium over potassium ratio of the Bastar Craton.

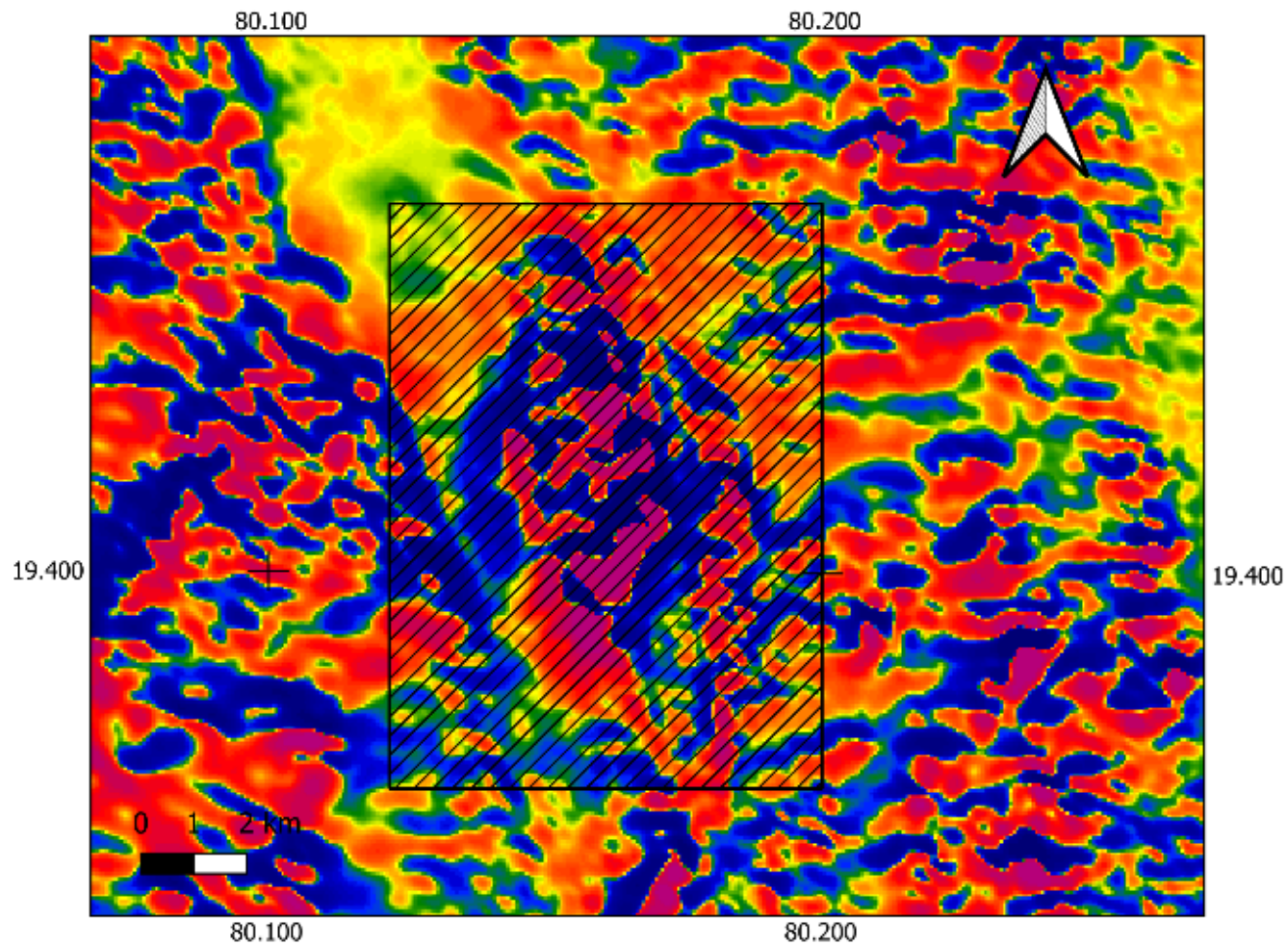


Figure 12.9.13: Medium priority Target Area L, area of high magnetism within a band of interpreted supracrustal rocks that may be related to volcanogenic massive sulphide mineralization, shown on the magnetic anomaly of the Bastar Craton.

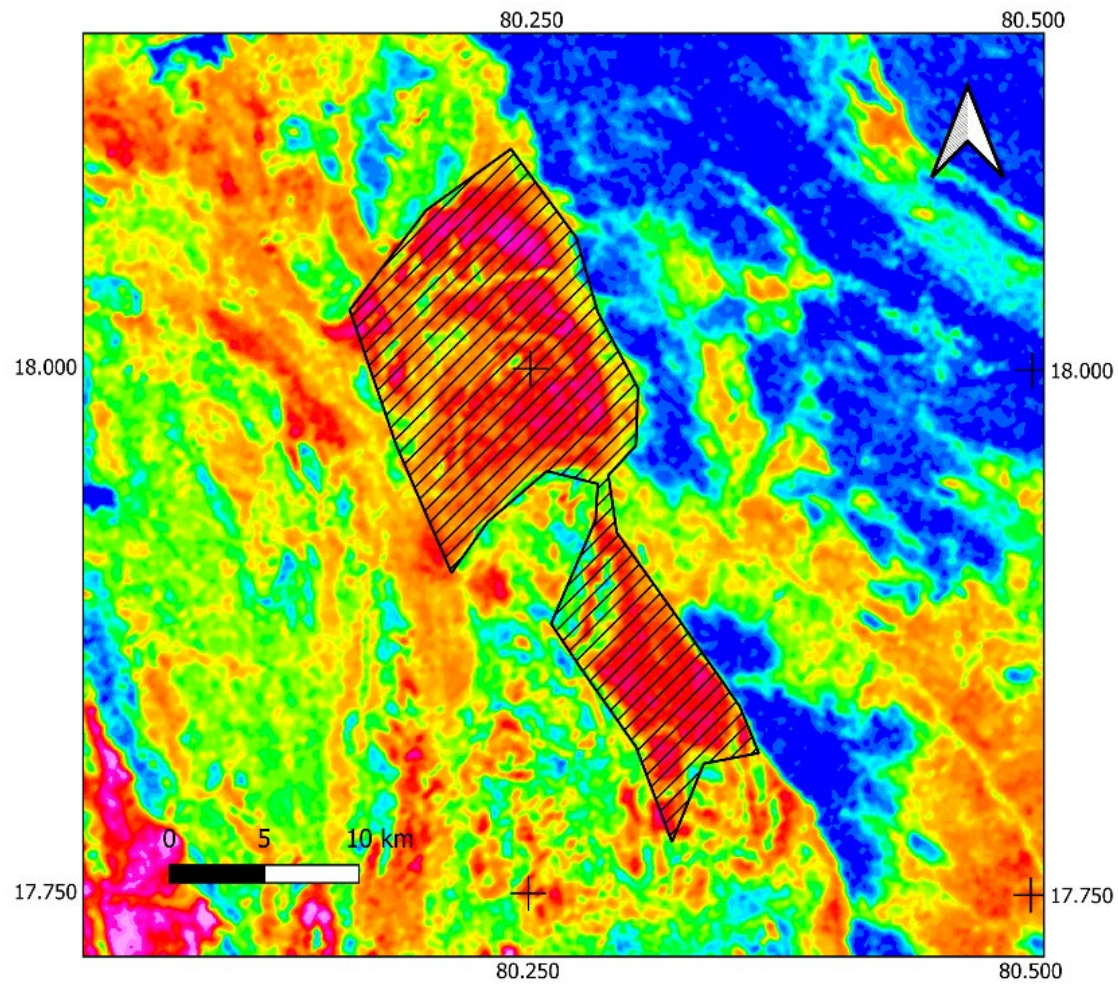


Figure 12.9.14: Medium priority Target Area M, areas of Godavari Supergroup sediments that are locally higher in potassium than elsewhere in the same mapped formations, shown on the potassium concentration of the Godavari Supergroup.

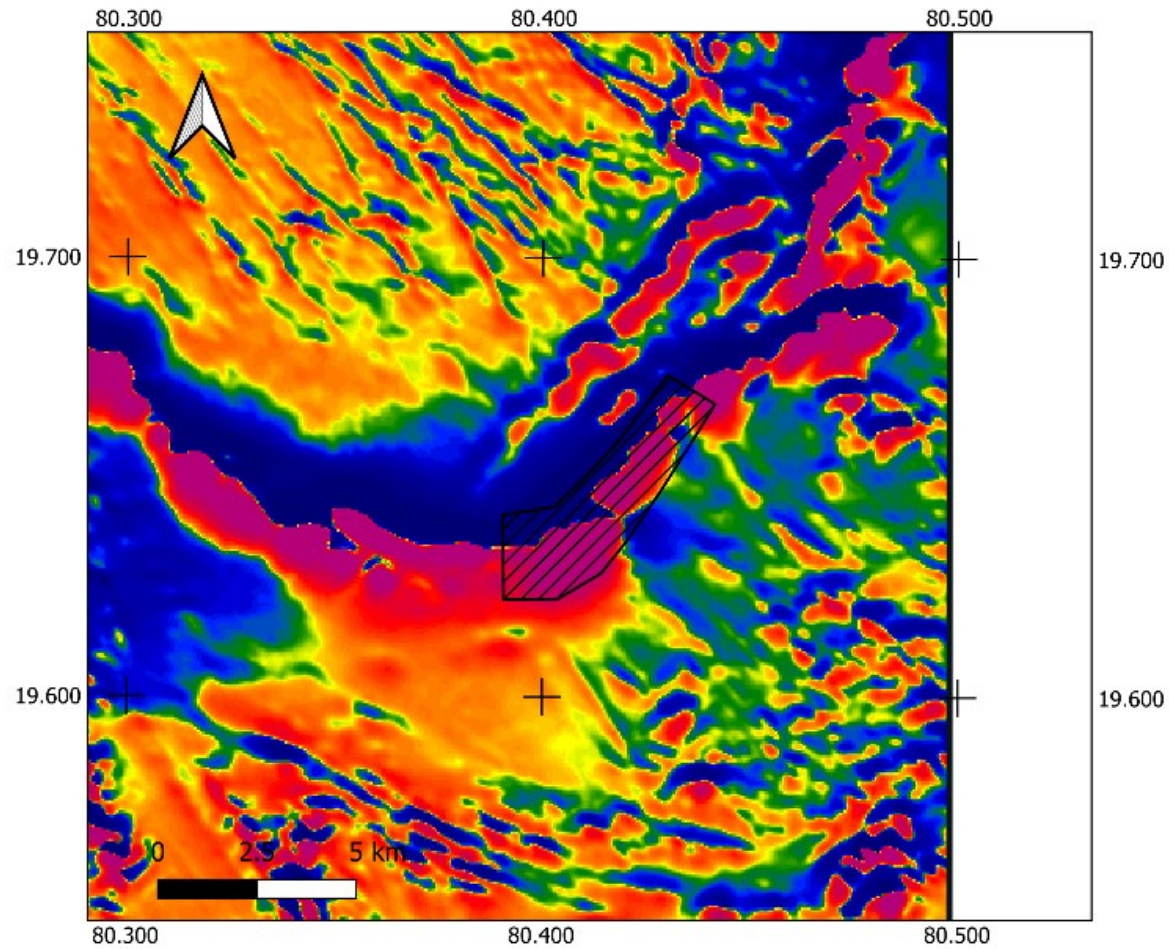


Figure 12.9.15: Medium priority Target Area N, previously mapped Bailadila Formation banded ironstone formation with a strong magnetic anomaly and fold structures that may act as a structural trap for enrichment, shown on the magnetic anomaly of the Bastar Craton.

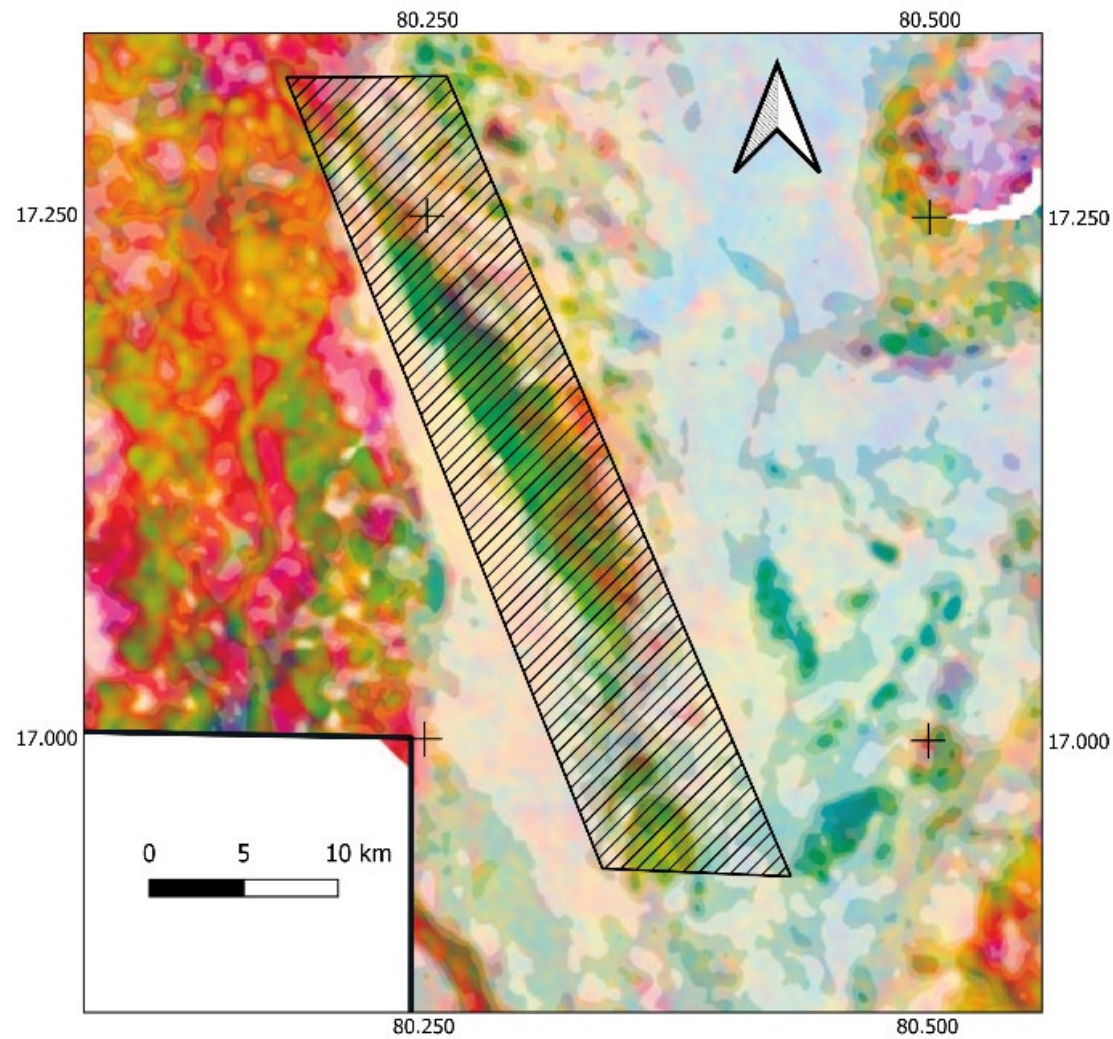


Figure 12.9.16: Low priority Target Area O, a line of previously mapped alkaline granites with high uranium and thorium character, shown on the radiometric ternary image of the Eastern Ghats Mobile Belt.

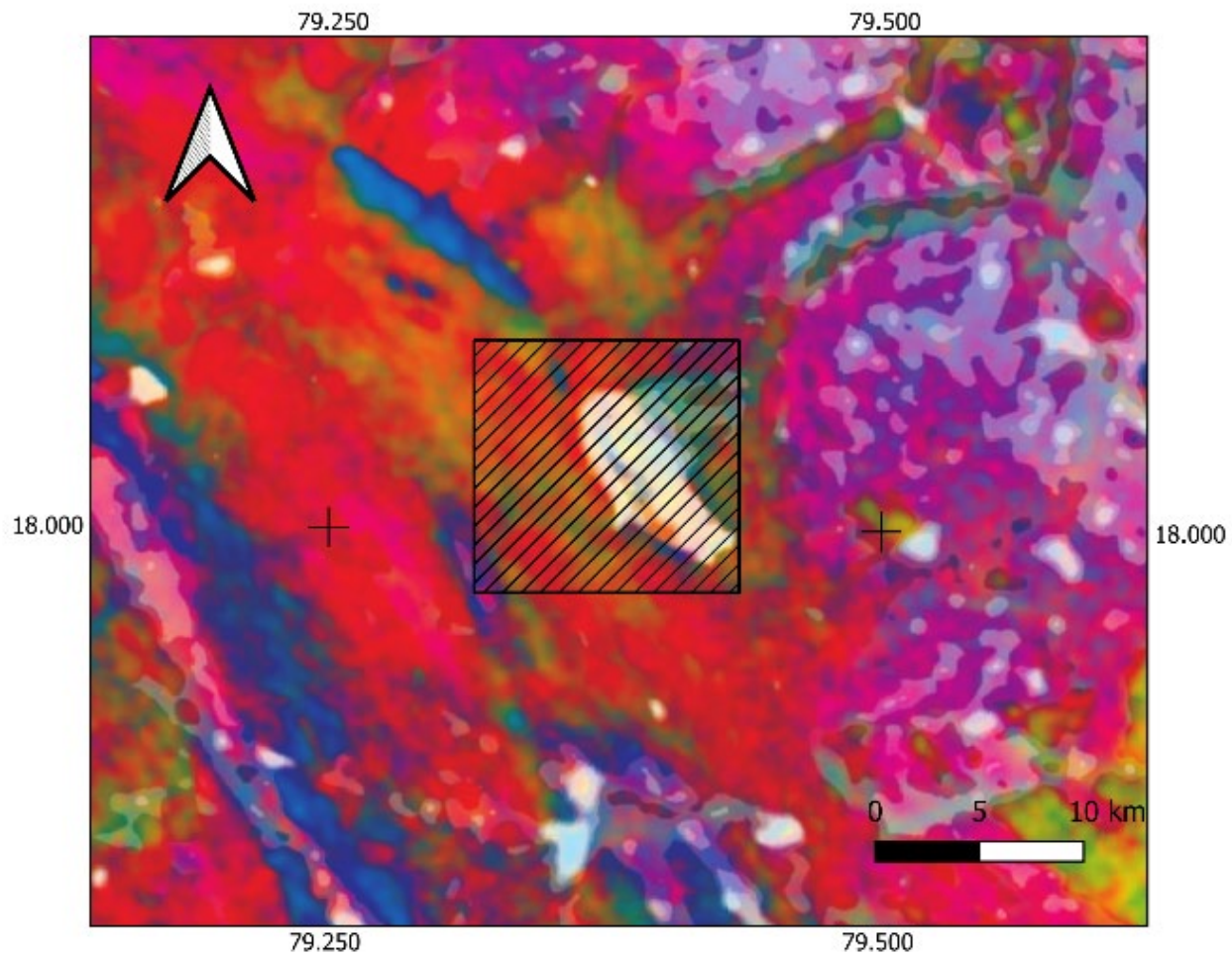


Figure 12.9.17: Low priority Target Area P, an outlier of previously mapped Karimnagar Granulite with very high magnetism and very low gamma-ray character, shown on the radiometric ternary image of the Eastern Dharwar Craton.

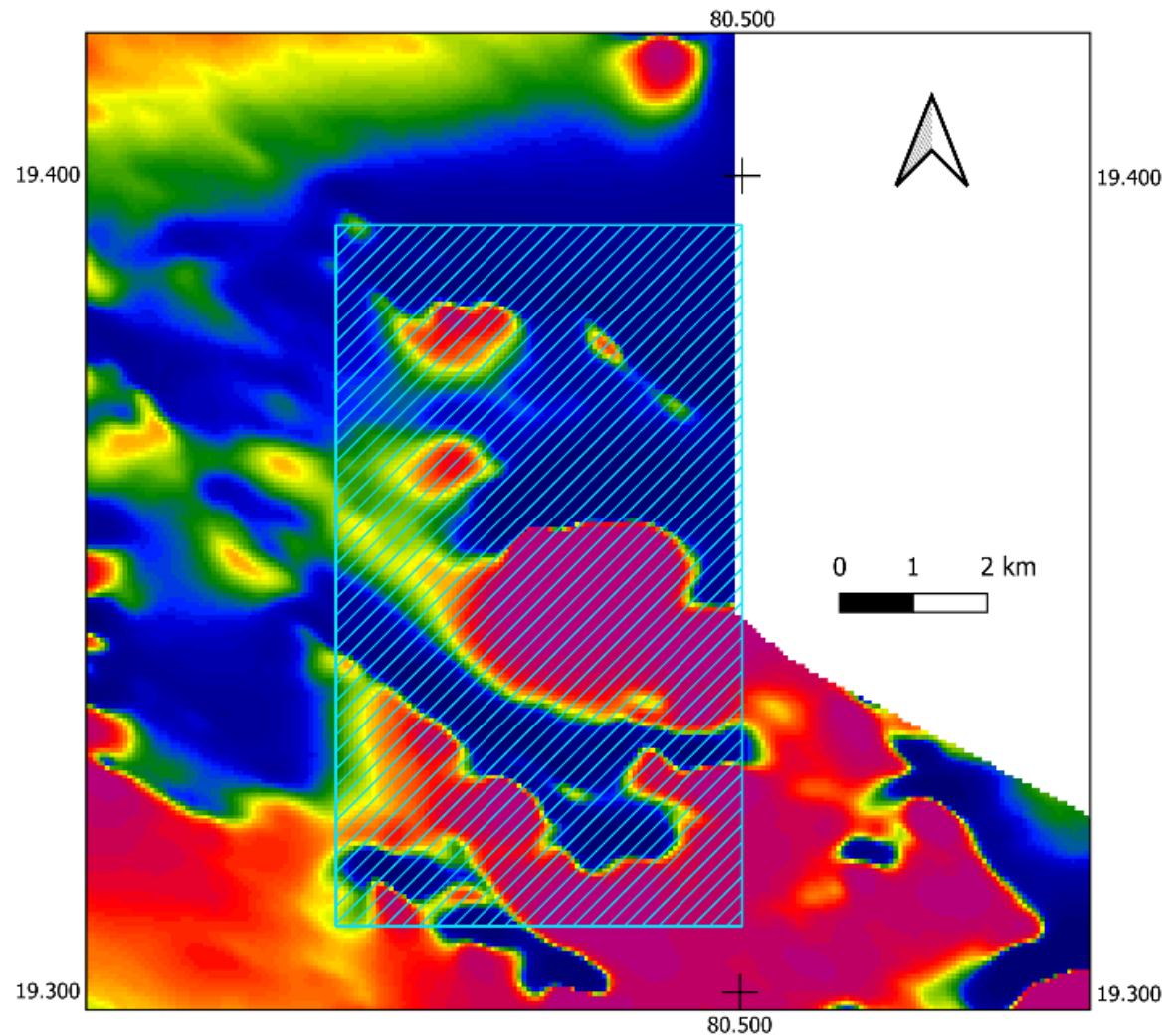


Figure 12.9.18: Low priority Target Area Q, previously mapped Bailadila Formation banded ironstone formation with a strong magnetic anomaly and fold that may act as a structural trap for enrichment, shown on the magnetic anomaly of the Bastar Craton.

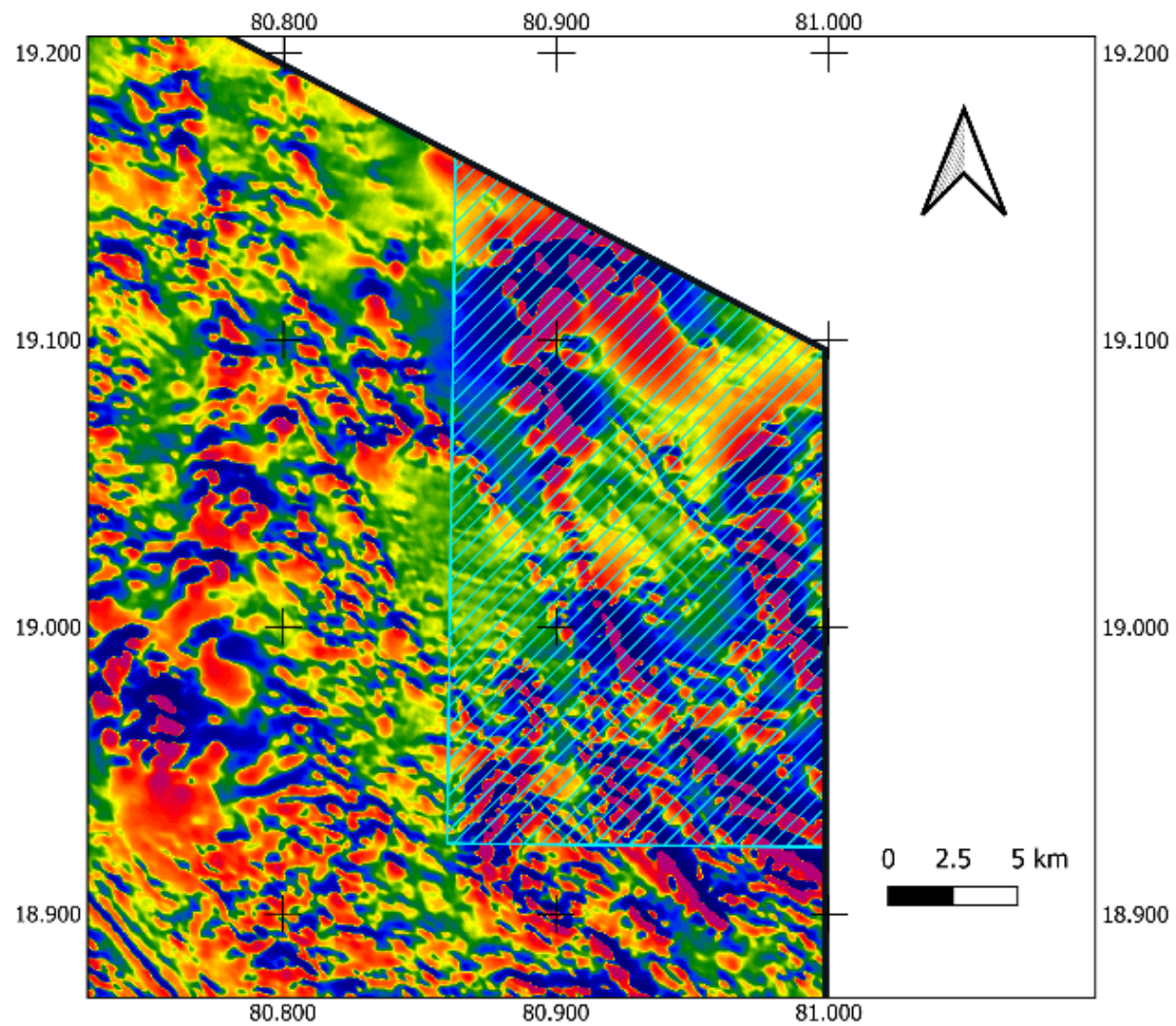


Figure 12.9.19: Low priority Target Area R, previously mapped folded supracrustal rocks, shown on the first vertical derivative of the magnetic anomaly of the Bastar Craton.